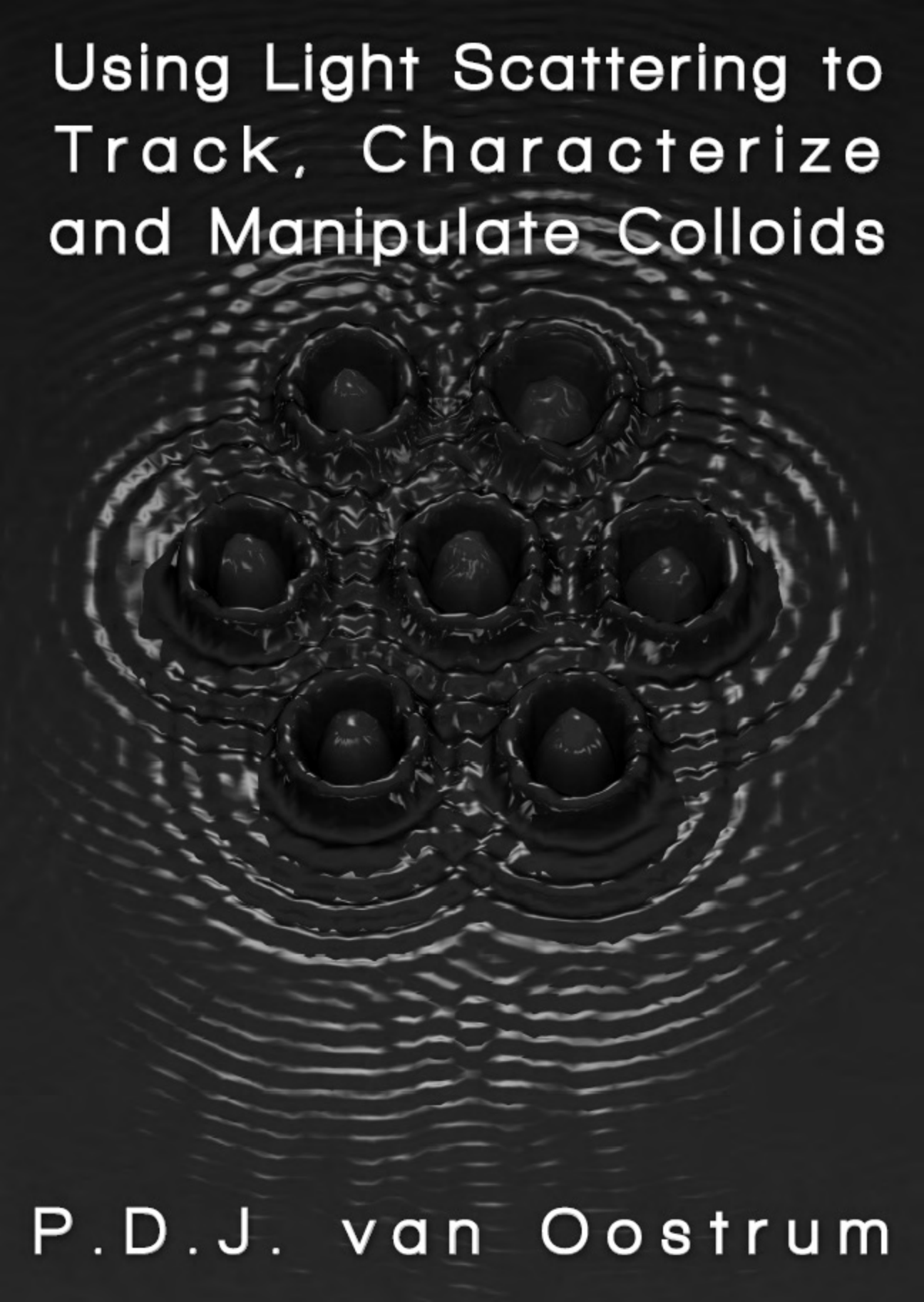


# Using Light Scattering to Track, Characterize and Manipulate Colloids



P.D.J. van Oostrum

Using Light Scattering to  
Track, Characterize  
and Manipulate Colloids

**Cover design:** Timo Rozendal & Peter van Oostrum

ISBN: 978-90-393-55321

A digital (color) version of this thesis is available at <http://www.colloid.nl>

# Using Light Scattering to Track, Characterize and Manipulate Colloids

---

## Licht Verstrooiing aanwenden om Colloïden te Volgen, Karakteriseren en Manipuleren

(met een samenvatting in het Nederlands)

### Proefschrift

ter verkrijging van de graad van doctor aan de Universiteit Utrecht  
op gezag van de rector magnificus, prof.dr. J. C. Stoof, ingevolge het  
besluit van het college voor promoties in het openbaar te verdedigen op

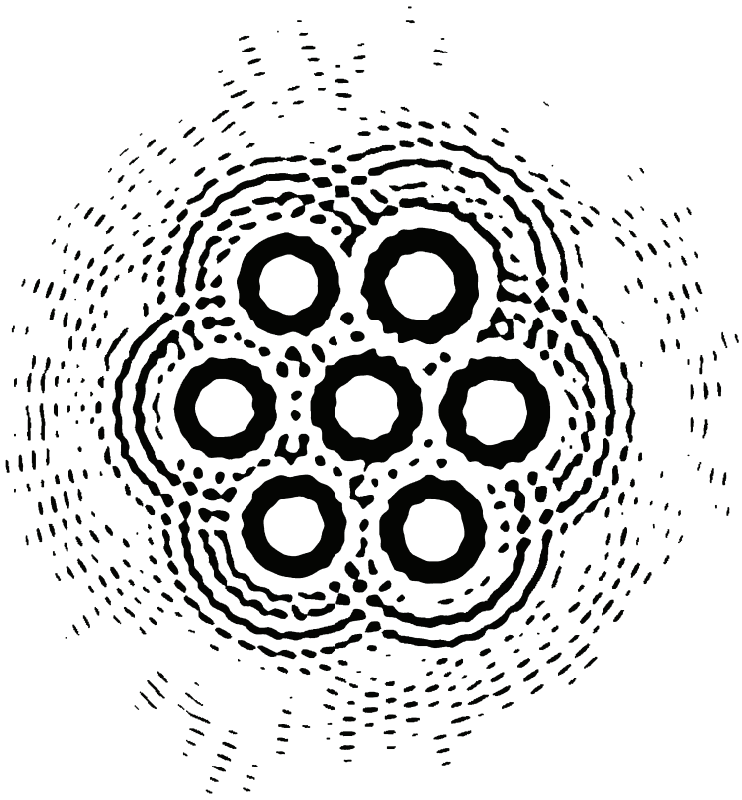
**dinsdag 22 maart 2011 des middags te 2.30 uur**

door

**Petrus Dominicus Joannes van Oostrum**

geboren op 11 oktober 1981 te Utrecht

**Promotor:** Prof.Dr. A. van Blaaderen  
**Co-promotor:** Dr. A. Imhof





# Contents

<b>1</b>	<b>Introduction</b>	<b>1</b>
1.1	Introduction	2
1.2	Colloids	3
1.3	Light Scattering	5
1.4	Track and Characterize	7
1.5	Manipulate	9
1.6	Used techniques and the Tweezers Setup	11
1.6.1	<i>The optical tweezers setup with adaptations for digital holographic microscopy</i>	11
1.6.2	<i>The used Imaging Techniques</i>	16
	Bibliography	17
<b>2</b>	<b>Digital Holographic Microscopy</b>	<b>21</b>
2.1	Holography	22
2.1.1	<i>In-line holograms</i>	23
2.2	Back Propagation	24
2.2.1	<i>An example: 1.4 <math>\mu\text{m}</math> silica in ethanol</i>	27
2.2.2	<i>Back propagated <math>g(\mathbf{r})</math></i>	29
2.2.3	<i>Back propagating a silica rod</i>	36
2.3	Lorenz-Mie-Debye Scattering	39
2.3.1	<i>The formulae</i>	40
2.3.2	<i>Interference between illuminating and scattered light: the hologram</i>	43
2.3.3	<i>An overview of the effect of the particle position, radius and refractive index on the hologram</i>	48
2.4	Inverse problem: Digital Holographic Microscopy	57
2.5	Characterization	60
2.5.1	<i>Characterizing <math>\text{SiO}_2</math> particles in ethanol</i>	60
2.5.2	<i>Characterizing titania particles; tuning the refractive index for trapping experiments</i>	64
2.5.3	<i>Characterizing melamine particles</i>	68
2.5.4	<i>Sedimentation</i>	70
2.5.5	<i>Gravity and Double-Layer Repulsion</i>	74
2.5.6	<i>Silica coated PS spheres</i>	79
2.6	Multiple particles	81
2.6.1	<i>2 particles</i>	82
2.6.2	<i>7 particles</i>	87
2.6.3	<i>Conclusion multiple particles</i>	92

2.6.4	<i>Dumbbell</i>	93
2.6.5	<i>Diffusion of a flexible string</i>	101
2.6.6	<i>Bending a string</i>	107
2.7	Acknowledgements	112
	Bibliography	112
<b>3</b>	<b>Measuring forces</b>	<b>121</b>
3.1	Introduction	122
3.2	Forces from equilibrium displacements in optical traps	123
3.3	Forces from mobility and friction factors	133
3.4	Silica in CHB	139
3.5	Advantages of holographic tracking	142
3.6	A future experiment: electrophoresis	143
3.7	Acknowledgement	147
	Bibliography	147
<b>4</b>	<b>Introduction to optical tweezers</b>	<b>153</b>
4.1	Introduction	154
4.2	Some applications of optical tweezers	155
4.3	How optical tweezers work	156
4.4	Characterizing optical traps	157
4.5	Basic experimental designs	161
4.6	Size regimes	162
4.6.1	<i>The Rayleigh regime</i>	162
4.6.2	<i>The ray optics regime</i>	163
4.6.3	<i>The intermediate or Lorenz-Mie regime</i>	164
4.7	Other relevant effects	166
4.7.1	<i>Spherical Aberration</i>	167
4.7.2	<i>Non-conservative forces</i>	168
4.7.3	<i>Temporal effects</i>	169
4.7.4	<i>Optical binding</i>	170
	Bibliography	170
<b>5</b>	<b>Exploration of trapping Parameters</b>	<b>177</b>
5.1	Introduction to calculations of trapping forces	178
5.2	The model	180
5.3	1.4 $\mu\text{m}$ silica spheres in ethanol	182
5.3.1	<i>Dependence of the trapping stiffness on the laser power</i>	184
5.3.2	<i>Spherical aberration</i>	189
5.3.3	<i>Non-conservative forces</i>	196
5.4	Measurements of setup specific phenomena	200
5.4.1	<i>The influence of the distance between imaging and trapping plane</i>	201
5.4.2	<i>The influence of the blinking nature of time-shared traps</i>	203
5.5	Size matters	207

5.5.1	<i>Force curves</i>	209
5.5.2	<i>Experiment</i>	210
5.5.3	<i>Size and Refractive index</i>	214
5.5.4	<i>Force curves; overview</i>	218
5.6	Trapping core-shell particles	221
5.6.1	$n_{\text{core}} > n_{\text{shell}} > n_{\text{medium}}$	223
5.6.2	$n_{\text{core}} > n_{\text{shell}} < n_{\text{medium}}, n_{\text{core}} > n_{\text{medium}}$	231
5.6.3	$n_{\text{core}} > n_{\text{shell}} < n_{\text{medium}}, n_{\text{core}} = n_{\text{medium}}$	239
5.6.4	$n_{\text{core}} < n_{\text{shell}} < n_{\text{medium}}$	242
5.6.5	$n_{\text{core}} < n_{\text{shell}} > n_{\text{medium}}$	242
5.7	Acknowledgements	246
	Bibliography	246
<b>6</b>	<b>Multiple traps together</b>	<b>253</b>
6.1	Introduction	254
6.2	Counter-propagating tweezers to trap high index materials	254
6.3	Trapping particles with an index of refraction below that of the immersion medium	266
6.4	line-traps	267
6.4.1	<i>line-traps: experiment</i>	273
6.4.2	<i>line-traps: lines of many traps</i>	276
6.5	Line traps to increase the trapping stiffness; Double Traps	278
6.5.1	<i>Double traps: experiment</i>	282
6.5.2	<i>More calculations on double traps</i>	284
6.6	Acknowledgements	289
	Bibliography	289
	<b>Summary</b>	<b>295</b>
	<b>Samenvatting in het Nederlands</b>	<b>302</b>
	<b>Samenvatting voor Leken</b>	<b>309</b>
	<b>Acknowledgements</b>	<b>310</b>
	<b>List of Publications</b>	<b>313</b>



# 1

## Introduction

---

Colloidal particles are widely used in industry and daily life. There are many interesting applications in which colloids play a crucial role. Also from a scientific perspective they are very interesting because of the bridge they form between atomic and molecular materials and objects of more human scales. Due to their size, which is comparable to the wavelength of visible light, it is possible to track colloids in real space using light microscopy techniques. On the other hand they are small enough to be considered a thermal system which means that in certain respects they show a phase behavior similar to that of atomic or molecular materials. The fact that colloids are comparable in size to the wavelength of light makes their interaction with light a very rich phenomenon. This thesis is dedicated to the application of light scattering in soft matter research. In this introductory Chapter we first introduce the terms in the title. We refer to various Chapters and sections where the topics are discussed in more detail. Then we proceed with a short introduction of the setup used in our experiments. We conclude the Chapter with an introduction of the imaging techniques used in this thesis.

## 1.1 Introduction

The title of this thesis, *Using Light Scattering to Track, Characterize and Manipulate Colloids* contains a few words that may need introduction. Although this is not the first word in the title, we start by introducing *Colloids* to the reader. The word colloid comes from the Greek word  $\chiόλλα$  for ‘glue’. It refers to the ‘sticky’ nature of colloidal dispersions. A colloidal dispersion is a dispersion of bits of some substance dispersed in another substance that perform Brownian motion under the influence of the thermal motion of the solvent. Typically, the size of colloids is taken to range from a few nm to several  $\mu\text{m}$ . Examples are silica beads in ethanol, gas bubbles in a liquid, but also oil droplets in water or vice versa. There are many industrial applications and daily life examples of colloids. One can think of paint, glue, ink, blood, toothpaste (solids in a liquid), fog, mist, clouds, smoke (solid/liquid particles in a gas), milk, mayonnaise (droplets in a solvent) and whipped cream (gas bubbles and droplets in a liquid). There are many examples of colloidal dispersions that can also be classified by the aggregation state of the medium in which the colloids are dispersed [1]. In this thesis most dispersions are solid particles dispersed in a liquid. In section 1.2 we introduce colloids in more detail.

The colloids that we look at in this thesis are studied mainly by looking at the *Light Scattering* that takes place at their interface. When the refractive index of the particles is different from that of the suspending medium, light shone on the interface is reflected and refracted. By studying the scattered light, it is possible to *Track* colloidal particles, i.e. determine their position. Since colloids are comparable in size to the wavelength of visible light, the interaction between the light and the particle depends strongly on the characteristics of a particle. This can be used to *Characterize* colloidal particles. The particles in a colloidal crystal are comparable in size to the wavelength of visible light, and so is the lattice parameter in colloidal crystals. As a consequence of the periodic refractive index variations in colloidal crystals, this gives rise to wavelength and direction dependent reflections that result in striking colors. Because of the strong and characteristic interactions between colloidal crystals and visible light [2], these structures can be used in electro-optical devices [3–5] and sensors [6]. Colloids need not be spherical. An example of non-spherical particles is formed by rod-like particles with hard interactions that form isotropic, nematic and smectic phases [7, 8], in analogy to the phases found in for instance the anisotropic molecules in liquid crystals. In section 1.3 we introduce light scattering in more detail.

The propagation direction of light changes in the process of scattering by a particle. Light carries momentum and thus the scattering process also changes the momentum of the light. Because of conservation of momentum, the momentum change of the light is accompanied by the opposite momentum change of the particle. The light thus exerts a force on the particle. It is possible to *Manipulate* colloids using light scattering by trapping them in an *Optical Tweezer* and move

them around. In section 1.5 we discuss optical tweezers in more detail. We introduce the setup on which all the experiments in this thesis are conducted in section 1.6.1 and point the attention of the reader to the relevant sections in the rest of the thesis.

## 1.2 Colloids

Using a light microscope, Robert Brown observed in 1827 that small pollen grains in water moved erratically without any preferential direction [9]. He could see these pollen due to their scattering behavior. The pollen grains have an index of refraction that differs from that of the water in which they are dispersed and as a result Robert Brown could follow them with his microscope [10]. In section 1.3 and in the Chapters to follow, we will discuss the scattering behavior of small particles in detail. The observed motion, which is now called *Brownian motion*, was explained by William Sutherland and Albert Einstein in 1905 in terms of statistical fluctuations [11, 12]. Thermal motion of the solvent molecules causes them to collide with the pollen grain, causing an effective pressure. The time average of this pressure is the same all around the grain but it fluctuates in time causing a random instantaneous net force. As a result, the object is moved around. The surface area of objects and thus the number of collisions generally increases with the radius of an object squared while many other forces, such as for instance gravity, increase with the radius cubed. This results in the fact that Brownian forces tend to be more important for smaller objects. Depending on the size of a particle and the strength of other forces, Brownian forces can either be dominant or negligible. For the movement of an oil tanker thermal fluctuations are of negligible relevance to its course while the oil droplets in milk diffuse over distances comparable to their radius in seconds. When Brownian motion dominates for an object that is significantly larger than the solvent molecules, it is justified to call an object a colloid.

In theoretical descriptions, colloids are often described as interacting while dispersed in a background with average properties. The individual solvent molecules are often not considered. The colloids are said to interact via a potential of mean force in which the effects of the solvent are taken into account. Onsager showed that colloidal dispersions are thermodynamically equivalent to atomic and molecular systems [13]. This means that colloidal dispersions are governed by the Boltzmann distribution; the probability of finding certain configurations is related to the exponent of the energy involved in that configuration. Due to the Brownian motion, colloidal particles explore microscopic configurations, the distribution of which is dictated by the Boltzmann distribution.

A famous example of a Boltzmann distribution is the barometric distribution of colloids, where the entropy competes with gravity. Jean Perrin counted the number of colloids he could observe in a barometric height distribution using a light microscope to measure the value of Boltzmann's constant [14]. This work

is one of the first examples where colloids are used for statistical mechanics experiments that are only possible because they are both small enough to perform Brownian motion and be in thermal equilibrium while they are large enough to be visualized using non-invasive light microscopy techniques in real space.

Not only are colloids subject to external fields such as gravity or electric fields, they also interact with each other. The simplest interaction that is present in almost all colloidal systems are the *excluded volume interactions* or *hard sphere interactions*. Two colloids cannot be simultaneously on the same point in space, similar to our daily life experience with hard objects, e.g. billiard balls do not interpenetrate. The hard sphere interaction between colloids causes them to not exert any force upon each other unless they are touching. The probability of collisions between the colloids increases with the volume fraction, the fraction of the volume of a dispersion which is occupied by particles. Because isolated thermodynamic systems maximize the entropy, or minimize the free energy, suspensions of hard spheres tend to order; they crystallize when the volume fraction increases [15–17]. In an ordered array, the particles have effectively more space to move around, the entropy is larger. Colloidal dispersions can thus, by changing the parameters, such as the volume fraction in this case, undergo phase transitions. When the volume fraction increases slowly enough for the system to find the crystalline minimum in the free energy landscape, a crystal is formed. When the compression is done too fast the particles that cannot interpenetrate may get stuck in a less optimal configuration that is referred to as a glass [18]. Colloidal crystals are for instance found in nature as so-called opals [19].

Apart from the intuitive hard sphere repulsion, colloids also interact via so-called *van der Waals attractions* [20]. These attractions are the result of attractions between permanent, induced and spontaneous electric dipoles in the colloids. The result is that colloids surrounded by some other material attract each other over short distances. The van der Waals attraction forms a very deep minimum from which the particles rarely escape by thermal fluctuations and as a result colloidal dispersions tend to coagulate [21]. Often, the van der Waals attractions can be reduced by refractive index matching of the colloids in their solvent. This does not generally exclude all van der Waals attractions because in most cases the index matching holds only for a limited range of the electro-magnetic spectrum. Another common strategy to prevent colloidal dispersions from coagulation is *steric stabilization*. Here the colloidal surface is grafted with polymers that prevent the particles from getting too close to each other. Also charge stabilization can effectively exclude the coagulation of a colloidal dispersion by preventing that the particles approach each other sufficiently close to experience the van der Waals attraction.

Colloids that are suspended in a sufficiently polar solvent acquire an electric charge by means of dissociation of surface groups or preferential adsorption of ions from the solvent. The charged colloids attract counter ions, which also attract ions of the same sign as the colloid, and all these ions form a diffuse double layer

around the particle. Again, the distribution of the ions around a charged colloid is the result of an equilibrium between two forces, electrostatic attraction and diffusion in this case, and is described by the Boltzmann distribution. Colloids with a surface charge of the same sign repel each other. The ions in the double layer screen the electrostatic charge on the particles and the range of the electrostatic interactions can be tuned by varying the ion concentration in the solvent [22, 23]. The Debye screening length is a measure of the range of the electrostatic interactions. Like charges repel and electrostatics thus play an important role in stabilizing colloidal dispersions against coagulation by the van der Waals attractions. The classical Derjaguin-Landau-Verwey-Overbeek theory, DLVO, describes the interaction between stable pairs of charged colloidal particles suspended in a dielectric medium as a sum of a screened repulsive electrostatic contribution and the generally shorter ranged attractive van der Waals attraction [22, 24]. In Chapter 3 we measure the charge repulsion between pairs of colloids in different solvents.

The repulsive interactions between charged colloids can be tuned in range from almost hard sphere interactions to several diameters by choosing the right solvent and by controlling the ion concentration [25]. Long-ranged systems show correlations between particles already at very low volume fractions. We study the order in a very dilute dispersion of charged colloids that interact over great distances by means of the radial distribution function in section 2.2.2.

### 1.3 Light Scattering

Light consists of electromagnetic waves that propagate through space or transparent media. In an alternative description, light consists of elementary, massless particles: photons. When light irradiates an object, several processes can occur. First of all it is possible that the object is transparent and that the light traverses the object without any changes. In that case the light is *transmitted*.

The refractive index  $n$  is defined as the ratio between the speed of light in vacuum and the speed of light in a material. The frequency of the electromagnetic waves remains unaltered such that the wavelength of light depends on the speed of light and thus on the refractive index  $n$  of the material in which the wave propagates. When light, in the form of plane waves, hits an interface between two materials with different refractive indices, basically two things can happen. The light can be transmitted or *reflected* at the interface between the two materials. When the interface is flat on the scale of the wavelength, the direction of the reflected light is mirrored around the normal direction of the interface. If the light is transmitted it will also change its propagation direction. This is called *refraction*. The direction into which the transmitted light propagates depends on the angle of the original direction of propagation with the normal of the interface and the ratio between the refractive indices of the two materials. The direction of the refracted light is described by Snell's law [26].

In general, a fraction of the light is reflected and a fraction of the light is

transmitted. The fraction of the transmitted and reflected light, or the probability that a photon is either transmitted or reflected, is described by Fresnel's law [26]. The electromagnetic waves of light are often transverse waves that propagate in the direction perpendicular to both the excitations of the electric field and to the direction of the magnetic excitations of the field, the two contributions to light that are also mutually perpendicular themselves. When the electric field is only non-zero in one direction, the light is said to be linearly *polarized*. The transmission and the reflection at an interface also depend on the angle between the polarization direction and the interface between the two materials. When there are excitations of the electromagnetic field in two directions, these two waves need not be in phase. When the two perpendicular components are of the same power and have a phase difference of 90 degrees, the orientation vector of the electric field rotates about the propagation direction of the light. The light is then said to be circularly polarized. Depending on the phase difference and the relative strength of the two contributions, the light can be lefthanded circularly polarized, righthanded circularly polarized or left- and righthanded elliptically polarized.

When a plane wave is focussed by a lens, that uses the change in propagation direction by refraction at curved surfaces, an extra axis that is relevant to the light propagation needs to be considered. This axis is referred to as the *optical axis*. The light is no longer a single plane wave, but can be described as the sum of many different plane-waves that all propagate in slightly different directions. When the electromagnetic waves in a focus of a lens are all oriented in the radial direction with respect to the optical axis, one speaks of radially polarized light. When all the waves are polarized perpendicular to the radial direction with respect to the optical axis, one speaks of azimuthally polarized light.

Apart from being transmitted or reflected at the interface between two materials, the light that propagates in a material can be *absorbed*. The energy that is associated with the light is then transformed to another form of energy. Usually, this other form of energy is heat. The amount of absorption in a material is quantified by the complex part of the refractive index. In this thesis we assume, unless stated otherwise, that absorption is of negligible importance for the phenomena under investigation.

When the object with which the light interacts is not flat on the scale of the wavelength of the light, the interaction is more complicated. The reflection of light from the object is no longer uniform. An example is the diffuse reflection of the coating of some photographs and common objects that are not shiny such as paper and walls. This phenomenon of diffuse reflections is called *scattering*, although in principle any change in propagation direction of radiation, also that by a mirror, is called scattering. Very many objects show diffuse reflections because their structure is not smooth on the length scale of visible light  $\sim 1 \mu\text{m}$ . Most objects in daily life are visible because they reflect light in a diffuse way such that the observer is not restricted to seeing objects at which their sightlines

make particular angles with respect to the local light source. Often only part of the *spectrum* is reflected, the rest is absorbed, such that the object is observed to have a color. Some materials do not (only) have a surface roughness but also an internal structure with many variations on the scale of the wavelength of visible light. One can think of for instance wood or cheese, or this paper if you are reading this thesis from (e-)paper. Also colloidal dispersions have many variations of the refractive index on the scale of the wavelength of the light. Milk, for instance, contains many colloidal fat droplets and protein blobs that scatter the light in many directions. As the absorption of both the water and the oil in the milk is very low and not particularly wavelength dependent, milk is observed to be a white liquid.

The reflection of light by objects that as a whole are comparable to the wavelength of the light is more complicated than the reflection by larger objects. As the object is comparable in size to the wavelength of the light, the interface at the other side of the object plays a crucial role in the reflection. A phenomenon that is also present in the case of reflection at an interface that is smooth at the length scale of the light waves is that of *evanescent waves*. Evanescent waves are non-propagating waves that decay exponentially in intensity with increasing distance to the interface from which light was reflected [26]. When the object at the surface of which light is reflected is comparable in size to the wavelength of the light, the other interface of the object will disturb the evanescent wave, scattering part of the energy away in other directions. Light waves, scattered by both interfaces might coincide on the same spot. The amplitude of the local electromagnetic field can simply be added, the intensity of the light in such a point in space is then the complex square of the local amplitude. This phenomenon is called *interference*. Although the superposition of any two waves is interference, one generally speaks of interference only when the two waves are of the same wavelength and have a constant phase difference. When the latter is the case these two waves are *coherent*. For spherical particles, the scattering of light has been described quantitatively by solving Maxwell's equations with appropriate boundary conditions [10]. Gustav Mie in 1908 [27] and Ludvig Lorenz [28, 29] in 1890 published their solutions independently and the scattering of light by spherical particles of about the wavelength of light is generally known as *Mie- or Lorenz-Mie-scattering*. In section 2.3 we will discuss the scattering by spherical particles, colloids in the size range of the waves of visible light in more detail.

## 1.4 Track and Characterize

The scattering of light by colloids depends strongly its the shape, size and refractive index distribution. Often, colloids in practice are spherical. As stated above, the scattering of light by such particles has been analytically solved. In Static Light Scattering (SLS) experiments, a dilute suspension of colloids is illuminated from one direction, usually by a laser beam, and a detector is rotated around the sam-

ple [10, 30]. Afterwards the angular dependence of the scattering can be approximated by varying the parameters of the particles in a numerical implementation of the Lorenz-Mie theory. As the angular dependent scattering by the particles is measured on a dispersion, the measured scattering is the sum of the scattering by all the particles in a certain volume. When the particles are not monodisperse or when the volume fraction of the dispersion is so high that a significant fraction of the light is scattered more than once, the measured scattering is not exactly described by the Lorenz-Mie theory for the scattering by single particles. In Chapter 2, in section 2.4, we discuss how we numerically solve the inverse problem posed by the recorded interference pattern between the light that was scattered by a single particle and the light that was not scattered at all and the Lorenz-Mie theory to *track* and *characterize* individual particles. This is a method to analyze Digital Holographic Microscopy, DHM images as published in reference [31].

Interference patterns that result from interference between light that was scattered by some object and coherent light that was not scattered at all, are generally called *holograms*. The interference pattern of light scattered by a microscopic object can be magnified using a microscope objective such that it can be conveniently recorded on a CCD camera. This is then called Digital Holographic Microscopy, DHM [32]. When the angle between the scattered light and the un-scattered light is zero we speak of *in-line holography*. In Chapter 2 we introduce two different methods to analyze in-line digital holographic micrographs.

Using the known phenomenon of interference it is possible to calculate what the intensity distribution throughout the sample looked like, using only the information in a single plane in the sample that has been recorded using a microscope and a CCD camera. This is called *back propagation*. In section 2.2 we discuss back propagation in detail. We show that it is possible to track single colloids in a dilute dispersion in 3D from 2D holographic snapshots. The coordinates of the particles are used to calculate the *radial distribution function* which is used to study the phase behavior of colloidal dispersions of a very dilute dispersion. Similarly, we present an experiment in which the three dimensional position and orientation of a silica rod is measured from a single 2D image.

Subsequently, in section 2.3, we discuss the scattering by small spherical colloids in more detail. The quantitative model for the scattering of light by such particles is then fit to experimental holograms. In section 2.4 and 2.5 we show that it is possible to fit Lorenz-Mie theory to experimental holograms to measure the radius and refractive index of individual colloids. An example of how such characterization can be useful in the process of synthesizing new colloidal systems is published in reference [33] where we apply the method to characterize the effect of several drying and sintering steps on the composition of titania particles. Similarly we studied the composition of melamine particles.

From the subsequent positions at which particles are found in 3D, it is possible to measure the Brownian motion and thus the hydrodynamic radius and weight of colloidal particles. Careful analysis of the diffusion allows one to check the error

estimates from the fitting algorithm used to determine the position of the particle from holographic snapshots. From the probability distribution of distances from the bottom of a sample cell of a single particle, it is possible to determine the interaction potential of the particle with the sample wall by application of the Boltzmann distribution discussed above. We proceed by showing that the positions and characteristics of multiple particles can, under certain conditions be determined from the same hologram in section 2.6. This is of great importance for the possibility to use holographic microscopy to measure inter-particle interactions as we present in Chapter 3.

Colloidal particles can be made to align in strings by inducing electric dipoles using alternating electric fields. Adjacent particles can be made to stick to each other by means of a simple thermal annealing step [25, 34] or by pushing the particles into the van der Waals minimum by optical tweezers. When the permanent connections between the particles in a string still allow bending by thermal fluctuations the string of particles can be used as a model system for (bio-)polymers and proteins. In sections 2.6.4, 2.6.5 and 2.6.6 we show that even in a string it is possible to track individual colloids that together form a string. We study the diffusion and bending of such strings in more detail.

## 1.5 Manipulate

The same scattering phenomenon that we use to track and characterize colloidal particles, can also be used to *manipulate* these particles. When the light is scattered by the particles, the direction of propagation of this light is changed. Consequently also the momentum that is associated with the light is altered. According to the conservation of momentum, a scattering particle is subject to a rate of momentum change, a force. These optical forces are negligible for human scale objects and even for colloids, these forces are negligible when they are illuminated these forces can generally be neglected. When, however, the light is concentrated in a (diffraction limited) focus of a microscope objective, these forces can become comparable to Brownian forces. Arthur Ashkin reported the first experiments in a lab in which optical forces were playing an important role [35, 36]. He observed that particles were pulled towards the optical axis of a mildly focussed laser beam and were then propelled along the optical axis. By carefully balancing the forces exerted by the laser light and by gravity, he managed to levitate particles in water [35]. He also managed to create a stable three dimensional trap based on counter propagating beams [36]. He coined the term *optical tweezers* in 1986, in an article in which the first single beam optical trap was demonstrated by using a high numerical aperture (NA) objective to focus the light [37].

All particles that scatter part of the light that they are irradiated with experience a force in the direction propagation of the illuminating light beam. This force is called the *scattering force*. Since the scattering by most spherical particles is cylindrically symmetric, the forces associated with the scattering away of the

light in various directions is canceled. When however, a colloid is not homogeneously illuminated, it will scatter more light in one direction than in another. The associated momentum change of the scattered light causes a net force in a direction perpendicular to the propagation direction of the illuminating light. This force is called the *gradient force*. Depending on the sign of the refractive index difference between the particle and the suspending medium, the gradient force can be directed either along or against the intensity gradient on the particle. In Chapter 4 we discuss the literature on optical tweezers in more detail.

Using optical tweezers it is possible to exert forces on colloidal particles and to confine them to a particular point in space. To a first approximation, the deviation of a particle from its equilibrium position in an optical trap is linear with the sum of all other forces on the particle. In other words, the optical trap acts as a hookian spring. It is possible to trap multiple particles with the time-averaged trapping potential of time-shared optical traps [38] as we also demonstrated in reference [39]. In section 5.6.2 and in reference [40] we demonstrate that arrays of time-shared traps trapping some high index tracer particles in a sample with many index matched host particles can be used to study nucleation. In Chapter 3 we present experiments in which the interaction force between charged colloids is measured by looking at the deviation of a colloid in a time-shared optical trap as a function of the distance to another particle in a similar optical trap. This work has also been published in reference [41].

Optical tweezers can also be used to bring colloids in predefined configurations, after which they can be switched off to study their trajectories under influence of Brownian motion, inter-particle forces, and forces exerted by external fields [42, 43]. In Chapter 3 of this thesis we present experiments in which electrostatic inter-particle forces are measured, as well as the force of gravity and the force on charged particles, exerted by an applied electric field.

The exact force field exerted by the light close to the focus of a laser beam depends on many parameters. To begin with, the exact shape of the focus depends on the microscope objective, the degree of overfilling, the wavelength of the laser used and the amount of spherical aberration which in turn depends on the refractive index contrast between the glass of the sample cell and that of the suspending medium as well as on the distance to the wall. Obviously also the size of the particle and the refractive index contrast between the particle and the suspending medium have a strong influence on the force field that the particle experiences in the vicinity of the focus. In Chapter 5 we present calculations based on the model by Viana *et al.* from the group of Nussensveig [44]. Using calculations and experiments we explored the possibilities offered by the time-shared tweezers that we have in the laboratory [45]. In the calculations we varied the particle composition over a broad range of values and found a few interesting phenomena that lead for instance to a new concept to trap particles with a negative refractive index contrast. Moreover, we present calculations on the trapping behavior of core-shell particles.

As mentioned before, it is possible to create multiple effective traps by means of time-sharing. The spatial extension of the force field exerted by optical tweezers in combination with multiple traps offers interesting possibilities. In chapter 6 we present calculations and experiments that demonstrate that, using counter propagating tweezers, it is possible to trap particles with an index of refraction that is too high to be otherwise trapped. This work has also been presented in reference [46]. Moreover, we explore the possibility to trap particles with an index of refraction that is lower than that of the surrounding solvent. Multiple traps in a linear array might be used as line-traps to measure the interaction potential between two particles [47]. We show in the same Chapter both with calculations and with experiments that this is in practice difficult to realize with arrays of point traps. This has also been published in reference [39]. In the course of the research we found that under given circumstances, it is possible to trap single particles in an array of point traps such that the stiffness of the array of traps is significantly higher than the stiffness of a single trap with the same total laser power. Simultaneously, the force-extension curves of such arrays or point traps are more linear than those of conventional traps. This makes these arrays of traps ideal for measuring the for the colloidal community relatively large forces that play key roles in biological systems with minimal laser power, minimizing photo-damage.

## 1.6 Used techniques and the Tweezers Setup

In this thesis we use several techniques to manipulate and track our colloids. We start with a brief introduction of our optical tweezers setup and the adjustments we made to it to facilitate Holographic Microscopy. We conclude this introduction with a short discussion of the various imaging techniques used in this theses.

### 1.6.1 *The optical tweezers setup with adaptations for digital holographic microscopy*

The basis of our setup is described in reference [45]. The setup is schematically depicted in Figure 1.1. For the trapping we use a diode-pumped Nd:YVO<sub>4</sub> laser (Spectra Physics, Millennia IR, 10 W cw) with a wavelength of 1064 nm and a TEM<sub>00</sub> mode profile. This wavelength was chosen because it is well separated from the emission and excitation wavelengths that are used in confocal microscopy. An other convenient property of this near-infrared wavelength is that it has a relatively small absorption in biological samples. The laser beam is expanded 6× using a beam expander (EXP, Newport). Consequently, the laser power is attenuated using a polarizing beam splitter cube BS1 (Newport) and half-lambda zero order wave plate W1 (Newport) that rotates the vertically polarized laser light.

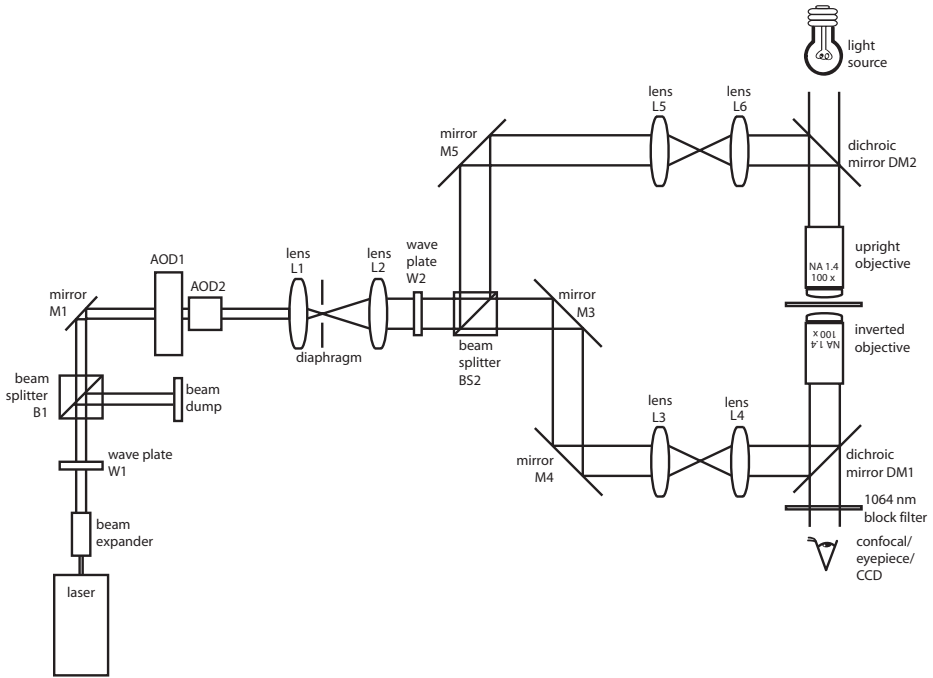


**Figure 1.1:** Schematic diagram of the tweezers setup. AODs were used to steer the trapping laser. Wave-plate W2 can be used to adjust the polarization of the laser beam to control the fraction of laser light that is transmitted and reflected by the polarizing beam splitter BS2. This allows one to switch between inverted, upright and counter-propagating trapping.

The vertically polarized fraction of the laser beam is subsequently coupled into a pair of orthogonal Acousto Optical Deflectors, AODs (IntraAction Corp., DTD-276HB6,  $6 \times 6 \text{ mm}^2$  aperture). Sound transducers excite waves of around 25 MHz in the  $\text{TeO}_2$  crystals. The periodic compressions and rarefactions associated with the wave train that travels through the crystal cause periodic variations in the refractive index of the crystal. Because of the long path-length of the light through the crystal, the AODs are operated as a Bragg device. As a result the crystal acts as a diffraction grating and the laser beam is diffracted in different horizontal and vertical directions by the first and second AOD respectively. By careful alignment of the orientation of the AODs it is possible to diffract up to 90% of the laser power to the first order diffraction peak. The wavelength of the sound is the spacing of the grating, so by changing the frequency, the direction in which the first order diffraction propagates can be changed. The two AODs are positioned around a plane conjugate to the back aperture of the objective such that a change in angle corresponds to a change in position of the focussed laser beam in the sample plane. The propagation speed of the sound and the width of the laser beam in the

crystal make that it is possible to change the position of the trap in about  $5.44 \mu\text{s}$ . By switching back and forth it is possible to trap multiple particles simultaneously, provided that the period during which a trapped particle is not illuminated is short enough for the particle not to diffuse away in the mean time. This is called time-shared trapping [38, 39]. In section 4.7.3 we discuss the phenomena associated with the blinking nature of time-shared traps that provoked a vivid discussion in the literature in more detail. In section 5.4.2 we present experiments in which we studied the effect of the blinking rate of a trap in more detail. The two AODs are both fitted on a four-axis kinematic stage (New Focus, 9071-M) at a mutual distance of 32 mm to allow optimal alignment. Because the diffraction pattern of both perpendicular AODs contains multiple peaks, the beam is diffracted in to a square array of beams. The (1,1)-order diffraction beam is selected for trapping by the diaphragm. In practice, careful alignment results in about 60% of the laser power that was diffracted into this order.

The signal to the AODs is generated by Direct Digital Synthesizers (DDS, Novatech Instruments Inc., DDS8m 100Mhz) and an amplifier (IntraAction Corp.), which allows for fast and accurate control of the positions, the rates at which is switched between the traps and the relative stiffnesses. The synthesizer board is controlled by a LabVIEW (National Instruments) program. To create two and three traps that were present simultaneously, we also used a synthesizer board (IntraAction Corp.) to create more signals that were then mixed and presented together to the amplifier.

The telescope formed by lens L1 ( $f = 250 \text{ mm}$ ) and L2 ( $f = 120 \text{ mm}$ ) expands the beam further such that the beam is expanded approximately 12 times to a width of  $2\omega_0 = 5.6 \text{ mm}$ . This is slightly overfilling the back aperture of a  $100 \times$  objective. All lenses are Melles Griot Achromatic Doublets, while the mirrors and the polarizing beam-splitters were obtained from Newport. All components have an antireflection coating for  $1064 \text{ nm}$ .

By rotating wave plate W2 (Newport) the orientation of the linear polarization can be changed. In this manner it is possible to select the fraction of laser power that is reflected into the upper (upright) beam path and transmitted into the lower (inverted) beam path. When both beam paths receive a comparable amount of laser light it is possible to trap particles at different planes in the axial direction.

When a focus of the upright objective and one from the inverted objective are overlaid they form a counter propagating trap. In section 6.2 we perform calculations and present experiments that demonstrate that by using counter propagating tweezers it is possible to trap titania particles that cannot be trapped in a single beam trap. The advantage of the counter propagating trapping of high index particles that cannot otherwise be trapped is that the stiffness by which such particles can be trapped is significantly higher as we demonstrated in reference [46].

When all the light is sent to the upper, upright objective the lower objective, the one used for imaging, can be moved independently from the trapped particles.

This was used to study the influence of trapped arrays of particles on the phase behavior of index matched bulk particles as presented in section 5.6.2 and in reference [40].

Finally, when sending all the light to the lower, inverted objective, many particles can still be trapped and because the upright objective is not needed for the trapping the illumination can be optimized for bright-field or holographic microscopy.

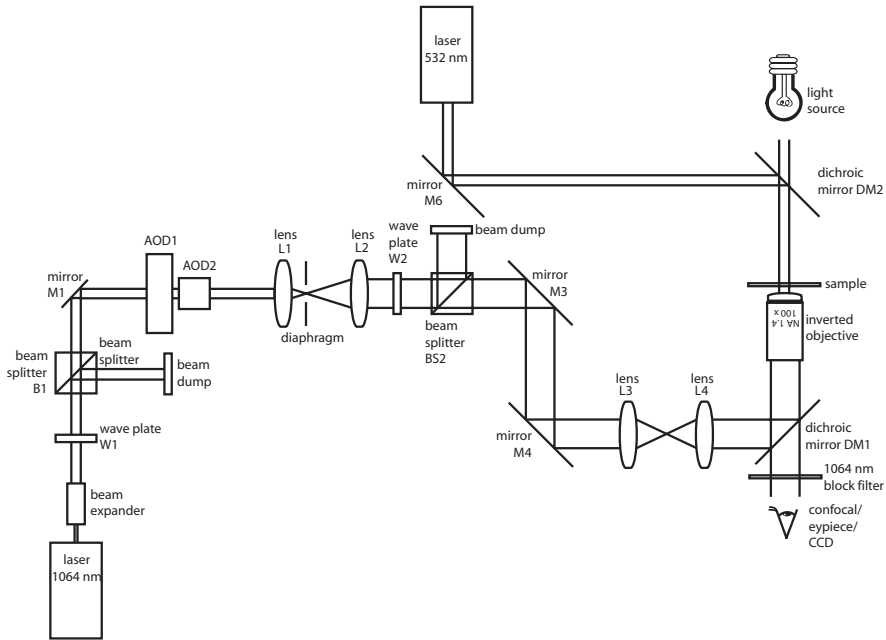


**Figure 1.2:** Schematic diagram of the tweezers setup in holography mode. When the setup is used in microscopy mode, flipping mirror M6 is flipped into the upper beam-path, coupling in the 532 nm laser beam for holographic illumination. The telescope lenses L5 and L6 and the upright objective are removed.

The fraction of the laser light that is transmitted by the beam splitter BS2 is guided by the mirrors M3 and M4 into the lower beam path. The light passes through the 1:1-telescope lenses L3 and L4 (both  $f = 80$  mm, Achromatic Doublets, Melles Griot). L3 is mounted on an  $xyz$ -stage equipped with micromanipulators. Like the AODs, also lens L3 is positioned close to a plane conjugate to the back aperture of the inverted objective. By moving L3 we tilt the beam in the back aperture of the inverted objective which results in a moving of the array of (time-shared) traps that is projected in the sample plane. The displacements of L3 in the lateral directions (perpendicular to the optical axis) are small and we did not observe a notable effect on the trapping stiffness. By moving lens L3 along the

optical axis, the beam at the back aperture of the objective can be made slightly convergent or slightly divergent. This results in out-of-plane displacements of the traps [48]. In section 5.4.1 we present experiments in which we evaluated the effect of displacements of the traps in the axial direction. The beam splitter BS2 together with mirror M3 guide the beam into the upper beam path. The two lenses L5 and L6 are identical to L3 and L4 and together they form a 1:1-telescope in analogy to these two lenses.

The revolver of an inverted microscope (Leica, DM IRB) is replaced by a block holding the inverted objective on a piezo microscope objective scanner (Physics Instruments, Pifoc P-721.20) and a dichroic mirror DM1 (Chroma Technology Corp.). This dichroic mirror reflects the 1064 nm trapping laser into the upright objective while it transmits the visible wavelengths for brightfield-, holographic- and confocal microscopy. The upright objective is mounted on an xyz-translation stage fitted with microscrews (Newport) for manipulation and alignment. The dichroic mirror DM2 (Chroma Technology Corp.) reflects both the 1064 nm trapping laser and 532 nm laser light used for holographic microscopy. To the rest of the visible spectrum DM2 is transparent such that we can also use the setup in bright-field mode. The upper objective can be used both for trapping and as condenser lens. We have several objectives: 100×(1.4-0.7 NA) oil immersion, 63×(1.4 NA) oil immersion, 63×(1.4 NA) oil immersion, 63×(1.3 NA) glycerol immersion, 63×(0.7 NA) air immersion, 50×(0.55 NA) air immersion, 40×(1.25-0.75 NA) oil immersion, and a 20×(0.7 NA) air immersion. All objectives were obtained from Leica. Unless stated otherwise we used the 100×(1.4-0.7 NA) oil immersion plan achromat objectives for the experiments presented in this thesis.

When the setup is used for holographic microscopy, the upright objective and lenses L5 and L6 were removed (Figure 1.2) such that the illuminating 532 nm laser beam, coupled in via flipping mirror M6, remains a parallel beam. The dichroic mirror DM2 then couples the 532 nm beam through the sample into the inverted objective. The holograms are then recorded on a CCD camera. For recording the holographic micrographs we used a Mikrottron EoSens CE camera. This system provides a total magnification of  $142 \pm 1$  nm/pixel over a  $182 \times 145$   $\mu\text{m}^2$  field of view. The 532 nm collimated laser we used was either a fibre coupled Spectra Physics Millennia V 532 nm or a Pegasus PE.P532 laser diode.

The maximum range over which the traps can be moved in the sample by the AODs is limited by the maximum deflection angle of the AODs and the optics. The accessible frequency range of 26 through 34 Mhz on our AODs correspond to a deflection range of 30  $\mu\text{rad}$ . The range of deflection angles was a factor of 2.1 less at the back aperture of the objectives due to the telescope behind the AODs. This resulted in a maximum displacement of the optical traps in the sample of 28  $\mu\text{m}$  when a 100× objective was used for trapping.

The samples were placed on an xyz-piezo stage (Physics Instruments, P-563.-3CD) with a range of  $300 \times 300 \times 300$   $\mu\text{m}^3$  in which the position is defined better than 0.5 nm. For long-range displacements of the sample the piezo-stage is

mounted on an adapted stage (Rolyn, 750-MS) with motorized actuators (Newport, 850G-LS).

## 1.6.2 *The used Imaging Techniques*

In the configuration of the setup as sketched in Figure 1.1, the imaging can be done via the eyepiece of the microscope when using the microscope in bright field mode. Similarly the bright field image can be recorded using the CCD to manipulate the traps using the computer interface of the motorized-stage, the piezo stage and the AODs. It is also possible to image the samples using confocal microscopy. The real space distribution of the particles in colloidal dispersions is routinely imaged in 3D using Confocal Laser Scanning Microscopy (CLSM) in combination with fluorescently labeled particles [49–52]. Using fluorescently labeled particles in combination with color filters and two pinholes, CLSM is able to provide 3D data stacks of the fluorescence by the particles. Analysis of confocal images can be used to track the particles in 2 or 3 dimensions [53]. This has allowed detailed studies of the melting of crystals, as well as the glass transition and certain interfacial phenomena, see for example references [25, 54–57]. The fluorescent response of the particle, which can be made more localized in space than the size of the particles themselves by concentrating the fluorescent dye in the core [58], is convolved with the point spread function of the microscope. As a result particles can be discerned when they are typically more than a micron apart in the lateral directions and about 2 micron in the axial direction. Factors that typically compromise confocal imaging are spherical aberration at the interface between the sample wall and the solvent and the scattering by the particles themselves which occurs if the refractive index of the particles is different from that of the particles.

In our experiments, we employed three different confocal microscopes that we could attach to the side-port of the tweezer-setup. The Leica-NT was used in the experiments on the nucleation of hard-sphere crystals as discussed in section 5.6.2 and reference [40]. This confocal microscope allows simultaneous confocal imaging using multiple channels for differently labeled particles and scans the sample literally with a single focus which makes the technique inherently slow. For faster confocal imaging, we used a Nipkow-disk confocal microscope (CSU10, Yokogawa) equipped with a sensitive digital video camera (Evolution<sup>TM</sup> QEi) as described in reference [59]. A spinning disk confocal microscope allows one to record confocal frames at much higher rates because it scans at typically 1000 different spots simultaneously. The spinning disk contains main pinholes in spirals, each forming a moving focus in the sample. The result is that every 1/360th of a second each place in the sample is visited once, and the image is recorded on a sensitive CCD camera. Sensitivity can be gained at the cost of speed by choosing the integration time of the camera a multiple of 1/360th of a second. In this thesis the Nipkow microscope was used to image the Rhodamine labeled particles between which we measured the screened Yukawa interaction in section 3.2. This

work has also been published in reference [41].

Later, we acquired a new confocal microscope, the Nikon C1 which, after some adjustments could also be coupled to the tweezer setup. This confocal is similar to the Leica NT in that it uses tilting mirrors to scan the sample with a single focus that can image three channels. It cannot be operated in reflection mode. However, the photo multiplier tubes are situated outside the scan head and the fluorescent light is coupled to them by an optical fibre. This allows one to couple the light to a spectrometer (Ocean Optics, HR4000).

When the microscope is used in transmission mode and the incandescent light is replaced by the 532 nm collimated laser beam, the CCD camera records magnified interference patterns that can be regarded as in-line holograms [32]. These digital holographic micrographs DHM can then be digitally analyzed by the methods described in Chapter 2 of this thesis and in reference [31, 60]. DHM is one of the most widely applied imaging technique in this thesis and is introduced in more detail in Chapter 2.

We also used two Quadrant Photo Diode QPD that can be coupled to the front port of the microscope and in the upper beam path. The QPD detects the 1064 nm light that leaks through the dichroic mirrors after being scattered by a trapped particle. The CPDs consist of four pixels and give three signals, the difference in voltage between the two northern and southern quadrants, the difference in voltage between the two eastern and two western quadrants and the sum of the voltages of all four quadrants. From the power spectrum of the variations in these signals it is possible to measure the stiffness of the trap. More about this technique is presented in section 4.2. In section 6.2 we present the experiments on counter-propagating trapping in which we used a QPD to measure the trap stiffness and that were published together with our calculations in reference [46].

## Bibliography

- [1] Evans, D. F. and Wennerström, H. *The Colloidal Domain: Where Physics, Chemistry, Biology, and Technology Meet (Advances in Interfacial Engineering)*. VCH Publishers, New York (1994).
- [2] Hynninen, A. P., Thijssen, J. H. J., Vermolen, E. C. M., Dijkstra, M., and Blaaderen, A. V. Self-assembly route for photonic crystals with a bandgap in the visible region. *Nature Materials* **6** 202 (2007).
- [3] Kamenetzky, E. A., Magliocco, L. G., and Panzer, H. P. Structure of Solidified Colloidal Array Laser Filters Studied by Cryogenic Transmission Electron Microscopy. *Science* **263** 207 (1994).
- [4] Vlasov, Y. A., Bo, X.-Z., Sturm, J. C., and Norris, D. J. On-chip natural assembly of silicon photonic bandgap crystals. *Nature* **414** 289 (2001).
- [5] Veinot, J. G. C., Yan, H., Smith, S. M., Cui, J., Huang, Q., and Marks, T. J. Fabrication and Properties of Organic Light-Emitting "Nanodiode" Arrays. *Nano Letters* **333** (2002).

- [6] Holtz, J. H. and Asher, S. A. Polymerized colloidal crystal hydrogel films as intelligent chemical sensing materials. *Nature* **389** 829 (1997).
- [7] Fraden, S., Maret, G., Caspar, D. L. D., and Meyer, R. B. Isotropic-nematic phase transition and angular correlations in isotropic suspensions of tobacco mosaic virus. *Phys. Rev. Lett.* **63** 2068 (1989).
- [8] Wen, X., Meyer, R. B., and Caspar, D. L. D. Observation of smectic-A ordering in a solution of rigid-rod-like particles. *Phys. Rev. Lett.* **63** 2760 (1989).
- [9] Brown, R. A brief account of microscopical observations made in the months of June, July and August, 1827, on the particles contained in the pollen of plants; and on the general existence of attractive molecules in organic and inorganic bodies. *Phil. Mag.* **4** 181 (1828).
- [10] Bohren, C. F. and Huffman, D. R. Absorption and Scattering of Light by Small Particles. Wiley Interscience, New York (1983).
- [11] Sutherland, W. Dynamical theory of diffusion for non-electrolytes and the molecular mass of albumin. *Phil. Mag.* **9** 781 (1905).
- [12] Einstein, A. Über die von der molekularkinetischen Theorie der Wärme geforderte Bewegung von in ruhenden Flüssigkeiten suspendierten Teilchen. *Ann. Phys. (Leipz.)* **17** 549 (1905).
- [13] Onsager, L. Theories of concentrated electrolytes. *Chem. Rev.* **13** 73 (1933).
- [14] Perrin, J. Atoms. Constable: London (1916).
- [15] Wood, W. W. and Jacobson, D. D. Preliminary results from a recalculation of the Monte Carlo equation of state for hard spheres. *J. Chem. Phys.* **27** 1207 (1957).
- [16] Wainwright, B. J. and Thijssen, T. E. Phase transition for a hard sphere system. *J. Chem. Phys.* **27** 1208 (1957).
- [17] Pusey, P. N. and Vanmegen, W. Phase-Behavior of Concentrated Suspensions of Nearly Hard Colloidal Spheres. *Nature* **320** 340 (1986).
- [18] van Blaaderen, A. and Wiltzius, P. Real-space structure of colloidal hard-sphere glasses. *Science* **270** 1177 (1995).
- [19] J. B. Jones, J. V. S. and Segnit, E. R. Structure of Opal. *Nature* **204** 990 (1964).
- [20] van der Waals, J. D. Over de continuïteit van den Gas- en Gloeïstoestanden. Ph.D. Thesis, Leiden University (1873).
- [21] Israelachvili, J. Intermolecular and Surface Forces. Academic Press, London (1991).
- [22] Verwey, E. J. W. and Overbeek, J. T. G. Theory of the Stability of Lyotropic Colloids. Elsevier, Amsterdam (1948).
- [23] Overbeek, J. T. G. Recent developments in understanding of colloid stability. *J. Colloid and Interface Sci.* **58** 408 (1977).
- [24] Derjaguin, B. and Landau, L. Theory of the stability of strongly charged lyophobic sols and of the adhesion of strongly charged particles in solutions of electrolytes. *Acta Physicochim. URSS* **14** 633 (1941).
- [25] Yethiraj, A. and van Blaaderen, A. A colloidal model system with an interaction tunable from hard sphere to soft and dipolar. *Nature* **421** 513 (2003).
- [26] Hecht, E. Optics. Addison Wesley, 3rd. ed. (1998).
- [27] Mie, G. Beiträge zur Optik trüber Medien, speziell kolloidaler Metallösungen. *Annalen der Physik* **25(3)** (1908).
- [28] Lorenz, L. Lysbevægelsen i og uden for en af plane Lysbølger belyst Kugle. *Videnskaberne Selskabs Skrifter* **6** 1 (1890).

- [29] Lorenz, L. Sur la lumière réfléchie et réfractée par une sphère (surface) transparente. *Oeuvres scientifiques de L. Lorenz. revues et annotées par H. Valentiner. Tome Premier, Libraire Lehmann & Stage, Copenhagen* 403 (1898).
- [30] Dhont, J. An Introduction to Dynamics of Colloids (Studies in Interface Science). Elsevier Science (1996).
- [31] Lee, S.-H., Roichman, Y., Yi, G.-R., Kim, S.-H., Yang, S.-M., van Blaaderen, A., van Oostrum, P., and Grier, D. G. Characterizing and tracking single colloidal particles with video holographic microscopy. *Opt. Exp.* **15** 18275 (2007).
- [32] Sheng, J., Malkiel, E., and Katz, J. Digital holographic microscope for measuring three-dimensional particle distributions and motions. *Appl. Opt.* **45** 3893 (2006).
- [33] Demirörs, A. F., Jannasch, A., van Oostrum, P. D. J., Schäffer, E., van Blaaderen, A., and Imhof, A. Seeded Growth of Titania Colloids with Refractive Index Tunability and Fluorophore-free Luminescence. *Langmuir*, DOI: 10.1021/la103717m (2010).
- [34] Vutukuri, H. R., Demirörs, A. F., Peng, B., van Oostrum, P., Imhof, A., and van Blaaderen, A. Colloidal analogues of charged and uncharged polymer chains with tunable stiffness. *in preparation* (2011).
- [35] Ashkin, A. Acceleration and trapping of particles by radiation pressure. *Phys. Rev. Lett.* **24** 156 (1970).
- [36] Ashkin, A. and Dziedzic, J. M. Optical levitation by radiation pressure. *Appl. Phys. Lett.* **19** 283 (1971).
- [37] Ashkin, A., Dziedzic, J. M., Bjorkholm, J. E., and Chu, S. Observation of a single-beam gradient force optical trap for dielectric particles. *Opt. Lett.* **11** 288 (1986).
- [38] Visscher, K., Brakenhoff, G. J., and Krol, J. J. Micromanipulation by multiple optical traps created by a single fast scanning trap integrated with the bilateral confocal scanning laser microscope. *Cytometry* **14** 105 (1993).
- [39] van Oostrum, P. D., van der Horst, A., and van Blaaderen, A. Mutual influence of time-shared optical traps studied by means of Video Holographic Microscopy. *Digital Holography and Three-Dimensional Imaging, OSA Technical Digest (CD) (Optical Society of America) DWD7* (2009).
- [40] Hermes, M., Vermolen, E. C. M., Leunissen, M. E., Vossen, D. L. J., van Oostrum, P. D. J., Dijkstra, M., and van Blaaderen, A. Nucleation of colloidal crystals on configurable seed structures. *Soft Matter*, DOI: 10.1039/COSM01219J (2011).
- [41] Masri, D. E., van Oostrum, P., Smalenburg, F., Vissers, T., Imhof, A., Dijkstra, M., and van Blaaderen, A. Measuring Colloidal Forces from Particle Position Deviations inside an Optical Trap. *Soft Matter*, DOI:10.1039/COSM01295E (2011).
- [42] Crocker, J. C. and Grier, D. G. Microscopic Measurement of the Pair Interaction Potential of Charge-Stabilized Colloid. *Phys. Rev. Lett.* **73** 352 (1994).
- [43] Sainis, S. K., Germain, V., and Dufresne, E. R. Statistics of Particle Trajectories at Short Time-Intervals Reveal Electrostatic Colloidal Interactions in Nonpolar Solvents. *Phys. Rev. Lett.* **95** 018303 (2007).
- [44] Viana, N. B., Rocha, M. S., Mesquita, O. N., Mazolli, A., Neto, P. A. M., and Nussenzeig, H. M. Towards absolute calibration of optical tweezers. *Phys. Rev. E* **75** 021914 (2007).
- [45] Vossen, D. L. J., van der Horst, A., Dogterom, M., and van Blaaderen, A. Optical tweezers and confocal microscopy for simultaneous three-dimensional manipulation and imaging in concentrated colloidal dispersions. *Rev. Sci. Instrum.* **75** 2960 (2004).

- [46] van der Horst, A., van Oostrum, P., Moroz, A., van Blaaderen, A., and Dogterom, M. High trapping forces for high-refractive index particles trapped in dynamic arrays of counterpropagating optical tweezers. *Appl. Opt.* **47** 3196 (2008).
- [47] Polin, M., Roichman, Y., and Grier, D. G. Autocalibrated colloidal interaction measurements with extended optical traps. *Phys. Rev. E.* **77** 051401 (2008).
- [48] Visscher, K., Gross, S. P., and Block, S. M. Construction of multiple -beam optical traps with nanometer-resolution position sensing. *IEEE J. Sel. Top. Quant. Electron.* **2(4)** 1066 (1996).
- [49] Minsky, M. Memoir on inventing the confocal scanning microscope. *Scanning* **10** (1988).
- [50] Wilson, T. *Confocal Microscopy*. Academic Press, London (1990).
- [51] van Blaaderen, A. and Vrij, A. Synthesis and characterization of colloidal dispersions of fluorescent, monodisperse silica spheres. *Langmuir* **8** 2921 (1992).
- [52] Kegel, W. and van Blaaderen, A. Direct observation of dynamical heterogeneities in colloidal hard-sphere suspensions. *Science* **287** 290 (2000).
- [53] Crocker, J. C. and Grier, D. G. Methods of Digital Video Microscopy for Colloidal Studies. *J. of Col. and Int. Sci.* **179** 289 (1996).
- [54] Gasser, U., Weeks, E. R., Schofield, A., Pusey, P. N., and Weitz, D. A. Real-space imaging of nucleation and growth in colloidal crystallization. *Science* **292** 258 (2001).
- [55] Dullens, R. and Kegel, W. Reentrant surface melting of colloidal hard spheres. *Phys. Rev. Lett.* **92** 195702 (2004).
- [56] Weeks, E., Crocker, J., Levitt, A., Schofield, A., and Weitz, D. Three-dimensional direct imaging of structural relaxation near the colloidal glass transition. *Science* **287** 627 (2000).
- [57] Aarts, D., Schmidt, M., and Lekkerkerker, H. Direct visual observation of thermal capillary waves. *Science* **304** 847 (2004).
- [58] van Blaaderen, A., Ruel, R., and P. Wiltzius. Template-directed colloidal crystallization. *Nature* **385** 321 (1997).
- [59] Lu, P. J., Sims, P. A., Oki, H., Macarthur, J. B., and A. Weitz, D. Target-locking acquisition with real-time confocal (TARC) microscopy. *Opt. Express* **15** 8702 (2007).
- [60] Cheong, F. C., Krishnatreya, B. J., and Grier, D. G. Strategies for three-dimensional particle tracking with holographic video microscopy. *Opt. Express* **18** 13563 (2010).

# 2

## Digital Holographic Microscopy

---

The light scattered from a particle contains much more information than what is recorded on conventional photographs. By recording the interference of this scattered light with a coherent and known beam of light, much more information is registered in a so-called *hologram*. In this Chapter we introduce in-line *Digital Holographic Microscopy*, DHM and two techniques to analyze the recorded holograms. First, we show that it is possible to calculate from a single 2D snapshot what the 3D light distribution in the sample must have been. We apply this method to measure the radial distribution function of a colloidal suspension at a volume fraction of only about  $10^{-4}$  and to study a rod-like particle. Then we present an alternative approach to analyze in-line Digital Holographic Micrographs, in which the inverse problem posed by the Lorentz-Mie-Debye scattering by micron size particles and the interference with the reference beam is solved numerically. This allows us to track colloids in 3D from 2D holographic snapshots to within a nanometer in the lateral direction and to within ten nanometer in the axial direction, while simultaneously measuring an individual particle's radius and refractive index. DHM is subsequently applied to various colloidal systems, to monitor the particle synthesis and the particle dynamics. We conclude this Chapter with holographic experiments on strings of spherical particles.

## 2.1 Holography

Conventional photographs and micrographs are 2D representations where the transmission, absorption and/or reflection have been modulated to represent the irradiance distributions. The real world is three dimensional. We are able to observe this 3D nature mainly because our eyes are slightly displaced with respect to each other giving a slightly different perspective on the world. In 1948 Dennis Gabor [1] introduced a technique that he coined *holography* after the Greek words *ὅλος* and *γραφή* meaning *whole script*, i.e. everything writes.

Holography is a technique that records not only the intensity but also the phase of the light that was scattered by the object. In the recording process the light that is scattered off the object, the *object beam*, is combined with a *reference beam*, of light that is *coherent* with the illuminating beam, and therefore also with the object beam. The resulting picture, the *hologram*, is a recording of the intensity distribution in the interference pattern that is formed by interference between the scattered light and the reference beam. Consequently, the hologram contains information on the amplitude and the phase of the diffracted light. After recording, it is then possible to illuminate the recorded interference pattern with a *reconstruction beam* that is collimated with the original reference beam. The reconstruction beam is diffracted on the recorded interference pattern. It can be shown that the diffracted light field is identical to the light field that was scattered off the object, containing the same phase distribution [2]. When looking into the hologram while it is illuminated by a reconstruction beam, one observes a light field identical to the one that is seen when looking at the original object. In particular, the reconstructed light object beam propagates in the same directions as the original object wave. When looking at the reconstructed light field with two eyes or from different positions, one sees the same 3 dimensional information, as is seen when looking at the light diffracted by the object itself.

Normally a photograph is taken by letting all the light pass through a small pinhole, be it a real pinhole or an effective pinhole formed by a lens. As a result the picture only contains the perspective of a pinhole. The light is allowed to interfere with a reference beam and in the plane where in normal photography one places the pinhole the interference pattern is recorded. Dennis Gabor thus invented a way to record all the light and the information it carries in that plane, rather than just the little bit of information that passes through the pinhole. This invention won him the 1971 Nobel prize in physics. Major advancements to the technique were the result of the invention of the laser in the early 1960s that made it much easier to obtain coherent light. The invention of digital recording media has greatly simplified the recording and analysis of holograms.

### 2.1.1 *In-line holograms*

There are many different holographic setups. One of the properties by which they are distinct is the angle between the object beam and the reference beam. The simplest form is called *in-line* holography where the illuminating beam and the reference beam are one and the same beam. When the illuminating beam and the reference beam are two separate beams it is possible to change the relative power of the two beams to tune the power of the scattered light, also referred to as *object beam*, with respect to the intensity to the reference beam. As stated before, in *in-line* holography, the angle between the illuminating beam and the reference beam is zero. Any object in the illuminating beam diffracts the light, changing its direction and phase. Part of this diffracted light continues more or less in the direction of the illuminating beam and reaches the *hologram plane* where it is recorded. The part of the illuminating beam that was not diffracted continues to propagate in the forward direction and interferes with the scattered light. Thus the illuminating beam also acts as the reference beam. Therefore the sample should not be too optically dense, otherwise there is no well-defined reference beam left. The coherence between the two is guaranteed. For Mie particles that scatter mainly in the forward direction [3], the intensity of the scattered light is comparable to that of the illuminating beam.

The conventional way to record *in-line* holograms is to place a recording medium in some plane, the hologram plane, behind the scattering object to record the interference pattern. To be able to record the interference on a CCD camera rather than on some photochemically sensitive medium that needs to be processed further, Sheng *et al.* [4] proposed applying a transmission microscope. By using the magnification of the microscope objective, the interference pattern can be recorded with sufficient resolution by a digital camera with pixels that are several microns in size. In this manner one generates a digital hologram that consists of pixels with different grey values that represent the intensity distribution in the hologram.

In this Chapter, we introduce two different methods to analyze these digital *in-line* holographic micrographs. Such an analysis can either be done by directly studying the 3D light distribution from the hologram or by fitting a model for the scattering and interference to the experimental hologram [5]. In section 2.2 we present a method to analyze the holograms by calculating the three dimensional light distribution from the recorded intensity distribution in the hologram plane. This method is henceforth referred to as *back propagating*. It is the numerical equivalent of illuminating the hologram with a reconstruction beam to be able to see the light field as it was scattered by the object and recorded by the hologram. To do this one only needs to know the wavelength of the light used to record the hologram and the size of the pixels. The 3D light distribution can then be further analyzed.

In section 2.2.1 we apply back propagation to a simulated hologram of a spherical particle. Then, in section 2.2.2, we show that back propagation can be used

to study the phase behavior of colloidal suspensions for instance by looking at the radial distribution function  $g(\mathbf{r})$ . Back propagation of in-line holograms can also be applied to study non-spherical particles such as colloidal rods [6]. In section 2.2.3, we show the holographic analysis of a silica rod.

For spherical dielectric particles, it is possible to quantitatively calculate the scattering. By allowing the calculated light field to interfere with a reference beam, one can thus quantitatively simulate in-line holograms. In section 2.3.1, we introduce a model, based on the Lorenz-Mie-Debye theory, for in-line holograms of spherical dielectrics. By fitting the model for the scattering by spherical particles as described in section 2.4 to experimental holograms, it is possible to characterize the individual particles radius and refractive index while simultaneously obtaining the particle position with 1 nm accuracy in the lateral directions and accurate up to around 10 nm in the axial direction [7].

This technique is applied to study individual particles in section 2.5. In section 2.5.1 we characterized silica particles of various sizes in ethanol. Fitting simulated in-line holograms was applied to characterize titania particles, following the changes in the refractive index in several steps in the particle preparation in section 2.19. In addition melamine particles were studied using these techniques as shown in section 2.20.

The information about the particle characteristics and position are all deduced from a single snapshot. By analyzing a time-sequence of in-line holographic micrographs we can study particle dynamics. This is shown in section 2.5.4, in which we study the sedimentation and diffusion of a silica particle in ethanol. In section 2.5.5, we study the interaction of the same particle with the bottom of the sample cell. From the distribution of the distances to the wall we measure the Debye screening length and the weight of the particle. The same technique was used to study the growth of a silica layer on polystyrene particles in section 2.5.6.

In section 2.6 the model for the in-line holograms of spherical particles is extended for multiple particles. The applicability of the model to study multiple particle dynamics was verified for two particles in section 2.6.1. In section 2.6.2, we study under which conditions the number of particles can be extended to seven. In section 2.6.4, we study the rotational and translational diffusion of a dumbbell of two PS particles in DMSO. Then, in section 2.6.5 we study the rotational and translational diffusion of a semi-flexible colloidal model for bio-polymers. Finally, in section 2.6.6 we demonstrated that in-line holographic microscopy combined with fitting to a model based on Lorenz-Mie-Debye scattering can be applied to study the bending of a string made of silica spheres in THF by means of optical tweezers.

## 2.2 Back Propagation

After the hologram has been recorded, the conventional method to further process the information, is to illuminate the hologram with a so-called *reconstruction*

*beam*. Such a beam should be as similar as possible to the original reference beam. The hologram then diffracts this light in such a way that the diffracted light is the same as the light that was originally diffracted by the object. A recorded hologram allows the study of the object, or more precisely the reconstructed hologram, under many different angles or from different positions.

When the hologram is recorded digitally, the illumination with a reconstruction beam is less straightforward. We can do so digitally in a process where the reconstruction is simulated on the computer rather than performed in reality. In the plane of the hologram we have an image of grey-values that we regard as a distribution of point scatterers that are all in phase and that are different in amplitude.

The recorded hologram is the interference between the object beam, the complex scattered light  $\tilde{S}$  that is diffracted in the direction of the recording medium, and the reference wave  $\tilde{R}$  [2, 4]. The intensity is thus given by:

$$\tilde{I}(\vec{\rho}_{xy}) = (\tilde{R} + \tilde{S})(\tilde{R}^* + \tilde{S}^*) = \tilde{R}\tilde{R}^* + \tilde{R}\tilde{S}^* + \tilde{S}\tilde{R}^* + \tilde{S}\tilde{S}^*. \quad (2.1)$$

Here the asterisk denotes complex conjugation and  $\vec{\rho}_{xy}$  represents the location in the hologram plane. The first term on the right side of equation 2.1 gives the average irradiance, the second and third term contain the information of the interference. The last term is referred to as halo [4] and contributes just noise when reconstructing the hologram.

When the reconstruction is done by simply irradiating the hologram with a reconstruction wave which is the same as the reference wave, the reconstruction wave is modulated by the hologram in the following manner:

$$\tilde{U}(\vec{\rho}_{xy}) = \tilde{R} \tilde{I} = \|\tilde{R}\|^2 \tilde{R} + \|\tilde{R}\|^2 \tilde{S}^* + \|\tilde{R}\|^2 \tilde{S} + \tilde{R} \|\tilde{S}\|^2. \quad (2.2)$$

The first term is the reference wave as before, the second term is the reconstructed object wave, the third term is the *virtual image* which is the complex conjugate of the reconstructed object wave. This wave propagates in the other direction, which for in-line holography means that it behaves as the mirror image of the object, mirrored in the hologram plane. In in-line holography the reference beam has the form  $\tilde{R} = \|\tilde{R}\|e^{i\Phi(\vec{k}, \vec{\rho})}$ . Here  $\Phi(\vec{k}, \vec{\rho})$  is the known phase distribution which depends only on the location  $\vec{\rho}$  and the wave vector  $\vec{k}$ . The object wave  $\tilde{S} = |\tilde{S}(\theta, \phi, \tilde{U}_{\text{ill}}, C)|e^{i\Phi_s(\theta, \phi, C)}e^{i\Phi(\vec{k}, \vec{\rho})}$  depends on the scattering angles  $\theta$  and  $\phi$ , the illumination beam  $\tilde{U}_{\text{ill}}$  and the object characteristics  $C$ . Not only the intensity but also the phase of the object beam depends on the scattering angles  $\theta$  and  $\phi$  and the object characteristics  $C$ . Depending on the nature of the particles,  $C$  can depend on the radius and refractive index, e.g. in the case of metallic or dielectric spheres. In general the shape, refractive index distribution and orientation affect the scattering. In section 2.3 we will go into the details of the object beam for so-called Mie particles, metallo-dielectric spheres.

When the reconstruction is performed digitally, the optical field is described as the light diffracted from a 2D complex aperture which generates the optical field:

$$\tilde{U}(\rho_x, \rho_y, z_h) = \int_{\rho'_x} \int_{\rho'_y} \tilde{U}(\rho_x, \rho_y, z_h=0) \left[ -\frac{\partial G}{\partial n}(\rho_x - \rho'_x, \rho_y - \rho'_y, z_h) \right] d\rho'_x d\rho'_y. \quad (2.3)$$

Here  $-\frac{\partial G}{\partial n}$  is the derivative in the direction  $n$ , normal to the hologram plane of the Green's function of light propagation in a homogeneous medium and describes the propagation of light. It describes the diffraction from a point source and the light field at any distance  $z_h$  can be calculated by performing a 2D convolution with this operator. The intensity distribution at a plane  $z_h$  is then  $\tilde{U}\tilde{U}^*(\vec{\rho}, z)$ . Two functions that are often used as the normal derivative of the Green's function of light propagation in a homogeneous medium are the Rayleigh-Sommerfeld formula and the Kirchhoff-Fresnel approximation [8].

The Rayleigh-Sommerfeld formula,

$$-\frac{\partial G}{\partial n}(\vec{\rho}_{xy}, z_h) = \frac{1}{\lambda} \frac{z_h e^{-ik\sqrt{\rho_{xy}^2 + z_h^2}}}{\rho_{xy}^2 + z_h^2} \quad (2.4)$$

can be approximated by using a binomial expansion and applying the paraxial approximation  $\sqrt{\rho_{xy}^2} \ll z_h$ :

$$-\frac{\partial G}{\partial n}(\vec{\rho}_{xy}, z_h) = \frac{e^{ikz_h}}{i\lambda z} e^{i\frac{k}{z_h}\rho_{xy}^2}. \quad (2.5)$$

This is called the Kirchhoff-Fresnel propagator.

The convolution in equation 2.3 can be performed by a computationally less intensive multiplication in the Fourier domain. To do so, equation 2.3 can be rewritten with the Fourier convolution theorem as:

$$\tilde{U}_F(q_x, q_y, z_h) = \tilde{U}_F(q_x, q_y, 0) G_F(q_x, q_y, -z_h) \quad (2.6)$$

where

$$\tilde{U}_F(q_x, q_y, z_h) = \int_{-\infty}^{\infty} \int_{-\infty}^{\infty} \tilde{U}(\rho_x, \rho_y, z_h) e^{-i(\rho_x + \rho_y)} d\rho_x d\rho_y \quad (2.7)$$

and the Rayleigh-Sommerfeld propagator in Fourier space [9, 10]

$$G_F(q_x, q_y, -z_h) = e^{-i(k^2 - (q_x^2 + q_y^2))z_h}. \quad (2.8)$$

The intensity distribution at any depth in the sample can then be calculated by inverse Fourier transform of equation 2.6.

Digital back propagation of in-line holograms yields 3D stacks of what look essentially like stacks of ordinary transmission microscopy images. In-line Digital

Holographic Microscopy (DHM), where the interference pattern is magnified using a microscope objective has been reported [4] to successfully reconstruct the light field containing several thousands of particles in a volume that is nearly 1000 times as thick as the depth of field of a conventional microscope while maintaining the lateral resolution. Micron-sized and sub-micron particles have been detected. This is impossible with lens-less in-line holography. In the back-propagated z-stack of holograms, the particles are visible as dark zones, so-called ‘particle-traces’. The position detection is based on the centroid finding of these particle traces. Thanks to the application of a magnifying objective, the particle traces have been reduced to about 2 – 10 diameters in the axial direction [4].

DHM has been applied successfully to detect 3D flow fields both by tracking individual particles in time sequences of holograms and by means of Holographic Particle Image Velocimetry, HPIV. Here the back propagated light fields of 2 or more consecutive holograms are cross-correlated to find local displacements [8].

### 2.2.1 An example: 1.4 $\mu\text{m}$ silica in ethanol

To demonstrate the working principle of back propagation we apply it to a typical hologram. We numerically generated an in-line hologram as might be recorded from a 1.4  $\mu\text{m}$  silica particle in ethanol using the methods that will be described in section 2.3. We chose this particular system because it shows all the relevant phenomena and because we used this system extensively in the lab. The particle was simulated to be  $z_h = 14 \mu\text{m}$  above the hologram plane and we assumed plane wave illumination with a wavelength of 532 nm. The hologram was assumed to be magnified using a microscope objective so that the pixels represent 141 nm. The in-line hologram is reproduced in Figure 2.1 **a**. The intensity distribution has been Fourier transformed and multiplied with the Fourier space version of the Rayleigh-Sommerfeld propagator with different distances  $z_h$  to the plane as give by equation 2.6. Images 2.1 **b-k** of the same Figure show the light distribution at distances of 5.66, 8.50, 11.33, 14.16, 16.99, 19.82, 22.66, 25.49 and 28.32  $\mu\text{m}$  respectively from the hologram.

We note that the concentric rings in the in-line hologram in Figure 2.1 **a** get smaller as the distance to the hologram is increased. The same observation could be made when literally moving the focal plane of the microscope closer to the particle. In Figure 2.1 **e**, at 14.16  $\mu\text{m}$  above the hologram, so well within the body of the particle, the light is concentrated in the center of the picture. Beyond that depth, in Figure 2.1 **f-k**, the center of the picture is darker than the rest of the plane. This black zone is referred to in the literature as the particle *trace*. The same black trace would also be observed if the focal plane were placed above the particle.

By calculating the light distribution at many depths this way we can generate a stack of 2D pictures that all together form a 3D picture of the light distribution. Something similar could be obtained by moving the objective lens through the sample, taking pictures at many different depths. In Figure 2.1 **l** we show a cross-

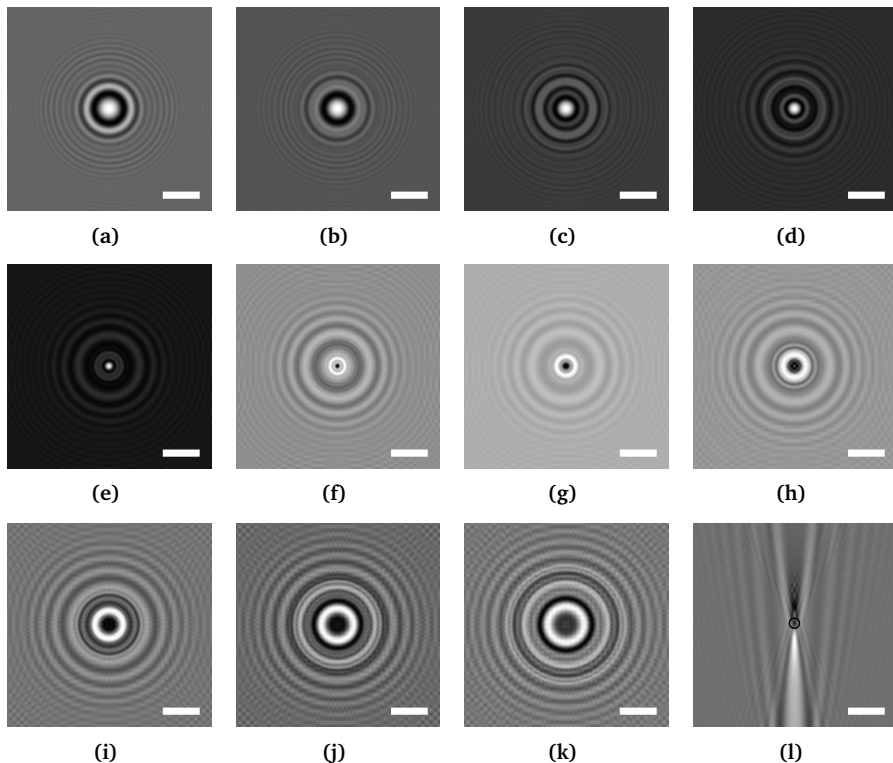


**Figure 2.1:** Rayleigh-Sommerfeld propagation of a simulated hologram of a silica sphere in Ethanol. The hologram, of a  $1.4 \mu\text{m}$  silica ( $n = 1.45$ ) sphere in ethanol ( $n = 1.36$ ),  $14 \mu\text{m}$  below the particle. The hologram has been simulated as described in section 2.3. **a.** The hologram at  $14 \mu\text{m}$  below the particle. **b.** The absolute intensity distribution  $2.83 \mu\text{m}$  above the hologram from the Rayleigh-Sommerfeld propagation. **c-k.** The same as in **b** at respectively  $5.66$ ,  $8.50$ ,  $11.33$ ,  $14.16$ ,  $16.99$ ,  $19.82$ ,  $22.66$ ,  $25.49$  and  $28.32 \mu\text{m}$  above the hologram. The scalebars indicate  $5 \mu\text{m}$ , all pictures are  $28.32$  by  $28.32 \mu\text{m}$ . **l.** A cross-section in the  $xz$  plane containing the particle, parallel to the polarization of the light, upward in the other frames. The black circle indicates the edge of the particle.

section through the 3D stack. The depths  $z_h$  at which we calculated the light distribution were chosen to lie  $141 \text{ nm}$  above each other, the same as the pixel size, so that both directions in the cross-section are of the same size. The lowest line of pixels in the cross-section corresponds to the central line of pixels in the hologram itself. The bright spot in the middle gets narrower and brighter with increasing distance to the hologram. The particle was positioned in the middle of this  $z$  stack.

Apart from the rings that move together with increasing depth there are also bright lines that slowly diverge. These belong to the so-called *virtual image*, given

by the third term in equation 2.2. If we were to propagate the light in the other direction, so down into the page, these lines would converge and form a mirror image of the cross-section in Figure 2.1 **l**.

When performing the digital Fourier transform we implicitly assume periodicity of the image. At larger depths, the consequence of this is that the lines that belong to the virtual image are ‘reflected’ at the boundary of the frame. This is clearly visible in Figures 2.1 **h-k**. In many cases one wants to use back-propagated holographic image stacks to detect the position or displacement of the scattering particles [4, 8]. The virtual image and reflections thereof can then be a disturbing factor [11]. In the same reference, a slightly different method of performing the back propagation is proposed. The reflections at the edge of the hologram can be postponed by taking a larger hologram. For a larger hologram these reflections occur at greater depths. An ideal hologram would be infinite so that it registers all the light scattered from the object of interest. A way to suppress these reflections is to pad the hologram with a rim of zeros before Fourier transforming.

In Figure 2.1 **a** the hologram is not perfectly rotationally symmetric. This is the result of a slight difference in the scattering by the particle of light in the direction of, and perpendicularly to, the direction of the linearly polarized illuminating beam. More about this can be read in section 2.3.1.

The position of the particle is traditionally determined as the darkest spot in a back propagated stack [4, 12, 13]. Within a 2D slice from such a back propagated  $z$ -stack, the lateral position of the particle is traditionally found by centroid finding algorithms as presented in [14]. In the axial direction, it is determined as the depth at which the particle trace is the darkest. From Figure 2.1 **l**, where the darkest region is clearly above the circle that indicates the edge of the particle, can be understood that this strategy tends to over-estimate the distance to the hologram plane. To a first approximation this is a constant offset (see reference [8] and references therein). Often particle coordinates determined using this method to study flow profiles of the liquid in which the particles are suspended. In the following subsection (2.2.2) we apply this technique to a new problem, to smaller particles, colloids, and with the aim of studying the phase behavior of the particles by determining their spatial distribution within a dispersion.

### 2.2.2 Back propagated $g(\mathbf{r})$

One method to characterize the behavior of colloidal suspensions is to look at the so-called *radial distribution function* or  $g(\mathbf{r})$  (say ‘ $g$ ’ of ‘ $\mathbf{r}$ ’), which quantifies the probability to find an other particle at a distance  $\mathbf{r}$  from a particle in the system. The calculation of the  $g(\mathbf{r})$  is based on the assumption that each particle can in principle be found anywhere, independent of the locations of the other particles [15]. The histogram of the found inter-particle-distances is normalized by dividing by the distribution of an equal number of ideal gas molecules in the same volume. In a perfect crystal, where the particles are regularly ordered by interaction with the other particles, the  $g(\mathbf{r})$  can therefore not formally be cal-

culated. This however, is commonly done to visualize the long-ranged order in a crystal. The  $g(\mathbf{r})$  in crystals with for instance Brownian movements around the lattice sites is peaked at characteristic distances. Also in a more isotropic phase, as for instance a liquid, we observe local maxima and minima in the probability of finding another particle. Closer than the diameter of the particles we do not expect any particles. A little further away, depending on the inter-particle interactions, there is an increased probability of finding a particle. In a liquid, the particle positions de-correlate with distance. For perfect crystals the correlation between particle positions extends to infinity. If the interaction between the particles can be assumed to be pair-wise additive, the  $g(\mathbf{r})$ 's at all volume fractions together, contain all thermodynamics of the system.

In order to gain sufficient statistics of the inter-particle distances, many particle positions are required [16–19]. A straightforward method to obtain real-space particle coordinates is to take fluorescently labeled and refractive index matched particles to image them in 3D using a confocal microscope [16]. Confocal microscopes are inherently slow, as they scan the sample point by point. This limits the size of the 3D stack that can be made as the time between recording the first and the last voxel of one 3D stack should be shorter than the time it takes for a particle to diffuse its diameter. Particularly when the volume fraction of particles in the sample is low, this can be a problem. In that case, the particles diffuse relatively fast and most of the data contains empty space. With decreasing volume fraction, it therefore becomes increasingly difficult to gather sufficient statistics to calculate a  $g(\mathbf{r})$ .

In-line holographic microscopy on the other hand, allows one to track scattering particles in a 3D volume from a 2D snap-shot, provided the volume is sufficiently empty to have enough unperturbed light to act as reference beam. The back propagation does not explicitly take the scattering by the particles into account, multiple scattering is therefore regarded as noise when determining the positions of scattering particles from a 2D in-line holographic snapshot. As all the coordinates are determined from a single 2D picture, in-line holographic microscopy inherently records all the particle coordinates simultaneously. It is also not necessary to register many empty voxels as would be the case when confocal microscopy were used.

To study the applicability of in-line holographic microscopy as a viable alternative to confocal microscopy for the determination of radial distribution functions in dilute systems with long range interactions, we prepared a dispersion of nominally  $1.4\ \mu\text{m}$  titania/silica particles in CycloHexyl Chloride, CHC. The particles were initially porous titania particles that were then coated with silica that also filled the pores. The CHC is therefore mainly in contact with the silica. These titania/silica particles have an effective refractive index of around 1.8 [20]. CHC has a refractive index of 1.4602. CHC is an oil with an intermediate dielectric constant,  $\epsilon = 7.6$ . In such a solvent, there are far fewer ions in the solvent than in water. The screening by ions is reduced and the Debye screening length is significantly

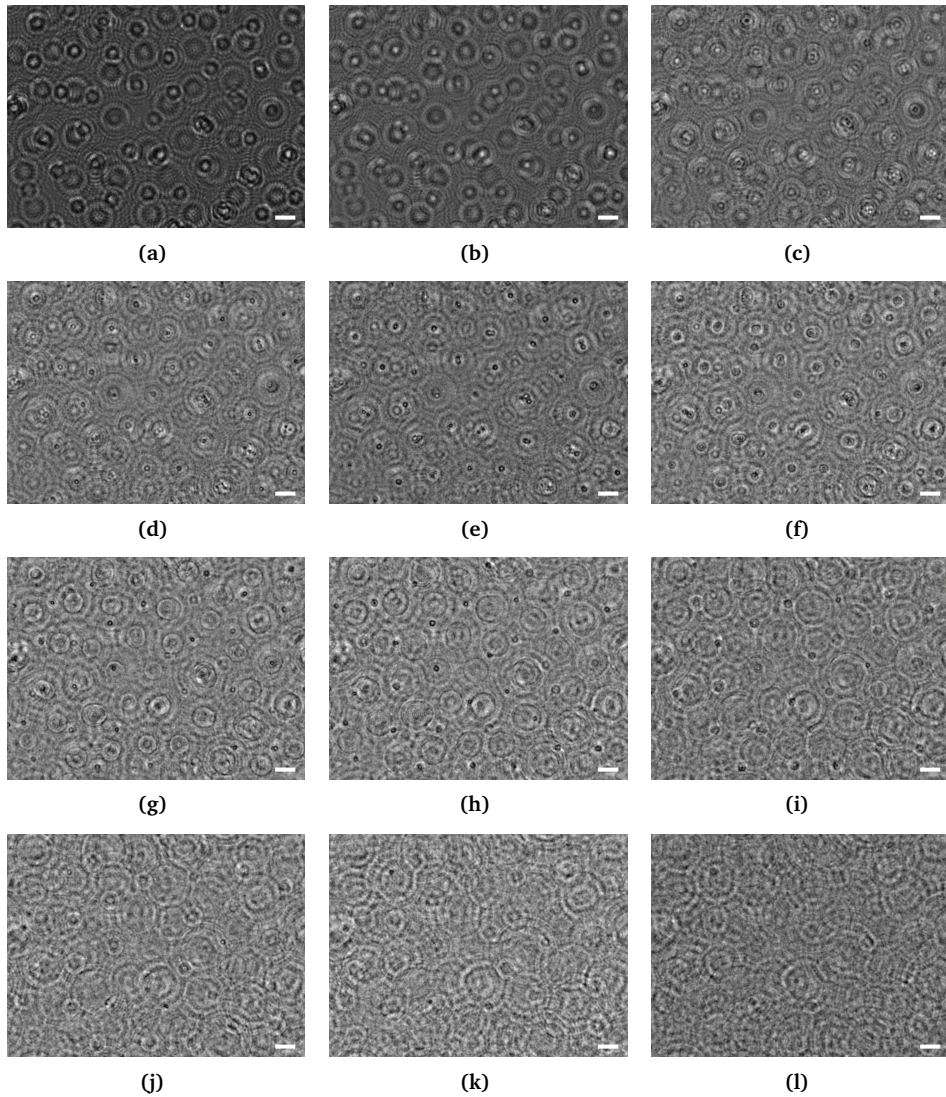


**Figure 2.2:** Rayleigh-Sommerfeld propagation of a hologram of silica/titania spheres in CHC. **a.** A hologram of a crystal of  $1.4 \mu\text{m}$  titania/silica particles with a refractive index  $\sim 1.8$ , in CycloHexyl Chloride, with a refractive index of  $1.46$ . The volume fraction of particles was  $1.1 \cdot 10^{-3}$ . The sample was illuminated with a  $543 \text{ nm}$  HeNe laser. **b-l.** The absolute intensity distribution the Rayleigh-Sommerfeld propagation at respectively  $3.17, 6.35, 9.53, 12.70, 15.88, 19.05, 22.23, 25.40, 28.58, 31.75$  and  $34.93 \mu\text{m}$  above the hologram. The scale bars are  $5 \mu\text{m}$ .

increased. Due to the lower screening, particles in such intermediate dielectric constant solvents can gather surface potentials similar to those in aqueous solutions [21–23]. As a result, the particles experience the influence of the other particles already at low volume fractions. At low volume fractions we already observe ordering and even the formation of long-ranged crystals. This means that a confocal microscope would have a hard time imaging sufficiently many particles in a sufficiently short time to calculate a reliable  $G(\mathbf{r})$ .

The suspension of titania/silica particles was transferred to a rectangular glass capillary (Vitrocom  $0.1 \times 2.0$  mm) and placed on an inverted microscope (Leica DRM-IRB), equipped with a  $100\times$  NA 1.4 PLAN APO objective. The condenser was replaced by a 543 nm HeNe laser (Melles Griot). The particles were left to sediment for about an hour, until a steady sedimentation-diffusion equilibrium was reached. In this steady state, we observed particles in the lowest  $\sim 40$   $\mu\text{m}$  of the sample. The focal plane of the microscope was placed close to the bottom of the cell and while illuminating with the 543 nm laser, images were recorded with around one frame per second on a CCD camera (Evolution QEi). The imaging system had a magnification such that a single pixel corresponded to 59.3 nm in the hologram plane. During recording, the sample was displaced horizontally so that the distances between the particles were uncorrelated from frame to frame.

The recorded holograms were normalized by dividing by the average intensity distribution in all the frames [5, 7, 24].

$$\tilde{B}(\vec{\rho}_{xy}) = \frac{\tilde{U}(\vec{\rho}_{xy})}{|\tilde{U}(\vec{\rho}_{xy})|} = \frac{\|\mathbf{R}\|^2 \tilde{\mathbf{R}} + \|\tilde{\mathbf{R}}\|^2 \tilde{\mathbf{S}}^* + \|\mathbf{R}\|^2 \tilde{\mathbf{S}} + \tilde{\mathbf{R}} \|\mathbf{S}\|^2}{|\tilde{U}(\vec{\rho}_{xy})|}. \quad (2.9)$$

Here  $|\tilde{U}(\vec{\rho}_{xy})|$  is the average intensity distribution throughout the sequence. This corrected for irregularities due to, for instance, dirty optics. A typical normalized in-line hologram  $B$  of this sample is presented in Figure 2.2 a.

The other pictures in Figure 2.2 are digitally giving an impression of the intensity distribution at respectively 3.17, 6.35, 9.53, 12.70, 15.88, 19.05, 22.23, 25.40, 28.58, 31.75 and 34.93  $\mu\text{m}$  above the hologram. Again, the rings get smaller with increasing distance to the hologram. The contrast of the dark spot just above each particle is much better than that of the bright spot in and below the particle. The particles that are at much higher positions are visible in the original hologram as much larger and fainter rings.

In general, the particles are on the order of 8  $\mu\text{m}$  away from each other. This is the result of charge repulsion and the low screening. Some particles however,  $\sim 2\%$ , a few examples of which are visible in Figure 2.2 e at 12.7  $\mu\text{m}$  above the hologram, seem to be stuck together. Such particles were observed to remain together for extended periods of time. This suggests that the particles were trapped in the minimum of the van der Waals interaction between them.

We applied the video microscopy technique as described by Crocker and Grier [14] to inverted pictures like the ones in Figure 2.2 to determine the particle posi-

tions. The spacing between the separate 2D frames in the 3D stack was chosen to be 20 times the size of the pixels in the  $x$ - and  $y$ -direction;  $1.186 \mu\text{m}$ . When a pixel in a dilated 2D cross-section was found to be brighter than a threshold, the lateral position of the corresponding particle was determined by centroid fitting. The threshold was chosen to be 7 standard deviations of the intensity above the average intensity. The procedure was repeated on all frames of a back-propagated  $z$ -stack. When a particle was found within 1.2 particle radii, 10 pixels, in at least three 2D frames above each other, the lateral particle position was taken to be the average lateral position of the particle trace. Due to fringes of other particles, we observed some variation in the lateral position of the particle trace as found by centroid fitting. We estimate that the lateral position of the particles was determined to within roughly 2 pixels,  $150 \text{ nm}$  in the  $xy$ -plane.

The axial coordinate was determined by fitting a gaussian to the intensity profile in that direction. We estimate that this yielded an accuracy in the  $z$  coordinate of better than  $0.5 \mu\text{m}$ . The procedure provided us with about 40 3D particle positions per frame. As discussed above, some particles were found to be in little aggregates of two or three particles. In an attempt to also find the distances between the particles in these clusters, we kept the maximum distance in the lateral directions that we allowed found centroids to belong to the same particle small, 1.2 particle radius. Due to the fringes of other particles in different planes, further away, this strategy may have caused some false positives.

In Figure 2.3 **a**, we give the dependence of the fraction of the volume occupied by the particles,  $\eta$  on the depth. We did this by binning the  $z$ -coordinates of all the particles to  $200 \text{ nm}$  boxes after which the number of particles at each depth was divided by the volume of the pillar boxes and the number of frames, 643, that contributed to the particle coordinates. There is a clear peak in the distribution of particle depths at a distance of about  $18 \mu\text{m}$  from the hologram plane. Above that height the volume fraction rapidly falls off in what appears to be an exponential decay.

In reference [25] several regimes for the sedimentation profiles were proposed, depending on the volume fraction and the long range interactions between the particles. For the lowest volume fractions, on top of the distributions an exponential decay governed by the particle weight was assumed. At intermediate volume fractions a linear relation between the particle density and the depth was predicted and experimentally found. At even higher volume fractions, again an exponential relation was proposed in which the length scale was modified by the particle charge. The left side of the density distribution in Figure 2.3 **a** suggests that the interactions between the particles and the sample bottom were rather long-ranged. This can also be seen from the shape of the  $g(\mathbf{r})$  in Figure 2.3 **b** and **c**. The  $g(\mathbf{r})$  for the lowest volume fraction of  $0.13 \cdot 10^{-3}$  did also take part of the tail for the density distribution, from which we determined the particle weight, into consideration. The peak in the  $g(\mathbf{r})$  however, is likely not present in the top  $15 \mu\text{m}$  of the distribution. The 247 particles that were found at these heights over

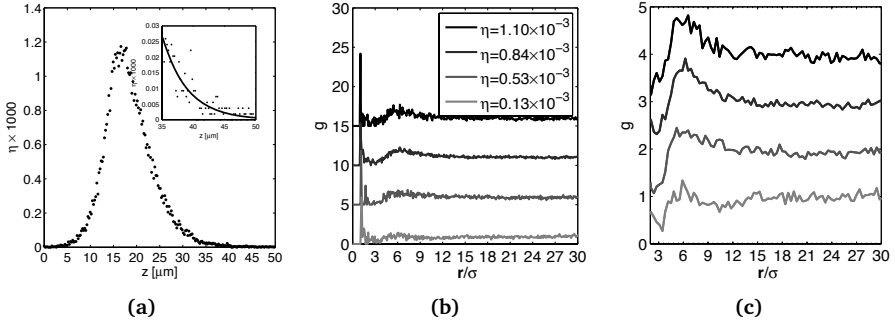


**Figure 2.3:**  $g(r)$  of a titania/silica spheres in CHC at four volume fractions. **a.** The depth dependence of the volume fraction of a liquid of  $1.4 \mu\text{m}$  titania/silica particles at an average volume fraction of  $\sim 2 \cdot 10^{-4}$  in CycloHexane Chloride. We acquired 643 holographic snapshots like the one shown in Figure 2.2 a. From these, we holographically determined 24,000 sets of particle coordinates. The distances between the particles were binned in bins of  $100 \text{ nm}$ . The full line in the inset is a fit to the barometric profile. **b.** The  $g(r)$  at four different volume fractions. The particles were separated into four groups based on the local volume fractions in the range from 0 to 0.4, from 0.4 to 0.7, from 0.7 to 1 and from  $1$  to  $1.3 \times 10^3$ , this resulted in average volume fractions of respectively  $0.13$ ,  $0.53$ ,  $0.84$  and  $1.10 \times 10^{-3}$ . The  $g(r)$  was calculated from the respectively 5366, 5829, 8534 and 4645 particle positions, yielding respectively 27166, 28025, 58641 and 17684 inter-particle-distances. The distances were binned in bins of a twelfth of the particle diameter. The  $g(r)$ 's were offset for clarity. **c.** The same as in **b** but plotted from  $r/\sigma = 3$ , to study the longer ranged behavior in more detail. Here the distances were binned in bins of a third of a particle diameter.

the 643 frames that were analyzed, could not be used to determine a  $g(r)$ . We assume that the volume fraction here was low enough to assume a barometric density distribution.

The probability distribution for the particles that were found more than  $35 \mu\text{m}$  above the hologram plane was fit to  $Ce^{-m_gz/k_B T}$  where  $C$  is a constant,  $m$  the mass of the particle,  $g$  the gravitational acceleration and  $k_B T$  Boltzmann's constant times the absolute temperature. This equation describes the equilibrium barometric distribution that is the result of the competition between sedimentation and diffusion.  $C$  and  $m$  are used as fitting parameters. We found that the effective mass  $m$  of the particle was  $1.04 \text{ pg}$ . Given the particle radius of  $700 \text{ nm}$  and the density of the CHC,  $0.99 \text{ g/cm}^3$ , this results in a density of the particles of  $2.03 \text{ g/cm}^3$ . The density of anatase titania is  $3.79 \text{ g/cm}^3$  [26], while the density of silica is around  $1.9$  [7]. In section 2.5.2 we will demonstrate that titania particles just after synthesis are porous. By sintering them in the oven the particles shrank to less than a sixth of their volume. Part of the volume of the pores was filled with silica. The remaining pores may contain some ethanol and may be partially filled with CHC. From density matching in mixtures of bromoform and methanol [27], it was found that the density of these particles indeed lies in between  $2$  and  $2.05 \text{ g/cm}^3$ , in agreement with the mass found from the barometric

tail of the distribution.

Also below the maximum in the depth distribution, we see that the volume fraction rapidly decreases. The particles cannot sediment any deeper due to charge repulsion of the bottom of the capillary. The bottom of the capillary is similar to silica and is charged while the screening is minimal. In section 3.4 we present force measurements on the interaction between silica coated PS particles in CycloHexyl Bromide, CHB, which is chemically and electrostatically similar to, CHC. Here, the charge of the silica spheres was determined to be 1140 elementary charges and a Debye screening length of  $9,72 \mu\text{m}$  was found. The apparent repulsion between the bottom of the capillary and the particles is in accordance with similar parameters.

From the distribution of the particle positions, we can also calculate the  $g(\mathbf{r})$ . From Figure 2.3 **a** we see that the volume fraction is not uniform. We therefore chose to divide the data over four groups based on the volume fractions in the range from 0 to 0.4, from 0.4 to 0.7, from 0.7 to 1 and from 1 to  $1.3 \times 10^{-3}$ , this resulted in average volume fractions of respectively 0.13, 0.53, 0.84 and  $1.10 \times 10^{-3}$ . The  $g(\mathbf{r})$  was calculated from the respectively 5366, 5829, 8534 and 4645 particle positions, yielding respectively 27166, 28025, 58641 and 17684 inter-particle-distances and is shown in Figure 2.3 **b** and **c**.

At short distances, up to around 2 diameters, we do find some particles, see Figure 2.3 **b**. Some of these were really there, in little clusters as could be seen in Figure 2.2. Others may be due to false positives. The height of the peak of around 10 at a distance of about 1 particle diameter in the densest  $g(\mathbf{r})$ , seems surprising at first. What this means is that the number of particles found at that distance was 10 times higher than the number of ideal gas molecules that one expects at that distance. Integrating  $4\pi g(\mathbf{r})r^2$  from  $r = 1$  to 2 and multiplication with the number density of per cubic diameter tells us that 1 % of the particles had another particle closer than 2 diameters away. At the other volume fractions we found less pairs. The peak at distance 1 in the  $g(\mathbf{r})$  for the lowest volume fraction is due solely to pairs in the lower region of the density distribution. The pairs are heavier than the single particles and pairs are also more likely to form at the higher volume fractions in the lower layers.

There is a minimum in the  $g(\mathbf{r})$ , apparently there were hardly any particles at a distance of about 3 diameters due to the large charge repulsion. There is a broad maximum in the  $g(\mathbf{r})$  around 6 diameters distance. Soon after that, the radial distribution flattens at unity, indicating there is no correlation. We note that the difference in the  $g(\mathbf{r})$  for volume fractions between  $10^{-4}$  and  $10^{-3}$  is small. The broad peak is displaced slightly to shorter distances and is more pronounced for the volume fractions 0.84 and  $1.1 \times 10^{-3}$ .

## Conclusion

We have shown that digitally reconstructed in-line holographic microscopy can be used to study the phase behavior of dilute colloidal (volume fractions  $\sim 10^{-3}$ )

dispersions by means of the  $g(\mathbf{r})$ . Particle positions are determined within 150 nm in the in-plane direction and to within 500 nm in the out-of-plane positions from single holographic snapshots. To study these samples, other real space techniques, like confocal microscopy, are too slow and involve much larger data sets. For the system analyzed in this section one could use a hybrid technique where confocal microscopy is used to examine the clusters, although it would be demanding great patience of the experimenter to focus the confocal on sufficiently many different clusters. One may expect little extra information from this when the particles are indeed bound by van der Waals attractions as the thermal excursions are likely to be smaller than the resolution of the confocal. In-line holographic microscopy might be applied to evaluate the behavior of dilute dispersions.

### 2.2.3 Back propagating a silica rod

Holographic microscopy is not limited in its application to spherical particles. Using the geometrical magnification that is inherent to point source illumination it has proven possible to study 3D structures within a single cell [28–30]. In-line holographic microscopy has been shown to be applicable to study the diffusion of copper oxide nano-rods [6].

Low index dielectric materials that can be index matched by solvents to allow 3D imaging by confocal laser scanning microscopy (CLSM) have been used before to fabricate anisotropic particles [31–33]. A new synthesis method was used to grow silica rods [34]. Silica has a refractive index of 1.45 and there are various mixtures of solvents in which it can be index matched. In ethanol however, with its refractive index of 1.36, silica scatters quite well. The silica rods were grown a little thicker to increase their scattering [35] and then dispersed in ethanol. Transmission Electron Microscopy, *TEM*, was used to determine that the rods were 1.9  $\mu\text{m}$  long (polydispersity, p.d. 10%) and 420 nm wide (p.d. 16%).

The dispersion was transferred to a rectangular glass capillary (Vitrocom 0.1  $\times$  2.0 mm) and placed on an inverted microscope (Leica DRM-IRB) equipped with a 100 $\times$  NA1.4 PLAN APO objective. The condenser was replaced by a 532 nm HeNe laser (Coherent). A single rod was filmed using a Mikrotron EoSens CE camera. The tube lens of the microscope was replaced by one that increased the magnification of the imaging system further such that a single pixel corresponded with 88.5 nm in the hologram plane.

In Figure 2.4 **a** and **b** we reproduce two snapshots  $B$  that were normalized, as in section 2.2.2, by the averaged intensity distribution in the sequence. The rod, the scattered light which interfered with the remaining part of the illuminating beam, was diffusing around at the bottom of the sample, approximately 10  $\mu\text{m}$  above the focal plane of the microscope. In Figure 2.4 **a**, the rod was oriented in a plane more or less parallel to the hologram plane. In Figure 2.4 **b** we present a typical hologram of when the particle was perpendicular to the plane.

The intensity distribution was again digitally propagated in the  $z$ -direction to find the 3D light distribution above the particle. At each depth, we recorded the

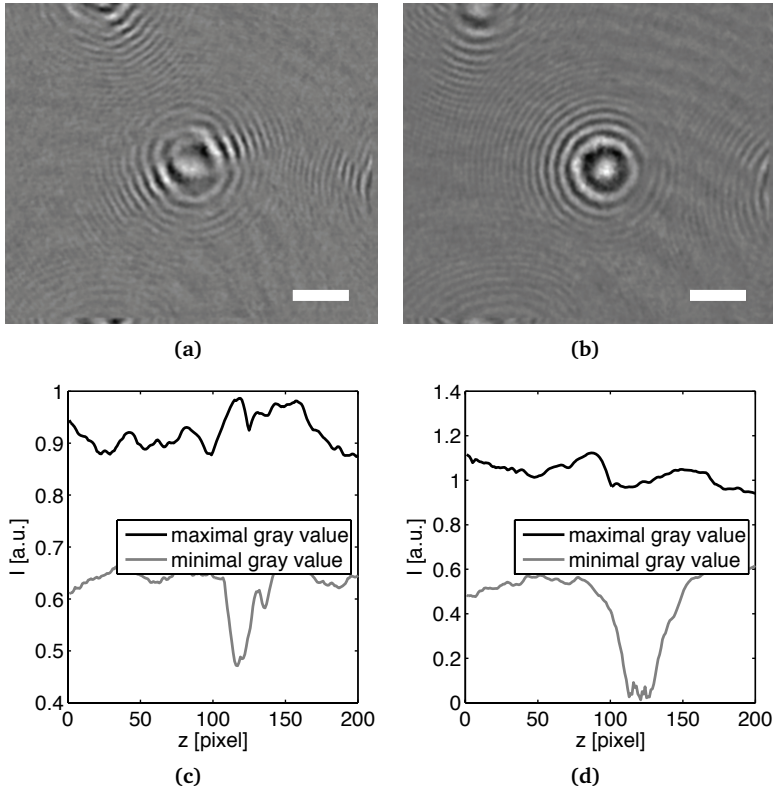


**Figure 2.4:** *In-line hologram of a silica rod in ethanol and Intensity vs.  $z_{\parallel}$ .* **a.** The normalized intensity of the hologram of a silica ( $n=1.45$ ) rod in ethanol ( $n=1.36$ ), that lies in a plane parallel to the hologram. **b.** An in-line hologram of the same rod, somewhat later, as Brownian motion has rotated the rod perpendicular to the hologram. **c, d.** The minimum and maximum intensity as a function of the distance to the hologram plane in pixels. The wavelength of the light was 532 nm and the scalebars are 5  $\mu\text{m}$ .

highest and the lowest intensity, the values of which are plotted for both orientations in respectively Figure 2.4 **c** and **d**. In both graphs there is a clear minimum in the intensity. The minimum in the case where the particle was orientated vertically (**d**) is much deeper than the minimum in the other orientation. We note that the minimum is much wider and has a more or less flat bottom. This is a clear indication that the rod was indeed orientated vertically. Taking the width of the minimum at the intensity value of 0.2 suggests that the particle is 2.2  $\mu\text{m}$  long, in agreement with the length distribution found by means of TEM.

In Figure 2.5 we show the light distribution in the plane where the darkest pixel in the entire  $z$  stack was found. In Figure 2.5 **a**, there is a clear black rod,

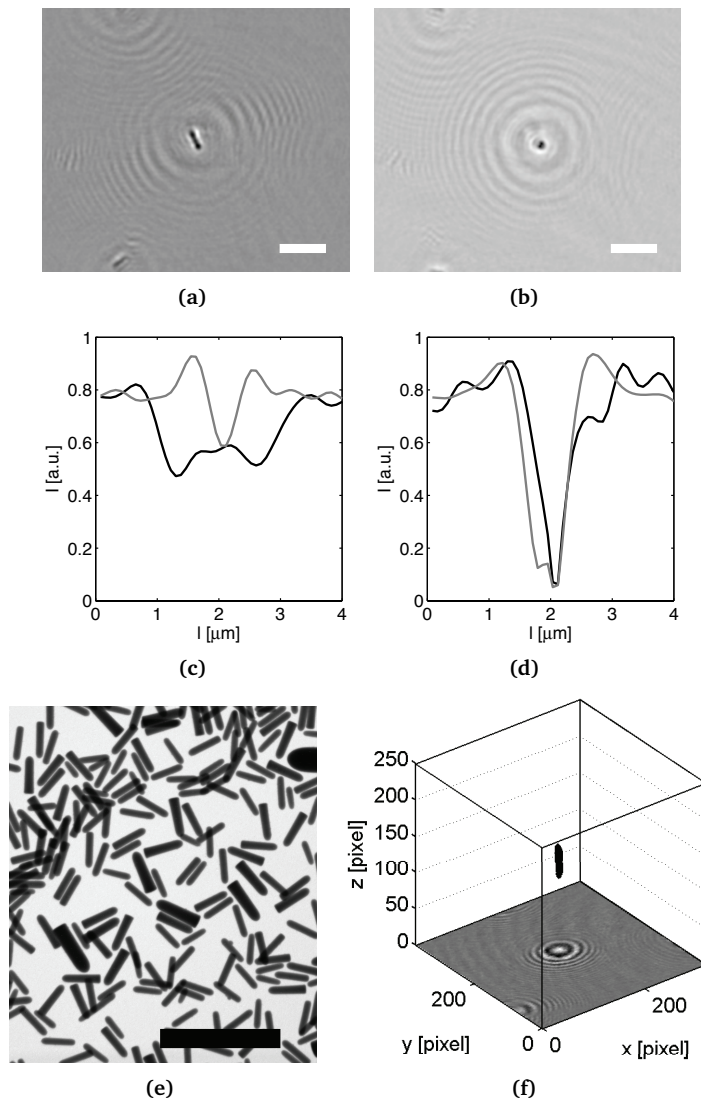


**Figure 2.5:** Holographically regenerated images of a silica rod in ethanol, TEM micrograph and 3D image. **a, b.** The intensity distribution of the plane in which the rod in Figure 2.4 was found. **c, d.** The intensity along and perpendicular to the rod in respectively **a, b.** **e.** A Transmission Electron Micrograph of the rods in the sample. **f.** A 3D representation of the vertical rod. All voxels with a normalized intensity lower than 0.4 were made black. At the bottom of the cube we projected the hologram. The wavelength of the light was 532 nm and the scalebars are 5  $\mu\text{m}$ .

while in the **b** section there is just a black dot. The intensity as a function of the distance along the rod, and perpendicular to the rod is plotted in Figure 2.5 **c** and **d**. The length of the rod as determined by looking at the length of minima (threshold at 0.6) was determined to have been  $1.83 \mu\text{m}$ , well within the distribution around the average length from TEM pictures as in Figure 2.5 **e**. The dip in the intensity in the direction perpendicular to the rod has a full width at half maximum of  $\sigma$  of  $520 \text{ nm}$  which, considering the broadening dip due to diffraction  $\sigma = \sigma_0 - 0.5\lambda^2/n_m^2$  [6], suggests that the rod was  $\sim 440 \text{ nm}$  in diameter, again in accordance with the TEM results. In 2.5 **f** we give an impression of the three dimensional intensity distribution by plotting in black all the voxels where the intensity was smaller than 0.4 in the back propagated stack for the vertical rod.

## Conclusion

We have shown that digital in-line holographic microscopy can be used to track and characterize silica rods in ethanol. These results for silica rods are similar to those obtained for colloidal copper oxide rods in reference [6], although this silica rod is shorter. Similar intensity-weighted skeletonization can be applied to study the (rotational) diffusion and sedimentation of silica rods.

## 2.3 Lorenz-Mie-Debye Scattering

Due to surface tension, a sphere is often a good approximation of the shape of droplets in clouds, but also for many colloids. The simplest shape for a scattering particle is that of a sphere. To analytically describe the scattering by a sphere, the Maxwell equations [36] need to be solved with the right boundary conditions on a spherical surface. It has already been quite a while since the problem posed by the scattering of a sphere of arbitrary radius and refractive index was analytically tackled, however it is unclear when this was done for the first time.

In 1908 Gustav Mie developed the theory, by solving the Maxwell equations, to explain the bright colors of dispersions of colloidal gold in water [37]. In the same period Peter Debye independently developed the solution to these equations while working on his PhD thesis on the radiation pressure as experienced by small particles in space [38]. Eighteen years before the famous paper by Gustav Mie was published, the Dane Ludvig Lorenz presented the theory in 1890 [39, 40]. Generally, the theory is referred to as Mie theory or Lorenz-Mie theory [3] but since also Peter Debye independently developed the theory, perhaps it is better to call it the Lorenz-Mie-Debye theory. Gustav Mie has gained the greatest fame for this feat, probably because he applied the theory to a practical example that fascinates.

Although the theory as such has been around for quite a while, the broad application to calculations had to wait until sufficiently powerful digital comput-

ers became available [3]. The scattering by the particles is most conveniently written as a series expansion in spherical harmonics, that converges rather quick (depending on the particle size and typically in less than 30 terms) [3, 41]. In section 2.3.1 we will not reproduce the derivation but we will limit ourselves to giving the solution. Then, we will apply the Lorenz-Mie-Debye theory to simulate in-line holograms by letting the theoretical wave fields interfere with the exciting beam. Consequently, we will briefly explore the colloidal parameter space to see what sort of holograms we may experimentally observe.

### 2.3.1 The formulae

First we need to define the scattering plane. We assume that the scatterer is illuminated by plane waves traveling along the  $z$ -direction that are linearly polarized in the  $x$ -direction. For convenience we place the origin of our frame of reference in the center of the particle. Sufficiently far away from the particle ( $k\rho \ll 1$ ), so multiple wavelengths away from the particle, the scattered electric field  $\vec{S}$  is transverse, *i.e.* is perpendicular to the direction in which the wave propagates. The direction in which the scattered wave propagates is called  $\vec{\rho}$  with length  $\rho$ , in the direction  $\hat{\rho}$ .

$\vec{\rho}$  makes an angle  $\theta$  to the optical axis, the  $z$ -axis, and an angle  $\phi$  in the  $xy$ -plane. The so-called scattering plane is uniquely defined by  $\theta$  and  $\phi$ . The scattering of single dielectric spheres is polarization maintaining. When  $\phi$  is zero or  $\pi$ , so when the scattering plane is the  $xz$ -plane, the scattered wave lies completely within the scattering plane. When  $\phi$  is  $\pi/2$  or  $3/2\pi$  the scattering plane is the  $yz$  plane and the scattered wave is purely perpendicular to the scattering plane. In other possible scattering planes, the polarization is still linear but lies partially in the scattering plane and partially perpendicular to the scattering plane.

The relation between incident and scattered fields can be written in matrix form:

$$\begin{pmatrix} E_{\parallel s} \\ E_{\perp s} \end{pmatrix} = \frac{e^{ik(\rho-z_h)}}{-ik\rho} \begin{pmatrix} S_1 & 0 \\ 0 & S_2 \end{pmatrix} \begin{pmatrix} E_{\parallel i} \\ E_{\perp i} \end{pmatrix}. \quad (2.10)$$

Here the subscripts  $i$  and  $s$  denote the illuminating and the scattered wave, and  $\parallel$  and  $\perp$  denote the polarization parallel and perpendicular to the scattering plane. The matrix elements  $S_1$  and  $S_2$  depend on the angle  $\theta$ , the relative refractive index of the particle  $m = n/n_{\text{med}}$  and the particle size  $\beta = kr$ , with  $r$  the radius of the sphere.

Figure 2.6 sketches the situation when the scattering plane is in the  $yz$ -plane. The illumination is polarized in the  $x$ -direction and so is the scattered field. The scattered field thus points in the  $\hat{e}_{\parallel}$  direction.

The matrix elements  $S_1$  and  $S_2$  in the far field are given by the series:

$$S_1 = \sum_n \frac{2n+1}{n(n+1)} (a_n \pi_n + b_n \tau_n), \quad (2.11)$$

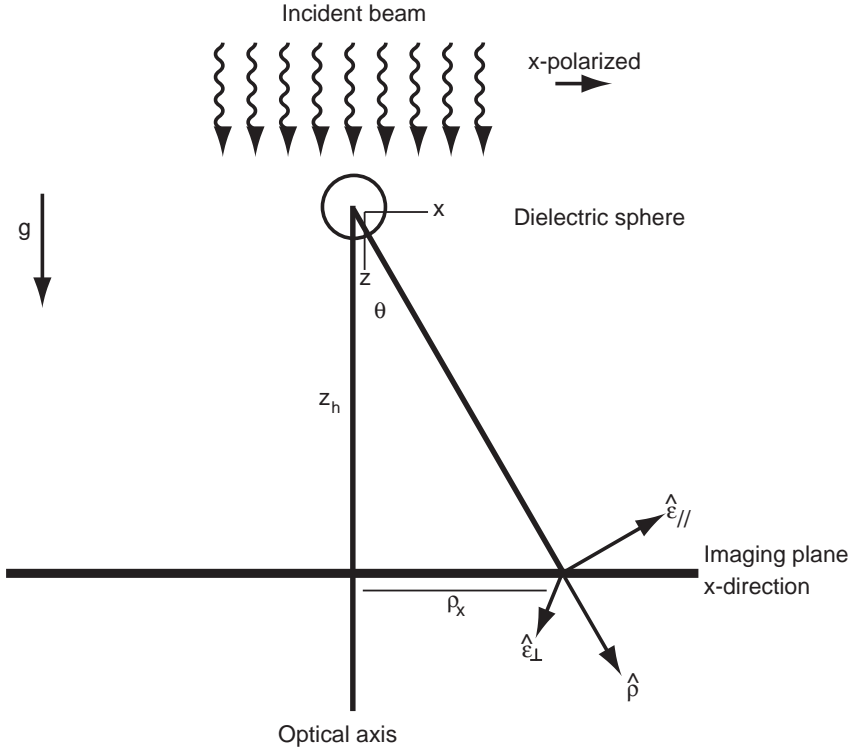


**Figure 2.6:** The scattering angles when the scattering plane is the  $yz$ -plane. The vector  $\vec{\rho}$  connects the center of the scattering colloid with a pixel at a radial distance  $\rho_{xy}$  within the hologram plane. The scattered electric field consists of two orthogonal contributions in the  $\vec{\epsilon}_{\perp}$  and  $\vec{\epsilon}_{\parallel}$  direction respectively perpendicular and parallel to the scattering plane.  $g$  Indicates the direction of gravity. The polarization of the light is assumed linear and oriented in the  $x$ -direction.

and

$$S_2 = \sum_n \frac{2n + 1}{n(n + 1)} (a_n \tau_n + b_n \pi_n). \tag{2.12}$$

Here  $\pi_n$  and  $\tau_n$  are the angle dependent functions,

$$\pi_n(\theta) = \frac{P_n^1(\theta)}{\sin(\theta)}, \quad \text{and} \quad \tau_n(\theta) = \frac{dP_n^1(\theta)}{d\theta}, \tag{2.13}$$

where  $P_n^1(\theta)$  is the associated Legendre polynomial. We find the scattering coefficients  $a_n$  and  $b_n$  for a dielectric sphere in the textbook by Craig F. Bohren and Donald R. Huffman [3]. These scattering coefficients are the coefficients in the expansion in spherical harmonics of the light scattered by a homogeneous spherical

particle under irradiation with a plane wave, as given by the Lorenz-Mie-Debye theory [37, 39, 40].

$$a_n = \frac{m\psi_n(m\beta)\psi_n'(\beta) - \psi_n(\beta)\psi_n'(m\beta)}{m\psi_n(m\beta)\xi_n'(\beta) - \xi_n(\beta)\psi_n'(m\beta)} \quad (2.14)$$

and

$$b_n = \frac{\psi_n(m\beta)\psi_n'(\beta) - m\psi_n(\beta)\psi_n'(m\beta)}{\psi_n(m\beta)\xi_n'(\beta) - m\xi_n(\beta)\psi_n'(m\beta)}. \quad (2.15)$$

Here  $\psi_n(x)$  and  $\xi_n(x)$  denote the Ricatti-Bessel functions  $xj_n(x)$  and  $xh_n^{(1)}(x)$  respectively, while the prime indicates differentiation with respect to the argument.  $\beta = kr$  refers to the particle size parameter. The scattering coefficients fall off rapidly with order  $n$ , and the series is found to converge after a number of terms  $n_c = kr + 4.05(kr)^{1/3} + 2$  [3]. Generally, for the colloids used in this thesis the series converged in less than 30 orders. We used Christian Mätzler's Matlab<sup>®</sup> code [42] to calculate the scattering coefficients. Possibly, this implementation of the Lorenz-Mie-Debye theory suffers from numerical instabilities for certain parameters [3, 41, 43]. However for the moderate particle sizes used ( $\beta < 20$ ) we do not expect problems.

The theory for the scattering of spherical particles has been extended to particles with a core-shell structure where the core is coated with another dielectric with a different refractive index [44]. The scattering coefficients for such particles are similar to those for homogeneous particles and are quoted in section 5.6.

The Lorenz-Mie-Debye theory [37–40] can be used to characterize colloidal particles by measuring the scattered intensity as a function of the scattering angle  $\theta$ , often with the azimuthal angle  $\phi$  kept constant at 0. In these Static Light Scattering (SLS) experiments, a dilute suspension of colloids is illuminated from one direction, usually by a laser beam, and the detector is rotated around the sample [45]. When the sample is dilute enough, the light is on average only scattered once and the intensity curve can be compared with calculations to find the size of the particles.

In Figure 2.7 we present two typical SLS curves, both for a 1.4  $\mu\text{m}$  silica ( $n = 1.45$ ) particle in ethanol ( $n = 1.36$ ), illuminated with a 532 nm (green) laser. The two curves differ only in the scattering plane. The black curve depicts the scattering intensity as a function of the scattering angle when the polarization is perpendicular to the scattering plane. The grey line gives the scattering intensity when the scattering plane is parallel to the scattering plane. The number and position of the minima in the intensity depend strongly on the particle size. Particle characterization by means of SLS relies on measuring these minima and trying to fit the particle size, and not to forget, the polydispersity of the particles to mimic the recorded scattering behavior. In SLS measurements, multiple particles contribute to the scattering behavior. When these particles are not all identical, the minima in their individual scattering curves will be different. The

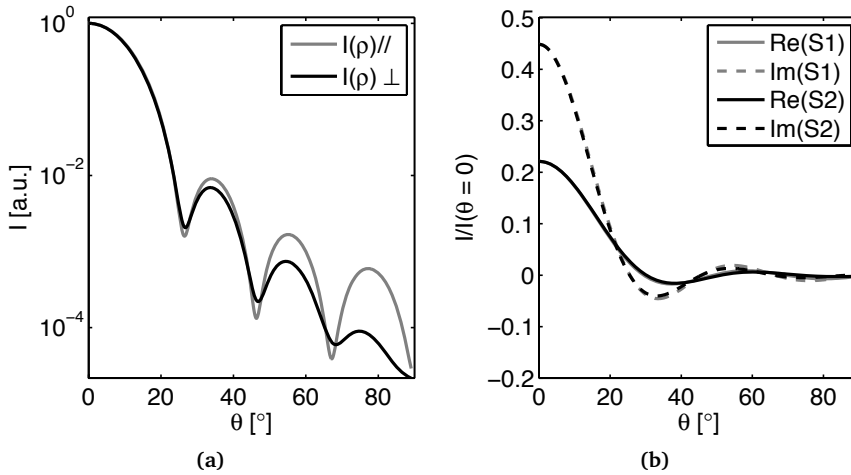


**Figure 2.7:** The Lorenz-Mie-Debye scattering of a silica sphere in Ethanol. **a.** The scattered intensity of  $1.4 \mu\text{m}$  silica sphere in ethanol as can be measured by SLS in the two polarization directions. **b.** The EM wave as scattered by a  $1.4 \mu\text{m}$  silica sphere in ethanol as a function of the angle theta.  $S_1$  describes the scattering in the plane of polarization while  $S_2$  describes the scattering in the plane perpendicular to it. The wavelength of the light here is  $532 \text{ nm}$ .

recorded intensity is the sum of the scattered intensities so the minima in the scattering curve for polydisperse particles are less sharp and less deep.

The scattered electric fields that do not only have an intensity but also a phase which also depends on the particle characteristics. In Figure 2.7 **b** we plot the real and the imaginary part of the scattered field. The phase of these waves is taken relative to the illuminating beam at the particle location

### 2.3.2 Interference between illuminating and scattered light: the hologram

The scattered wave interferes with the remaining illumination beam as described by equation 2.1. This also happens in the *image plane* in Figure 2.6. As the scattering is different between the  $x$ -direction, parallel to the polarization, and the  $y$ -direction perpendicular to the polarization, the intensity of the interference in the two directions differs (slightly). By considering the different optical path lengths to the points in the image plane and thus the relative phase, the light intensity at any point in the image plane can be calculated.

In Figure 2.8, the intensity of the interference pattern, relative to the intensity of the illuminating beam,  $B$ , is plotted for both the direction parallel and perpendicular to the polarization. As the particle scatters different fields in different directions  $\theta$ , the intensity distribution in the image plane is not homogeneous. We

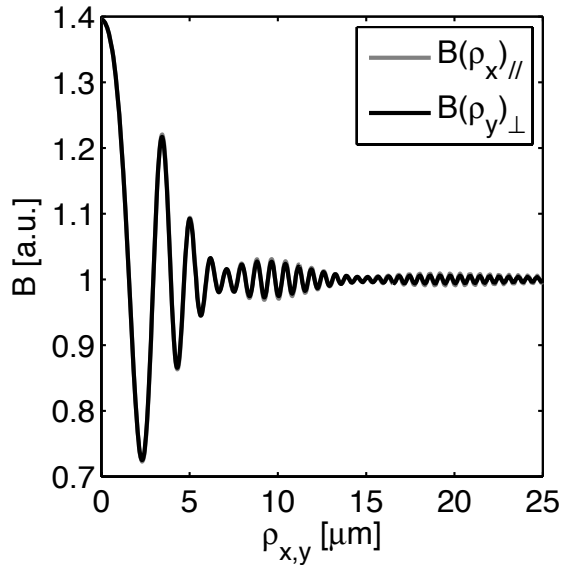


**Figure 2.8:** Interference of the scattered light from a  $1.4 \mu\text{m}$  silica sphere in Ethanol with the illuminating beam. The patterns of interference between the light scattered from a  $1.4 \mu\text{m}$  silica ( $n = 1.45$ ) in ethanol ( $n = 1.36$ ) and the remaining light of the illuminating plane wave for the two polarization directions separately (not visible because the two curves are so similar). The interference has been normalized with respect to the intensity of the illuminating beam. The illuminating beam is assumed to be linearly polarized in the  $x$ -direction. The wavelength of the light here is  $532 \text{ nm}$ . The particle was assumed to be  $14 \mu\text{m}$  above the interfering plane.

note that there are more maxima and minima in the intensity in the image plane than there are in the scattered fields in Figure 2.7. This is the result of the different optical path lengths the light has to traverse to get to the respective locations in the image plane. The distance from the optical axis of the minima and maxima depends to a first approximation linearly on the distance along the optical axis  $z_{\text{h}}$  (see Figure 2.6) between the scattering particle and the image plane, and simple geometry. The envelope on the intensity curve in Figure 2.8 reflects the minima in Figure 2.7, as can be seen from equation 2.10. The difference between the intensity of the interference in the plane parallel to the polarization of the illuminating beam and that in the direction perpendicular to the scattering plane is smaller than the width of the line in Figure 2.8.

If we were to place some recording medium in the image plane  $14 \mu\text{m}$  below a  $1.4 \mu\text{m}$  diameter silica ( $n = 1.45$ ) particle in ethanol ( $n = 1.36$ ) we would record the intensity as plotted in Figure 2.8 in the  $x$ - and  $y$ -direction, parallel and perpendicular to the polarization of the illuminating beam. In the other directions the recorded intensity is a linear combination between the two curves as a result of the superposition principle. The two curves are very similar to each other. The

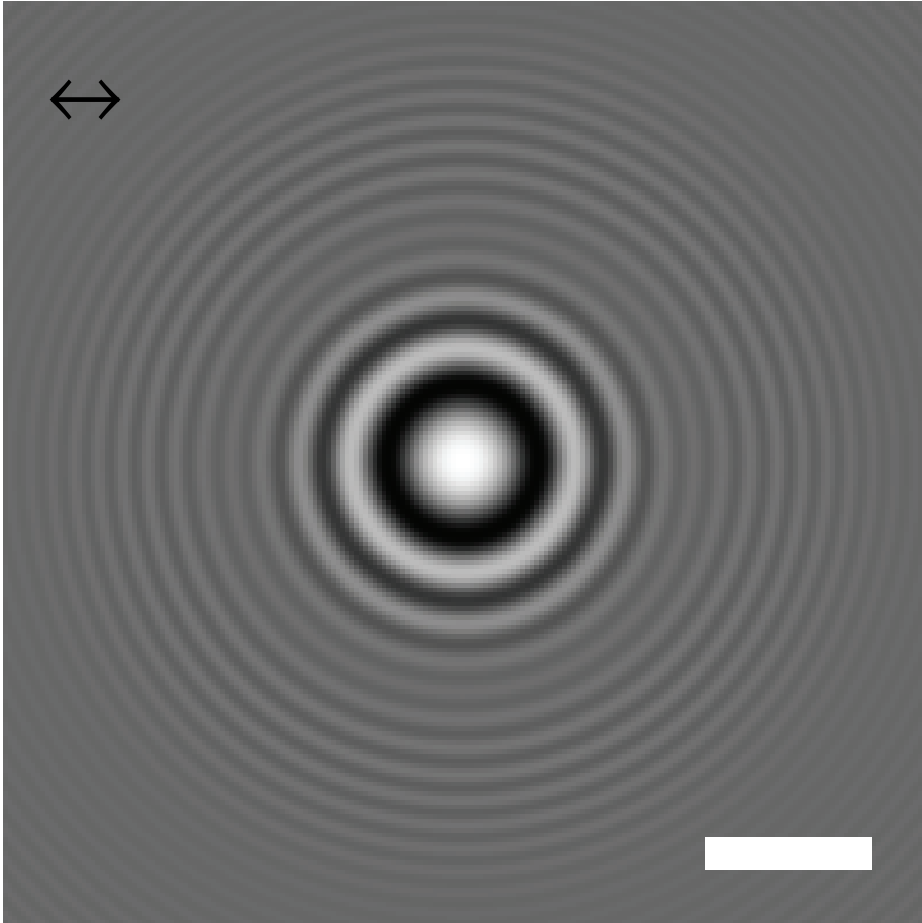


**Figure 2.9:** *In-line hologram from Lorenz-Mie-Debye theory.* The interference pattern between the scattered light from a  $1.4\ \mu\text{m}$  silica ( $n = 1.45$ ) in ethanol ( $n = 1.36$ ) that is located  $14\ \mu\text{m}$  above the image plane and the remaining light of the illuminating plane wave. The double arrow signifies  $x$ -direction, the direction of the polarization. The wavelength of the light is  $532\ \text{nm}$ . The scale bar is  $5\ \mu\text{m}$  long.

calculated intensities can also be represented as a (simulated) in-line hologram. Such an in-line hologram has been reproduced in Figure 2.9, the same Figure as was used in section 2.2.1 to demonstrate digital back propagation.

The polarization of the light in this hologram was oriented along the horizontal  $x$ -direction, as indicated by the double arrow in the upper left corner. In line with the plots in Figure 2.9 there are many concentric rings around a bright spot in the middle. The difference between the hologram in the direction parallel and

perpendicular to the polarization is so small that the finite bit depth (8 or 12) of the cameras used in this thesis does not allow to measure this difference.

For reasons that will be made clear in section 2.4, we will simplify the holograms by assuming that intensity in all directions varies with the distance as the radial average about the azimuth centered in the particle. This means that the intensity in the hologram is assumed to depend only on the length of the projection of  $\vec{\rho}$  on the hologram plane,  $|\rho_{xy}|$ , and not on the azimuthal angle  $\phi$ . The dependence on  $|\rho_{xy}|$  is taken to be the average of the two curves in Figure 2.8.

This radially averaged hologram intensity can be calculated by simplifying equation 2.10 in the following manner:

$$\mathbf{E}_s = \frac{e^{ik(\rho-z)}}{-i2k\rho} (S_1(\theta, \beta, m) + S_2(\theta, \beta, m)) \mathbf{E}_i. \quad (2.16)$$

The scattered electric field  $\mathbf{E}_s$  can then be inserted in equation 2.1 to calculate the in-line hologram, which can then be normalized by dividing by the average intensity distribution [5, 7, 24]:

$$\begin{aligned} B(\vec{\rho}) &= \frac{(\tilde{\mathbf{R}} + \tilde{\mathbf{E}}_s(\rho, \beta, m))(\tilde{\mathbf{R}}^* + \tilde{\mathbf{E}}_s^*(\rho, \beta, m))}{\tilde{\mathbf{R}}\tilde{\mathbf{R}}^*} \\ &= \frac{\tilde{\mathbf{R}}\tilde{\mathbf{R}}^* + \tilde{\mathbf{R}}\tilde{\mathbf{E}}_s^*(\rho, \beta, m) + \tilde{\mathbf{E}}_s(\rho, \beta, m)\tilde{\mathbf{R}}^* + \tilde{\mathbf{E}}_s(\rho, \beta, m)\tilde{\mathbf{E}}_s^*(\rho, \beta, m)}{\tilde{\mathbf{R}}\tilde{\mathbf{R}}^*}. \end{aligned} \quad (2.17)$$

This radial dependence of the intensity of the in-line hologram is equal to that which would be found if circularly or non-polarized light was used for the illumination.

In Figure 2.10, we reproduce the in-line hologram in Figure 2.9 as calculated by equation 2.17, averaging the scattered intensity in the two polarization directions. The difference between Figure 2.10 and 2.9 is not large, as can be seen from Figure 2.11. The relative difference between the intensity in the  $x$ - and  $y$ -direction parallel and perpendicular to the polarization is no larger than 3 parts in thousand of the background intensity, which for normalized holograms is unity. For most pixels, the difference is even smaller as the intensity in directions other than the  $x$ - and the  $y$ -direction are a linear combination of the hologram in these two directions. In general, the difference between the light scattered in the directions parallel and perpendicular to the polarization of the illuminating beam increases with the particle size and with the scattering angle. For the practical purposes discussed in the rest of this thesis, the difference is neglected for the relatively small particles studied and for the limited range of scattering angles  $\theta$  recorded in the holograms. In the following, unless stated differently we will neglect the difference between the hologram intensities in the direction parallel and perpendicular to the polarization of the illuminating beam. Conversely we will plot the radially averaged intensities versus the length of the projection of  $\vec{\rho}$  on the hologram plane,  $\rho_h$ .

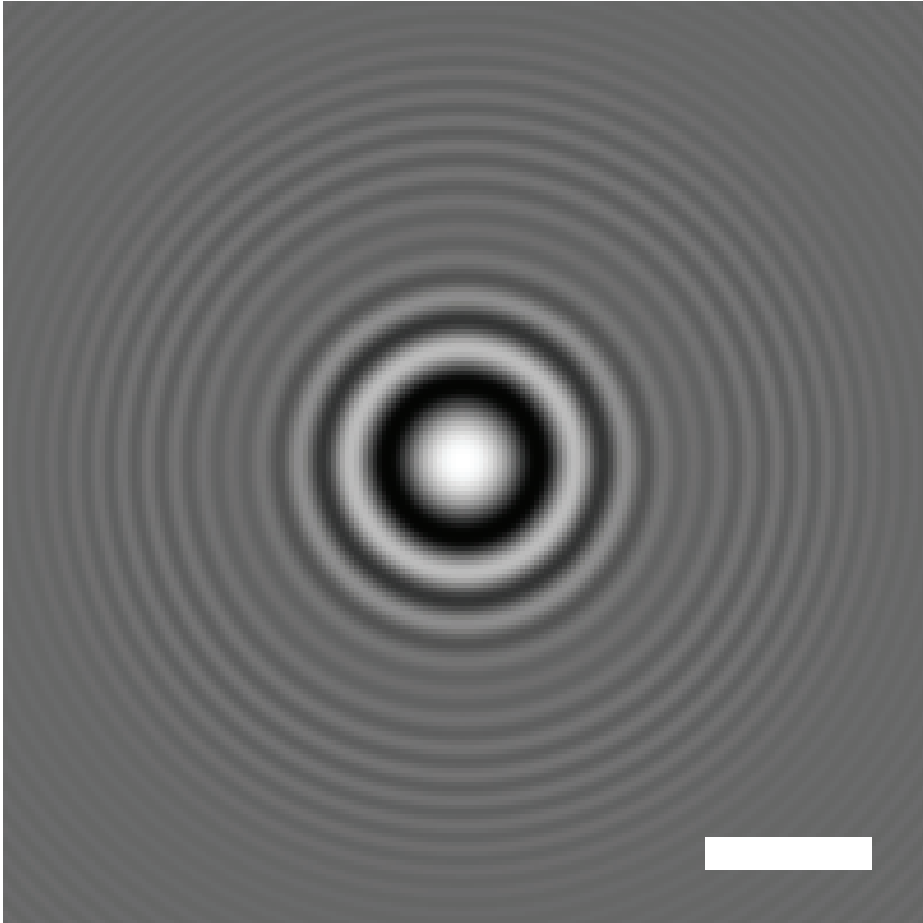


**Figure 2.10:** *In-line hologram from Lorenz-Mie-Debye theory.* The interference pattern between the scattered light from a  $1.4 \mu\text{m}$  silica ( $n = 1.45$ ) in ethanol ( $n = 1.36$ ) that is positioned  $14 \mu\text{m}$  above the image plane and the remaining light of the illuminating plane wave. Contrary to in Figure 2.9, the intensity in all directions is assumed to be equal to the intensity averaged over the polarization. The wavelength of the light is  $532 \text{ nm}$ . The scale bar is  $5 \mu\text{m}$  long.

In the experiments the in-line holograms are magnified by the microscope objective as described in Sheng *et al.* [4]. The hologram is recorded on a CCD chip, in a plane conjugate to the focal plane of the microscope in the sample, about  $40 \text{ cm}$  away from the physical hologram plane. As a result, the only components of the electric field around the scattering particle contributing to the intensity of the hologram are the propagating parts. Near field evanescent waves that are present in the immediate vicinity (closer than  $\sim \lambda$ ) of the particle under investigation are

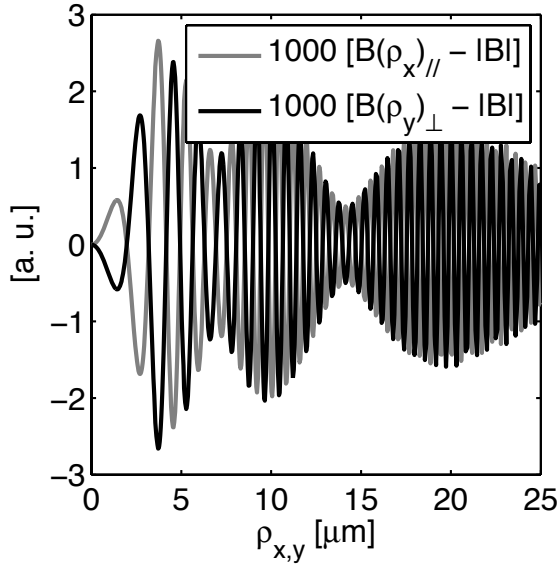


**Figure 2.11:** Difference between the two directions parallel and perpendicular to the polarization and the radially averaged intensity. The difference between the intensity in the  $x$ -direction and the  $y$ -direction, parallel and perpendicular to the polarization of the illuminating beam respectively, relative to the radially averaged intensity. The difference between the in-line hologram in Figure 2.10 and the one in Figure 2.9 are thus no greater than 7 %. The wavelength of the light is 532 nm.

not propagated to the CCD. The paraxial approximation [3] that was applied in the formulation of equation 2.10 and 2.16 is assumed to be applicable in the analysis of in-line holograms of particles that are more than  $\sim 4 \mu\text{m}$  away from the hologram plane.

In the following we will first discuss the influence of the particle position and particle parameters on the holograms. Then, we will discuss a practical method to solve the inverse problem posed by an experimental hologram in section 2.4. Some examples of this method will be presented in section 2.5 where single particles are analyzed. Finally, in section 2.6, we will look at examples of holograms of multiple particles. In the same section we will give examples of how digital in-line holographic microscopy can be applied to study the behavior of multiple particles assembled together into a string.

### 2.3.3 An overview of the effect of the particle position, radius and refractive index on the hologram

As is clear from the above, the exact intensity distribution in an in-line hologram depends on both the particle characteristics and on the particle position. We first,

section 2.3.3, discuss the influence of the particle position on the hologram. Then in section 2.3.3, we discuss the effect of the radius of the particle on the way the particle scatters light and the effect on the hologram. We proceed in section 2.3.3 with a discussion on the effect of the refractive index of the particle on its scattering and on the holograms. Finally, in section 2.3.3 we give an overview of combined effect of the radius and refractive index.

### The effect of the particle position

Since in in-line holography a parallel beam is used both for the illumination and as the reference beam, the lateral position of the particle corresponds directly to the in plane position of its hologram. As can be understood from the triangle in Figure 2.6, the axial position of the particle has more effect on the shape of the hologram. The hologram is stretched simply because the scattered waves diverge. The position on the hologram plane where the light that was scattered in the  $\theta$  direction interferes with the reference beam depends on the position of the particle in the lateral directions and on the depth  $z_h$  times the tangent of  $\theta$ . The amplitude of the scattered wave goes like  $1/\rho$  and the intensity goes like  $1/\rho^2$ . To a first approximation, the effect of increasing the distance  $z_h$  between the particle and the hologram is thus a magnification and a fading of the hologram, both linear in  $z_h$ .

The actual effect on the hologram of a displacement in the  $z$ -direction is the result from interference and depends on the phase of the light. The phase of the scattered light relative to that of the reference beam in the hologram plane depends on the distance along the hypotenuse of the triangle. At a constant angle  $\theta$  the phase difference with the reference beam obviously is a periodic function of the depth  $z_h$ . But as the hologram consist of light scattered in many directions  $\theta$ , the in-plane dependence of the phase difference between the scattered light and the reference beam is unique for one particular depth, even when scaling out the depth dependent magnification. As a result, it is a simplification to say that moving the particle twice as far from the hologram plane results in magnifying the hologram by a factor of two.

In Figure 2.12 **a** we plotted the radial intensity profile for a  $1.4 \mu\text{m}$  silica sphere in ethanol, at a range of different depths. For clarity, each curve was given a different offset. In Figure 2.12 **b** we placed many radial averages of holograms for different depths  $z_h$  in a row.

The first impression of Figure 2.12 is that the first maximum does not occur at the same angle  $\theta$  when the depth of the particle is changed. Instead, all maxima shift towards smaller angles with increasing depth  $z_h$ . This is the result of the phase difference that is non constant for a fixed angle with increasing depth  $z_h$ . The result is that the angles at which constructive interference between the scattered light and the plane waves takes place change.

In Figure 2.12 **b** the location of the maxima do not only change in the  $\theta z$ -plane, but the brightness of the rings also changes with the depth. The central

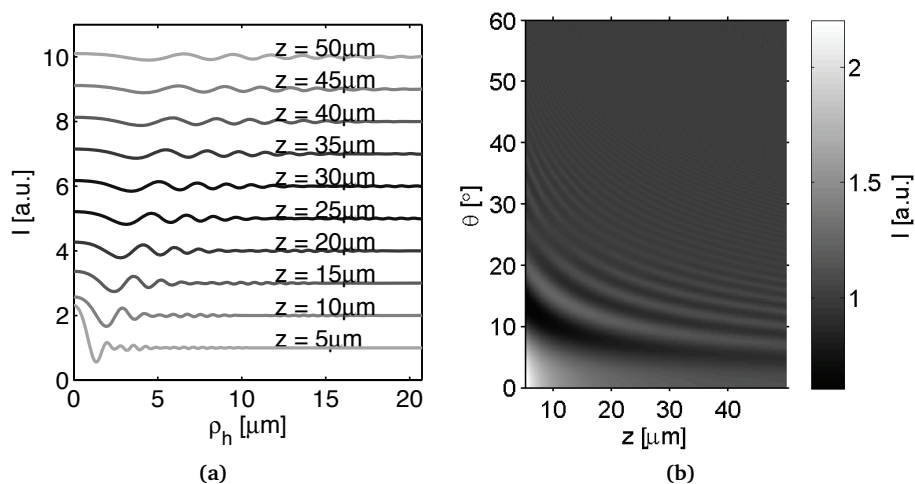


**Figure 2.12:** In-line hologram from Mie-Lorenz theory as a function of the depth. **a.** The normalized intensity of the hologram of a  $1.4\ \mu\text{m}$  silica ( $n=1.45$ ) particle in ethanol ( $n=1.36$ ) plotted versus the radial distance in the hologram plane with the optical axis, as a function of the distance  $z_h$  along the optical axis. For clarity the curves have been given different offsets. **b.** The same as in **a** but here the intensities are represented by grey values in the  $\theta z_h$ -plane. The wavelength of the light was taken to be  $532\ \text{nm}$ .

peak gets relatively less bright with increasing depth.

The increased size of the rings at greater depths  $z_h$  makes it easier to register them on a CCD chip with finite pixel size. The diminished brightness of the central spot eases the demands for the dynamic range of the camera used. Whenever there is the possibility to choose  $z_h$ , and whenever the particle scatters enough light to also discern the somewhat fainter rings when the particle is at greater depths, possibly by manipulating also the sensitivity or integration time of the camera, it is recommendable to increase  $z_h$ , increasing the number of pixels that contribute information about the hologram.

### The effect of the particle radius

As stated before, the radius of the particle strongly influences the scattering. The exact dependence of the brightness and the phase of the scattering is given by equations 2.10 through 2.15. In general, one can state that for particles that are larger than the wavelength of the light, one observes minima in the scattering intensity. The larger the particle, the more minima and the closer the first minimum is found to the forward direction.

The important parameter is not so much the size of the particle, but more the size of the particle relative to the wavelength of the light used for the holography.

Particles that are much smaller than the wavelength of the light, behave as point scatterers and are often referred to as Rayleigh particles. Here the scattering is isotropic and the only effect of the size of the particle on the scattering is that the strength of the scattering changes with the polarizability and thus with the volume of the particle. Since in in-line holography the illuminating beam is the same as the reference beam, the reference beam tends to be relatively strong for weakly scattering particles. The advantage of in-line holography is that since the illuminating beam is recorded, one measures the absolute scattering strength of the particles.

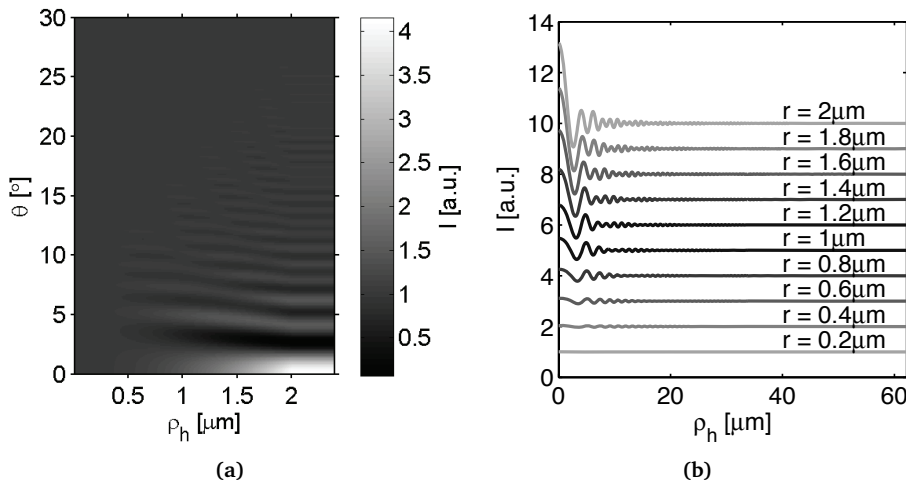


**Figure 2.13:** In-line hologram from Mie-Lorenz theory as a function of the particle radius. **a.** The normalized intensity of the hologram of a silica ( $n=1.45$ ) particle in ethanol ( $n=1.36$ ) versus the angle with the optical axis, as a function of the particle radius. The particle was assumed to be  $30\ \mu\text{m}$  above the image plane. **b.** The same as in **a** but as curves. For clarity the curves have been given different offsets. The wavelength of the light was taken to be  $532\ \text{nm}$ .

As the particles get larger, the scattering starts to become anisotropic. Relatively more and more light is scattered in the forward directions. A first minimum is formed and, as the particle gets larger, this minimum moves towards smaller angles. As the hologram is recorded on a finite plane, and because we use a microscope objective with a finite numerical aperture to magnify the interference pattern in the focal plane, this minimum is not immediately visible using in-line holographic microscopy. The finite numerical aperture of the microscope lens is, for most particle sizes, not the limiting factor in our setup for the holographic characterization because the amplitude of the scattered field at larger angles is small with respect to the scattering in the forward directions. The particles generally scatter so little light to larger angles that the associated fringes would not be registered by the finite bit depth of the camera.

From Figure 2.13 **a** can be seen that the minimum for the smallest particle for silica particles in ethanol, illuminated with 532 nm light, is observed for particles that are around 750 nm in radius. This minimum is found at an angle of around 15° as a region where the amplitude of the intensity variation has a minimum. For particles smaller than this, the angular dependence of the scattered field, though less characteristic, certainly does vary with the particle size.

When the particle gets even larger, the first minimum moves towards smaller scattering angles and more minima appear. These minima act as an envelope over the amplitude of the oscillations in the hologram intensity. This is particularly visible from the curves for the particles larger than 1 μm in Figure 2.13 **b**.

### The effect of the refractive index

The particle under investigation only scatters light if it gets polarized by an exciting beam. This requires that the particle has an index of refraction different from the refractive index of the surrounding medium. The relative refractive index determines how much the particle is polarized but also how it scatters the light. For large particles ( $r \gg \lambda$ ), where one can apply ray optics, it is easy to understand that the relative refractive index does not change the directions into which the light is reflected and refracted at the interface but that it does change the relative intensities. The most extreme effect is that of the critical angle, the angle above which total internal reflection within the particle takes place, which changes with the refractive index difference over an interface.

There is a wide variety of possible refractive indices of both particle and surrounding medium. Often it is easier to change the (mixture of) surrounding solvents and to measure the refractive index thereof than it is to change and measure the refractive index of the particle. To simplify, we only present the radial hologram intensity for a 1.4 μm particle with varying refractive index in ethanol, in Figure 2.14. Some refractive indices of the particle may be difficult to obtain, but particular scattering behavior may be realized by choosing a solvent with the appropriate refractive index. What matters is the relative refractive index (and the size of the particle with respect to the wavelength).

In Figure 2.14 **a** we present the radial hologram intensity for various refractive indices stitched together. As the refractive index of the solvent is 1.36 particles with that refractive index, or indices close to that do not scatter a lot of light. It is also in these cases where the formulae for the scattering coefficients tend to be numerically unstable [3, 43].

For particles that have a higher index of refraction than that of the solvent, the center of the hologram is bright, as we have seen before for silica ( $n = 1.45$ ) in ethanol ( $n = 1.36$ ), and for titania/silica particles ( $n \sim 1.8$ ) in CHC ( $n = 1.46$ ) in section 2.2.2. The light that is scattered in the forward direction is (partially) in phase with the remaining part of the illuminating beam that acts as the reference beam and there is constructive interference. In the ray optics approximation, which is certainly not justified for 1.4 μm particles illuminated the 532 nm laser

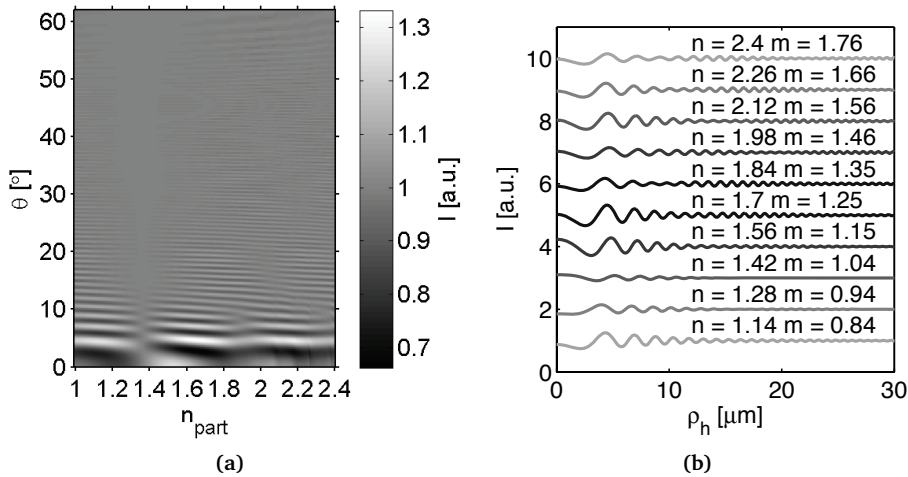


**Figure 2.14:** In-line hologram from Mie-Lorenz theory as a function of the particle refractive index. **a.** The normalized intensity of the hologram of a  $1.4 \mu\text{m}$  spherical dielectric in ethanol ( $n=1.36$ ) versus the angle with the optical axis, as a function of the refractive index of the particle. The particle was assumed to be  $30 \mu\text{m}$  above the image plane. **b.** The same as in **a** but as curves. For clarity the curves have been given different offsets. They have been provided with the refractive index of the particles and with the ratio between the refractive index of the particles and that of the ethanol,  $m$ . The wavelength of the light was taken to be  $532 \text{ nm}$ .

light, the particle acts as a little positive lens, focusing the light below it. When the refractive index of the particle is around 1.8, so when the relative refractive index  $m$  is around 1.32, the central spot is a little less bright as the particle as a whole acts as a anti-reflection coating. See also sections 5.5 and 5.6.

For particles with an index of refraction that is slightly lower than that of the solvent the center of the hologram is dark. This is the result of negative interference of the scattered wave with the reference beam. Light that enters and leaves the particle does not undergo a rotation of the phase by  $180^\circ$ , but light that reflects inside the particle does. In the, once again for these particles not justifiable ray optics limit, the particle acts as a negative lens with a virtual focus above the particle. When the refractive index is even lower, the central spot gets bright again. An air bubble with a refractive index of 1 in ethanol will give holograms with a bright central spot.

We note that the depth of the minima and location of the maxima changes with varying refractive index. Moreover, the number of maxima changes with the refractive index of the particle. The third and the fourth maximum in the intensity seem to merge at a refractive index of about 1.8, so with a relative refractive index of about 1.32. This is also visible in the curves for the  $n = 1.70$  and the  $n = 1.84$  particle in Figure 2.14 **b**.

### All effects together

The combination of the distance to the hologram plane, the radius of the particle and the refractive index contrast with the solvent gives a unique radial dependence of the hologram intensity. The parameter space is rather large and in the above we have attempted to give an impression of the possibilities by intersecting the parameter space through the  $r = 1.4 \mu\text{m}$ ,  $n = 1.45$  plane, the  $z = 30 \mu\text{m}$ ,  $n = 1.45$  plane and the  $r = 1.4 \mu\text{m}$ ,  $z = 30 \mu\text{m}$  plane, keeping the refractive index of the solvent constant at 1.36, the value for ethanol and the wavelength of the light constant at 532 nm.

In Figure 2.15 and 2.16 we give a number of possible holograms for various sizes and refractive indices, for particles in ethanol, 20  $\mu\text{m}$  above the hologram plane. For completeness, these holograms are given with the correct polarization dependent intensities that were discussed in section 2.3, where the polarization of the light is in the  $x$ -direction, horizontal on the paper.

The larger particles scatter more light, although the intensity of the holograms increases less for particles that are larger than 0.5  $\mu\text{m}$  in radius. We note that the black central spot that was observed above for a particle with a radius of 0.7  $\mu\text{m}$  and a refractive index of 1.15, so lower than that of the surrounding ethanol, is not present for all particle sizes with that refractive index.

Apart from the distance to the hologram plane, the radius and the refractive index, also other factors can play a role in the formation of the holograms. First of all we should state that these calculations assume that the particles are homogeneous and spherical. Often people are tempted to apply the Lorenz-Mie-Debye theory also to non spherical particles [3], but one has to be careful with applying this simplification. It is also possible that the refractive index distribution within the particle is inhomogeneous. An example of this will be presented in section 2.5.3. When the characteristic features of the refractive index inhomogeneities is smaller than the wavelength of the light, the scattering behavior of such particles may be approximated by the scattering of a sphere with some sort of effective refractive index.

In the magnification step by the microscope objective [4] of the actual interference pattern in the focal plane of the microscope onto the image plane on the CCD of the camera, one assumes that the imaging system works correctly. That is, that the light beams that interfere at some point in the focal plane of the microscope are all refracted in such a way that they all go to the same corresponding point on the CCD, regardless of the direction in which they propagate. We assume that the optical path to get from any point  $A$  in the object plane to any point  $A'$  in the image plane is the same for all propagation directions. Generally that is just what the microscope has been designed to do. However, there are possible aberrations, for instance spherical aberration. This aberration can be caused for instance by the angle dependent refraction at the interface between the microscope glass or capillary and the solvent. For a description of the effects of spherical aberration on the trapping behavior of particles in optical tweezers, see sections 4.7.1 and 5.3.2.

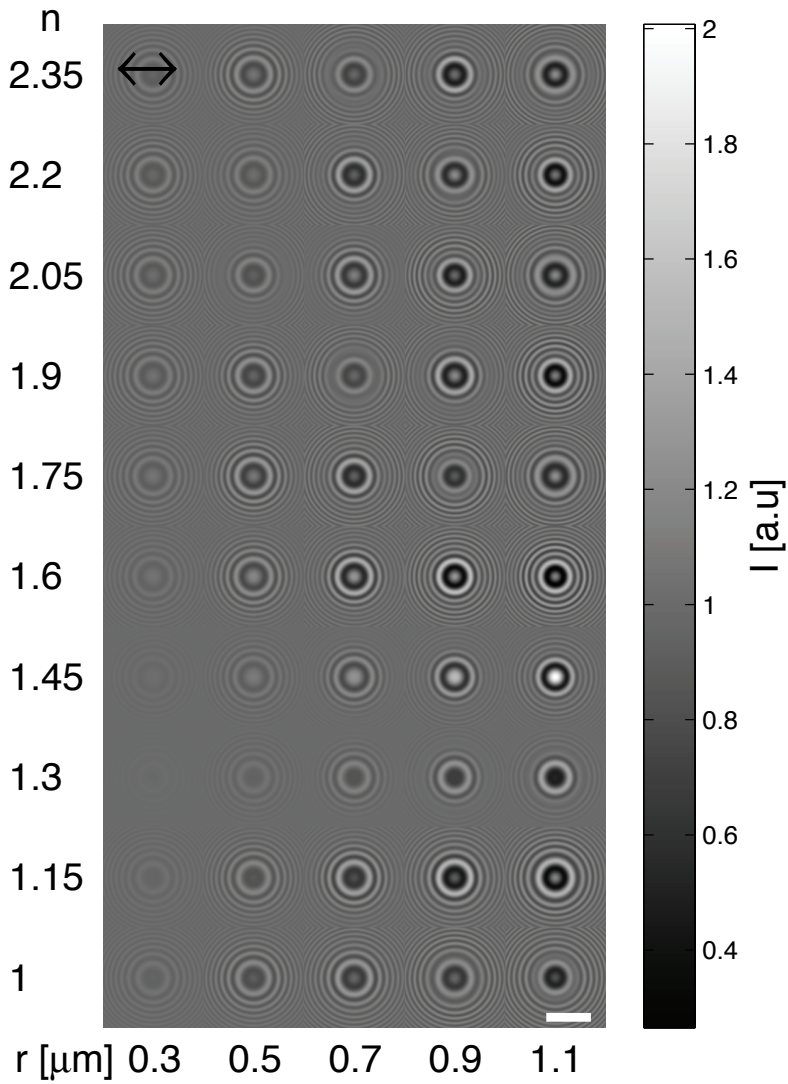


**Figure 2.15:** In-line holograms from Mie-Lorenz-Debye theory as a function of the particle radius between 0.3 and 1.1  $\mu\text{m}$  and refractive index between 1 and 2.35 in ethanol ( $n = 1.36$ ). Normalized holograms of spherical dielectrics in ethanol ( $n = 1.36$ ) as a function of the particle size and refractive index. The wavelength of the light is to be 532 nm and the particles are placed 20  $\mu\text{m}$  above the image plane. The scale bar indicates 10  $\mu\text{m}$  and the double arrow indicates the direction of the polarization.

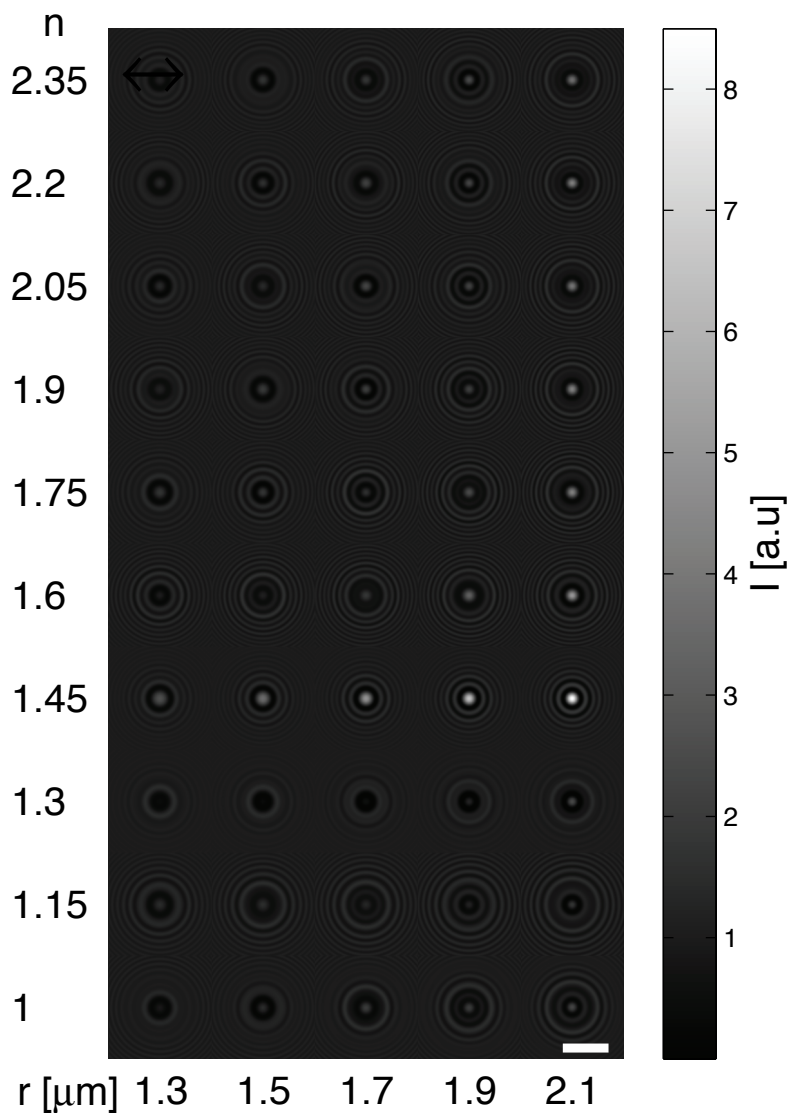


**Figure 2.16:** In-line holograms from Mie-Lorenz-Debye theory as a function of the particle radius between 1.3 and 2.1  $\mu\text{m}$  and refractive index between 1 and 2.35 in ethanol ( $n = 1.36$ ). Normalized holograms of spherical dielectrics in ethanol ( $n = 1.36$ ) as a function of the particle size and refractive index. The wavelength of the light is to be 532 nm and the particles are placed 20  $\mu\text{m}$  above the image plane. The scale bar indicates 10  $\mu\text{m}$  and the double arrow indicates the direction of the polarization.

In principle it is possible to also include the effect of spherical aberration in the calculation of what a hologram looks like. The five primary geometric aberrations of which spherical aberration is one, can be described with Zernike's orthogonal polynomials [46]. In this thesis, when discussing holograms, we assume that these aberrations are negligible.

In the following section, we will discuss how the information about the particle position and the particle characteristics can be distilled by fitting the model for the in-line holograms to an experimental in-line holographic micrograph.

## 2.4 Inverse problem: Digital Holographic Microscopy

In the previous section we saw how Lorenz-Mie-Debye theory can be used to quantitatively calculate the electric field as scattered by spherical colloids. Using the phase information from the Lorenz-Mie-Debye theory and simple geometry to calculate the interference in a plane underneath the particle, we can quantitatively calculate in-line holograms for given parameters as in equations 2.12 through 2.17.

Equation 2.17 can be fit to a normalized experimental hologram by treating the particle's three-dimensional position, its radius and its refractive index as free parameters [7]. Numerical fitting of the Lorenz-Mie-Debye theory [3, 37–39, 41] to experimentally recorded and appropriately normalized in-line holograms can be done by using the Levenberg-Marquardt non-linear least squares minimization algorithm [47, 48]. In this technique the parameters in the model,  $x$ ,  $y$ ,  $z$ ,  $r$  and  $n$  are optimized to minimize the squared differences between corresponding pixels. This technique of fitting to Lorenz-Mie-Debye theory and interference to experimental in-line holograms to characterize and track spherical particles is an alternative to back-propagation (see section 2.2) to analyze the in-line holographic images from *Digital Holographic Microscopy*, DHM [5, 7].

The typically tens of thousands of pixels in a hologram all contribute a little bit of information, although some pixels are influenced more and others less, by the scattered light and its interference with the reference beam. In principle there are multiple combinations of the parameters that yield a relatively good fit in the 5 or 6 dimensional error landscape. The Levenberg-Marquardt algorithm mediates between the slow but secure steepest descent method and the much faster Newton optimization algorithms and will, when properly parameterized find a local minimum from a start position. Generally, knowledge of the type of material and a rough size estimate of the particles in the system is good enough for the Levenberg-Marquardt algorithm to find the global minimum. Sometimes, it is necessary to start the minimization algorithm at different depths  $z_{h_0}$ , to then judge based on the values of the total error in the local minima and prior knowledge about the nature of the particles, which is the right depth to start fitting from.

Equation 2.17 can be simplified in the following manner;

$$\begin{aligned} B(\vec{\rho}_{xy}) &= \frac{\widetilde{R}\widetilde{R}^* + \widetilde{R}\widetilde{E}_s^*(\rho, \beta, m) + \widetilde{E}_s(\rho, \beta, m)\widetilde{R}^* + \widetilde{E}_s(\rho, \beta, m)\widetilde{E}_s^*(\rho, \beta, m)}{\widetilde{R}\widetilde{R}^*} \\ &= 1 + \frac{2\widetilde{R}\widetilde{E}_s^*(\rho, \beta, m)}{\widetilde{R}\widetilde{R}^*} + \frac{\widetilde{E}_s(\rho, \beta, m)\widetilde{E}_s^*(\rho, \beta, m)}{\widetilde{R}\widetilde{R}^*}. \end{aligned} \quad (2.18)$$

The first term, 1, is the normalized intensity of the background. An in-line hologram should be of homogeneous intensity in the absence of a scattering particle. The second term contains most information about the scattering by the particle. As the term depends linearly on the scattered field rather than on the scattered intensity, DHM can be applied to a relatively wide range of particles with only a limited dynamic range of the camera. The third term is generally rather small, although it can in principle be as much as 25% of the intensity in the central spot.

To account for variations in the illumination, the scattered intensity in equation 2.16, is multiplied with  $\alpha \approx 1$ , which is treated as a 6<sup>th</sup> fitting parameter. Although in many cases the fitting works well by only replacing  $\widetilde{E}_s(\rho, \beta, m)$  with  $\alpha\widetilde{E}_s(\rho, \beta, m)$  [7], we found that the algorithm is more stable when the background is set to  $\alpha$ , so that  $\alpha$  is constrained to 1.

$$B(\vec{\rho}_{xy}) = \alpha + \frac{2\alpha\widetilde{R}\widetilde{E}_s^*(\rho, \beta, m)}{\widetilde{R}\widetilde{R}^*} + \alpha^2 \frac{\widetilde{E}_s(\rho, \beta, m)\widetilde{E}_s^*(\rho, \beta, m)}{\widetilde{R}\widetilde{R}^*}. \quad (2.19)$$

The normalization by the background can be done in experiments by dividing by the average frame of a movie in which the particle has diffused enough to be effectively averaged out. Alternatively, the background can be recorded in absence of the particles. The particle can then be brought into the field of view using optical tweezers or an external (electric) field. Typically we record 8 bits images which after normalization leaves us with 5 or 6 bits grey values for what should be quantitatively described by equation 2.19. For some cameras it can be advisable to separately record the black level and subtract this from both the nominator and the denominator in the normalization.

According to equation 2.19, the intensity of a pixel in the hologram varies only with the lateral position of the particle and the radial distance to the lateral position of the particle, the center of the rings. In the calculation of the holograms, we make use of this cylindrical symmetry by calculating the radial intensity profile and applying a spline interpolation to the radial distance of each pixel to the lateral position of the particle to calculate the intensities of all the pixels. This speeds up the fitting procedure substantially. Typically fitting a hologram of 400 by 400 pixels takes less than 1 second on a 3.00 GHz Pentium 4 processor. In the process several hundreds of trial holograms are calculated.

The simplification made by calculating the radially averaged intensity rather than the intensity for the direction parallel and perpendicular to the polarization

separately, is less bad for the fitting than one might think at first sight. In the experimental hologram, both orientations with respect to the polarization are represented. The averaged radial intensity calculated by averaging over all orientations with respect to the polarization of the illuminating beam however, is by definition the averaged intensity that we are fitting to the experimental hologram. The particle parameters in the minimum are barely altered by this simplification which was confirmed by fitting equation 2.19 to simulated holograms that were generated by taking the polarization direction into account as described by equation 2.10. From Figure 2.15 and 2.16 in section 2.3.3 can be seen that the difference in intensity of the hologram in both directions is rather small for most particle sizes used in this thesis. Fitting holograms taking the polarization into account, for particles that scatter sufficiently different in both directions, demands that the orientation and degree of polarization of the illuminating beam be accurately known. As already stated however, the effect of polarization was not observed to be recorded by our cameras for the holograms discussed in this thesis.

In some previous studies, phenomenological models were fit to non-normalized holograms [49–57] or Lorenz-Mie-Debye scattering theory [58] for some of these quantities, but never all five. Because errors in the adjustable parameters are strongly correlated, failing to optimize them all simultaneously yields inaccurate results. The camera noise is measured and used for the estimation of the single-pixel error which is used to weigh the pixel contributions to the error. The  $\chi^2$  deviates for many of the fits we report are of order unity, so that the calculated uncertainties in the fit parameters accurately reflect their precision [47, 59]. The calculated uncertainties are related to the second derivative of the error that is minimized with respect to the parameter that is optimized. In the here presented work we used the Matlab<sup>®</sup> implementation of the Levenberg-Marquardt algorithm in the function `smarquardt.m` [60].

DHM allows one to track colloidal trajectories with nm accuracy in the lateral directions while measuring the particle position in the  $z_h$ -direction with a accuracy of around 10 nm [5, 7, 61, 62]. Simultaneously, the particle radius and refractive index are found to within 1%, [5, 7, 20, 63]. The technique works so well because, due to the inherent de-focusing, the information of the scattering of the particle is spread over thousands of pixels. An interesting alternative method to measure the individual particle's refractive index consists in comparing the measured trapping stiffness with calculated trapping stiffnesses using a T-matrix formalism [64], see also Chapter 4 and 5 about the calculation of trapping forces. The method requires that the particle be trappable which limits the applicability and relies on careful calibration.

For the fitting of in-line holograms, DHM, to be applicable the only requirements are that the particle scatters enough and can be accurately modeled by Lorenz-Mie-Debye scattering, while the only calibration needed consists of knowing the wavelength of the laser light used and the pixel size.

In the following sections we will apply DHM in combination with fitting of the

full Mie-Lorenz-Debye model to various types of particles and solvents to give an impression of the capabilities and limitations.

## 2.5 Characterization

In this section we will show what typical results can be achieved by fitting equation 2.19 to experimental holograms of various particles. First, in section 2.5 we will apply DHM to various sizes of silica particles in ethanol the properties of which are well known. Then, in section 2.5.2, we will show how the fitting of Lorenz-Mie-Debye theory to measured holograms can be useful for the development of new colloidal systems by characterization of the refractive index of particles made of materials like titania particles. We also apply DHM to melamine particles in section 2.5.3.

Subsequently, in section 2.5.4, we will study the dynamical processes of sedimentation and diffusion to measure the hydrodynamic radius and sedimentation coefficient of the particles. The mean squared displacements of the particles allow to confirm the error estimates from the  $\chi^2$  deviates of DHM fits. In section 2.5.5 we will show that a holographically determined height distribution can be applied to measure the weight of the individual particle and the interaction potential between a colloidal particle and the glass wall. As discussed before, the Lorenz-Mie-Debye theory has been extended for particles with a core-shell structure. In section 2.5.6, we will shortly discuss the applicability of our fitting technique to holograms of these particles.

### 2.5.1 Characterizing $\text{SiO}_2$ particles in ethanol

In Figure 2.13 we saw how the radial dependence of the intensity of in-line holograms depends on the size of silica particles. Here we show several experimental examples of these holograms.

Silica particles with average diameters from SLS measurements of 758, 1080, 1400, 1640 and 1750 nm were dispersed in technical grade ethanol. The suspensions were transferred to a rectangular glass capillary (Vitrocom  $0.1 \times 2.0$  mm) and placed on an inverted microscope (Leica DRM-IRB) equipped with a  $100\times$  NA 1.4 PLAN APO objective. This system provides a total magnification of  $142 \pm 1$  nm/pixel over a  $182 \times 145$   $\mu\text{m}^2$  field of view. The condenser was replaced by a mirror reflecting the beam from a fibre coupled Spectra Physics Millennia V 532 nm laser at minimum power through the sample, into the objective. The laser intensity was attenuated using polarizers. The resulting irradiance of roughly  $10$  nW/ $\mu\text{m}^2$  is comparable to that of conventional microscope illumination and is too weak to exert measurable forces on the illuminated objects or to heat the sample appreciably. The integration time of the camera was set to 100  $\mu\text{s}$ . The holograms were recorded at 200 fps (frames per second) on a Mikrotрон EoSens CE camera. To save space on the hard drive only a field of view of 160 by 450

pixels was recorded. In the actual analysis of the holograms we only considered a section of 160 by 160 pixels.

The particles were trapped in an optical tweezer at about 5  $\mu\text{m}$  above the hologram plane and moved out of the field of view. The camera was set to record and during the first few tens of frames the illuminating laser beam was blocked to record the offset level of the camera. The next 1000 frames were used to register the background in absence of the particle. Then the trapped particle was moved into the field of view.

In Figure 2.17 and 2.18 we present the experimental holograms of respectively the 758, 1080 and 1400  $\text{nm}$  diameter particles and those of the 1640 and 1750  $\text{nm}$  diameter particles. The holograms were normalized through division by the background after subtraction of the camera's measured offset level. The holograms of the particles are clearly visible as concentric rings. The stripes in the holograms are interference patterns caused by the scattering of objects in the light path such as the edge of the capillary that were apparently displaced since the background was recorded.

Next to the experimental holograms we include the fitted hologram, which should look identical to the experimental hologram in the absence of noise in the background. On the far right pictures we plot the radially averaged intensities as a function of the radial distance from the particle position in the hologram plane  $\rho_h = \sqrt{\rho_x^2 + \rho_y^2}$ . The radial dependence of the intensity of the fitted hologram is plotted in black. In grey we plot the radially averaged intensity in the experimental hologram, to give an impression of the noise we plotted this twice, with the statistical error added and subtracted to indicate the error range in the measurement of the intensity as a function of the radial distance.

The maximum intensity in the hologram increases with the particle diameter. For clarity, the grey scales in the representation of the holograms have been adapted by linear stretching of the grey values. The consequence is that the noise in the background seems more pronounced for the smaller particles that scatter less. Although the noise level is in reality comparable between the various holograms, the signal to noise ratio is smaller for smaller particles. This is one of the challenges of holographing smaller particles.

Most of the background noise is actually removed by the division of the recorded background. The noise that remains is the result of changes of the background over time. The amount of background noise can thus be reduced by using a more stable laser and sturdier mounting of the optics. Reducing the airflow around the optics would also improve the stability of the illumination. The manually moving back of the trapped particles into the field of view after recording the background is also a problem.

The intensity of the hologram decreases with increasing distance to the center of the hologram. The effect on the signal to noise ratio at larger radial distances is compensated by the increasing number of pixels at an increasing distance from the central spot. This reflected in the fact that the two grey lines at distances of

around  $5 \mu\text{m}$  lie closer together than those at the center.

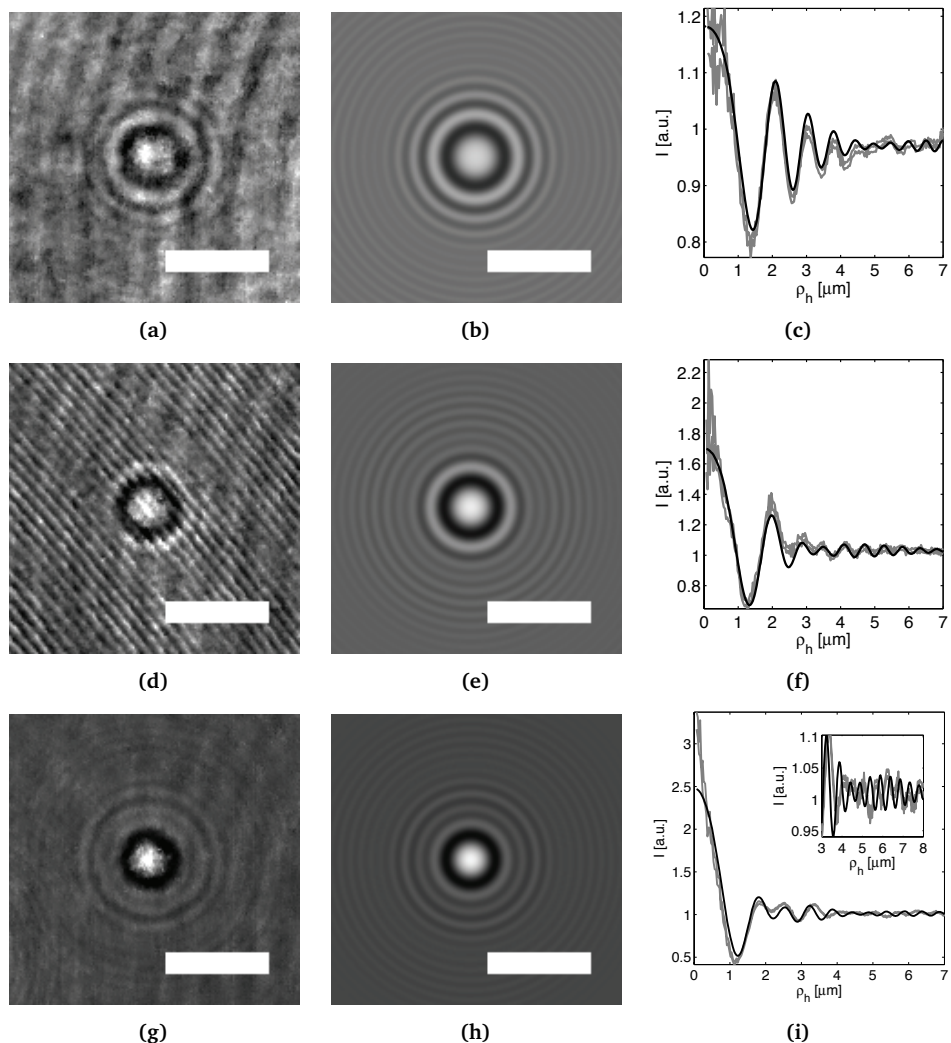


**Figure 2.17:** Holograms of a 758, a 1080 and a 1400 nm  $\text{SiO}_2$  particle in ethanol. **a, d** and **g.** In-line holograms of respectively a 758, 1080 and 1400 nm  $\text{SiO}_2$  particle in ethanol. **b, e** and **h.** Fitted holograms. The particles were fitted respectively to be  $5.695$ ,  $5.755$  and  $4.920 \pm 0.01 \mu\text{m}$  above the focal plane and their lateral positions have been determined to within about  $5 \text{ nm}$ . The particles were found to have a radius of  $449$ ,  $585$  and  $732 \pm 2 \text{ nm}$  and to have a refractive index of  $1.43$ ,  $1.47$ ,  $1.46 \pm 0.02$ . **c, f** and **i.** Azimuthally averaged radial profiles. The black lines represent the intensities in the fitted holograms. The grey lines indicate the averages in the experimental holograms plus and minus the statistical error. The wavelength was  $532 \text{ nm}$ . The scalebars are  $5 \mu\text{m}$ .

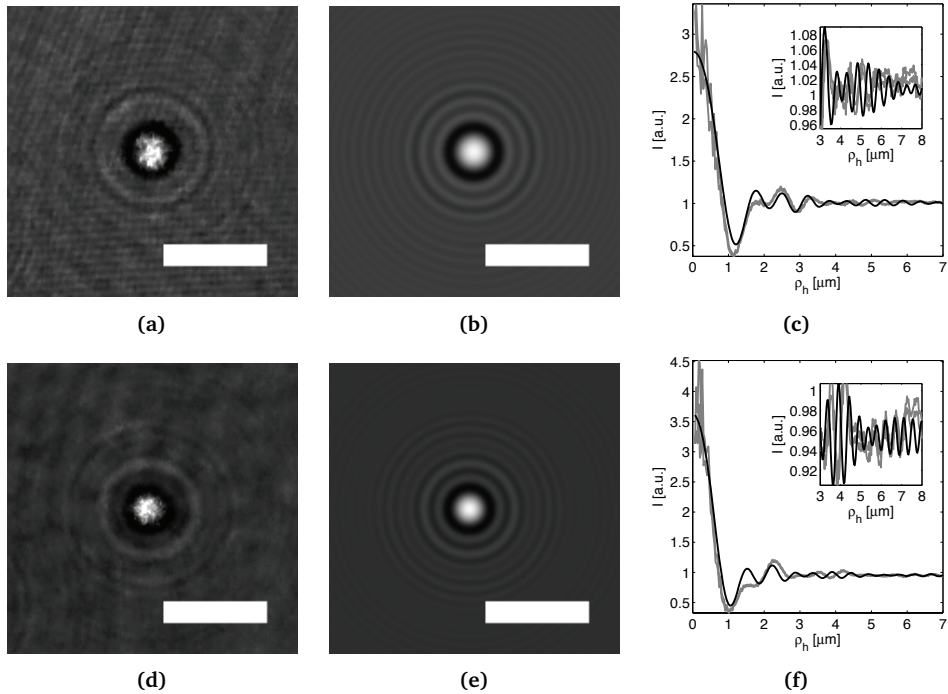


**Figure 2.18:** Holograms of a 1640 and a 1750 nm  $\text{SiO}_2$  particle in ethanol. **a** and **d**. In-line holograms of respectively a 1640 and 1750 nm  $\text{SiO}_2$  particle in ethanol. **b** and **e**. Fitted holograms. The particles were fitted respectively to be  $5.572$  and  $4.777 \pm 0.01$   $\mu\text{m}$  above the focal plane and their lateral positions have been determined to within about  $5$  nm. The particles were found to have a radius of  $834$  and  $887 \pm 5$  nm and to have a refractive index of  $1.46$  and  $1.46 \pm 0.05$ . **c** and **f**. Azimuthally averaged radial profiles. The black lines represent the intensities in the fitted holograms. The grey lines indicate the averages in the experimental holograms plus and minus the statistical error. The wavelength was  $532$  nm. The scalebars are  $5$   $\mu\text{m}$ .

In Figure 2.18 the fits for the 1640 and 1750 nm diameter particles are less good than those for the smaller particles in Figure 2.17. This is the result of the fact that the central spot is too bright. The camera we used was not linear in the intensity for the brightest 10% of the possible grey values of the pixels. The non-linear response of the camera can be circumvented by choosing a shorter integration time or less laser power. This has the disadvantage that the less intense part of the holograms is then even darker and the fainter rings are no longer recorded in the limited dynamic range of the camera. Given the parameters of the camera used, the bright central spot appears less bright in the photograph than it must have been in reality. In Figure 2.15 the central spot gets less bright when the refractive index of the particle is higher. As a result our particles are fitted with relatively high refractive indices.

The fit values for the radii of the particles agree well with the obtained using Static Light Scattering, SLS, and the fit values for the refractive indices of the silica agree with each other and with values obtained by index matching in mixtures of ethanol and DiMethylSulfOxide, DMSO. The fit values for the smallest particle in Figure 2.17 are estimated to be less accurate due to the relatively lesser and less characteristic scattering of smaller particles. For the larger particles in Figure 2.18, it is also reasonable to assume that the fit values from the holograms deviate more due to the relatively lesser sensitivity to light of the camera for the intensities in the central spot.

It is clear that the fits could be improved by using a camera with a greater dynamic range. An alternative strategy to improve the characterization of these particles would consist in defocusing even more. Making the distance between the hologram plane and the particles larger, the intensity of the bright central spot rapidly drops as we have seen in Figure 2.12. This would accommodate the limited dynamic range of the camera. Clearly, we should then also fit to holograms consisting of more pixels, to gather more statistics and because the holograms would be larger.

The scope of these experiments was, however, to characterize the size dependence of the trapping behavior of the particles in the optical traps, presented in section 5.5.2, and the influence of the spacing between multiple traps, presented in sections 6.4.1 and 6.5. The axial distance between the focal plane of the microscope, the hologram plane, and the trapping plane was limited to not alter the trapping behavior too radically. For more information on the effect of changing the distance between the hologram plane and the trapping plane on the trapping behavior we refer to section 5.4.1. The limited distance between the hologram plane and the particle did compromise the characterization of the particles, but the information in the trajectories was satisfactory for the purpose of studying the interaction between optical tweezers and the particles.

## Conclusion

Differently sized silica particles can be tracked and characterized in ethanol by fitting a model for the interference pattern between the light scattered by the particles and the remaining illuminating beam. The characterization of the particles can be improved by increasing the distance between the hologram plane and the particle and by using a camera with a greater dynamic range.

### 2.5.2 *Characterizing titania particles; tuning the refractive index for trapping experiments*

Titania is key in modern material science for its importance in many fields such as catalysis both as a catalyst [65] and as a support [66]. In Grätzel-type solar cells titania is used as a semiconductor for conversion of light to electricity [67]. In colloidal photonic crystals and as a paint pigment titania is applied for its high re-

fractive index [68–70]. Crystalline titania cores were synthesized according to the procedure of Yu *et al.* [71] with slight modifications. Seeded growth, well known for the growth of silica particles, gives control over particle growth and generally helps to decrease the polydispersity of the particles [35]. It was observed that amorphous titania as-synthesized is highly porous, but that it becomes more dense upon drying [72]. Thus, drying reduces particle size but increases the density and the refractive index. Higher index particles can be trapped stiffer and can be used to exert larger forces with optical tweezers as demonstrated in Chapter 5. For details on the synthesis and further characterization of titania particles with tunable refractive indices please refer to Demirörs *et al.* [20].

We applied DHM to amorphous, dried and calcined titania particles of the same original batch. The particles immediately after synthesis were amorphous. Some of the particles are dried in an oven at 50°C. Another part of the batch was calcined by placing the particles in an oven at 450°C. The size and refractive indices of these particles were determined by SLS and TEM to be respectively 850 nm p.d. 5%, 580 nm p.d. 5% and 490 nm p.d. 5% in radius. From the SLS measurements the refractive indices were found to be respectively 1.55, 1.8, 2.2 for amorphous, dried and calcined titania particles respectively. The particles were dispersed in ethanol and holograms were recorded on the same setup as described in section 2.5.1. Only here, we recorded the background by just letting the particle diffuse freely and averaging over sufficiently many frames to effectively average its hologram away. This way we induced less motion in the setup with as a result a smoother background after normalization.

Figure 2.19 a-c shows the typical hologram, the fit and the intensity profile for a non-dried (amorphous) titania particle. The particle was found to be 22.82  $\mu\text{m}$  above the focal plane of the microscope. The fit values for the radius and refractive index of this particle were  $902 \pm 5$  nm and  $1.55 \pm 0.02$ . This agrees with what was to be expected from the SLS measurements. In the radial intensity profile there are many minima that are the result of the interference between the scattered light and the reference beam. Thus the position can be determined rather accurately. On top of the many minima there is an envelope of three clear minima. These are part of the characteristic way this particle scatters the light and this is the basis for the particle characterization by both DHM and SLS. Moreover, the central spot is less bright than that of the 887 nm  $\text{SiO}_2$  particle in ethanol in Figure 2.18. This is a result of the high refractive index of the titania particle, see also Figure 2.15.

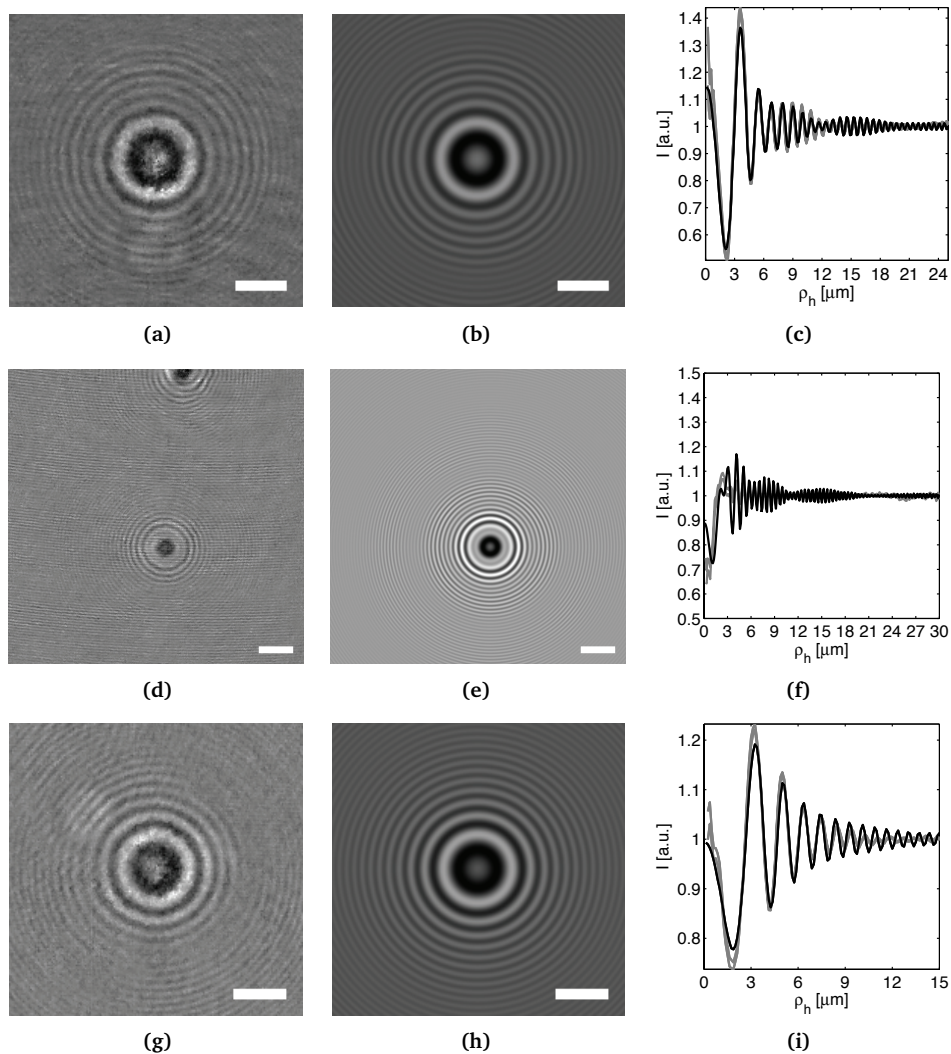


**Figure 2.19:** Holograms of untreated, dried and calcined  $\text{TiO}_2$  particles in ethanol. **a**, **d** and **g**. In-line holograms of respectively a freshly synthesized  $\text{TiO}_2$  particle, a dried  $\text{TiO}_2$  particle and a calcined  $\text{TiO}_2$  particle in ethanol. **b**, **e** and **h**. Fitted holograms. The particles were fitted to be 22.82, 10.04 and  $18.68 \pm 0.01$   $\mu\text{m}$  above the focal plane, have a radius of 902, 417 and  $485 \pm 5$   $\text{nm}$  and to have a refractive index of 1.55, 1.88 and  $2.35 \pm 0.05$ . **c**, **f** and **i**. Azimuthally averaged radial profiles. The black lines represent the intensities in the fitted holograms. The grey lines indicate the averages in the experimental holograms plus and minus the error. The wavelength was 532  $\text{nm}$ . The scalebars are 5  $\mu\text{m}$ .

An example of a hologram of a particle after drying is presented in Figure 2.19 **d-f**. The distance to the focal plane, the radius and the refractive index were  $10.04 \pm 0.01 \mu\text{m}$ ,  $417 \pm 5 \text{ nm}$  and  $1.88 \pm 0.05$  respectively. These values agree with the values obtained with SLS and TEM measurements. The particle has shrunk significantly in the drying step. The intensity of the hologram is significantly less bright than that of the larger amorphous particle. This reduces the signal to noise ratio of the measurement. To compensate for this, the particle was holographed at a smaller distance  $z_h$  from the hologram plane.

The central spot of this hologram is even darker, this means that the light that is scattered in the forward direction is practically rotated by  $\pi/2$ . This is apparently the result of the higher refractive index. The higher refractive index corresponds to the smaller volume in which a similar amount of titania is concentrated. The pores in the amorphous particle had probably been filled with ethanol which has a lower refractive index. Also for this particle there are a few minima in the envelope over the interference fringes that are the signature of the particle characteristics.

Finally in Figure 2.19 **g-i**, we include a hologram, its fit and the corresponding intensity profile for a titania particle that has been calcined at  $450^\circ\text{C}$ . We found the particle at a depth of  $18.36 \pm 0.01 \mu\text{m}$ , with a radius of  $553 \pm 5 \text{ nm}$  and a refractive index of  $2.35 \pm 0.05$ . These values agree with measurements using SLS and TEM on particles from the batch. The hologram of this particle is again a little brighter than that of the dried particle. This, notwithstanding the fact that the particle was even smaller than the dried particle. The intensity of the hologram varies a lot with the particle size and refractive index for particle radii and refractive indices between 1.6 and 2.2 in Figure 2.15. This is the result of the different optical path lengths within the particle which vary both with the particle size and the wavelength of the light within the particle, which in turn depends on the refractive index of the particle. Because the particle is smaller, its scattering pattern shows less minima. Nevertheless, the envelope over the amplitude of the fringes in the hologram still has a characteristic shape to which the particle radius was fit.

## Conclusion

The general trend in the shrinkage and the rise in refractive index when the particles are subsequently dried and calcined from DHM agrees with the SLS and TEM results [20]. The observed particle sizes fall within the size distribution as determined by SLS, a polydispersity of 5% was found for all three types of particles. Given the porous and polydisperse nature of the titania particles it is not surprising that we found different values for individual particles. Since we measure the size and refractive index of individual particles, it is possible to measure the size and index distributions in a batch of particles and to then study correlations between these parameters. This is impossible with any bulk measurement technique. Moreover, we noticed that fitting to the holograms of some particles

resulted in fit values that varied from frame to frame. The holograms in question occasionally lacked rotational symmetry, suggesting that the particle in question was not spherical. We have applied DHM to characterize titania particles and followed the evolution of their composition as a result of different treatments. We have shown that DHM can be applied to characterize particles made of high index materials.

### 2.5.3 Characterizing melamine particles

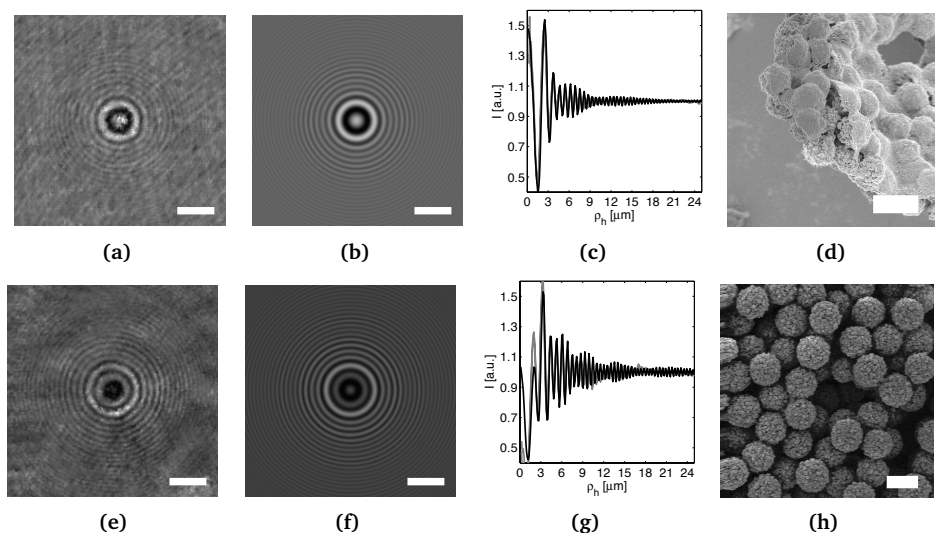


**Figure 2.20:** Holograms of melamine particles. **a** and **e**. In-line holograms of respectively a 1.3 and 2.2  $\mu\text{m}$  melamine particle in ethanol. **b** and **f**. Fitted holograms. The particles were fitted respectively to be 10.010 and  $12.191 \pm 0.01 \mu\text{m}$  above the focal plane, have a radius of 658 and  $1222 \pm 10 \text{ nm}$  and to have a refractive index of 1.58 and  $1.59 \pm 0.05$ . The scalebars are 5  $\mu\text{m}$ . **c** and **g**. Azimuthally averaged radial profiles. The black lines represent the intensities in the fitted holograms. The grey lines indicate the averages in the experimental holograms plus and minus the error. The wavelength was 532 nm. **c** and **h** SEM images of the same batches of particles. The scale bars in the SEM pictures are 2  $\mu\text{m}$ .

Melamine is a nitrogen rich polymer that is used for instance in household items and fire retarders. The high refractive index of 1.68 makes it potentially an interesting material for optical tweezer experiments when appropriately coated with for instance silica, see section 5.6.

Two batches of melamine particles were synthesized using the methods in [73, 74]. Holograms of two batches of melamine particles in ethanol were recorded. The particles were holographed in a similar setup to the one used to record the holograms of the titania particles in section 2.19. The Spectra Physics Millennia

V 532 nm laser was replaced by a Pegasus PE.P532 laser diode with the same wavelength, which was mounted on the optical table and could be attenuated electrically rather than by means of polarizers. Again, the particle was left to freely diffuse while we recorded holograms that were averaged to get the background and subsequently analyzed by fitting the Lorenz-Mie-Debye theory to the normalized in-line holograms.

The fit values for the particle sizes agree reasonably well with the particle sizes from the microscopic study of dried crystals (not included) and the SEM pictures. We note that the fits to the experimental holograms match reasonably well. The minimum in the amplitude of oscillations in the radial intensity of the hologram of the 1.3  $\mu\text{m}$  particle at around 8  $\mu\text{m}$  in Figure 2.20 **b** falls on top of the curve for the experimental hologram. In **g** the fit clearly matches the experiment but there remains a slight mismatch between the fitted and the experimental hologram. The first few fringes in the fit are less pronounced than in the experimental hologram. The shape however, of the envelope over the fringes and the phase of the fringes of the fit does follow the experimental intensity profile. We particularly note the brighter central spot in the fitted hologram. This is in line with the relatively low refractive indices that were found for these melamine particles. The values of 1.584 and  $1.593 \pm 0.05$  are rather low for melamine which should have a refractive index of 1.68. The particles were immersed in different index liquids from Cargille [75]. From the bright spot respectively dark spot below the particles as observed with a bright field microscope without condenser lens, the refractive index of the particles was determined to be larger than 1.68 and smaller than 1.69. The particles were subsequently studied using a Scanning Electron Microscope, SEM, the result of which is reproduced in Figure 2.20 **d** and **h**. The particles of respectively 1.3 and 2.2  $\mu\text{m}$  are clearly visible. The particles look porous and consist of clumps of many smaller particles. The 1.3  $\mu\text{m}$  batch also contains a film of even smaller stuff. These are either remains of the surfactant that was used to stabilize the particles or even smaller second nucleation. The observation that the fits to the holograms yield smaller refractive indices in ethanol than the measurement by index matching can be explained by supposing that the fitted values represent an effective volume average of the refractive index. The pores in between the smaller constituent particles that are visible in the SEM pictures can either be filled with low index ethanol or with the index liquids. The roughness of the particles is typically smaller than 532 nm, the wavelength of the laser light used. However, the smaller particles are not that much smaller and are likely to scatter themselves as well. This may be the cause of the smaller deviations between the fit and the experimental hologram that was observed in Figure 2.20 **g** for the 2.2  $\mu\text{m}$  particle, of which the roughness is also larger than that of the 1.3  $\mu\text{m}$  particle.

## Conclusion

DHM was applied to characterize two batches of melamine particles. The results indicated that the particles have a lower refractive index than one would expect

for melamine particles. This observation was explained by the observation from SEM pictures that the particles consisted of clusters of smaller particles leaving free pores to be filled with the lower index solvent. DHM can thus indicate that particles have a porous structures.

### 2.5.4 Sedimentation

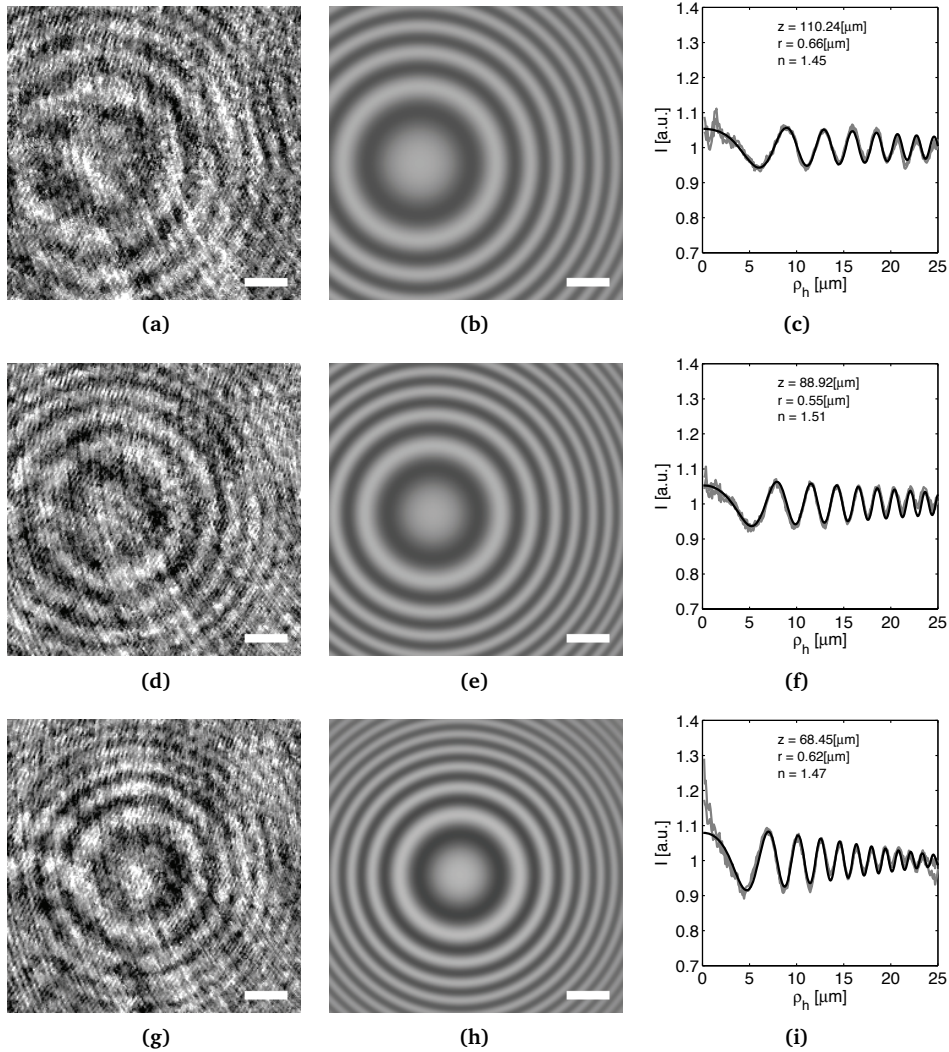
Apart from using DHM to characterize the static properties of individual particles, the technique can also be used to track the particles in space. By studying the dynamics of particles, one can measure many particle properties. One can determine the hydrodynamic radius of the particle by studying the diffusion, and its sedimentation coefficient by studying its sedimentation velocity. By applying a constant electric field, one can study the charge of the particles [76–78], by applying an AC field one can induce dipolar interactions [21, 79] which can also be measured by tracking individual particles [80]. Also interactions between multiple particles can be measured using single particle tracking, see [81] and references therein.

Here we study the diffusion and sedimentation of a  $1.4\ \mu\text{m}$  silica particle in ethanol. The dispersion was transferred to a rectangular glass capillary (Vitrocom  $0.1 \times 2.0\ \text{mm}$ ) and placed on an inverted microscope (Leica DRM-IRB) equipped with a  $100\times$  NA1.4 PLAN APO objective. The condenser was replaced by a Pegasus PE.P532 laser diode. The holograms were recorded using a Mikrotron EoSens CE camera.

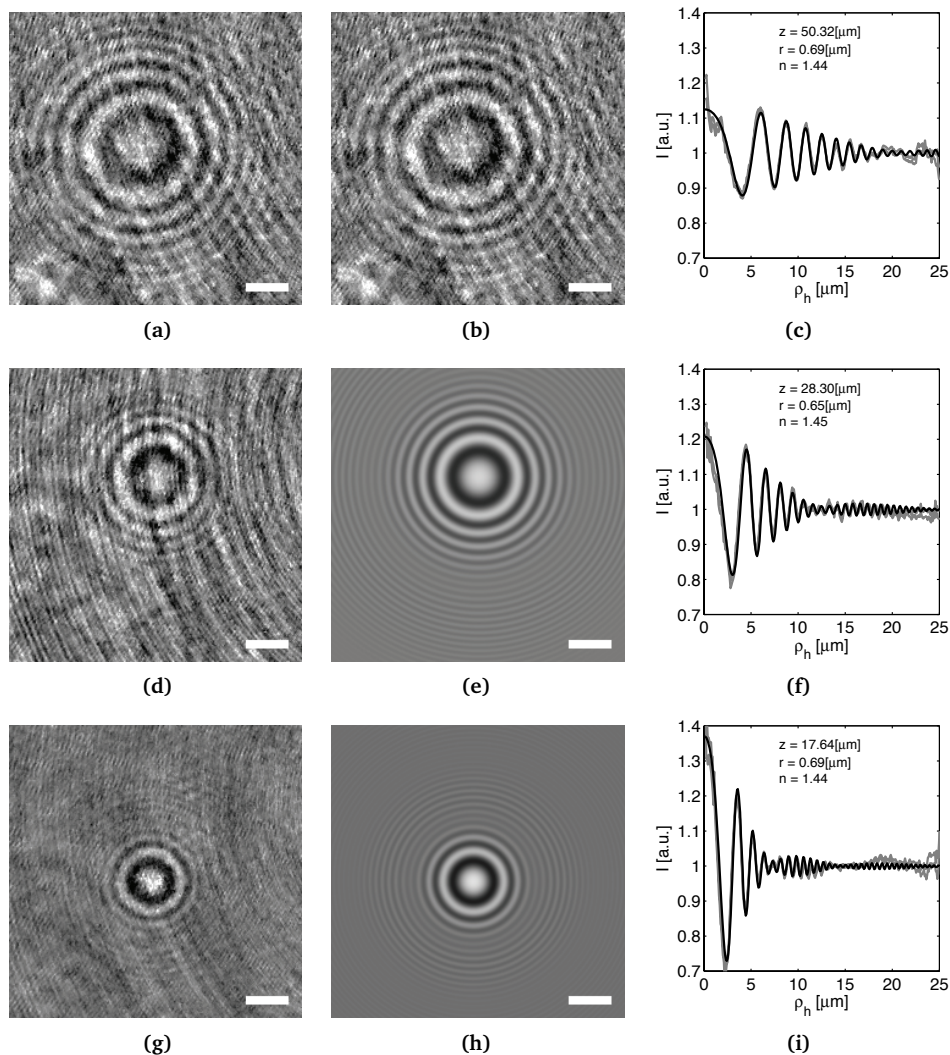
The particle was trapped in an optical trap and brought to  $\sim 100\ \mu\text{m}$  above the bottom of the sample. Both the illuminating laser and the trapping laser were interrupted. The camera started recording the black level while the focus of the microscope was manually brought back down. Then the illuminating laser was switched back on. The hologram of the particle was recorded on a field of view of  $240$  by  $240$  pixels at a frame rate of  $50\ \text{fps}$ .

Figure 2.21 and 2.22 reproduces a few snapshots of the interference pattern between the scattered light and the reference beam while the particle sediments. The magnifying effect of an increased the distance between the particle and the hologram plane is evident. At the greatest distance of  $110.7 \pm 0.1\ \mu\text{m}$  above the hologram plane, in Figure 2.21 **a-c**, the first minimum is at a distance of  $\sim 7\ \mu\text{m}$  and there are only seven minima visible. The characterization of this hologram would definitely benefit from a larger field of view that records more fringes. At the smallest depth of  $17.48 \pm 0.05\ \mu\text{m}$  in Figure 2.22 **g-i**, there are 34 minima, although only about 15 of these are clearly visible in the radial average of the experimental hologram.

The bright central spot in Figure 2.21 **a** has around a quarter of the relative intensity of that in Figure 2.22 **g**. The result is that the relative strength of the background noise is much bigger. This is compensated by the greater statistics in the larger holograms. Of the central spot itself there are relatively less measurements, which can cause the background to have a significant effect, as for instance



**Figure 2.21:** Sedimentation of a  $1.4 \mu\text{m}$   $\text{SiO}_2$  particle from  $110 \mu$  to  $70 \mu$  above the hologram plane in ethanol. In-line holograms of a sedimenting  $1.4 \mu\text{m}$  silica particle in ethanol. **a.** The normalized hologram of the particle at  $110.7 \pm 0.1 \mu\text{m}$  above the hologram plane. **b.** The fitted hologram. The fit value for the radius was  $0.817 \pm 0.02 \mu\text{m}$  and the refractive index was fitted at  $1.44 \pm 0.01$ . In the lateral direction the estimate for the uncertainty from the fit was  $0.01 \mu\text{m}$ . **c.** The radially averaged intensity at the particle location. In black: the fitted hologram, in grey: the experimental hologram plus and minus the statistical uncertainty. **d-f.** The same as in **a-c** for the same particle at  $80.85 \pm 0.09 \mu\text{m}$ . **g-h.** The same as in **a-c** for the same particle at  $68.91 \pm 0.07 \mu\text{m}$ . The error estimates from the fitting algorithm suggest that the lateral position was determined to within  $10 \text{ nm}$ , the axial positions to within  $100 \text{ nm}$ . The particle radius and refractive index were determined to within respectively  $20 \text{ nm}$  and  $0.01$ . The scale bars are  $5 \mu\text{m}$ , the wavelength used was  $532 \text{ nm}$ .



**Figure 2.22:** Sedimentation of a  $1.4 \mu\text{m}$   $\text{SiO}_2$  particle from  $50 \mu$  to  $18 \mu\text{m}$  above the hologram plane in ethanol. In-line holograms of a sedimenting  $1.4 \mu\text{m}$  silica particle in ethanol. **a.** The normalized hologram of the particle at  $50.88 \pm 0.06 \mu\text{m}$  above the hologram plane. **b.** The fitted hologram. **c.** The radially averaged intensity at the particle location. In black: the fitted hologram, in grey: the experimental hologram plus and minus the statistical uncertainty. **d-f.** The same as in **a-c** for the same particle at  $28.48 \pm 0.02 \mu\text{m}$ . **g-h.** The same as in **a-c** for the same particle at  $17.48 \pm 0.01 \mu\text{m}$ . The error estimates from the fitting algorithm suggest that the lateral position was determined to within  $10 \text{ nm}$ , the axial positions to within  $100 \text{ nm}$ . The particle radius and refractive index were determined to within respectively  $10 \text{ nm}$  and  $0.01$ . The scale bars are  $5 \mu\text{m}$ , the wavelength used was  $532 \text{ nm}$ .

in Figure 2.21 **g-i** when the particle was at a depth of  $68.91 \pm 0.07 \mu\text{m}$ . This does not have a dramatic influence on the fitting result, as all the pixels are fitted and because there are many more measurements of the hologram intensity at greater radial distances.

The fit values of the particle radius and refractive index are fairly constant over the almost  $100 \mu\text{m}$  distance over which the particle sedimented. However, the calculated uncertainties in the fit parameters seem to overestimate the precision. This suggests that the model that is fitted to the experimental holograms does not capture all the physics. We think that the problem is in the variation in the background intensity. In Figure 2.23 **a** we plot the particle position versus time.

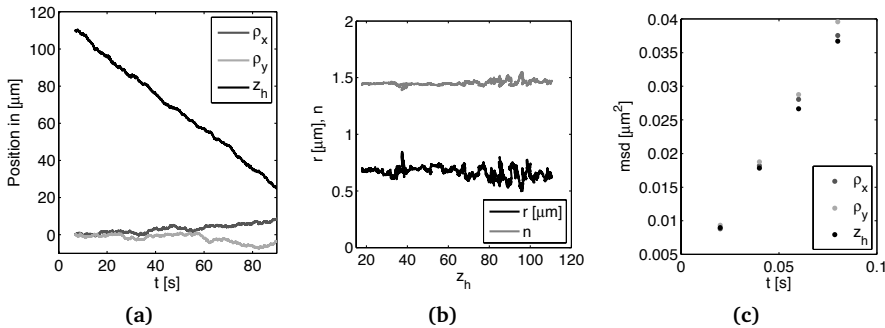


**Figure 2.23:** Analyzing the sedimentation. **a.** The  $\rho_x$ ,  $\rho_y$  and  $z_h$  coordinates of the particle as a function of the time. **b.** The fit value for the radius and the refractive index as a function of the distance from the hologram plane. **c.** The mean square displacement in the three directions over the last  $10 \mu\text{m}$  for the three directions. The errors are estimated to be of the size of the symbols.

After  $\sim 5$  seconds the focal plane of the microscope was moved to its final position and the illuminating laser was turned on. The particle sedimented over  $90 \mu\text{m}$  at an average velocity of  $1.01 \pm 0.01 \mu\text{m/s}$  while performing Brownian motion.

In Figure 2.23 **b** we plot the fit value for the particle radius and the refractive index. The values are boxcar averages over 50 frames. The fit values vary in time and show some correlation. The variation is due to the background noise, the influence of which changes with the particle position. Over the whole measurement the average fit value of the radius was  $0.66 \pm 0.02 \mu\text{m}$ , while the average value that was found for the refractive index was  $1.4476 \pm 0.0004$ . It seems better to average only over the last  $10 \mu\text{m}$  of the sedimentation path as the fit values seem more stable and because the size of the field of view was more adapted to the size of the hologram. The result of that averaging is  $0.680 \pm 0.01 \mu\text{m}$  for the radius and  $1.4476 \pm 0.003$  for the refractive index.

From the sedimentation velocity and the particle radius which give the friction factor, the density of the particle can be determined via  $\rho_p = \rho_m + 9\eta v / (2r^2g)$ , where  $\rho_p$  and  $\rho_m$  are the density of the particle and the solvent respectively.  $\eta$

is the viscosity of the ethanol and  $g$  is the gravitational acceleration,  $9.81 \text{ m/s}^2$ . The viscosity of ethanol is strongly temperature dependent [82] and is take to be  $1.2 \text{ mPas}$ . Taking the average optically fit radius  $0.680 \pm 0.01 \text{ }\mu\text{m}$ , we find that the density of the particle was about  $1.8 \pm 0.2 \text{ g/cm}^3$ , in accordance with the literature value [7].

The mean square displacements,  $\Delta r_j^2(\tau) = \langle (r_j(t + \tau) - r_j(t))^2 \rangle$ , in Figure 2.23 c show that fluctuations in the trajectory's individual Cartesian components agree with each other and all three display linear Einstein-Smoluchowsky scaling,  $\Delta r_j^2(\tau) = 2D\tau$ , with a diffusion coefficient  $D = 0.24 \pm 0.05 \text{ }\mu\text{m/s}$ . This is consistent with the anticipated Stokes-Einstein value,  $D = k_B T / (6\pi\eta r) = 0.24 \pm 0.06 \text{ }\mu\text{m/s}$ , where  $k_B T$  is Boltzmann's constant. Using the friction factor from the diffusion constant to determine the weight of the particle yields a value of  $1.79 \pm 0.03 \text{ pg}$ , which agrees with the value based on the optically determined radius and the densities from the literature  $4/3\pi * r^3 * (1.9 - 0.79) = 1.84 \pm 0.10 \text{ pg}$ .

The mean squared displacements of the components of the particle's position provide additional consistency checks. Using the methods of reference [83], we then interpret the offsets obtained from linear fits to  $\Delta r_j^2(t)$  over the last  $10 \text{ }\mu\text{m}$  to be consistent with no worse than  $10 \text{ nm}$  accuracy for the lateral positions and  $20 \text{ nm}$  for axial positions throughout the trajectory. The optical characterization is thus consistent with the particle dynamics.

## Conclusion

DHM can be applied to movies of holograms to track colloidal particles in time. From the dynamics it is possible to measure the sedimentation coefficient and the diffusion coefficient. Studying the diffusion offers a consistency check for the accuracy of the position detection, which suggests that the particle position is measured to within  $10 \text{ nm}$  in the lateral directions and to within  $20 \text{ nm}$  in the axial direction.

### 2.5.5 Gravity and Double-Layer Repulsion

At a certain depth, the sedimentation discussed in section 2.5.4 stopped, as a result of the fact that the gravitational attraction was counter-balanced by the screened charge repulsion of the charged glass wall. It was observed that the average depth was still decreased linearly in time with a slope of  $0.01 \text{ }\mu\text{m/s}$ . This is the result of the drift of the microscope objective. The focal plane of the microscope would ideally be stable but relatively short after being moved, the  $\sim 90$  seconds during which the particle sedimented as can be seen from Figure 2.23 b, there is still some residual drift. This continuous movement of the focal plane makes that the background is continuously changing. Probably the errors of the measurements in section 2.5.4 could have been smaller had the objective been stable and the field of view larger.

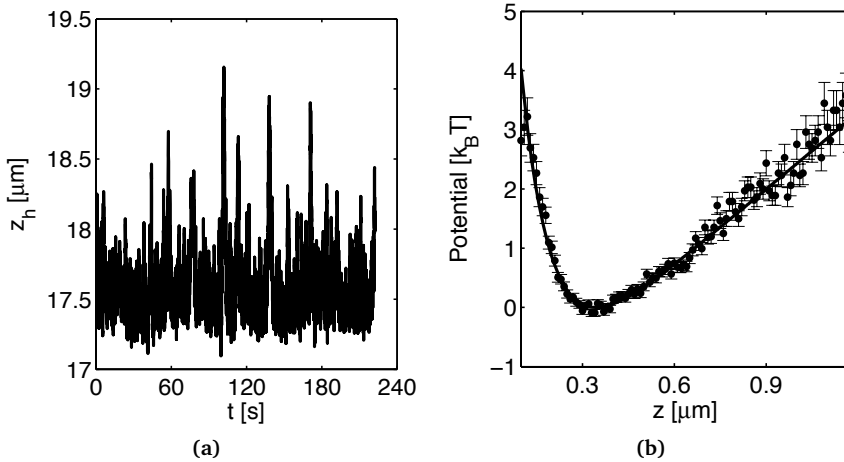


**Figure 2.24:** *Bouncing around on the bottom.* After sedimenting, the  $1.4 \mu\text{m}$  silica particle in ethanol from Figures 2.21 and 2.22 diffused freely over the bottom of the capillary. **a.** The heights of the particle as a function of the time. **b.** The probability density function, pdf from the positions in **a.** The full line is a fit to equation 2.22.

The axial distance of the particle from the hologram plane varied with time, even after correction for the linear component of the drift of the objective as plotted in Figure 2.20 **a.** The particle depth was assumed to be in thermal equilibrium and thus the potential energy as a function of the depth can be determined from the Boltzmann distribution. The  $10^4$  particle depths were binned in bins of  $10 \text{ nm}$  and the logarithm of the probability distribution was taken. The apparent potential is represented in Figure 2.20 **b** by statistical error-bars.

This method of analyzing the interaction potential between the wall and a colloidal particle is similar to the analysis of Total Internal Reflection Microscopy, TIRM, measurements [84, 85]. In this technique the distance between the glass wall and a colloidal particle is determined from the intensity of the light scattered away by the particle from the evanescent field due to total internal reflection. This way many different wall particle interactions such as a depletion interaction and the effect of steric stabilization can be studied. For an overview of the literature on wall particle interactions we refer to a review paper [86].

Dennis C. Prieve wrote a review paper on the achievements of the first decade of TIRM [87] in which also the simplest case where the potential the particle experiences is the result of two factors, gravity and charge repulsion is discussed. When the separation distance between the wall and the particle is several nanometers, the van der Waals attraction is severely retarded and screened. When the screening of the charge is sufficiently small, for Debye screening lengths of more than  $10 \text{ nm}$ , the interaction between the wall is correctly described consid-

ering only the charge repulsion. The total potential energy profile is expected to obey:

$$\frac{U(z)}{k_B T} = \frac{B}{k_B T} e^{-\kappa z} + \frac{mg}{k_B T} z. \quad (2.20)$$

Here  $U(z)$  is the potential energy as a function of the depth  $z$ ,  $k_B T$  Boltzmann's constant multiplied with the absolute temperature,  $\kappa$  the inverse Debye screening length,  $m = 4/3\pi r^3(\rho_p - \rho_m)$  the weight of the particle and  $g$  the gravitational acceleration. The factor  $B$  for monovalent ions is given by:

$$B = 16\epsilon r \left( \frac{k_B T}{e} \right)^2 \tanh \left( \frac{e\Psi_{\text{particle}}}{4k_B T} \right) \tanh \left( \frac{e\Psi_{\text{wall}}}{4k_B T} \right), \quad (2.21)$$

where  $\epsilon$  is the dielectric constant of the solvent,  $r$  the radius of the particle,  $e$  the elementary charge and  $\Psi_{\text{particle}}$ , respectively  $\Psi_{\text{wall}}$  are the surface potentials of the particle and the sphere.

When exact the position of the wall is unknown we cannot quantitatively determine the charge of the particle and the wall, we then refer to the height with respect to the minimum in the potential given by  $z_{\text{min}} = \frac{1}{\kappa} \ln \left( \frac{\kappa B}{mg} \right)$ .  $B$  can be eliminated from equation 2.20:

$$\frac{U(z - z_{\text{min}})}{k_B T} = \frac{mg}{\kappa k_B T} \left( e^{-\kappa(z - z_{\text{min}})} - 1 \right) + \frac{mg}{k_B T} (z - z_{\text{min}}). \quad (2.22)$$

We fitted equation 2.22 to the apparent potential in Figure 2.24 **b**, the result of which is plotted as the full line. The weight of the particle was found to be  $1.77 \pm 0.01$  pg while the Debye screening length was found to be  $93 \pm 3$  nm. Taking the density of the ethanol to be  $0.79$  g/cm<sup>3</sup> and the density of the particle to be  $1.92$  g/cm<sup>3</sup>, this weight agrees within the uncertainty with  $4/3\pi * r^3 * (1.9 - 0.79) = 1.81 \pm 0.01$  pg.

## Conclusion

TIRM is limited to measuring particle positions that are closer to the wall than the penetration depth of the evanescent field. We have shown that DHM can also be used to measure interaction potentials between the wall and the particle. DHM is not limited in depth and can thus be used to measure long-ranged particle wall interactions. When DHM is applied to a system with long-ranged interactions [21, 88–97] it could be used to measure the screening length. If the position of the wall is known, for instance from a second particle that is stuck to the wall in the primary van der Waals minimum, the technique could also be used to measure the charge repulsion between the wall and the particle from a fit value of the factor  $B$ , for the charge on the wall and the particle, in equation 2.22.

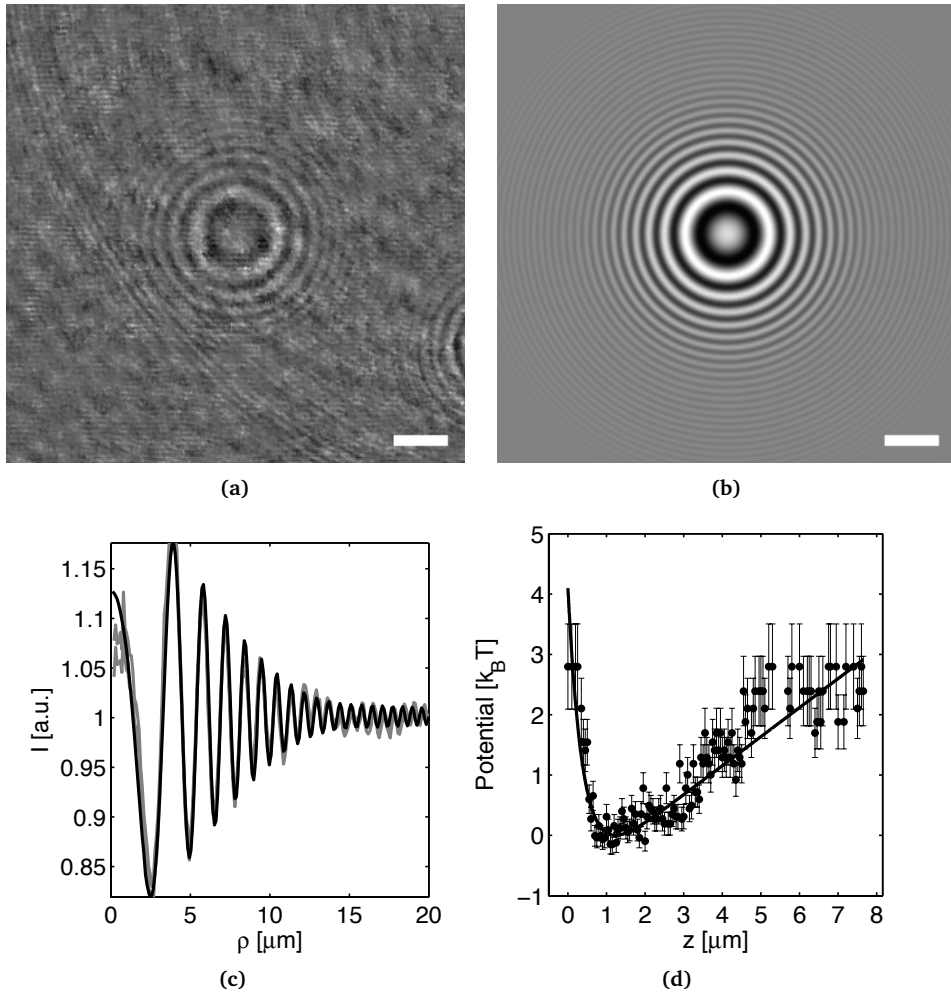


**Figure 2.25:** DHM applied to a PS particle. **a.** In-line holograms of a PolyStyrene PS particle in ethanol. **b.** Fitted hologram. The particle was fitted to be  $22.82 \pm 0.01 \mu\text{m}$  above the focal plane. The pure PS particle was fitted to have a radius of  $0.51 \pm 0.01 \mu\text{m}$  and to have a refractive index of  $1.573$  and  $\pm 0.001$ . The scalebar is  $5 \mu\text{m}$ . **c.** Azimuthally averaged radial profile. The black line represents the intensities in the fitted holograms. The grey lines indicate the averages in the experimental holograms plus and minus the statistical error. The wavelength was  $532 \text{ nm}$ . **d.** The wall induced potential. The full line is a fit to equation 2.22

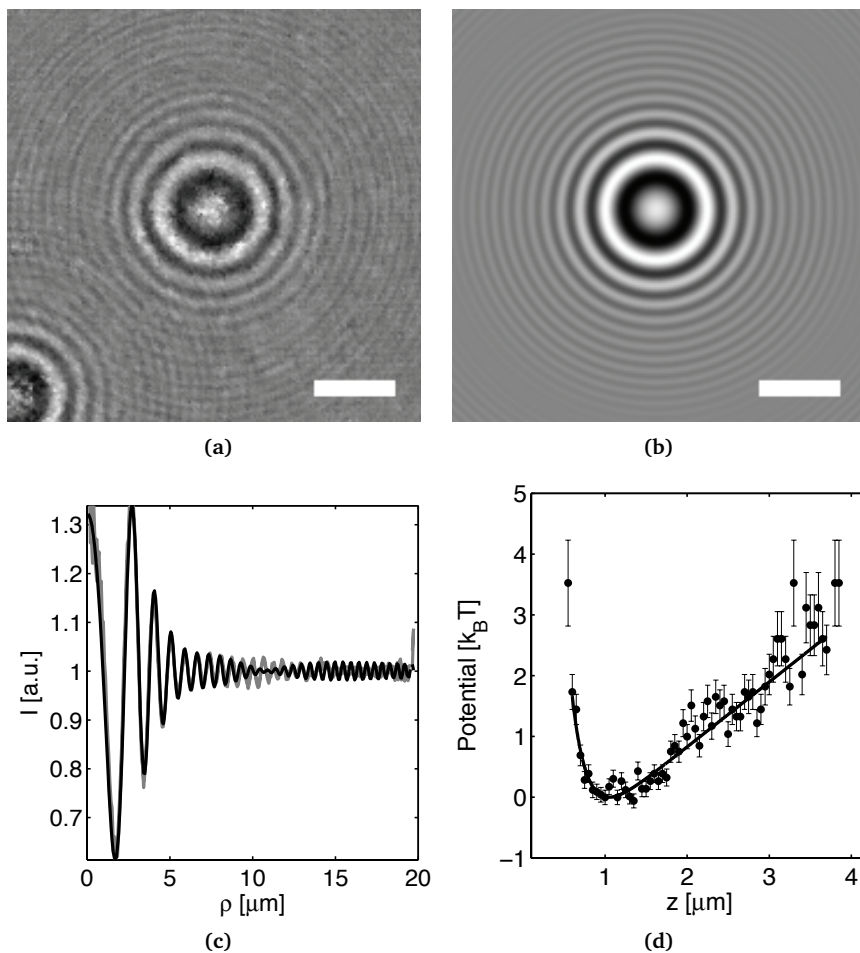


**Figure 2.26:** DHM applied to a  $\text{SiO}_2$  coated PS particle. **a.** In-line holograms of a silica coated PS particle in ethanol. **b.** Fitted hologram. The particle was fitted respectively to be  $15.28 \pm 0.01 \mu\text{m}$  above the focal plane. The scalebar is  $5 \mu\text{m}$ . **c.** Azimuthally averaged radial profile. The black line represents the intensities in the fitted holograms. The grey lines indicate the averages in the experimental holograms plus and minus the error. The wavelength was  $532 \text{ nm}$ . **d.** The wall induced potential. The full line is a fit to equation 2.22

### 2.5.6 Silica coated PS spheres

The theory for the scattering of uniform dielectric scatterers was extended to particles with a core-shell structure where the shell material has an index of refraction that deviates from that of the core [44]. Particles can be made to reflect less light with a carefully chosen coating. Such an anti-reflection coating reduces the scattering force and creates favorable trapping behavior in optical traps [20, 98–101]. For a more extensive discussion of the trapping of core-shell particles the reader is referred to section 5.6.

To facilitate better trapping of  $\sim 1 \mu\text{m}$  PolyStyrene PS particles in water, these can be coated with a silica layer [101]. A silica coating around PS particles [102], also allows them to be used as trappable tracer particles [103, 104] in a system of otherwise index matched particles [21, 88–97, 104] by preventing the dissolution of the core [105].

990 nm PS particles (BANGS laboratories) were acquired and coated with 87 nm silica using the techniques described in [102, 105]. The thickness of the silica was determined using TEM. Both the particles as received and the coated particles were dispersed in pure ethanol and holograms were recorded with the same setup as was used in section 2.5.3.

In Figure 2.25 **a-c** we present an in-line hologram, its fit and the radially averaged intensity of a bare PS particle in ethanol. The particle was  $22.82 \pm 0.01 \mu\text{m}$  above the focal plane. The radius and refractive index were fit to be  $0.51 \pm 0.01 \mu\text{m}$  and to have a refractive index of 1.573 and  $\pm 0.001$  respectively. The average values from the entire trajectory of 2000 frames were  $0.53 \pm 0.03 \mu\text{m}$  and  $1.55 \pm 0.04$  respectively. In literature, values in the range from 1.55 to 1.60 are mentioned [106]. These particles are relatively small which means they do not scatter light in a characteristic manner. The scattering pattern of this particle in 2.25 **c** barely shows any minima in the envelope over the fringes. The consequence of this is that the particle size and refractive index cannot be determined with great accuracy. The calculated uncertainties in the fit parameters do not reflect their precision as the model error which is minimized does not depend sensitively on the particle parameters in this range. The fitting algorithm sometimes finds another minimum that suggests that the particle has a refractive index of 1.54. These particles can however be characterized using SLS measurements as this method has access to information about larger scattering angles.

The position of the particle however, can still be determined quite accurately with an uncertainty of  $0.005 \mu\text{m}$  and  $0.01 \mu\text{m}$  in the lateral directions and in the axial direction respectively. These error estimated were gathered from the mean squared displacement [83] as in section 2.5.4.

The information of the particle depths was used to determine the interaction potential between the glass wall of the capillary and the particle in the same way as was done in section 2.5.5. In Figure 2.25 **d** we plot the interaction potential of this bare PS particle in ethanol with the glass wall of the capillary and gravity. Equation 2.22 was fit to this potential to find the Debye screening length in

the system and the weight of the particle. From this analysis it was found that the particle's weight was  $0.202 \pm 0.06$  pg. This agrees with the value given by  $4/3\pi r^3(\rho_{\text{PS}} - \rho_{\text{ethoh}}) = 0.42 \pm 0.05$  pg. The Debye screening length  $\kappa^{-1}$  was fit to  $0.37 \pm 0.08$   $\mu\text{m}$ . The screening length is a reasonable value in ethanol. We did not attempt to verify the screening length.

A particle that was coated with nominally 87 nm of silica was holographed in the same way. In Figure 2.26 a-c we provide the same analysis of this particle. The particle was at a distance of  $11.45 \pm 0.01$   $\mu\text{m}$  from the hologram plane. The scattering coefficients that describe the scattering of spherical dielectrics in the model (equation 2.14 and 2.14) in an expansion of spherical harmonics, can be replaced by those for particles with a core-shell structure [3, 44]. For the calculation of trapping forces on such core-shell particles these are given in Chapter 5 in equation 5.13 and 5.14. An attempt to fit a model for in-line holograms of core-shell particles with adapted version of equation 2.16 to holograms like the one in Figure 2.25 a did not yield consistent results. We conclude that the scattering by these particles is not characteristic enough to characterize the two radii and two refractive indices of the particles simultaneously. We found that for 1  $\mu\text{m}$  PS particles in ethanol the addition of a thin  $< 1$   $\mu\text{m}$  silica layer on the particle surface does not change enough to be able to characterize the silica layer separately. Instead, we ignored the fact that the particle is coated with silica and fit the particle as if it were homogeneous. The average fit value for the radius was  $0.58 \pm 0.01$   $\mu\text{m}$  while the refractive index was found on average as  $1.57 \pm 0.01$ .

Because the interference pattern resulting from the different optical path-lengths still contains more than enough information in the fringes, see Figure 2.25 a-c, we could analyze the distribution of depths as we did for the bare PS particle in Figure 2.25 d. Again we fitted equation 2.22 to the potential to find the Debye screening length in the system and the weight of the particle. From this analysis it was found that the particles weight was  $0.46 \pm 0.1$  pg. The Debye screening length  $\kappa^{-1}$  was fit to  $0.11 \pm 0.03$   $\mu\text{m}$ . This suggests that the ethanol contained more ions than in the sample in Figure 2.24. The  $0.4 \pm 0.1$  pg the particle gained in weight is in agreement with the theoretical weight of a 87 nm thick layer of silica around a particle with a radius  $\sim 0.509$   $\mu\text{m}$ . The measurement could be made more accurate if more holographic snapshots are considered to gather better statistics.

## Conclusion

We have shown that DHM can be applied to core shell particles but that the optical characterization is challenging for particles with a core radius of around half a micron. Fitting an equation for the interaction potential between the particle and the glass of the capillary to the measured interaction potential allows one to measure the weight increase upon coating of the particles.

## 2.6 Multiple particles

The illuminating beam, which in the case of in-line holography also acts as reference beam, will be disturbed if too many particles are scattering the light in various directions. However, it is possible to register the scattering of multiple particles in a single frame. It can be interesting to track multiple particles simultaneously, for instance to directly measure inter-particle forces, as will be shown in Chapter 3. For the moment, we assume that the volume fraction is sufficiently low for most of the reference beam to reach the hologram plane unperturbed. In this case, the intensity distribution in the hologram plane can be described accurately by an extension of equation 2.19. For two particles this becomes:

$$B(\vec{\rho}_{xy}) = \frac{\left| \tilde{R} + \tilde{E}_{1s}(\vec{\rho}_1, \beta_1, m_1) + \tilde{E}_{2s}(\vec{\rho}_2, \beta_2, m_2) \right|^2}{\tilde{R}^2}, \quad (2.23)$$

where  $\vec{\rho}_1$  respectively  $\vec{\rho}_2$  stand for the distance from the center of particle 1 respectively 2 to the pixel at  $\vec{\rho}_{xy}$ .  $\beta_1$  And  $\beta_2$  are the size parameters of respectively particle 1 and 2 and the same holds for the relative refractive indices  $m_1$  and  $m_2$ . Evaluation of equation 2.23 involves cross terms:

$$\begin{aligned} B(\vec{\rho}_{xy}) &= \frac{\tilde{R}\tilde{R}^*}{\tilde{R}\tilde{R}^*} + \frac{\tilde{R}\tilde{E}_{1s}^*(\vec{\rho}, \beta, m)}{\tilde{R}\tilde{R}^*} + \frac{\tilde{E}_{1s}(\vec{\rho}, \beta, m)\tilde{R}^*}{\tilde{R}\tilde{R}^*} \\ &+ \frac{\tilde{R}\tilde{E}_{2s}^*(\vec{\rho}, \beta, m)}{\tilde{R}\tilde{R}^*} + \frac{\tilde{E}_{2s}(\vec{\rho}, \beta, m)\tilde{R}^*}{\tilde{R}\tilde{R}^*} \\ &+ \frac{\tilde{E}_{1s}(\vec{\rho}, \beta, m)\tilde{E}_{1s}^*(\vec{\rho}, \beta, m)}{\tilde{R}\tilde{R}^*} + \frac{\tilde{E}_{2s}(\vec{\rho}, \beta, m)\tilde{E}_{2s}^*(\vec{\rho}, \beta, m)}{\tilde{R}\tilde{R}^*} \\ &+ \frac{\tilde{E}_{1s}(\vec{\rho}, \beta, m)\tilde{E}_{2s}^*(\vec{\rho}, \beta, m)}{\tilde{R}\tilde{R}^*} + \frac{\tilde{E}_{2s}(\vec{\rho}, \beta, m)\tilde{E}_{1s}^*(\vec{\rho}, \beta, m)}{\tilde{R}\tilde{R}^*} \\ &= \alpha + \frac{2\alpha\tilde{R}\tilde{E}_{1s}^*(\vec{\rho}, \beta, m)}{\tilde{R}\tilde{R}^*} + \frac{2\alpha\tilde{R}\tilde{E}_{2s}^*(\vec{\rho}, \beta, m)}{\tilde{R}\tilde{R}^*} \\ &+ \alpha^2 \frac{\tilde{E}_{1s}(\vec{\rho}, \beta, m)\tilde{E}_{1s}^*(\vec{\rho}, \beta, m)}{\tilde{R}\tilde{R}^*} + \alpha^2 \frac{\tilde{E}_{2s}(\vec{\rho}, \beta, m)\tilde{E}_{2s}^*(\vec{\rho}, \beta, m)}{\tilde{R}\tilde{R}^*} \\ &+ 2\alpha^2 \frac{\tilde{E}_{2s}(\vec{\rho}, \beta, m)\tilde{E}_{1s}^*(\vec{\rho}, \beta, m)}{\tilde{R}\tilde{R}^*}. \end{aligned} \quad (2.24)$$

For simplicity we left out the subscripts 1 and 2 for the arguments  $\rho, \beta, m$  of the  $\tilde{E}_{2s}$  and  $\tilde{E}_{1s}$  terms respectively. When the two particles are far enough away from each other in the lateral direction to not be in their mutual near fields, nor in the significantly brighter part of the scattered light, this is a valid description of an in-line hologram of two particles. The fitting of holograms with two particles involves the optimization of more parameters. If we assume  $\alpha$  to be the same for

both particles this gives 11 variables to be optimized. Naturally this is easier when the particles are separated in space so that the information about the two particles arrives, mostly, on separate pixels. In other words, the worst case scenario is when the two particles are located above each other. In that case the information of both particles ends up on the same pixels. Apart from that, assuming the particles are more than a wavelength apart, the lower particle is also directly irradiated by the scattered field of the upper particle which is not taken into account in equation 2.24.

In section 2.6.1, we will fit equation 2.24 to holograms of two silica particles in ethanol at different distances and look at the influence of the distance between the particles on the quality of the fits.

In section 2.6.2, we proceed by extending the number of particles in the hologram to seven particles in a honeycomb structure that is formed by means of time-shared optical tweezers as described in the Chapters 4, 5 and 6. Subsequently we shall show that the technique of fitting the Lorenz-Mie-Debye theory to experimental holograms can even be applied to particles that are clearly in their mutual near fields with a study of the diffusion of a dumbbell in section 2.6.4. Then in section 2.6.5 we study the diffusion of a semi-flexible analogue of bio-polymers consisting of PS spheres. Finally, we show a few snapshots of a string of silica particles which have been stuck to each other with optical tweezers using the van der Waals attraction while it is bent by optical tweezers in section 2.6.6.

### 2.6.1 2 particles

The simplest form of inter-particle interactions are pair potentials. Here the interaction between many particles is simplified as if it were the sum of the interaction between all the couples of two particles. There are many techniques to measure the pair potential. Some are based on the study of a dilute dispersion, for instance by considering the radial distribution function, the so-called  $g(\mathbf{r})$ , see also section 2.2.2. Here, the radial pair correlation function is inverted using the Boltzmann distribution or compared with simulated  $g(\mathbf{r})$ 's [16, 18, 107, 108].

One can also look at the collective modes of the particles in a crystal to quantify the interaction from the apparent potential the particles experience [17, 19]. It can be hard to gather enough statistics, particularly for the less likely distances between particles. A solution might be to increase the volume fraction but this has the drawback that multiple particle interaction may start to play too large a role.

Alternative techniques aimed at measuring the interactions between colloids actually measure the interactions between a colloid and a flat plate, as in TIRM [84, 85], see also section 2.5.5, or the interaction forces acting on the tip of an atomic force microscope that may or may not have a colloid on its surface [109].

The measurement of inter-particle interactions can be helped greatly by bringing the particles together in relatively improbable configurations using optical tweezers [81, 110, 111]. The actual particle interactions can then be obtained from

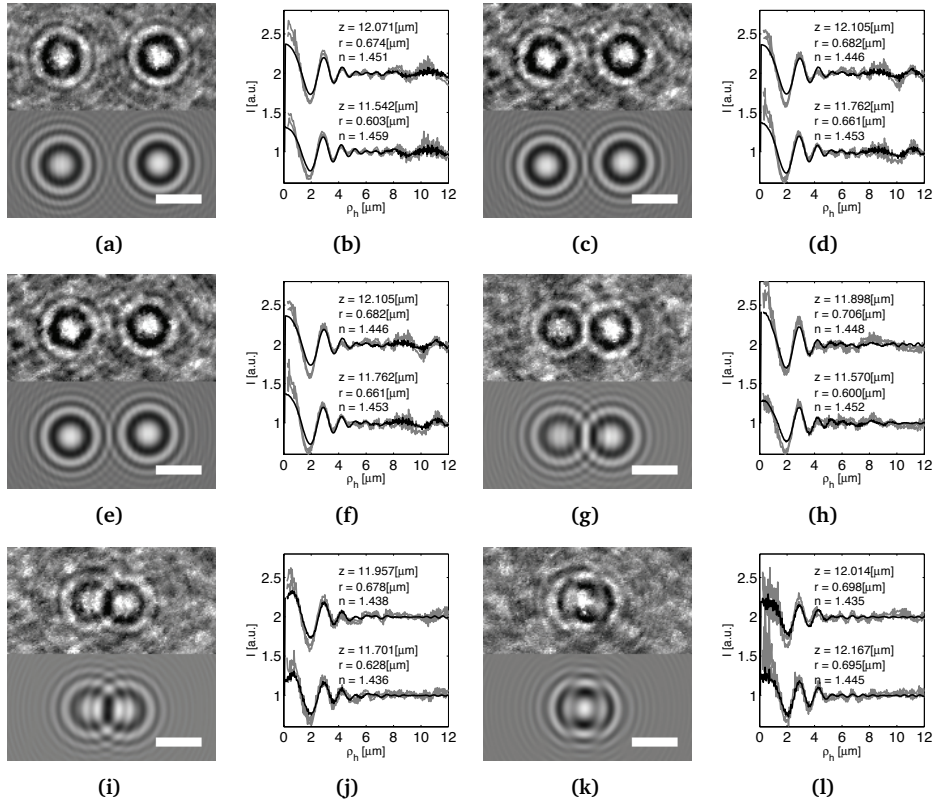


**Figure 2.27:** DHM applied to two silica spheres in Ethanol. Holograms of two  $1.4 \mu\text{m}$   $\text{SiO}_2$  ( $n = 1.45$ ) spheres in ethanol ( $n = 1.36$ ),  $\sim 12 \mu\text{m}$  below the particles. **a.** A hologram (top) and its fit (bottom) at spacing  $S = 10.585 \pm 0.005 \mu\text{m}$ . **b.** The radial averages centered at both particles, the left particle corresponds to the lower curve. The black curve is the radial average in the fit. The grey curves are experimental radial averages plus and minus the statistical error. **c-d.** The same as in **a-b** with a spacing of  $S = 8.440 \pm 0.005 \mu\text{m}$ . **e-f.**  $S = 6.896 \pm 0.005 \mu\text{m}$ . **g-h.**  $S = 5.516 \pm 0.005 \mu\text{m}$ . **i-j.**  $S = 3.624 \pm 0.005 \mu\text{m}$ . **k-l.**  $S = 1.582 \pm 0.005 \mu\text{m}$ . The error estimate for the particle radii from the fit was  $0.005 \mu\text{m}$  for the radii and  $0.001$  for the refractive indices. Scalebars are  $5 \mu\text{m}$ .

the distribution of particle separations that yield a potential through the Boltzmann distribution where the potential then needs to be corrected for the trap potential, see [81] and references therein. Alternatively, one can measure the displacement of the particle in an optical trap of calibrated stiffness to measure the force [80, 112]. A variation to this is the technique presented by Sainis *et al.* [113] where the forces on the particles are measured against the Stokes drag which yields superior force resolution. In Chapter 3 we discuss this method in more detail.

All these techniques rely on accurate particle position detection, which can be problematic when the particles are close to each other [114, 115]. Baumgartl and Bechinger [115] showed that when the images of the particles start to overlap, this results in a systematic error in the position measurement. The sign of this error changes as a function of the distance which can show up in the force measurements as an attraction that is solely due to the imaging error. In the same paper however, they showed that these errors can be corrected for by taking the individual particle images as proposed by Ovryn *et al.* [116, 117] into account rather than applying a simple centroid finding algorithm like the one proposed by Crocker and Grier [14]. Often, the Debye screening length is long enough to prevent that the particles get as close to each other as to have their images overlap. When the suspension is forced in between two glass plates, the particles are located in the double layer of the walls, the higher ion concentration there makes that the Debye screening length is shorter so that the particles get close enough together for these imaging artifacts to occur. The appearance of an ‘attraction’ has provoked a vivid discussion in the literature on the existence of like charge attractions [114, 118–121] where the existence of like charge attractions have been confirmed, contested and explained by hydrodynamics [122].

To be able to use DHM to measure forces between multiple particles, we thus have to be aware of the risk that the position measurement suffers from an inaccuracy that is a function of the distance between the particles. This is a particular risk as the interference patterns between the light scattered by the particle and the reference beam are large. As can be seen in the examples above, the fringes extend over an area many times larger than the particle and the fringes from both particles overlap.

However, if we fit equation 2.24 to holograms in which two particles are imaged, we take the effect that the image of particle 1 may have on the image of particle 2 into account. We even take the interference between the scattered waves of the two particles into account.

To test the ability of DHM to track two particles and to test the ability of measuring the positions even when the particles are close, we placed two  $1.4\ \mu\text{m}$  silica particles, from the same batch as was used for the sedimentation experiments in section 2.5.4 in two optical traps. The condenser was replaced by a mirror, reflecting the beam from a fibre coupled Spectra Physics Millennia V 532 nm laser at minimum power through the sample, into the objective. The integration time of the camera was set to  $80\ \mu\text{s}$ . The holograms were recorded at 100 fps on Mikrotron EoSens CE camera. Only a field of view of 160 by 450 pixels was recorded, this saves space on the memory card of the camera and allows one to record sufficient images to gather statistics for possible force measurements.

To record the background and the intensity offset, the traps with the particles were moved out of the field of view. After 1000 frames, the particles were moved back into the field of view and the actual measurement began. Figure 2.27 represents some experimental snapshots, the fit and also the radially averaged intensity centered at both particles. The black line represents the radially averaged intensity in the fit while the grey lines represent the radially averaged intensity plus and minus the statistical error in the experimental hologram.

In these radial averages the presence of the other particle is clearly present. In Figure 2.27 **b**, **d**, **f** and **h** a clear image of the hologram of the other particle can be seen in the radial averages of both particles. This appears as noise, even in the radial averages of the model, because the intensity varies wildly with the distance. This is due to the binning of the pixels to radial distances. The fact that the signature of the other particle appears most clearly in Figure 2.27 **b** is emphasized due to the finite field of view which makes that the pixels occupied by the other particle are weighed more heavily in the average. When the particles get closer to each other, the fringe patterns of the particles start to overlap. This has strong repercussions on the radially averaged intensities in Figure 2.27 **i-l**. The first minimum in the intensity starts to overlap with the central bright spot of the other particles. This is reflected in the lower intensity in the central spots of the holograms of particles at smaller separations.

The fits seem to be an accurate representation of the experimental holograms, it looks as if the fit is equal to the experiment with the noise in the background deduced. Nevertheless, the fit values for the particle radius and the particle refractive index varies with the particle position. We think this is due to the irregularities in the background that remained visible even after dividing out the background.

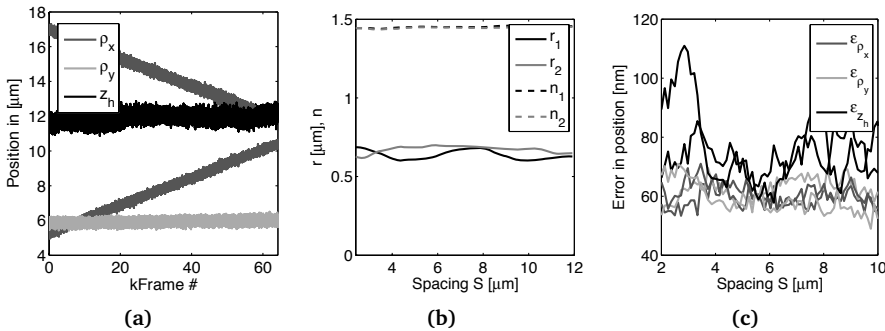


**Figure 2.28:** DHM applied to two silica spheres in Ethanol. **a.** The trajectories of the two particles in Figure 2.27. The larger noise in the  $z_h$  coordinates is due to the lower trap stiffness in that direction and the fact the curves for the two particles overlap. **b.** Boxcar averaged of the particle radii and refractive indices as a function of the inter-particle spacing  $D$ . **c.** Error estimates in the particle positioning from the offset of the mean squared displacements.

In Figure 2.28 **a** the trajectories in space are plotted as a function of the frame number. It is clearly visible that the particles move closer together in the  $x$ -direction. The larger noise in the axial positions is only partially due to the larger error in the position measurement in that direction. The main component to the noise in the axial direction is Brownian motion that has more freedom to move the particles in that direction due to the smaller trap stiffness in that direction. See also the Chapters 4, 5 and 6 for a more elaborate evaluation of the trapping of colloids.

The fit values for the particle radii and refractive indices are plotted as a function of the spacing  $S$  between the particles in Figure 2.28 **b**. There is some variation in the fit value for the particle radius. The curves as a function of the particle spacing do not seem to reflect the shape of the intensity distribution of the other particle in any way. Moreover, the curves do not look alike. We therefore think that the variation in the fit values of the particle radii is not due to the presence of the other particle but more due to the remaining variation in the background intensity, visible in Figure 2.27, as a function of the particle position. The variation in the fit values for the particle refractive indices is much less than the variation in the particle radius which agrees with the uncertainty estimates from the minimization.

Similar as in reference [113] the two traps were periodically switched off, leaving the particles free to diffuse and to move under influence of the forces they experience due to interactions with each other and external fields. When the traps are off, the camera is triggered to take three holographic snapshots at 100 Hz. Then the traps are switched back on, putting the particles back in place so that they are not lost. The procedure is repeated 20,000 times while the two traps are slowly moved closer to each other. For each trajectory of three positions we calculated the average distance between the particles. The trajectories are binned in bins with a spacing of 50 nm. This leaves about 125 trajectories per bin. The mean square displacements,  $\Delta r_j^2(\tau) = \langle (r_j(t + \tau) - r_j(t))^2 \rangle$ , are calculated for the Cartesian components of the particle's positions in each bin. All three mean squared displacements display linear Einstein-Smoluchowsky scaling. Using the methods of reference [83], we then interpret the offsets obtained from linear fits to  $\Delta r_j^2(t)$  to estimate the accuracy for the lateral positions and axial positions as a function of the distance between the particles, Figure 2.28 **c**.

For most of the trajectories this gives error estimates for the position detection in the order of 60 nm in the lateral direction and around 100 nm in the axial direction. These numbers are greater than those reported in section 2.5.4. The error seems to depend more on the particle position than on the spacing in between the particles. Probably the noise in the background was larger when this experiment was conducted. This can be due to the fact that the optical traps were moved manually in between the recording of the background and the recording of the holograms themselves. Another contribution to the noise can be found in the camera, of which the sensitivity seems to depend slightly on the time between

two frames, which was not constant because we did not record any frames while the traps were on to position the particles. It is reasonable to assume that further improvements can be implemented to reduce the variation in the background and increase the precision of DHM measurements of the positions.

## Conclusion

We have shown that taking the light scattered by both particles simultaneously into account when fitting the holograms of two particles allows DHM to be applied to pairs of particles. This allows DHM to be utilized for force measurements. An elegant technique to which it may be applied is described by Sainis *et al.* [113] where the particles are not influenced by the optical traps while the forces are measured. The advantage of DHM above bright field microscopy is that it allows one to track the particles in the axial direction as well.

### 2.6.2 7 particles

The interaction between colloids is often assumed to be pairwise additive. This, however is not always the case and not at all volume fractions [123, 124]. When the interactions are long-ranged, multiple particle interactions can be important for particles that are not even close with respect to their diameter. This is also the case at high volume fractions or under confinement [115], where the particles are located in each other's double layers. Three-body interactions can play a role in 2D and 3D systems [125–129]. Also the hydrodynamics between multiple particles shows interesting behavior [129].

For the investigation of these kind of interactions it is important to be able to perform accurate and fast 3D position measurements. First of all, because out of plane motion can make the position detection and the measured forces inaccurate [128, 129]. Secondly, it might be interesting to measure the interactions between particles in a three dimensional rather than a 2D configuration.

To study the possibility to apply in-line holography with fitting to Lorenz-Mie-Debye theory to measure multiple particle interactions we study here an array of 7 particles that is made using time-shared optical tweezers. In that case equation 2.19 for the interference between the scattered light and the reference beam is extended as follows:

$$B(\vec{\rho}_{xy}) = \frac{\left| \tilde{R} + \sum_{i=0}^7 \tilde{E}_{is}(\vec{\rho}_i, \beta_i, m_i) \right|^2}{\tilde{R}^2}. \quad (2.25)$$

We leave the listing of all 64 terms after evaluation of the squares as an exercise to the reader. The evaluation of equation 2.25 costs roughly seven times as much time as it takes to evaluate equation 2.17, if the same number of pixels is considered. Fitting the equation to an experimental hologram also takes more hologram evaluations as there are more variables to be optimized.

Alternatively, one can also choose to fit the particles one by one and deduce the fitted hologram from the experimental hologram before proceeding, in a process that is similar to that reported in [55, 56]. The consequence of this strategy is that the cross terms for the interference between the scattered light of different particles are not taken into account, which may be reasonable when the particles are spaced far enough to have only the fainter outer rings overlap. Another result is that the scattered light of the other particles acts as noise when fitting a particle. The Levenberg-Marquardt algorithm may find parameters that produce a hologram that resembles this noise. Again, this effect is worse in the case that the particles are closer. This second effect that the fits of the individual particles are influenced by the holograms of neighboring particles, can be reduced by subtracting the fits of all particles but one and fit that one. When this is done iteratively, the order in which the particles are fit becomes irrelevant.

As this is an iterative process in which all seven individual holograms have to be fitted several ( $\sim 4$ ) times, it may not be faster than directly fitting equation 2.25 to the experimental hologram. The latter also has the advantage that the cross terms are considered and that the problem of fitting the parameters of one particle to the scattering by others is reduced. In the following we show some results of both strategies.

We placed seven silica particles with a nominal radius of 875 nm in TetraHydroFurane, THF with a refractive index of 1.406 and a dielectric constant at zero frequency of  $\epsilon = 7.52$ . As was the case for CHC in section 2.2.2, it is more difficult than it is in aqueous systems for ions to dissociate in THF. As a result, there are fewer ions in the solvent, and thus there is less screening. As the screening by ions is reduced, the Debye screening length is significantly increased. Particles in such intermediate dielectric constant solvents can acquire surface potentials similar to those in aqueous solutions 50-100 mV [22]. As a consequence, the resulting interaction between silica spheres in THF can be rather long-ranged.

In this section, we will focus on the tracking of colloids. The particles were trapped in a honeycomb array. The array was moved out of the field of view to record the background. After 1000 frames, the array was slowly moved into the field of view and a hologram of seven particle was recorded. During the movie, the particles were slowly brought closer together as in section 2.27, see also Chapter 3. Again, the images were recorded on a Mikrotron EoSens CE camera, while the particles were illuminated using a fibre coupled Spectra Physics Millennia V 532 nm laser at minimum power. The laser intensity was attenuated using polarizers. The integration time of the camera was set to 80  $\mu\text{s}$ .

In Figure 2.29 a we present a typical snapshot of the experiment. Apart from the holograms of the particles themselves there are also fringes in two different directions. Apparently a rather large scattering object such as the edge of the capillary or a mirror has moved a little with respect to the recorded background. This is the disadvantage of manually moving a trapped particle into the field of view after the background has been recorded.

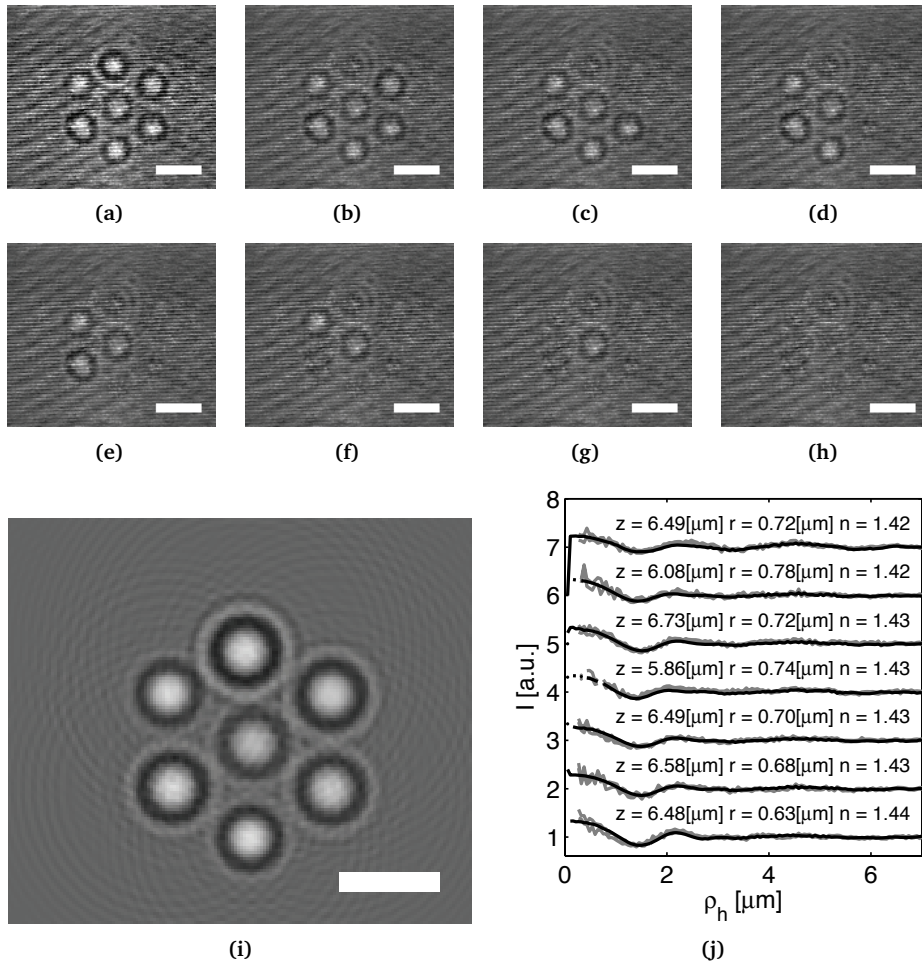


**Figure 2.29:** In-line hologram of 7 silica particles in THF-I. Seven silica ( $n = 1.45$  nm) particles with a radius of 875 nm have been trapped about 12  $\mu\text{m}$  above the hologram plane in a hexagonal array of time-shared traps at 14  $\mu\text{m}$  above the bottom glass wall. **a.** The hologram itself. **b-h.** The particles have been fitted and the corresponding holograms were subtracted from the hologram one by one. **i.** The fit of all seven particles simultaneously to the hologram in **a.** **j.** The radial averages centered on the particles in **i** in black. The radial averages are offset with the numbers of the sequence in **b-h.** The radial averages of the holograms in **a** plus and minus the standard deviation are plotted in grey.

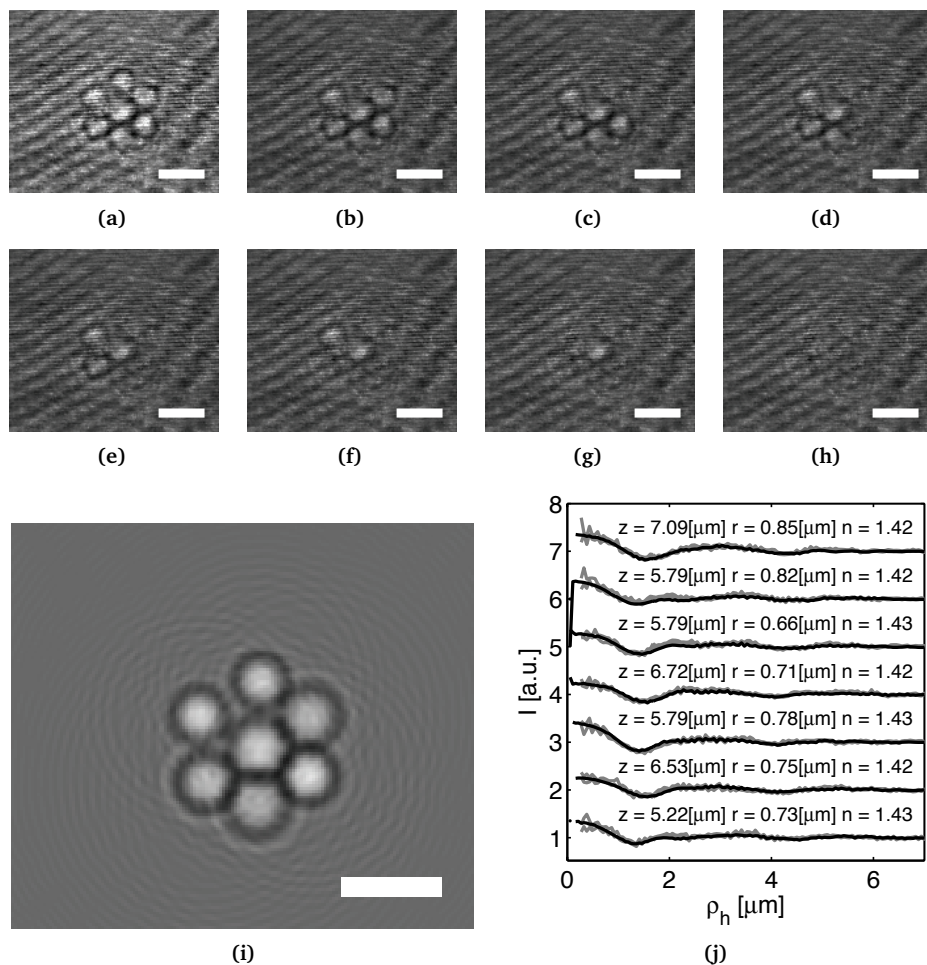


**Figure 2.30:** In-line hologram of 7 silica particles in THF-II. Seven silica ( $n = 1.45$  nm) particles with a radius of 875 nm have been trapped about 12  $\mu\text{m}$  above the hologram plane in a hexagonal array of time-shared traps as in Figure 2.29 but closer together. The array was trapped 14  $\mu\text{m}$  above the bottom glass wall. **a.** The hologram itself. **b-h.** The particles have been fitted and the corresponding holograms were subtracted from the hologram one by one. **i** The fit of all seven particles simultaneously to the hologram in **a.** **h.** The radial averages centered on the particles in **i** including also the other present particles in black. For clarity, the radial averages have been offset with the numbers of the sequence in **b-h.** The radial averages of the holograms in **a** plus and minus the standard deviation are plotted in grey.

In Figure 2.29 **b-h** we show the hologram with progressively more fitted holograms, from the first iteration, subtracted. If the fits were perfect, Figure 2.29 **h** would show only the background, that is the intensity profile that is not modeled by equation 2.25. The fits for these particles were fairly good. Only the first particle to be removed from the experimental hologram leaves a trace. Presumably, this particle was actually two particles, one above the other. The hologram for this particle looks different from that of the other particles. It often occurred that we un-intentionally trapped a second particle in the same trap. Modeling the scattering of two particles as if it were just one particle does not yield good fits. This means that it is possible to detect the presence of a second particle in the trap from the hologram.

In Figure 2.30 we performed the same analysis as in Figure 2.29 on a snapshot from another experiment with only single particles in the traps. In this particular snapshot, the spacing between the particles was smaller. Again the fitted hologram seems to capture most features of the experimental hologram. The radially averaged intensities are similar to those of the experimental holograms.

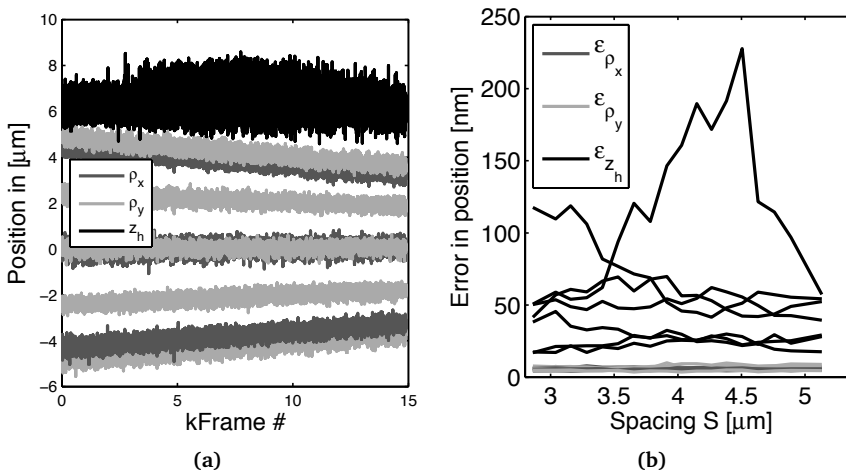


**Figure 2.31:** DHM applied to seven silica spheres in THF. **a.** The trajectories of the seven particles in Figure 2.27. The larger noise in the  $z_h$  coordinates is due to the lower trap stiffness in that direction and the fact the curves for the seven particles overlap. **c.** Error estimates in the particle positioning from the offset of the mean squared displacements.

In Figure 2.31 **a** we plot the traces of the seven particles in Figure 2.30 that move together as the spacing of the hexagonal array of traps gets smaller. The coordinates considered were the result of fitting all seven particles simultaneously by fitting equation 2.25 to the experimental holograms. The seven time-shared traps are occasionally all switched off, similar to in the experiment described in section 2.6.1 where we studied the applicability of DHM to track two particles.

When the traps were all off the particles were free to diffuse and to move under the influence of their mutual interactions and external fields, in this case gravity. During these intervals the camera was triggered to take four frames at 500 fps. The 13000 analyzed frames thus yielded 3250 trajectories. From the positions of the 7 particles, averaged over the trajectories, we calculated the twelve distances between them that should all be the same on a perfect hexagonal lattice. The average of these twelve distances was taken to be the spacing  $S$  of the array. The trajectories were binned into 16 bins each containing 200 trajectories.

From each trajectory we calculated the squared displacements in the  $\rho_x$ -,  $\rho_y$ - and  $z_h$ -directions over the 3, 2 and 1 time lapses of respectively 1, 2 and 3 time steps. These squared displacements were averaged over the trajectories in the bin. From the mean squared displacements,  $\Delta r_j^2(\tau) = \langle (r_j(t + \tau) - r_j(t))^2 \rangle$ , one can calculate the diffusion constant in all three Cartesian coordinates. All three mean squared displacements for all seven particles display linear Einstein-Smoluchowsky scaling. Using the methods of reference [83], we then interpret the offsets obtained from linear fits to  $\Delta r_j^2(t)$  to estimate the accuracy for the lateral positions and axial positions as a function of the distance between the particles. The error estimates thus obtained are reproduced in Figure 2.31 **b** suggests that the accuracy in the lateral positions were determined to within 50 nm throughout the experiment where the particles approach each other to within 3.5  $\mu\text{m}$ . In the axial direction the position was determined with a slightly lower accuracy of around 150 nm, depending on the background noise at the location of the individual hologram. There is one unfortunate exception. The axial position was much less accurate for the central particle, here the error estimate rises to as much as 230 nm. This is due to the fact that the surrounding particles are positioned on the rings in the hologram of the central particle. It is the information in these rings that contributes to the accuracy of the axial position detection.

### 2.6.3 Conclusion multiple particles

The above results suggest that DHM might be applied to also measure the interactions between multiple particles as in reference [128]. This allows the study of many body interactions and mimic the effect of slightly higher effective volume fractions. The advantage of applying in-line holography over bright-field microscopy for the measurements of inter-particle interactions lies in the slightly higher accuracy in the lateral position detection. The major advantage though is the axial position detection. Since optical tweezers are less stiff in the axial direction, see Chapters 4, 5 and 6, there is quite some displacement in that direction. Particularly when the repulsive forces between the particles are strong and when the particles are close to each other, a significant part of the distance and the forces between the particles lies in that direction. Being able to also accurately measure the particle displacements in the axial direction at hundreds of frames per second allows one to also measure forces 3D, as will be demonstrated in Chapter 3.

### 2.6.4 Dumbbell

In sections 2.6.1 and 2.6.2 we have seen that multiple particles can be fitted simultaneously in one hologram. The particles in those experiments were at the closest  $\sim 200$  nm apart (see Figure 2.27 **k-l**). When the particles are this close to each other, closer than the wavelength of the light, they start to be located in their mutual near fields. Around the particles that are scattering propagating waves, there is also a non-propagating, so-called near-field. The evanescent field used in Total Internal Reflection Microscopy is an example of such a non-propagating field. The model we use to fit to our experimental in-line holograms does not include these fields.

That is fine when considering single particles, or when considering particles that are more than a wavelength of the light apart. When two particles are close to each other, there is a finite probability that a photon first encounters one particle, is coupled to the other and then scatter by the second particle. In other words, particle 2 in the near field of particle one gets polarized and scatters light in the direction of the camera. Our model does not include this effect and it may be that the optimizing algorithm finds the wrong parameters. The strength of the near field falls off exponentially with the distance from the particles with a penetration depth that depends on the refractive indices of the particle and the solvent. The penetration depth is around a third of the wavelength [87]. The contribution of mutually scattered evanescent fields to the hologram of two particles is thus negligible unless the particles are closer than 100 nm. When the Debye screening length is at least 200 nm the scattering of two particles is probably not measurably influenced by the near field.

Another effect that is much larger is the phenomenon of multiple scattering. When the particles are positioned such that the part of the scattered light that is otherwise recorded in the hologram first hits another particle, part of this scattered light is scattered again. As most of the light is scattered in the forward direction, this happens in particular when the particles are above each other. The result of this multiple scattering is twofold. First of all, the hologram of the particle that scattered the light first is distorted. Secondly, the lower particle is not only illuminated by the plane waves of the illuminating beam, but also by the scattered light of the upper particle. Near field effects and multiple scattering is not taken into account in equation 2.24.

It is possible to calculate the scattering by any shape of dielectric matter or array of spherical particles by applying the so-called T-matrix formalism [41, 130, 131]. The advantage of the T-matrix formalism for the calculation of trapping forces is that it allows one to calculate the scattering by an object once for a particular size, shape (or orientation) and refractive index and then apply this as many times as needed for the evaluation of the trapping forces [130, 131]. In this sense it is similar to the Lorenz-Mie-Debye theory for the scattering of spherical particles. To characterize particles by fitting a model for the scattering to an experimental hologram however, requires that the model be evaluated for

many sets of trial parameters. The application of the T-matrix formalism may therefore become computationally intensive.

To experimentally test whether or not the contribution to the scattering of near field light of other particles to the total of the scattered light is relevant for the position detection by DHM, we study here the diffusion of a so-called colloidal dumbbell particle. A dumbbell consists of two spherical particles that are stuck together or that are even interpenetrating. There is no doubt that these two constituent spheres are close enough to scatter away part of their mutual near fields [132, 133]. From these experiments we will also see the effect of multiple scattering when the constituent spheres are, partially, above each other.

We used  $1.35\ \mu\text{m}$  PS particles that were sterically stabilized with polyvinylpyrrolidone, PVP, that were synthesized by dispersion polymerization [134]. These particles had a polydispersity, from SLS and TEM measurements of 4-5%. The particles were dispersed in DiMethylSulfOxide, DMSO, with a refractive index of 1.479. Two thin metal wires were pulled through a Vitrocom capillary ( $0.1 \times 2.0\ \text{mm}$ ) which was then filled with the dispersion. A radio frequency electric field was applied to the sample to induce dipoles in the particles that made the particles align parallel to the field as in reference [21, 80], typical field applied were  $\sim 50\ \text{V/mm}$  at 1 MHz. The connection between the spherical particles was made permanent by a simple thermal annealing step [135]. Among strings of other lengths there were also dimers in the dispersion.

One of these dimers was studied using DHM. We used the setup as in section 2.5.4 for the imaging. The integration time was set to  $100\ \mu\text{s}$ . We used optical tweezers to place the dumbbell in the center of the capillary where lubrication effects are minimal [136, 137]. Subsequently a movie was recorded at 20 frames per second where the frames were  $320$  by  $340$  pixels large.

Somewhere in the first few seconds of the movie, the dumbbell was observed to be positioned more or less horizontally. This means that its hologram looks like a hologram of two spherical particles that are close together, next to each other. A snapshot of such a frame is shown in Figure 2.32 a. The two constituent particles are located a distance of  $10.53$  and  $10.57 \pm 0.01\ \mu\text{m}$  above the hologram plane. In Figure 2.32 e we print the fit to the hologram in Figure 2.32 a, where we simply assume that the dumbbell is two particles by fitting to equation 2.24. The fit value for the distance between the two particles is  $1.30 \pm 0.05\ \mu\text{m}$ , which is close to the sum of the radii of the two constituent particles, that were in this case both fit to be  $0.69 \pm 0.05\ \mu\text{m}$ , in accordance with the SLS and TEM measurements. In the inset we drew the two spheres from a side-view along the  $y$  axis. The radii of the spheres in the inset are the optically determined radii. In Figure 2.32 i we finally plot the radial averages centered on both constituent particles. The black line plots the radial averages in the fitted hologram while the grey lines represent the radial averages in the experimental hologram plus and minus the statistical uncertainty.

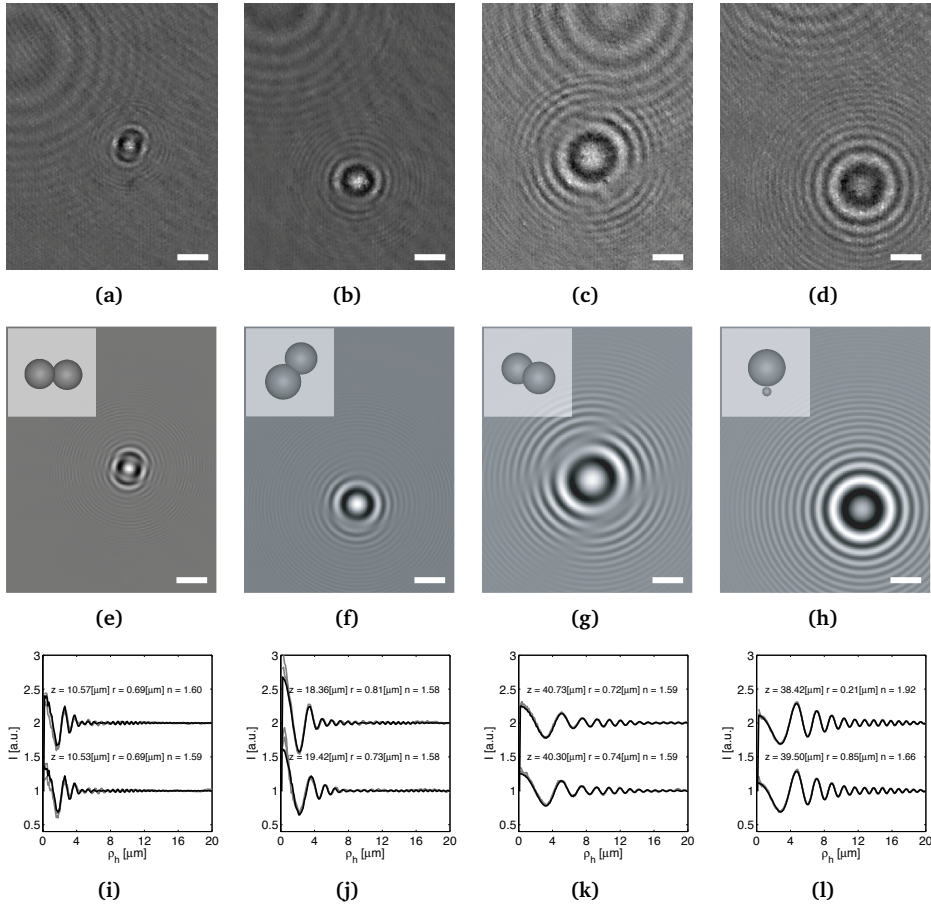


**Figure 2.32:** Diffusion of a PS dumbbell in DMSO: the holograms. In-line holograms of a freely diffusing dumbbell of  $1.35 \mu\text{m}$  PS ( $n = 1.59$ ) in DMSO ( $n = 1.4785$ ). **a-d.** Experimental holograms when the particle was respectively  $10.55$ ,  $18.89$ ,  $40.52$  and  $38.96 \pm 0.02 \mu\text{m}$  above the hologram plane. **e-h.** Fits of equation 2.24 to the holograms in **a-d**, the insets show a real space representation of the fitted parameters in the  $xz$  plane. The distances between the particles were estimated to be  $\text{dist } 1.30 \pm 0.05$ ,  $1.33 \pm 0.04$ ,  $1.33 \pm 0.04$  and  $1.1 \pm 0.5$ . **i-l.** Radial averages centered on the constituent particles. The black lines were taken from the fitted holograms and the grey lines were obtained from the experimental holograms plus and minus the statistical uncertainty. The scalebars are  $5 \mu\text{m}$ .

As the particle diffused, it also rotated and slowly rose due to the slightly higher density of the DMSO ( $1.101 \text{ g/cm}^3$ ) with respect to the particles ( $1.050 \text{ g/cm}^3$ ). This is also visible from the holograms in Figure 2.32 **b-d** and the fits in Figure 2.32 **e-h** with the corresponding radially averaged intensities in Figure 2.32 **j-l**. In Figure 2.32 **b** and **c** the dumbbell is also (partially) oriented horizontally, as can also be seen from the inset in which we drew the two spheres looking along the  $y$  axis. Due to the larger distance between particles and the hologram plane, the interference patterns corresponding to the two constituent particles overlap and interfere. This causes the appearance of lines where the two interference patterns more or less cancel each other as the bright rings of one particle fill up part of a dark ring of the other particle. The long axes of the dumbbell is oriented perpendicular to these lines. Despite the large number of pixels that receive scattered light by both particles, the fit values for the particle radii,  $0.81$  and  $0.73 \pm 0.04$  for the fit to Figure 2.32 **b** and  $0.72$  and  $0.74 \pm 0.08$  are almost consistent with the distance between the particles, respectively  $1.33 \pm 0.04$  and  $1.33 \pm 0.04 \text{ }\mu\text{m}$ . Also the fit values for the refractive indices,  $1.60$ ,  $1.58$  and  $1.59$   $1.58 \pm 0.01$  are reasonable for PS particles. The grey zones on either side of the particle center in Figure 2.32 **b** that are the result of the filling of the intensity minima of one hologram with the maxima of the other which are not of the same size due to the different distance  $z_h$  between both particles and the hologram plane. This is due to the fact that the particle was not level.

The particle in Figure 2.32 **d** is oriented vertically. The holograms of the two particles overlap completely. The information about the light scattered by the two particles is hard to separate. Apart from this, the light scattered by the top particle has to traverse the lower particle that will also scatter some of this light. In addition, the lower particle receives rather distorted illumination. There is also the fact that the particles are in their mutual near fields but this is the case for all orientations. That the holograms overlap and that the holograms are distorted by multiple scattering, makes the fitting of the scattering of two particles to this hologram particularly difficult. This is reflected in the rather strange fit values for the particle radii  $0.2 \pm 0.9$  and  $0.85 \pm 0.09 \text{ }\mu\text{m}$  for the upper and lower particle respectively. Also the fit values for the particle refractive index do not appear to be realistic with  $1.66 \pm 0.01$  and  $1.9 \pm 2$ . As the fitting is started with the fit values of the previous frame, the start values for the position are not that far besides the minimum that the Levenberg-Marquardt algorithm finds. The distance between the particles in the fit was  $1.08$  which is clearly an underestimate of what must have been the real distance between the particles.

All in all, the fits to the experimental holograms of a dumbbell to a model that describes the scattering of the individual spheres but that does not take multiple scattering nor near field effects into account do at least visually resemble the experimental holograms. The fit values do vary strongly with the orientation of the particles with the most realistic values occurring when the particles are more or less at the same distance from the hologram plane.

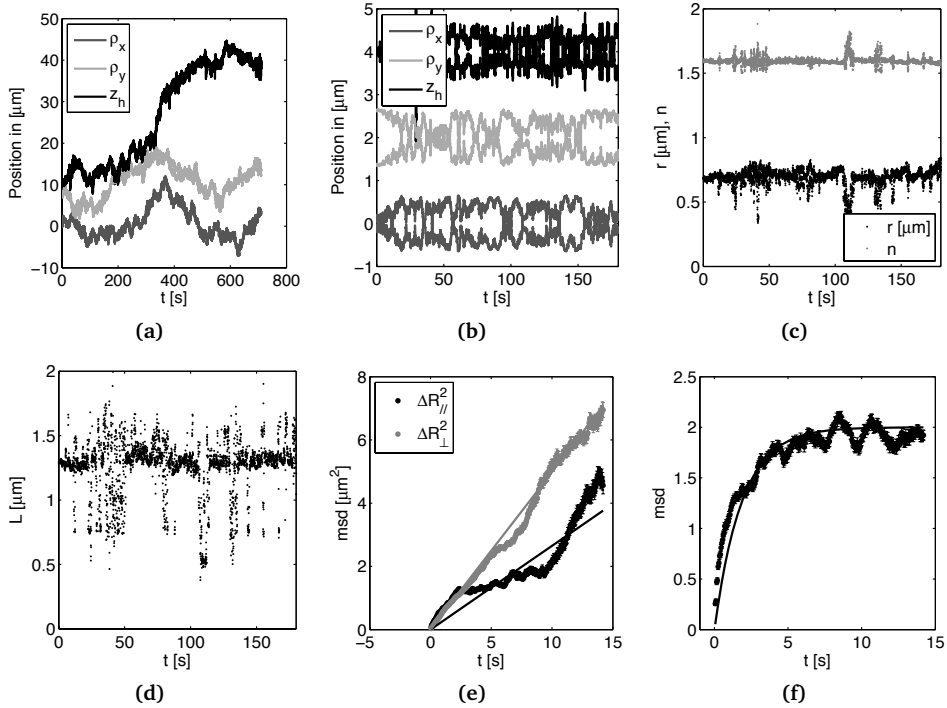


**Figure 2.33:** Diffusion of a PS dumbbell in DMSO: the graphs. **a.** The coordinates from DHM of the two PS particles forming a dumbbell in DMSO while it diffused and slowly rose in the DMSO, about 50  $\mu\text{m}$  into the sample. **b.** The coordinates of the two constituent particles relative to the center of mass of the dumbbell, leaving the rotational diffusion as the only contribution to the curve. For clarity, the relative coordinates in the  $\rho_y$ - and  $z_h$ -direction have been offset by 2 and 4  $\mu\text{m}$ . **c.** The fit values for the two particle radii and the particle refractive indices from the fits. **d.** The distance between the particles as a function of time. **e.** The mean squared displacements of the center of mass in the two directions along and perpendicular to the dumbbell axis. The many error bars together look like a thin line. The full lines are fits to equation 2.27 and 2.28. **f.** The mean squared displacements of the orientational diffusion as a function of time. The uncertainty is estimated to be comparable to the size of the symbols. The full curve represents a fit to equation 2.31.

In Figure 2.33 **a** we plot the three coordinates of the two particles that form the dumbbell. The particle was diffusing around while it slowly rose. Apart from the diffusion in the position the two lines for each sphere separately cross regularly. This is better visible in Figure 2.33 **b** with the position of the center of mass,  $\bar{R}$ , subtracted leaving the rotation as the only contribution to the curves. The two lines for each coordinate cross each other quite regularly, a signature of rotation. The proper fitting of the particle position is particularly difficult in the axial direction when the particle is positioned vertically. In Figure 2.33 **c** we plot the fit values for the radii and refractive indices of both particles. There are more outliers

when the particle is further away from the hologram plane. The average particle radius over the entire trajectory was  $0.73 \pm 0.01$ . This agrees with the average fit value for a single particle in the same capillary of  $0.71 \pm 0.02 \mu\text{m}$ , considering a small polydispersity. The average fit value for the refractive index was  $1.584 \pm 0.001$ . The refractive index from DHM for this PS dumbbell in DMSO agrees with the literature value [106]. The particle size is a bit large for two particles from this batch.

The distance between the two spheres is plotted in Figure 2.33 **d**. The average distance between the particles was  $1.299 \pm 0.002 \mu\text{m}$ . The average particle size does not match the distance between the two particles. It could be that the particles are slightly interpenetrating if the thermal annealing step to make the dumbbell permanent was overdone. SEM images of samples that received similar treatments did not suggest that the particles were significantly interpenetrating. More likely, the dumbbell as a whole has an optical cross-section that exceeds the sum of that of the two constituent particles, this may be due to the scattering of a fraction of the mutual near fields. The fitting algorithm might compensate this by increasing the particles size.

From the coordinates and orientations of the two particles we can study the Brownian motion of our dumbbell. The rotational diffusion can be separated from the translational diffusion [138]. The orientation of the dumbbell at any given moment in time is given by the orientation vector:

$$\tilde{s}(t) = (\cos(\theta_d(t))\sin(\phi_d(t)), \sin(\theta_d(t))\sin(\phi_d(t)), \cos(\theta_d(t))), \quad (2.26)$$

where  $\theta_d(t)$  and  $\phi_d(t)$  are polar and azimuthal angles of the dumbbell respectively. The translational diffusion of an elongated colloid depends on the orientation. To study the translational diffusion, the diffusion should be studied in the reference frame of the dumbbell. The axial and transverse projections of the center-of-mass translations satisfy the standard Einstein-Smoluchowski relations:

$$\Delta R_{\parallel}^2(t) \equiv \left\langle \left| [\bar{\mathbf{R}}(t) - \bar{\mathbf{R}}(s)] \cdot \tilde{s} \right|^2 \right\rangle = 2D_{\parallel} \left( t - \frac{\tau}{3} \right) + 2\epsilon_{\parallel}^2 \quad (2.27)$$

and

$$\Delta R_{\perp}^2(t) \equiv \left\langle \left| [\bar{\mathbf{R}}(t) - \bar{\mathbf{R}}(s)] \times \tilde{s} \right|^2 \right\rangle = 4D_{\perp} \left( t - \frac{\tau}{3} \right) + 4\epsilon_{\perp}^2. \quad (2.28)$$

Equations 2.27 and 2.28 are corrected for the camera's exposure time  $\tau$  [138]. These equations also account for measurement errors  $\epsilon_{\parallel}$  and  $\epsilon_{\perp}$  along and normal to the dumbbell's axis under the assumption that these errors are independent of orientation,  $\tilde{s}$ .

The diffusion coefficients for stiff rods are given by:

$$D_{\parallel} = \frac{k_B T}{2\pi\eta L} \left[ \ln \left( \frac{L}{2r} \right) - \gamma_{\parallel} \right] \quad \text{and} \quad D_{\perp} = \frac{k_B T}{4\pi\eta L} \left[ \ln \left( \frac{L}{2r} \right) + \gamma_{\perp} \right]. \quad (2.29)$$

The viscosity of the liquid is  $\eta$ ,  $\tau$  is the integration time of the camera and the  $\gamma$ 's are constants that depend on the detailed shape of a cylindrical rod and are

known analytically only for special cases, such as prolate ellipsoids [138].  $L$  is the length of the particle under study and is taken to be equal to  $4r$ . For cylindrical rods of length  $L$  and radius  $r$ , Tirado, Martinez and de la Torre [139] proposed:

$$\gamma_{\parallel} = 0.839 + \frac{0.185}{\frac{L}{2r}} + \frac{0.233}{\left(\frac{L}{2r}\right)^2} \quad \text{and} \quad \gamma_{\perp} = -0.207 + \frac{0.980}{\frac{L}{2r}} - \frac{0.133}{\left(\frac{L}{2r}\right)^2}. \quad (2.30)$$

For single spheres, the corresponding cylinder would have length  $L$  equal to  $2r$ , in which case equation 2.30 gives a 6% smaller diffusion constant in the direction ‘perpendicular’ to the cylindrical rod when compared to the diffusion constant of a sphere. For longer chains of rods this is probably even a better approximation [140].

In Figure 2.33 e we plot the translational diffusion in both directions according to equation 2.27 and 2.28, with the statistical uncertainties represented by the error-bars. In the same Figure we plot fits to the right hand side of equation 2.27 and 2.28. From the fit we find  $D_{\parallel} = 0.133 \pm 0.003 \mu\text{m}^2/\text{s}$  and  $D_{\perp} = 0.125 \pm 0.002 \mu\text{m}^2/\text{s}$ . The diffusion constant in the perpendicular direction is smaller than in the parallel direction but the total mean-squared-displacement in the perpendicular direction is larger, because there are two directions perpendicular to the dumbbell. In the following we will come back to these values.

The experimentally determined translational diffusion is well described by the Einstein-Smoluchowski relations. The fit suggests that the error in the position detection over the whole trajectory independent of the dumbbell orientation was  $0.25 \mu\text{m}$  in the direction parallel to the dumbbell and  $0.64 \mu\text{m}$  in the direction perpendicular to the dumbbell. The error in the positioning probably is orientation dependent where the accuracy is thought to be better than these values when the dumbbell is more or less level to the hologram plane. We assume that the accuracy can still be improved upon when applying careful selection and rejection rules for the found coordinates. A fit may be rejected on the ground that the distance between the particles is too large or too small to make sense, after which new attempt to fit the hologram can be attempted.

The rotational diffusion for a cylinder is defined as [138]:

$$\Delta s^2(t) \equiv \langle |\tilde{s}(t) - \tilde{s}(0)|^2 \rangle = 2 \left[ 1 - (1 - \epsilon_s) e^{-2D_r(t - \frac{\tau}{3})} \right], \quad (2.31)$$

where the rotational diffusion is

$$D_r = \frac{3k_B T}{\pi\eta L^3} \left[ \ln \left( \frac{L}{2r} \right) - \gamma_r \right], \quad (2.32)$$

and  $\epsilon_s$  is the error in the orientation measurement. Tirado, Martinez and de la Torre [139] proposed

$$\gamma_r = -0.662 + \frac{0.917}{\frac{L}{2r}} - \frac{0.050}{\left(\frac{L}{2r}\right)^2}. \quad (2.33)$$

In Figure 2.32 **d**, **h** and **l** the fitting of the holograms of two individual spheres is more problematic because the dumbbell is more or less oriented vertically. Therefore we considered only the coordinates of the snapshots in which  $\pi/4 > \phi_d > 3/4\pi$ . We find the same translational diffusion constants (to three decimals) as when considering all coordinates and a rotational diffusion constant of  $0.2682 \pm 0.005 \text{ s}^{-1}$ . The rotational diffusion constant gives the slope of the curve for the decay orientation correlation at small times  $t$ ; this allows it to be fit relatively accurately. The rotational diffusion of anisotropic colloids has been studied before by means of confocal microscopy of nanorods in viscous media [141]. Much faster rotational diffusion was recorded by means of back propagation of in-line holograms as in section 2.2.3 and reference [6]. One of the first studies of rotational diffusion was conducted using bright-field microscopy by Jean Perrin [142].

Using  $D = \frac{k_B T}{6\pi\eta r}$ , where  $\eta$  is the viscosity of DMSO, for which we take 1.996 cP (the value at 20°C) we find a diffusion constant for a single sphere of  $0.147 \mu\text{m}^2/\text{s}$ , for a single sphere we looked at in the same sample we found  $D = 0.130 \pm 0.05 \mu\text{m}^2/\text{s}$ . The difference can probably be explained by a slightly different temperature in the sample. The parallel and perpendicular diffusion of the PS dumbbell  $D_{\parallel} = 0.133 \pm 0.003 \mu\text{m}^2/\text{s}$  and  $D_{\perp} = 0.125 \pm 0.002 \mu\text{m}^2/\text{s}$  on the contrary were a little higher than what equations 2.29 and 2.30 give;  $D_{\parallel} = 0.207 \mu\text{m}^2/\text{s}$  and  $D_{\perp} = 0.1845 \mu\text{m}^2/\text{s}$ . The disagreement could be due to the fact that the dumbbell is significantly smaller than a cylinder with the same diameter. The rotational diffusion from the experiment  $0.2682 \pm 0.005 \text{ s}^{-1}$  on the other hand, was a little lower than what equations 2.32 and 2.33 suggest. Our experimental results for the diffusion of this dumbbell are in qualitative agreement with the theory for the diffusion of cylinders.

## Conclusion

We have shown that DHM can be applied to study the rotational and translational diffusion of a dumbbell of micrometer sized PS particles by fitting the scattering of two separate spheres simultaneously. The contribution of the near fields around both particles does not impede position detection and particle characterization when the dumbbell lies more or less in a plane parallel to the hologram plane. When the particle is oriented progressively more vertical, the analysis is more complex. The holograms of the individual particles overlap, making the separation of the information difficult. An other effect that starts to become problematic when the two particles are somewhat aligned with the optical axis, is multiple scattering. Fitting a model for the scattering of an array of in this case 2 spheres using the T-matrix formalism [130, 131] to experimental holograms may improve the accuracy of  $0.25 \mu\text{m}$  in the direction parallel to the dumbbell and  $0.64 \mu\text{m}$  in the direction perpendicular to the dumbbell axis. This improvement will be more due to the consideration of multiple scattering than by the consideration of near field contributions. Alternatively, one could apply back propagation as described

in section 2.2, which has been applied to a silica rod in section 2.2.3, to enhance the position detection for the snapshot with a vertical dumbbell similar to the work presented in [6]. In that reference the positional accuracy was estimated to be about 100 nm. The slightly lower accuracy found here is probably due to the fact that our dumbbell was significantly smaller than the copper oxide rod in this reference. Possibly, taking the result from back propagation for the position of the constituent spheres as starting points for the error minimization results in more accurate measurements. The results presented in this section support the conclusion of section 2.6.1 and 2.6.2 that fitting holograms of multiple particles simultaneously to experimental holograms can be successfully applied to measure inter-particle forces, particularly when the particles are not directly above each other.

### 2.6.5 Diffusion of a flexible string

Depending on the molecular weight of the steric stabilizer polyvinylpyrrolidone, PVP, the connection between the particles, made permanent a simple thermal annealing step [135], can allow more or less movement of the particles in the chain. As in the previous section, we dispersed sterically stabilized PS particles, 1.54  $\mu\text{m}$  in diameter, in DMSO as received. The dispersion was subjected to a radio frequency electric field to induce dipoles in the particles causing the particles to align and form strings. These spherical particles were connected in a thermal annealing step [135]. A distribution of string lengths of semi-flexible strings was the result. The flexibility is clearly visible in bright-field microscopy from random shape fluctuations. From a comparison of typical images to simulation snapshots similar to those in reference [143] it was concluded that the persistence length  $\lambda_b$  must have been about 9 particle diameters. The capillary was opened and the dispersion of strings was further diluted with more DMSO before a new sample was prepared in another glass capillary (Vitrocom 0.1  $\times$  2.0 mm).

Using the same imaging system as was used in the previous section, we studied the diffusion of a semi-flexible string of five particles. The integration time was set to 1 ms. Because of the length of the strings and the fact that the particles were slightly larger, the diffusion was much slower than in the previous section. From the results in the previous section it can be understood that the tracking is a lot easier when the particles are more or less at the same distance from the focal plane. To ensure that the string was initially level, the string was trapped in an array of three time-shared point traps that released the string just before the diffusion was recorded. This also facilitated the recording of the background for which the diffusion was found to be too slow. The traps with the string were moved out of the field of view and the background was recorded for 1000 frames before the array of traps was moved back into the field of view. The frames were analyzed by fitting a variation of equation 2.19 for the interference between the scattered

light and the reference beam for five particles to the experimental holograms:

$$B(\vec{\rho}_{xy}) = \frac{\left| \tilde{R} + \sum_{i=0}^5 \tilde{E}_{is}(\vec{\rho}_i, \beta_i, m_i) \right|^2}{\tilde{R}^2}. \quad (2.34)$$

In Figure 2.34 we reproduce some of the experimental in-line holograms, the fits to equation 2.34 and the radially averaged intensities in both the fit and the experimental hologram. The time between consecutive snapshots was around 12 seconds. From the experimental holograms in Figure 2.34 **a-d** it is clear that the string was not only performing translational and rotational diffusion, but also that its shape is fluctuating.

The simulated holograms in Figure 2.34 **e-h** clearly resemble the experimental counterparts they were fitted to. In addition, from the radial intensity distributions in Figure 2.34 **i-l** where the fit can be quantitatively compared to the experiment, one sees that the model follows the intensity in the experimental holograms. The holograms of the five individual particles are overlapping. The fit values for the particle radii and the refractive indices agree with 5 PS particles of around 1.54  $\mu\text{m}$  from SLS. The error estimate from the Levenberg-Marquardt algorithm are underestimates of the error.

An alternative strategy to fitting an individual radius and refractive index for all 5 particles separately is to enforce mono-dispersity by fitting only one radius and one refractive index for all particles. The advantage is that there are fewer fitting parameters which makes the fitting slightly faster. More important however is the observed result that the distances between the fitted locations of the individual particles are more consistent, suggesting that the position measurements are more accurate. The fitted holograms look identical, but having only one radius and refractive index to manipulate, the algorithm is forced to place the particles on the right position.

The string is clearly observed to bend. There is an elastic potential energy involved in the bending. As can be seen from the undulations of the freely diffusion string, this energy is small compared to the thermal energy  $k_B T$ . Let  $\vec{\rho}_n$  be the position of the  $n^{\text{th}}$  particle in the string. We can then define the local orientation vector  $\tilde{s}_l$ . The bending energy then goes like:

$$U_{\text{bend}} = \frac{k_B T}{4\lambda_b} \int_0^L \frac{\partial \tilde{s}_l}{\partial l} \cdot d\vec{l} \quad (2.35)$$

where  $l$  is the distance along the contour of the string and  $\lambda_b$  the persistence length. This is known as the Kratky-Porod or worm-like chain model [138, 144]. The persistence length can be defined as the distance over which the orientation of the segments is correlated. For sufficiently flexible strings, the orientation between two segments that are far enough from each other are totally uncorrelated.

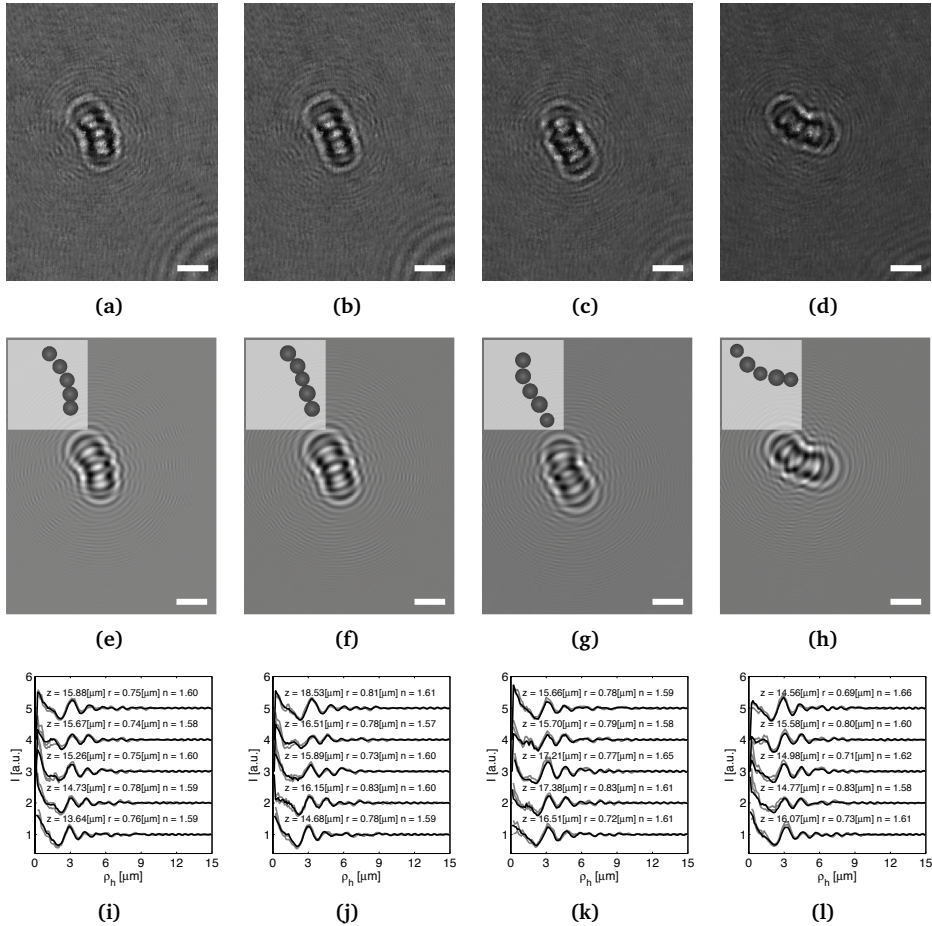


**Figure 2.34:** Diffusion of a semi-flexible string of PS particles in DMSO: the holograms. In-line holograms of a freely diffusing semi-flexible string of  $1.54 \mu\text{m}$  PS ( $n = 1.59$ ) in DMSO ( $n = 1.4785$ ). **a-d.** Experimental holograms when the string was respectively  $15.03, 16.35, 16.49$  and  $15.19 \pm 0.02 \mu\text{m}$  above the hologram plane. **e-h.** Fits of equation 2.34 to the experimental holograms. **i-l.** Radial averages centered on the constituent particles. The black lines were taken from the fitted holograms and the grey lines were obtained from the experimental holograms plus and minus the statistical uncertainty. The scalebars are  $5 \mu\text{m}$ .

The correlation between the orientation of two segments is expressed as the scalar product of the orientational vectors of two segments that are separated by a distance  $l$  along the contour of the chain. This correlation is predicted by random coil statistics to decay exponentially with the curvilinear distance  $l$  expressed in

the persistence length  $\lambda_b$ :

$$\langle \vec{s}_l(l) \cdot \vec{s}_l(0) \rangle = \exp(-l/\lambda_b), \quad (2.36)$$

where  $\vec{s}_l(i)$  is the orientation vector of segment  $l(i)$ . In the limit of long chains, that are hundreds of elements long, the persistence length can also be obtained from the average projection of the end-to-end vector onto the first bond of the chain [145]:

$$\lambda_b = \left\langle \sum_{i=1}^{N-1} \vec{s}(i) \cdot \vec{s}(1) \right\rangle / l_s. \quad (2.37)$$

Here  $l_s$  is the length of the segments. For strings of particles a natural choice for the segments would be the distance between the centers of the constituent spheres. For stiff rods equation 2.37 yields the contour length of the string.

For a discrete chain of straight segments with arbitrary isotropic elasticity in the joints of finite length, the persistence length can be approximated in segment lengths from the average cosine of the bending angle  $\theta_b$  in any joint:

$$\lambda_b = \frac{1}{1 - \langle \cos(\theta_b) \rangle}. \quad (2.38)$$

The persistence length as calculated by equation 2.38 can be longer than the contour length of the string. Another approximation that can be used to determine the persistence length of the coil is given by:

$$\langle R^2 \rangle = 2\lambda_b L_C - 2\lambda_b^2 (1 - \exp(-L_C/\lambda_b)). \quad (2.39)$$

Here  $\langle R^2 \rangle$  is the average end-to-end distance and  $L_C$  the contour length along the string. The different approximation can yield different values as a result of the different assumptions and approximations that were made in the formulation of these estimates.

In Figure 2.35 **a** we plot the trajectories followed by all 5 constituent particles. These are the coordinates obtained by fitting the three coordinates of all five particles independently while fitting only one set of particle characteristics, one radius and one refractive index. Clearly, there has been some diffusion. In Figure 2.35 **b** the trajectory of the particles is plotted with respect to the center of mass of the string. It is clear that the string was more or less parallel to the hologram plane throughout the trajectory. Towards the end of the analysis of the movie, the string started to be tilted partially vertical. The analysis was stopped when one of the five particles was not fit close to the other particles. Due to the flexibility of the string, the correlation between the coordinates in the three directions is less than one would expect for a stiff rod.

In Figure 2.35 **c** we plot the fit values for the radius and the refractive index for the 5 constituent particles as a function of time. The variation in the fit values for the radius is smaller than in Figure 2.33 **c**. Possibly this is due to the larger

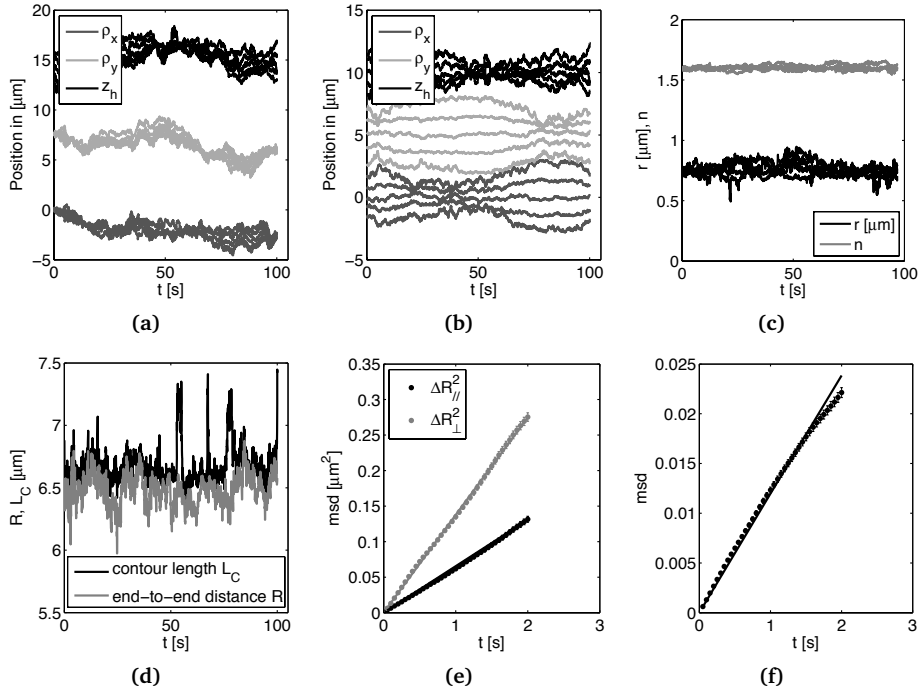


**Figure 2.35:** Diffusion of a semi-flexible string of PS particles in DMSO: the holograms. **a.** The coordinates from DHM, fitting all particle locations and 1 radius and 1 refractive index for the five PS particles forming a semi-flexible string in DMSO while it diffused freely. **b.** The coordinates of the five constituent particles, relative to the center of mass of the string, leaving the rotational diffusion as the only contribution to the curve. For clarity, the relative coordinates in the  $y$ - and  $z$ -direction have been offset by 5 and 10  $\mu\text{m}$ . **c.** The fit values for the five particle radii and the particle refractive indices from the fits in Figure 2.34. **d.** The end-to-end distance and contour length for the single particle characteristic fits, as a function of time. **e.** The mean squared displacements in the two directions along and perpendicular to the string. The full lines are fits to equation 2.27 and 2.28. **f.** The mean squared displacements of the orientational diffusion as a function of time. The full curve represents a fit to equation 2.31.

distance between the hologram and the dumbbell in that Figure, which makes the individual holograms overlap even more. Another important factor is that the string discussed here stays more or less parallel to the hologram plane throughout the trajectory. The average optical radius of the particles was  $0.759 \pm 0.001 \mu\text{m}$  and the average refractive index was found to be  $1.600 \pm 0.001$ . When all five particles are fit together with one radius and one refractive index, we find a radius of  $0.753 \pm 0.001 \mu\text{m}$  and  $1.598 \pm 0.001$ .

In 2.35 **d** we plot the end-to-end distance  $R$  calculated as the distance between the center of the first and the center of the last particle. The average value is 6.475

$\pm 0.003 \mu\text{m}$ . In the same Figure we plot the sum of all the four distances between the particles which we take as the contour length  $L_C$  as a function of time. There is still quite some variation in this parameter that should be constant. The average value is  $L_C = 6.672 \pm 0.003 \mu\text{m}$ , this is more than 8 times the average fit value for the individual particle radii. This difference may be due to the fact that the model for the scattering by the five particles in the string does not include the effects of multiple scattering and the effect the scattering of near-field components of nearby particles.

The fact that the average end-to-end distance is shorter than the contour length is the result of the flexibility and there are many studies of the end-to-end distance distribution that either do or do not take the orientation of the end-sections into consideration, see [146] and references therein. While the end-to-end distance distribution function for a flexible polymer is well known to be Gaussian, an exact solution for the corresponding distribution function for a worm like chain of finite length is not trivially found. Using equation 2.39 we find a persistence length of 37 particle diameters.

If we use the individual coordinates of the particles to calculate the bond angles, from which we can calculate the persistence length using equation 2.38, we find a persistence length of 20 particles. The exact formula for the persistence length 2.37 cannot really be applied to this string as it will by definition find a value that is shorter than the contour length, and it is clear from the snapshots in Figure 2.34 that there is still a strong correlation between the orientation of the first and the last bond. Because this string consists of only five particles, which give four bonds and three bond-angles we cannot apply the Fourier mode analysis as used in reference [147]. Also equation 2.36 cannot really be applied because it requires fitting of an exponential decay of the orientational correlation that does not decay significantly over the four bonds. That the two estimates of the persistence length, 37 from equation 2.39 which considers the strings overall behavior and 20 from equation 2.38 which considers the individual bond angles is not too surprising. Both approximations for the persistence length are the result of different approximations [145]. Since individual outliers can cause too high values for the bond angles it is likely that the estimate of  $\lambda_b = 20$ , based on equation 2.38 is an underestimate.

In Figure 2.35 e we plot the mean squared displacement of the center of mass of the string in the directions parallel and perpendicular to the end-to-end vector of the string. The full lines are fits to equation 2.27 and 2.28 for the diffusion parallel and perpendicular respectively. The length  $L$  is assumed to be  $10 r$  where  $r$  is the average optical radius of the particles,  $0.759 \pm 0.001$ . One might also argue that  $L$  should be the average end-to-end distance. The width of the string in that case is ill defined. The fit values for the translational diffusion constants are  $D_{\parallel} = 0.036 \pm 0.001 \mu\text{m}^2/\text{s}$  and  $D_{\perp} = 0.035 \pm 0.001 \mu\text{m}^2/\text{s}$ . The error estimate for the position measurement in the parallel and perpendicular direction from the fit to equation 2.27 and 2.28 were  $0.1 \mu\text{m}$  in the parallel and perpendicular

direction [83].

Fitting equation 2.31 to the experimental rotational diffusion is well possible as the rotational diffusion constant gives the slope at small  $t$ . We took orientation of the end-to-end vector as the orientation of the string. We find  $D_r = 0.0030 \pm 0.0001 \text{ s}^{-1}$ . This is a hundred times as slow as the rotational diffusion of the dumbbell.

For the parallel and perpendicular diffusion of a PS string of 5 particles in DMSO, treating it as a stiff rod, we find by applying equations 2.29 and 2.30;  $D_{\parallel} = 0.137 \text{ }\mu\text{m}^2/\text{s}$  and  $D_{\perp} = 0.107 \text{ }\mu\text{m}^2/\text{s}$ . Also in the experiment we find a slightly smaller diffusion constant in the direction perpendicular to the string that is smaller than in the direction along the end-to-end vector. The rotational diffusion from the experiment  $0.00370 \pm 0.00001 \text{ s}^{-1}$ , was a lot lower than what equations 2.32 and 2.33 suggest;  $0.0404 \pm 0.00001 \text{ s}^{-1}$ . The flexibility offers extra degrees of freedom that stiff cylinders lack. It would be interesting to compare these experimental results to a theory that for the diffusion of a flexible string that takes the damping effect of the flexibility on the diffusion [138] into account.

## Conclusion

DHM was successfully applied to study the rotational, translational and conformational diffusion of a semi-flexible worm like chain that consisted of 5 PS spheres in DMSO. When the string is more or less horizontal, increasing the number of particles in the chain does not seem to be a problem to DHM. It was estimated that the accuracy in the position detection was in the order of 100 nm. Considering the outliers in the bond angles we can improve upon the analysis of these holograms by formulating better starting conditions for the minimization. Also applying a rule to reject fitting results by looking at for instance the inter-particle distances may improve the accuracy.

### 2.6.6 *Bending a string*

In the previous section we have seen that it is possible to track semi-flexible strings of PS particles in DMSO when they lie more or less in a plane perpendicular to the hologram plane. We applied an array of three optical tweezers to trap the particles and move them in and out of the field of view to record the background in the absence of the string. Here we show that a horizontally trapped string can also be bent as was shown for strings of PMMA and PS particles in water [148].

The lower dielectric constant of DMSO,  $\epsilon = 47.2$ , allows the Debye screening length to be made longer than in water. Using BioRad ion exchangers the concentration of ions in the DMSO was reduced. This increased the Debye screening length to around 1100 nm, which is comparable to the colloidal radius. Also in the case of DNA in saline conditions the Debye screening length is comparable to the width of the chain [149, 150]. The consequence of a screening length comparable to the particle size is that the charge repulsion between the particles starts

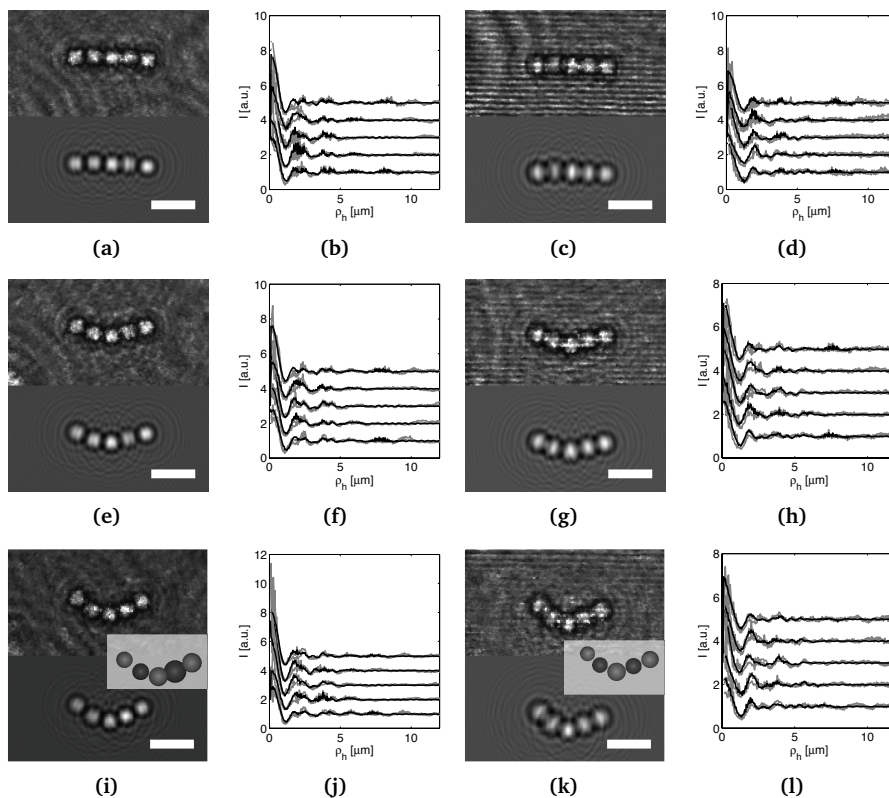


**Figure 2.36:** DHM applied to the bending two strings of PS particles in DMSO. In-line holograms of two strings of 5 PS 1.9  $\mu\text{m}$  particles in DMSO while they are trapped and bent by an array of three time-shared optical traps. **a, e, i.** In-line holograms and fits thereof of a string in sample I: purified DMSO, at progressive bending steps. **b, f, j.** Radially averaged intensity profiles for the holograms in **a, e, i**. The black line is taken from the fit, the grey lines are taken from the experiment plus and minus the statistical uncertainty. Particles from left to right were given offsets in steps of 1  $\mu\text{m}$ . **c, g, k.** In-line holograms and fits thereof of a string in sample II, DMSO 3% saturated with LiCl, at progressive bending steps. **d, h, l.** Radially averaged intensity profiles for the holograms in **a, e, i** as in **b, f, j**. Typical fit values for the radius and the refractive index are 900 nm and 1.59. Scalebars are 5  $\mu\text{m}$ .

to give a relevant contribution to the bending energy. To bend the particles have to approach each other which costs energy if the interaction between the particles is long-ranged.

It is also possible to add salt to DMSO to increase the screening and reduce the Debye screening length. The consequence is that it costs less energy to bring the particles closer together. The remaining stiffness is the mechanical stiffness associated with the bonds between the spheres that make up the string.

Flexible strings were made out of  $1.9\ \mu\text{m}$  PS particles in DMSO as described in section 2.6.4 and 2.6.5, using the methods described in reference [135]. After preparation of the strings these were redispersed in two different samples. In sample I we used DMSO that was purified and deprived of ions by contact with BioRad ion exchanger beads (BioRad AG 501-X8 Resin, 20-50 Mesh, Biotechnology grade) for several weeks. In sample II the strings were dispersed in DMSO that was for 3% saturated with the salt LiCl, corresponding  $3.087\ \text{g/l}$ , to increase the screening. Both dispersions were transferred to a glass capillary (Vitrocom  $0.1 \times 2.0\ \text{mm}$ ).

In both samples a single string of 5 beads was isolated using optical tweezers and brought to the center of the capillary at a depth of  $\sim 50\ \mu\text{m}$ . The string was trapped horizontally in an array of three time-shared optical traps, see Chapter 6. The first, the third and the fifth particle were trapped. The string was moved out of the field of view and around a thousand frames were recorded as the background for hologram normalization. Subsequently, the string was brought back in the field of view after which the center trap was moved away stepwise, bending the string similar to experiments reported by Furst *et al.* [148]. In this reference, the exerted force that bent the strings was measured by studying the displacement of the string within the trap, similar to how forces are measured on single particles in reference [112]. The trap stiffness was measured in a separate experiment studying the trapping behavior of a single particle. This is not guaranteed to give an accurate calibration for the force-extension curve of a trapped string of these particles. The radiation pressure is exerted on the edge of the particle, at refractive index discontinuity, see Chapter 6. The spatial distribution of the refractive index around a particle in a string of particles is clearly different than that around a single particle. During the manipulation of our strings of PS particles in DMSO we noticed that the string was trapped less stiff than the single particles that we trapped to move them out of the field of view. We thus believe that the force measurements reported in reference [148], though a good indication of the physics of the bending, may not be quantitatively accurate. The forces are likely to be off by some constant factor.

In Figure 2.36 we demonstrate that semi-flexible strings made of PS particles in DMSO can be trapped and bent by three time-shared optical point traps while the interference pattern between scattered light and the remaining illuminating beam can be fitted to a Lorenz-Mie-Debye model for the scattering of the constituent traps to measure the particle coordinates. In Figure 2.36 **a**, **e** and **i** we reproduce in-line holographic snapshots of a typical bending experiment on a string in the purified DMSO of sample I and fits of equation 2.34. The corresponding radial intensity plots in Figure 2.36 **b**, **f** and **j** illustrate the resemblance of the fits to the experimental intensity distribution. The three traps act on the two outer particles and the central particle, the lighter colored particles in the inset in Figures 2.36 **i** and **k**. In Figure 2.36 **c**, **g** and **k** we present holograms and fits thereto of the same experiment conducted on sample II with the higher salt

concentration. Figure **d**, **h** and **l** show the radially averaged intensity around the in-plane particle positions.

From a comparison between Figure 2.36 **i** and **k** for respectively the low-screening and high-screening case, we conclude that the charge repulsion between the constituent spheres in sample I is a significant contribution to the bending energy. The distance between the second and the fourth particle is visibly larger in the low-screening case. The curve of the string is more rounded in the low-screening case of sample I, while it looks more like a triangle in sample II. The semi-flexible strings of PS particles in DMSO are thus modeling the flexibility of DNA strands and other polyelectrolytes in the sense that part of the bending rigidity is due to charge repulsion.

Strings can also be made by soft welding [151, 152] PMMA-particles using the enhanced heating by absorption of the trapping laser which can be increased by incorporation of the commercial dye Epolin 1151 can be trapped and bent in CHC to study the rigidity of the welds and possibly the contribution of charge repulsion to the bending rigidity.

## Yielding

In section 2.6.2 we discussed the tracking of silica particles in THF. This is one of several systems where the dielectric constant  $\epsilon$  is close to 7, for THF  $\epsilon = 7.52$ . In these systems we generally observe low ion concentrations so the Debye screening length in these systems can be several micrometers long while the particles still gain a non-negligible charge. The result is that the particles start to interact with each other at low volume fractions and long range crystals, as in section 2.2.2, can be formed. At shorter distances there is a van der Waals attraction.

In Figure 2.37 **a**, **c**, **e**, **g**, **j** and **k** we reproduce in-line holograms of a string of nine silica particles and a fit of a variant of equation 2.25 for nine particles. The deviation in the  $y$ -direction of the middle trap is progressively increased. In Figure 2.37 **b**, **d**, **f**, **h**, **j** and **l** we plot the radially averaged intensity in both the fit, in black and the experimentally averaged intensity plus and minus the statistical uncertainty. From the shape of the string and the changes therein over several sequences of bending and relaxing we conclude that the string shows non elastic rearrangements under stress. When the string was released it did not bend back to its original shape. The bonds between the particles, caused by van der Waals attractions, are not ruptured in the process. What we think happens is a stick-slip behavior. The string maintained its mechanical integrity. From the information about the axial coordinates of the spheres we deduce that the deformations are real and not rotations of an already curved string.

Similar results were obtained on strings of silica spheres in a mixture of hexane and hexanol which allows the experimenter to vary the dielectric constant of the solvent between 2 and 13.5 [153], changing the strength of the van der Waals attraction and the charge repulsion. Also strings made of silica coated PS spheres similar to those presented in section 2.5.6 in CycloHexyl Bromide, a solvent

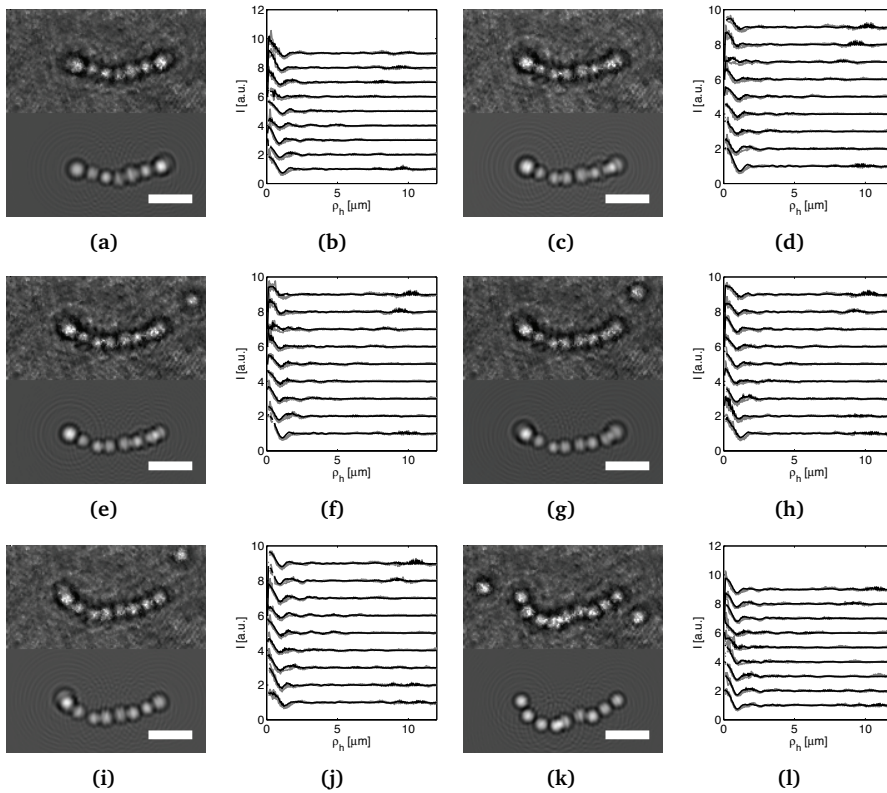


**Figure 2.37:** DHM applied to the bending of string of silica particles in THF. In-line holograms of a string of 9 silica particles with a diameter of 1750 nm in THF while they are trapped and bent by an array of three time-shared optical traps. **a, c, e, g, j, k.** In-line holograms and fits thereof of a string in of silica particles in THF at progressive bending steps. **b, d, f, h, j, l.** Radially averaged intensity profiles for the holograms in **a, c, e, g, j, k.** The black line is taken from the fit, the grey lines are taken from the experiment plus and minus the statistical uncertainty. Particles from left to right were given offsets in steps of 1  $\mu\text{m}$ . Scalebars are 5  $\mu\text{m}$ .

that is similar to CHC, were observed to show yielding of the bonds between the individual spheres.

## Conclusion

DHM in combination with dynamically changed arrays of time-shared point traps have been successfully used to study the bending behavior of strings of colloids. We have shown that the stiffness of semi-flexible strings of PS particles in DMSO can be manipulated by changing the Debye screening length similar to they way in which the screening length influences the stiffness of DNA. In addition, we can

induce rearrangements of strings that are connected by van der Waals attractions.

## 2.7 Acknowledgements

We thank Anke Kuijk for the silica rod. Jacob Hoogenboom is thanked for synthesis of the 1.4  $\mu\text{m}$   $\text{SiO}_2$  particles. Dannis 't Hart is thanked for the synthesis of the 758 nm silica particle. It is a pleasure to thank Ahmet Faik Demirör for the synthesis of the titania particles and interesting discussions. Henry Martin and Roel Dullens from the University of Cambridge are thanked for the synthesis of the melamine particles. Frank Smalenburg is thanked for interesting discussions and the error calculus of the wall induced potential. We owe our thanks to Bo Peng for the SEM pictures of the melamine particles. Gulşen Heessels-Gürboğa and Carlos van Kats are thanked for growing the silica layers on the PS particles. Peter Helfferich is thanked for many useful discussions, help with the experiments and in particular help with the electronic timing of the optical traps and the camera in section 2.6.1, 2.6.2 and 2.6.6. Bo Peng and Rao Vutukuri are thanked for the synthesis of polystyrene particles and the sticking together of these to form strings. Michiel Hermes is thanked for the rendering of some of the insets. Finally, Johan Stiefelhagen is thanked for the synthesis all the other sizes of silica particles used in this Chapter, also those that were calcined and stuck together using optical tweezers in THF and for the synthesis of PMMA spheres with the Epolin 1151 dye. Sang-Hyuk Lee, Yohai Roichman, Gi-Ra Yi, Shin-Hyun Kim, Seung-Man Yang and David Grier are thanked for interesting discussions.

## Bibliography

- [1] Gabor, D. A New Microscopic Principle. 1948 177 777 (1948).
- [2] Hecht, E. Optics. Addison Wesley, 3rd. ed. (1998).
- [3] Bohren, C. F. and Huffman, D. R. Absorption and Scattering of Light by Small Particles. Wiley Interscience, New York (1983).
- [4] Sheng, J., Malkiel, E., and Katz, J. Digital holographic microscope for measuring three-dimensional particle distributions and motions. *Appl. Opt.* **45** 3893 (2006).
- [5] Cheong, F. C., Krishnatreya, B. J., and Grier, D. G. Strategies for three-dimensional particle tracking with holographic video microscopy. *Opt. Express* **18** 13563 (2010).
- [6] Cheong, F. C. and Grier, D. G. Rotational and translational diffusion of copper oxide nanorods measured with holographic video microscopy. *Opt. Express* **18** 6555 (2010).
- [7] Lee, S.-H., Roichman, Y., Yi, G.-R., Kim, S.-H., Yang, S.-M., van Blaaderen, A., van Oostrum, P., and Grier, D. G. Characterizing and tracking single colloidal particles with video holographic microscopy. *Opt. Exp.* **15** 18275 (2007).
- [8] Katz, J. and Sheng, J. Applications of Holography in Fluid Mechanics and Particle Dynamics. *Annu. Rev. Fluid Mechanics* **42** 531 (2010).

- [9] Sherman, G. C. Application of the convolution theorem to Rayleigh's integral formulas. *J. Opt. Soc. Am.* **57** 546 (1967).
- [10] Schnars, U. and Jüptner, W. P. O. Digital recording and reconstruction of holograms. *Meas. Sci. Technol.* **13** R85 (2002).
- [11] Ooms, T., Koek, W., and Westerweel, J. Digital holographic particle image velocimetry: eliminating a signambiguity error and a bias error from the measured particle field displacement. *Meas. Sci. Technol.* **19** 074003 (2008).
- [12] Satake, S., Kunugi, T., Sato, K., Ito, T., and Taniguchi, J. Three-dimensional flow tracking in a micro channel with high time resolution using micro digital-holographic particle-tracking velocimetry. *Opt. Rev.* **12** 442 (2005).
- [13] Kim, S. and Lee, S. J. Measurement of 3D laminar flow inside a micro tube using micro digital holographic particle tracking velocimetry. *J. Micromech. Microeng.* **17** 2157 (2007).
- [14] Crocker, J. C. and Grier, D. G. Methods of Digital Video Microscopy for Colloidal Studies. *J. of Col. and Int. Sci.* **179** 289 (1996).
- [15] Hansen, J. P. and McDonald, I. R. Theory of Simple Liquids. Academic Press; 3 ed. (2006).
- [16] Royall, P. C., Leunissen, M. E., Hynninen, A., Dijkstra, M., and van Blaaderen, A. Re-entrant melting and freezing in a model system of charged colloids. *The Journal of Chemical Physics* **124** 244706 (2006).
- [17] Weiss, J. A., Larsen, A. E., and Grier, D. G. Interactions, dynamics, and elasticity in charge-stabilized colloidal crystals. *J. Chem. Phys.* **109** 8659 (1998).
- [18] Behrens, S. H. and Grier, D. G. The pair interaction of charged colloidal spheres near a charged wall. *Phys. Rev. E.* **64** 050401(R) (2001).
- [19] Dufresne, E. R. and Grier, D. G. Erratum: "Interactions, dynamics, and elasticity in charge-stabilized colloidal crystals" [J. Chem. Phys. 109, 8659 (1998)]. *J. Chem. Phys.* **110** 8845 (1999).
- [20] Demirörs, A. F., Jannasch, A., van Oostrum, P. D. J., Schäffer, E., van Blaaderen, A., and Imhof, A. Seeded Growth of Titania Colloids with Refractive Index Tunability and Fluorophore-free Luminescence. *Langmuir*, DOI: 10.1021/la103717m (2010).
- [21] Yethiraj, A. and van Blaaderen, A. A colloidal model system with an interaction tunable from hard sphere to soft and dipolar. *Nature* **421** 513 (2003).
- [22] Vanderhoeven, P. H. C. and Lyklema, J. Electrostatic Stabilization in Nonaqueous Media. *Advances in Colloid and Interface Science* **42** 205 (1992).
- [23] Morrison, I. D. Electrical Charges in Nonaqueous Media. *Colloids and Surfaces a-Physicochemical and Engineering Aspects* **71** 1 (1993).
- [24] Lee, S.-H. and Grier, D. G. Holographic microscopy of holographically trapped three-dimensional structures. *Opt. Express* **15** 1505 (2007).
- [25] Royall, C. P., van Roij, R., and van Blaaderen, A. Extended sedimentation profiles in charged colloids: the gravitational length, entropy, and electrostatics. *J. Phys. Cond. Matt.* **15** 2315 (2005).
- [26] Banfield, J. F., Veblen, D. R., and Smith, D. J. The identification of naturally occurring TiO<sub>2</sub> (B) by structure determination using high-resolution electron microscopy, image simulation, and distance-least-squares refinement. *American Mineralogist* **76** 343 (1991).
- [27] Tolpekin, V. A., Duits, M. H. G., van den Ende, D., and Mellema, J. Aggregation

- and Breakup of Colloidal Particle Aggregates in Shear Flow, Studied with Video Microscopy. *Langmuir* **20** 2614 (2004).
- [28] Xu, W., Jericho, M. H., Meinertzhagen, I. A., and Kreuzer, H. J. Digital in-line holography for biological applications. *Proc. Natl. Acad. Sci. USA* **98** 11301 (2001).
- [29] Xu, W., Jericho, M. H., Meinertzhagen, I. A., and Kreuzer, H. J. Digital in-line holography of microspheres. *Appl. Opt.* **41** 5367 (2002).
- [30] Garcia-Sucerquia, J., Xu, W. B., Jericho, S. K., Klages, P., Jericho, M. H., and j. Kreuzer, H. Digital in-line holographic microscopy. *Appl. Opt.* **45** 836 (2006).
- [31] Keville, K., Franes, E., and Caruthers, J. Preparation and characterization of monodisperse polymer microspheroids. *J. Coll. Int. Sc.* **144** 103 (1991).
- [32] Ho, C., Keller, A., Odell, J., and Ottewill, R. Preparation of monodisperse ellipsoidal polystyrene particles. *Coll. Pol. Sc.* **271** 469 (1993).
- [33] van Kats, C., Johnson, P., Meerakker, J., and van Blaaderen, A. Synthesis of Monodisperse High-Aspect-Ratio Colloidal Silicon and Silica Rods. *Langmuir* **20** 11201 (2004).
- [34] Kuijk, A., van Blaaderen, A., and Imhof, A. Synthesis of monodisperse rod-like silica colloids with tunable aspect ratio. *JACS*, DOI: 10.1021/ja109524h (2010).
- [35] van Blaaderen, A. and Vrij, A. Synthesis and characterization of colloidal dispersions of fluorescent, monodisperse silica spheres. *Langmuir* **8** 2921 (1992).
- [36] Maxwell, J. C. On Physical Lines of Force. *Phil. Mag. J. Sci.* **42** 161 (1861).
- [37] Mie, G. Beiträge zur Optik trüber Medien, speziell kolloidaler Metallösungen. *Annalen der Physik* **25(3)** (1908).
- [38] Debye, P. Der Lichtdruck auf Kugeln von beliebigem Material. *Annalen der Physik* **4(30)1** 57 (1909).
- [39] Lorenz, L. Lysbevægelsen i og uden for en af plane Lysbølger belyst Kugle. *Videnskaberens Selskabs Skrifter* **6** 1 (1890).
- [40] Lorenz, L. Sur la lumière réfléchie et réfractée par une sphère (surface) transparente. *Oeuvres scientifiques de L. Lorenz. revues et annotées par H. Valentiner. Tome Premier, Libraire Lehmann & Stage, Copenhague* 403 (1898).
- [41] Mishchenko, M. I., Travis, L. D., and Lacis, A. A. Scattering, Absorption and Emission of Light by Small Particles. Cambridge University Press (2001).
- [42] [http://diogenes.iwt.uni-bremen.de/vt/laser/wriedt/Mie\\_Type\\_Codes/body\\_mie\\_type\\_codes.html](http://diogenes.iwt.uni-bremen.de/vt/laser/wriedt/Mie_Type_Codes/body_mie_type_codes.html) .
- [43] Sun, B. and Grier, D. G. Comment: The effect of Mie resonances on trapping in optical tweezers. *Opt. Exp.* **17** 2658 (2009).
- [44] Aden, A. L. and Kerker, M. Scattering of electromagnetic waves from two concentric spheres. *J. Appl. Phys.* **22** 1242 (1951).
- [45] Dhont, J. An Introduction to Dynamics of Colloids (Studies in Interface Science). Elsevier Science (1996).
- [46] Born, M. and Wolf, E. Principles of Optics. Cambridge University (1980).
- [47] Moré, J. The Levenberg-Marquardt algorithm: Implementation and theory. in Numerical Analysis, G. A. Watson, ed., vol. 630, p. 105 (Springer-Verlag, Berlin (1977)).
- [48] Gill, P. E. and Murray, W. Algorithms for the solution of the nonlinear least-squares problem. *SIAM J. Numer. Anal.* **15** 977 (1978).
- [49] Thompson, B. J. Holographic particle sizing techniques. *J. Phys. E: Sci. Instru.* **7** 781 (1974).

- [50] Soontaranon, S., Widjaja, J., and Asakura, T. Improved holographic particle sizing by using absolute values of the wavelet transform. *Opt. Commun.* **240** 253 (2004).
- [51] Pu, S. L., Allano, D., Malek, B. P.-R. M., Lebrun, D., and Cen, K. F. Particle field characterization by digital in-line holography: 3D location and sizing. *Exp. Fluids* **39** 1 (2005).
- [52] Guerrero-Viramontes, J. A., Moreno-Hernández, D., Mendoza-Santoyo, F., and Funes-Gallanzi, M. 3D particle positioning from CCD images using the generalized Lorenz-Mie and Huygens-Fresnel theories. *Meas. Sci. Technol.* **17** 2328 (2006).
- [53] Denis, L., Fournier, C., Fournel, T., Ducottet, C., and Jeulin, D. Direct extraction of the mean particle size from a digital hologram. *Appl. Opt.* **45** 944 (2006).
- [54] Park, Y.-K., Popescu, G., Badizadegan, K., Dasari, R. R., and Feld, M. S. Fresnel particle tracing in three dimensions using diffraction phase microscopy. *Opt. Lett.* **32** 811 (2007).
- [55] Soulez, F., Denis, L., Fournier, C., Thiébaud, E., and Goepfert, C. Inverse problem approach for particle digital holography: accurate location based on local optimisation. *J. Opt. Soc. Am. A* **24** 1164 (2007).
- [56] Soulez, F., Denis, L., Thiébaud, E., Fournier, C., and Goepfert, C. Inverse problem approach in particle digital holography: out-of-field particle detection made possible. *J. Opt. Soc. Am. A* **24** 3708 (2007).
- [57] Gire, J., Denis, L., Fournier, C., Thiébaud, E., Soulez, F., and Ducottet, C. Digital holography of particles: benefits of the 'inverse problem' approach. *Meas. Sci. Technol.* **19** 074005 (2008).
- [58] Alexandrov, S. A., Hillman, T. R., and Sampson, D. D. Spatially resolved Fourier holographic light scattering angular spectroscopy. *Opt. Lett.* **30** 3305 (2005).
- [59] Dennis, J. E. and Schnabel, R. B. Numerical Methods for Unconstrained Optimization and Nonlinear Equations. *SIAM, Philadelphia* (1996).
- [60] Madsen, K. and Nielsen, H. B. Introduction to Optimization and Data Fitting. Section 6.4, DTU Informatics, DTU, Denmark, ([http://www2.imm.dtu.dk/pubdb/views/publication\\_details.php?id=5938](http://www2.imm.dtu.dk/pubdb/views/publication_details.php?id=5938)) (2010).
- [61] Roichman, Y., Sun, B., Stolarski, A., and Grier, D. G. Influence of Nonconservative Optical Forces on the Dynamics of Optically Trapped Colloidal Spheres: The Fountain of Probability. *Phys. Rev. Lett.* **101** 128301 (2008).
- [62] van Oostrum, P. D., van der Horst, A., and van Blaaderen, A. Mutual influence of time-shared optical traps studied by means of Video Holographic Microscopy. *Digital Holography and Three-Dimensional Imaging, OSA Technical Digest (CD) (Optical Society of America) DWD7* (2009).
- [63] Cheong, F. C., Xiao, K., and Grier, D. G. Characterization of individual milk fat globules with holographic video microscopy. *J. of Dairy Sci.* **92** 95 (2009).
- [64] Knöner, G., Parkin, S., Nieminen, T. A., Heckenberg, N. R., and Rubinsztein-Dunlop, H. Measurement of the index of refraction of single microparticles. *Phys. Rev. Lett.* **97** 157402 (2006).
- [65] Hoffmann, M. R., Martin, S. T., Choi, W. Y., and Bahnemann, D. W. Environmental Applications of Semiconductor Photocatalysis. *Chemical Rev.* **95** 69 (1995).
- [66] Valden, M., W., X. L. D., and Goodman. Onset of catalytic activity of gold clusters on titania with the appearance of nonmetallic properties. *Science* **281** 1647 (1998).

- [67] Oregan, B. and Gratzel, M. A Low-Cost, High-Efficiency Solar-Cell based on Dye-Sensitized Colloidal  $\text{TiO}_2$  Films. *Nature* **353** 737 (1991).
- [68] Imhof, A. and Pine, D. J. Ordered microporous materials by emulsion templating. *Nature* **389** 948 (1997).
- [69] Wijnhoven, J. and Vos, W. L. Preparation of photonic crystals made of air spheres in titania. *Science* **281** 802 (1998).
- [70] Lodahl, P., van A. F. Driel, Nikolaev, I. S., Irman, A., Overgaag, K., Vanmaekelbergh, D. L., and Vos, W. L. Controlling the dynamics of spontaneous emission from quantum dots by photonic crystals. *Nature* **430** 654 (2004).
- [71] Yu, H. K., Yi, G. R., Kang, J. H., Cho, Y. S., Manoharan, V. N., Pine, D. J., and Yang, S. M. Surfactant-assisted synthesis of uniform titania microspheres and their clusters. *Chem. Mater.* **20** 2704 (2008).
- [72] Demirrs, A. F., van Blaaderen, A., and Imhof, A. Synthesis of Eccentric Titania-Silica Core-Shell and Composite Particles. *Chem. Mater.* **21** 979 (2009).
- [73] Cheong, I. W., Shin, J. S., Kim, J. H., and Lee, S. J. Preparation of Monodisperse Melamine-Formaldehyde Microspheres via Dispersed Polycondensation. *Macromolecular Research* **12** 225 (2004).
- [74] Friedel, B. and Greulich-Weber, S. Preparation of Monodisperse, Submicrometer Carbon Spheres by Pyrolysis of Melamine-Formaldehyde Resin. *small* **2** 859 (2006).
- [75] (<http://www.cargille.com/refractivestandards.shtml>) .
- [76] Yang, C., Dabros, T., Li, D. Q., Czarnecki, J., and Maslyah, J. H. Measurement of the zeta potential of gas bubbles in aqueous solutions by microelectrophoresis method. *Journal of Colloid and Interface Science* **243** 128 (2001).
- [77] Yan, D. G., Yang, C., Nguyen, N. T., and Huang, X. Y. A method for simultaneously determining the zeta potentials of the channel surface and the tracer particles using microparticle image velocimetry technique. *Electrophoresis* **27** 620 (2006).
- [78] Roberts, G. S., Wood, A. T., Frith, W. J., and Bartlett, P. Direct measurement of the effective charge in nonpolar suspensions by optical tracking of single particles. *The Journal of Chemical Physics* **126** 194503 (2007).
- [79] Leunissen, M. E., Vutukuri, H. R., and van Blaaderen, A. Directing colloidal self-assembly with biaxial electric fields. *Advanced Materials* **21** 3116 (2009).
- [80] Mittal, M., Lele, P. P., Kaler, E. W., and Furst, E. M. Polarization and interactions of colloidal particles in ac electric fields. *The Journal of Chemical Physics* **129** 064513 (2008).
- [81] Polin, M., Roichman, Y., and Grier, D. G. Autocalibrated colloidal interaction measurements with extended optical traps. *Phys. Rev. E* **77** 051401 (2008).
- [82] Pure Component Properties (Queryable database), Chemical Engineering Research Information Center. <http://www.cheric.org/research/kdb/hcprop/showcoef.php?cmpid=818prop=VSL> (Retrieved 9 August 2010).
- [83] Savin, T. and Doyle, P. S. Role of finite exposure time on measuring an elastic modulus using microrheology. *Phys. Rev. E* **71** 041106 (2005).
- [84] Prieve, D. C., Lanni, F., and Luo, F. Brownian Motion of a Hydrosol Particle in a Colloidal Force Field. *Faraday Discuss. Chem. Soc.* **83** 297 (1987).
- [85] Walz, J. Y. Measuring particle interactions with total internal reflection microscopy. *Curr. Opin. Colloid Interface Sci.* **2** 600 (1997).

- [86] Kleshchanok, D., Tuinier, R., and Lang, P. R. Direct measurements of polymer-induced forces. *J. Phys.: Condens. Matter* **20** 073101 (2008).
- [87] Prieve, D. C. Measurement of Colloidal Forces with TIRM. *Adv. Colloid Interface Sci.* **82** 93 (1999).
- [88] Lin, K.-H., Crocker, J. C., Prasad, V., Schofield, A., Weitz, D. A., Lubensky, T. C., and Yodh, A. G. Entropically Driven Colloidal Crystallization on Patterned Surfaces. *Phys. Rev. Lett.* **85** 1770 (2000).
- [89] Gasser, U., Weeks, E. R., Schofield, A., Pusey, P. N., and Weitz, D. A. Real-space imaging of nucleation and growth in colloidal crystallization. *Science* **292** 258 (2001).
- [90] Frank, M., Anderson, D., Weeks, E. R., and Morris, J. F. Particle migration in pressure-driven flow of a Brownian suspension. *Journal of Fluid Mechanics* **493** 363 (2003).
- [91] Mohraz, A. and Solomon, M. J. Direct Visualization of Colloidal Rod Assembly by Confocal Microscopy. *Langmuir* **21** 5298 (2005).
- [92] Leunissen, M. E., Christova, C. G., Hynninen, A. P., Royall, C. P., Campbell, A. I., Imhof, A., Dijkstra, M., van Roij, R., and van Blaaderen, A. Ionic colloidal crystals of oppositely charged particles. *Nature* **437** 7056 (2005).
- [93] Cohen, I., Davidovitch, B., Schofield, A., Brenner, P., and Weitz, D. Slip, Yield, and Bands in Colloidal Crystals under Oscillatory Shear. *Physical Review Letters* **97** 215502 (2006).
- [94] Nugent, C. R., Edmond, K. V., Patel, H. N., and Weeks, E. R. Colloidal Glass Transition Observed in Confinement. *Physical Review Letters* **99** 025702 (2007).
- [95] Leunissen, M. E., van Blaaderen, A., Hollingsworth, A. D., Sullivan, M. T., and Chaikin, P. M. Electrostatics at the oil-water interface, stability, and order in emulsions and colloids. *Proceedings of the National Academy of Sciences of the United States of America* **104** 2585 (2007).
- [96] Leunissen, M. E., Sullivan, M. T., Chaikin, P. M., and van Blaaderen, A. Concentrating colloids with electric field gradients. I. Particle transport and growth mechanism of hard-sphere-like crystals in an electric bottle. *Journal of Chemical Physics* **128** 164508 (2008).
- [97] van Schooneveld, M. M., de Villeneuve, V. W. A., Dullens, R. P. A., Aarts, D. G. A. L., Leunissen, M. E., and Kegels, W. K. Structure, Stability, and Formation Pathways of Colloidal Gels in Systems with Short-Range Attraction and Long-Range Repulsion. *The Journal of Physical Chemistry B* **113** 4560 (2009).
- [98] Hu, Y., Nieminen, T. A., Heckenberg, N. R., and Rubinsztein-Dunlop, H. Antireflection coating for improved optical trapping. *J. Appl. Phys.* **103** 093119 (2008).
- [99] Bormuth, V., Jannasch, A., van Blaaderen, A., Howard, J., and Schäffer, E. Optical trapping particle and optical trapping method. *European Patent Application EP 08 15 2033.0* (filed 27 February 2008).
- [100] Bormuth, V., Jannasch, A., Ander, C. M. v. K., van Blaaderen, A., Howard, J., and Schäffer, E. Optical trapping of coated microspheres. *Opt. Exp.* **16** 13831 (2008).
- [101] Jannasch, A., Bormuth, V., van Kats, C. M., van Blaaderen, A., Howard, J., and Schäffer, E. Coated microspheres as enhanced probes for optical trapping. *Proc. of SPIE* **7038** (2008).
- [102] Graf, C., Vossen, D. L. J., Imhof, A., and van Blaaderen, A. A general method to coat colloidal particles with silica. *Langmuir* **19** 6693 (2003).

- [103] Vossen, D. L. J., van der Horst, A., Dogterom, M., and van Blaaderen, A. Optical tweezers and confocal microscopy for simultaneous three-dimensional manipulation and imaging in concentrated colloidal dispersions. *Rev. Sci. Instrum.* **75** 2960 (2004).
- [104] Hermes, M., Vermolen, E. C. M., Leunissen, M. E., Vossen, D. L. J., van Oostrum, P. D. J., Dijkstra, M., and van Blaaderen, A. Nucleation of colloidal crystals on configurable seed structures. *Soft Matter*; DOI: 10.1039/COSM01219J (2011).
- [105] Zhang, L., D'Acunzi, M., Kappl, M., Auernhammer, G. K., Vollmer, D., van Kats, C. M., and van Blaaderen, A. Hollow Silica Spheres: Synthesis and Mechanical Properties. *Langmuir* **25** 2711 (2009).
- [106] <http://www.plasticsusa.com/refract.html> .
- [107] Vondermassen, K., Bongers, J., Mueller, A., and Versmold, H. Brownian Motion: A Tool To Determine the Pair Potential between Colloid Particles. *Langmuir* **10** 1351 (1994).
- [108] Carbajal-Tinoco, M. D., Castro-Román, F., and Arauz-Lara, J. L. Static properties of confined colloidal suspensions. *Phys. Rev. E* **53** 3745 (1996).
- [109] Ducker, W. A., Senden, T. J., and Pashley, R. M. Direct measurement of colloidal forces using an atomic force microscope. *Nature* **353** 239 (1991).
- [110] Crocker, J. C. and Grier, D. G. Microscopic Measurement of the Pair Interaction Potential of Charge-Stabilized Colloid. *Phys. Rev. Lett.* **73** 352 (1994).
- [111] Crocker, J. C., Matteo, J. A., Dinsmore, A. D., and Yodh, A. Entropic Attraction and Repulsion in Binary Colloids Probed with a Line Optical Tweezer. *Phys. Rev. Lett.* **82** 4352 (1999).
- [112] Masri, D. E., van Oostrum, P., Smallenburg, F., Vissers, T., Imhof, A., Dijkstra, M., and van Blaaderen, A. Measuring Colloidal Forces from Particle Position Deviations inside an Optical Trap. *Soft Matter*; DOI:10.1039/COSM01295E (2011).
- [113] Sainis, S. K., Germain, V., and Dufresne, E. R. Statistics of Particle Trajectories at Short Time-Intervals Reveal Electrostatic Colloidal Interactions in Nonpolar Solvents. *Phys. Rev. Lett.* **95** 018303 (2007).
- [114] Han, Y. and Grier, D. G. Confinement-Induced Colloidal Attractions in Equilibrium. *Phys. Rev. Lett.* **91** 038302 (2003).
- [115] Baumgartl, J. and Bechinger, C. On the limits of digital video microscopy. *Europhys. Lett.* **71** 487 (2005).
- [116] Ovryn, B. and Izen, S. H. Imaging of transparent spheres through a planar interface using a high-numerical-aperture microscope. *J. Opt. Soc. Am. A* **17** 1202 (2000).
- [117] Ovryn, B. Three-dimensional forward scattering particle image velocimetry applied to a microscope field-of-view. *Exp. Fluids* **29** S175 (2000).
- [118] Kepler, G. M. and Fraden, S. Attractive potential between confined colloids at low ionic strength. *Phys. Rev. Lett.* **73** 356 (1994).
- [119] C.Léon, G., Saucedo-Solorio, J. M., and Arauz-Lara, J. L. Colloidal Interactions in Partially Quenched Suspensions of Charged Particles. *Phys. Rev. Lett.* **81** 1122 (1998).
- [120] Trizac, E. and Raimbault, J.-L. Long-range electrostatic interactions between like-charged colloids: Steric and confinement effects. *Phys. Rev. E* **60** 6530 (1999).
- [121] Sader, J. E. and Chan, D. Y. C. Long-Range Electrostatic Attractions between Identically Charged Particles in Confined Geometries and the Poisson-Boltzmann Theory.

- Langmuir* **16** 324 (2000).
- [122] Squires, T. M. and Brenner, M. P. Like-Charge Attraction and Hydrodynamic Interaction. *Phys. Rev. Lett.* **85** 4976 (2000).
- [123] Rojas-Ochoa, L. F., neda Priego, R. C., Lobaskin, V., Stradner, A., Scheffold, F., and Schurtenberger, P. Density Dependent Interactions and Structure of Charged Colloidal Dispersions in the Weak Screening Regime. *Phys. Rev. Lett.* **100** 178304 (2008).
- [124] Brunner, M., Bechinger, C., Strepp, W., Lobaskin, V., and von Grünberg, H.-H. Density-dependent pair interactions in 2D. *Europhys. Lett.* **58** 926 (2002).
- [125] Russ, C., von Grünberg, H.-H., Dijkstra, M., and van Roij, R. Three-body forces between charged colloidal particles. *Phys. Rev. E.* **66** 011402 (2002).
- [126] Brunner, M., Dobnikar, J., and von Grünberg, H.-H. Direct Measurement of Three-Body Interactions amongst Charged Colloids. *Phys. Rev. Lett.* **92** 078301 (2004).
- [127] Reinke, D., Stark, H., von Grünberg, H.-H., Schofield, A. B., Maret, G., and Gasser, U. Noncentral Forces in Crystals of Charged Colloids. *Phys. Rev. Lett.* 038301 (2007).
- [128] Merrill, J. W., Sainis, S. K., and Dufresne, E. R. Many-Body Electrostatic Forces between Colloidal Particles at Vanishing Ionic Strength. *Phys. Rev. Lett.* **103** 138301 (2009).
- [129] Merrill, J. W., Sainis, S. K., Bławdziewicz, J., and Dufresne, E. R. Many-body force and mobility measurements in colloidal systems. *Soft Matter* **6** 2187 (2010).
- [130] Nieminen, T. A., Rubinsztein-Dunlop, H., and Heckenberg, N. R. Calculation of the T-matrix: general considerations and application of the point-matching method. *Journal of Quantitative Spectroscopy and Radiative Transfer* **79-80** 1019 (2003).
- [131] Mishchenko, M. I., Zakharova, N. T., Videen, G., Khlebtsov, N. G., and Wriedt, T. Comprehensive T-matrix referencedatabase:A2007-2009update. *Journal of Quantitative Spectroscopy & Radiative Transfer* **111** 650 (2010).
- [132] Johnson, P. M., van Kats, C. M., and van Blaaderen, A. Synthesis of colloidal silica dumbbells. *Langmuir* **21** 11510 (2005).
- [133] Demirörs, A. F., Johnson, P. M., van Kats, C. M., van Blaaderen, A., and Imhof, A. Directed self-assembly of colloidal dumbbells with an electric field. *Langmuir* **26** 14466 (2010).
- [134] Okubo, M., Fujibayashi, T., Yamada, M., and Minami, H. Micron-sized, monodisperse, snowman/confetti-shaped polymer particles by seeded dispersion polymerization. *Colloid Polym. Sci.* **283** 1042 (2005).
- [135] Vutukuri, H. R., Demirörs, A. F., Peng, B., van Oostrum, P., Imhof, A., and van Blaaderen, A. Colloidal analogues of charged and uncharged polymer chains with tunable stiffness. *in preparation* (2011).
- [136] Zahn, K., Lenke, R., and Maret, G. Friction coefficient of rod-like chains of spheres at very low Reynolds numbers. I. Experiment. *J. Phys. II France* **4** 555 (1994).
- [137] Meunier, A. Friction coefficient of rod-like chains of spheres at very low Reynolds numbers. II. Numerical simulations. *J. Phys. II France* **4** 561 (1994).
- [138] Doi, M. and Edwards, S. F. *The Theory of Polymer Dynamics*. Clarendon Press, Oxford (1986).
- [139] Tirado, M. M., Martínez, C. L., and de la Torre, J. G. Comparison of theories for the translational and rotational diffusion coefficients of rod-like macromolecules. Application to short DNA fragments. *J. Chem. Phys.* **84** 2047 (1984).

- [140] Löwen, H. Brownian dynamics of hard spherocylinders. *Phys. Rev. E* **50** 1232 (1994).
- [141] Mukhija, D. and Solomon, M. J. Translational and rotational dynamics of colloidal rods by direct visualization with confocal microscopy. *J. Colloid Interface Sci.* **314** 98 (2007).
- [142] Perrin, J. Mouvement brownien et réalité moléculaire. *Annales de Chimie et de Physique* 19 (8e série), <http://gallica.bnf.fr/ark:/12148/bpt6k349481> (1909).
- [143] Chelakkot, R., Winkler, R. G., and Gompper, G. Migration of semiflexible polymers in microcapillary flow. *EPL* **91** 14001 (2010).
- [144] Stepanow, S. On the behaviour of the short Kratky-Porod chain. *J. Phys.: Cond. Mat.* **17** S1799 (2005).
- [145] Cifra, P. Differences and limits in estimates of persistence length for semi-flexible macromolecules. *Polymer* **45** 5992 (2004).
- [146] Spakowitz, A. J. and Wang, Z.-G. End-to-end distance vector distribution with fixed end orientations for the wormlike chain model. *Phys. Rev. E* **72** 041802 (2005).
- [147] Brangwynne, C. P., Koenderink, G. H., Barry, E., Dogic, Z., MacKintosh, F. C., and Weitz, D. A. Bending Dynamics of Fluctuating Biopolymers Probed by Automated High-Resolution Filament Tracking. *Biophys. J.* **93** 346 (2007).
- [148] Furst, E. M. and Pantina, J. P. Yielding in colloidal gels due to nonlinear microstructure bending mechanics. *Phys. Rev. E* **75** 050402 (2007).
- [149] Robertson, R. M., Laib, S., and Smith, D. E. Diffusion of isolated DNA molecules: Dependence on length and topology. *PNAS* **103** 7310 (2006).
- [150] Tomić, S., Babić, S. D., Ivek, T., Vuletić, T., Kča, S., Livolant, F., and Podgornik, R. Short-fragment Na-DNA dilute aqueous solutions: Fundamental length scales and screening. *EPL* **81** (2008).
- [151] Mazur, S., Beckerbauer, R., and Buckholz, J. Particle Size Limits for Sintering Polymer Colloids without Viscous Flow. *Langmuir* **13** 4287 (1997).
- [152] George, M. C., Mohroz, A., Piech, M., Bell, N. S., Lewis, J. A., and Braun, P. V. Direct Laser Writing of Photoresponsive Colloids for Microscale Patterning of 3D Porous Structures. *Adv. Mat.* **21** 66 (2009).
- [153] Singh, R. P. and Sinh, C. P. Dielectric behavior of the Binary Mixtures of n-Hexane with Toluene, Chlorobenzene and 1-Hexanol. *J. Eng. Data.* **27** 283 (1982).

# 3

## Measuring forces

---

In this Chapter we introduce two methods to measure colloidal interactions using two time-shared optical tweezers and particle tracking. We show that by calibrating an optical trap and varying the distance between two particles one can measure colloidal forces in the pN range. The particles were tracked using confocal laser scanning microscopy. Alternatively, when the particles are released from the two traps, the forces between the colloids act against the hydrodynamic friction. From many trajectories it is possible to deduce both the average velocity and the diffusion constant and thus the friction factor. The force can then be obtained from both the mobility and the friction factor. In this way it is possible to measure colloidal interactions in the fN range. We applied this last technique to measure colloidal forces. Here we used Digital Holographic Microscopy for the particle tracking. We compare the two methods to measure forces and the application of the two particle tracking methods for application in force measurements. Moreover we demonstrate that it is possible using these methods to measure external forces as in sedimentation and electrophoresis.

## 3.1 Introduction

Understanding the interactions between (charged) particles is of great importance from a fundamental point of view to many natural, biological and industrial processes, which require control over the structure, stability and many other properties of a dispersion [1]. According to the classical Derjaguin-Landau-Verwey-Overbeek DLVO theory, the interaction between stable pairs of charged colloidal particles suspended in a dielectric medium is a sum of a repulsive electrostatic part and a generally shorter ranged attractive Van der Waals part [2, 3]. To quantitatively confront DLVO theory with experiments, some refinements are required [4, 5]. For example, the adsorption of charged species at the colloidal surface and the complex charging mechanisms in nonaqueous media with low polarity [6, 7], make it unclear as to what extent the electrostatic interactions can be described with a sum of pair potentials [8, 9] that are independent of the volume fraction and phase.

Different experimental techniques have been developed to directly or indirectly measure forces acting between (charged) objects ranging from a few femto Newtons to pico Newtons. Total Internal Reflection Microscopy (TIRM) can measure the interaction forces between a microscopic sphere and a flat surface [9]. The Magnetic Chaining Technique, MCT, has been used to directly probe the force-distance profile between magnetic colloidal particles [10, 11]. Alternatively, the interaction potential between the colloids is determined by inverting a measured  $g(\mathbf{r})$  [12–15], or in Fourier space, by studying the scattering of a dispersion measuring the so-called  $S(\vec{q})$  [16–19]. Although in principle the inversion of scattering data could also be used to obtain inter-particle potentials, the finite range of  $\vec{q}$ -vectors available, difficulties with dividing out the formfactor and the finite accuracy almost always make this approach less accurate than a real space approach. Atomic force microscopes, equipped with a colloid on the tip of the cantilever have been applied to measure colloidal interaction forces [20]. Optical Tweezers, see also Chapters 4, 5 and 6, provide a powerful tool to optically manipulate colloidal systems and have been widely used in recent years to investigate colloidal interactions. Optical tweezers have been used to place particles in improbable configurations to gather more statistics [21–24]. A different approach to measure forces is to study the deviations from the equilibrium position in an optical trap [25, 26].

In this Chapter we present two techniques to measure colloidal interaction forces between particles by trapping them in optical tweezers. First, in section 3.2, we present measurements of the electrostatic repulsion between PMMA particles in cyclohexyl chloride, CHC where the forces were measured by means of the particle displacements in a calibrated trap. Here, the particles were tracked by confocal microscopy. The influence of ions, either originating from solvent decomposition or, more controlled, in the form of added salt TetraButylAmmonium Chloride, TBAC, on the interaction strength is studied. Ions in the suspension in-

fluence the interaction between the charged colloids in two ways. Ions in solution influence the range of the interaction by charge screening and the charge of the particles themselves may change in the presence of ions due to charge regulation and/or more specific adsorption of the ions on the particle surface.

In section 3.3 we present measurements of much smaller forces between silica particles in ethanol. The tracking was done by means of Digital Holographic Microscopy, DHM (see Chapter 2). The particles were periodically released from the traps after which the interaction forces equilibrate with the hydrodynamic friction. From local trajectories both the drift velocity and the hydrodynamic friction were determined, allowing to measure forces in the fN range [23].

The same technique to measure colloidal interaction forces was applied in section 3.4 to measure the interaction between silica coated PS particles in Cyclo-Hexyl Bromide, CHB. In section 3.5 we show a few of the advantages of the 3D tracking that holographic microscopy provides. In addition, DHM allows one to evaluate the out-of-plane component of the inter-particle distance and the force in that direction. We show an example in which it is clear that the out-of-plane component of the inter-particle interaction needs to be considered. Finally, in section 3.6, we show that it is possible to measure different forces in mutually perpendicular directions. We study the effect of the distance between two particles on their surface charges.

## 3.2 Forces from equilibrium displacements in optical traps

Here, we used the displacements in optical tweezers as determined by confocal microscopy to measure electrostatic forces between colloids. We used a Nipkow scanning disk confocal microscope to measure interaction forces between pairs of charged PMMA colloidal particles suspended in a relatively low-polar medium, HycloHexyl chloride, CHC, which has a dielectric constant  $\epsilon = 7.6$ , as was also used in section 2.2.2. Like the titania/silica composite particles described in section 2.2.2, PMMA particles in CHC gain a non-negligible charge which, in combination with relatively low screening results in long-ranged interactions. We varied the salt concentration, and thus the degree of screening by either adding a salt to the dispersion or by illuminating the sample with a UV lamp which caused the solvent to decompose into ions, among other products. Two particles were trapped: one was held in a stationary trap and the other particle was brought closer in small fixed steps. We calculate the inter-particle forces from the observed deviations of the particle positions inside the traps, see also Chapter 4 and 5.

In our study, we used sterically stabilized and fluorescently labeled Poly-Pethyl-MethAcrylate particles, PMMA [14] with a diameter of  $1.4 \mu\text{m}$  and size polydispersity of 3% from SLS. The refractive index of CHC is  $n = 1.462$ , which is lower than that of the particles  $n = 1.494$ , at the trapping wavelength of  $1064 \text{ nm}$ ,

which allows the particles to be trapped using optical tweezers. In this low-polar solvent, charge dissociation still occurs spontaneously [27], contrary to in truly apolar media that require charge stabilizing surfactants [28–30]. We performed electrophoresis measurements in dilute dispersions, using the methods described in references [31] and [32], which showed that the particles carried a positive charge of about  $+500 e$ , with  $e$  the elementary charge. We studied systems at a volume fraction  $\eta = 0.001$ , determined by particle tracking. Three different samples were studied. The first one consisted of a PMMA dispersion in purified CHC. The CHC was purified using activated alumina as described in reference [27]. The ion concentrations in the three other systems were observed to be increased by exposing the sample to UV (UVL-58 Handheld UV-lamp, UVP) illumination for different exposure times. It is known that UV exposure accelerates the partial degradation of the solvent into ions and none-charged products, but it is difficult to quantify the salt concentration by conductivity measurements without knowing the exact nature of the ions.

However, our measurements give an idea of how the different parameters in the same sample vary when exposed to UV-light. The dried particles were initially mixed with the purified CHC and allowed to equilibrate for 48 hours before the measurements were performed. The sample was then gently remixed, placed in a glass capillary of 0.1 by 1.0 mm inner dimensions and a wall thickness of 90  $\mu\text{m}$  (VitroCom) and sealed with Norland 68 UV glue. While curing the glue with UV-light, the sample was covered with aluminium foil to prevent solvent degradation. The measurement of particle interactions was performed using the optical tweezers setup described in reference [33] and in chapter 1. The wavelength of the laser used to trap the particles is 1064 nm. The trapping focus is formed by the same lens as used for the imaging confocal. We applied time-sharing using *Acousto-Optical Deflectors*, AODs, see also the Chapters 4, 5 and 6 to generate two traps and to vary their positions. Particle imaging was performed with a spinning Nipkow-disk confocal microscope (CSU10, Yokogawa) and recorded on a digital video camera (Evolution<sup>TM</sup> QEi) as in [34]. A 100 $\times$  NA1.4 PLAN APO objective from Leica was used. The particles were synthesized using the methods described in reference [35] were dyed with covalently bonded Rhodamine. The dye was excited with a Millennia V diode-pumped laser beam ( $\lambda = 532 \text{ nm}$ ). The trapped particles were located in the plane around 14  $\mu\text{m}$  above the bottom of the capillary glass wall to avoid possible effects of the sample boundaries. One of the traps was brought closer to the other one in small steps of about 500 nm every 2-3 seconds. For every step, 1000 confocal images of 80 by 21 pixels were recorded to sample the Brownian motion of the particles inside the traps. All images were processed to extract particle positions using home-made software based on methods similar to those described by Crocker and Grier [36].

One of the two particles was held in a stationary trap (at the origin) and the other particle (situated at distance  $S$  from the first particle) was brought closer in small steps, see Figure 3.1. The particle in the stationary trap experienced both

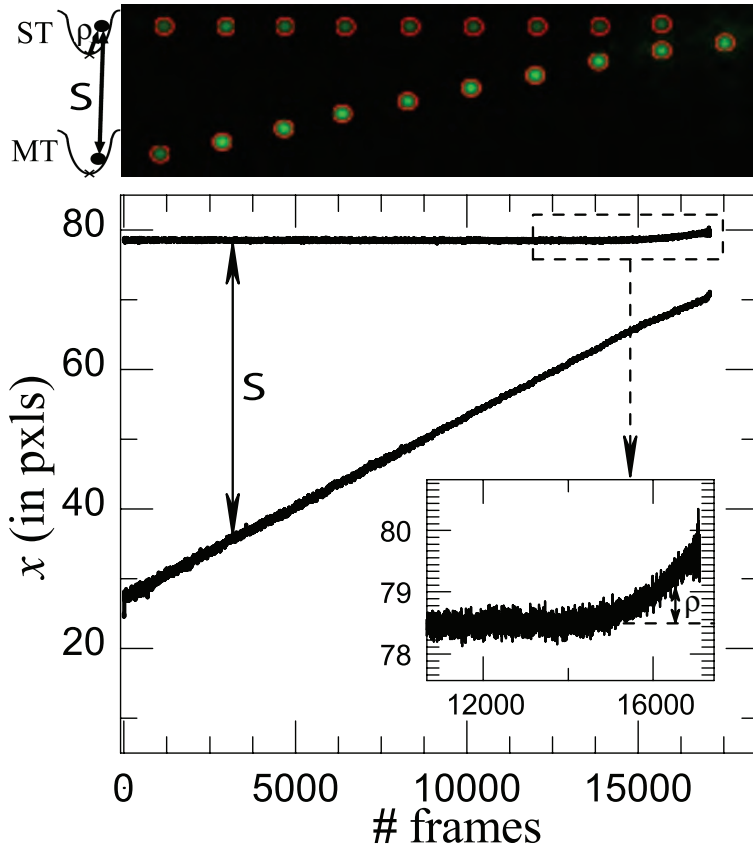


**Figure 3.1:** *Bringing two traps closer to one-another.* (Top left) A sketch of two particles confined to two optical traps. (Top right) Confocal microscopy images of the two particles as the mobile trap, MT, approaches the stationary trap, ST. The red contours on the particles are centered on the positions taken from the tracking code. (Bottom) Trajectories of the two trapped particles (1 pixel = 0.181  $\mu\text{m}$ ) projected onto the  $x$ -axis (chosen along the line connecting the two traps) for different frames. Inset: a zoom of the particle position deviations inside the stationary trap.

the potential of the optical trap  $U_{\text{well}}(\vec{\rho})$ , which varied with the position of the particle with respect to its equilibrium position in the trap  $\vec{\rho}$  and a force  $F(S)$  due to the presence of the other particle at a separation distance  $S$ . The additional force  $F$  caused the equilibrium position of the particle in the stationary trap to shift by a small amount. As the mobile trap was moved closer to the stationary one, the strength of this force increased and the particle deviated further. The particle in the mobile trap was similarly pushed in the opposite direction. For sufficiently large forces, Brownian motion caused one of the particles to escape from its trap. Figure 3.1 shows the positions of the two particles as the mobile

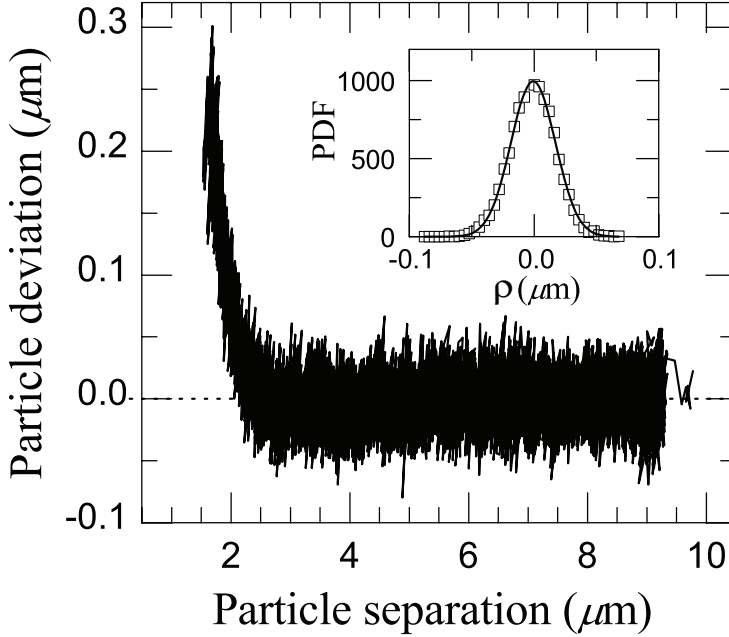


**Figure 3.2:** *Particle deviations in the trap.* Measured particle deviations inside the stationary trap plotted against particle separations for the sample with the highest salt concentration studied in this work. The particle starts being deviated due to the forces exerted by the approaching other particle in the mobile trap at a particle separation of about 2  $\mu\text{m}$ . Inset: the probability distribution of displacements inside the stationary trap before any deviation. The fitted line is a Gaussian approximation to the experimental data.

trap approached, until one of the particles escaped. At large distances, the pair interaction between the particles was negligible, but as the traps approached, each particle deviated from its well center due to the electrostatic repulsion. If the trap potential is known, the equilibrium position of the particle in the trap can be calculated from the Boltzmann distribution. If we assume that the force  $\vec{F}$ , exerted on the first particle by the second particle, did not vary significantly over the volume in which the particle fluctuates;  $\vec{F}(S) \approx \vec{F}(S \pm d\rho)$ , where  $d\rho$  is the typical fluctuation displacement of the particle inside the trap, the expected position is given by:

$$\langle \vec{\rho} \rangle = \frac{\int \vec{\rho} \exp(-\beta \{U_{\text{well}}(\vec{\rho}) - \vec{F} \cdot \vec{\rho}\}) d\vec{\rho}}{\int \exp(-\beta \{U_{\text{well}}(\vec{\rho}) - \vec{F} \cdot \vec{\rho}\}) d\vec{\rho}}, \quad (3.1)$$

Here, the integrations are carried out over the volume explored by the particle around the equilibrium position of the trap. After (numerically) calculating the integral, this relation can be inverted to calculate the force on a particle from

its measured position. For perfectly harmonic traps,  $\vec{F}_{\text{well}} \sim \langle \vec{\rho} \rangle$ . This is not generally the case [37, 38]. To calculate the exact shape of the well potential at larger displacements in the trap, we used the Mie-Debye representation given in [39, 40] (see also Chapter 4 and 5). In these calculations, the parameters describing the laser trap configuration are the beam opening angle  $\theta$  and  $\gamma$ , the ratio of the objective focal length to the beam waist  $\omega_0$ . We used  $\theta = 64.245^\circ$ ,  $\gamma = 1.21$  to model our laser spot with the  $100\times$  NA 1.4 PLAN APO objective from Leica used to trap the particles, with appropriate overfilling [41, 42]. See Chapter 5 and 6 for an elaborate description of the calculations of the forces exerted by a laser focus on colloidal particles.

The spherical aberrations, due to the refractive index mismatch between coverslip and solvent, depend on the distance from the geometric focus to the glass surface, here chosen to be  $14\ \mu\text{m}$ . To calculate the potential energy of the particle in the trap, the trapping force was integrated in the lateral direction at the trapping depth. The calculations show, for the parameters used in our experiments, a distinct deviation from harmonic behavior, a relative increase in the stiffness at larger deviations, as was also reported in [37, 38]. For the measured forces with the largest deviations, this effect can be as large as 20%. By using the trapping potential from calculations, we rest reassured that we do not underestimate these relatively larger forces. The trapping forces and potential are assumed to scale with the power of the trap, such that the well potential is  $U_{\text{well}}(r) = \alpha U_{\text{calculated}}(r)$ . The prefactor  $\alpha$  was measured from the standard deviation in the particle positions at large distances.

From our measurements, we determine the particle deviation in the stationary well  $\rho$  versus the particle separation  $S$ , see Figure 3.2. Initially, the particle exhibited Brownian motion inside the trap of a magnitude less than  $0.1\ \mu\text{m}$ , i.e.  $< 12\%$  of the particle diameter as demonstrated by the probability distribution of displacements plotted in the inset of Figure 3.2. From the standard deviation of this distribution, we determine the proportionality factor  $\alpha$ , which sets the well depth. We then calculate average deviations at different inter-particle distances by binning the data shown in Figure 3.2. Then we convert these deviations to forces using equation 3.1. Performing measurements with different laser powers, in the range from 200 to 800 mW, gave the same results for the inter-particle forces within our experimental resolution. This clearly demonstrates that possible light-induced particle interactions can be neglected [24, 43], which is partially due to the fact that the laser is always only illuminating a single particle in the time-shared tweezers used. See also Chapter 4 on optical tweezers, section 4.7.4.

Our data of the pair-interaction forces are compared with the prediction of the linearized Derjaguin approximation [1] with constant surface potential of the form:

$$F(S) = \frac{k_B T}{4\lambda_B} \phi^2 \kappa \sigma \frac{\exp(-\kappa\sigma(S/\sigma - 1))}{1 + \exp(-\kappa\sigma(S/\sigma - 1))}. \quad (3.2)$$

Here  $\phi = e\Psi_0/k_B T$  is the dimensionless surface potential, with surface potential

$\Psi_0$ ,  $\lambda_B$  the Bjerrum length, in CHC  $\lambda_B = 7.3$  nm,  $\kappa = \sqrt{4\pi\lambda_B C_s}$  the inverse Debye length assuming only monovalent ions at concentration  $C_s$ ,  $\sigma$  the particle diameter and  $S$  the distance between the trapped particles.

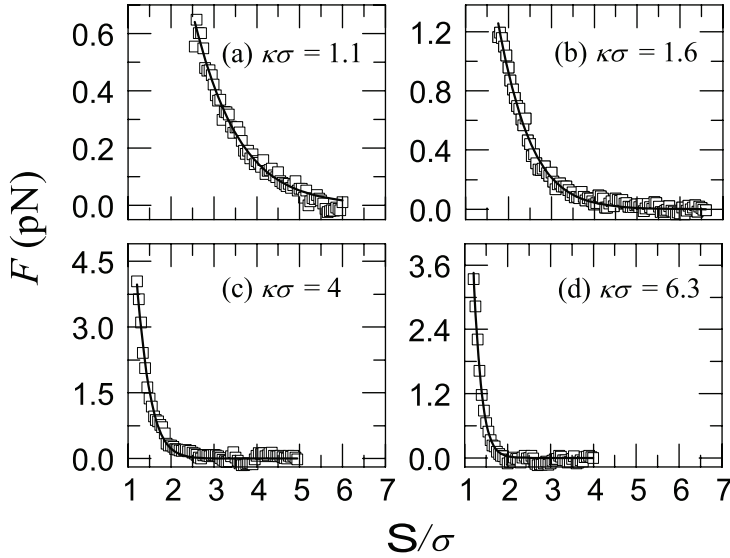


**Figure 3.3:** Screened charge repulsion between PMMA particles in CHC after different durations of UV exposure. Interaction forces between charged colloidal PMMA particles suspended in CycloHexyl Chloride with different salt concentrations resulting from different UV exposure times: **a** initial purified sample. **b** after 1 hour of UV exposure. **c** after 12 hours and **d** after 16 hours. The lines are fits based on the DLVO theory, equation 3.2 with fixed surface potential  $\Psi_0 = 135$  mV, giving values for Debye screening lengths  $\kappa^{-1}$  of 1.3, 0.87, 0.35 and 0.22  $\mu\text{m}$  respectively.

Figure 3.3 shows the results for the different sets of measurements as the concentration of salt is increased by exposing the initial purified sample under an UV-lamp at different exposure times: 0, 1, 12, and 16 hours respectively. The data are well fitted with the DLVO force given by equation 3.2 with a fixed surface potential  $\psi \simeq 5.3$  or  $\psi_0 \simeq 135$  mV and a Debye screening length decreasing from  $\kappa^{-1} \simeq 1.3$   $\mu\text{m}$  in a purified sample to  $\kappa^{-1} \simeq 0.2$   $\mu\text{m}$  in the sample with the longest UV exposure time. The interaction force  $F(S)$ , initially soft and extremely long-ranged, became shorter-ranged after longer exposure to UV. We thus conclude that UV exposure degrades the solvent, effectively increasing the higher salt concentration. This process was also observed in the chemically very similar solvent CycloHexyl Bromide, CHB [44].

When we performing the same measurements in the same sample with a different speed of approach, the resulting interactions did not differ significantly. This suggests that hydrodynamic effects due to the movement of the traps are negligible. Since with the 2D confocal imaging we cannot follow the deviations

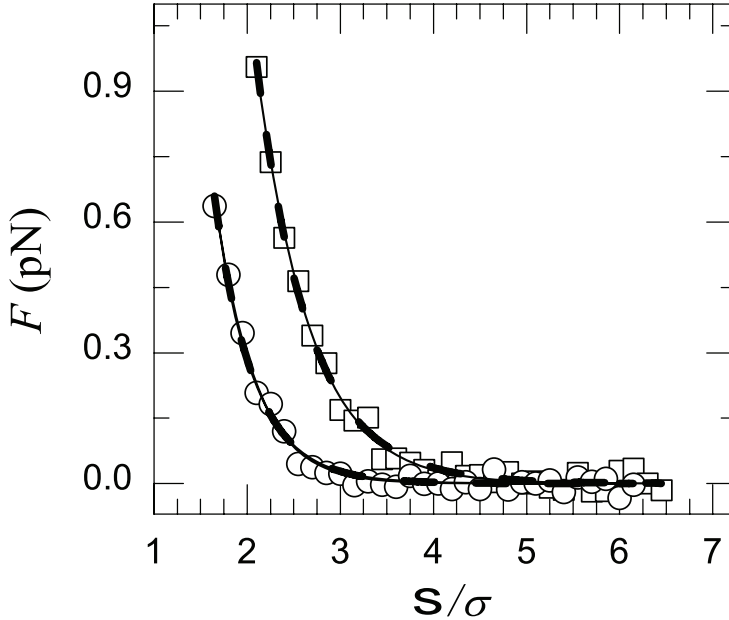


**Figure 3.4:** Screened charge repulsion between PMMA particles in CHC with 0.026 and 0.26  $\mu\text{M}$  added TBAC salt respectively. Interaction forces between charged colloidal PMMA particles in samples I and II with 0.026 and 0.26 mM added TBAC salt respectively. The lines are fits based on the DLVO theory with constant surface potential (full lines) with  $\phi = 5.64$  and 3.37, giving values for screening lengths  $\kappa\sigma$  of 1.86 and 2.58 respectively, and with constant surface charge (dashed lines) with  $Q = 4.56$  and 2.55, giving values for screening lengths  $\kappa\sigma$  of 1.6 and 2.06 respectively.

in the  $z$ -direction, which is the direction in which optical traps show the smallest stiffness (see Chapter 4), we instead measure the projection of the particle separation onto the  $xy$ -plane and thus we slightly underestimate the distance between the two particles. It is the limited speed of acquisition of confocal laser scanning microscopy that limits us to tracking in 2D. In principle it is possible to calibrate the intensity of the individual particles as a function of bleaching and out-of-plane position to also obtain an estimate of the  $z$ -displacement. Using two  $z$ -planes in the imaging can also give the sign of the displacement. In addition, the assumption that the force is approximately constant over the integration volume in equation 3.1 will lead to a small systematic error in the measured forces. We performed Monte Carlo simulations to estimate the magnitude of these effects, simulating two particles in two optical traps with the interactions and well shape based on our experimental parameters. After analyzing the resulting data in the same way as the experimental data, the deviations in the obtained values for the  $\kappa\sigma$  and  $\Psi_0$  were at most 3% and 1%, respectively.

To further test the reliability of this method, we conducted two more mea-

Constant Surface Potential (Equation 3.2)					
Sample	$\kappa\sigma$	$\phi$	$Z^*$	$\phi_{el}$	$Z_{el}^*$
I	1.86	5.64	1833	4.5	1130
II	2.58	3.37	910	2.42	585
Constant Surface Charge (Equation 3.3)					
	$\kappa\sigma$	Q	$Z^*$	$\phi_{el}$	$Z_{el}^*$
I	1.6	4.56	547	4.38	980
II	2.06	2.55	237	2.43	510

**Table 3.1:** Measured parameters for the two samples I and II with 0.026 and 0.26  $\mu\text{M}$  added TBAC respectively: the screening length  $\kappa\sigma$ , the dimensionless surface potential  $\phi = e\Psi_0/k_B T$ , the dimensionless surface charge  $Q = eZ^*/4\pi\epsilon k_B T\kappa^{-1}$ , and the effective charge  $Z^*$ . The effective charges quoted for the constant potential fits were evaluated at infinite particle spacing. The last two columns are based on the electrophoresis measurements.

measurements using two other dispersions containing a controlled amount of the salt tetrabutylammonium chloride (TBAC, Sigma-Aldrich). We independently estimated the Debye screening lengths from the scaling law for the liquid-solid phase transition in Yukawa systems [45], and measured the particle surface charges by means of electrophoresis. We prepared a solution of TBAC in purified CHC, which we allowed to equilibrate for a week. We then filtered the saturated solvent (260  $\mu\text{M}$  TBAC) and diluted it by adding an amount of purified CHC to prepare two solvents, I and II containing 0.026 and 0.26  $\mu\text{M}$  of TBAC, respectively. The measured force-distance profiles of PMMA particles in these two salt added solvents are again well fitted with the DLVO force but with different surface potentials. See Figure 3.4 for the fit and table 3.1 for the fit-values. The data are also well fitted with the constant surface charge formula [1]:

$$F(S) = \frac{k_B T}{4\lambda_B} Q^2 \kappa\sigma \frac{\exp(-\kappa\sigma(S/\sigma - 1))}{1 - \exp(-\kappa\sigma(S/\sigma - 1))}, \quad (3.3)$$

where  $Q = eZ^*/4\pi\epsilon k_B T\kappa^{-1}$  is the dimensionless surface charge (see Figure 3.4 and table 3.1 for the different parameters).

The fit values for the screening lengths and the charges obtained from fits of equation 3.2, for the force between two charged colloids under the assumption of a constant surface potential and of equation 3.3 for this force under the assumption of constant charge, are not the same. In the derivation of these equations it was assumed that the dimensionless charge or the dimensionless potential would be smaller than unity. However, comparison with exact numerical solutions to the non-linear Poisson-Boltzmann equation leads to the conclusion that violation of this limit does not cause big deviations [46]. In reality the charge of the particles

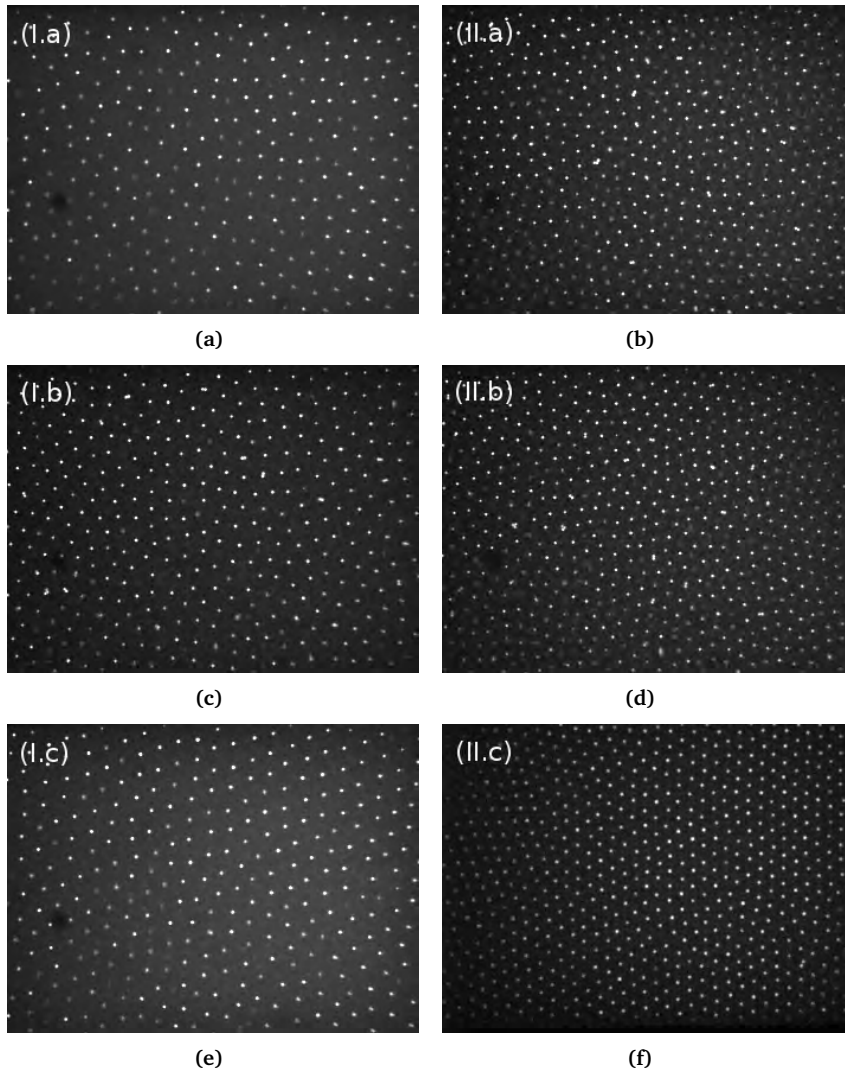


**Figure 3.5:** Confocal images of the two samples I and II with 0.026 and 0.26  $\mu\text{M}$  added TBAC salt respectively at freezing. The average particle-particle separations are 5.3 and 4.1  $\mu\text{m}$  respectively. Using the coupling parameter needed for crystallization, equation 3.4, this gives an estimate for the screening lengths  $\kappa\sigma$  of about 2.3 and 2.8 respectively. **a.** Sample I in the liquid, close to freezing. **b.** Sample II in the liquid, close to freezing. **c.** Sample I with some more local order. **d.** Sample II the liquid with some more local order. In **a,b,c** and **d** we did observe long time self diffusion, particle sometimes exchanged places. **e.** Sample I in the crystal where no long time self diffusion was observed, close to freezing. **f.** Sample II in the crystal where no long time self diffusion was observed, close to freezing.

might depend on the ion concentration but not as strong as the constant surface potential assumption prescribes.

To get an independent estimate of the screening length, the two samples were left vertically. The sedimentation of the particles induced crystallization in the lower part of the sample. The samples were imaged with a tilted confocal microscope that allows one to scan at all heights. The average particle-particle separation  $|S|$  for the two systems at freezing were 5.3 and 4.1  $\mu\text{m}$  respectively (see Figure 3.5). Vaulina *et al.* [45] introduced a relation between the screening length and the coupling parameter needed for crystallization:

$$\frac{U(S')}{k_B T} \left( 1 + \kappa S' + \frac{(\kappa S')^2}{2} \right) = 106.6, \quad (3.4)$$

where  $U(S')$  is the potential energy at the typical particle-particle separation  $S'$ . From the average particle-particle spacing one can thus estimate  $\kappa\sigma$ . Using surface potentials from our force fits, this gives values for  $\kappa\sigma$  of about 2.3 and 2.8 respectively, in the same order of magnitude as the values we obtained from our force measurements.

In addition, we obtained independent measurements of the ionic strength from the conductivity of the particle free solvents. A commercial Conductivity meter (Scientifica 627) was used to measure the conductivity of the two solvents with the added salt. This yielded conductivities of 1600 and 9800 pS/cm respectively. Using Walden's rule [47, 48], the corresponding screening lengths are  $\kappa\sigma = 2.1$  and 5.5 respectively. The measured conductivity values are not in agreement with those obtained from Yukawa fits. It seems likely that part of the ions were adsorbed onto the metal surface of the conductivity meter during the measurement. Similarly, the ions in the sample might have been adsorbed at the wall of the capillary. Also the different approximations using Walden's rule to translate the measured conductivities to screening lengths make it difficult to compare with our force measurements. For this reason we resorted to the scaling law of the liquid-solid phase transition.

These two alternative techniques to estimate the amount of screening are clearly not accurate enough to favor either the constant surface potential or constant charge assumption. An alternative approach would be to fit the numerical solution of the non-linear Poisson-Boltzmann equation directly to the measured interaction potential.

Electrophoretic measurements on the same dilute samples were conducted by driving the particles in a dc-electric field ( $|E| \approx 1 - 3 \text{ V/m}\cdot\text{m}$ ) and measuring the electrophoretic mobility from particle tracking in a time series of confocal images. Using the values of the Debye screening length  $\kappa^{-1}$  from our force fits and the measured mobilities, the surface potentials were obtained using recent calculations for electrophoresis [17, 31, 32, 49]. This gives values of  $\phi_{el} = 4.5$  and 2.42 for samples I and II respectively when using the screening lengths from the constant surface potential fits and, 4.38 and 2.43 for the case of constant

surface charge. Finally, to translate the surface potential into a particle charge  $Z^*$ , we used the empirical relationship proposed by Loeb *et al.* [50]. The results of the electrophoresis measurements are slightly lower than the measured force parameters with a constant surface potential but slightly higher than the parameters obtained under the assumption of a constant surface charge. These results suggest the importance of charge regulation [15] in the case of PMMA dispersed in CHC with added TBAC.

## Conclusion

In summary, we have measured the interaction forces acting between charged PMMA colloidal particles suspended in a relatively low dielectric medium directly from the deviations of particle positions inside an optical trap. In principle, the measured forces include all possible effects such as the influence of the surrounding particles. Confocal microscopy can be used to track the particles at relatively high volume fractions  $\sim 15\%$  where optical tweezers can still be used to trap individual particles. As a result, this method allows one to measure particle interactions at higher volume fractions. Additionally, our measurements quantified for the first time the effect of exposing a PMMA/CHC dispersion to UV-light. When increasing the salt concentration by exposing the sample to UV-light, the force measurements agree well with the classical DLVO theory assuming a constant surface potential. On the other hand, when adding TBAC to vary the salt concentration, surface charge regulation seemed to play an important role. Future work will explore the effect of particle concentration and the nature of the interactions in dense systems.

## 3.3 Forces from mobility and friction factors

In section 3.2, we measured the charge repulsion between PMMA particles in CHC with different amounts of salt, either added purposely or resulting from solvent degradation. The forces were measured using calibrated optical traps. It is also possible to measure the interaction forces between colloidal particles from equilibrium distributions by inverting the Boltzmann equation [51, 52], see also section 2.5.5. These techniques rely on the assumption that the system is in thermal equilibrium and are limited to interactions of a few  $k_B T$ . Optical tweezers can be used to bring particles to improbable configurations to measure the interactions between them. This can be done by means of so-called line tweezers that confine the particles to a 1D section of space (see section 6.4 and [24] and references therein). These techniques are limited to measuring the interaction between two particles and one has to be aware of possible optically induced forces [43], see also section 4.7.4 and [24]. An alternative method to measure colloidal interactions between colloids relies on blinking traps that place the particles at improbable distances to then let them evolve freely in the absence of the

optically induced force field. This was introduced by Crocker and Grier [21]. This technique analyzes the probability fluxes between adjacent bins. The advantage is that it allows one to sample higher interaction energies. The disadvantage is that it needs to also measure the interactions to a distance large enough to let the interactions be negligible because it measures only relative energies. Furthermore it is difficult to rule out any hydrodynamic artifacts and it is hard to quantify the effect of sampling errors on the measured value for the interaction.

Sunil Sainis, Vincent Germain and Eric Dufresne developed a technique to essentially analyze the conservative forces between pairs of colloids over a short spatial interval [23]. This has the advantage that it is no longer necessary to evaluate all of the interaction potential because it measures the local force rather than relative potential energies. The method can be applied to any over-damped thermal system with normal modes. At sufficiently small time intervals the evolution of a normal mode is described by the Einstein-Smoluchowski or Stokes-Einstein relation with a constant drift velocity. Using the fluctuation-dissipation theory, it was shown that the conservative force on the normal mode is related to the drift velocity  $v$  and the diffusion constant  $D$  by:  $F = k_B Tv/D$ . From the same trajectories as from which the average drift velocity  $v$  is measured, also the diffusion constant  $D$  is determined. By doing so the method accounts for hydrodynamic forces through their effects on the diffusion coefficients. As a result, the technique requires no calibration or assumptions on the friction force against which the force of interest is measured.

Here we show that it is also possible to measure colloidal interaction forces using the technique proposed by Sainis *et al.* when Digital Holographic Microscopy, see Chapter 2 and [53], is used for the particle tracking. This is favorable due to its superior accuracy and the fact that it allows tracking the particles in 3D [53].

We first analyze the coordinates of the two 1.4  $\mu\text{m}$  silica particles in ethanol that we discussed in section 2.6.1. These two particles were trapped in time-shared optical traps that were intermittently switched off. Whenever both traps were switched off, the camera was triggered to record 3 frames at 100 fps. The time that both traps were off simultaneously was set to 0.04 seconds, after which the two traps were consecutively switched on for 0.02 seconds each. During this time the optical forces, see Chapters 4, 5 and 6, put the particles back to their initial position. One of the two particles is thus released 0.02 seconds prior to the release of the other particle. During this time the particle is free to move under influence of Brownian motion and external forces such as those resulting from the interaction with the other particle and external fields like gravity or electric fields. The result of the longer time since release is visible in the larger apparent noise in the position of the particle that starts at  $\rho_x = 17$  in Figure 3.6 a.

The condenser of an inverted microscope (Leica DRM-IRB) was replaced by a mirror, coupling the beam from a fibre coupled Spectra Physics Millennia V 532 nm laser at minimum power (200 mW) through the sample, into the objective. The integration time of the camera was set to 80  $\mu\text{s}$ . The holograms were recorded

at 100 fps on Mikrotron EoSens CE camera. Only a field of view of 160 by 450 pixels was recorded, this saves space on the memory card of the camera to optimize the statistics.

Figure 3.6 a shows the trajectories of the two particles. The two traps are slowly moved towards each other in the  $\rho_y$ -direction. The result is that the spacing  $S$  between the particles is decreased during the experiment. From each holographic snapshot we measured the 3D positions of both particles by fitting a model that describes the Mie scattering of the individual particles and the interference between the scattered light and the remaining illumination beam [53]. We fit both particles simultaneously to minimize the influence of imaging artifacts, see section 2.6 and reference [54]. The camera we used records a movie with

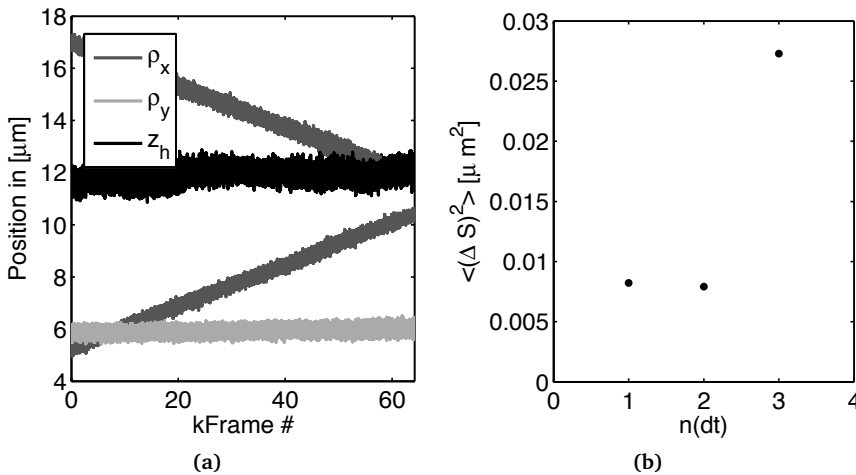


**Figure 3.6:** Trajectories and mean squared displacements over three frame intervals as a function of the initial frame. **a.** The same trajectories of the two silica particles in ethanol as in Figure 2.28 measured from analysis of holographic snapshots like the ones in Figure 2.27. **b.** Variance in the change of the inter-particle spacing  $S$  over three frames, as a function of the begin frame.

frame intervals given by triggering pulses. Unfortunately it did not allow us precise control over the moment it started recording and as a result we do not know a-priori which frames are the first frames of the trajectories of 3 frames. We solve this by studying the variance in the collection of changes in the spacing between the particles from frame to frame. Since the two particles are put back by the optical tweezers after three frames, we calculate the variance of all third time steps. Depending on the first time step considered, this variance is either dominated by the mean squared displacement during one time step or during two time steps as the particles are moved back to the initial positions by the optical tweezers. The mean squared displacement is therefore maximum for the displacements between the last frames of the trajectories and the first frames of the subsequent trajec-

ries. We plot the mean squared displacement over three frames as a function of the begin frame in Figure 3.6. Clearly one of these mean squared displacements is much larger than the others allowing us to determine which frames are the first in the sequences. For each trajectory, the average spacing  $S$  is calculated. The

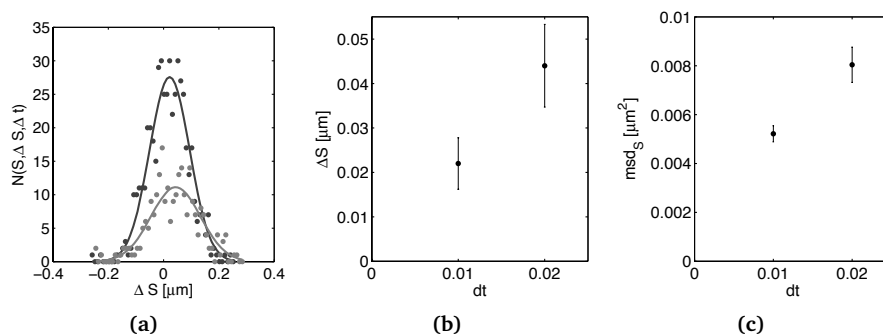


**Figure 3.7:** Short time statistics of the distance between two silica spheres in ethanol. **a.** A histogram of the changes in the distance between two  $1.4 \mu\text{m}$  particles about  $1.6 \mu\text{m}$  apart in ethanol  $\Delta S$  at two time lapses  $\Delta t$ . Dark grey; the displacements after  $0.01$  s, light grey; the displacements after  $0.02$  s. **b.** Plotting the mean displacement as a function of time. **c.** The mean squared displacement as a function of time. From these curves we deduce the average velocity and the diffusion constant.

trajectories are binned in bins containing 250 trajectories based on the spacing  $S$ . From these 750 particle coordinates, the average drift velocity and the average diffusion is determined. Figure 3.7 **a** represents two histograms for the displacements as a function of time. As each trajectory consists of 3 frames we have twice as many measurements for the displacement after  $0.01$  s as for the displacements after  $0.02$  s. The mean displacement over 1 and 2 frame intervals, when the two particles are on average  $1.6 \mu\text{m}$  apart, are plotted in Figure 3.7 **b**. By applying linear regression, the average drift velocity is determined. In Figure 3.7 **c** we give the mean squared displacements as a function of the time lapse. We determine the diffusion constant from the slopes of these curves and we gather an estimate of the accuracy of the position detection from the offset [55]. The error in the position detection thus estimated is given in Figure 2.28 **c**.

For each separation distance we thus measure the average drift velocity and the diffusion constant. These are plotted as a function of the spacing  $S$  in Figure 3.8 **a** and **b** respectively. The drift velocity in the spacing between the two silica spheres is positive, meaning that the distance between the particles increased on average during a trajectory, at short distances and falls off rapidly with increasing distance between the two spheres. The diffusion constant increases with the distance between the spheres as the hydrodynamic coupling between them decreases. For distances between the cores of more than  $4 \mu\text{m}$  the diffusion is more or less constant.

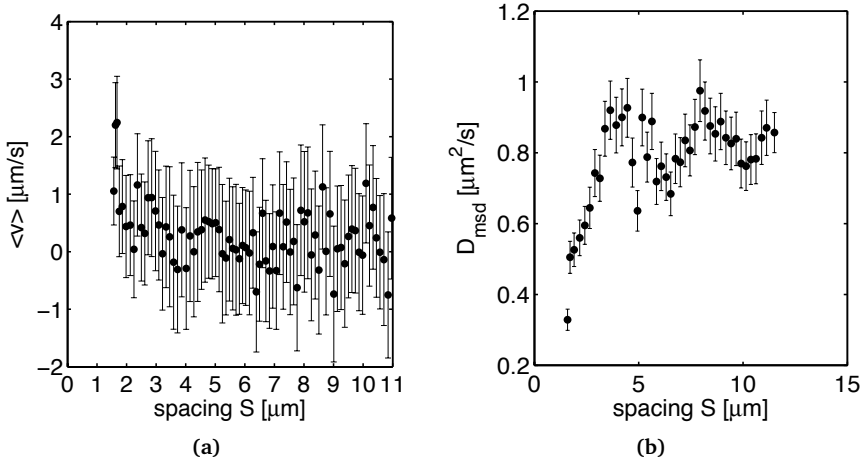


**Figure 3.8:** Separation dependence. **a.** Separation dependence of the velocity  $v$  of the separation between two  $1.4 \mu\text{m}$  silica spheres in ethanol. **b.** Plotting the mean displacement and the mean squared displacement. From these curves we deduce the average velocity and the diffusion constant.

The drift velocity is the result of charge repulsion between the two spheres. The velocity of a single sphere is the result of an equilibrium between the driving force and the Stokes friction,  $F = 6\pi\eta r v$  where  $\eta$  is the viscosity of the solvent,  $r$  the radius of the sphere and  $v$  its velocity. When two spheres are close to each other, the friction factor deviates from  $6\pi\eta r$  [56]. When the particles are charged and surrounded by ions this influences the friction factor as well [57]. Without *a priori* knowledge of the charge and screening in the experiment the friction factor is not known. When the parameter of interest, here the spacing  $S$  between the two particles, is a normal mode of an over-damped thermal system however, the friction factor and the diffusion constant are related through the Einstein-Smolukowski equation  $D = k_B T / \gamma$ , where  $\gamma$  is the friction factor on the mode under investigation [23]. The external force can thus be expressed as:

$$F = k_B T \left( \frac{v}{D} + \frac{D'}{D} \right). \quad (3.5)$$

Here  $D'$  denotes the spatial derivative of the diffusion constant. In reference [58] the apparent force due to the spatial variation of the diffusion constant  $k_B T \frac{D'}{D}$  was of significant importance. Often, also here, this force is negligible. We can thus determine the force from:

$$F = k_B T \frac{v}{D}. \quad (3.6)$$

Equation 3.6 can be used to measure the local forces on any normal mode  $x$  of a thermal system from short trajectories provided that:  $\langle \Delta x(\tau) \rangle v' \ll v$ ,  $\sqrt{\langle \Delta x(\tau)^2 \rangle}$

$v' \ll v$ ,  $\langle \Delta x(\tau) \rangle D' \ll D$  and  $\sqrt{\langle \Delta x(\tau)^2 \rangle} D' \ll D$ , where the primes denote spatial derivatives and  $\tau$  the time interval over which the system is allowed to evolve [23]. In short, both the drift velocity and the diffusion constant should be approximately constant over the range of displacements. It is important to choose  $\tau$  sufficiently short, such that these requirements are met and long enough for the physical displacements to be significantly larger than the measurement error. When the displacements are small compared to their lengths also the vector nature of normal modes such as the spacing  $S$  between two particles can be ignored. By application of equation 3.6, we can thus calculate the force between the two

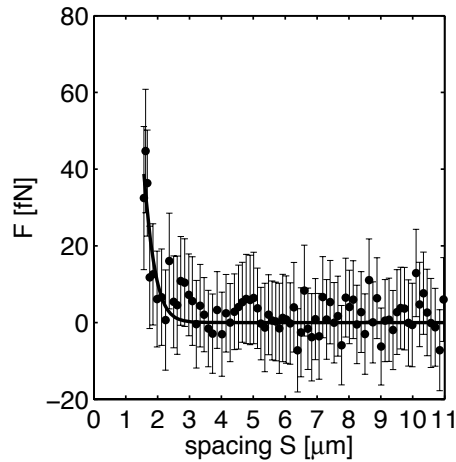


**Figure 3.9:** Interaction force between two silica spheres in ethanol. The force between two  $1.4 \mu\text{m}$  silica spheres in ethanol as a function of the distance  $S$  between them. The force is calculated from the transport coefficients in Figure 3.8. The full line is a fit to equation 3.2 for the force due to electrostatic repulsion at constant surface potential.

silica spheres in ethanol from the average drift velocities and diffusion constants in Figure 3.8. The resulting forces are plotted in Figure 3.9. Note that the forces here are measured in fN's rather than the pN's in section 3.2. There is a clear repulsive force that falls off exponentially with increasing distance between the two spheres. The interaction force is of negligible magnitude after circa  $3 \mu\text{m}$ . Since  $\kappa\sigma$  is relatively large, we have to apply one of Derjaguin's approximations for the charge repulsion between these two spheres [46]. The full line in Figure 3.9 is a fit to equation 3.2 for the charge repulsion in the case of a constant surface potential. We found a screening length of  $0.26 \pm 0.01 \mu\text{m}$  which is somewhere in between the values found in the experiments in section 2.5.5 and 2.5.6, where the interaction between a colloid from the same batch in ethanol and the sample wall were determined from the probability distribution. The dimensionless surface potential was found to be 0.22 which corresponds to a surface potential of

either +5.6 mV or -5.6 mV. In general the charge of silica at moderate pH is expected to be negative due to dissociation of silanol groups at the particle surface. The fit value of -5.6 mV value is relatively small [59]. Probably the poor statistics about the interaction force between these particles resulted in a large error in the measured particle charge. The bins were rather large with respect to the spatial change of the repulsive force, which results in a smaller maximum force.

As stated above, equation 3.6 can be applied to any normal mode of a thermal system. The simplest example of such a normal mode is the force in one of a Cartesian directions on a particle, as for instance the force of gravity that acts only in the  $z_h$  direction. From the analysis of the force in the  $z_h$ -direction, we gather that both particles had a mass of  $15 \pm 1.5$  pg, which almost agrees with what was found for similar particles in section 2.5.5. The difference is likely caused by a slightly different temperature and thus a slightly different density of the ethanol and perhaps some convection due to local heating of the solvent by the trapping laser. In general the viscosity of a liquid changes more strongly with the temperature than the density does, but here the viscosity is implicitly measured with the friction factor.

The accuracy of the measurement would benefit from both a larger number of particle coordinates per trajectory and from a larger number of trajectories. The number of frames the camera we used can record in one movie however, is limited by the requirement that the total movie be smaller than 1 GB. Given the fact that holographic particle tracking is accurate to tens of nm, in this case measurement errors contribute little to the noise on the force. We therefore assumed that optimal statistics would be gained by choosing to record more, but less long, trajectories in order to average out Brownian noise. This assumption was confirmed by Brownian dynamics simulations.

## Conclusion

In conclusion, the force measurements introduced by Sainis *et al.* [23] can be applied to data obtained using Digital Holographic Microscopy. Combining holographic tracking with this statistical analysis of particle trajectories allows one to measure fN forces in 3D, which is not possible using bright-field microscopy.

## 3.4 Silica in CHB

A different interesting system in which electrostatic colloidal interactions can be measured consists of PS particle that have been coated with a layer of silica in CycloHexyl Bromide. Particles from the same batch as was used in section 2.5.6 were dried under a nitrogen flow and dispersed in CycloHexyl Bromide, CHB. CHB has a dielectric constant  $\epsilon$  of  $7.92 \epsilon_0$ , which results in relatively little amounts of dissociated ions and a poor charge screening.

Again the particles were trapped in two time-shared traps and slowly brought closer to each other. When both traps were off the camera was triggered to take 3 holographic snapshots at 200 fps. From the holographic snapshots we measured the particle positions as introduced in Chapter 2. From the particle coordinates, we determined the particle-particle spacing  $S$ . Then we binned the trajectories in groups of 500. From these 500 trajectories we determined the average drift

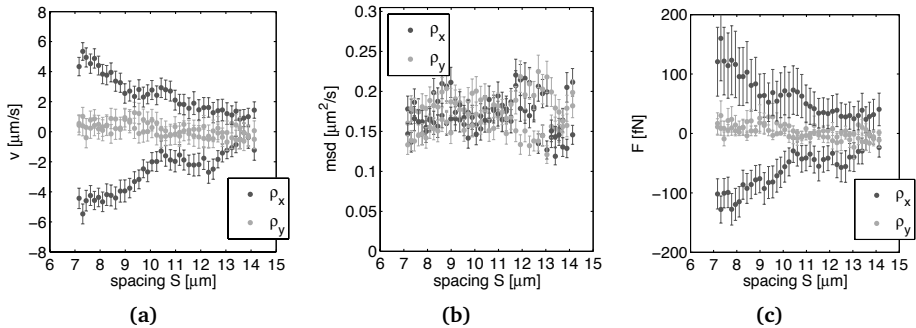


**Figure 3.10:** Interaction force between two silica coated PS particles in CHB. **a.** The velocities  $v_x$  and  $v_y$  as a function of the separation between two silica coated PS spheres in CHB. **b.** The separation dependence of the diffusion constants. **c.** Applying equation 3.6 to the coordinates in the  $\rho_x$  and  $\rho_y$ -directions separately, we determined the forces in those directions.

velocities and diffusion constants in the  $\rho_x$  and  $\rho_y$ -direction. In Figure 3.10 **a** we plot the dependence of the drift velocities. The separation between the particles is mainly in the  $\rho_x$ -direction. One of the two particles moves to smaller  $\rho_x$  values while the other particle moves towards larger  $\rho_x$  values. This indicates that the two particles were repelling each other. When the particles were at a mutual distance of about 11  $\mu\text{m}$  they seem to drift towards larger  $\rho_x$  values. This is probably due to some flow in the sample. Both particles move much less in the  $\rho_y$ -direction. The particles moved slightly towards larger  $\rho_y$  values as the experiment proceeded and the particles were brought closer to each other. In Figure 3.10 **b** the diffusion constants in both directions and for both particles were very similar. Figure 3.10 **c** depicts the forces in the  $\rho_x$  and  $\rho_y$ -direction as determined by application of equation 3.6. Clearly the particles repel each other.

As in section 3.3, it is also possible to directly calculate the forces between these two silica coated PS particles in CHB from the rate of change of the distance between the particles and the diffusion thereof. Results of this analysis are presented in Figure 3.4. Clearly part of the variation in the drift velocity of the individual particles in Figure 3.10 **a** represents a collective drift. We observe that even at the largest spacing measured, 14  $\mu\text{m}$  there was a significant repulsion between the two particles. As the distance between the two particles decreases, the interaction force between the two particles increases. When the spacing between

the particles was reduced to  $7\ \mu\text{m}$  the force had grown to about  $150\ \text{fN}$ . Attempts to bring the particles closer together resulted in loss a of the particles. The power of the trapping laser used was  $3\ \text{W}$  and could not be increased to increase the trapping forces without risking to damage the optics. The fact that the particles escaped is not only due to the finite power of the trapping laser, but also due to the fact that the trap was intermittently switched off to allow the force measurement. During this time, the particles moved on average  $200\ \text{nm}$ , see Figure 3.10 a. As a result, the particles had a good chance of ending up outside the range of interaction with the trap. We already increased the frame rate of the camera to  $200\ \text{fps}$  to minimize the times the particle was free to be pushed away. Increasing the frame rate further makes the error in the position detection relative to the displacements larger. Even for the detection of the larger forces this would be a problem as also the diffusion needs to be measured accurately.

Integration of the force between the two particles shows that there must be a potential energy difference of about  $150\ k_B T$  between the configuration where the particles are  $14$  and  $7\ \mu\text{m}$  apart. In the absence of the external forces exerted by the optical tweezers it is thus extremely unlikely that two particles be as close as  $7\ \mu\text{m}$  apart.

Clearly the screening length is very long such that linear superposition can be used to approximate the electrostatic interactions-[46]. We fit the spatial derivative of the Yukawa potential, the electrostatic part of the DLVO potential by Derjaguin, Landau, Verwey and Overbeek [2, 3] to the measured force as a function

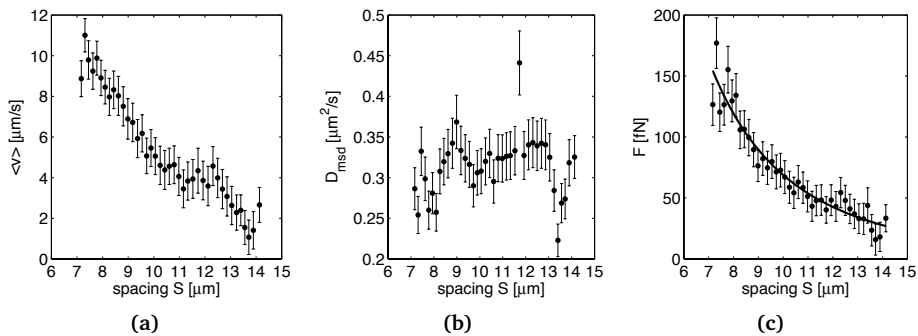


**Figure 3.11:** Interactions between two silica coated PS particles in CHB. **a.** Velocity  $v$  of the separation distance between two silica coated PS spheres in CHB as a function of the spacing between the particles. **b.** The diffusion constant as a function of the spacing between the particles. **c.** The force on the separation between the two particles from the drift velocities and the diffusion constants as a function of the spacing between the particles. The full line is a fit to equation 3.7.

of the particle spacing  $S$ ;

$$F(R) = \frac{\lambda_B k_B T Z^2}{(1 + \kappa\sigma/2)^2} \exp(-\kappa\sigma(S/\sigma - 1)) \frac{1 + \kappa S}{S^2}. \quad (3.7)$$

Again, the diameter of the particles is represented by  $\sigma$ ,  $\kappa$  is the inverse Debye screening length and  $\lambda_B$  is the Bjerrum length in the solvent. Fitting equation 3.7 to the measured interaction force in Figure c. The fit value for the screening length is  $9.72 \mu\text{m}$  which clearly the application of equation 3.7 rather than 3.2 or 3.3. Such long screening lengths in CHB have been reported before [44]. From the fit we find a charge on the particles of  $Z = 1140 e$ .

These measurements show that the analysis of local particle trajectories as proposed by Sainis *et al.* [23] can be combined with Digital Holographic Microscopy as presented in Chapter 2, to measure colloidal interactions also when the interactions are longer ranged than the largest spacing at which the force was measured.

### 3.5 Advantages of holographic tracking

As can be seen from the analysis of the trajectories in the  $z_h$ -direction of the silica particles in ethanol in section 3.3, holographic particle tracking can be applied to also measure forces on the colloids in the out of plane direction. This is not only relevant to measure the gravitational force on colloids but can also play an important role in the determination of the particle-particle interaction forces.

As can be read in Chapters 4, 5 and 6 on optical tweezers, optical traps tend to be less stiff in the axial direction than in the lateral directions. This results in the possibility that, during the measurement of the repulsive interaction between two colloids they push each other up and down in their respective traps. This is similar to the effect one experiences when trying to push two magnets together with similar poles facing each other. One then tends to displace the magnets perpendicularly.

This phenomenon carries the risk that the particle-particle spacing is underestimated when only considering the lateral coordinates of the particles to calculate the inter-particles spacing. Not only will this make the interaction between the particles appear less long-ranged, the component of the force in the axial direction is not measured such that the interaction forces are underestimated.

The interaction between silica particles in THF, a system we introduced in section 2.6.2, is dominated by electrostatic repulsion. As can be seen from Figure 3.12 a, the repulsion is sufficiently strong for the two particles to push each other up, respectively down in the trap. Again, the data was binned depending on the inter-particle spacing in bins containing 100 trajectories. Fitting equation 3.2 to the measured force in Figure 3.12 b results in a screening length of  $0.46 \mu\text{m}$  and a dimensionless potential of  $1.04 \pm 0.05$ , which corresponds to a surface potential of  $27 \pm 1 \text{ mV}$ . In the inset in Figure 3.12 b we plot the force as a

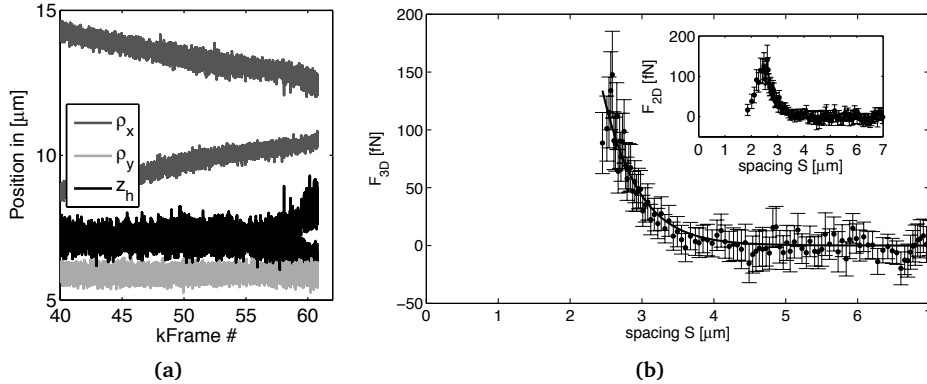


**Figure 3.12:** Interaction force between two silica spheres in THF. **a.** The trajectories of two 1.75 μm silica particles while they are moved together in two blinking optical traps. **b.** The interaction force between these two particles from 3D analysis of the trajectories after the particles have been released using equation 3.6. The full line is a fit to equation 3.2. The inset shows the interaction force that would have been measured if only the in-plane (2D) coordinates were considered.

function of the particle-particle spacing in the plane. As the particles get closer together, the distance between the particles is underestimated because the out-of-plane component is ignored. Because the distance between the particles is for a significant fraction oriented in the vertical direction, so is the force. In the inset we plot the in-plane force that is clearly different from the force in 3D. Not measuring this contribution to the inter-particle force gives rise to an apparent decrease in the interaction force as the particles approach each other.

From Figure 3.12, it is clear that both for the determination of the inter-particle spacing and for the determination of the particle-particle interaction, it was necessary to include the axial component of the spacing. The application of holographic tracking for force measurements can thus be useful.

### 3.6 A future experiment: electrophoresis

As was stated in section 3.3 and as can also be seen from Figure 3.10 one can apply equation 3.6 to the individual coordinates of colloids. One can use this to measure different forces as long as these forces act in mutually perpendicular directions. This was for instance applied in section 3.3 to measure the weight of the two silica particles in the axial direction while simultaneously measuring the interaction force between the two particles as a function of the distance between them, mainly in the ρ<sub>y</sub>-direction.

In this section, we show that it is also possible to combine the techniques presented in reference [23] to measure the inter-particle forces with electrophore-

sis. Being able to measure the interaction forces between the particles and the electrophoretic mobility of the particles in the same measurement allows one to compare the electrophoretic charge with the effective surface charge. Such comparisons also allow to determine whether the colloids carry a constant charge or a constant surface potential; as the distance between the colloids is varied such the double layer around them inter-penetrate. To measure the electrophoretic mobility, one needs to apply an external electric field to the dispersion and measure the electrophoretic mobility of the particles [60, 61]. The mobility under influence of an external electric field can be related to the particle charge. One has to be careful, as many factors play a role in the process of electrophoresis. For instance, one should consider the forces exerted on and the extra friction caused by the ions in the double layer around the particles [62]. Also hydrodynamic coupling and the volume fraction are important for the electrophoretic mobility [63–65]. A numerical calculation of the electrophoretic mobility of spherical colloidal particles at high concentrations for arbitrary  $\zeta$ -potentials that fully takes into account overlapping double layers was given by Carrique *et. al.* [49].

The counter-ions close to the charged sample walls move under influence of the electric field, this results in a plug flow of the liquid in the cell. This is called electro-osmosis. In a closed cell this results in a counter-flow with a Poiseuille profile [66]. The colloids, of which the mobility has to be determined, move with respect to this flow. In order to subtract the contribution of the flow to the particle velocity, one can measure the velocity profile as a function of the depth in the sample to determine at which depth the Poiseuille flow and the plug flow cancel each other. In this so-called zero velocity plane the solvent is stationary and the total particle movement can be ascribed to electrophoresis [66]. An alternative method to circumvent electro-osmosis is to apply an alternating current and to be sufficiently far away from the charge sample wall [29].

Apart from the effect of the volume fraction on the electrophoretic mobility [63–65], it is also conceivable that the charge itself is a function of the volume fraction. When the screening length is long, the concentration of ions around the particles changes considerably as they get closer to each other. In combination with charge regulation, this may result in a volume fraction dependence of the particle charge and thus also the stability of suspensions [67]. Merrill, Sainis and Dufresne used the analysis of local trajectories of normal modes of arrays of different numbers of colloids to show that the vicinity of the other particles reduces the strength of the interaction [68]. In other words, the interaction was shown to not be pairwise additive [69, 70].

Here, we show that it is possible to measure the charge of two colloids as a function of the distance to another particle. In order to do so we measured the interaction force between two charged colloids as we have shown above. The spacing  $S$  between the particles was mainly oriented in the  $\rho_y$ -direction. In the  $\rho_x$ -direction we applied an electric field. To reduce the effect of electro-osmosis, the electric field was switched on only when the optical traps were off. The electric

field is thus an alternating current with a block-wave shape. When the frequency of the electric field and the distance to the charged wall is large enough, the effect of electro-osmosis will be negligible [29].

We show the results of a preliminary experiment in which we measured both the interaction force and the electrophoretic mobility as a function of the spacing  $S$  between two colloids. The colloids, 1675 nm diameter PMMA particles, were dispersed in a density matching mixture of 50 weight percent CHC and 50 weight percent MethoxyPerFluoroButane, MPFB. This mixture has the same density as the PMMA particles,  $1.188 \text{ g/cm}^{-3}$ , but the refractive index is much lower than that of the particles,  $n_{\text{part}} = 1.49$ . With an Abbe refractometer (ATAGO 3T) the refractive index of the mixture was determined to be 1.3875 at  $21^\circ\text{C}$  for 530 nm light. As a result the particles can be trapped in this solvent using optical tweezers, see Chapter 4 and 5. The contrast between the refractive index of the particles and that of the solvent allows these particles to be tracked using Digital Holographic Microscopy, see also Chapter 2.

A glass capillary (Vitrocom  $0.1 \times 2.0 \text{ mm}$ ) was provided with two electric wires in the length direction and filled with a dilute (volume fraction  $< 10^{-6}$ ) dispersion of PMMA particles in CHC-MPFB. The sample was placed on our microscope and the distance between the two wires was determined to be 1.851 mm. Two particles were trapped in optical traps in the middle between the two wires at a depth of 14  $\mu\text{m}$ . The traps were intermittently switched off. When both traps were switched off, the sample was subject to 10 V. The traps were left off and the field was left on for 0.022 seconds during which the camera made 4 holographic snapshots at 200 fps. After this, the electric field was switched off and the optical tweezers were switched on to place the particles back at their initial configuration.

In Figure 3.13 a, we plot the trajectories of the two PMMA particles in CHC-MPFB as they are brought closer together. Similar to section 3.5, it is clear that the two particles repel each other quite strongly as the two particles push each other respectively up and down in the trap. A careful look at the trajectories in the  $\rho_y$ -direction gives the same hint as the trend is not entirely linear.

From the particle coordinates, we calculated the particle spacings  $S$ . For the individual particle trajectories we calculated the average spacing. The trajectories were then divided in bins containing 300 trajectories each. From the average drift and the mean squared displacements for these trajectories we measured the local force on the spacing between the particles using equation 3.6. In Figure 3.13 b we plot the forces in the spacing direction. The full line is a fit the equation 3.2 which assumes a constant surface potential. From this fit we find that the surface potential on the surface of the two  $1.42 \mu\text{m}$  PMMA particles in CHC-MPFB was 67.4 mV. The inverse Debye screening length was found to be  $0.85 \mu\text{m}$ .

In Figure 3.13 c we plot the forces on the Cartesian coordinates of both particles measured from the local trajectories using equation 3.6. Clearly the two particles repel each other in the two directions that contribute to the spacing between

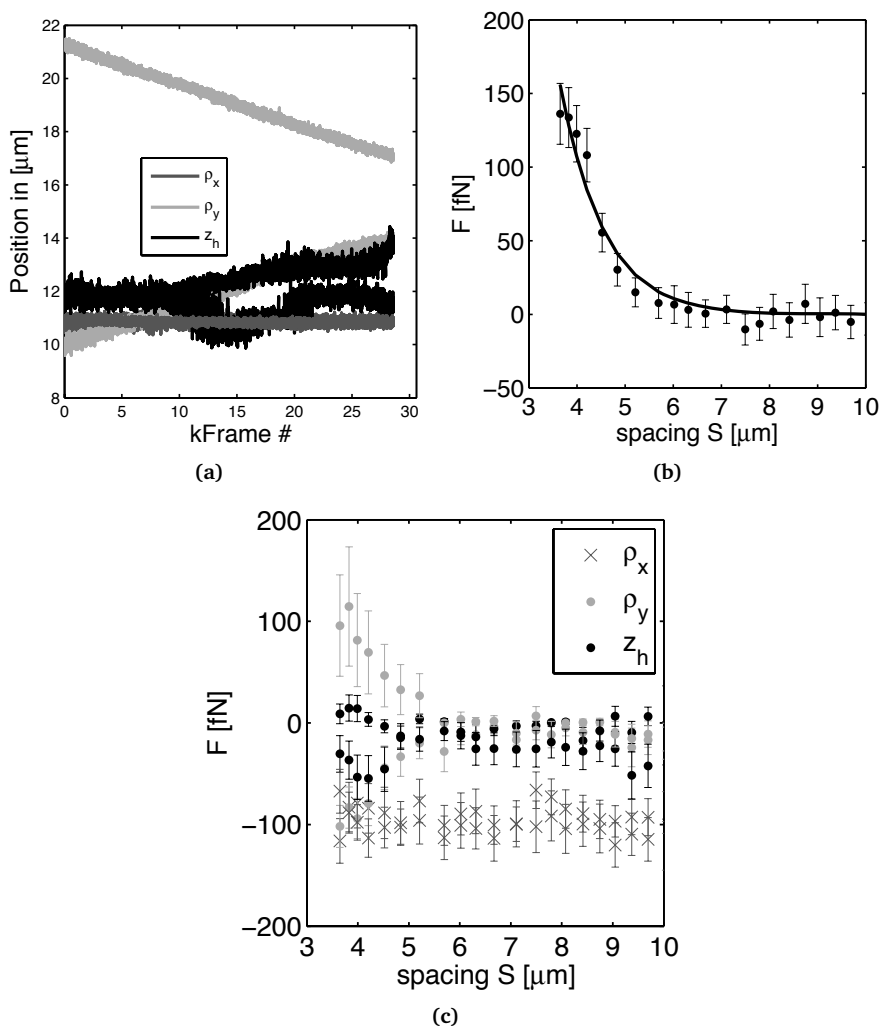


**Figure 3.13:** Interaction force between two PMMA particles in CHC-MPFB. **a.** The trajectories of two 1.675  $\mu\text{m}$  PMMA particles in a 50-50 weight percent mixture of CHC and MPFB as their traps are brought together. In the  $\rho_x$ -direction, the particles are subject to an electric field of 551 V/m. **b.** The force on the separation between the two particles. The full line is a fit to equation 3.2. **c.** The forces on the cartesian coordinates of the two particles.

the two particles, the  $\rho_y$ - and the  $z_h$ -direction. In the  $\rho_y$ -direction we observe that both particles experience a strong force in the same direction. This is the result of the external electric field that we apply in that direction. The electrophoretic force on the two particles seems to be constant over the inter-particle spacing

range tested. The force measurement corrects for the increase in the friction factor as the particles get closer as this is measured simultaneously. The particles are forced deeper into each others double layer. The locally increased ion concentration could shift the equilibrium that generates charge. Further research into this matter is needed.

The electrophoretic mobility of  $0.7 \text{ nm}^2/\text{Vs}$  is lower than what was found from electrophoretic measurements using the methods as described in the PhD thesis of Teun Vissers [31], conducted on the same sample on the same day:  $1.7 \text{ nm}^2/\text{Vs}$ . Further research is necessary to exclude the influence of electro-osmosis. Our measurements were conducted at  $14 \text{ }\mu\text{m}$  from the charged bottom of the sample and the frequency of the electric field was not slower than  $40 \text{ Hz}$ . This will certainly have reduced the effect of electro-osmosis, but the effect may have still contributed to the measured mobilities. Future research will have to point out to what extent the lower electrophoretic mobility from the simultaneous measurement of the particle-particle force can be ascribed to electro-osmosis.

In conclusion, we have shown that holographic tracking of colloids can be used in combination with optical tweezers and triggered electric fields to measure both the inter-particle interaction and the electrophoretic mobility in different directions. More work needs to be done to evaluate and further reduce the effect of electro-osmosis. Possibly these experiments can help to assess the relevance of the constant charge and the constant surface potential assumptions for the modeling of the interaction between colloids in different solvents.

### 3.7 Acknowledgement

We are grateful to Djamel El Masri, Frank Smalenburg, Teun Vissers for help with sample preparation, the Monte Carlo simulations and data analysis for the work presented in section 3.2. Michiel Hermes is thanked for performing Brownian dynamics simulations to learn how to optimize the statistics from a limited number of particle coordinates. René van Roij, Joost de Graaf and Marjolein Dijkstra are thanked for helpful discussions. Johan Stiefelhagen is thanked for particle synthesis and building the electrophoretic cells. Peter Lu is thanked for the automated acquisition software for the work on the PMMA particles in CHC. Jacob Hoogenboom is thanked for synthesis of the  $1.4 \text{ }\mu\text{m}$   $\text{SiO}_2$  particles. Gulşen Heessels-Gürboğa and Carlos van Kats are thanked for growing a silica layer around the PS particles in section 5.6.2. Peter Helfferich is thanked for technical support and creative solutions for the triggering and timing of the camera for the force measurements.

## Bibliography

- [1] Russel, W. B., Saville, D. A., and Schowalter, W. R. *Colloidal Dispersions*. Cambridge University Press, Cambridge (1989).
- [2] Derjaguin, B. and Landau, L. Theory of the stability of strongly charged lyophobic sols and of the adhesion of strongly charged particles in solutions of electrolytes. *Acta Physicochim. URSS* **14** 633 (1941).
- [3] Verwey, E. J. W. and Overbeek, J. T. G. *Theory of the Stability of Lyotropic Colloids*. Elsevier, Amsterdam (1948).
- [4] Hsu, J.-P. and Liu, B.-T. Stability of Colloidal Dispersions: Charge Regulation/Adsorption Model. *Langmuir* **15** 5219 (1999).
- [5] Behrens, S. H., Christl, D. I., Emmerzael, R., Schurtenberger, P., and Borkovec, M. Charging and Aggregation Properties of Carboxyl Latex Particles: Experiments versus DLVO Theory. *Langmuir* **16** 2566 (2000).
- [6] Lyklema, J. Principles of the stability of lyophobic colloidal dispersions in non-aqueous media. *Adv. Colloid Interface Sci.* **2** 65 (1968).
- [7] Morrison, I. D. Electrical Charges in Nonaqueous Media. *Colloids and Surfaces a-Physicochemical and Engineering Aspects* **71** 1 (1993).
- [8] Reinke, D., Stark, H., von Grünberg, H.-H., Schofield, A. B., Maret, G., and Gasser, U. Noncentral Forces in Crystals of Charged Colloids. *Phys. Rev. Lett.* 038301 (2007).
- [9] Prieve, D. C. Measurement of Colloidal Forces with TIRM. *Adv. Colloid Interface Sci.* **82** 93 (1999).
- [10] Calderon, F. L., Stora, T., Monval, O. M., Poulin, P., and Bibette, J. Direct measurement of Colloidal Forces. *Phys. Rev. Lett.* **72** 2959 (1994).
- [11] Li, D., Lam, C. N., and Biswal, S. L. Measuring short-range repulsive forces by imaging directed magnetic-particle assembly. *Soft Matter* **6** 239 (2010).
- [12] Vondermassen, K., Bongers, J., Mueller, A., and Versmold, H. Brownian Motion: A Tool To Determine the Pair Potential between Colloid Particles. *Langmuir* **10** 1351 (1994).
- [13] Carbajal-Tinoco, M. D., Castro-Román, F., and Arauz-Lara, J. L. Static properties of confined colloidal suspensions. *Phys. Rev. E.* **53** 3745 (1996).
- [14] Behrens, S. H. and Grier, D. G. The pair interaction of charged colloidal spheres near a charged wall. *Phys. Rev. E.* **64** 050401(R) (2001).
- [15] Royall, P. C., Leunissen, M. E., Hynninen, A., Dijkstra, M., and van Blaaderen, A. Re-entrant melting and freezing in a model system of charged colloids. *The Journal of Chemical Physics* **124** 244706 (2006).
- [16] Pedersen, J. S. Analysis of small-angle scattering data from colloids and polymer solutions: modeling and least-squares fitting. *Adv. in Coll. and Int. Sci.* **70** 171 (1997).
- [17] Hunter, R. J. *Foundations of colloid science / Robert J. Hunter*. Oxford University Press, Oxford ; New York : (2001). TY-BOOK 2nd ed.
- [18] Innerlohinger, J., Wyss, H. M., and Glatter, O. Colloidal Systems with Attractive Interactions: Evaluation of Scattering Data Using the Generalized Indirect Fourier Transformation Method. *J. Phys. Chem. B* 18149 (2004).
- [19] Fritz, G. and Glatter, O. Structure and interaction in dense colloidal systems: evaluation of scattering data by the generalized indirect Fourier transformation method. *J. Phys.: Condens. Matter* **18** (2006).

- [20] Ducker, W. A., Senden, T. J., and Pashley, R. M. Direct measurement of colloidal forces using an atomic force microscope. *Nature* **353** 239 (1991).
- [21] Crocker, J. C. and Grier, D. G. Microscopic Measurement of the Pair Interaction Potential of Charge-Stabilized Colloid. *Phys. Rev. Lett.* **73** 352 (1994).
- [22] Crocker, J. C., Matteo, J. A., Dinsmore, A. D., and Yodh, A. Entropic Attraction and Repulsion in Binary Colloids Probed with a Line Optical Tweezer. *Phys. Rev. Lett.* **82** 4352 (1999).
- [23] Sainis, S. K., Germain, V., and Dufresne, E. R. Statistics of Particle Trajectories at Short Time-Intervals Reveal Electrostatic Colloidal Interactions in Nonpolar Solvents. *Phys. Rev. Lett.* **95** 018303 (2007).
- [24] Polin, M., Roichman, Y., and Grier, D. G. Autocalibrated colloidal interaction measurements with extended optical traps. *Phys. Rev. E.* **77** 051401 (2008).
- [25] Mittal, M., Lele, P. P., Kaler, E. W., and Furst, E. M. Polarization and interactions of colloidal particles in ac electric fields. *The Journal of Chemical Physics* **129** 064513 (2008).
- [26] Masri, D. E., van Oostrum, P., Smalenburg, F., Vissers, T., Imhof, A., Dijkstra, M., and van Blaaderen, A. Measuring Colloidal Forces from Particle Position Deviations inside an Optical Trap. *Soft Matter*, DOI:10.1039/COSM01295E (2011).
- [27] Vanderhoeven, P. H. C. and Lyklema, J. Electrostatic Stabilization in Nonaqueous Media. *Advances in Colloid and Interface Science* **42** 205 (1992).
- [28] Hsu, M. F., Dufresne, E. R., and Weitz, D. A. Charge stabilization in nonpolar solvents. *Langmuir* **21** 4881 (2005).
- [29] Roberts, G. S., Wood, A. T., Frith, W. J., and Bartlett, P. Direct measurement of the effective charge in nonpolar suspensions by optical tracking of single particles. *The Journal of Chemical Physics* **126** 194503 (2007).
- [30] Strubbe, F., Beunis, F., and Neyts, K. Detection of Elementary Charges on Colloidal Particles. *Phys. Rev. Lett.* **100** 218301 (2008).
- [31] Vissers, T. Oppositely Charged Colloids Out of Equilibrium. PhD Thesis, Utrecht University (2010).
- [32] Vissers, T. and *et al.* Electrophoresis on Concentrated Colloidal Suspensions in Low-polar Solvents. *in preparation* (2011).
- [33] Vossen, D. L. J., van der Horst, A., Dogterom, M., and van Blaaderen, A. Optical tweezers and confocal microscopy for simultaneous three-dimensional manipulation and imaging in concentrated colloidal dispersions. *Rev. Sci. Instrum.* **75** 2960 (2004).
- [34] Lu, P. J., Sims, P. A., Oki, H., Macarthur, J. B., and A. Weitz, D. Target-locking acquisition with real-time confocal (TARC) microscopy. *Opt. Express* **15** 8702 (2007).
- [35] Bosma, G., Pathmamanoharan, C., Hoog, E. H. A. D., W. Kegel, Blaaderen, A. V., , and Lekkerkerker, H. N. W. Preparation of monodisperse, fluorescent pmma-latex colloids by dispersion polymerization. *J. Coll. Int. Sci.* **54** 292 (2002).
- [36] Crocker, J. C. and Grier, D. G. Methods of Digital Video Microscopy for Colloidal Studies. *J. of Col. and Int. Sci.* **179** 289 (1996).
- [37] Neves, A. A. R., Fontes, A., de Y. Pozzo, L., de Thomaz, A. A., Rodriguez, E. C. E., Barbosa, L. C., and Cesar, C. L. Electromagnetic forces for an arbitrary optical trapping of a spherical dielectric. *Opt. Exp.* **14** 13101 (2006).
- [38] Richardson, A. C., Reihani, S. N. S., and Oddershede, L. B. Non-harmonic potential of a single beam optical trap. *Opt. Exp.* **16** 15709 (2008).

- [39] Mazolli, A., Neto, P. A. M., and Nussenzveig, H. M. Theory of trapping forces in optical tweezers. *Proceedings of the Royal Society of London A* **459** 3021 (2003).
- [40] Viana, N. B., Rocha, M. S., Mesquita, O. N., Mazolli, A., Neto, P. A. M., and Nussenzveig, H. M. Towards absolute calibration of optical tweezers. *Phys. Rev. E* **75** 021914 (2007).
- [41] van der Horst, A., van Oostrum, P., Moroz, A., van Blaaderen, A., and Dogterom, M. High trapping forces for high-refractive index particles trapped in dynamic arrays of counterpropagating optical tweezers. *Appl. Opt.* **47** 3196 (2008).
- [42] van Oostrum, P. D., van der Horst, A., and van Blaaderen, A. Mutual influence of time-shared optical traps studied by means of Video Holographic Microscopy. *Digital Holography and Three-Dimensional Imaging, OSA Technical Digest (CD) (Optical Society of America) DWD7* (2009).
- [43] Burns, M. M., Fournier, J.-M., and Golovchenko, J. A. Optical Binding. *Phys. Rev. Lett.* **63** 1233 (1989).
- [44] Leunissen, M. Manipulating Colloids with Charges & Electric Fields. PhD Thesis, Utrecht University (2007).
- [45] Vulina, O. S. and Khrapak, S. A. Simulation of the dynamics of strongly interacting microparticles in a weakly ionized plasma. *J. of Exp. and Theo. Phys.* **90** 287 (2000).
- [46] Carnie, S. L. and Chan, D. Y. C. Interaction Free Energy between Identical Spherical Colloidal Particles: The Linearized Poisson-Boltzmann Theory. *J. Coll. Intf. sci.* **155** 297 (1992).
- [47] Walden, P. Über organische Lösungs- und Ionisierungsmittel. III. Teil: Innere Reibung und deren Zusammenhang mit dem Leitvermögen. *Z. Phys. Chem* **55** 129 (1906).
- [48] Fuoss, R. Ionic Association III. The equilibrium between ion pairs and free ions. *J. Am. Chem. Soc.* **80** 5059 (1958).
- [49] Carrique, F., Arroyo, F. J., and Delgado, A. V. Electrokinetics of concentrated suspensions of spherical colloidal particles with surface conductance, arbitrary zeta potential, and double-layer thickness in static electric fields. *Journal of Colloid and Interface Science* **252** 126 (2002).
- [50] Loeb, A. L., Wiersema, P. H., and Overbeek, J. T. G. The Electrical Double Layer Around a Spherical Colloid Particle. MIT Press, Cambridge, MA (1961).
- [51] Prieve, D. C., Lanni, F., and Luo, F. Brownian Motion of a Hydrosol Particle in a Colloidal Force Field. *Faraday Discuss. Chem. Soc.* **83** 297 (1987).
- [52] Biancaniello, P. L. and Crocker, J. C. Line optical tweezers instrument for measuring nanoscale interactions and kinetics. *Rev. Sci. Instrum.* **77** 113702 (2006).
- [53] Lee, S.-H., Roichman, Y., Yi, G.-R., Kim, S.-H., Yang, S.-M., van Blaaderen, A., van Oostrum, P., and Grier, D. G. Characterizing and tracking single colloidal particles with video holographic microscopy. *Opt. Exp.* **15** 18275 (2007).
- [54] Baumgartl, J. and Bechinger, C. On the limits of digital video microscopy. *Europhys. Lett.* **71** 487 (2005).
- [55] Savin, T. and Doyle, P. S. Role of finite exposure time on measuring an elastic modulus using microrheology. *Phys. Rev. E* **71** 041106 (2005).
- [56] Batchelor, G. K. Brownian diffusion of particles with hydrodynamic interaction. *J. Fluid Mech.* **74** 1 (1976).
- [57] O'Brien, R. and White, L. Electrophoretic Mobility of a Spherical Colloidal Particle. *J. Chem. Soc. Faraday II* **74** 1607 (1978).

- [58] Volpe, G., Helden, L., Brettschneider, T., Wehr, J., and Bechinger, C. Influence of Noise on Force Measurements. *Phys. Rev. Lett.* **104** 170602 (2010).
- [59] Kosmulskis, M. and Matijević, E.  $\zeta$ -Potentials of Silica in Water-Alcohol Mixtures. *Langmuir* **8** 1060 (1992).
- [60] Yang, C., Dabros, T., Li, D. Q., Czarnecki, J., and Masliyah, J. H. Measurement of the zeta potential of gas bubbles in aqueous solutions by microelectrophoresis method. *Journal of Colloid and Interface Science* **243** 128 (2001).
- [61] Yan, D. G., Yang, C., Nguyen, N. T., and Huang, X. Y. A method for simultaneously determining the zeta potentials of the channel surface and the tracer particles using microparticle image velocimetry technique. *Electrophoresis* **27** 620 (2006).
- [62] Dukhin, S. S. and Deryaguin, B. V. *Surface and Colloid Science*, volume 7. John Wiley, New York (1974).
- [63] Long, D. and Ajdari, A. A note on the screening of hydrodynamic interactions, in electrophoresis, and in porous media. *European Physical Journal E* **4** 29 (2001).
- [64] Anderson, J. L. Concentration-Dependence of Electrophoretic Mobility. *Journal of Colloid and Interface Science* **82** 248 (1981).
- [65] Zukoski, C. F. and Saville, D. A. Electrokinetic Properties of Particles in Concentrated Suspensions. *Journal of Colloid and Interface Science* **115** 422 (1987).
- [66] Pelton, R., Miller, P., McPhee, W., and Rajaram, S. Strategies for Improving Electrophoresis Data from the Coulter Delsa. *Colloids and Surfaces a-Physicochemical and Engineering Aspects* **80** 181 (1993).
- [67] Albers, W. and Overbeek, J. T. G. Stability of emulsions of water in oil : I. The correlation between electrokinetic potential and stability. *Journal of Colloid Science* **14** 501 (1959).
- [68] Merrill, J. W., Sainis, S. K., and Dufresne, E. R. Many-Body Electrostatic Forces between Colloidal Particles at Vanishing Ionic Strength. *Phys. Rev. Lett.* **103** 138301 (2009).
- [69] Rojas-Ochoa, L. F., neda Priego, R. C., Lobaskin, V., Stradner, A., Scheffold, F., and Schurtenberger, P. Density Dependent Interactions and Structure of Charged Colloidal Dispersions in the Weak Screening Regime. *Phys. Rev. Lett.* **100** 178304 (2008).
- [70] Brunner, M., Bechinger, C., Strepp, W., Lobaskin, V., and von Grünberg, H.-H. Density-dependent pair interactions in 2D. *Europhys. Lett.* **58** 926 (2002).



# 4

## Introduction to optical tweezers

---

In this Chapter we introduce optical tweezers by giving an overview of the literature on optical tweezers. First, we introduce the various applications that optical traps have found in many active fields of research. Subsequently, we discuss the underlying physics and the various techniques to characterize optical traps and the different approaches to realize optical traps. We proceed with a more detailed discussion about the trapping forces and the various theories used to calculate them. Finally, we discuss non-conservative forces, temporal effects and optical binding.

## 4.1 Introduction

The first noted observation of forces exerted by light may be the observation of Johannes Kepler in 1619 that the tail ‘behind’ a comet always points away from the sun. This is due to the radiation pressure of the light from the sun that pushes away the dust in the tail. Later, in the end of the sixties and beginning of the seventies of the last century Arthur Ashkin reported the first experiments in the lab in which optical forces were playing an important role [1, 2]. He observed that particles were pulled towards the optical axis of a mildly focussed laser beam and were then propelled along the optical axis. By carefully balancing the forces exerted by the laser light and by gravity, he managed to levitate particles in water [1]. He also managed to create a stable three dimensional trap based on counter propagating beams [2]. He coined the term ‘optical tweezers’ in 1986, in an article in which the first single beam optical trap was demonstrated by using a high numerical aperture, NA, objective to focus the light [3].

In this Chapter we will first, in section 4.2, give a brief overview of the applications of optical tweezers in various fields. In section 4.3, we shortly address the working principle of optical tweezers. An optical trap is usually characterized by a trapping stiffness. In section 4.4, we introduce some commonly used techniques to measure the trapping stiffness. Subsequently, in section 4.5, we briefly introduce the most common designs of optical tweezers.

We proceed with a more detailed analysis of the physics behind optical tweezers in section 4.6. For clarity, we make a distinction based on particle size. First, we treat the trapping of particles, smaller than the wavelength of the light used to trap the particles, so-called Rayleigh scatterers, in section 4.6.1. Then we proceed with a short treatment of the trapping behavior of particles that are much larger than the wavelength, for which we can apply ray-optics in section 4.6.2. Finally, we discuss the most interesting and most complicated size regime: when the particles are comparable in size to the wavelength of the light, the simplifications of the Rayleigh-regime, where the particles can be treated as point-scatters, and those of the ray-optics regime, in which the light is modeled as rays, cannot be justified. Interaction of the light with one side of the particle cannot be understood without considering the effect of the other side of the particle. This so-called Lorenz-Mie regime is treated in section 4.6.3, in which we also introduce a number of theoretical models to calculate the trapping forces. One of these models will be used extensively in Chapters 5 and 6.

The Chapter is finalized with section 4.7 about other effects that (can) play a role in optical trapping. First, we discuss the phenomenon of spherical aberration in section 4.7.1. The forces exerted by optical tweezers are not always conservative. That means that the force field cannot generally be integrated to obtain a potential energy landscape. Depending on the trajectory followed to go from point A to point B, the work performed by the light field on the particle can be different. These non-conservative forces are discussed in section 4.7.2. Next

we discuss so-called *temporal effects* in section 4.7.3. In this section we treat the discussions in literature about the alleged effect of trapping with pulsed lasers instead of with continuous lasers. We also address the discussion about parametric excitation. Finally, in section 4.7.4, we discuss the effect of *optical binding*, where an interaction force between two trapped particles is reported.

## 4.2 Some applications of optical tweezers

Since the first paper in which dielectric particles have been trapped, Ashkin and co-workers have demonstrated their applicability in various fields like cooling atoms [4] and trapping live bacteria and viruses [5, 6]. The interface that optical tweezers form between human scales and microscopic scales, with the ability to apply and measure pico Newton forces and enforce nm displacements have made them an excellent tool in many different types of research. One of the first works in which optical tweezers featured as force transducers in biology dates from 1990 when optical tweezers were used to follow kinesin moving along a single microtubule-track [7]. Since then, optical tweezers have been applied to measure the forces exerted by single molecular motors in many articles [8–12] and to measure the mechanical properties of (bio-)polymers [13, 14]. Another fascinating application of optical tweezers is found in an experiment in which was studied how cells are deformed and stretched to make distinction between healthy cells and cancerous cells [15].

Techniques based on Quadrant Photo-Diodes, QPD's, to track a particle at a high temporal resolution, developed to characterize optical traps, have successfully been applied to measure rheological properties in a field called  $\mu$ rheology [16, 17]. These experiments have also found applications in biomedical science [18]. The detection of the power spectrum of trapped micro-spheres has undergone several improvements [19, 20]. To measure the rheological properties of liquids with a low elasticity, there are even setups that apply blinking traps to vary the elasticity of the trap to provide for sufficient sensitivity in the measurements without losing the particle from the trap [17].

Also in the field of colloids, do optical tweezers find ample application [21–29]. They can for instance be used to pattern a substrate with colloids to study epitaxial growth of colloidal crystals [30]. Optical tweezers allow the measurement of the pair potential between two colloidal particles. This can be done by creating a line-shaped trap in which two particles are confined as were they on a one dimensional set of rails. Looking at the probability density function of distances that occur between particles, one can then obtain the pair potential by applying the Boltzmann distribution [31]. It is also possible to use two optical traps to position two particles at an improbable distance [29] and study the displacements in the trap, see Chapter 3. Alternatively it is possible to let the particles loose at a particular distance and to study the statistics of where they go next [28, 32–34]. See also Chapter 3. The interpretation of the trajectories the particles follow can

differ but the key ingredient to these techniques is the use of optical tweezers to bring colloidal particles in improbable positions. Doing this, one has to be careful with the interpretation of the results as hydrodynamic effects may be a source of errors in the measurement of the interaction forces [35–37].

### 4.3 How optical tweezers work

Generally speaking, each photon carries a certain amount of energy  $\frac{hc}{\lambda}$  and an amount of momentum  $\frac{h}{\lambda}$ , where  $\lambda$  is the wavelength of the light in the medium,  $c$  the speed of light in vacuum, and  $h$  is Planck's constant. When light interacts with matter it can be absorbed, refracted or reflected. Each of these interactions has an effect on the energy and momentum of the photon. If the photon is absorbed, it transfers all its energy and momentum to the object that absorbs it. The object will warm up a little by absorption of the photon's energy and it will also absorb the momentum of the photon. For total absorption of a light beam of power  $P$  the force  $F$  on the absorber is equal to

$$F = \frac{n_m P}{c} \left[ \frac{\text{Nms}^{-1}}{\text{ms}^{-1}} \right] \quad (4.1)$$

where  $n_m$  is the refractive index of the surrounding medium. If light is reflected, the photon maintains its energy but its direction of propagation changes sign and as a result its momentum also changes. Due to momentum transfer, a force is exerted on the object that reflects. Similarly, the momentum of the photon changes when it is refracted, i.e. when its direction of propagation is changed by interaction with an interface. If we study the exertion of forces with light, for instance to trap them in optical tweezers, we often use the dimensionless efficiency factor  $Q$  on the particle. This gives the fraction of the force that would be exerted if the light were fully absorbed [38]:

$$F = \frac{QPn_m}{c}. \quad (4.2)$$

Common values of  $Q$  are a few hundredths to at maximum about 0.25 [39].

Often, a distinction is made between a so-called 'scattering' force and a so-called 'gradient' force. For isotropic- or Rayleigh-scatterers, the momentum of the scattered photons is redistributed homogeneously, such that the time-averaged momentum transfer on the particle is equal in all directions and cancels itself. As a result, the effective force on the particle is equal to the rate of momentum transfer from the photons that are redistributed in the scattering process and points in the direction of propagation of the beam. This is called the *scattering force*,  $F_{\text{scat}}$ . When the particle is located in an intensity gradient it will scatter somewhat more photons in one direction than in the other. A resulting non-zero force appears in the direction of the intensity gradient: the *gradient force*,  $F_{\text{grad}}$ .

This force can also be regarded as the time-averaged Lorentz force. Depending on the sign of the refractive index contrast between the particle and the surrounding medium, the gradient force can point either towards the higher or towards the lower intensity. Depending on the relative magnitude of the particle with respect to the wavelength of the light, this picture is either correct for small particles or only formally correct though somewhat oversimplified for the situation for large particles. For particles larger than the wavelength of the light, the distinction between  $F_{\text{scat}}$  and  $F_{\text{grad}}$  can still formally be made although it is no longer as clear from the equations describing the forces. In any case, the distinction between the scattering and the gradient force is intuitive and instructive.

We can divide the light scattering and thus the trapping in three regimes, depending on the size of the particle. The smallest particles, where  $r$ , the radius of the particle is much smaller than the wavelength of the light ( $\lambda \ll r/20$ ) we speak of a *Rayleigh* scatterer. In this regime, the particle can be regarded as a point-dipole. The other extreme, where the particle is much larger than the wavelength of the light, ( $r \gg \lambda$ ) is called the *ray-optics* regime. Here we can simply apply ray-optics to study the interaction between the object and the light. One can for instance apply Snell's law to determine the refraction of the light at the interface of the particle. The momentum flows associated with these light rays can be used to model the trapping forces exerted on these large particles [3].

In the intermediate regime where  $r \sim \lambda$ , the situation is more complicated. The particle is so large that the electric field can no longer be considered homogeneous throughout the particle as in the Rayleigh-regime. Simultaneously the particle is so small that we cannot study the interaction of the light with one of the faces of the particle without considering the influence of the other side of the particle. This is the regime in which the simple pictures of point dipoles or rays of light are oversimplifications and Maxwell's equations or the vector Helmholtz-equation, need to be solved to determine what the interaction between the light and the particle will be. This regime is referred to as the *Lorenz-Mie* regime and here modeling the interaction with light is more complicated. It is also the size regime that is of most interest since most particles that are used in experiments fall well within this regime.

## 4.4 Characterizing optical traps

Usually, optical traps are assumed to be modeled successfully by a harmonic potential where the force on the trapped particle is linear in the displacement from the trapping position. In other words, the optical trap is modeled as a Hookian spring.

$$F_{\text{spring}} = -\kappa x. \quad (4.3)$$

Here  $F$  is the force needed to displace the particle a distance  $x$  from its equilibrium position. The constant  $\kappa$  between the force and the displacement is generally

referred to as the *stiffness* of the trap. Often, the stiffness is not the same in all directions. Particularly in the axial direction, the stiffness tends to be much smaller than in the axial directions due to the finite NA of the objectives used and the fact that the destabilizing scattering force points in the direction of propagation of the light. Moreover, spherical aberration, see also section 4.7.1, that is often present in experiments, makes the trap in the axial direction less stiff. For the in-plane directions, there are sometimes small differences in the trapping forces along with and perpendicular to the polarization of the light [40]. Since the particles that are generally trapped in experiments are a few hundred nm to a few  $\mu\text{m}$  in size, and dispersed in a solvent, these particles undergo Brownian motion. Equation 4.3 should therefore be applied on time averaged values for the displacement.

If a particle is trapped while we have the possibility to track the particle it is possible to calibrate the trap. Techniques that can be used to track optically trapped particles are for instance given by Quadrant Photo Diode, QPD, [16, 17], bright field microscopy [41], confocal microscopy [42, 43] or Digital Holographic Microscopy [44], see also Chapter 2. Once the stiffness of the trap is known, it can be used to measure other forces by multiplying the measured displacement that resulted from the applied force [29].

The most intuitive method to measure the trap stiffness is to apply a known force to the particle and measure the displacement of the particle from its equilibrium position. The most widely applied force to measure the trap stiffness is using the so-called Stokes friction [45], to provide a known force to calibrate the trap with. Here the particle is dragged through the medium, or the medium is made to flow along the trapped particle at a known speed. When the viscosity of the medium and the radius of the particle are both known, the drag or Stokes friction on the particle is:

$$F_{\text{Stokes}} = 6\pi\eta rv = \gamma v, \quad (4.4)$$

where  $\eta$  is the viscosity of the fluid,  $r$  the radius of the particle,  $v$  the particle velocity and  $\gamma$  the friction factor. When applying this *drag force method*, one has to be careful to be far enough from the wall to eliminate an increase in the effective friction factor [45]. A particle experiences a larger friction due to so-called lubrication effects. In the case of a nearby wall, Faxen's law can be applied to include the effect of the nearby wall due to lubrication effects. In those cases Faxen's law should be used to calculate the friction factor [46]. This way of calibrating the trap depends strongly on the particle radius and the temperature through the strong temperature dependence of the viscosity. All in all this method yields the trap stiffness with an error of about 21% [47].

The consequence of equation 4.3 is that the potential energy associated with a certain displacement  $x$  has the form:

$$E = \frac{1}{2}\kappa x^2. \quad (4.5)$$

Other methods to measure the trap stiffness are based on the (harmonic) potential energy associated with the trap. Due to Brownian motion, the particle is sampling

the trapping potential. The simplest method to deduce the trapping stiffness from a sequence of particle positions is to relate the mean squared displacement  $\langle x^2 \rangle$  to the thermal energy as prescribed by the equipartition theorem. This yields the simple equation:

$$\kappa = \frac{k_B T}{2\langle x^2 \rangle}. \quad (4.6)$$

For this method to be reliable, it is necessary to have the position detection calibrated. One has to be careful applying this method as it assumes that all of the standard deviation in the particle position is physical rather than the result of measurement noise.

A more sophisticated method to characterize the trapping potential makes use of the Boltzmann distribution. This equation relates the probability that a parameter in thermal equilibrium reached a certain value, to the potential energy associated with this value of the parameter:

$$P = C e^{-\frac{E(x)}{k_B T}}. \quad (4.7)$$

Here,  $C$  is a normalization constant to make sure that the total probability of finding the parameter at some value is unity. Florin *et al.* [47], measured the potential landscape of an optical trap by determining the probability of finding the particle in a certain bin. They simply used a Quadrant Photo Diode, which they calibrated later with the same particle after it had been stuck on a glass plate, to record 250,000 positions. From the probability distribution, the trapping potential was determined using equation 4.7. To this energy landscape, a harmonic potential (equation 4.5) was fitted to determine the trap stiffness. The advantage of this technique is that only the temperature  $T$  needs to be known. The disadvantage is that the position detection needs to be calibrated. Both in Chapter 5 and 6, we apply this method to characterize our optical traps from a collection of holographically measured particle positions [44].

Yet another set of techniques to measure the trapping stiffness is based on dynamics. The displacement of an over-damped Brownian particle in a harmonic potential well shows a Lorentzian power spectrum with a corner frequency  $\omega_C = \frac{\kappa}{\gamma}$  [48], where  $\gamma$  is the drag coefficient. A qualitative understanding of the corner frequency is that the optical trap impedes all Brownian motion that takes place at shorter timescales [49]. Movements that are faster than the timescale associated with the corner frequency still occur and a stiffer trap impedes more motion, so it has a higher corner frequency. When the displacement, or a signal that is linear in the displacement (such as the voltage over a Quadrant Photo Diode) is recorded at a sufficiently high sample frequency, one can determine the corner frequency, and thus the stiffness of the trap. The Lorentzian power spectrum is given by [50]:

$$S_{xx} = \frac{k_B T}{\pi^2 \gamma (\omega_C + \omega)}, \quad (4.8)$$

where  $\omega_C$  is the corner frequency. Equation 4.8 can then be fitted to its experimental counterpart to determine the corner frequency. To get the trapping stiffness from the corner frequency it is required to also know the drag coefficient, and thus the particle diameter, the liquid viscosity and the distance to the wall. The advantage is that the Quadrant Photo Diode does not need to be calibrated. In section 6.2, we use a Quadrant Photo Diode, and the fitting of a Lorentzian power spectrum to measure the trapping stiffness of high refractive index titania particles trapped in counter propagating tweezers [51].

Wong *et al.* [20] showed that the sample frequency of the measurement equipment can be effectively ten folded using intensity modulation spectral analysis, allowing for the measurement of the trap stiffness from the corner frequency using video rate position detection.

An other method that uses the dynamics to measure the trap stiffness and that can be applied to data taken at video rates, makes use of the one-dimensional Langevin equation for the motion of a Brownian particle in a harmonic potential well:

$$\dot{x}(t) = -\frac{x(t)}{\tau} + \xi(t). \quad (4.9)$$

Here, the autocorrelation time  $\tau = \frac{\gamma}{\kappa}$  is the period associated with the corner frequency discussed above. The Brownian motion is described by the Gaussian random noise  $\xi(t)$ . If the particle position is determined at  $t = 0$  and at  $t = \Delta t$  the two positions are related by:

$$x(\Delta t) = e^{-\frac{\Delta t}{\tau}} x(0) + \alpha(\Delta t), \quad (4.10)$$

where  $\alpha(\Delta t)$  is a Gaussian random variable with mean zero and variance  $\frac{k_B T}{\kappa} (1 - e^{-\frac{\Delta t}{\tau}})$ . In 2005 Marco Polin *et al.* published a method [52] to extract the trapping stiffness  $\kappa$  and the friction factor  $\gamma$  from a particles trajectory by fitting the inverted equation 4.10 to the measured trajectory. This analysis also yields an error estimate. This method has the advantage that as input one only needs a particle trajectory. Using the information provided by the sequence of the positions as well as the Langevin equation, both the trap stiffness and the friction factor can be measured. Moreover, the analysis works best if the time steps in the trajectory are about as long as the autocorrelation time  $\tau$ . This is much slower than the several kHz needed for spectral analysis, usually video rates are fast enough. Accurate tracking is more important than speed because the stiffness and the friction factor are determined from correlations between consecutive particle positions rather than from the characteristic timescales. Bright field microscopy [41] or Digital Holographic Microscopy [44] provide sufficient accuracy and allow the trap characterization to be simultaneously applied to multiple trapped particles [52]. Also this method is applied in Chapters 5 and 6 to measure trap stiffnesses.

## 4.5 Basic experimental designs

To be able to trap a particle, one needs a tight focus, preferably diffraction limited. In principle, light from any light source can be used, but to make a diffraction limited focus one needs a pure parallel beam. The simplest optical tweezers consist of a Gaussian laser beam, focussed at some point in the sample using a high numerical aperture microscope objective [3]. There are various ways of making more systems of traps.

First of all it is possible to make two traps, or even a line of light in the sample using a rapidly moving mirror [32]. Alternatively, an *Acousto-Optical Deflector*, AOD, can be used to create two or more traps by time-sharing [53–55]. The basic idea behind time-sharing is to simply shine the beam intermittently on different locations. This should be done at a frequency high enough to not have the particles diffuse away in the time that other particles are trapped elsewhere. In this way, hundreds of particles can be manipulated simultaneously [55]. In sections 4.7.3 and 5.4.2, more details are provided on the effect of a temporally varied laser intensity on the trapping behavior. Most of the experiments with multiple traps in this thesis have been performed by time-sharing the trap. In some cases, multiple traps were created simultaneously by providing a combined signal consisting of multiple frequencies to the AODs. The setup that was used for the experiments in this thesis uses AODs to control the optical traps and allows for the trapping of particles counter-propagatingly while simultaneously allowing the application of confocal- and brightfield-microscopy is described in reference [55]. After minor adjustments also in-line holographic microscopy [44] could be performed on the setup.

A different way of making traps is provided by holographic traps. Here, the phase-distribution and/or the intensity-distribution in a plane conjugate to that of the back aperture is altered such that the light in the sample interferes to form the desired intensity distribution. One has to manipulate the wavefront that enters the objective in such a way that it is the Fourier transform of the desired light distribution in the trapping plane. This can be done with a permanent diffractive optical element, DOE, or with computer addressed liquid crystal displays [52, 56–60] that either address the phase or the intensity of the light, or both.

For some particles in combination with some objectives, the scattering force is always larger than the gradient force. This happens for instance for particles with a high refractive index, depending on the NA of the objective used, typically particles with an index of refraction higher than 1.2 times that of the surrounding medium. Also particles made of absorbing materials such as metals, experience a scattering force that is too large to allow optical trapping in a single beam trap. A method to trap these particles is using counter-propagating tweezers by squeezing the sample between two objectives such that the particle is trapped in two traps that cancel their respective scattering forces, leaving only the gradient forces to trap the particle [2, 51, 55]. Often one needs a minimum numerical

aperture lens to trap a specific particle. Using counter-propagating traps, one can trap particles with two objectives of a lower NA. There are also examples of counter-propagating traps using spatial light modulators to manipulate the light distribution [61].

## 4.6 Size regimes

In this section we explain the mechanism of the trapping in optical tweezers in more detail. As discussed above we can divide the trapping in three regimes depending on the size of the particle relative to the wavelength of the light. First, we treat the trapping of particles that are smaller than the wavelength of the light, so-called Rayleigh scatterers, in section 4.6.1. Then we proceed with a short discussion of the trapping behavior of particles that are much larger than the wavelength, for which we can apply ray-optics in section 4.6.2. Finally we discuss the most interesting and most complicated size regime. When the particles are comparable in size to the wavelength of the light, the simplifications of the Rayleigh-regime, where the particles can be treated as point scatterers, and those of the ray-optics-regime, in which the light is modeled as rays, cannot be justified. Interaction of the light with one side of the particle cannot be understood without considering the effect of the other side of the particle. This so-called Lorenz-Mie regime is discussed in section 4.6.3, in which we also introduce a number of theoretical models to calculate the trapping forces.

### 4.6.1 The Rayleigh regime

In the Rayleigh regime, as stated above, the particle is much smaller than the wavelength of the light. Therefore, the particle will be polarized homogeneously by the incident light and will then interact with the light field that induced it. In this regime, the particle can also be regarded as a point dipole: the induced dipole, that minimizes its energy in the light field [62]. The particle is polarized through interaction with some of the photons of the trapping light, the momentum of which contributes to the scattering force. In the Rayleigh regime the scattering force is given by:

$$F_{\text{scat}} = I_0 \frac{\sigma_{\text{scat}} n_m}{c}, \quad (4.11)$$

where  $I_0$  is the intensity of the light and  $c$  the speed of light in vacuum. The scattering cross-section  $\sigma_{\text{scat}}$  of the sphere is a measure of the amount of light the particle interacts with:

$$\sigma_{\text{scat}} = \frac{128\pi^5 r^6}{3\lambda^4} \left( \frac{m^2 - 1}{m^2 + 2} \right)^2, \quad (4.12)$$

where  $r$  is the particle radius,  $m$  is the ratio between the refractive index of the particle and that of the medium ( $m = n_p/n_m$ ). The resulting point dipole will

radiate the associated energy out like a point scatterer. As this is done in an isotropic manner, there are no net forces associated with this radiative process. Under homogeneous illumination the particle therefore experiences only the scattering force described by equation 4.11.

However, if the point dipole is located in an intensity gradient it will experience a time-averaged Lorentz force, or gradient force:

$$F_{\text{grad}} = 2 \frac{\pi \alpha}{c_m} \nabla I_0 \quad (4.13)$$

where  $\alpha$  is the particle's polarizability,  $\alpha = n_m^2 a^3 \frac{m^2 - 1}{m^2 + 2}$ . Note that although the scattering force always points in the direction of propagation of the light, the gradient force can point either up or down the gradient depending on the sign of  $\alpha$ , i.e. on whether the refractive index of the particle is larger or smaller than the refractive index of the medium. A particle can be stably trapped if the scattering force and gradient force cancel one another at a certain point in space [3]. Suppose we have a diffraction limited focus and a Rayleigh particle with an index of refraction slightly above that of the medium. Then the gradient force will pull the particle towards the optical axis, where the intensity is maximum. On the optical axis, the particle will be pushed along the optical axis by  $F_{\text{scat}}$ , in the direction of the propagation of the light. Just beyond the focus there will be an intensity gradient which will result in a gradient force back to the focus. If there is a point where the gradient force is equal in magnitude (but in the opposite direction) to the scattering force these two forces will cancel and the particle is trapped. Obviously the particle will in practice only be stably trapped if the 'potential' well is deeper than a few  $k_B T$ , because otherwise the particle will escape by thermal fluctuations.

### 4.6.2 The ray optics regime

For particles that are large, i.e. where the radius of the particle is much larger than the wavelength of the light,  $r \gg \lambda$ , ray optics can be applied to calculate the forces on a dielectric in the focus of a Gaussian beam [38]. In this regime, the light is considered as rays transporting linear momentum. When the rays strike the interface of a particle, part of the light is reflected and part of it enters the particle. The same holds for the momentum that is associated with the light. The reflection and refraction can be calculated by applying Fresnel's law. In reference [38], Arthur Ashkin developed two equations for the force exerted in the parallel and perpendicular direction with respect to a light ray. He showed that incident rays with a larger angle contribute more to the gradient force than the rays that are closer to the optical axis. In other words, for stiff trapping, it is better to use a high NA objective. To calculate the total force, the contributions of the light coming from various directions are summed for all angles smaller than some angle  $\theta_0$  which corresponds to the NA. The trapping stiffness in the ray optics regime decays with  $1/r$ , with increasing particle radius.

Another way of regarding the axial gradient force on larger particles is by considering the particle to be a small positive lens [63] that makes the tightly focussed beam more parallel. The tightly focussed beam of a high NA objective carries a relatively small amount of momentum in the propagation direction. Because the particle makes the beam more parallel it increases the momentum of the light and hence the particle experiences a force opposite to the direction of propagation of the light [64].

### 4.6.3 *The intermediate or Lorenz-Mie regime*

The most demanding regime for calculating (trapping-) forces is the intermediate regime where neither the simplifications of point dipoles in the Rayleigh regime nor those in the ray optics regime can be applied, because the size of these particles is of the order of the wavelength of the light. In the Rayleigh regime the trapping stiffness increases with  $r^3$ , while in the ray optics regime the trapping stiffness decreases like  $1/r$ . In the Lorenz-Mie regime both regimes meet and the physics gets interesting. In many experiments the particles are right in the middle of this regime where the behavior is richest.

It is important to have good models of the functioning for optical tweezers, because it allows one to optimize optical traps in a relatively cheap way. Generally speaking one is looking for more efficient traps that generate maximum forces with minimum light intensity to minimize photo-damage in, for instance, biological samples [9, 65]. Furthermore, theoretical models can help validate novel measurement systems and they can help understand new phenomena [66].

To arrive at equations giving the force on the particles, formally Maxwell's equations should be solved to calculate the scattering by the particle at any given location with respect to the focus, after which the Maxwell stress tensor has to be applied to calculate the rate of momentum transfer or the forces.

A way to avoid solving Maxwell's equations is by discretizing the scatterer under consideration into many point dipoles: Rayleigh scatterers. The problem is then to calculate the multiple scattering of simple scatterers. Here, one also has to take into account the contributions of the non-propagating fields as the point dipoles in this approximation are inevitably close to one another. This discrete dipole method has the advantage that it is general and that it allows for the calculation of internal stresses in the trapped object that result from the interaction with light [67]. Because of the large number of point scatterers this approach is computationally expensive.

A brute force method to calculate the scattering of an arbitrary scatterer and the associated forces is the numerical solution of the Maxwell equation on a discretized grid in and around the particle using either a finite-difference time-domain or a finite element method [66]. These methods are rather computationally intensive as well.

For homogeneous scatterers, the scattering can be calculated using surface integral methods. For spherical particles the Lorenz-Mie-Debye theory [68–71] is

often used, which, when speaking of non-plane wave illumination, is often referred to as *generalized* Lorenz-Mie-Debye theory. The convenient feature of this theory is that it describes the scattering by the particles as a series of spherical harmonics that are each by themselves a solution to the Maxwell equations. The scattering of a particular particle is then described by an infinite analytical series of coefficients that describes the strength of each spherical harmonic contribution. Fortunately, these series usually converge rather fast so that the scattered fields can be calculated numerically [72]. Although the Lorenz-Mie-Debye theory was originally developed for homogeneous spheres, A. L. Aden and M. Kerker have been able to derive analytical results for the more complicated particle architecture of core-shell particles [73]. There are various theories that use the generalized Lorenz-Mie-Debye theory to calculate the scattering by the particle in one way or another to calculate the forces that are exerted by optical tweezers [74–88].

For particles that are only slightly larger than the Rayleigh scatterers and that have an index of refraction that differs little enough from that of the surrounding medium, the Born approximation can be applied. A theory of the trapping forces on these particles, that correctly describes the shape of the focus including the effect of spherical aberration, is provided by Rohrbach *et al.* [74–76]. They have developed an extension of the Rayleigh-Gans-Debye theory to calculate the forces exerted by an EM wave on a dielectric object described by Mie theory. In the work, the surface integral method of Lorenz-Mie-Debye is applied to calculate the scattering of dielectric spheres. To arrive at an expression of the force, they apply the Born approximation, i.e. they assume the particles to be in the so-called Rayleigh-Gans regime. There are many names for the approximations made: *Born approximation*, *Rayleigh-Gans*, *Rayleigh-Gans-Debye etc.*, but essentially it takes the exciting field as the only contribution to the local field in any given point in space. The scattered field is assumed to be small in comparison to the incident field. The scattered field is then simply the sum of the far field scattering of the dipoles. This saves the laborious calculation of the electric fields around and inside the particles but it limits the applicability to smaller particles and particles with a small refractive index contrast. The great merit of this work is the correct description of the diffraction limited focus of a high NA objective which includes the effect of spherical aberration. In section 4.7.1 the effects of spherical aberration will be discussed in more detail.

The application of the Lorenz-Mie theory to describe the scattering of spherical particles and also applying the correct description of the diffraction limited focus in combination with the full integration of the Maxwell stress tensor, was first described for the axial direction by P. A. Maia Neto and H. M. Nussensveig [79]. Later, the theory was extended in the same group to include the lateral forces [80]. The effect of spherical aberration on the shape of the diffraction limited focus was included finally in 2007 by N. B. Viana *et al.*, also from the Nussensveig group [82]. The results of this theory match well with experimental

results [81]. Thanks to the application of the Lorenz-Mie theory for the scattering of dielectric spheres, this model is widely applicable, agreeing quantitatively for small particles with the models for Rayleigh scattering and for large particles with ray optics. For simplicity these models assume the incident beam to be circularly polarized. This simplifies the calculations because of the cylindrical symmetry that can be used while the deviations in the forces are rather small in most cases [40]. We have adopted the model of the Nussensveig group to explore the possibilities with our setup. This model and the results we obtained with it are described in more detail in Chapters 5 and 6.

The Lorenz-Mie based theories have the advantage that they require the calculation of the scattering by the particle only once, which can then be used to calculate the scattering under different circumstances, for instance at different locations in the light field. The spherical symmetry of the scattered field allows for the decomposition of the scattered field in spherical harmonics that are each solutions of the Maxwell equations. However, for this decomposition to be applied, the particle does not need to be spherical. An alternative method to calculate trapping forces is given by the T-Matrix formalism. This formalism allows one to calculate the relation between the incident and the scattered light only once, just like the Lorenz-Mie based methods. The T-Matrix method can be applied to scatterers of arbitrary shape [66, 89]. Another feature of the T-Matrix formalism is that there is no need to apply the integration of the Maxwell stress tensor to calculate the optical forces.

In [90] a fully vectorial theory that calculates the forces on a particle exerted by the plane wave due to each individual pixel of a Diffractive Optical Element, DOE is given. Decomposing the light field into contributions from each single pixel of a DOE makes this model applicable to general optical force fields as projected by holographic optical tweezers. This model also takes into account the local change of the polarization. A thorough review on the various exact methods was written by Kahnert [91].

## 4.7 Other relevant effects

Apart from considerations like the particle size and refractive index, and the numerical aperture of the trapping objective, there are more effects that are relevant to the trapping process. In this section, we first discuss the effect of *spherical aberration*. Then we discuss the *non-conservative* nature of forces that are exerted by optical tweezers. Also *temporal effects* such as the influence of the pulse duration when pulsed lasers are used instead of continuous wave lasers and parametric excitation are discussed. Finally in section 4.7.4, we will discuss the phenomenon of *optical binding*.

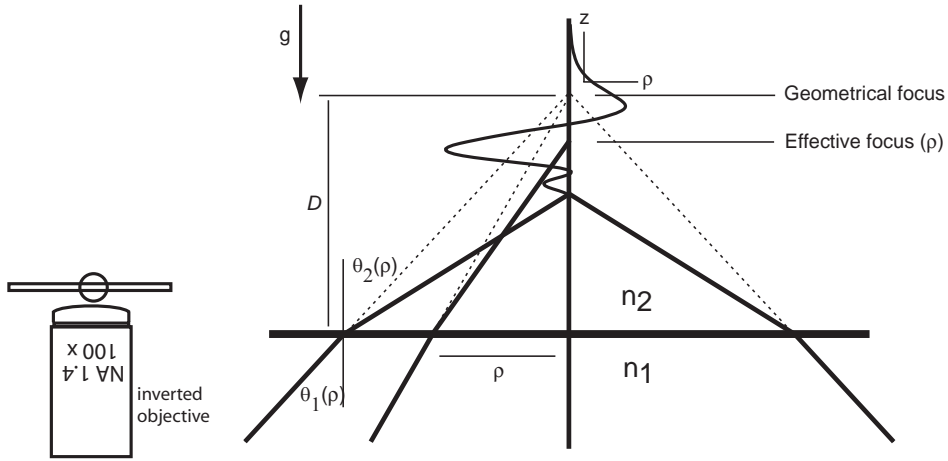


**Figure 4.1:** Schematic geometrical optics representation of spherical aberration. The focusing of a laser beam through a coverlip into the sample, where the refractive index of the medium is lower than that of the glass, ( $n_1 > n_2$ ), is schematically drawn. The light rays hit the interface under different angles to focus the light to a point in the focal plane. The dotted lines trace the path the light would take in absence of the interface. Depending on the angle of incidence, the light is deflected more or less at the interface. In this case ( $n_1 > n_2$ ) this results in an effective focus below the geometrical focus. The axes indicate the coordinates used in the calculations of the trapping forces with the origin at the geometrical focus, which is positioned a distance  $D$  above the bottom glass plate. The curve indicates the shape of the axial force on a silica particle in ethanol. The arrow  $g$  indicates the direction of gravity when an inverted microscope is used.

#### 4.7.1 Spherical Aberration

Often there is a difference between the refractive index of the immersion fluid and the glass holding the sample. At this interface the trapping laser is refracted as described by Fresnel's law [92]. The light entering the sample perpendicular to the sample glass is not refracted. The outer rays, the more convergent part of the light, which contribute relatively more to the gradient force [38], are refracted more strongly. In most cases the refractive index of the solvent is lower than that of the glass so the more deflected beams are refracted towards the optical axis. As can be seen in Figure 4.1, this results in that the outer beams are focussed closer to the sample wall than the less deflected rays. This causes the total focus, or point spread function, PSF, which describes the response of an imaging system to a point source, to be stretched. The focus becomes less confined and the maximal intensity and intensity gradients are reduced. This is called spherical aberration. Spherical aberration has negative consequences for the maximum trapping forces and the stiffness [45]. The outer beams converge stronger, so that the light intensity is focussed closer to the glass, with the result that the particle is

trapped less deep in the sample. Sometimes there appear even multiple trapping locations [81].

The effect gets stronger as the light is focussed deeper in the sample. If the refractive index of the solvent is higher than the refractive index of the glass, the effect of the spherical aberration is exactly the opposite, with the more deflected beams refracted outward so that they are focussed beyond the geometric focus or nominal focal point. In other words there exist two types of spherical aberration, positive and negative. A way to reduce the effect of spherical aberration is to use an objective that compensates the spherical aberration in a certain immersion fluid, usually water, and at a certain depth  $\sim 10 \mu\text{m}$ . When the optical tweezers make use of computer addressed spatial light modulators, it is possible to correct for the effect of spherical aberration by applying the opposite spherical aberration in the hologram to cancel the spherical aberration that occurs at the glass-medium interface [93]. S. N. S. Reihani *et al.* have shown that it is possible to cancel the negative spherical aberration at a certain depth in a sample with a lower index of refraction by introducing positive spherical aberration, by intentionally using an immersion oil with an index of refraction that is higher than that of the coverslip [94].

In reference [95] we find a nice evaluation of the effect of spherical aberration on the trapping properties in the ray-optics regime. One of the more surprising conclusions is that sometimes the higher numerical aperture objectives do not yield optimal trapping. This is due to the fact the outer rays get refracted more strongly inwards such that they focus at a smaller distance to the glass. The result is generally that the focus is stretched, having smaller intensity gradients and thus smaller gradient forces. As the outer rays are refracted inwards however, they focus under a shallower angle which corresponds to a higher NA.

In the Rayleigh regime, Rohrbach *et al.* [74–76] provided a model that captures the effect of spherical aberrations on the trapping of small particles, under application of the Born approximation. An exact trapping model which is applicable for all particle sizes that also includes the effect of spherical aberration is given by the Nussensveig group [79, 80, 82] and is also described in section 4.6.3. The model as given by Viana *et al.* from the Nussensveig group was the basis for the exploration of the trapping parameters presented in Chapters 5 and 6.

### 4.7.2 Non-conservative forces

Although optical traps are often referred to as potential wells in which the particle is trapped, optical traps form *non* conservative force fields, as Arthur Ashkin [38] already pointed out for the ray-optics regime. The exact method of the Nussensveig group [79–82] which applies to all particle sizes shows distinct non-conservative forces, as can be seen from Figure 3 in [81]. Although the gradient force is clearly conservative in nature, the scattering force, or radiation pressure, is not.

In reference [96], Y. Roichman elegantly showed that phase gradients can cause significant forces by creating line traps and circular traps with homogeneous intensity distributions but with a phase gradient. These traps were made using a digitally addressed DOE and sophisticated algorithms.

In the same year Y. Roichman published another experiment in which a silica particle was trapped in water and tracked using video holographic microscopy [44], described in Chapter 2. From the trajectories it was deduced that the particle was rotating more often in the clockwise direction than in the counter clockwise direction [97]. Similar experiments are presented in section 5.3.3. Using quadrant photo detectors Wu *et al.* [98] measured a non-zero curl, signifying non-conservativeness, in the force field exerted on a Rayleigh particle (a 200 nm diameter PS particle).

### 4.7.3 Temporal effects

For variations in the electric field that are much slower than the oscillations associated with the light waves itself, when using pulsed lasers rather than continuous wave, *cw*, lasers, there have been reports of interesting phenomena in the form of ponderomotive forces by Wang *et al.* [99]. Arijit Kumar De *et al.* have shown experiments that indicated that ultrashort pulsed traps can trap nanometer-sized particles with powers that are too low to trap particles with *cw* lasers [100].

In the Dholakia group however, careful experiments have been performed in which the pulse duration was varied over 1.5 orders of magnitude, that seem to indicate that there are no material-independent temporal dependencies [101]. This suggests that the results obtained by De *et al.* [100] were due to material specific phenomena like two photon effects. In addition, the theoretical results by Wang *et al.* have been addressed. Although it is true that the peak forces are larger if a pulsed laser is used, in the general case, the total momentum transfer depends on the average power only.

Another temporal effect that is not particularly optical but rather mechanical in nature is that of parametric excitation first reported by Joykuty *et al.* [102]. Here, the laser power is oscillated at twice the resonance frequency of the particle in its harmonic trap. This is called parametric excitation because one of the parameters of the optical trap, the stiffness, is varied. It is the variation of a parameter rather than an external driving force that pumps energy into the system. The variance in the position of a Brownian particle in a harmonic trap allegedly increased when the laser power and thus the trap stiffness were varied sinusoidally in time at about twice the corner frequency of the trap. Pederson and Flyvbjerg [103] published a comment in which they showed that damping dominates the dynamics, such that no such resonance should appear in the dynamics. Deng *et al.* [104] also argued and experimentally showed that the severe overdamping that colloids in a liquid experience makes the appearance of a resonance impossible. Their observations also have implications for time-shared trapping as they observed an increase in the positional variance when the trap stiffness was

modulated at frequencies below the corner frequency. Venkataraman *et al.* [105] argued that the experimental observations in reference [102] may be due to not only the periodic modulation of the trap strength but also partially to slight variations in the trap-shape. In reference [102] an Acousto Optical Modulator, AOM was used to provide for the variation in trap strength. This may as a side-effect result in a small variation in the shape of the trap which may be essential for the appearance of the parametric resonance. In section 5.4.2 we will discuss experiments on the effect of the switch-rate of time-shared traps on the trapping behavior that support this hypothesis.

Strictly speaking, the driving of the over-damped harmonic oscillator by the periodic variation of the trap position is not a parametric excitation. Roberto di Leonardo *et al.* [106] showed that when the damping is much less, in the so-called liquid-damped regime, as is the case for micron-sized particles in for instance air, a parametric resonance *can* be excited.

#### 4.7.4 *Optical binding*

If a particle is trapped by an optical trap, it scatters light in various directions. Moreover, close to the particle, there is the so-called near-field, a non-propagating part of the EM field such as evanescent waves. All this light might interact with a nearby second particle, exerting also forces on this second particle. Note that in the absence of the first particle in the trap this light and the associated forces would not be there. This phenomenon was demonstrated by Micheal M. Burns [107] and coined *Optical binding*.

For these interactions to be strong, it is important that both particles are irradiated simultaneously such that their scattered fields can interact. Using time-sharing to trap multiple particles minimizes the optical binding because there is always only one particle irradiated at a time. Optical binding forces can also be reduced by coating the particles with a layer of a material that is refractive index matched by the solvent, thus effectively increasing the distance between the scattering particles. For more on the trapping of particles with a core-shell architecture see section 5.6.

M. I. Antonoyiannakis and J. B. Pendry performed calculations on the time average EM forces in macroscopic matters such a colloidal crystals [108]. Although traveling waves always produce a repulsion between the particles, this is the so-called scattering force discussed above, evanescent waves may induce either attractions or repulsions. Particularly at wavelengths that cause so-called Mie resonances, corresponding to the EM eigenmodes of the spheres, the forces induced by the near fields may be even stronger than gravity or van der Waals forces. Bayindir *et al.* [109] and Bayer *et al.* [110] were the first to experimentally show the light-induced bonding and anti-bonding interactions that were predicted by M. I. Antonoyiannakis and J. B. Pendry.

## Bibliography

- [1] Ashkin, A. Acceleration and trapping of particles by radiation pressure. *Phys. Rev. Lett.* **24** 156 (1970).
- [2] Ashkin, A. and Dziedzic, J. M. Optical levitation by radiation pressure. *Appl. Phys. Lett.* **19** 283 (1971).
- [3] Ashkin, A., Dziedzic, J. M., Bjorkholm, J. E., and Chu, S. Observation of a single-beam gradient force optical trap for dielectric particles. *Opt. Lett.* **11** 288 (1986).
- [4] Chu, S., Bjorkholm, J. E., Ashkin, A., and Cable, A. Experimental Observation of Optically Trapped Atoms. *Phys. Rev. Lett.* **57** 314 (1986).
- [5] Ashkin, A., Dziedzic, J. M., and Yamane, T. Optical trapping and manipulation of single cells using infrared laser beams. *Nature* **330** 769 (1987).
- [6] Ashkin, A. and Dziedzic, J. M. Optical trapping and manipulation of viruses and bacteria. *Science* **235** 1517 (1987).
- [7] Block, S. M., Goldstein, L. S. B., and Schnapp, B. J. Direct observation of kinesin stepping by optical trapping interferometry. *Nature* **348** 721 (1990).
- [8] Svoboda, K., Schmidt, C. F., Schnapp, B. J., and Block, S. M. Direct observation of kinesin stepping by optical trapping interferometry. *Nature* **365** 721 (1993).
- [9] Svoboda, K. and Block, S. M. Biological applications of optical forces. *Annu. Rev. Biophys. Biomol. Struct.* **23** 247 (1994).
- [10] Kuo, S. C. and Sheetz, M. P. Force of Single Kinesin Molecules Measures with Optical Tweezers. *Science* **260** 773 (1993).
- [11] Abbondanzieri, E. A., Greenleaf, W. J., Shaevitz, J. W., Landick, R., and Block, S. M. Direct observation of base-pair stepping by RNA polymerase. *Nature* **438** 460 (2005).
- [12] Footer, M. J., Kerssemakers, J. W. J., Theriot, J. A., and Dogterom, M. Direct measurement of force generation by actin filament polymerization using an optical trap. *PNAS* **104** 2181 (2007).
- [13] Bustamante, C., Macosko, J. C., and Wuite, G. J. Grabbing the cat by the tail: manipulating molecules one by one. *Nat. Rev. Mol. Cell Biol.* **1** 130 (2000).
- [14] Bryant, Z., Stone, M. D., Gore, J., Smith, S., Cozzarelli, N. R., and Bustamante, C. Structural transitions and elasticity from torque measurements on DNA. *Nature* **424** 338 (2003).
- [15] Guck, J., Ananthakrishnan, R., Mahmood, H., Moon, T. J., Cunningham, C. C., Hallworth, R., and Kas, J. The Optical Stretcher: A Novel Laser Tool to Micromanipulate Cells. *Biophys. J.* **80** 767 (2001).
- [16] Gittes, F., Schnurr, B., Olmsted, P. D., MacKintosh, F. C., and Schmidt, C. F. Microscopic Viscoelasticity: Shear Moduli of Soft Materials Determined from Thermal Fluctuations. *Phys. Rev. Lett.* **79** 3286 (1997).
- [17] Pesce, G., Luca, A. C. D., Rusciano, G., Netti, P. A., Fusco, S., and Sasso, A. Microrheology of complex fluids using optical tweezers: a comparison with microrheological measurements. *J. Opt. A: Pure Appl. Opt.* **11** 034016 (2009).
- [18] Alcaraz, J., Buscemi, L., Grabulosa, M., Trepas, X., Fabry, B., Farré, R., and Navajas, D. Microrheology of Human Lung Epithelial Cells Measured by Atomic Force Microscopy. *Biophys. J.* **84** 2071 (2003).
- [19] Berg-Sørensen, K., Peterman, E. J. G., Weber, T., Schmidt, C. F., and Flyvbjerg, H.

- Power Spectrum Analysis for Optical Tweezers, II: Laser Wavelength Dependence of Parasitic Filtering, and how to Achieve High Band-Width. *Rev. Sci. Instrum.* **77** 063106 (2006).
- [20] Wong, W. P. and Halvorsen, K. Beyond the frame rate: measuring high-frequency fluctuations with light-intensity modulation. *Opt. Lett.* **34** 277 (2009).
- [21] Grier, D. G. A revolution in optical manipulation. *Nature* **424** 810 (2003).
- [22] Grier, D. G. Optical tweezers in colloid and interface science. *Curr. Opin. Colloid Interface Sci.* **2** 264 (1997).
- [23] Hoffmann, G. P. and Löwen, H. Freezing and melting criteria in non-equilibrium. *J. Phys.: Condens. Matter* **13** 9197 (2001).
- [24] Bar-Ziv, R., Moses, E., and Nelson, P. Dynamic excitations of membrane induced by optical tweezers. *Biophys. J.* **75** 294 (1998).
- [25] P. T. Korda and, M. B. T. and Grier, D. G. Kinetically Locked-in Colloidal Transport in an Array of Optical Tweezers. *Phys. Rev. Lett.* **89** 128301 (2002).
- [26] Hough, L. A. and Ou-Yang, H. D. Correlated motions of two hydrodynamically coupled particles confined in separate quadratic potential wells. *Phys. Rev. E* **65** 021906 (2002).
- [27] Lin, K.-H., Crocker, J. C., Prasad, V., Schofield, A., Weitz, D. A., Lubensky, T. C., and Yodh, A. G. Entropically Driven Colloidal Crystallization on Patterned Surfaces. *Phys. Rev. Lett.* **85** 1770 (2000).
- [28] Sainis, S. K., Germain, V., and Dufresne, E. R. Statistics of Particle Trajectories at Short Time-Intervals Reveal Electrostatic Colloidal Interactions in Nonpolar Solvents. *Phys. Rev. Lett.* **95** 018303 (2007).
- [29] Masri, D. E., van Oostrum, P., Smalenburg, F., Vissers, T., Imhof, A., Dijkstra, M., and van Blaaderen, A. Measuring Colloidal Forces from Particle Position Deviations inside an Optical Trap. *Soft Matter*, DOI:10.1039/COSM01295E (2011).
- [30] Hoogenboom, J. P., Vossen, D. L. J., Faivre-Moskalenko, C., Dogterom, M., and van Blaaderen, A. Patterning surfaces with colloidal particles using optical tweezers. *Appl. Phys. Lett.* **80** 4828 (2002).
- [31] Crocker, J. C., Matteo, J. A., Dinsmore, A. D., and Yodh, A. Entropic Attraction and Repulsion in Binary Colloids Probed with a Line Optical Tweezer. *Phys. Rev. Lett.* **82** 4352 (1999).
- [32] Crocker, J. C. and Grier, D. G. Microscopic Measurement of the Pair Interaction Potential of Charge-Stabilized Colloid. *Phys. Rev. Lett.* **73** 352 (1994).
- [33] Crocker, J. C. and Grier, D. G. When like charges attract: The effects of geometrical confinement on long-range colloidal interactions. *Phys. Rev. Lett.* **77** 1897 (1996).
- [34] Crocker, J. C. and Grier, D. G. Methods of Digital Video Microscopy for Colloidal Studies. *J. Colloid Interface Sci.* **179** 298 (1996).
- [35] Squires, T. M. and Brenner, M. P. Like -Charge Attraction and Hydrodynamic Interaction. *Phys. Rev. Lett.* **85** 4976 (2000).
- [36] Popov, Y. O. Effects of Flow on Measurements of Interactions in Colloidal Suspensions. *J. of Col. and Int. Sci.* **252** 320 (2002).
- [37] Lutz, C., Reichert, M., Stark, H., and Bechinger, C. Surmounting barriers: The benefit of hydrodynamic interactions. *Europhys. Lett.* **74** 719 (2006).
- [38] Ashkin, A. Forces of a single-beam gradient laser trap on a dielectric sphere in the ray optics regime. *Biophys. J.* **61** 569 (1992).

- [39] Merenda, F., Rohner, J., Fournier, J.-M., and Salathé, R.-P. Miniaturized high-NA focusing-mirror multiple optical tweezers. *Opt. Exp.* **15** 6075 (2007).
- [40] Dutra, R. S., Viana, N. B., Neto, P. A. M., and Nussenzveig, H. M. Polarization effects in optical tweezers. *J. Opt. A Pure Appl. Opt.* **9** S221 (2007).
- [41] Crocker, J. C. and Grier, D. G. Methods of Digital Video Microscopy for Colloidal Studies. *J. of Col. and Int. Sci.* **179** 289 (1996).
- [42] Minsky, M. Memoir on inventing the confocal scanning microscope. *Scanning* **10** (1988).
- [43] Wilson, T. *Confocal Microscopy*. Academic Press, London (1990).
- [44] Lee, S.-H., Roichman, Y., Yi, G.-R., Kim, S.-H., Yang, S.-M., van Blaaderen, A., van Oostrum, P., and Grier, D. G. Characterizing and tracking single colloidal particles with video holographic microscopy. *Opt. Exp.* **15** 18275 (2007).
- [45] Felgner, H., Müller, O., and Schliwa, M. Calibration of light forces in optical tweezers. *Appl. Opt.* **34** 977 (1995).
- [46] Happel, J. and Brenner, H. *Low Reynolds Number Hydrodynamics*. Kluwer Academic, Dordrecht (1993).
- [47] Florin, E.-L., Pralle, A., Stelzer, E. H. K., and Hörber, J. K. H. Photonic force microscope calibration by thermal noise analysis. *App. Phys. A* **66** S75 (1998).
- [48] Ghislain, L. P. and Webb, W. W. Scanning-force microscope based on an optical trap. *Opt. Lett.* **18** 1678 (1993).
- [49] Allersma, M. W., Gittes, F., de Castro, M. J., Stewart, R. J., and Schmidt, C. F. Two-dimensional tracking of ncd motility by back focal plane interferometry. *Biophys. J.* **74** 1074 (1998).
- [50] Wang, M. and Uhlenbeck, O. On the theory of the Brownian motion II. *Rev. Mod. Phys.* **17** (1945 Reprinted in *Selected Papers on Noise and Stochastic Processes*, ed. N Wax, pp. 113-32. New York, NY: Dover).
- [51] van der Horst, A., van Oostrum, P., Moroz, A., van Blaaderen, A., and Dogterom, M. High trapping forces for high-refractive index particles trapped in dynamic arrays of counterpropagating optical tweezers. *Appl. Opt.* **47** 3196 (2008).
- [52] Polin, M., Ladavac, K., Lee, S.-H., Roichman, Y., and Grier, D. Optimized holographic optical traps. *Opt. Exp.* **13** 5831 (2005).
- [53] Visscher, K., Brakenhoff, G. J., and Krol, J. J. Micromanipulation by multiple optical traps created by a single fast scanning trap integrated with the bilateral confocal scanning laser microscope. *Cytometry* **14** 105 (1993).
- [54] Fällman, E. and Axner, O. Design for fully steerable dual-trap optical tweezers. *Appl. Opt.* **36** 2107 (1997).
- [55] Vossen, D. L. J., van der Horst, A., Dogterom, M., and van Blaaderen, A. Optical tweezers and confocal microscopy for simultaneous three-dimensional manipulation and imaging in concentrated colloidal dispersions. *Rev. Sci. Instrum.* **75** 2960 (2004).
- [56] Dufresne, E. R. and Grier, D. G. Optical tweezer array on optical substrates created with diffractive optics. *Rev. Sci. Instrum.* **69** 1974 (1998).
- [57] Reichert, M., Haist, T., Wagemann, E. U., and Tiziani, H. J. Optical particle trapping with computer-generated holograms written on a liquid-crystal display. *Opt. Lett.* **24** 608 (1999).
- [58] Dufresne, E. R., Spalding, G. C., Dearing, M. T., Sheets, S. A., and Grier, D. G.

- Computer-generated holographic optical tweezer arrays. *Rev. Sci. Instrum.* **72** 1810 (2001).
- [59] Curtis, J. E., Koss, B. A., and Grier, D. G. Dynamic holographic optical tweezers. *Optics comm.* **207** 169 (2002).
- [60] Leonardo, R. D., Ianni, F., and Ruocco, G. Computer generation of optimal holograms for optical trap arrays. *Opt. Exp.* **15** (2007).
- [61] Rodrigo, P. J., Gammelgaard, L., Bøggold, P., Perch-Nielsen, I. R., and Glückstad, J. Actuation of microfabricated tools using multiple GPC-based counterpropagating-beam traps. *Opt. Exp.* **13** 6899 (2005).
- [62] Malignino, N., Pesce, G., Sasso, A., and Arimondo, E. Measurements of trapping efficiency and stiffness in optical tweezers. *Opt. Comm.* **214** 15 (2002).
- [63] Marlow, F. and Eiden, S. Refractive index determination on microscopic objects. *Eur. J. Phys.* **25** 439 (2004).
- [64] Hu, Y., Nieminen, T. A., Heckenberg, N. R., and Rubinsztein-Dunlop, H. Antireflection coating for improved optical trapping. *J. Appl. Phys.* **103** 093119 (2008).
- [65] Neuman, K. C., E. H. Chadd, G. F. Liou, K. B., and Block, S. M. Characterization of Photodamage to *Escherichia coli* in Optical Traps. *Biophys. J.* **77** 2856 (1999).
- [66] Nieminen, T. A., Heckenberg, N. R., and Rubinsztein-Dunlop, H. Computational modelling of optical tweezers. *Proc. SPIE* **5514** 514 (2004).
- [67] Hoekstra, A. G., Frijlink, M., Waters, L. B. F. M., and Sloot, P. M. A. Radiation forces in the discrete-dipole approximation. *J. Opt. Soc. Am. A* **18** 1944 (2001).
- [68] Lorenz, L. Lysbevægelsen i og uden for en af plane Lysbølger belyst Kugle. *Videnskaberne Selskabs Skrifter* **6** 1 (1890).
- [69] Lorenz, L. Sur la lumière réfléchie et réfractée par une sphère (surface) transparente. *Oeuvres scientifiques de L. Lorenz. revues et annotées par H. Valentiner. Tome Premier; Libraire Lehmann & Stage, Copenhagen* 403 (1898).
- [70] Mie, G. Beiträge zur Optik trüber Medien, speziell kolloidaler Metallösungen. *Annalen der Physik* **25(3)** (1908).
- [71] Debye, P. Der Lichtdruck auf Kugeln von beliebigem Material. *Annalen der Physik* **4(30)** 1 57 (1909).
- [72] Bohren, C. F. and Huffman, D. R. Absorption and Scattering of Light by Small Particles. Wiley Interscience, New York (1983).
- [73] Aden, A. L. and Kerker, M. Scattering of electromagnetic waves from two concentric spheres. *J. Appl. Phys.* **22** 1242 (1951).
- [74] Rohrbach, A. and Stelzer, E. H. K. Optical trapping of dielectric particles in arbitrary fields. *J. Opt. Soc. Am. A* **8** 839 (2001).
- [75] Rohrbach, A. and Stelzer, E. H. K. Trapping forces, force constants, and potential depths for dielectric spheres in the presence of spherical aberrations. *Appl. Opt.* **41** 2494 (2002).
- [76] Rohrbach, A. Stiffness of Optical Traps: Quantitative Agreement between Experiment and Electromagnetic Theory. *Phys. Rev. Lett.* **95** 168102 (2005).
- [77] Ren, K. F., Gréehan, G., and Gouesbet, G. Prediction of reverse radiation pressure by generalized Lorenz-Mie theory. *App. Opt.* **35** 2702 (1996).
- [78] Rosin, T. W. A. and Stelzer, E. H. K. Theoretical determination of the influence of the polarization on forces exerted by optical tweezers. *Optik* **102** 181 (1996).
- [79] Neto, P. A. M. and Nussenzweig, H. M. Theory of optical tweezers. *Europhysics*

- Letters* **50** 702 (2000).
- [80] Mazolli, A., Neto, P. A. M., and Nussenzeig, H. M. Theory of trapping forces in optical tweezers. *Proceedings of the Royal Society of London A* **459** 3021 (2003).
- [81] Viana, N. B., Mazolli, A., Neto, P. A. M., and Nussenzeig, H. M. Characterization of objective transmittance for optical tweezers. *Appl. Phys. Lett.* **88** 4263 (2006).
- [82] Viana, N. B., Rocha, M. S., Mesquita, O. N., Mazolli, A., Neto, P. A. M., and Nussenzeig, H. M. Towards absolute calibration of optical tweezers. *Phys. Rev. E* **75** 021914 (2007).
- [83] Lock, J. A. Calculation of the radiation trapping force for laser tweezers by use of generalized Lorenz-Mie theory. I. Localized model description of an on-axis tightly focussed laser beam with spherical aberration. *App. Opt.* **43** 2532 (2004).
- [84] Lock, J. A. Calculation of the radiation trapping force for laser tweezers by use of generalized Lorenz-Mie theory. II. On-axis trapping force. *App. Opt.* **43** 2545 (2004).
- [85] Neves, A. A. R., Fontes, A., Padilha, L. A., Rodriguez, E., C. H. de Brito Cruz, L. C. B., and Cesar, C. L. Exact partial wave expansion of optical beams with respect to an arbitrary origin. *Opt. Lett.* **31** 2477 (2006).
- [86] Neves, A. A. R., Fontes, A., de Y. Pozzo, L., de Thomaz, A. A., Rodriguez, E. C. E., Barbosa, L. C., and Cesar, C. L. Electromagnetic forces for an arbitrary optical trapping of a spherical dielectric. *Opt. Exp.* **14** 13101 (2006).
- [87] Ganic, D., Gan, X., and Gu, M. Exact radiation trapping force calculation based on vectorial diffraction theory. *Opt. Exp.* **12** 2670 (2004).
- [88] Gouesbet, G. Generalized Lorenz-Mie theories, the third decade: A perspective. *J. Quant. Spect. & Rad. Trans.* **110** 1223 (2009).
- [89] Nieminen, T. A., Rubinsztein-Dunlop, H., and Heckenberg, N. R. Calculation of the T-matrix: general considerations and application of the point-matching method. *Journal of Quantitative Spectroscopy and Radiative Transfer* **79-80** 1019 (2003).
- [90] Sun, B., Roichman, Y., and Grier, D. G. Theory of holographic optical trapping. *Opt. Exp.* **16** 15765 (2008).
- [91] Kahnert, F. M. Numerical methods in electromagnetic scattering theory. *Journal of Quantitative Spectroscopy and Radiative Transfer* **79** 775 (2003).
- [92] Hecht, E. Optics. Addison Wesley, 3rd. ed. (1998).
- [93] Roichman, Y., Waldron, A. S., Gardel, E., and Grier, D. G. Performance of optical traps with geometric aberrations. *Appl. Opt.* **45** 3425 (2005).
- [94] Reihani, S. N. S. and Oddershede, L. Optimizing immersion media refractive index improves optical trapping by compensating spherical aberrations. *Opt. Lett.* **32** 1998 (2007).
- [95] Fällman, E. and Axner, O. Influence of a Glass-Water Interface on the On-Axis Trapping of Micrometer-Sized Spherical Objects by Optical Tweezers. *Appl. Opt.* **42** 3915 (2003).
- [96] Roichman, Y., Sun, B., Roichman, Y., Amato-Grill, J., and Grier, D. G. Optical Forces arising from phase gradients. *Phys. Rev. Lett.* **100** 013602 (2008).
- [97] Roichman, Y., Sun, B., Stolarski, A., and Grier, D. G. Influence of Nonconservative Optical Forces on the Dynamics of Optically Trapped Colloidal Spheres: The Fountain of Probability. *Phys. Rev. Lett.* **101** 128301 (2008).
- [98] Wu, P., Huang, R., Tischer, C., Jonas, A., and Florin, E.-L. Direct Measurement of

- the Nonconservative Force Field Generated by Optical Tweezers. *Phys. Rev. Lett.* **103** 108101 (2009).
- [99] Wang, L.-G. and Zhao, C.-L. Dynamic radiation force of a pulsed Gaussian beam acting on a Rayleigh dielectric sphere. *Opt. Exp.* **15** 10615 (2007).
- [100] De, A. K., Roy, D., Dutta, A., and Goswami, D. Stable optical trapping of latex nanoparticles with ultrashort pulsed illumination. *Appl. Opt.* **48** G33 (2009).
- [101] Shane, J. C., Mazilu, M., Lee, W. M., and Dholakia, K. Effect of pulse temporal shape on optical trapping and impulse transfer using ultrashort pulsed lasers. *Opt. Exp.* **8** 7554 (2010).
- [102] Joykutti, J., Mathur, V., Venkataraman, V., and Natarajan, V. Direct Measurement of the Oscillation Frequency in an Optical-Tweezers Trap by Parametric Excitation. *Phys. Rev. Lett.* **95** 193902 (2005).
- [103] Pedersen, L. and Flyvbjerg, H. Comment on "Direct Measurement of the Oscillation Frequency in an Optical-Tweezers Trap by Parametric Excitation". *Phys. Rev. Lett.* **98** 189801 (2007).
- [104] Deng, Y., Bechhoefer, J., and Forde, N. R. Brownian motion in a modulated optical trap. *J. Opt. A: Pure Appl. Opt.* **9** S256 (2007).
- [105] Venkataraman, V., Natarajan, V., and Kumar, N. Comment on: Comment on "Direct Measurement of the Oscillation Frequency in an Optical-Tweezers Trap by Parametric Excitation". *Phys. Rev. Lett.* **98** 189802 (2007).
- [106] Leonardo, R. D., Ruocco, G., Padgett, M. J., and J. M. Girkin, A. J. W., Burnham, D. R., and McGloin, D. Parametric Resonance of Optically trapped Aerosols. *Phys. Rev. Lett.* **99** 010601 (2007).
- [107] Burns, M. M., Fournier, J.-M., and Golovchenko, J. A. Optical Binding. *Phys. Rev. Lett.* **63** 1233 (1989).
- [108] Antonoyiannakis, M. I. and Pendry, J. B. Electromagnetic forces in photonic crystals. *Phys. Rev. B* **60** 2363 (1999).
- [109] Bayindir, M., Temelkuran, B., and Ozbay, E. Tight-Binding Description of the Coupled Defect Modes in Three-Dimensional Photonic Crystals. *Phys. Rev. Lett.* **84** 2140 (2000).
- [110] Bayer, M., Gutbrod, T., Reithmaier, J. P., Forchel, A., Reinecke, T. L., Knipp, A., Dremin, A. A., and Kulakovskii, V. D. Optical Modes in Photonic Molecules. *Phys. Rev. Lett.* **81** 2582 (1998).

# 5

## Exploration of trapping Parameters

---

In this Chapter we briefly introduce the theory for the trapping forces exerted on dielectric particles that was developed in several papers from the group of Nussensveig. These calculations are based on a Debye-type integral of the radiation pressure on spherical particles in a diffraction limited focus, the description of which takes the effect of spherical aberrations into account. We apply this model to map the phenomena that play a roll in the trapping of a model system. We experimentally study the non-conservativeness of the forces exerted by our optical trap using Digital Holographic Microscopy, DHM. Then, we experimentally investigate the effect of the space between the focal plane of the microscope and the trapped particle that facilitates the application of DHM on the trapping. In our setup, it is possible to trap multiple particles simultaneously by means of time-sharing. We experimentally study the effect of the rate at which the laser focus is switched on the trapping performance. We explore the trapping behavior of various particles that might be trapped in our setup, including particles with a core-shell structure.

## 5.1 Introduction to calculations of trapping forces

In this Chapter we explore the various parameters that play a role in the trapping of colloids. This is mainly done using calculations, that, at some points are supported by experimental results. For our calculations we used the Mie-Debye representation, first given by P. A. Maia Neto and H. M. Nussensveig for the axial direction [1]. The model was subsequently extended to include also the lateral forces [2], and complemented to include spherical aberrations by Viana *et al.* within the same group [3]. The calculations presented here were performed on desktop computers using a home built Matlab<sup>®</sup> implementation of the model as described in [3].

The model uses the Lorenz-Mie [4–6] theory to describe the scattering of spherical particles. This theory describes the scattering of spherical homogeneous and core-shell [7] particles as an analytical infinite series that converges generally quite fast, depending on the particle size within 10 or 20 terms [8]. The correct shape of the diffraction limited focus is described by a Debye-type integral which describes the focus as a superposition of plane waves [9].

Polarization is an important factor in the scattering of light and thus also for the calculations of optical forces. Because of the singularity that is created on the optical axis in the case of radially polarized light for instance, these traps have a dark center. Moreover, for a particle in the focus, all the light rays with respect to the colloid surface are p polarized, minimizing reflection and thus the scattering force [10]. In the ray optics regime [11] and in the Lorenz-Mie regime [10], calculations have been performed on the effects of the type of polarization on the trapping behavior. The radially polarized traps are predicted to trap particularly high refractive index contrast particles significantly better than the linearly polarized Gaussian trap. However, the differences between the trapping forces in traps of different polarization type are typically smaller than a few percent when the refractive index of the particle is no more 1.2 times that of the surrounding medium. The creation of radially polarized light requires significant changes to a setup that also reduce the intensity of the laser light. It is therefore better to first calculate the benefits of using a radially polarized beam to trap the particles under investigation to see if the benefits justify the costs of adapting the setup and the loss of laser power in the additional optics.

Dutra *et al.* [12], from the Nussensveig group, have presented calculations that include the effect of polarization in which they compared trapping with linearly polarized light with the trapping using circularly polarized light. They concluded that the difference between the trapping with circularly and linearly polarized beams is not of experimental interest. Only for larger particles ( $r \approx 5 \lambda$ ), they found differences between the forces exerted in the two lateral directions at larger displacements ( $\rho > r$ ) which they ascribe to Mie-resonances. In our calculations, circularly polarized light is assumed for simplicity. In our experiments, and in the vast majority of experiments done, linearly polarized light is used.

Since the deviations from theory assuming circularly polarized light of experiments using linearly polarized light are so small, we prefer to use the calculations as described by reference [3] from the Nussensveig group to explore our parameter space. We do include the strong effects of spherical aberration.

There is a large parameter space: many different types of particles in combination with a great many combinations of solvents to be trapped using different objectives and wavelengths. To form an idea of the possibilities with our setup, without all the work involved in synthesizing particles and trying, we used the model by the Nussensveig group [3]. Our interest goes out to both finding the limits of what our setup can do and to find the particle characteristics that optimize the trapping stiffness and stability. In this Chapter we describe our findings for single particles in single traps. In Chapter 6 we discuss some of the benefits of using multiple optical traps to trap a single particle.

First, in section 5.2 we will introduce the model used in more detail. Then, in section 5.3, we show typical results of the calculations for a model system chosen for experimental convenience. We will choose a particle-solvent combination with which we have performed many experiments, a  $1.4\ \mu\text{m}$   $\text{SiO}_2$  bead in ethanol, and we will gauge the effects of spherical aberration in this system. Experiments showing the linear dependence of the trapping forces on the laser power are presented. We showed experimentally how the non-conservative nature of optical traps, see also section 4.7.2, influences the trapping behavior. In the same experiments, we study the effect of spherical aberration on the non-conservative behavior of the trap.

In section 5.4 we experimentally investigate the effect of the distance between the trapping plane and the imaging plane on the trapping behavior. We purposefully create this distance to facilitate the application of the Digital Holographic Microscopy, DHM technique we presented in Chapter 2. The laser beam is made divergent at the back focal plane of the objective to trap the particle deeper into the sample. This also influences the effective overfilling of the back aperture. On a different note, we also study the effect of the timing when applying time-sharing to make multiple traps on the trapping behavior in these traps.

Next, in section 5.5, we show what effect the particle size has on the forces exerted by the optical tweezer. In the same section we also give an overview of the effect of the index of refraction of both the particle and the medium.

Finally, in section 5.6 we will look at somewhat more complicated particles with a core-shell structure. There are many examples of colloids that have a shell or coating of some material on their surface. This can have rather surprising effects on the trapping behavior of these particles. For some combinations of materials, the shell can function as an anti-reflection coating reducing the scattering forces, thus facilitating better trapping. Normally a particle of a material with an index of refraction lower than that of the surrounding medium cannot be trapped in a point trap due to its negative polarizability. However, we show that it can be trapped when provided with a core that has an index of refraction that is larger

than that of the shell, but still smaller than that of the solvent. The refractive index of that core does not need to be higher than the refractive index of the suspending medium, it suffices to have the index of refraction of that core above that of the shell material.

## 5.2 The model

For spherical particles trapped by an ordinary point trap the important parameters are the particle radius and the refractive index contrast. We define the ratio  $m$ :

$$m = n_{\text{part}}/n_{\text{med}}, \quad (5.1)$$

where respectively  $n_{\text{med}}$  and  $n_{\text{part}}$  are the refractive index of the medium and the particle. The next dimensionless parameter of interest is the size of the particle relative to the wavelength:

$$\beta = kr, \quad (5.2)$$

where  $k$  is the wave number of the trapping light in the medium,  $\frac{2\pi n_m}{\lambda}$ , and  $r$  is the radius of the particle. In a sense  $\beta$  is thus the number of light waves that can be ‘wrapped’ around the circumference of the particle.

These two parameters are sufficient to quantitatively describe the scattering of plane waves by the particle [4–6]. In the textbook by Craig F. Bohren and Donald R. Huffman [8] we find the expressions for the scattering coefficients of a spherical particle that consists of a dielectric or a metallic material. These scattering coefficients are the coefficients in the expansion in spherical harmonics of the light scattered by a homogeneous spherical particle under irradiation with a plane wave, as given by the Lorenz-Mie theory [4–6]:

$$a_n = \frac{m\psi_n(m\beta)\psi_n'(\beta) - \psi_n(\beta)\psi_n'(m\beta)}{m\psi_n(m\beta)\xi_n'(\beta) - \xi_n(\beta)\psi_n'(m\beta)} \quad (5.3)$$

and

$$b_n = \frac{\psi_n(m\beta)\psi_n'(\beta) - m\psi_n(\beta)\psi_n'(m\beta)}{\psi_n(m\beta)\xi_n'(\beta) - m\xi_n(\beta)\psi_n'(m\beta)}. \quad (5.4)$$

Here,  $\psi_n(x)$  and  $\xi_n(x)$  denote the Ricatti-Bessel functions  $xj_n(x)$  and  $xh_n^{(1)}(x)$  respectively, while the prime indicates differentiation with respect to the argument.  $\beta$  refers to the particle size as referred to in equation 5.2. The scattering that plays such a crucial role in the optical forces used to trap particles is the same scattering that we used in Chapter 2 to track and characterize the particles by means of so-called holographic microscopy. As in Chapter 2 for the calculation of the holograms, we used Cristian Mätzler’s Matlab<sup>®</sup> [13] code to calculate the scattering coefficients.

Another parameter of relevance for the trapping is the refractive index of the glass interface through which the light is focussed into the sample. In many experimental systems the refractive index of the solvent is lower than that of the glass,

which introduces spherical aberrations. See also section 4.7.1 in Chapter 4. In the following, the refractive index of the glass,  $n_{\text{glass}}$ , is assumed to be 1.51. The amount of refraction at an interface depends not solely on the refractive index contrast at this interface, but also on the angle of incidence through Snell's law. Finally, the actual amount of deformation of the focus due to spherical aberration depends on the distance from the geometric focus to the glass surface  $D$ , see also Figure 4.1. Unless stated otherwise  $D = 14 \mu\text{m}$ .

Because the more deflected beams contribute more to the trapping, it is useful to apply high numerical aperture lenses [14]. To get relatively much light in the outer beams, the back aperture of the objective is usually overfilled, effectively throwing away the light in the tails of the Gaussian intensity distribution. The effective fraction of power that enters the sample is given by:

$$A = 16\gamma_{\text{optical}}^2 \int_0^{\sin \theta_0} s \exp(-2\gamma^2 s^2) \frac{\sqrt{(1-s^2)(N^2-s^2)}}{(\sqrt{1-s^2} + \sqrt{N^2+s^2})^2} ds, \quad (5.5)$$

where  $\theta_0$  is the opening angle of the focussed beam,  $N = \frac{n_{\text{med}}}{n_{\text{glass}}}$  and  $\gamma_{\text{optical}}$  is the ratio between the *focal length* or *tube length* of the objective and the beam waist  $\omega_0$  at the back aperture of the objective. Equation 5.5 takes into account that the transmission at the glass-medium interface is a function of the angle of incidence. We do not take the angle dependence of the transmission of the objective [15] into account. Following the results of Astrid van der Horst [16] p. 131, we use

$$\gamma_{\text{optical}} = (n_{\text{med}}R_0)/(NA\omega_0), \quad (5.6)$$

where  $R_0$  is the radius of the back aperture of the objective and  $\omega_0$  is the beam waist, the radius of the beam at the  $1/e^2$ -point. For our setup with a beam width  $\omega_0 = 2.80 \text{ mm}$ , equipped with a  $100 \times 1.4 \text{ NA}$  oil immersion lens from Leica with  $R_0 = 3.4 \text{ mm}$ , used in a sample with ethanol ( $n_{\text{med}} = 1.36$ ), this comes down to  $\gamma_{\text{optical}} = 1.21$ . Furthermore we used  $\theta_0 = 64.245^\circ$ , and a laser wavelength  $\lambda = 1064 \text{ nm}$  in our calculations.

We represent the performance of optical traps with the dimensionless trapping efficiency in the lateral direction  $Q_\rho$  as defined by equation 4.2. For stable trapping there should be a spot in 3D to which the optical forces from all direction are directed. These optical forces should be stronger than the other forces acting on the particle. Examples of other forces acting on the particle are gravity, Coulomb forces, dipolar interactions and Brownian fluctuations. Should the particle be displaced by a non optical force it will then be pushed back to the trapping position [17].

With the parameters that characterize the focus in our setup using a  $100 \times 1.4 \text{ NA}$  oil immersion lens from Leica fixed, there are still quite some parameters to vary. In the following sections we will first introduce the trapping behavior of a  $1.4 \mu\text{m}$  silica ( $n_2 = 1.45$ ) spheres in ethanol ( $n_1 = 1.36$ ). This system has been chosen because it was often used in our experiments. Silica in ethanol forms a

rather stable dispersion which does not suffer from the growth of microorganisms. A diameter of  $1.4\ \mu\text{m}$  was chosen for imaging convenience and availability. For these particles we will first show the typical forces that are exerted by the laser. Then we will show how this varies with the trapping depth as a result of spherical aberration.

### 5.3 1.4 $\mu\text{m}$ silica spheres in ethanol

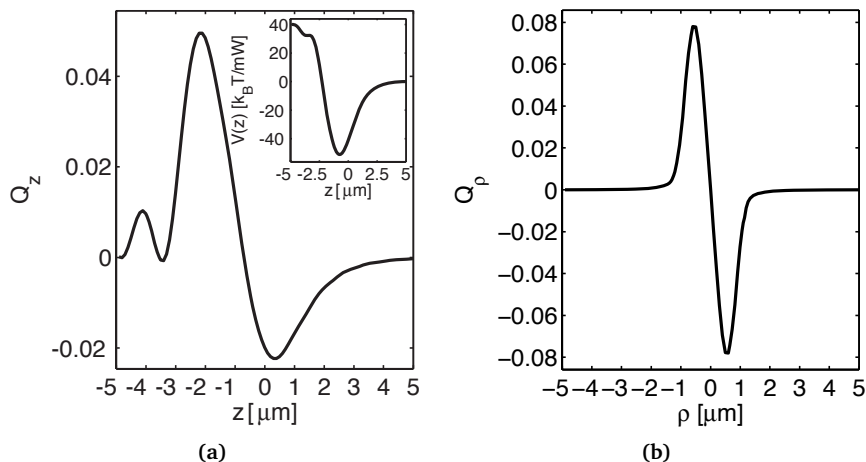


**Figure 5.1:** The trapping efficiency as a function of the distance to the geometric focus. **a.** The axial trapping efficiency  $Q_z$  as a function of the axial distance  $z$  from the geometric focus for a  $1.4\ \mu\text{m}$  silica particle trapped in ethanol at a depth of  $14\ \mu\text{m}$ , inset: the ‘potential’ obtained by integrating the optical forces over the optical axis. **b.** The lateral trapping efficiency  $Q_\rho$  as a function of the distance from the optical axis  $\rho$  at a trapping depth  $z_0 = -696\ \text{nm}$ .

A system that shows all the basic features of trapping dielectric spheres in some liquid, consists of a  $1.4\ \mu\text{m}$  silica ( $n_2 = 1.45$ ) sphere in ethanol ( $n_1 = 1.36$ ). This yields the moderate contrast  $m = 1.07$  and the particle is somewhat larger than a diffraction limited spot, which is similar in size to the wavelength of the trapping laser in the suspending medium, i.e. be a little over  $\lambda/n_{\text{med}} \approx 800\ \text{nm}$ .

We plot the axial trapping efficiency  $Q_z$ , or normalized force, as defined by equation 4.2, as a function of the distance to the geometrical focus, in Figure 5.1 **a.** When  $Q_z$  is positive, this means that the total force exerted by the light on the particle is in the positive  $z$ -direction. When  $Q_z$  is negative, the particle experiences a force, due to the so-called gradient force, in the direction opposite to the direction of propagation of the light.

For an inverted microscope, where the direction of propagation of the light is upwards, a negative trapping efficiency  $Q_z$  means literally a force downwards.

In the setup used, see also Chapter 1, we can trap either from below or from above, or both (see also section 6.2). In the following, unless stated otherwise, we assume trapping from below such that ‘up’ and ‘down’ correspond to the direction of the propagation of the light and the opposite direction respectively.

The curve in Figure 5.1 **a** clearly consists of two regions. Below a certain height,  $z_0$ , the particle experiences a positive force, i.e. the particle is pushed further up. If the particle is located above  $z_0$  however, it is pushed down. At a height  $z_0 = -696$  nm, the total force on the particle is zero. Whenever the particle, for instance due to a Brownian fluctuation, is located a bit below or above this location, it experiences a force back. We plot the force integrated over the optical axis, in the direction opposite to the direction of propagation of the light in the inset. There is a clear minimum of about  $50 k_B T$  at  $z_0 = -696$  nm, so below the focus, when 1 Watt of laser power is used to form the trap. When the well depth is a few  $k_B T$  deep, thermal fluctuations cannot overcome the well depth at reasonable timescales (depending on the experiment minutes or hours) and the particle is trapped.

At height  $z_0$  we calculated the trapping efficiency  $Q_\rho$ , or simply  $Q_\rho$ , as a function of the distance to the optical axis,  $\rho$ . This is plotted in the **b** section of Figure 5.1. The meaning of  $Q_\rho$  is similar to that of  $Q_z$ ; wherever  $Q_\rho$  is positive the particle is pushed to the right, while it is pushed to the left when  $Q_\rho$  is negative. Also in the lateral direction there is a point, on the optical axis, where the force on the particle is zero and where the particle is pushed back to. The particle is thus confined to one point in space.

As stated above, the particle experiences a force back down/up whenever the particle is located above/below the trapping plane and the same holds for excursions within the trapping plane. For excursions smaller than  $\sim \lambda / (2n_{\text{med}}) \approx 400$  nm, the force back is more or less linear with the displacement and the effect of the optical trap can be modeled as an (over-damped) harmonic oscillator, see also section 4.4. It is as if the particle were attached to the trapping location with little springs. The spring constants of the optical trap in respectively the axial and lateral direction are given by the spatial derivative of the force to the position;

$$\kappa_z = -\frac{n_1 P}{c} \frac{\partial Q_z}{\partial z} \quad (5.7)$$

and

$$\kappa_\rho = -\frac{n_1 P}{c} \frac{\partial Q_\rho}{\partial \rho}. \quad (5.8)$$

Here  $P$ , once again, is the power of the light in the sample and  $c$  is the speed of light in vacuum. The stiffnesses of the trap,  $\kappa_z$  and  $\kappa_\rho$  are often used to specify how strong the traps are. An method that is often used to measure forces is based on the stiffness. One can measure the force by measuring the displacement from the trapping location; multiplication with the stiffness gives the force [18].

For our  $1.4 \mu\text{m}$  silica particle trapped in ethanol with the geometrical focus at a depth of  $14 \mu\text{m}$ , using 1 W of laser power, we find a lateral trapping stiffness of

661.6 pN/ $\mu\text{m}$ , while in the axial direction we find the much smaller value of 192.6 pN/ $\mu\text{m}$ . That is roughly a factor 3 less in the axial direction than in the lateral direction, which is due to the fact that the focus is elongated in the  $z$ -direction. This is an inevitable result of the finite numerical aperture, with smaller gradients in the intensity in that direction.

A force of 4 fN corresponds to an energy penalty of  $1 k_B T$  per micrometer. The force-distance relation is generally considered linear. This is a fair approximation for excursions of the particle in the trap that are smaller than half the particle radius. For particles that are significantly larger than the laser focus, the deviation from the linear relation are larger at larger displacements [19, 20].

### 5.3.1 *Dependence of the trapping stiffness on the laser power*

Both the trapping efficiencies, or normalized forces  $Q_z$  and  $Q_\rho$ , as defined by equation 4.2, and the trapping stiffnesses as defined in equations 5.7 and 5.8 are linear in the laser power. The force exerted on the particle is the direct result of the rate of momentum change of the photons, the rate of momentum transfer is linear in the number of photons and thus in the laser power. In the following we will present experiments that confirm the linear dependence of the trapping stiffness on the laser power.

A 1.4  $\mu\text{m}$  silica particle was trapped in a continuous point trap made by the inverted objective of our setup, as described in Chapter 1. The particle was trapped at a depth  $D$  of 14  $\mu\text{m}$  above the bottom glass plate, see also Figure 4.7.1 for a graphical definition of depth  $D$ .

To facilitate holographic particle tracking as described in Chapter 2 and reference [21], it is important that the particle be trapped above the focal plane of the microscope. To realize this, the first lens of the telescope, lens L3, see also Chapter 1, was positioned such that laser beam was slightly divergent in the back aperture of the objective so that the particle was trapped a distance  $z_h$  of  $\approx 11 \mu\text{m}$  above the focal plane of the microscope. The distance between the particle and the glass bottom of the sample was again chosen to be 14  $\mu\text{m}$ . This means that the focal plane of the microscope was  $\approx 3 \mu\text{m}$  above the bottom glass plate. This situation is similar to the case for which we calculated the trapping forces above. The major difference is the fact that the particle is not trapped in the focal plane of the microscope but above it. The effect of this on the trapping will be discussed below in section 5.4.1.

The holograms of the particles were recorded on 160 by 182 pixels and the frame rate was set to 100 fps. To record a nice background (see Chapter 2), L3 was moved sideways to move the hologram of the particle out of the frame. After 1000 frames the particle was moved back in the frame. The power of the laser was kept constant for 3000 frames and then altered and again kept constant for 3000 frames, etcetera. This procedure was repeated three times in slightly different power ranges. The power at the back aperture of the inverted objective was measured separately using a Melles Griot Broadband Power/Energy 13PEN001

placed just before the dichroic mirror underneath the inverted objective. The laser power at the back aperture was found to be linear in the power sent to the laser. From the holographic snapshots we measured the particle coordinates using the method described in Chapter 2 and reference [21].

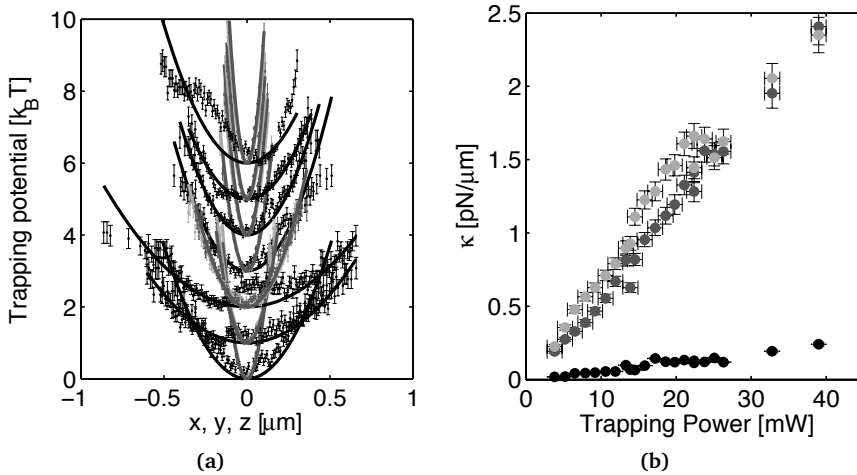


**Figure 5.2:** *Trapping and laser power.* **a.** The trapping potential in  $k_B T$  as a function of the distance to the average trapping location measured at different laser powers. The points are obtained from a histogram with  $10 \text{ nm}$  bins. The full lines represent fits to a harmonic potential, black was used for the axial trapping, grey and light grey were used for the two lateral directions,  $x$  and  $y$  respectively. For clarity we limited the powers to be represented in this plot to 3.8, 10.6, 17.2, 23.8, 32.8 and 39.0 mW of laser power at the back aperture of the objective, these potentials were given an offset of respectively 1, 2, 3, 4, 5 and 6  $k_B T$ . **b.** The fit values of the stiffness plotted versus the laser power in the back aperture of the objective using the same color coding as in **a.**

Figure 5.2 shows the result of applying the harmonic approximation to 3000 holographic measurements of the particle position for 22 different laser powers. Using the same method as presented by Florin *et al.* [22], we used the Boltzmann distribution to calculate the trapping potential from the probability distribution. These potentials have been determined by assuming that the system is in thermal equilibrium, such that we can apply the Boltzmann distribution to calculate the relative energy from the probability distribution as determined from the measured trajectories. Here we also assume that we can model the optical trap by three mutually perpendicular trapping stiffnesses, factoring the three dimensional probability distribution in three separate one-dimensional distributions. (See section 4.4.)

Figure 5.2 **a** shows the parabola associated with a harmonic trapping potential that is much wider in the axial direction than in the two lateral directions. This is due to the fact that the light is less focussed in that direction, due to the finite

numerical aperture of the objective [23], and it is also predicted by theory (see section 4.6.3). The linear increase with the laser power is clearly visible in Figure 5.2 b.

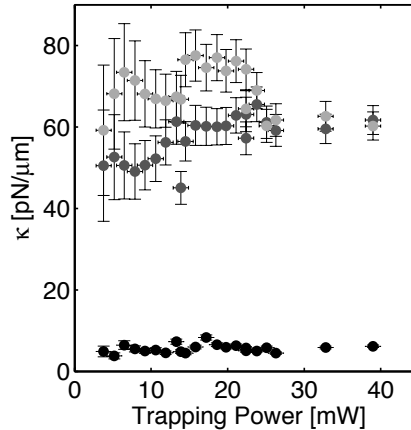


**Figure 5.3:** *Trapping efficiency.* The trapping stiffnesses per watt laser power  $\kappa_x$ ,  $\kappa_y$  and  $\kappa_z$  as a function of the laser power, black was used for the axial trapping, grey and light grey was used for the two lateral directions  $x$  and  $y$  respectively. The average stiffness in the  $x$ -direction, parallel to the polarization, was  $68 \pm 6$  pN/ $\mu\text{m}/\text{W}$ , in the  $y$ -direction perpendicular to the polarization we found an average stiffness of  $57 \pm 6$  pN/ $\mu\text{m}/\text{W}$ . The average stiffness in the  $z$ -direction was found to be  $5.6 \pm 1$  pN/ $\mu\text{m}/\text{W}$ .

The trapping stiffness per Watt is plotted as a function of the laser power in Figure 5.3 to show that it does not vary with the laser power. Apart from the noise, there is no power dependence of the trapping stiffness per Watt. We find a trapping stiffness of  $68 \pm 6$  pN/ $\mu\text{m}/\text{W}$  in the  $y$ -direction, along the polarization direction of the trap. In the  $y$ -direction, perpendicular to the polarization of the trap, we find a trapping stiffness of  $57 \pm 6$  pN/ $\mu\text{m}/\text{W}$ . The difference between the stiffness in the  $x$ -direction, along the polarization of the light and the  $y$ -direction, perpendicular to the polarization of the light, has been reported before [12, 24, 25].

In the axial direction we find a lower trapping efficiency of  $5.6 \pm 1$  pN/ $\mu\text{m}/\text{W}$ . The factor between the lateral and axial trapping efficiency in the calculations was about 3.4 for this trapping depth. This ratio generally depends also on the numerical aperture, the amount of spherical aberration, details of the objective and the optics present in front of the objective.

The experimentally observed trapping efficiency is much lower than what was calculated, although this type of trapping efficiency has been reported before for traps that have been placed above the focal plane of the microscope to facilitate Digital Holographic Microscopy [26, 27]. The quantitative disagreement between the calculations and experiments here presented is partially due to some absorp-

tion in the objective and the dichroic mirror that were positioned between the sample and the location where we measured the laser power. Another factor is the ‘misalignment’ introduced by positioning L3 such that the particle is trapped at a distance  $z_h = 11 \mu\text{m}$  above the focal plane of the microscope to facilitate holographic tracking. See also section 5.4.1. Last but certainly not least it could very well be that the alignment of the setup was sub-optimal. If the beam was not well centered, for instance, this may have caused a deformation of the trap such that the trapping in the axial direction was less stiff.

As described in section 4.4, Marco Polin *et al.* developed a technique to use the information that is contained in the actual trajectory of the particle in combination with the Langevin equation [28]. We applied this algorithm to the particle trajectories to check the results obtained with the fitting of the harmonic potential to the apparent localizing potential.

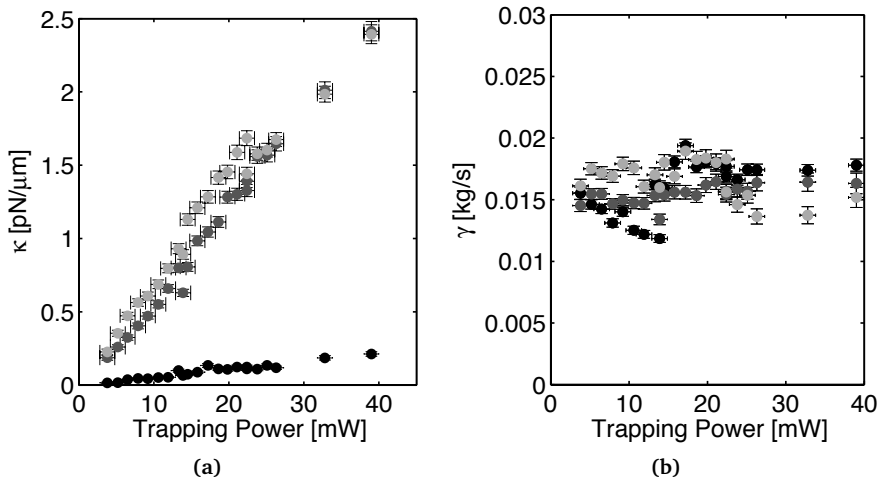


**Figure 5.4:** *Trapping stiffness from the Langevin equation.* **a.** The values of the stiffness from fitting to the Langevin equation plotted versus the laser power in the back aperture of the objective. Black was used for the axial trapping, grey and light grey was used for the two lateral directions,  $x$  and  $y$  respectively. **b.** The fit values for the drag coefficient  $\gamma$  versus the laser power in the back aperture of the objective, the average value of  $\gamma$  was  $0.016 \pm 0.002 \text{ kg s}^{-1}$ .

From a comparison between Figure 5.2 and Figure 5.4 can be seen that these methods yield similar results for the trapping stiffness, as the values fall in their mutual range of uncertainty, about 2 % of the value. The noise around the linear trend is somewhat different between the two measurement techniques and the error estimate is a little smaller when using the extra information from the trajectory that the particle followed. In this method, the correlation between consecutive positions contributes to the measurement of the trapping stiffness. We note that this is different from the method based on the probability density distri-

bution via the Boltzmann distribution, as here the statistics get poorer when the individual measurements of the particle positions are correlated.

Another advantage of fitting to the Langevin equation is that it also gives an accurate value for the Stokes friction factor  $\gamma = 6\pi\eta r$  when the frame rate of the trajectory is comparable to the corner frequency of the trap [28].

The estimate of the friction factor is fairly constant over the data presented in Figure 5.4. The stiffnesses in the axial and in the lateral directions cover two orders of magnitude from  $0.016 \pm 0.005$  pN/ $\mu\text{m}$  in the axial direction to  $2.39 \pm 0.06$  pN/ $\mu\text{m}$  in the  $x$ -direction. The average friction factor of  $0.016 \pm 0.002$  kgs $^{-1}$  agrees within the error with the friction factor based on the optically fitted radius of  $0.730 \pm 0.005$   $\mu\text{m}$ , where the viscosity is the largest uncertain factor.

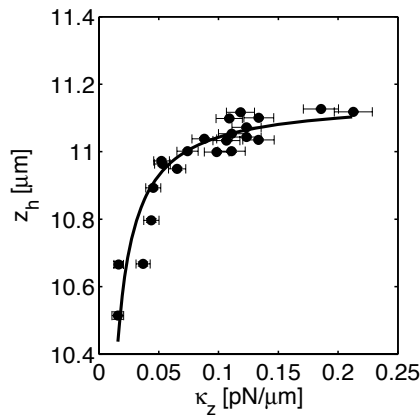


**Figure 5.5:** *Trapping depth versus trapping stiffness.* The depth  $z_h$  as a function of the axial trapping stiffness. The solid black line is a fit to  $z' = F/\kappa_z$ .

As the laser power was increased, the distance between the focal plane and the microscope,  $z_h$ , also increased. The trap stiffness increases with increasing laser power. If the particle is trapped, the effective gravitational force on the particle is counter-balanced by the optical forces on the particle. In order to realize this force the ‘optical spring’ that connects the particle to its equilibrium position has to be stretched. When we increase the power of the trapping laser, we effectively make this spring stiffer. The displacement of the particle from the equilibrium position,  $z'$ , the stiffness of the trap  $\kappa_z$  and the buoyant force on the particle are related via  $z' = F/\kappa_z$ . The full line in Figure 5.5 corresponds to a buoyant mass of the particle of  $1.2 \pm 0.6$  pg. This is in agreement with the weight of the particle  $1.81 \pm 0.04$  pg, based on the optical radius and a density of silica of  $1.92$  g/cm $^3$  [21] and the density of the ethanol of  $0.789$  g/cm $^3$ . The fit suggests that the equilibrium position of the trap in the absence of gravity or at infinite laser power would have been  $11.16$   $\mu\text{m}$  above the focal plane of the microscope.

## Conclusion

We have shown that our setup can optically trap a  $1.4\ \mu\text{m}$  silica particle in ethanol while we track the particle using Digital Holographic Microscopy. The trapping stiffness was observed to be linear in the power of the trapping laser. This indicates that the optical tweezer was working correctly. From the variation in the trapping position of the particle with different laser powers the weight of the particle could be deduced. This indicates that the tracking of the particle worked correctly, also in the out-of-plane direction.

### 5.3.2 Spherical aberration

Another observation in Figure 5.1 **a** on page 182 for the axial trapping efficiency  $Q_z$  is the small wiggle at some about  $4\ \mu\text{m}$  below the geometrical focus. This is the result of spherical aberration; some of the outer rays are refracted inwards at the glass/ethanol interface creating paraxial focuses below the geometric focus. These paraxial, secondary focuses also exert forces on the particle. Due to interference, there are intensity gradients with resulting gradient forces. In this case, the local minimum of the trapping force is still above zero, so the particle is still pushed upwards there. However, this effect is stronger for smaller particles or traps that are focussed deeper in the sample, and can result in multiple trapping locations [15].

The fact that the particle is trapped a distance  $z_0$ , below the geometrical focus is a result of spherical aberration as well. In the absence of spherical aberration, the particle would be trapped beyond the geometric focus such that the gradient force compensates the scattering force. In the presence of spherical aberration the particle is trapped somewhat above the effective focus, but the effective focus is located below the geometrical focus.

From Figure 5.6 **a** we learn that also for the  $1.4\ \mu\text{m}$  silica particle in ethanol, the effect of spherical aberration can be such that there is a second effective trap ( $4.72\ \mu\text{m}$  below the focus) when the geometrical focus is placed deeper ( $30\ \mu\text{m}$ ) in the sample. The energy barrier to escape from this second trap is only  $0.37\ k_B T$  when the laser power on the back aperture of the objective is  $1\ \text{W}$ . The horizontal forces at this trapping depth in Figure 5.6 **b** are smaller than in the primary trap but there is a region in space in which the optical forces are all directed to one point. So strictly speaking this is an optical trap. However the region over which this secondary trap extends is relatively small and, depending on the laser power, eventually the particle will probably end up in the primary trap, closer to the geometrical focus.

The spherical aberration gets progressively worse for larger trapping depths as can be seen in Figure 5.7. The effect is particularly visible for the curves representing the trapping efficiency in the axial direction  $Q_z$ , these curves are stretched along with the focus. On the other hand, the curves for the lateral trapping efficiency retain more or less their shape under the influence of an increasing trap-

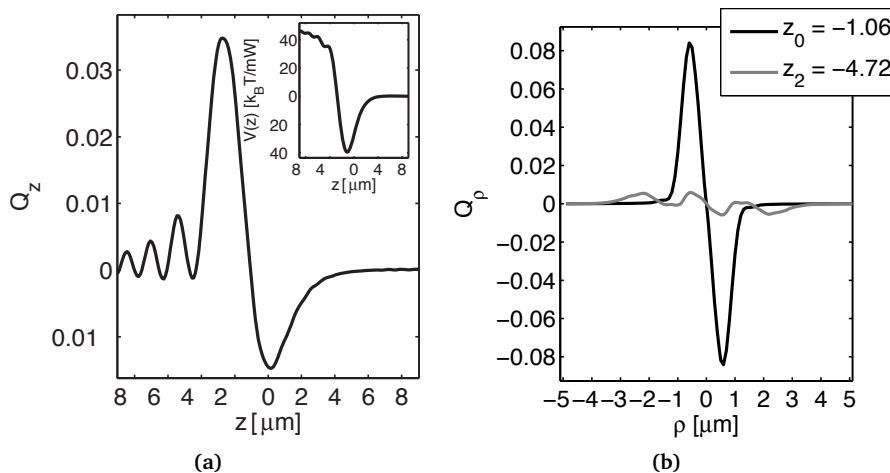


**Figure 5.6:** The trapping efficiency as a function of the distance to the geometric focus, further from the wall. **a.** The axial trapping efficiency  $Q_z$  as a function of the axial distance  $z$  from the geometric focus for a  $1.4 \mu\text{m}$  silica particle trapped in ethanol at a distance of  $30 \mu\text{m}$  from the glass wall. **b.** The lateral trapping efficiency  $Q_\rho$  as a function of the distance from the optical axis  $\rho$  at the trapping height  $z_0 = -1.06 \mu\text{m}$  and the secondary trapping height  $z_2 = -4.72 \mu\text{m}$ .

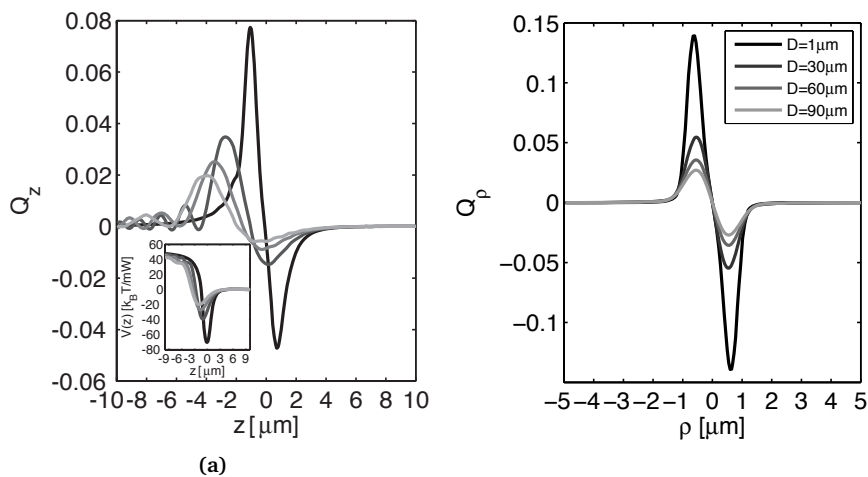


**Figure 5.7:** Trapping efficiencies at different depths. **a.** The axial trapping efficiency  $Q_z$  as a function of the axial distance  $z$  from the geometric focus for a  $1.4 \mu\text{m}$  silica particle trapped in ethanol at depths of respectively 1, 30, 60, and 90  $\mu\text{m}$ . **b.** The lateral trapping efficiency  $Q_\rho$  as a function of the distance from the optical axis  $\rho$  at the trapping height  $z_0$ .

ping depth. The main effect is that the forces become smaller as the intensity and thus the gradients in the intensity become smaller with increasing spherical aberration and trapping depth.

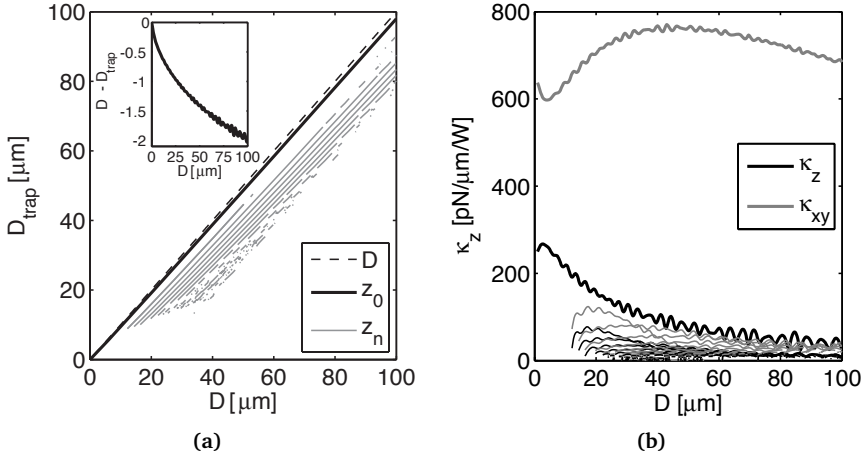


**Figure 5.8:** The influence on the trapping stiffness of the distance to the glass wall. **a.** The axial trapping position in  $\mu\text{m}$  with respect to the bottom of the sample as a function of the trapping depth. The dotted line represents the position of the geometrical focus, the full line gives the position of the main trap  $z_0$ , while the grey lines represent the depths of the secondary traps. The inset shows the distance between the geometrical focus and the main trapping location as a function of the trapping depth. **b.** The influence of the trapping depth on the axial and lateral trapping stiffnesses. Thick lines represent the properties for the main trap, black is used for the axial direction while grey is used for the lateral directions. Thin lines are used for the secondary traps.

We varied the trapping depth more systematically in Figure 5.8 **a.** We give the trapping location  $z_0$  with respect to the geometrical focus as a function of the distance between this focus and the glass-ethanol interface that caused the spherical aberration. The particle is progressively trapped further below the geometrical focus as the geometrical focus is positioned deeper into the sample. This is consistent with the qualitative image of the spherical aberration in Figure 4.1. The outer light rays are focussed closer to the glass providing even shallower angles of illumination, corresponding to high(er) numerical apertures. This would potentially give rise to larger intensity gradients and thus trapping forces. However, as every ray is refracted in a slightly different manner, focusing at a different depth, the intensity gradient in the  $z$ -direction diminishes and also in the lateral direction the intensity gradients are reduced. One might expect that the trapping location shifts more that, roughly like the effective focus  $n_1/n_{\text{glass}}D \sim 0.9D$  [29, 30], but apparently, the decrease of the intensity gradient is such the particle is trapped (further) above the paraxial focus. This is all the more clear from the inset in Figure 5.8 **a,** in which we plotted the distance between the actual trap

and the depth of the geometrical focus. Not only is it clear that this distance is by far not similar to roughly a tenth of the depth of the geometrical focus, the distance between the geometrical focus and the trapping location seems to even level off. This qualitatively agrees with the results by Neuman *et al.* [31].

For larger trapping depths there appear secondary traps, as was observable in Figures 5.1, 5.6 and 5.7. These traps are further below the geometrical focus, also for these traps the actual trapping depth does not really seem to follow the paraxial focus.

We examine the effects on the trapping stiffnesses of the depth  $D$  into the sample in Figure 5.8 **b**. At small depths of roughly  $5\ \mu\text{m}$ , the increased intensity gradients cause a slight increase in the axial trapping stiffness (black line); effectively we have a slightly higher numerical aperture. However, for larger depths we there is a steady decrease in the stiffness with the trapping depth which is in agreement with the picture of the focus that gets stretched.

The trend in the lateral direction is quite different. Due to the absence of the scattering force, there are impressive stiffnesses for every trapping depth. For small trapping depths we find a slight decrease in lateral stiffness. For larger depths however, we first there is a rather interesting increase in stiffness with a rather broad maximum at a depth of roughly  $50\ \mu\text{m}$ , which is some about 25% higher than at the minimum. This is an interesting observation which contrasts with the findings of Im *et al.* [32], in the ray optics regime. Larger gradient forces suggest larger intensity gradients. Although one might naively think that a stiffer trap is formed by a smaller focus, this is not always the case for larger particles as we will also show in section 6.5. In this section we will look into the effect of multiple traps that are overlapping on the stiffness. We find an explanation for the increase in trapping stiffness in the lateral direction for greater trapping depths in Figure 5.8.

Both in Figure 5.8 **a** and in Figure 5.8 **b**, there are some oscillations on top of the general trends of the curves. The lens is designed such that all the light interferes constructively in the geometrical focus when there is no spherical aberration, i.e. all the light is in phase when it passed through the focal point. Due to the spherical aberration the light is no longer all focussed on the same spot. The outer beams are focussed closer to the glass/ethanol interface. This has also implications for the relative phase. The path length to the optical axis where the light is focussed is no longer the same throughout the whole focal region. This results in positive and negative interference, which in turn gives rise to local intensity gradients that change the trapping positions. The oscillations in the trapping depth and trapping stiffness are caused by the same phenomenon that causes the appearance of secondary traps.

The representation of the lateral trapping efficiency in Figures 5.1, 5.6 and 5.7 is slightly misleading in the sense that they have been calculated in the lateral plane at the stable trapping depth  $z_0$ . However, as mentioned in literature, these calculations predict [2] and experiments in the ray optics regime [33] and in the

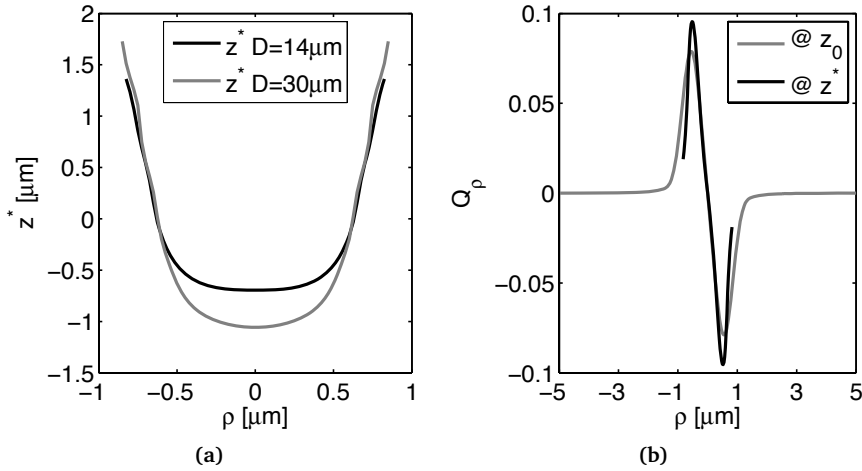


**Figure 5.9:** The trapping depth as a function of the lateral displacement. **a.** The actual axial trapping position,  $z^*$ , in  $\mu\text{m}$  with respect to the geometrical trapping depth as a function of the lateral displacement for a  $1.4\ \mu\text{m}$  silica particle in ethanol. The black and grey lines indicate the behavior with the geometrical focus at a depth of  $14\ \mu\text{m}$  and  $30\ \mu\text{m}$  respectively. **b.** In black, the trapping efficiency at the actual trapping position at a trapping depth of  $14\ \mu\text{m}$ , the grey line indicates the horizontal trapping efficiency at the trapping depth at the optical axis,  $z_0 = -696\ \text{nm}$ .

Lorenz-Mie regime [20, 34] confirm, that when a particle is, by some an external force, laterally displaced, it finds a different stable trapping depth,  $z^*$ . We plot the axial trapping position as a function of the lateral displacement in Figure 5.9.

At a certain displacement of roughly  $900\ \text{nm}$  sideways, there is no longer a stable trapping depth. The grey line for the trapping position with respect to the geometrical focus at depth  $D$  of  $30\ \mu\text{m}$  in Figure 5.9 **a** shows once more that the particle is trapped further below the geometrical focus when this lies deeper in the sample, causing more spherical aberration. For larger lateral displacements, however, this effect is more than compensated as the smaller intensity gradient necessitates a larger axial displacement to compensate the larger off-axis scattering force. The lateral trapping force is slightly larger at the actual trapping depths that are associated with the larger lateral displacements as can be seen in Figure 5.9 **b**.

### Spherical aberration in an experiment

The refractive index of ethanol ( $n = 1.36$ ) is lower than that of the glass plate ( $n = 1.51$ ) which causes spherical aberration. The light is refracted when entering the sample, changing direction. The amount of deflection is larger when the angle with the normal of the interface is larger. This causes a deformation of the focus, that is also a function of the distance between the trap and the particle. See

section 4.7.1.

In the experiments here presented, we trapped a  $1.4 \mu\text{m}$  silica particle in ethanol while we varied the distance  $D$  from the glass plate to the geometrical focus. We tracked the particle using Digital Holographic Microscopy, as described in Chapter 2. To facilitate holographic tracking the particle was trapped a distance  $d_h = 9.8 \mu\text{m}$  above the imaging plane. At each depth we recorded 6000 frames of 160 by 168 pixels, at a framerate of 200 Hz. In the experiment we determined the distance to the bottom of the sample by moving the sample upwards in steps of  $1 \mu\text{m}$ , using our piezostage, until we observed that the particle was pushed upward by the bottom, after which we moved the sample down. This gives our estimate of  $D$  an error of  $\sim 1 \mu\text{m}$ . The depth was then varied in  $5 \mu\text{m}$  steps.

From the trajectories we deduced the trapping stiffness and the friction factor as described in [28]. In Figure 5.10 we plot both the trapping stiffness and the friction factor  $\gamma$ . Figure 5.10 a gives the trapping stiffnesses as a function of the trapping depth. The trapping stiffnesses from our calculations are shown in Figure 5.8. Both lines have been rescaled to correct for the different power used in the experiment and other effects that cause weaker trapping in our experiments, such as the distance between the trapping plane and the focal plane of the microscope. Similar to section 5.3.1, we find that the axial stiffness is relatively weaker with respect to the lateral stiffnesses when compared to the calculations. In section 5.4.1 we will discuss this more in detail.

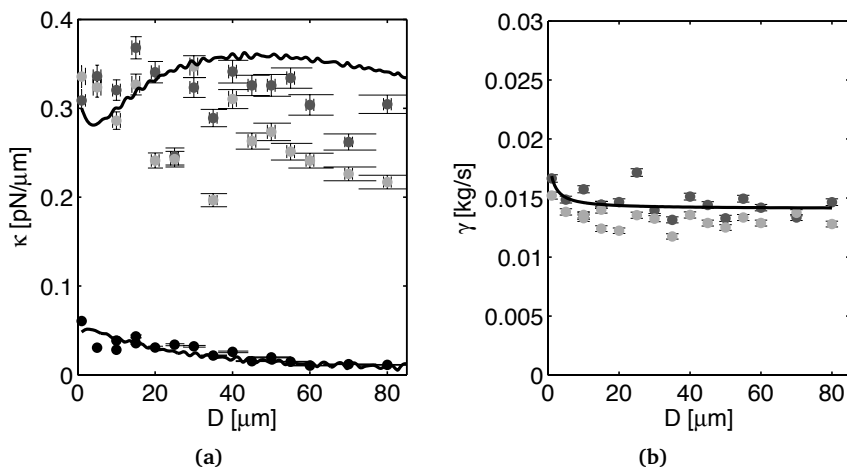


**Figure 5.10:** The trapping behavior as a function of the trapping depth. **a.** The trapping stiffnesses in the two lateral directions (light grey  $\times$  and dark grey  $\text{y}$ , and the axial direction  $z$  (in black), as deduced from measured trajectories, plotted against the trapping depth. Full lines mark the trapping stiffnesses from Figure 5.8 scaled by a factor of  $4.8 \cdot 10^{-4}$  in the lateral direction, and by a factor of  $1.7 \cdot 10^{-4}$  in the axial direction. **b.** The hydrodynamic drag in the lateral directions as a function of the trapping depth. The full curve is a fit to Faxen's law.

For the axial stiffness we find that the calculations fit well with the experimental results. The shape of the decline of the axial trapping stiffness is well described by the theory. In the lateral directions however, we find experimentally that the trapping stiffness decreases stronger with increasing trapping depth than the calculations suggest. We also note a relatively large spread in the measured values. Possibly this is due to irregularities in the bottom glass plate and the fact that we trap the particle at slightly different positions from point to point. Why this had a smaller effect on the axial trapping we do not know.

The friction factor in the lateral directions is plotted in Figure 5.10 **b** as a function of the trapping depth. In the axial direction we found that the trapping stiffness was so low that the corner frequency of the trap was too different from the frame rate to estimate the friction factor [28]. The friction factor at depths less than about 10  $\mu\text{m}$  is significantly higher than at larger depths. This is due to lubrication effects that are modeled by Faxen's rule [35]:

$$\gamma = \frac{6\pi\eta r}{1 - \frac{9}{16}\left(\frac{r}{D-D_0}\right) + \frac{1}{8}\left(\frac{r}{D-D_0}\right)^3 - \frac{45}{256}\left(\frac{r}{D-D_0}\right)^4 - \frac{1}{16}\left(\frac{r}{D-D_0}\right)^5}. \quad (5.9)$$

Here  $\eta$  is the viscosity of the liquid,  $r$  the radius of the particle and  $D - D_0$  the distance from the wall. For large distances to the wall this equation goes to the Stokes friction in equation 4.4;  $\gamma = 6\pi\eta r$ . The full line is a fit of equation 5.9 to the measured friction factors. The fitting parameters we used were the viscosity of ethanol and the offset of our depths. The particle radius was kept constant at the optical fit value of  $0.69 \pm 0.3 \mu\text{m}$ . The offset we found was  $1.67 \mu\text{m}$  which is a reasonable value considering the method we used to determine the trapping depth  $D$ . The viscosity of the ethanol was found to be  $1.024 \pm 0.003 \text{ mPa s}$ . This is in accordance with the temperature in the lab of  $26^\circ\text{C}$  [36].

## Conclusion

We have shown calculations of the effect of spherical aberration on the trapping behavior of a  $1.4 \mu\text{m}$  silica sphere in ethanol. We also performed measurements on this system. A qualitative agreement between the calculations and the measurements was observed in the lateral directions for the effect of spherical aberrations on the trapping behavior. In the axial direction the effect was described almost quantitatively by the calculations. The disagreement in the lateral directions between the calculations are probably the result of an inhomogeneous glass plate. From the same measurements we determined the friction factor on the particle as a function of the distance from the wall. The increase of the friction due to lubrication effects as the particle approaches the wall was experimentally observed and could be effectively fit with Faxen's law.

### 5.3.3 Non-conservative forces

In Figure 5.1 **a**, (on page 182), the total areas of the curve above and below zero are not equal to each other. This is due to the scattering force that points in the direction of the propagation of the light, everywhere. In the inset of the same Figure, the integral of the trapping efficiency over the optical axis is plotted. One can easily understand that the energy at the beginning is higher than at the end of the curve. Clearly, the integration of the force field does not yield the same ‘potential’ independent of the integration path. This means that the forces exerted by optical traps are non-conservative, as was mentioned before in literature [14, 26, 37, 38], see also section 4.7.2. It is easy to understand why the non-conservativeness of the total force should be due to the scattering force if we allow ourselves to regard the forces exerted by optical tweezers as consisting of two contributions i.e. if we consider optical traps in the Rayleigh regime, the gradient force (equation 4.13) and the scattering force (equation 4.11). The gradient force, after all, is linear in the *gradient* of the intensity. If the particle follows a closed path, rising along the optical axis where it is pushed up by the scattering force, and comes down somewhat further away from the optical axis, experiencing a smaller scattering force before it goes back to the optical axis, the optical force field exerts work on the particle.

It is clear that the gradient force, which is the only force playing a role in the lateral direction, is conservative in Figure 5.1 **b**. This can be seen from that fact that the area under the positive part of  $Q_\rho$  is equal to that above the negative part. The fact that the force field exerted by the optical tweezers is non-conservative, makes that we cannot speak of the potential landscape. Instead, we depict the force field in both the axial and lateral directions separately. This has been done in Figure 5.11 for the 1.4  $\mu\text{m}$  silica particle in ethanol. The force is represented by grey values such that for the brighter shades the particle is pushed in the positive direction. Dark shades mean that the particle is pushed in the negative direction. The axial forces are depicted in Figure 5.11 **a**. In the lateral direction in Figure 5.11 **b**, brighter shades indicate that the particle is pushed to the right. Clearly there is a region where the particle would be pushed back to the optical axis and along the optical axis to the trapping position. These graphs can help in understanding the trapping behavior of certain particles as we will see in the following sections.

The fact that the optical forces in the axial direction at off-axis positions balance at a different depth as was plotted in figure 5.9 is also visible from the curved shape of the bright, positive axial trapping efficiency zone in Figure 5.11, or, more accurately from the curved shape of the iso-force curve at zero force in the same Figure.

We can also represent the force field as a vector field as is shown in Figure 5.12. In this representation one can see the direction of the local force. In this Figure we drew a possible trajectory that a particle might follow under the influence of thermal fluctuations and the optical forces. In the inset the optical forces

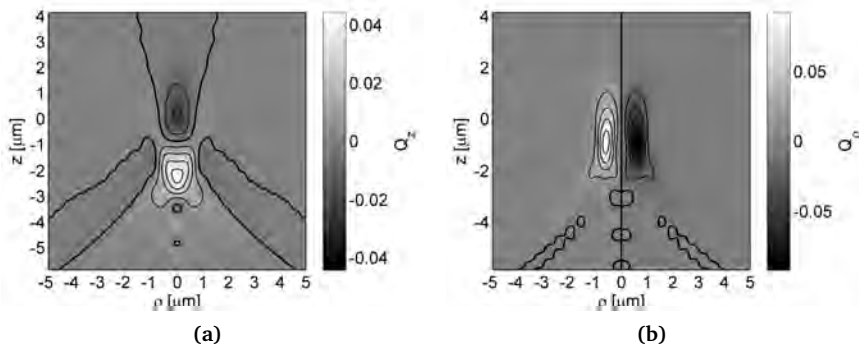


**Figure 5.11:** The trapping forces as a function of the position. **a.** The axial trapping efficiency  $Q_z$  a  $1.4 \mu\text{m}$  silica particle trapped in ethanol as a function of the position. The origin is located in the geometric focus for at a depth of  $14 \mu\text{m}$ . **b.** The lateral trapping efficiency  $Q_\rho$  as a function of the position. The trapping efficiencies in both graphs are represented by grey values, for clarity some iso-force curves were added with the one for  $Q = 0$  slightly thicker.

have been integrated over this trajectory. The light field performs  $7.9 k_B T$  of work on the particle in a trap powered by only  $1 \text{ mW}$  that follows the drawn trajectory, once again illustrating that the optical forces exerted by a diffraction limited focus are non-conservative.

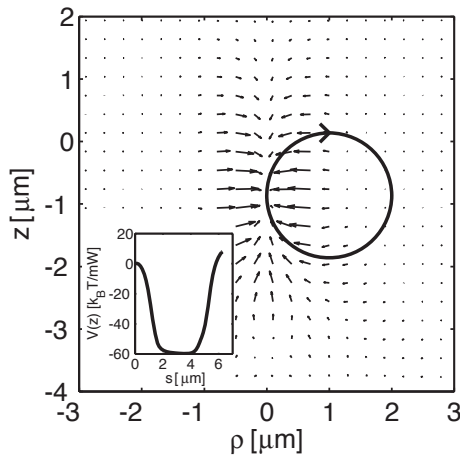


**Figure 5.12:** Vector representation of the optical forces. The force field around the geometric focus for a  $1.4 \mu\text{m}$  silica particle trapped in ethanol at a depth of  $14 \mu\text{m}$  represented as vectors. The full line represents a possible trajectory. In the inset the optical forces were integrated clockwise along the trajectory as drawn the main figure, one round on this particular trajectory gives a  $7.9 k_B T$  energy gain per  $\text{mW}$  of laser power.

### Experiment on the non-conservative nature of optical traps

To test the nonconservativeness of our traps we trapped a  $1.4 \mu\text{m}$  silica particle in ethanol using  $\approx 15 \text{ mW}$  of laser power at the back aperture of the objective. The particle was trapped at 7 different depths while we recorded 30,000 holographic snapshots of 320 by 360 pixels at 40 Hz. From the 30,000 measurements of single particle positions we determined the apparent trapping potential to which we fitted a harmonic potential to determine the trapping stiffnesses [22].

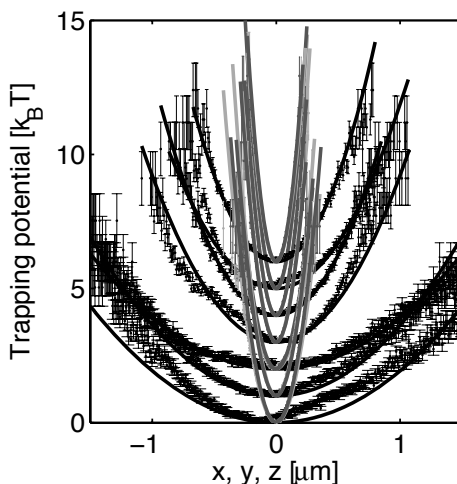


**Figure 5.13:** *Trapping potential.* The trapping potential in  $k_B T$ , in the axial, black, and lateral directions, grey and light grey. The points are obtained from a histogram with  $10 \text{ nm}$  bins. For clarity the potentials taken at respectively 92, 72, 52, 32, 22, 12 and  $2 \mu\text{m}$  above the bottom glass plate have been given offsets of 0, 1, 2, 3, 4, 5, 6 and  $7 k_B T$ .

The apparent trapping potentials in the three different directions is plotted in Figure 5.13 as a function of the deviation from the equilibrium position. These potentials have been determined by assuming that the system is in thermal equilibrium such that we can apply the Boltzmann distribution to calculate the relative energy from the probability distribution as determined from the measured trajectories. Here, we also assume that we can model the optical trap by three mutually perpendicular trapping stiffnesses, factoring the three dimensional probability distribution in three separate one-dimensional distributions. We note that the spherical aberration increases with the trapping depth  $D$ ; this causes the particle to be less confined as was also shown in section 5.3.2. With Yohai Roichman *et al.* [26] we study the extent to which the trap is not conservative for our particle by quantifying the circulation the particle performs. Since the axial stiffness is smaller than the lateral stiffnesses, the particle explores a roughly elliptical region around the equilibrium position. Therefore we consider the particle trajectory in

cylindrical coordinates  $\mathbf{r} = (\rho, \phi, z)$ . If the trap is nonconservative, the particle should rotate (clockwise) in the  $\rho, z$  plane. We quantify the instantaneous circulation rate over the  $\tau = 1/40$  s interval between consecutive frames;

$$\Omega(t) = \frac{1}{2\pi\tau} \frac{[\mathbf{r}(t+\tau) \times \mathbf{r}(t)] \cdot \hat{\Phi}}{\sqrt{\langle (\rho - \langle \rho \rangle)^2 \rangle \langle (z - \langle z \rangle)^2 \rangle}} \quad (5.10)$$

The angle brackets denote the average over the trajectory and  $\hat{\Phi}$  is the unit vector in the  $\Phi$  direction.  $\Omega$  is positive for clockwise rotation in the  $\rho, z$  plane. The force field in this plane has been represented by vectors in Figure 5.12. To identify trends that would normally be swamped in thermal noise in  $\Omega(t)$  we define:

$$\chi(t) = \int_0^t \Omega(t') dt', \quad (5.11)$$

which measures the accumulation of clockwise circulation.

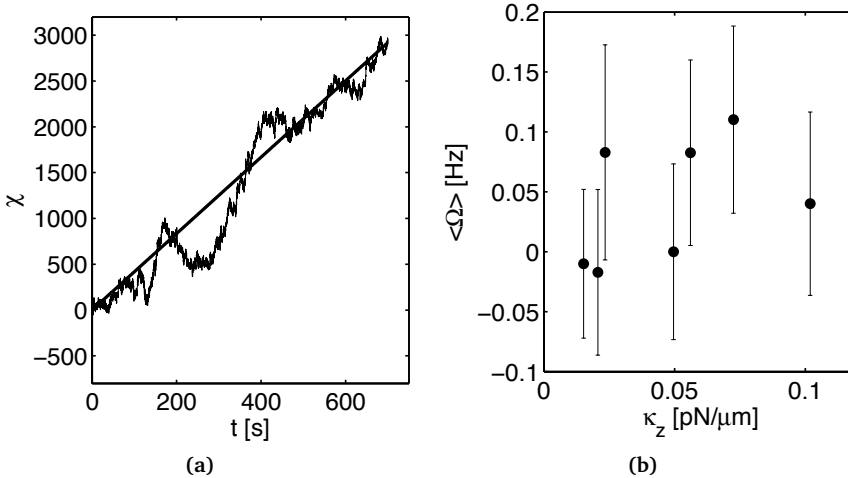


**Figure 5.14: Accumulated circulation.** **a.** The accumulated circulation  $\chi$  of a single  $1.4 \mu\text{m}$  silica particle in ethanol at a trapping depth of  $22 \mu\text{m}$ . The straight line has a slope of  $\langle \Omega \rangle$ . **b.** The average circulation rate  $\langle \Omega \rangle$  as a function of the axial trapping stiffness.

There is an increasing trend in the accumulated circulation with time for the particle in the trap at a depth  $D$  of  $22 \mu\text{m}$  in Figure 5.14 **a**. This shows that there is a circulating steady state in which the particle on average makes one net cycle in 10 seconds. In Figure 5.14 **b** we plot the average circulation rate as a function of the axial stiffness. The error bars are large but it seems that the rotation rate does increase with increasing trapping stiffness. Roichman *et al.* [26] observed an increase in the rotation rate with increasing laser power, and thus

with increasing trap stiffness. In our case, with constant laser power but varying degrees of spherical aberration by varying the depth in the sample, a stiffer trap means more focussed light and thus larger scattering forces that contribute to the rotation in the  $\rho, z$  plane. The least focussed beam conceivable would be a parallel beam, the radiation pressure of which is the same everywhere such that the force field is conservative. A result of the non-uniform radiation pressure is an underestimation of the forces as measured by thermal fluctuation analysis. The circulation is excited by thermal fluctuations, which suggests that the example of trapped particle is an example of a Brownian motor [26, 39], but because there is no time-dependent forcing to break detailed balance, this is Brownian vortex [40]. Depending on the effective temperature, which can be manipulated by changing the strength of the potential, the laser power, or as was demonstrated in this section, the amount of spherical aberration. The rotation direction can be inverted [40, 41].

## Conclusion

Both in calculations and in experiments we demonstrated that the force-field exerted by optical traps is non-conservative as a result of the radiation pressure. The particle in the experiments was observed to perform clockwise rotations in the trap that were the result of the effective work performed by the scattering force. The trap forms a Brownian vortex.

## 5.4 Measurements of setup specific phenomena

In order to form a good focus, one needs to shine a perfectly parallel beam into the back aperture of the objective. In the calculations above, we assumed this was the case. To allow for holographic measurements however, the trapping plane and the microscope plane have to be separated by a few micrometer, height  $d_h$ , see Chapter 2. This is realized by moving lens L3, see Chapter 1, along the optical axis as described in [42] to make the beam slightly divergent.

In some experiments we use time-sharing to create multiple traps [43–45]. Here, the laser light is scanned rapidly between multiple locations, using for instance an Acousto Optical Deflector, AOD. Each individual trap is then blinking on and off. On the longer time scale, the particle experiences the time averaged potential. The traps should be switched off only for a limited amount of time to make sure that the particle does not diffuse away, out of the range of the trap. Deng *et al.* [46], reasoned that the switching of the traps should happen at rates higher than the corner frequency of the traps to prevent an increase in the variance of the particle position. There has been discussion about the influence of non-linear effects of variations in the laser power on extremely short timescales (fs), like the so-called ponderomotive forces, see [47] and references therein. See also section 4.7.3. Using the AODs in our setup we can vary the switching rate

of our traps over several orders of magnitude, from switching the traps every 3.2  $\mu\text{s}$  to every few seconds. This switching we normally do to make multiple time-shared traps, so it is interesting to know what the effect of the switching rate on the trapping behavior is.

In this section we will first, (section 5.4.1) study the influence of the distance  $z_h$ , between the trapping and imaging plane on the trapping behavior. Then we will show experimental results on the effect of the switching rate of the traps on the trapping behavior in section 5.4.2.

### 5.4.1 *The influence of the distance between imaging and trapping plane*

To allow for Digital Holographic Microscopy [21], the distance  $z_h$  between the focal plane of the microscope and the particle under investigation has to be at least a few micrometer to allow for good particle characterization, see also Chapter 2. The larger the distance  $z_h$  between the scattering particle and the focal plane of the microscope, the larger the hologram and the more pixels record the interference pattern. To a first approximation, the hologram can be enlarged, at the cost of a decreased brightness, by increasing the distance between the particle and the focal plane. The calculations of the trapping behavior assume that the laser is focussed in the focal plane of the microscope. In reference [42], a telescope with a magnification of unity was used to be able to position the trap. To this end the first lens of the telescope, in the plane conjugate to the focal plane of the microscope, was mounted on an  $xyz$  stage, to be able to move the trap in the  $x$ -,  $y$ - and  $z$ -direction. We use the same technique to provide for the distance between the trapping plane and the focal plane of the microscope, see also Chapter 1 and reference [45].

In the following, we present experiments where we varied the position of the first lens L3 of the telescope along the optical axis. For every position of we recorded 6000 frames of 320 by 320 pixels at 100 fps. From these in-line holograms we measured the particle position in 3D, from the trajectories we then determined the stiffness and trapping location. After the lens L3 was placed in position the sample was moved up until the bottom visually touched the particle, a 1.4  $\mu\text{m}$  diameter silica particle in ethanol. Then the sample was moved down 14  $\mu\text{m}$ . As a consequence the distance  $D$  between the glass-ethanol interface and the particle was  $14 \pm 1 \mu\text{m}$  for all the measurements. In this way we assured that the spherical aberration remained constant for all measurements while we varied the distance between the image plane and the trapping plane,  $z_h$ .

The depth at which we trap the particle with respect to the focal plane of the microscope varies indeed almost linearly with the position of the first lens of the telescope as we see in Figure 5.15 a. The deviation from the linear relation between the distance position of lens L3, and the distance between the particle and the hologram plane  $d_h$  in Figure 5.15 a is ascribed to the reduced axial stiffness

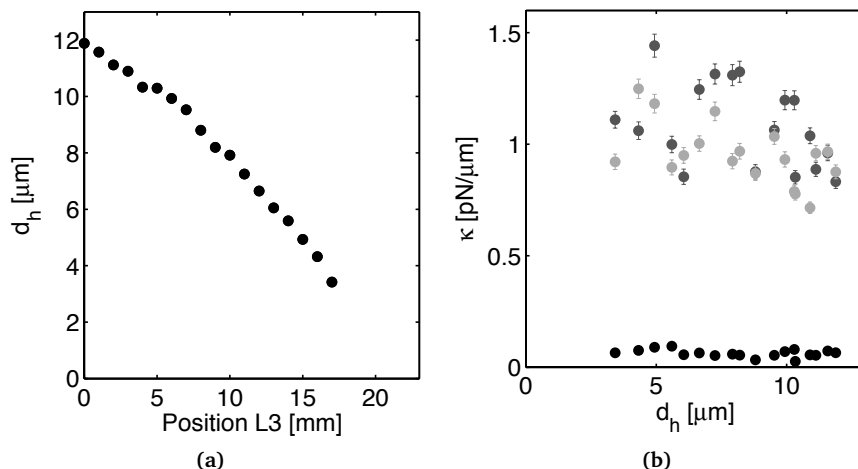


**Figure 5.15:** *The trapping behavior as a function of the distance between focal plane and particle. a.* The distance  $d_h$ , as measured using holography, between the focal plane of the microscope and the equilibrium position of the particle in the trap as a function of the position of lens L3. The errors are estimated to be similar to the size of the symbols. **b.** The trapping stiffness in the lateral directions,  $x$  in light grey and  $y$  in dark grey, and the axial direction in black, as a function of the distance  $d_h$ .

at larger distance  $d_h$ , as plotted in Figure 5.15 **b**. The weight of the particle was constant, and had to be counterbalanced by the changing radiation pressure. For weaker traps, this means that the particle is trapped further below the geometric focus. This mechanism is similar to the relation between the trapping stiffness and the trapping depth as plotted in Figure 5.5 on page 188. We therefore conclude that the relation between the position of lens L3 and the position of the focus in the sample is very close to linear.

When the beam is more divergent we may be effectively changing the overfilling of the back aperture of the objective and the numerical aperture of the focus. This may be the mechanism for the decrease in the trapping stiffness with increasing distance  $d_h$ . We plot the results for the trapping stiffnesses as a function of the distance between the trap and the focal plane in Figure 5.15 **b**. The trapping stiffnesses decrease slightly with increasing distance between the focal plane and the trapping plane. For distances even smaller than the 3.5  $\mu\text{m}$  between the imaging plane and the trapping plane in Figure 5.15, we noticed that there was too little information in the holograms, the fringes were too small as compared to the pixel size and we could not obtain reliable trajectories to measure the trap stiffnesses. We think that part of the discrepancy between the calculations and the experiments, as for instance in section 5.3.1 is due to the fact that in the experiments the particle is trapped well above the focal plane of the microscope. The large ratio between the lateral and the axial stiffness however seems to be grosso

modo independent from the distance  $d_h$  for the values that we have been able to study. The most likely explanation is that the overfilling at the back aperture of our objective is less than what we assumed in the calculations.

## Conclusion

Experiments were performed to study the effect of the distance between the focal plane of the microscope and the trapped particle, created to facilitate DHM, on the trapping behavior. The trapping depth was observed to depend linearly on the position of the first lens of the telescope, L3. A slight decrease of the trapping stiffness for increasing trapping depths was observed.

### 5.4.2 *The influence of the blinking nature of time-shared traps*

As shortly described in section 4.5 and 4.7.3, it is possible to create multiple effective traps by means of time-sharing. In this technique, the laser beam is somehow, often using Acousto Optical Deflectors, AODs, switched back and forth to shift the focus in the sample. If the repeat period with which the traps are addressed by the laser is short enough such that the particles do not diffuse out of the range of the trap in the time the trap is switched off, the particle is pushed back to the trapping location. When the trap is strong enough to push the particle back to the equilibrium position during the intervals in which the trap is on, the particle experiences the trap as a trap with a time-averaged stiffness [43–45]. During the time the trap is switched off, the laser can be used to form another trap. This way, it is possible to trap multiple, even hundreds of particles, provided the focus is moved fast enough and has enough power to keep all the particles at their corresponding trapping locations. In our setup as described in [45] and in Chapter 1, we use Acousto Optical Deflectors, AODs, to change the direction of the beam. The AOD consists of a telluriumdioxide ( $\text{TeO}_2$ ) crystal in which radio frequency acoustic waves are produced. The tellurium crystal is an optically transparent medium in which the sound waves form a periodic variation in the refractive index due to the compressions and rarefactions of the sound wave. The periodic variation of the refractive index thus created, forms a grating that is capable of diffracting an incident laser beam. By changing the frequency and thus the wavelength of the sound waves, the spacing of the diffraction grating can be changed. This also changes the angle of the first diffraction order that we use to form our traps. The AODs are positioned in a plane conjugate to the back aperture of the objective such that a different angle corresponds to a different position in the sample plane. The frequency of the sound wave can be changed extremely fast, changing the position of the trap in micro seconds, which allows one to scan multiple trapping sites rapidly enough for time-shared trapping.

The two DTD-274HA6 AODs from the IntraAction Corporation in our setup are operated as a Bragg device. The light-sound interaction length of 334 mm is much longer than  $\Lambda^2/\lambda$ , where  $\Lambda$  is the wavelength of the sound waves (25.3  $\mu\text{m}$

at 25 MHz) and  $\lambda$  is the wavelength of the laser (1.064  $\mu\text{m}$ ). This, or a quality factor of more than 7 means that the AOD is used as a Bragg device. In this mode the incident laser should enter the sound field at the Bragg angle  $\theta_B = \frac{\lambda}{2\Lambda}$ . The first diffraction peak can, depending on the design of the device contain up to 90 % of the energy when the AOD is aligned such that the incident beam and the first order diffraction beam make symmetric angles with the sound field. The rise time  $T_r$  is defined as the time it takes for the intensity of the first diffraction order to increase from 10 % to 90 % of the maximum intensity. For a Gaussian laser beam the rise time is given by [48]:

$$T_r = 0.64\tau. \quad (5.12)$$

$\tau$  is the transit time, the time it takes a sound wave to propagate a distance equal to the width of the laser beam. For our setup, the diameter of the laser beam at the location of the AODs is 2.69 mm. The speed of sound in tellurium is 0.632 mm/ $\mu\text{s}$  so the rise time in our setup is 5.55  $\mu\text{s}$ . The period associated with the fastest possible switching between 90 % and 10 % of the maximum intensity therefore is 5.44  $\mu\text{s}$ .

In our setup we have two of these AODs to be able to position multiple traps in 2 different directions. Suppose we want to form two traps with both the  $x$  and the  $y$  coordinate different. Then we have to choose the period during which we have the laser in either one of the two traps short enough for the other particle not to diffuse away. When we switch the laser from position  $x_1, y_1$  to  $x_2, y_2$  we start to excite the crystals at the frequency associated with  $x_2$  and  $y_2$  respectively. During the rise time the wavefront of the new wave moves through the laser beam, moving the laser power from  $x_1$  to  $x_2$ . During this time there is a little bit of light diffracted in both directions. The same process happens in the  $y$ -direction. As a result there is effectively also some light focussed on the positions  $x_2, y_1$  and  $x_1, y_2$ . The time averaged power in these two ‘ghost’ traps increases if the laser is switched more frequently between the two intended trapping locations  $x_1, y_1$  to  $x_2, y_2$ . During the transition time, part of the laser beam is still diffracted in the ‘old’ direction and part of the beam is diffracted in the ‘new’ direction. To study the effect of the fact that it takes time to change the diffraction grating, we tracked a particle trapped in a blinking trap. For the behavior of the particle in a blinking trap it does not matter where the laser light is diffracted to when the trap is off, as long as that light is not focussed too close by (see also section 6.4). We made a trap at 14  $\mu\text{m}$  depth and switched it on and off using the AODs. The AODs were excited using waves that were generated by Direct Digital Synthesizers (DDS, Novatech Instruments Inc., DDS8m 100 MHz) which were controlled using a LabVIEW (National Instruments) program.

As the trap was switched on and off, the fraction of time during which the trap was on was kept constant at 50 %. The period of the square wave was varied between 3.2  $\mu\text{s}$  and 6400  $\mu\text{s}$ . At the fastest switching rate, the crystal was excited for 1.6  $\mu\text{s}$ , forming a wave train that was 1.0120 mm long that consisted of 40 full cycles of the sound wave. As the beam width was 2.69 mm, the beam was

continuously diffracted partially in the direction of the first diffraction order. The laser power in the trap was only slightly modulated in this case. When the period of the switching was  $6.4 \mu\text{s}$  the intensity was rising and decreasing the most. For longer switching periods, the traps were at times completely on or completely off. We used a Melles Griot Broadband Power/Energy 13PEN001 power meter to assure that the time averaged laser power that arrived on the back aperture of the objective did not vary within measurement accuracy. The laser power on the back aperture of the objective was  $26.2 \pm 0.2 \text{ mW}$  throughout the trajectory. At every switching rate we recorded 6000 frames of 160 by 160 pixels at 100 fps. From the holographically [21] measured trajectories (see also Chapter 2), we determined the average trapping depth of the particle above the focal plane and the trapping stiffnesses.

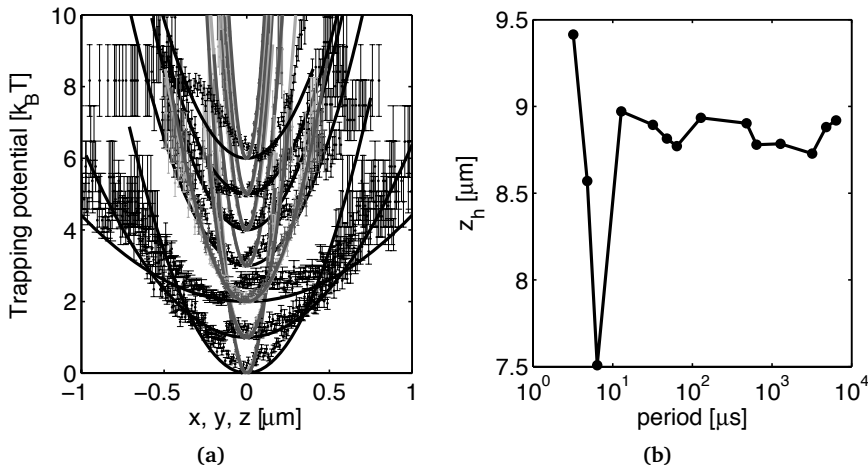


**Figure 5.16:** The trapping position as a function of the switching rate of the traps. **a.** The apparent trapping potential as a function of the distance from the equilibrium position. For clarity the curves associated with a switching period of respectively  $3.2$ ,  $4.8$ ,  $6.4$ ,  $12.8$ ,  $32$ ,  $48$  and  $64 \mu\text{s}$  have been given an offset of respectively  $0$ ,  $1$ ,  $2$ ,  $3$ ,  $4$ ,  $5$  and  $6 k_B T$ . The full lines represent a fit to the harmonic potential. The two lateral directions have been plotted with grey and light-grey for the  $x$ - and  $y$ -direction respectively. The axial direction is plotted in black. **b.** The distance  $d_h$ , as measured using holography, between the focal plane of the microscope and the equilibrium position of the particle in the trap as a function of the period of the laser switching. The errors are estimated to be similar to the size of the symbols.

The trapping potential for the seven fastest switching rates is plotted in Figure 5.16 **a.** We note that the trapping potentials are particularly wide for a switching period of  $6.4 \mu\text{s}$ . From Figure 5.16 **b** shows that the particle was also trapped by far the lowest at this switching rate. Apparently the particle had to be displaced significantly before the optical forces could counteract gravity. This agrees with the observation of the weaker axial confinement, similar to the case where a

particle is trapped in a less brightly illuminated and thus weaker trap as discussed in section 5.3.1. The particle in the weaker trap has to be displaced more for the trap to be able to counterbalance its weight.

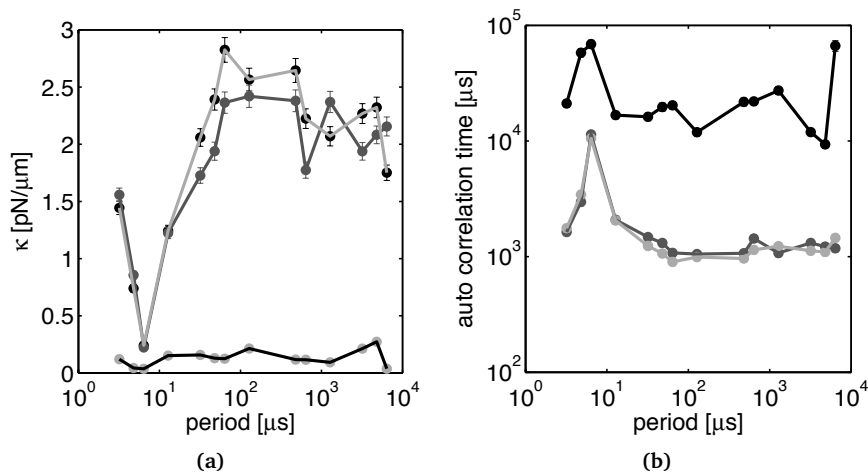


**Figure 5.17:** The trapping behavior as a function of the switching rate of the traps. **a.** The trapping stiffness in the lateral directions  $x$  and  $y$ , in light grey and grey, and the axial  $z$ -direction in black, as a function of the switching period. The stiffnesses have been determined by fitting a harmonic potential to the measured trapping potential. **b.** The correlation time, based on harmonic fitting, in the lateral directions  $x$  and  $y$ , in light grey and grey, and the axial  $z$ -direction in black, as a function of the switching period.

The lateral and axial stiffnesses are plotted as a function of the switching period in Figure 5.17 **a**. Similar to in Figure 5.16, there is a clear drop in the trapping stiffness when the trap is switched on and off once every 6.4  $\mu\text{s}$ . Also when the switching period was 4.8  $\mu\text{s}$  the trapping stiffnesses were significantly reduced. At the shortest switching period the trapping stiffness is almost the same as at much longer switching times. When the switching period is shorter, the fraction of time during which only part of the Gaussian beam is diffracted in the direction of the microscope to form a trap is larger. At a switching period of 5.44  $\mu\text{s}$  always only 50 % of the Gaussian beam encounters the grating sound wave-train. This yields much weaker trapping as can be seen from Figure 5.17 **a**. At higher switching rates, shorter wave trains, the Gaussian beam still encounters gratings over only half its cross-section. These 50 % however, are distributed progressively more evenly over the cross-section of the beam as the extension of the gratings gets shorter and shorter with respect to the beam diameter. This causes the focus to be progressively more confined with increasing switching rates, with stiffer trapping as a result. Also the observation of constant irradiance on the back aperture of the objective when the switching rate is varied, suggests that the decrease

in trapping stiffness at a switching period of  $6.4 \mu\text{s}$  is due to the deformation. Similar effects may have been causing what was wrongfully interpreted as ‘parametric resonance’ by Joykuty *et al.* [49], as stated in [46, 50]. See also section 4.7.3.

The autocorrelation time, the inverse of the corner frequency (section 4.4), is plotted versus the switching time in Figure 5.17 **b**. A shorter autocorrelation time means a stiffer trap. These autocorrelation times are based on the stiffnesses as determined by fitting a harmonic to the trapping potentials from Figure 5.16. As stated by Deng *et al.* [46], the switching time in time-shared trapping should be chosen shorter than the autocorrelation time to not induce an increase of the variance in the particle position. Indeed, when the period of the switching on and off of the traps is longer than roughly the autocorrelation time, that than the apparent stiffness decreases and the associated autocorrelation time increases.

## Conclusion

Here we have shown that the switching period should be much longer than the rise time of the AODs used for the time-sharing. Deng *et al.* [46] showed that the switching time in time-shared trapping should be chosen shorter than the autocorrelation time for optimal trapping. We confirmed this result. For our setup, these two restraints leave us about one order of magnitude between 100 and 1000  $\mu\text{s}$  for the switching rate of time-shared traps without compromising the trapping stiffness. If more than 10 particles are to be trapped, our results strongly suggest to not compromise the shortest switching period but to choose to let the modulation in the trap power to be of the order of the autocorrelation time.

## 5.5 Size matters

Not only the shape of the trapping beam and the spherical aberration play a role in the trapping behavior. The size and refractive index of the particle that is trapped are of great influence on the trap performance, as was discussed in chapter 4. In the Rayleigh regime (small ( $r \ll \lambda$ ) particles) the trapping stiffness increases with the polarizability of the particles. The trapping stiffness thus increases with the cubed radius of the particles and with the refractive index contrast between the particle and the medium. For large particles in the ray optics regime, ( $r \gg \lambda$ ), the trend is that the trapping stiffness goes down with  $1/r$ . In the intermediate range, the Lorenz-Mie regime, there is a cross-over between these two regimes.

The dependence of the trap stiffness with the particle size is plotted in Figure 5.18. For consistency we assumed a trapping depth of  $14 \mu\text{m}$  and silica ( $n = 1.45$ ) in ethanol ( $n_2 = 1.36$ ) as the materials of choice. Just for reference we included curves for the effect of the size on the trapping stiffness for particles with a slightly higher index of refraction,  $n \sim 1.49$ , these could for instance be made out of Polymethylmethacrylate, PMMA.

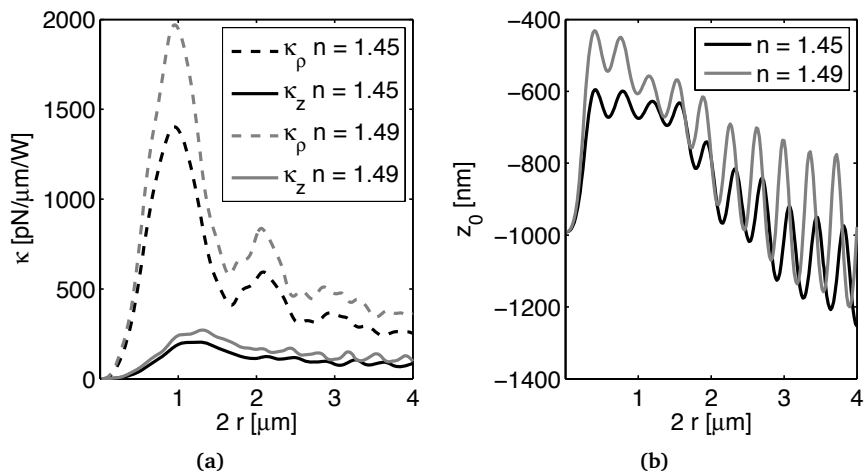


**Figure 5.18:** The influence of the particle size on the trapping stiffnesses. **a.** The trapping stiffness in the axial and the lateral direction for a silica ( $n = 1.45$ ) and a PMMA ( $n = 1.49$ ) particle in ethanol ( $n = 1.36$ ), with the geometrical focus  $14 \mu\text{m}$  above the glass plate, as a function of the particle diameter. **b.** The trapping depths  $z_0$ , with respect to the geometrical focus for these particles.

In these curves, there is a clear optimal size for stiff trapping. Particles that are approximately as large as the diffraction limited focus ( $\sim \lambda/n_1 \approx 800 \text{ nm}$ ) used to trap them, are trapped significantly stiffer than particles that are either larger or smaller. Small particles inevitably consist of less material to be polarized. This limits both the scattering and the gradient force. Particles that are much larger than the wavelength experience a relatively smaller gradient force, mainly because the gradient in the light intensity is not present at their edge. This makes that their polarization does not decrease appreciably when they move out of the focus, causing smaller restoring forces and thus lower stiffnesses.

Note that the maximum stiffness in the axial direction occurs for a larger particle size than that which yields maximum lateral trapping stiffness. This difference in the optimal size for stiff trapping is not only due to the absence of the scattering force in the lateral direction. It illustrates once more the anisotropic shape of the focus as can be seen from the generally smaller axial stiffness. The focus is longer in the axial direction than in the lateral direction due to the finite numerical aperture of the objective lens used to focus the light. This results in smaller intensity gradients in the axial direction, and more importantly the maximum intensity gradients in the axial direction lie further apart. Again, this illustrates the importance of the intensity gradient at the edge of the particle.

The oscillations in the trapping stiffness and the trapping location for the larger particles are due to interference of light in the particle [1, 2]. For certain sizes, the optical path length,  $4nr$ , roughly associated to traversing the particle

twice (after being reflected once), is exactly a multiple of one wavelength plus half a wavelength. This causes destructive interference between light that has been reflected on the first interface of the particle and light that has been reflected by the other interface and traversed the particle twice. The result is less reflection and a smaller radiative pressure. Thus the particle is trapped closer to the effective focus. This corresponds to the minima in the trapping depth in Figure 5.18 **b**. When the scattering force, due to the particle's 'antireflection effect' is minimum, the particle gets trapped further below the geometrical focus. In effect it gets trapped less far beyond the effective focus. The minima in the trapping depth in Figure 5.18 **b** correspond to the maxima in the axial trapping stiffness in Figure 5.18 **a**. The different refractive indices of PMMA and silica yield different optical path lengths within the particle and therefore the period of the oscillations is slightly smaller for PMMA which has a higher refractive index.

### 5.5.1 Force curves

We plot some force curves for differently sized particles in Figure 5.19. For the smaller particles, the effect of the spherical aberration is much larger. Some of the smaller particles ( $r < 0.5 \mu\text{m}$ ) already experience secondary traps when the geometrical focus is  $14 \mu\text{m}$  above the glass, while larger particles do not. For the larger particles, the intensity gradients, associated with the paraxial focuses caused by the spherical aberration, are simply too small. Moreover, we note that the general size of the features grows with the particle size. For most sizes the interaction in the lateral direction extends roughly over a distance similar to the particle size. In fact the shape of the trap is roughly like a convolution of the particle with the focus.

For particles of  $\sim 2 \mu\text{m}$  in radius, the calculations predict that in the lateral direction there is a significant stiffening of the traps for larger displacements from the optical axis, see Figure 5.19 **b**. This gives rise to significantly larger maximum forces than one might expect based on measurement of the stiffness when the particle is only making small excursions, as described in [19, 20]. All these observations suggest that the shape of the gradient force is mainly due to interaction between the intensity gradient at the edge of the focus and the refractive index step at the edge of the particle. To illustrate how the particle size influences the effect of spherical aberration, we calculated a few trapping efficiency curves at different trapping depths in Figure 5.20. There is a clear decrease in the maximum forces exerted on the particles with increasing trapping depth. Furthermore, we note that the larger particles are less likely to experience a secondary trap in the paraxial focuses caused by spherical aberration. They clearly experience oscillations in the total optical force as a function of the depth, but nowhere is the restoring gradient force associated with the local focuses strong enough to overcome the scattering force. Generally speaking, this is what one expects as the gradient force increases less strongly with the particle polarizability and thus its size than the scattering force does. There is another, more subtle effect, that also

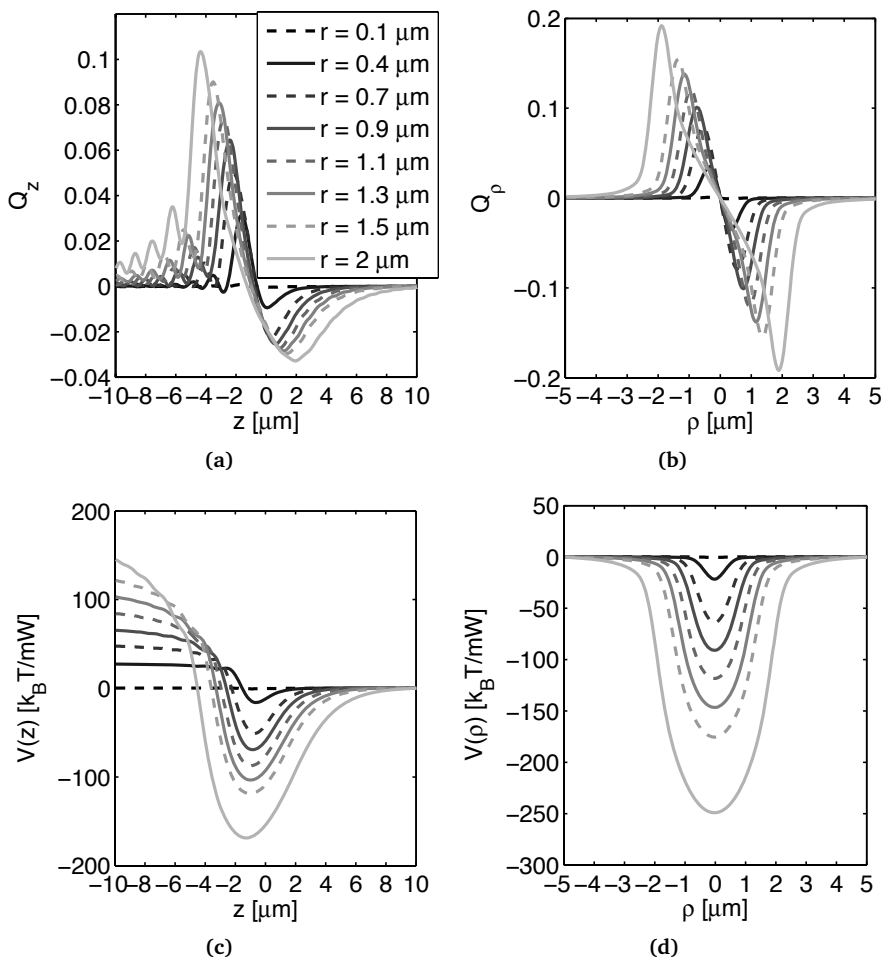
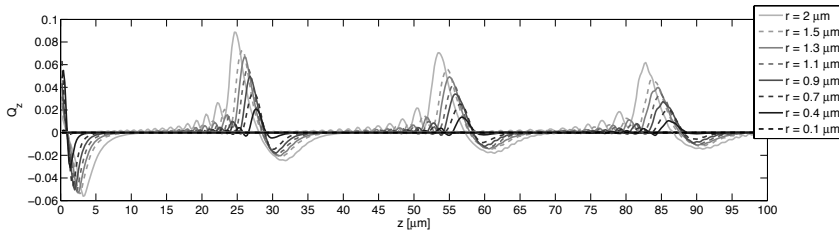
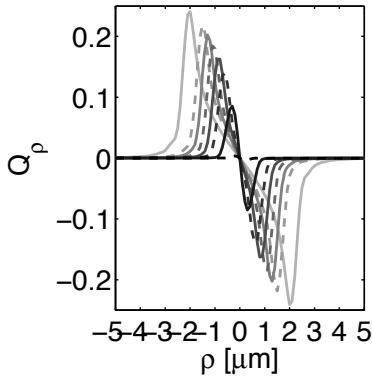


**Figure 5.19:** The influence of the particle size on the trapping efficiency. **a.** The axial trapping efficiency is as a function of the distance in  $z$  from the geometrical focus,  $14 \mu\text{m}$  above the bottom glass plate, for differently sized silica particles in ethanol. **b.** The lateral forces for the same particles, at their respective trapping depth. **c, d** the trapping efficiencies integrated in respectively the axial and the lateral direction.

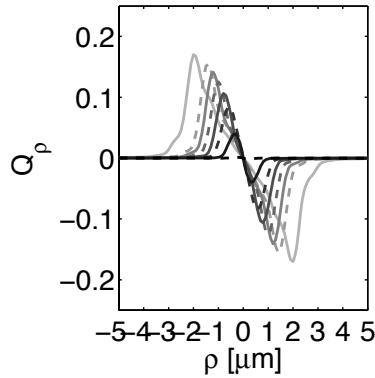
plays a role. The larger particles are also larger than the secondary focuses that are of the order of the wavelength. These particles are therefore never located in a single intensity gradient. The effect of the secondary focuses on the total force is smeared out by the particles sampling always multiple focuses.



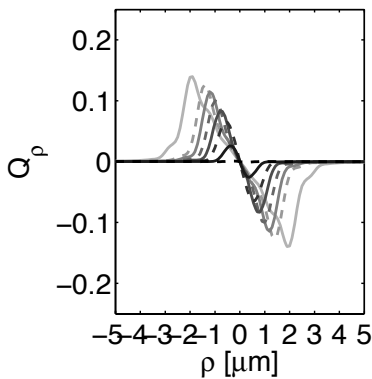
(a)



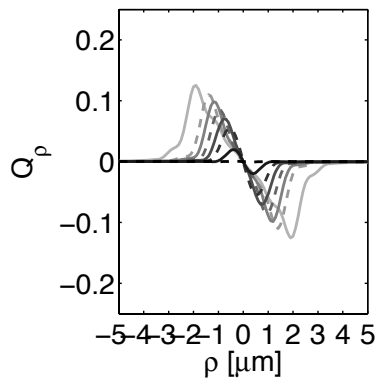
(b)



(c)



(d)



(e)

**Figure 5.20:** The effect of spherical aberration and particle size on the trapping efficiency. **a.** The axial trapping efficiency as a function of the distance in  $z$  from the geometrical focus, 1, 30, 60 and 90  $\mu\text{m}$  above the bottom glass plate, for silica particles of different radius in ethanol. **b, c, d** and **e.** The lateral trapping efficiencies for the same particles with the geometrical focus at 1, 30, 60 and 90  $\mu\text{m}$  respectively from the bottom glass plate.

### 5.5.2 Experiment

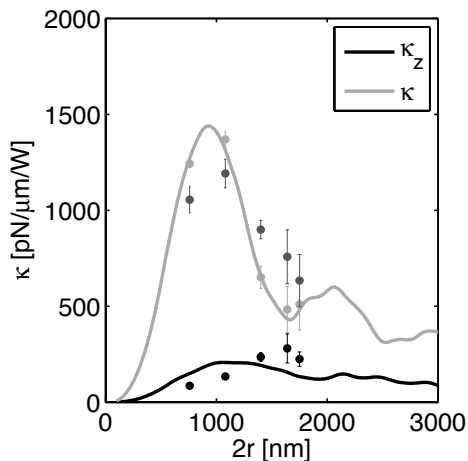


**Figure 5.21:** *The influence of the particle size on the trapping stiffnesses, experiment.* The trapping stiffness in the axial and the lateral direction for silica ( $n = 1.45$ ) spheres in ethanol ( $n = 1.36$ ), with the geometrical focus  $14 \mu\text{m}$  above the glass plate, as a function of the particle diameter. The points represent experimental stiffnesses measured from holographically measured trajectories for silica particles with diameters of 758, 1080, 1400, 1640 and 1750 nm. Black was used for the axial direction, dark grey was used in the  $y$ -direction along the polarization and light grey was used for the stiffness in the  $y$ -direction perpendicular to the polarization.

To experimentally test the above predictions, we performed the following experiments. We trapped silica particles of respectively 758, 1080, 1400, 1640 and 1750 nm in diameter in ethanol. Digital Holographic Microscopy [21] was applied to track the particle movement. For each particle we recorded about 5000 holographic frames at 200 frames per second. We applied the algorithm as proposed by Marco Polin [28], to solve the Langevin equation for an over-damped Brownian particle in a harmonic potential, for the trap stiffness from the holographically measured particle trajectories. The experiment was done at three different laser powers, 200, 500 and 1000 mW. All the particles were trapped at a distance of  $14 \mu\text{m}$  above the glass bottom of the cell. The trapping stiffnesses we measured were normalized to 1 Watt of laser power at the laser output and then averaged.

The calculated trapping stiffnesses are plotted together with the experimental trapping stiffnesses in Figure 5.21. The lateral and axial calculations were normalized separately as we already noted that the ratio between these stiffnesses in our experiments does not quantitatively match with the calculations, see section 5.3.1 and 5.4.1. The smaller particles in this series of particle sizes are trapped significantly stiffer than the larger particles. Contrary to previous reports [12], we do experimentally observe a clear maximum in the trapping stiffness for particles of about the size of the wavelength. The larger particles appear to be trapped more stiffly in the direction parallel to the polarization of the light. However, we think that this effect is not the only explanation of the observed higher stiffness in this direction for the particles with diameters of 1400, 1640 and 1750 nm. We note that the smaller particles, 758 and 1080 nm in diameter were trapped less stiff in that direction. Similar to the observation that the maximum size for stiff trapping is slightly larger in the axial direction than in the lateral directions because the focus is less confined in that direction, we hypothesize that the focus was not perfectly symmetric. A slight misalignment is assumed to have caused the focus to have been slightly larger in the  $y$ -direction.

Similarly, we note that there is a clear maximum in the axial stiffness. The maximal stiffness for axial trapping in our setup seems to be close to 1.6  $\mu\text{m}$  in diameter rather than the roughly 1  $\mu\text{m}$  in the calculations. This suggests that the focus in the axial direction is significantly longer. The extension in the axial direction is in agreement with the observation that the particles in our traps are not trapped as stiff in the axial direction as the calculations predict, as was observed in section 5.3.1 and 5.4.1. We note that more optimal alignment could improve the axial trapping. Perhaps we should adjust the objective parameter,  $\gamma$  which represents the ratio between the tube length and the beam waist, see equation 5.5, to better model the objective used.

## Conclusion

Experiments were performed on the trapping stiffness of differently sized silica spheres in ethanol. The particle trajectories from which the trapping stiffnesses were deduced were measured using DHM. The size dependence of the trapping stiffnesses confirmed that the focus of the laser beam in the sample was longer in the axial direction than it was in the lateral directions. Moreover, the measured size dependence of the trapping stiffnesses suggested that the alignment of the trap was sub-optimal, resulting in a larger focus in the  $x$ -direction. The trapping stiffnesses were compared with calculations. We conclude that the model as presented by the Nussensveig group [3] accurately describes the trapping behavior of dielectric spheres in optical traps.

### 5.5.3 Size and Refractive index

In Figure 5.22 all the above on the effects of size and refractive index on the trapping stiffness is summarized for a particle trapped in a focus with the geometrical focus  $14\ \mu\text{m}$  above the bottom glass plate. The medium in which the particles are dispersed has a refractive index of 1.33, which agrees with water. The axial trapping stiffness is given in Figure 5.22 **a** in false colors as a function of the position in the  $r, n$  plane. Wherever no stable trapping plane is found, the corresponding pixel is left white. There is a maximum stiffness per watt of  $482\ \text{pN}/\mu\text{m}/\text{W}$  for particles with a radius of  $740\ \text{nm}$  and a refractive index of 1.71. In the lateral direction this particle would have a much higher stiffness per watt of  $1680\ \text{pN}/\mu\text{m}/\text{W}$ .

The maximum trapping stiffness in the lateral directions, in Figure 5.22 **b**, is found for a slightly smaller particle of a slightly lower refractive index; here the optimal size is a radius of  $600\ \text{nm}$  for a particle made of a material with a refractive index of 1.68, yielding a stiffness per watt of  $3098\ \text{pN}/\mu\text{m}/\text{W}$ . This is similar in refractive index to e.g. melamine. In the axial direction, this particle would experience a much lower stiffness per watt of  $57\ \text{pN}/\mu\text{m}/\text{W}$ . The fact that the maximum stiffness in the lateral directions is found for a smaller particle than in the axial direction is due to shape of the focus which is slightly smaller in the lateral direction, than in the axial direction. The absence of the scattering force in the lateral direction is responsible for the fact that the optimal refractive index of the particles is slightly higher. In principle, the lateral trapping stiffness would be even larger for higher refractive indices. The lateral stiffness is limited by the fact that higher index particles experience a larger scattering force in the axial direction, resulting in a higher trapping location or even no trapping.

The stiffness decreases steadily with increasing particle radius for particles with a good contrast like PolyStyrene, PS, with a refractive index  $n = 1.6$ . In the geometric optics regime, the stiffness decreases like  $\sim 1/r$ . We also observed this decrease for silica and PMMA particles in ethanol in Figure 5.22. The information in the curves in this Figure is similar (mind the different refractive index of the medium) to the information in the intensities in Figure 5.22 **a** and **b**, here represented in false colors on horizontal lines at the respective refractive indices. We observe oscillations in the scattering force and consequently in the trapping depth and the axial stiffness for the larger particles. These oscillations are due to interference of light that was 'reflected' from both ends of the particle. Note that the particles that are trapped the closest to the effective focus yellowish zones in Figure **c** 5.22 are the particles that are generally trapped stiffer in the axial direction [15].

The interference effect becomes even stronger for higher index particles. This is mainly due to the larger reflection at interfaces with a larger index discontinuity. The optimal size for stiff trapping goes down with increasing refractive index of the particle. This is due to the fact that the wavelength of the light in a higher refractive index medium, here the particle, is shorter. For the lateral trapping

efficiency the interference effect is not too important because the scattering force plays no role in the lateral direction. Surprisingly, the partial canceling of the reflected light for certain particle sizes causes trappability for larger, higher index particles. This phenomenon will be hard to use to trap high index particles since it is hard to synthesize particles with the required accuracy in size and refractive index. Moreover, the details of the focus become important so that the assumption of circularly polarized light and, last but not least, imperfections in the optics will affect the trappability. A way to trap a larger, high index particle would be to vary the wavelength of the trapping laser to minimize the particle's reflection. This could be realized using a white laser and an Acousto Optical Modulator, although

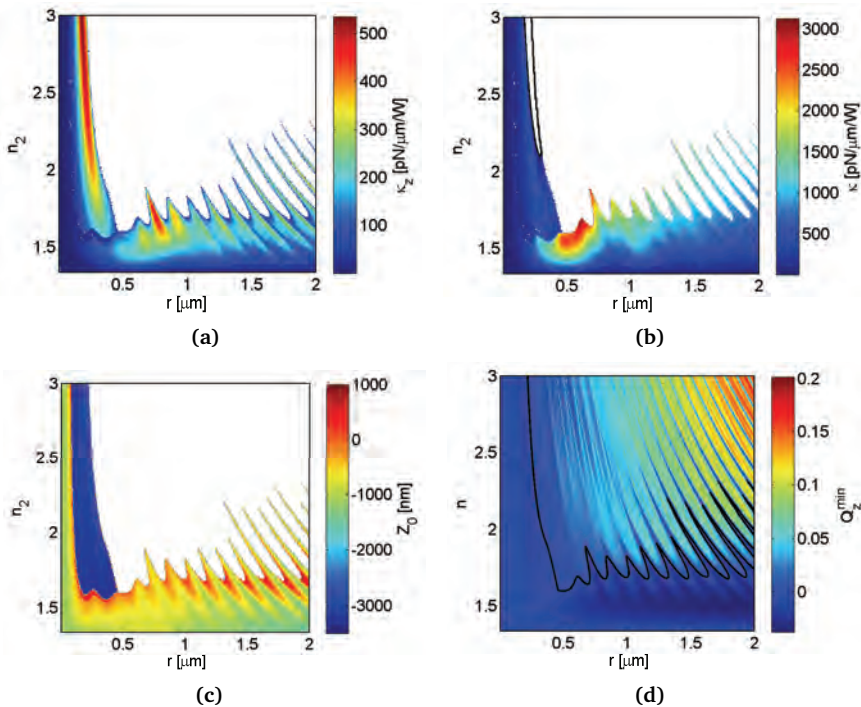


**Figure 5.22:** The trapping stiffness as a function of particle size and refractive index. **a.** The trapping stiffness in the axial direction in false colors as a function of the particle's radius in  $\mu\text{m}$  and the particle's refractive index. The particle is assumed to be trapped in water ( $n = 1.33$ ) with the geometrical focus at a depth of  $14 \mu\text{m}$  above the bottom glass plate. When there was no stable trapping the corresponding pixel was left white. **b.** The same for the stiffness in the lateral direction. The black line indicates the region where there is stable trapping in the axial direction but not in the lateral direction. **c.** The trapping depth with respect to the geometrical focus. Also here, the pixel was left white when no stable trapping location could be found. **d.** The maximal restoring force, the black line indicates the particles on the verge of trappability as the maximum restoring force is zero.

the power per wavelength is still a bit low for trapping.

If it were not for the different trapping plane with varying refractive index and particle size, in Figure 5.22 c, the lateral stiffness of the trap would continue to increase with the particles' polarizability and thus its refractive index. The optimal size for trapping is not only determined by the optimal polarizability of the particle, but obviously also by the relative size of the particle with respect to the focus.

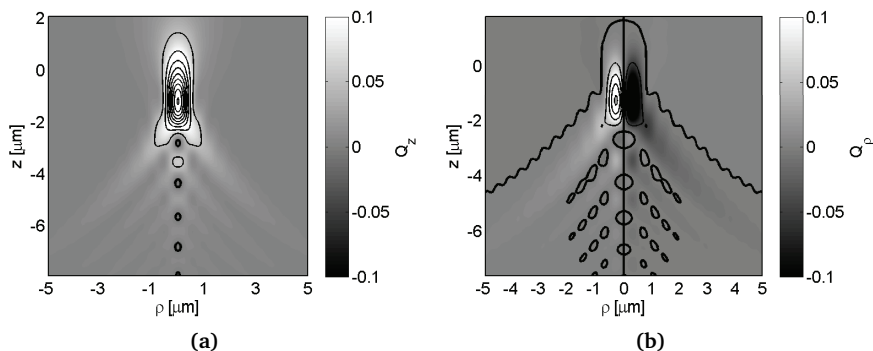


**Figure 5.23:** The trapping efficiency of a titania particle in water as a function of the position. **a.** The axial trapping efficiency  $Q_z$  as a function of the position with the origin in the geometric focus for an anatase titania ( $n = 2.4$ ) particle with a radius of 260 nm, trapped in water at a depth of 14 μm. **b.** The lateral trapping efficiency  $Q_\rho$  as a function of the position with the origin in the geometric focus. The trapping efficiencies in both graphs are represented by grey values, for clarity an iso-force curve was added for  $Q = 0$ .

For a particle to be trapped at all, it is crucial to have a depth at which the axial trapping efficiency is negative so that the particle gets pushed back to the trapping location. The larger the restoring force is, the more probable it is that a particle remains trapped. The minimal trapping efficiency is depicted in Figure 5.22 d in false colors. Also in the minimal trapping efficiency we recognize the interference effect. The effect is much smaller than for the trapping depth. For particles with a refractive index higher than circa 1.6 also the largest restoring force varies significantly with the exact particle size. For many sizes, the gradient force can no longer overcome the scattering force and the particles are not trapable. For clarity we included a black line in Figure 5.22 d where the maximum restoring force is zero. Below this line, particles can be trapped, above this line the total force exerted on the particle points upwards everywhere.

Another interesting observation in Figure 5.22, is that for the smallest particles, about 100 nm in radius, apparently there is the possibility to trap particles with high refractive indices. Despite their high refractive index, the scattering force is relatively small due to the small volume of the particles. The particle that is trapped most stiffly of all in the axial direction is in fact a 180 nm radius par-

ticle with a refractive index of 2.93. This particle experiences an axial stiffness of  $532 \text{ pN}/\mu\text{m}/W$ . In the axial direction there is a minimum in the trapping position rather deep, 2.84 micron below the geometrical focus, due to the spherical aberration. The lateral stiffness, however is calculated to be  $-288 \text{ pN}/\mu\text{m}/W$ . A negative stiffness means that the particle is not trapped, instead any perturbation is amplified. The particle will be pushed away from the optical axis. Further away from the optical axis we find the light that will be focussed further upwards. Apparently the intensity away from the optical axis is higher, and the particle will be drawn away from the optical axis. There, it will be pushed upward and the particle will not be trapped. When particles of such a high refractive index material are made any larger, rapidly the scattering force becomes dominant at all depths and the gradient force can no longer provide enough restoring force. The range of particle parameters for which our calculations predict a positive axial stiffness in combination with a negative lateral stiffness is circumscribed in black in the upper left corner of Figure 5.22 **b**.

The force field exerted on a particle with a radius of 260 nm and a refractive index of 2.4 in an optical trap with the geometrical focus at a depth of  $14 \mu\text{m}$  above the glass is depicted in Figure 5.23. Such a particle may be made out of an anatase titania. In Figure 5.23 **a** and **b**, the upward, respectively lateral forces, are depicted in grey values as a function of the trapping position with respect the geometrical focus. According to Figure 5.22 this particle should be trapped in the axial direction on the optical axis, while it is predicted not to be trappable in the lateral direction. The particle experiences alternately upward and downward forces due to the local paraxial focuses caused by the spherical aberration as can be seen in the lower half of Figure 5.23 **a**. At several depths along the optical axis, the particle experiences a zero force, also indicated with iso-force curves in black, for half the occasions on the optical axis with a negative slope in the trapping efficiency. One of these trapping locations is located at a depth of  $-2.92 \mu\text{m}$ , so below the geometrical focus. If we now look at the lateral trapping efficiency at the same region in Figure 5.23 **b**, we see that the particle, when it is positioned to the left of the optical axis experiences a force that pushes it even further to the left. Clearly, not all secondary axial minima that are generated by spherical aberration are good traps.

The trapping depth is represented by false colors in Figure 5.22 **c** as a function of the particle radius and its refractive index. A large range of particle parameters, roughly particles smaller than 500 nm in radius, and with a refractive index higher than about 1.6, are trapped much deeper below the geometrical focus in a secondary trap caused by the spherical aberration. Many more particles experience one or more secondary traps (see also Figure 5.8), but these particles can, due to the large scattering force they experience in the effective focus, only be trapped in the secondary trap. These secondary traps effectively have a higher numerical aperture, see also section 5.3.2.

### 5.5.4 Force curves; overview

We study the underlying force curves in more detail in Figure 5.24. We plotted a patchwork of little graphs that represent the lateral trapping efficiency, again with the geometrical focus about  $14\ \mu\text{m}$  above the glass plate. In every patch we plotted the axial trapping efficiency  $Q_\rho$  as a function of the distance to the geometrical focus along the optical axis. When there is a trap in the axial direction, we plotted the lateral trapping efficiency, at that depth, in grey, as a function of the distance to the optical axis  $\rho$ .

There are many observations to be made. We start by stating that the trapping efficiency, the dimensionless force, generally increases with increasing refractive index. The maximum value of the trapping efficiency for one refractive index does not show a clear trend with varying particle radius. Clearly ‘trapping efficiency’ is not such a good term. It is clear that trapping, for instance, a particle with a radius of  $800\ \text{nm}$  and a refractive index of  $2.67$  is impossible. The graph for a  $800\ \text{nm}$  particle with a refractive index of  $1.66$  shows that, in accordance with Figure 5.22, this particle can be trapped. As we learn from the same Figure, the stiffness with which the particle is trapped is even relatively high. The stiffness, however, is not all there is to trapping. The stiffness is merely the slope of the trapping efficiency versus the position at the position where the total force is zero. That this slope may be large does not say anything about the largest restoring force or the well depth. The  $800\ \text{nm}$  particle with a refractive index of  $1.66$ , although it experiences a significant axial trapping stiffness of  $204\ \text{pN}/\mu\text{m}/\text{W}$ , the maximal restoring force is rather small. The associated trapping efficiency is only  $-0.01$ , small compared to the maximum upward force  $0.23$ . This means that even though the particle is trapped rather stiffly, only a small perturbation suffices to loose the particle; a small upward excursion would result in the particle pushed even further up and the energy barrier for escape is small.

When the refractive index is higher than about  $1.7$ , it depends on the particle size whether or not the gradient force wins it from the scattering force. A particle with a radius of  $1800\ \text{nm}$  and a refractive index of  $1.83$  does experience a minimum in the trapping efficiency, but this minimum is not deep enough to actually trap the particle. A slightly larger particle with a radius of  $2000\ \text{nm}$  can be trapped, thanks to the reduced scattering force caused by the interference effect discussed above. It is clear however, that this trap is not stable as only a small energy barrier needs to be overcome to get to the region where the particle is inevitably pushed further away from the focus.

Below the effective focus which sometimes acts as a trap, the particles experience an oscillating force as they follow the optical axis. This is caused by the spherical aberration at the glass-water interface that focusses the outer rays less deep in the sample. The intensity gradients of these local focuses also generate gradient forces that are, in some cases sufficient to trap the particle.

We calculated the same trapping behavior for particles in a medium with a refractive index of  $1.52$  as for instance CycloHexyl Bromide, CHB [51]. This which

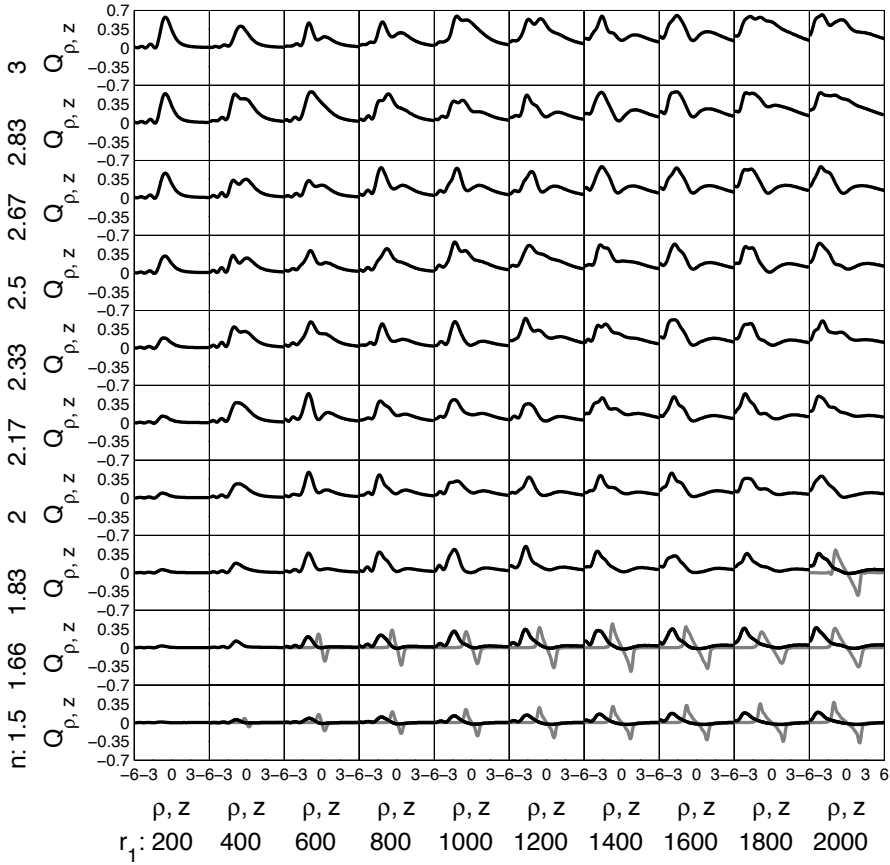


**Figure 5.24:** The trapping behavior as a function of the particle’s radius in  $\mu\text{m}$  and refractive index. The particle is assumed to be trapped in water ( $n = 1.33$ ) with the geometrical focus at a depth of  $14 \mu\text{m}$  above the bottom glass plate. For each particle size and refractive index we plot the axial trapping efficiency in black as a function of the position with respect to the geometrical focus. When there is a stable trapping location in the  $z$ -direction we include the lateral trapping efficiency as a function of the distance from the optical axis in the trapping plane in grey.

is similar to the refractive index of glass (1.51). The result is that the outer beams are much less refracted, so the focus is hardly affected by spherical aberration. Care was taken to make sure that the particle radii were chosen such that the size parameter  $\beta$  (equation 5.2) and the relative refractive index of the particles  $m$ , equation 5.1, were the same as in Figure 5.24. The calculations are summarized in Figure 5.25. Were it not for the spherical aberration in Figure 5.24, these two Figures would be the same.

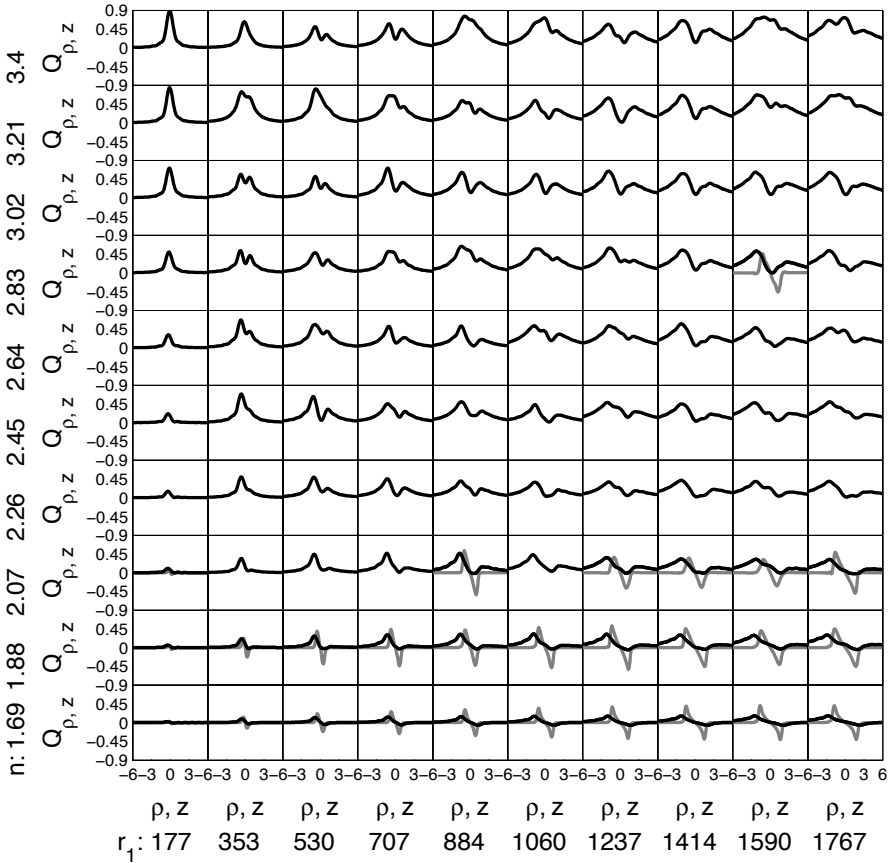


**Figure 5.25:** The trapping behavior as a function of the particle's radius in  $\mu\text{m}$  and refractive index. The particle is assumed to be trapped in CHB ( $n = 1.5051$ ), to minimize the effect of spherical aberration with the geometrical focus at a depth of  $14 \mu\text{m}$  above the bottom glass plate. The particle sizes and refractive indices are chosen such that their size parameter ( $\beta = k r$ ) and refractive index contrast ( $m = n_{\text{particle}}/n_{\text{medium}}$ ) correspond to the situation in Figure 5.24, be it without spherical aberration. For each particle size and refractive index we plot the axial trapping efficiency in black as a function of the position with respect to the geometrical focus. When there is a stable trapping location in the  $z$ -direction we include the lateral trapping efficiency as a function of the distance from the optical axis in the trapping plane in grey.

From the shape of the trapping efficiency as a function of the trapping depth of the smaller particles, we can conclude that the spherical aberration was in fact making the effective focus larger. The peak in the trapping efficiency for the particles with a radius of  $177 \text{ nm}$  in CHB ( $\beta = 1.57$ ) clearly extends over a much

smaller region and reaches a higher maximum than their 200 nm counterparts in water. These small particles are smaller than the focus itself and therefore fit completely in the brightest part of the focus allowing an efficient transfer of momentum from the light to the particles. Larger particles all clearly show a local minimum in the trapping efficiency due to the gradient force. Particles with a refractive index of 2.07 in CHB, which is to be compared with a refractive index of 1.83 in water, can be trapped in many cases. The spherical aberration in water hinders the trapping of these particles with a relative refractive index of 1.37. Note also that the interference effect discussed above allows a 1590 nm particle with a refractive index of 2.83 to be trapped in CHB. The maximal restoring force on the corresponding particle in water, with a slightly lower refractive index of 2.64, cannot be trapped as the gradient force is slightly smaller. For most particles there is a local minimum in the trapping efficiency due to the gradient force. There is always a depth at which the gradient force opposes the scattering force. For the lower refractive indices the scattering force is small enough to be overcome by the scattering force. For particles with a refractive index above about 1.7 in water and about 2 in CHB, it depends a lot on the particular size of the particle whether or not the reflection is small enough to ensure that the gradient force dominates over the scattering force creating a viable trap.

## 5.6 Trapping core-shell particles

Apart from the particle radius and the refractive index, the trapping behavior can also be manipulated by playing with the architecture of the particle. A structure that is often used is that of a core shell particle [52]. It is for instance possible to synthesize core-shell particle by coating particles with silica [53–55]. But not only silica can be grown around colloidal particles. It is also possible to make, for instance, amorphous titania [56, 57] or PMMA [58–60] shells. Also hollow particles of silica can be synthesized [61]. For two recent overviews of hollow particles see references [62] and [63].

A shell of a different material around a particle can have quite a strong effect on the scattering behavior and thus on the trapping behavior of colloidal particles. If the refractive index of the shell is lower than that of the core, but still higher than that of the medium, for instance, the shell can act as an ‘anti-reflection’ coating. Such a coating can reduce the backscattering and thus the scattering force on the particles [64–67], which allows for the trapping of higher index particles. These particles might then be trapped stiffer and facilitate the exertion of larger trapping forces. For biological applications it is favorable that the particles be ‘bio-compatible’, for this reason it would be useful to have silica on the outside of the particles. This allows many different ‘of the shelf’ surface treatments to be applied, preparing the particles for a wide variety of biological experiments. The refractive index of silica, 1.45, lies in between the higher index materials like melamine, PS and titania and that of most physiological solutions that consist of

mostly water. This implies that the silica layer would act as an ‘anti-reflection’ coating, reducing the scattering force on the particle [57, 64–67] and thereby allowing the particles to be trapped stiffer. The larger trapping forces that are made possible this way have been successfully applied in, for instance, experiments on molecular motors [68].

As described in section 4.6.3 and 5.2, the calculation of the optical forces on particles in the Lorenz-Mie regime can be done with generalized Lorenz-Mie theory [4–6] to calculate the scattering behavior of the particle under investigation. The theory for the scattering of spherical particles has been extended to particles with a core-shell structure where the core is coated with another dielectric with a different refractive index [7].

In the textbook by Craig F. Bohren and Donald R. Huffman [8] we find the scattering coefficients of particles with a core-shell structure:

$$a_n = \frac{\psi_n(\beta_2)[\psi'_n(m_2\beta_2) - A_n\chi'_n(m_2\beta_2)] - m_2\psi'_n(\beta_2)[\psi_n(m_2\beta_2) - A_n\chi_n(m_2\beta_2)]}{\xi_n(\beta_2)[\psi'_n(m_2\beta_2) - A_n\chi'_n(m_2\beta_2)] - m_2\xi'_n(\beta_2)[\psi_n(m_2\beta_2) - A_n\chi_n(m_2\beta_2)]} \quad (5.13)$$

and

$$b_n = \frac{m_2\psi_n(\beta_2)[\psi'_n(m_2\beta_2) - B_n\chi'_n(m_2\beta_2)] - \psi'_n(\beta_2)[\psi_n(m_2\beta_2) - B_n\chi_n(m_2\beta_2)]}{m_2\xi'_n(\beta_2)[\psi'_n(m_2\beta_2) - B_n\chi'_n(m_2\beta_2)] - \xi'_n(\beta_2)[\psi_n(m_2\beta_2) - B_n\chi_n(m_2\beta_2)]} \quad (5.14)$$

with

$$A_n = \frac{m_2\psi_n(m_2\beta_1)\psi'_n(m_1\beta_1) - m_1\psi'_n(m_2\beta_1)\psi_n(m_1\beta_1)}{m_2\chi_n(m_2\beta_1)\psi'_n(m_1\beta_1) - m_1\chi'_n(m_2\beta_1)\psi_n(m_1\beta_1)} \quad (5.15)$$

and

$$B_n = \frac{m_2\psi_n(m_1\beta_1)\psi'_n(m_2\beta_1) - m_1\psi_n(m_2\beta_1)\psi'_n(m_1\beta_1)}{m_2\chi'_n(m_2\beta_1)\psi_n(m_1\beta_1) - m_1\psi'_n(m_1\beta_1)\chi_n(m_2\beta_1)}. \quad (5.16)$$

Here, as before  $\psi_n(x)$ ,  $\xi_n(x)$  and  $\chi_n(x)$  denote the Ricatti-Bessel functions  $xj_n(x)$ ,  $xh_n^{(1)}(x)$  and  $-xy_n(x)$  respectively, while the prime indicates differentiation with respect to the argument.  $m_1$  and  $m_2$  are the relative refractive indices of the core and the shell, both with respect to the refractive index of the medium.  $\beta_1$  and  $\beta_2$  are the size parameters of respectively the core and the shell of the particles, analogous to the particle size as defined in equation 5.2.

These scattering coefficients describe the scattering of core-shell particles in the same way as before, for uniform particles. Thus we can also calculate optical forces on particles with a core-shell structure, see for instance reference [64]. By simply inserting the scattering coefficients for core-shell particles in the model given by [3], replacing the scattering coefficients of uniform particles, we can calculate the forces that we can exert on core-shell particles. In the following we give an overview of the trapping behavior of core-shell particles. We first (section 5.6.1) consider high index particles with a shell of a lower index material where

the coating might act as an anti-reflection coating. It is also possible that the shell material has an index of refraction that is not only lower than that of the core but also lower than that of the suspending medium. An example would be a PS ( $n_{\text{core}} = 1.59$ ) particle with a silica ( $n_{\text{shell}} = 1.45$ ) coating in CycloHexyl Bromide, CHB, ( $n_{\text{medium}} = 1.5052$ ). The trapping behavior of this kind of particles will be treated in section 5.6.2. Then, because the CHB sometimes dissolves the PS, leaving a hollow silica shell, we describe the trapping behavior of such hollow shells in a high index oil (5.6.3). It is also conceivable to have the index of refraction of the core lower than both that of the medium and that of the shell, we present calculations on these particles, in section 5.6.4. Finally in section 5.6.5 we discuss the trapping behavior of hollow shells in a lower index medium.

### 5.6.1 $n_{\text{core}} > n_{\text{shell}} > n_{\text{medium}}$

We depict the trapping stiffness and the trapping depth of a silica coated melamine ( $n_{\text{core}} = 1.68$ ) particle in water ( $n_{\text{medium}} = 1.33$ ) in Figure 5.26 in false colors, as a function of the radius of the melamine core and the thickness of the silica ( $n_{\text{shell}} = 1.45$ ) shell. The geometrical focus is assumed to be at a depth of 14  $\mu\text{m}$ . The silica coated melamine particle is used as an example of particles with a coating of a material with a refractive index between that of the core and that of the medium. Whenever there was no stable trapping location, the pixel was left white. When there was a stable trapping location in the axial direction (Figure 5.26 c), where the optical upward forces and those downward cancel, the derivative of the trapping efficiency was taken to calculate the axial trapping stiffness (Figure 5.26 a). At the same depth we calculated the lateral trapping stiffness (Figure 5.26 b). Almost all combinations of core size and shell thickness yield trappable particles. Only particles with a shell thinner than about 100 nm are not trappable.

In section 5.5, Figure 5.22 suggests that bare melamine particles of most radii in water can be trapped. From Figure 5.22 we learn that although bare melamine particles in water are trappable, the maximal restoring force is small as the scattering force is relatively large. In Figure 5.26 we show that not all sizes of melamine particles with a thin silica shell are trappable.

Figure 5.26 c gives the trapping depth with respect to the geometric focus. There is a periodic variation of the trapping depth as a function of the radius of the core, at constant shell thickness. This is caused by the same interference phenomenon mentioned in section 5.5 and for instance in references [1, 2]. For certain sizes, the optical path length the light has to travel when it goes into the core, is reflected on the other side of the core and then leaves the core in the same direction as which it came from is exactly a multiple of half a wavelength. As a result, this light interferes destructively with the light that was reflected directly, this reduces the reflection by the particle and thus the scattering forces. This simplified picture works amazingly well. If the core is slightly larger or smaller, this light that traversed the core twice interferes less destructively.

It is also possible to increase the reflectivity of a particle with constructive in-

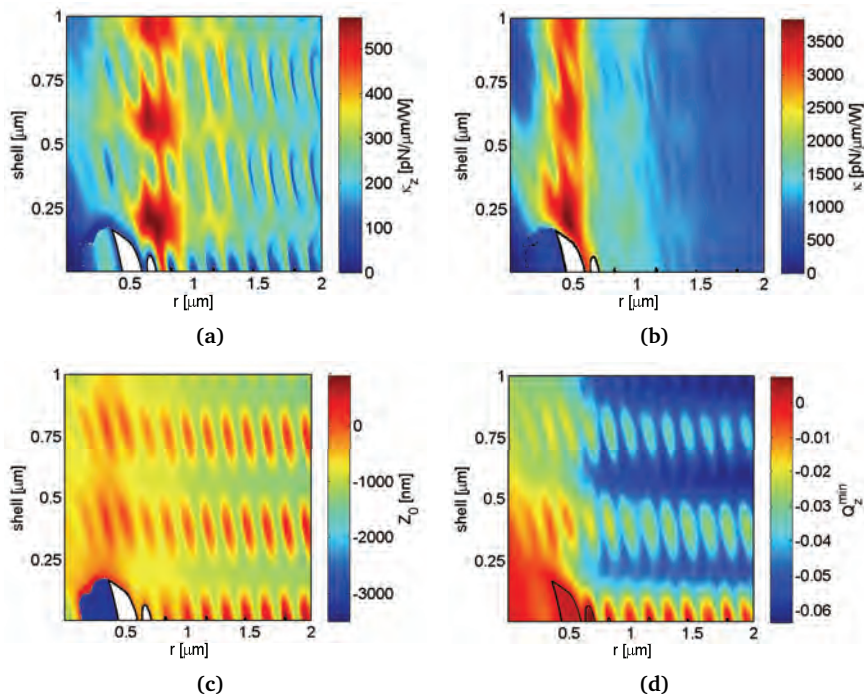


**Figure 5.26:** The trapping behavior of a silica coated melamine particle in water. **a.** The axial trapping stiffness in the axial direction in false colors as a function of the radius of a melamine ( $n_{\text{core}} = 1.68$ ) core in  $\mu\text{m}$  and the thickness of a silica ( $n_{\text{shell}} = 1.45$ ) shell. The particle is assumed to be trapped in water ( $n_{\text{medium}} = 1.33$ ) with the geometrical focus at a depth of  $14 \mu\text{m}$  above the bottom glass plate. When there was no stable trapping the corresponding pixel was left white. **b.** The same for the stiffness in the lateral direction. **c.** The trapping depth with respect to the geometrical focus. The pixel was left white when no stable trapping location could be found. **d.** The maximal restoring force, also when this is positive so that the particle cannot be trapped. The black line is drawn around the region where the maximal restoring force is positive such that no stable trapping is possible.

terference, for instance with a layer of silica around it. Particles with a melamine core of  $1 \mu\text{m}$  in radius and with a silica shell of  $400 \text{ nm}$  are trapped at much greater depths than those with a shell of only  $200 \text{ nm}$  thickness as can be seen from Figure 5.26 **c**. Apparently, they experience a larger scattering force due to constructive interference. The reflectivity of the particle is strongly dependent on the particle radius. Whenever the reflectivity is higher, the scattering force is larger and the particle is trapped further along the direction of propagation of the light. This is what explains the oscillations in the trapping depth. The different amounts of reflectivity and thus of the scattering force in the effective focus obviously also have their effect on the axial trapping stiffness. Although the scattering force itself plays no role in the lateral directions the varying trapping depth has

some influence on the exact value of the lateral trapping stiffness, as can be seen in Figure 5.26b.

When the silica shell becomes thicker, the optical path length the light has to traverse to get to the core and back increases. When the thickness is  $\sim 180$  nm we observe a minimum in the amplitude of the variation in the trapping depth. The wavelength of the trapping laser in the silica shell is 731.6 nm, a quarter of which amounts to 182.9 nm. When the shell is this thick the light that was reflected from the first shell-core interface will have traversed a half a wavelength longer optical path than the light which was reflected on the water-silica interface. As a result, there is destructive interference minimizing the reflectivity and thus the scattering force. When the reflectivity is minimized by the silica shell, the remaining variation in the reflectivity with varying core radius is minimal.

Also when the shell is a multiple of 182.9 nm thick,  $\frac{\lambda}{4n_{\text{silica}}}$ , we observe minimal influence of the core size on the trapping depth as the scattering force is already minimized by the silica shell. The optimal trapping stiffness, in the axial and the lateral direction 570 pN/ $\mu\text{m}/\text{W}$  and 3830 pN/ $\mu\text{m}/\text{W}$  respectively, occurs for core radii of 720 nm and 460 nm respectively. For the lateral stiffness this means that the particle is roughly as large as the wavelength of the trapping laser in silica. In a way, it is as if the core is optically trapped in silica as a suspending medium. The focus is significantly larger in the axial direction leading to a larger optimal size. The optimal shell thickness is only slightly different with 180 nm for the lateral directions and 200 nm for the axial direction.

Note that the maximum stiffnesses for melamine coated with silica are higher than the stiffness we observed for un-coated particles as in Figure 5.22. Particularly in the axial direction the silica coated melamine particle is trapped stiffer, 570 pN/ $\mu\text{m}/\text{W}$  versus 486 pN/ $\mu\text{m}/\text{W}$  in ethanol, or, due to the even larger scattering forces there, 474 pN/ $\mu\text{m}/\text{W}$  in water. The silica coating works quite well as an anti-reflection coating to minimize the scattering force that comes with the high index of the core. The difference in trapping depth, caused by the silica shell, causes also the lateral trapping stiffness to be higher. Bare melamine in water, with the geometrical focus at 14  $\mu\text{m}$  above the glass plate has a maximum lateral stiffness of 3098 pN/ $\mu\text{m}/\text{W}$  versus 3830 pN/ $\mu\text{m}/\text{W}$  for a melamine particle with an optimal silica coating. This optimal shell thickness is slightly smaller than the optimal for axial trapping stiffness. Probably the extra bit of lateral stiffness is partially caused trapping forces exerted on the silica shell. The different trapping depth cause the particle to be trapped closer to the effective focus which makes that the particle experiences greater intensity gradients in the lateral directions, resulting in larger gradient forces and thus larger lateral stiffnesses.

We reproduce the trapping behavior of silica coated melamine particles in more detail in Figure 5.27. For different combinations of core radius and shell thickness, we plot the dependence of the axial trapping efficiency as a function of the distance to the geometrical focus in black. Whenever there was a stable trapping depth, which was always the case for the parameters tested here, we

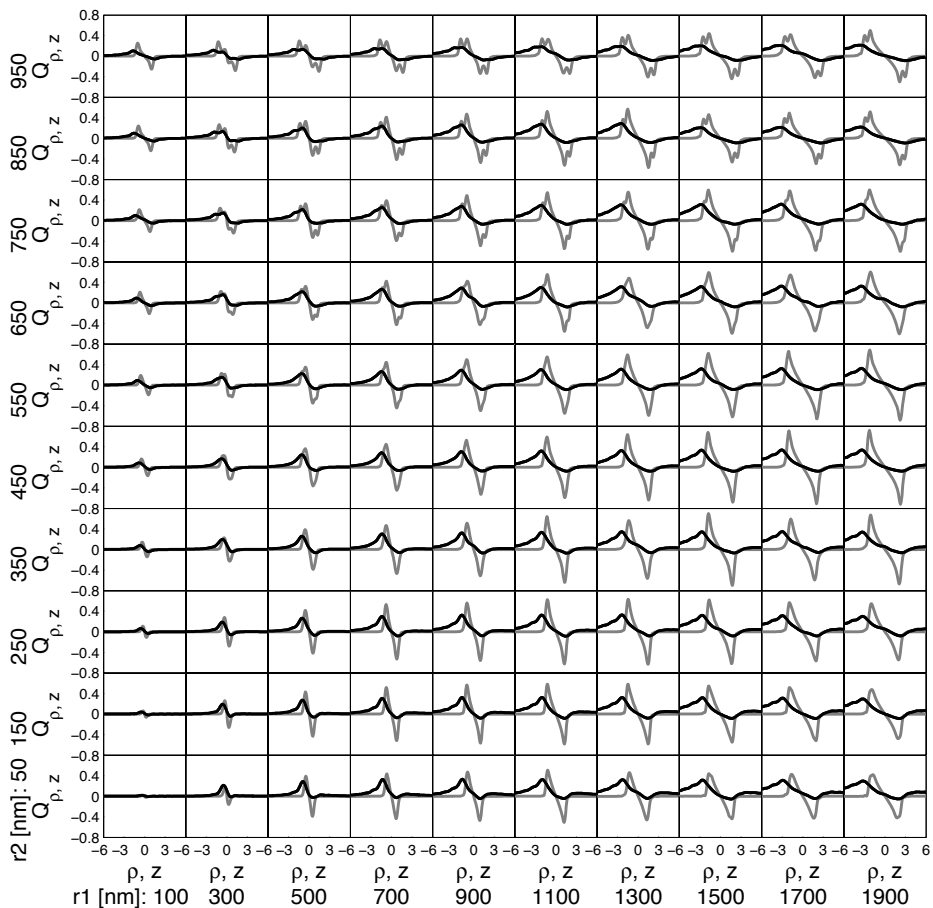


**Figure 5.27:** The trapping behavior of a silica ( $n_{\text{shell}} = 1.45$ ) coated melamine ( $n_{\text{core}} = 1.68$ ) particle in water ( $n_{\text{medium}} = 1.33$ ). The particle's core radius  $r_1$  in  $\mu\text{m}$  and the thickness of the silica shell  $r_2$  in  $\mu\text{m}$  are varied to study the trapping behavior. The geometrical focus is assumed at a depth of  $14 \mu\text{m}$  above the bottom glass plate. For each particle size and refractive index we plot the axial trapping efficiency in black as a function of the position with respect to the geometrical focus. When there is a stable trapping location in the  $z$ -direction we include the lateral trapping efficiency as a function of the lateral distance in the trapping plane to the optical axis, in grey.

plotted the dependence of the lateral trapping efficiency on the distance to the optical axis in grey. A nice feature of particles that have a coating that is bit thicker than the size of the focus is a little wiggle in the lateral trapping efficiency

for particle displacements of about a wavelength. Both the silica shell and the melamine core are attracted to the focus. When also the core is entering the effective focus, the attraction increases even more. When the shell is thicker than about 650 nm, the lateral trapping efficiency shows a local minimum. We think that this is due to the silica shell that has to leave the focus to make place for the melamine core.

The maximal restoring force, the largest force down, for all combinations of core radius and shell thickness is rather small with respect to the maximum upward force. This is due to the high refractive index of the melamine core. The silica shell helps to reduce the scattering force on the melamine core but the trapping remains potentially unstable.

When the refractive index of the core material is even larger than that for melamine, both the scattering force and the gradient force become larger. We should be careful ascribing too much significance to the value of the trapping stiffness. The maximal restoring force is much more important when we are interested in trappability. A high stiffness is only useful when the particle is actually trapped.

As an example for the trapping of high index particles with an anti reflection coating we calculated the trapping behavior of an anatase titania ( $n_{\text{core}} = 2.4$ ) particle with an amorphous titania shell in water. We assumed the refractive index  $n_{\text{shell}}$  to be about 1.8 as experimentally determined in section 2.5.2 and reference [56, 57]. This kind of particles was used to achieve higher trapping stiffnesses that were useful doing experiments on molecular motors [66–68].

Figure 5.28 is similar to Figure 5.26 in that it depicts the trapping stiffnesses, the trapping depth and the maximum restoring force in false colors as a function of the particle's core and shell dimensions. The physics is similar as before, but now the scattering force is more dominant. As a result, many particles are predicted to be not trappable. Only particles with an anti-reflection coating are foreseen to be trappable. Due to the higher refractive index of the shell material the thinnest shell for which the coating works as an antireflection coating is about 140 nm.

This is comparable to a quarter of the wavelength of the trapping laser in amorphous titania with a refractive index of 1.8. Note also the small region in parameter space where the particles are trappable in the axial direction but not in the lateral direction, similar to Figure 5.22 for the trapping of uniform particles with different sizes and refractive indices. Also here, we think it is mainly the result of spherical aberration that the light intensity a little away from the optical axis is slightly higher. In Figure 5.29 we plot, in analogy to Figure 5.27, the axial trapping efficiency as a function of the trapping depth in black. If a particle with a particular core radius and shell thickness is trappable, we calculated the lateral trapping efficiency. In this case, where the index of refraction of the core is even higher, the major trends are the same as for melamine. Titania particles with similar shell thickness are trapped deeper below the geometrical focus. The scattering

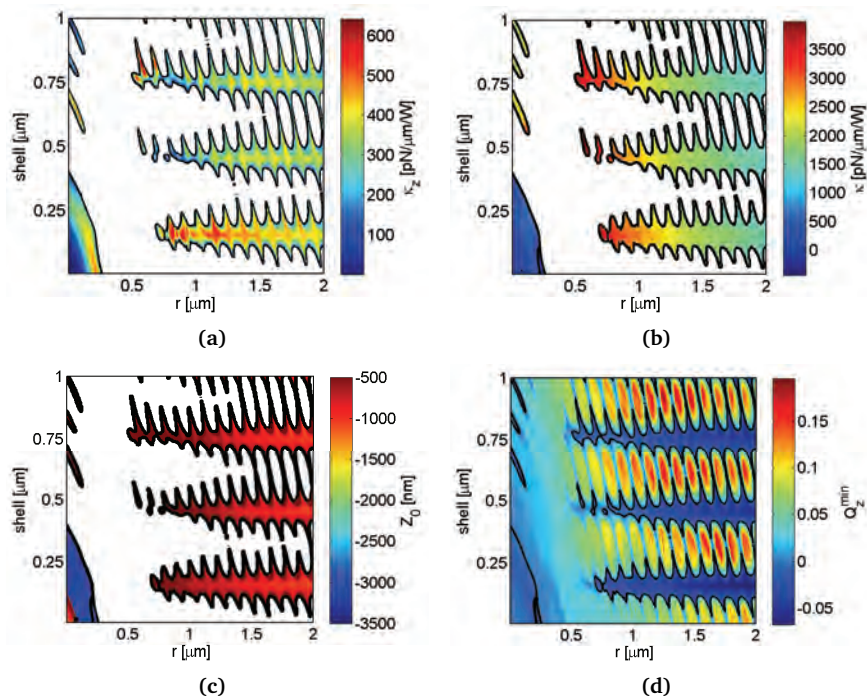


**Figure 5.28:** The trapping behavior of an amorphous titania ( $n_{\text{shell}} = 1.8$ ) coated anatase titania ( $n_{\text{core}} = 2.4$ ) particle in water ( $n_{\text{medium}} = 1.33$ ). **a.** The trapping stiffness in the axial direction in false colors as a function of the radius of an anatase titania ( $n_{\text{core}} = 2.4$ ) core in  $\mu\text{m}$  and the thickness of the amorphous titania ( $n_{\text{shell}} = 1.8$ ) shell. The particle is assumed to be trapped in water ( $n_{\text{medium}} = 1.33$ ) with the geometrical focus at a depth of  $14 \mu\text{m}$  above the bottom glass plate. When there was no stable trapping the corresponding pixel was left white. The border between trappable and not trappable has been encircled with a black line. **b.** The same for the stiffness in the lateral direction. There are particle configurations that yield axial, but no lateral trapping, this region has been encircled with the thick line. **c.** The trapping depth with respect to the geometrical focus. Also here, the pixel was left white when no stable trapping location could be found. **d.** The maximum restoring force  $Q_z$ . The black lines mark the edge between the trappable and the non-trappable regions in parameter space.

force in is this case even larger so that the antireflection coating is really necessary to be able to trap the particles at all. Some of the smaller core sizes that yielded particles that were trapped deeper below the geometric focus in Figure 5.27 and 5.26 are now no longer trappable.

The axial trapping efficiency is plotted in Figure 5.29 as a function of the position with respect to the geometrical focus for a selection of anatase ( $n_{\text{core}} = 2.4$ ) core radii and amorphous titania ( $n_{\text{shell}} = 1.8$ ) shell thicknesses. The variation of the scattering force around the effective focus due to the varying anti reflection effect is rather subtle. They do sometimes allow the particle to be trapped but the

Core Mat.	Shell Mat.	RI	RI	Core radius nm	Shell radius nm	$\kappa_z$ $\frac{pN}{\mu mW}$	$\kappa_\rho$ $\frac{pN}{\mu mW}$	Max. $Q_{rest.}$
TiO <sub>2</sub> anatase	TiO <sub>2</sub> amorph.	2.4	1.8	2000	860	<b>347</b>	1022	-0.002
				1920	1000	179	<b>1320</b>	-0.001
				1940	1000	300	1259	<b>-0.003</b>
TiO <sub>2</sub> anatase	SiO <sub>2</sub>	2.4	1.45	220	10	<b>472</b>	-52	-0.010
				1100	610	427	<b>2286</b>	-0.003
				80	1000	151	996	<b>-0.028</b>
TiO <sub>2</sub> amorph.	SiO <sub>2</sub>	1.8	1.45	700	190	<b>692</b>	2036	-0.033
				540	180	112	<b>3980</b>	-0.003
				1920	970	285	846	<b>-0.053</b>
Mel.	SiO <sub>2</sub>	1.68	1.45	720	180	<b>570</b>	1532	-0.040
				460	200	232	<b>3830</b>	-0.015
				1920	980	235	682	<b>-0.064</b>
PS	SiO <sub>2</sub>	1.59	1.45	640	190	<b>453</b>	1466	-0.038
				420	180	271	<b>3134</b>	-0.019
				2000	1000	141	504	<b>-0.065</b>

**Table 5.1:** The trapping stiffnesses and size parameters for either optimized axial stiffness, lateral stiffness or optimized restoring force (here negative is good) of some combinations of core and shell material. The optimized parameter is given in **bold numbers**. The geometrical focus is positioned at 14  $\mu m$  from the glass.

maximal restoring forces are rather small, ( $\sim 0.001-0.01$ ). As the energy barrier for escape is be low, it will be difficult to actually trap these particles.

There are various materials that could be used to construct core shell particles. In table 5.6.1 we give the optimal axial trapping stiffnesses for some of the imaginable combinations of core and shell material, to be trapped in water, with the geometrical focus at 14  $\mu m$ . Because apart from a high trapping stiffness,

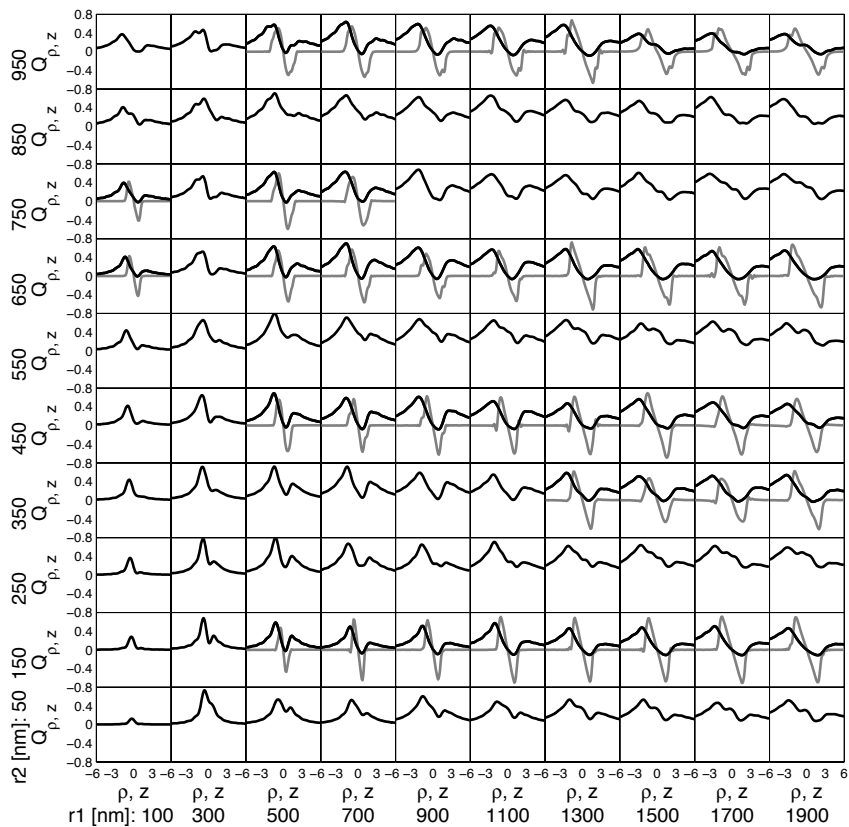


**Figure 5.29:** The trapping behavior of a anatase titania ( $n_{\text{core}} = 2.4$ ) particle with an amorphous titania ( $n_{\text{shell}} = 1.8$ ) shell in water ( $n_{\text{medium}} = 1.33$ ). The trapping behavior as a function of the particle's core radius  $r_1$  in  $\mu\text{m}$  and the thickness of the shell  $r_2$  in  $\mu\text{m}$ . The geometrical focus is assumed at a depth of  $14 \mu\text{m}$  above the bottom glass plate. For each particle size and refractive index we plot the axial trapping efficiency in black as a function of the position with respect to the geometrical focus. When there is a stable trapping location in the  $z$ -direction we include the lateral trapping efficiency as a function of the distance from the optical axis in the trapping plane in grey.

also the maximal trapping efficiency or the restoring force is important for good trapping we include these values. The values correspond to the optimal in the **bold faced** parameter, either the axial or lateral trapping stiffness or the maximal restoring force. Indeed, when an antireflection coating sufficiently minimizes the scattering force to be able to trap a higher index particle, this generally yields stiffer trapping. This trend certainly holds for the lateral trapping stiffness as here

the scattering force plays no role. An antireflection coating works better if both surfaces have the same reflection coefficient such that the amplitude of the waves that should be interfering destructively are similar in amplitude. A particle which consists of an anatase titania core ( $n_{\text{core}} = 2.4$ ) can obviously not be coated with an optimal antireflection coating made out of silica. A melamine particle which is coated with silica, on the contrary works quite well. Note that melamine scores also good as bare material to be trapped stiffly.

If we want to minimize the risk of loosing our trapped particle, rather than maximizing the stiffness with which we trap them, we should optimize the maximum restoring force. This, is generally achieved for the larger particles. Larger particles interact over much larger distances with the focus and as a result the slopes in the force curves are smaller and thus the stiffnesses are smaller as well.

### 5.6.2 $n_{\text{core}} > n_{\text{shell}} < n_{\text{medium}}, n_{\text{core}} > n_{\text{medium}}$

An often used system in soft matter research consists of PMMA particles in a mixture of CycloHexyl Bromide and cisdecahydronaphthalene, (CHB-decalin) [51]. This is an interesting combination of materials because it allows one to almost simultaneously index- and density-match the particles. Moreover, by adding an appropriate salt, it is possible to tune the screening length from almost hard sphere to soft and long range [69–79]. Index matching of the particles is done to minimize the scattering by the particles, this allows one to apply confocal microscopy to image deep into a concentrated sample. Moreover the refractive index of the dispersion is similar enough to that of the glass to have spherical aberration at the glass-oil interface not hinder the imaging. As the particles are index matched and do not scatter light, the optical tweezer does not exert any force on the particles [45]. A minimal refractive index mismatch of  $\sim 0.001$  for the wavelength of the trapping laser can cause the trap to also exert significant forces on the host particles. The correct matching can be experimentally verified by averaging several confocal micrographs of a dispersion of host particles as they diffuse through the ‘empty’ trap [45]. Polystyrene is an example of a common material with an index of refraction that is even higher than that of the PMMA and the CHB-decalin. As a result, it is possible to trap PS particles in CHB or in a dense dispersion of index matched PMMA particles in a mixture of CHB-decalin. The latter is interesting because it gives us handles to manipulate single particles in the bulk without exerting forces on the surrounding particles. This can be used to study for instance nucleation on a template of particles [80].

Unfortunately, un-crosslinked PS dissolves in CHB. Moreover it is of interest to make sure that the interaction between a tracer, the trappable particle, and a host, the index matched particle, is the same as the interaction between two host particles. In order to make the interactions between tracers and hosts identical to the interactions between the hosts amongst themselves one could coat the particles with a layer of (index matched) PMMA. To facilitate the growth of PMMA on PS and in order to protect the PS against dissolving in the CHB, the PS can first

be coated with silica [45].

The particles that formed the bulk of the experimental dispersion in reference [80] were PMMA particles which were completely dyed with 1,1'-dioctadecyl-3,3,3',3'-tetramethylindocarbocyanideperchlorate (DiIC) and sterically stabilized with poly(12-hydroxystearic acid), PHS. The PHS was not locked to the particles. These host particles were  $0.93\ \mu\text{m}$  in diameter. The seed particles were made from polystyrene cores with a diameter of  $0.99\ \mu\text{m}$  onto which a  $50\ \text{nm}$  silica shell was grown as described in reference [54]. Subsequently, the silica shell was coated with 3-(trimethoxysilyl) propyl methacrylate and the PMMA-PHSA steric stabiliser [45]. The final diameter of the tracer particles was  $1.1\ \mu\text{m}$ . The solvent matched the index of refraction of the PMMA host particles at  $1064\ \text{nm}$  and consisted of a mixture of CHB and cis-decalin. We verified that the bulk fluid particles were unaffected by the presence of an empty optical trap. The interactions between the particles were tuned to be nearly hard-sphere-like by saturating the solvent with the salt TetraButylAmmonium Bromide, TBAB. The dielectrophoretic compression was obtained by a 'slit-like' geometry as described in reference [78]. The cell was approximately  $15\ \text{mm}$  by  $8\ \text{mm}$  by  $70\ \mu\text{m}$  and the slit was approximately  $0.3\ \text{mm}$  wide.

The tracer particles were trapped in a time-shared array of either 25 traps in a square array with the spacing chosen to be twice the distances between the particles in the (100)-plane of a Face Centered Cubic, FCC, hard sphere crystal of the host particles at coexistence. Similarly, 16 tracer particles were trapped in a hexagonal array with a spacing that matches the spacing between the particles in the (111)-plane of an FCC-crystal at coexistence. Although the particles are refractive index matched by the solvent at the wavelength of the trapping laser, the dielectric constant at zero frequency of the particles is different, (lower) from that of the solvent. When an alternating current is applied between the electrodes outside of the slit, the particles are polarized. Similar to in the optical case, this polarized the particles. As the polarizability of the particles is negative, the particles experience a negative gradient force at the edge of the slit. The particles are pushed into the slit where the field-strength is less than in between the electrodes [78].

In about 180 minutes this increased the volume fraction in the slit between about  $\eta = 0.30$  to  $0.50$ , close to coexistence between a hard sphere crystal and a liquid. After this, the volume fraction was increased a bit further and the nucleation of a crystal on the seed array of trapped particles was observed. In Figure 5.30 we reproduce confocal micrographs recorded, with a Leica NT scanhead, of the host particles with among them, the trapped arrays. The images have been averaged over 5-10 frames such that a clear distinction can be made between the crystalline and the liquid particles.

The square seed was observed to lower the nucleation barrier more than the hexagonal array did. While the square seeds lower the nucleation barrier remarkably well, they result in crystals with significantly more defects than the hexag-

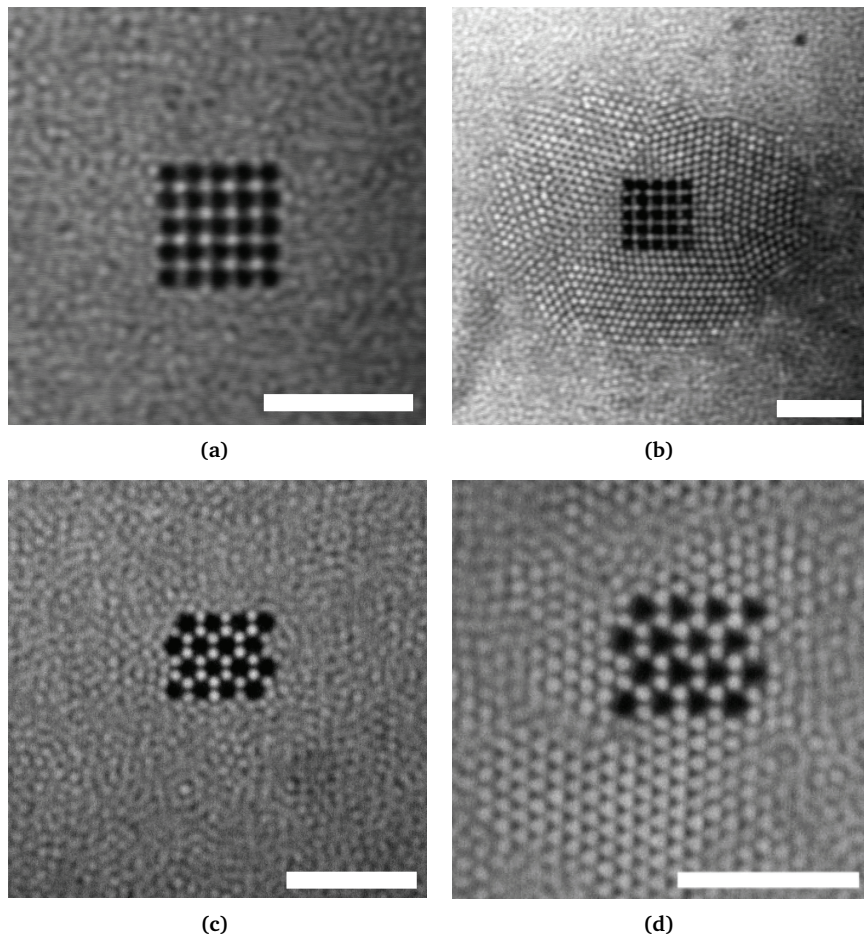


**Figure 5.30:** Crystals growing on 2D square and hexagonal seeds. **a.** Averaged confocal micrograph of a dispersion of  $0.93 \mu\text{m}$  PMMA particles in an index-matching CHB-decalin mixture in grey at a volume fraction below coexistence ( $\eta \approx 0.49$ ). The black particles are the  $1.1 \mu\text{m}$  silica coated PS particles, trapped in a square array of 5 by 5 particles, with the spacing chosen to match the (100)-plane of an FCC crystal. **b.** The crystal on the square seed has grown beyond its critical size at a volume fraction of  $\eta = 0.515$  (Molecular dynamics simulation value). To visualize the solid and the liquid particles, the frame has been averaged over 5-10 frames. **c.** As in **a** but with a hexagonal array of 4 by 4 tracer particles, with the spacing chosen to match the (111)-plane of an FCC crystal. **d.** The crystal on the square seed has grown beyond its critical size at a volume fraction of  $\eta = 0.535$  (Molecular dynamics simulation value). To visualize the solid and the liquid particles, the frame has been averaged over 5-10 frames. The scalebars are  $10 \mu\text{m}$ .

onal seeds and do not lead to large FCC crystals. For a more detailed discussion of the implications to nucleation theory and details of the simulations we refer to

reference [80].

In order to do these experiments, the tracer particles had to be trappable in the mixture of CHB and decalin with a refractive index close to that of PMMA, ( $n_{\text{medium}} = 1.494$ ), the refractive index of the tracer particles should be higher. Particles made of PS meet that requirement. The PS particles had to be coated with the same stabilizer as on the surface of the PMMA host particles to ensure that the tracer-host interaction was identical to the host-host interaction. In order to facilitate this coating, and to prevent the dissolution of the PS particle in the solvent, they were first coated with a silica layer. Silica, has an index of refraction of 1.45, much lower than that of the dispersion medium, the CHB-decalin (1.494) [80]. A particle of pure silica cannot be trapped in CHB.

It is interesting to know what the effect of a silica coating on the trapping behavior is. In order to understand the trapping behavior of PS particles with a layer of silica around them, we did calculations on the trapping behavior of these particles. Since a PMMA layer around the silica coating of the PS core is refractive index matched in the CHB-decalin mixture, it does not influence the trapping behavior of the particle so we ignore it in this analysis.

We depict the trapping behavior of silica coated PS particles in CHB as a function of the core radius ( $r_1$ ) and the thickness of the silica layer ( $r_2$ ) in Figure 5.31. The spherical aberration is in this case much smaller than in for instance ethanol, because of the smaller refractive index difference between the medium and the glass. We placed the geometrical focus 14  $\mu\text{m}$  above the bottom glass plate.

We give the trapping stiffnesses of these particles in Figure 5.31 **a** and **b** in false colors in the core-shell plane. Some particles scatter light in such a way that the restoring gradient force is never totally compensating the scattering force, and these particles could not be trapped. In that case, the corresponding pixel was left white. When the particle was indeed trappable, the axial and the lateral trapping stiffness were calculated at the trapping depth, which is depicted in Figure 5.31 **c**. The first observation is that almost all combinations of core size and shell thickness are trappable. Only particles with a PS core that is smaller than about 300 nm in radius and with more than about 400 nm of silica coating around them are not trappable. Some of the smaller PS cores with a silica coating with a thickness between about 200 and 400 nm are trappable, but these particles are trapped in a secondary trap caused by the small amount of spherical aberration.

The edge between trappable and not trappable zone in this 'trapping phase diagram' is almost vertical, at a core radius of about 300 nm. The fact that most particles even in the north western quadrant of the plot are trappable is surprising. The volume of the particle, occupied by the silica coating rapidly increases with the coating thickness. In general one would think that more silica, in CHB not trappable, means worse trapping. Instead, generally particles with a thicker coating are not trapped with a lower stiffness. For those particles that are trappable, the key factor determining the stiffness with which they are trapped, seems to depend mainly on the size of the core. A particle with a core radius of half a

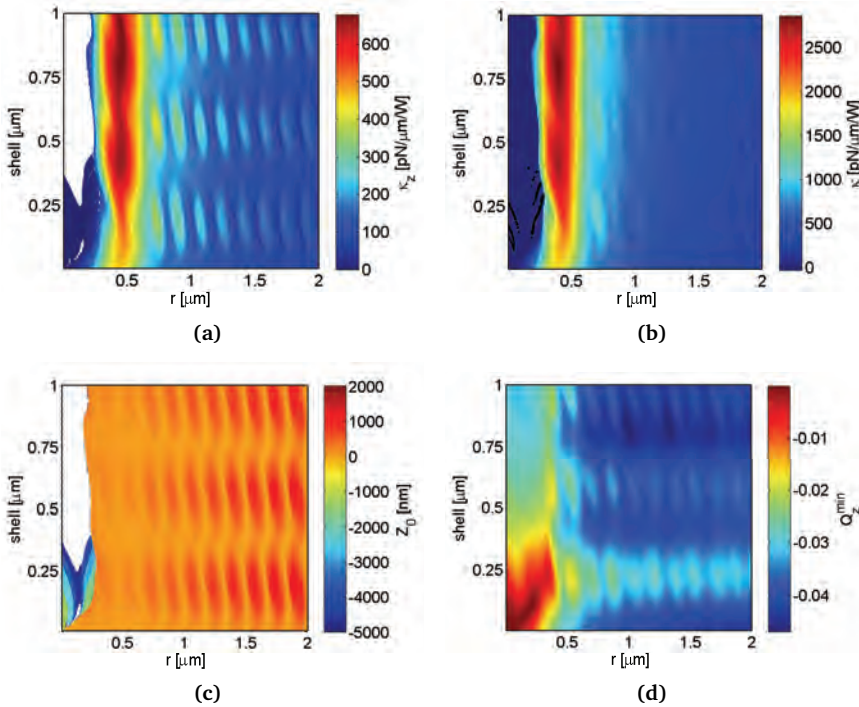


**Figure 5.31:** The trapping behavior of silica ( $n_{\text{shell}} = 1.45$ ) coated PS ( $n_{\text{core}} = 1.59$ ) particles in CHB ( $n_{\text{medium}} = 1.52$ ). **a.** The trapping stiffness in the axial direction in false colors as a function of the radius of a PS ( $n_{\text{core}} = 1.59$ ) core in  $\mu\text{m}$  and the thickness of the silica ( $n_{\text{shell}} = 1.45$ ) shell. The particle is assumed to be trapped in CHB ( $n_{\text{medium}} = 1.52$ ) with the geometrical focus at a depth of  $14 \mu\text{m}$  above the bottom glass plate. When there was no stable trapping the corresponding pixel was left white. **b.** The same for the stiffness in the lateral direction. **c.** The trapping depth with respect to the geometrical focus. Also here, the pixel was left white when no stable trapping location could be found. **d.** The maximal restoring force. The black line marks the frontier between the trappable and the non-trappable zone in parameter space.

micron and a shell thickness of one micron is trapped no worse than the bare PS core would. In fact it is trapped even stiffer. Apparently, for this type of particle, consisting for 88 % of silica does not mean that it is untrappable in the higher index CHB. We could state that in the case of a thick shell, the PS core is effectively trapped in the silica, where the silica shell acts as the suspending medium to the core. This yields a higher index contrast than there would be for a bare PS particle in CHB. The PS core is attracted stronger to the focus than the silica shell is repelled.

The stiffness that keeps the particles at the trapping location reaches impressive values both in the lateral directions, and more importantly, in the axial direction. The maximum trapping stiffness in the lateral directions reaches a value

of  $2854 \text{ pN}/\mu\text{m}/W$  and the maximum axial stiffness is  $678 \text{ pN}/\mu\text{m}/W$ . These are considerable, because a bare PS core in CHB would experience a maximum trapping stiffness of  $1867 \text{ pN}/\mu\text{m}/W$  and  $460 \text{ pN}/\mu\text{m}/W$  in the lateral and axial directions respectively (the optimum radii are  $400 \text{ nm}$  with and  $440 \text{ nm}$  respectively). Coating with an appropriate layer of silica apparently enhances the trapping stiffness. The maximal trapping stiffnesses in the silica coated case, occur for the same shell thickness;  $800 \text{ nm}$ . The optimal core radius is almost the same for both stiffnesses,  $400 \text{ nm}$  and  $440 \text{ nm}$ , for lateral and axial trapping respectively. The outer diameter of such a particle therefore amounts to about  $2.4 \mu\text{m}$ . This particle consists for almost 94 volume percent of the, in CHB, not trappable silica. The volume averaged refractive index of this particle is only slightly higher than that of silica: 1.4535. A particle, of any size, with this refractive index homogeneously distributed over the particle is not trappable in CHB, because not only the scattering force, but also the gradient force pushes these particles away from the focus. Clearly the distribution of the refractive index throughout the particle is crucial for the trapping behavior.

If we look at the trapping stiffness for a certain, fixed shell thickness, for instance  $200 \text{ nm}$ , and vary the core size, there is an oscillation in the trapping depth and in the trapping stiffness. These oscillations are caused by the same interference effect we discussed in section 5.5. For instance in Figure 5.22 we observed similar undulations in the trapping stiffness. Indicative is the distance, about  $170 \text{ nm}$ , between two minima in the scattering force with the resulting minima in the trapping depth. This corresponds to steps of one wavelength in the double path length that the light which reflects on the second interface of the core has to traverse through the particle, as also described in section 5.5. If we assume the refractive index of the interferometer to be the 1.59 of PS we should get a period of  $167 \text{ nm}$  in the core radius, for silica we expect  $183 \text{ nm}$ . We thus concluded that the interferometer here is the silica layer around the PS core.

The undulations in the trapping location are also influenced by the vicinity of the silica-CHB interface. We observe that the amplitude of the oscillations in the trapping depth and the trapping stiffness as a function of the core size, is significantly reduced for certain shell thicknesses. This occurs for instance for a shell thickness of about  $375 \text{ nm}$  and also for a shell thickness of about  $745 \text{ nm}$ . Note that the wavelength of the trapping laser in silica, with its refractive index of 1.45 is only  $733.8 \text{ nm}$ . The scattering force can apparently also be minimized with a shell thickness of multiples of half a wavelength such that the total path length through the silica is causing destructive interference, reducing the scattering force. Whenever this is the case, the amplitude in the oscillations in the trapping location as a function of the varying core radius is much smaller, as the reflection is already minimized by the silica shell. A silica shell with a thickness of  $360 \text{ nm}$  or  $740 \text{ nm}$  can therefore be used as an anti-reflection coating. This reduces the scattering of the PS core, as it also does in the case that the particle is dispersed in water [57, 64–67] and section 5.6.1.

We note that the variation in the trapping depth and the axial trapping stiffness in the (practical) absence of a silica layer is similar to the variation that we observe in the case of an antireflection coating. The oscillations with varying core size are minimized. In fact, the silica coating which has a higher contrast with the PS core than the CHB, increases the scattering. The amplitude of the variation in reflectivity with varying core radius, or more accurately, the reflectivity of the shell varies with the shell thickness. Contrary to what we found in section 5.6.1 for the case where the refractive index of the shell is in between that of the dispersion medium and that of the core, there is a minimum in the reflectivity of the particle at a shell thickness of  $0 \mu\text{m}$ . The oscillation of the reflectivity with the shell thickness is shifted by half a period,  $\pi$ . If light reflects on the interface between two refractive indices it depends on the sign of the index jump if the phase of the reflected light is shifted by  $\pi$ , or not. In section 5.6.1, where the refractive index increased, both when entering the shell and when entering the core, the light that was reflected from both interfaces experienced a phase shift of  $\pi$ . To the contrary, here the light that reflects off the CHB-silica interface does not experience a phase shift of  $\pi$ . The result is clear, when the shell is thin, the light beams that reflect off both interfaces of the shell have a mutual phase difference close to  $\pi$  and interfere destructively.

If we choose the wrong shell thickness we can effectively increase the reflection of the particle by constructive interference. This increases the scattering force on the particle. Note also that the steps in the thickness of the silica shell, necessary to minimize the scattering force, are twice those in the variation in the core radius direction. This is because it is the shell on only one side of the particle that acts as an interferometer, whereas for the core it is the diameter that counts. A convenient consequence is that the precision with which one has to coat the particle in order to minimize the scattering force is half that with which the size of a homogeneous particle needs to be optimized.

We have a closer look at the trapping behavior of silica coated PS in CHB in a focus made with the geometrical focus  $14 \mu\text{m}$  above the glass plate in Figure 5.32. The setup of this Figure is similar to that of Figure 5.24. A patchwork of little graphs represents the trapping efficiency as a function of the position for various particles. The trapping efficiency in the axial direction is plotted in black. Whenever the particle under investigation could be trapped in the axial direction we plot the lateral trapping efficiency at the trapping depth in grey.

The most striking observation to be made is the great similarity between the various graphs. This is in accordance with the observation made from Figure 5.22, that most combinations of shell thickness and core radius yield trappable particles. We note that the particles experience only a small restoring force. In general, the maximal axial forces are not at all large as the trapping efficiency never exceeds values of about 0.1. If we take a closer look at the profiles for the scattering efficiency in the axial direction for the particles with a core radius of respectively 1200 and 1400 nm, both with a shell thickness of 200 nm, we note that the larger

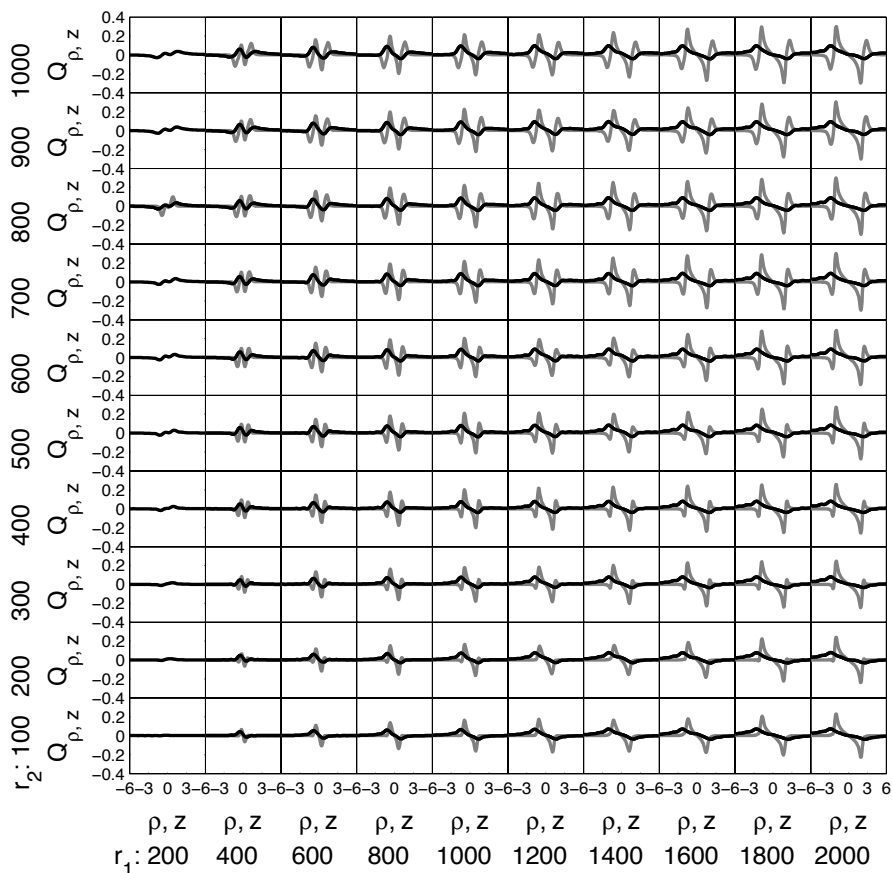


**Figure 5.32:** The trapping of silica ( $n_{\text{shell}} = 1.45$ ) coated PS ( $n_{\text{core}} = 1.59$ ) particles in CHB ( $n_{\text{medium}} = 1.52$ ). The trapping behavior of a PS ( $n_{\text{core}} = 1.59$ ) particle with a silica ( $n_{\text{shell}} = 1.45$ ) shell in CHB ( $n_{\text{medium}} = 1.52$ ), as a function of the particle's core radius  $r_1$  in  $\mu\text{m}$  and the thickness of the shell  $r_2$  in  $\mu\text{m}$ . The geometrical focus is assumed at a depth of  $14 \mu\text{m}$  above the bottom glass plate. For each particle size and refractive index we plot the axial trapping efficiency in black as a function of the position with respect to the geometrical focus. When there is a stable trapping location in the  $z$ -direction we include the lateral trapping efficiency as a function of the distance from the optical axis in the trapping plane in grey.

particle experiences a larger force upward around the geometrical focus than the smaller one. This is in line with the corresponding zone in Figure 5.22.

The larger particle is trapped further upwards due to the larger scattering force. The thickness of the silica layer quite efficiently optimizes the reflection of the particle such that the specific size of the core has a great influence on the

final reflectivity and thus scattering force. The axial force curve, in black, shows a small bump that the curve for the smaller particle does not have.

The lateral trapping efficiency profiles (grey lines) show an interesting pattern. At small distances from the optical axis, say smaller than the core diameter, we observe the standard profile where the particle is pushed back to the optical axis. When the silica shell is thicker than about 200 nm we start to observe a remarkable peak in the force in the other direction. At larger displacements from the optical axis, the particle is pushed even further away from the optical axis. This is obviously due to the fact that when the particle is positioned far enough away from the focus, the focus interacts practically only with the silica shell. The silica shell, due to its negative refractive index contrast with the CHB, is pushed away from the focus.

That a particle beyond a certain distance from the optical axis would be pushed even further away means that for instance if we want to trap the particle in an array of time-shared traps that then the trapping is more difficult than in the absence of a silica layer. The particle would have to diffuse a smaller distance in the time interval during which the trap is off in order to be no longer trapped. The effect is even more of a problem when the time interval during which the trap is left off is intentionally increased, for instance to measure a force on the particle as done in the technique describe in reference [81] and Chapter 3. With increasing shell thickness the repulsive effect of the shell becomes stronger, in some cases the maximal repulsive force is even larger than the maximal attractive force. Practically, this makes it also harder to trap the particle, or more precisely to get the particle into the trap. This can be avoided by choosing the silica shell as thin as possible but certainly not thicker than 200 nm.

### 5.6.3 $n_{\text{core}} > n_{\text{shell}} < n_{\text{medium}}, n_{\text{core}} = n_{\text{medium}}$

As already mentioned before, PS can be dissolved in CHB. It is therefore possible that, in case the silica layer is porous, the PS core is dissolved by the CHB, leaving a hollow shell of silica in CHB. Since silica has an index of refraction that is lower than that of CHB, we might expect such hollow shells to not be trappable.

To our surprise this is not the case. We depict the trapping stiffness and trapping depth of hollow silica shells with a thickness of  $r_2$  around a droplet of CHB with a radius of  $r_1$  in CHB, with the geometrical focus again at 14  $\mu\text{m}$  above the glass plate in Figure 5.33. Contrary to our expectations, we notice that many of these particles are trappable. The maximal trapping stiffness we observe for a silica coated CHB droplet in CHB is in the axial and lateral directions respectively 1010 pN/ $\mu\text{m}/W$  and 246 pN/ $\mu\text{m}/W$ . This is lower than the 2854 pN/ $\mu\text{m}/W$  and 678 pN/ $\mu\text{m}/W$  we found for the case PS in the silica shell was not dissolved. Nevertheless these are very good trapping stiffnesses, particularly when considering that these particles are made of silica that cannot normally be trapped in CHB. Here, there is no other explanation than that we are effectively trapping a CHB droplet in silica as the dispersion medium. The silica is repelled less strong

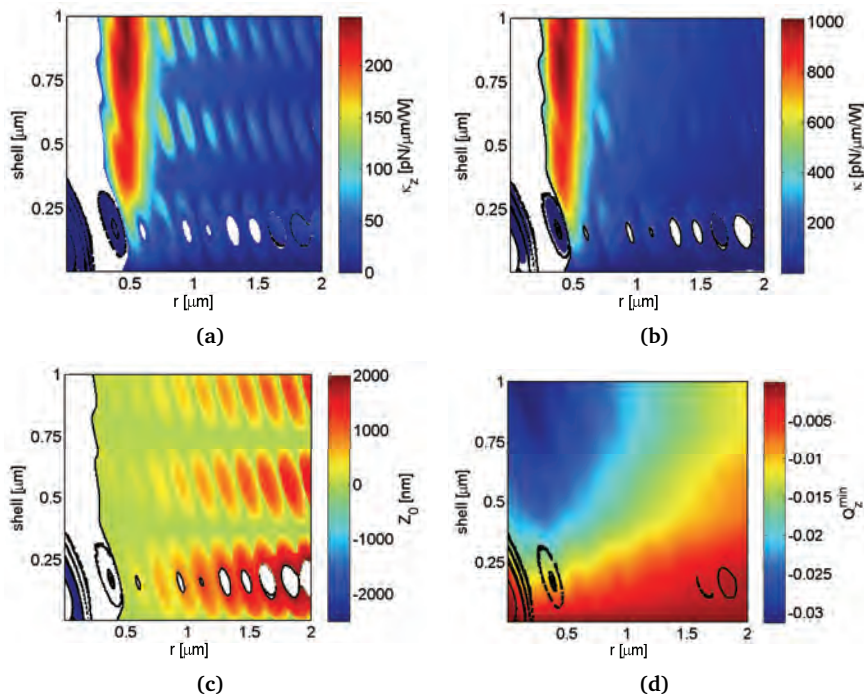


**Figure 5.33:** The trapping stiffness of hollow ( $n_{\text{core}} = n_{\text{medium}}$ ) silica shells ( $n_{\text{shell}} = 1.33$ ) in CHB ( $n_{\text{medium}} = 1.52$ ). **a.** The trapping stiffness in the axial direction in false colors as a function of the radius of a hollow silica ( $n_{\text{shell}} = 1.45$ ) shell, in and filled with CHB ( $n_{\text{medium}} = n_{\text{core}} = 1.52$ ). The geometrical focus is placed at a depth of  $14 \mu\text{m}$  above the bottom glass plate. When there was no stable trapping, the corresponding pixel was left white. **b.** The same for the stiffness in the lateral direction. **c.** The trapping depth with respect to the geometrical focus. Also here, the pixel was left white when no stable trapping location could be found. **d.** The maximal restoring force. The black lines demarcate the zones where the particle cannot be trapped in the lateral direction.

than the CHB is attracted to the focus. The refractive index of the CHB is lower than that of PS which makes that the CHB core in the silica shell experiences smaller scattering and gradient forces.

The structure in the local maxima and minima in the trapping depth and the trapping stiffness for these silica coated CHB droplets in CHB is similar to that in the case where the refractive index of the core is higher than that of the dispersion medium. (Figure 5.31) We still observe the periodic undulations of the trapping depth with increasing core radius. Although the refractive index of the CHB core is lower than that of the PS core, it is still higher than that of the silica shell that surrounds the particle. When either the core diameter or the shell thickness is an integer multiple of half the wavelength of the light in the material under consideration, the reflected light can again interfere destructively, reducing the

scattering force.

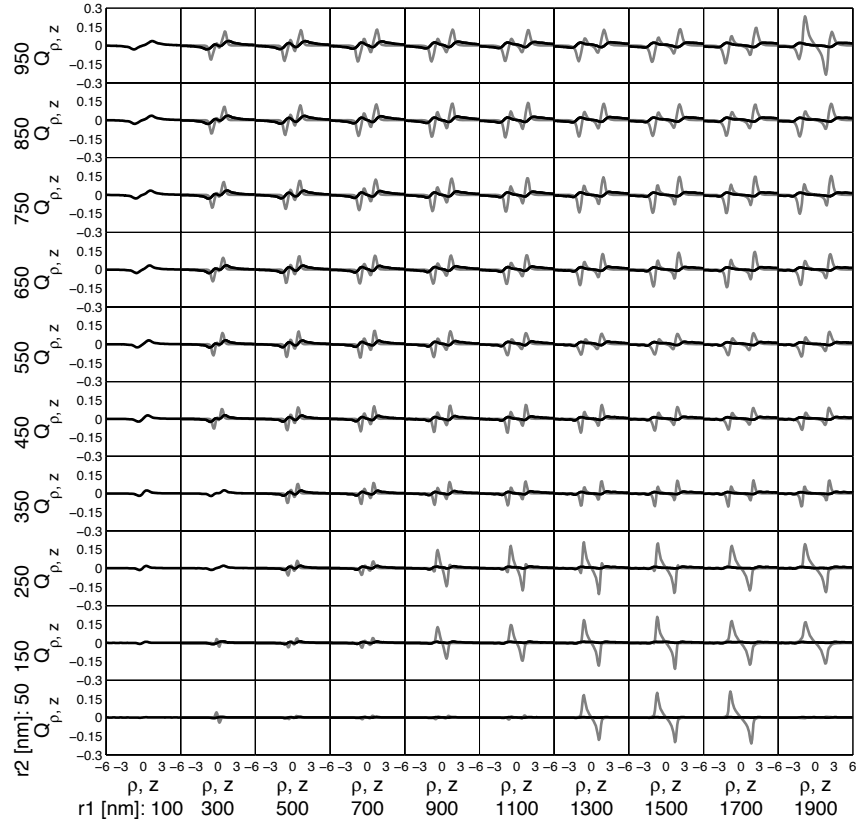


**Figure 5.34:** Trapping hollow ( $n_{\text{core}} = n_{\text{medium}}$ ) silica shells ( $n_{\text{shell}} = 1.33$ ) in CHB ( $n_{\text{medium}} = 1.52$ ). The trapping behavior of a hollow silica ( $n_{\text{shell}} = 1.45$ ) shell immersed in and filled with CHB ( $n_{\text{core}} = n_{\text{medium}} = 1.52$ ), as a function of the droplets radius  $r_1$  in  $\mu\text{m}$  and the thickness of the shell  $r_2$  in  $\mu\text{m}$ . The geometrical focus is assumed at a depth of  $14 \mu\text{m}$  above the bottom glass plate. For each particle size and refractive index we plot the axial trapping efficiency in black as a function of the position with respect to the geometrical focus. When there is a stable trapping location in the  $z$ -direction we include the lateral trapping efficiency as a function of the distance from the optical axis in the trapping plane in grey.

The trapping efficiency is plotted in Figure 5.34 for various core radii and shell thicknesses. The axial trapping efficiency is plotted as a function of the depth with respect to the geometrical focus in black. Whenever there was a stable trapping location, the lateral trapping efficiency at the trapping depth is plotted in grey.

We can say two things about this. First of all, although formally the particles can be trapped in the axial direction, not only are the trapping stiffnesses low, also the maximum forces are small. These coated droplets will be trappable but hard to manipulate. In the lateral directions the characteristic signature of a particle that can be trapped but that has a shell that cannot, as we saw in Figure 5.32 can be recognized. This means that, at larger distances from the optical axis, we observe that the particle is pushed even further away. The sign of the refractive index steps in these hollow particles filled with CHB are the same as those in silica coated PS particles. This makes that, other than that the trapping is less good, the trapping behavior of hollow silica shells in CHB is qualitatively similar to that of silica coated PS particles. Also the scattering signature looks very similar between these two types of particles. It is therefore important to assure oneself that the PS cores did not dissolve in the CHB when the trapping behavior is unsatisfactory. When the silica layer is thin enough the coated PS particle will rise in the denser CHB. And 'empty' silica shell in CHB will sediment.

#### 5.6.4 $n_{\text{core}} < n_{\text{shell}} < n_{\text{medium}}$

If these hollow silica shells, or those describe in reference [61], but filled with water are dispersed in a high index oil, like CHB, one might imagine that the water stays inside the shell as the water does not mix with the oil. We plot the trapping efficiency for these particles in Figure 5.35 as a function of the position with respect to the geometrical focus. Again, for some of these particles, there are two minima in the axial trapping efficiency. In a few cases one of the two minima is actually negative such that the particle can be trapped. When the particle is trapped in the axial direction it can also be trapped in the lateral direction. This is due to the fact that the silica shell around the water is pushed away. Only a small excursion from the optical axis is enough to push the particle even further away though. These particles are therefore not very suitable to be trapped in a single laser focus.

#### 5.6.5 $n_{\text{core}} < n_{\text{shell}} > n_{\text{medium}}$

It is also possible to have a hollow shell of a higher index material immersed in a lower index liquid. An example is given the hollow shells of silica in water or ethanol as described in reference [61]. Similar hollow shells may be used for targeted drug delivery. The trapping stiffnesses, the trapping depth and the maximal restoring force are depicted in Figure 5.36 in false colors as a function of the inner and outer radius of such shells in a trap with the geometrical focus at a distance of 14  $\mu\text{m}$  above the glass plate. Roughly half of these hollow shells are trappable. Some particles are not trappable because there is no stable trapping location along the optical axis, these zones are encircled with the thick black lines. Others are non trappable because the lateral stiffness is negative at the trapping depth, these parameters are encircled with the thin black lines. Very similar to

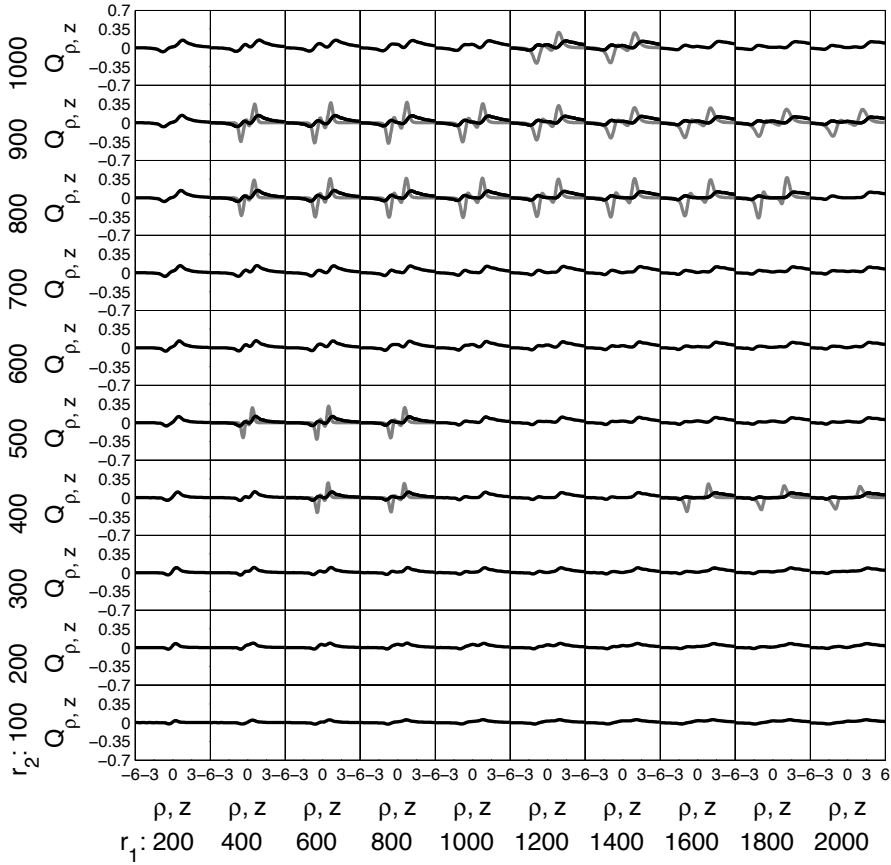


**Figure 5.35:** The trapping of a water droplet ( $n_{\text{core}} = 1.33$ ) with a silica shell  $n_{\text{shell}} = 1.45$  in CHB  $n_{\text{medium}} = 1.52$ . The trapping behavior of a hollow silica ( $n_{\text{shell}} = 1.45$ ) shell immersed in CHB ( $n_{\text{medium}} = 1.5052$ ) and filled with water ( $n_{\text{core}} = 1.33$ ), as a function of the particle's core radius  $r_1$  in  $\mu\text{m}$  and the thickness of the shell  $r_2$  in  $\mu\text{m}$ . The geometrical focus is assumed at a depth of  $14 \mu\text{m}$  above the bottom glass plate. For each particle size and refractive index we plot the axial trapping efficiency in black as a function of the position with respect to the geometrical focus. When there is a stable trapping location in the  $z$ -direction we include the lateral trapping efficiency as a function of the distance from the optical axis in the trapping plane in grey.

the silica coated particles in CHB discussed above, the reflection of these particles can be optimized with a silica shell of about  $200 \text{ nm}$ . The reflection enhancement by the shell is minimized for thin shells as the phase difference between the light that was reflected off either interface is close to  $\pi$ .

Also here this is caused by the phase-shift that light undergoes when it reflects

off an interface with a lower index of refraction. Only now it is the interface between the shell and the core at which the reflected light undergoes a  $\pi$  phase shift. Many of the water droplets with a very thin shell are not trappable though, because the particle is pushed away from the optical axis. From Figure 5.36 c there are two different types of trapping for these hollow shells. Shells with shell thickness larger than about 300 nm and with an inner radius of more than 1000 nm are often trapped significantly deeper below the geometrical focus. These particles can only be trapped in a secondary minimum caused by the spherical aberration.

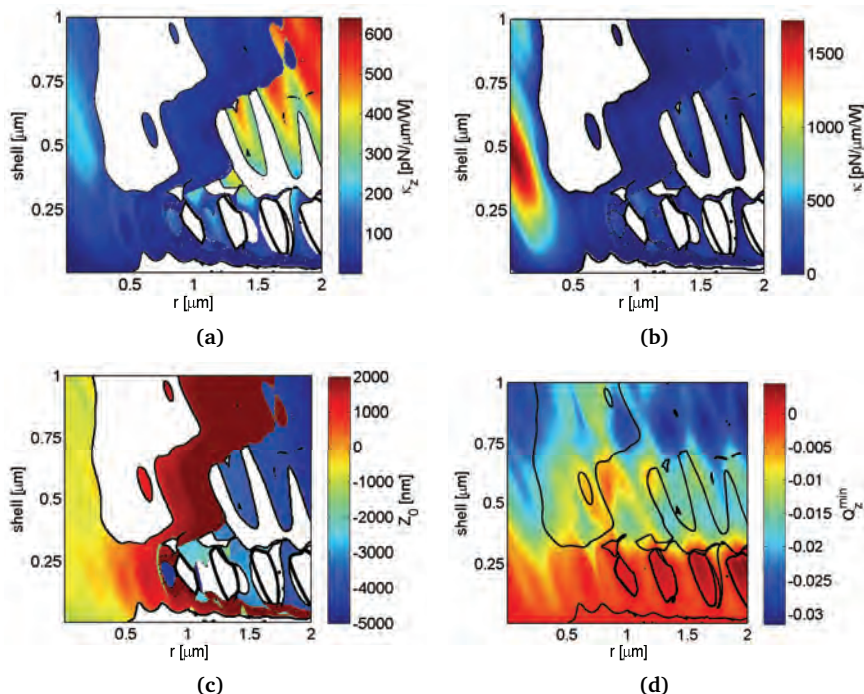


**Figure 5.36:** Trapping water filled ( $n_{\text{core}} = 1.33$ ) silica shells ( $n_{\text{shell}} = 1.45$ ) in water ( $n_{\text{medium}} = 1.45$ ). **a.** The trapping stiffness in the axial direction in grey values as a function of the radius of a hollow silica ( $n_{\text{shell}} = 1.45$ ) shell, in and filled with water ( $n_{\text{core}} = n_{\text{medium}} = 1.33$ ). The geometrical focus is placed at a depth of 14  $\mu\text{m}$  above the bottom glass plate. When there was no stable trapping the corresponding pixel was left white. **b.** The same for the stiffness in the lateral direction. **c.** The trapping depth with respect to the geometrical focus. Also here, the pixel was left white when no stable trapping location could be found. **d.** The maximal restoring force. The thin black lines indicate the borders of the regions where the shells cannot be trapped because of the negative lateral stiffness. The thicker lines indicate the borders of the zones where the shells cannot be trapped because the maximal axial restoring force is too large.

The trapping of these hollow shells is strongly influenced by the presence of

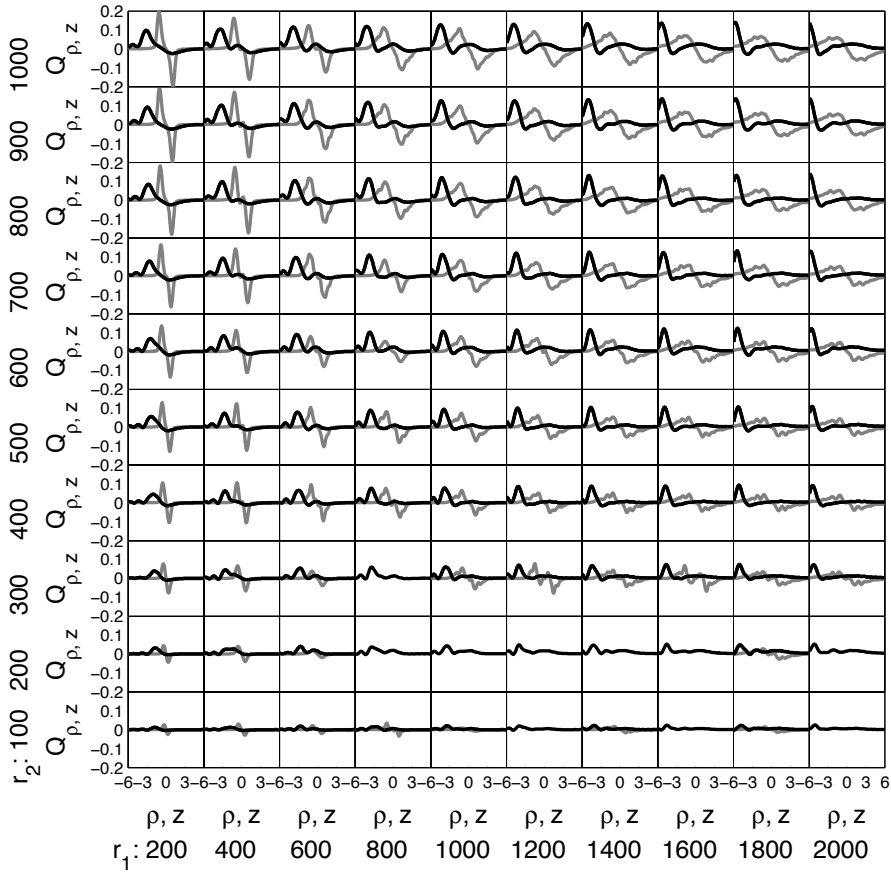


**Figure 5.37:** The trapping forces on hollow ( $n_{\text{core}} = 1.33$ ) silica shells ( $n_{\text{shell}} = 1.33$ ) in water ( $n_{\text{medium}} = 1.33$ ). The trapping behavior of a hollow silica ( $n_{\text{shell}} = 1.45$ ) shell immersed in and filled with water ( $n_{\text{medium}} = n_{\text{core}} = 1.33$ ), as a function of the particle’s core radius  $r_1$  in  $\mu\text{m}$  and the thickness of the shell  $r_2$  in  $\mu\text{m}$ . The geometrical focus is placed at a depth of 14  $\mu\text{m}$  above the bottom glass plate. For each particle size and refractive index, we plot the axial trapping efficiency in black as a function of the position with respect to the geometrical focus. When there is a stable trapping location in the  $z$ -direction we include the lateral trapping efficiency as a function of the distance from the optical axis in the trapping plane.

the spherical aberration. The particles are generally trapped quite deep, far below the geometrical focus. We compare the graphs in Figure 5.37, to a similar plot for solid particles trapped in water (depicted on the bottom row of Figure 5.24). At for instance the axial trapping efficiency for the hollow shells with an inner radius of 600  $\text{nm}$  and a shell thickness of 400  $\text{nm}$  or 500  $\text{nm}$ , the curves have

two local minima. For some of these particles this even results in two distinct trapping locations. The silica shell is trapped but the water droplet inside the silica is repelled due to its negative contrast with its surrounding silica layer. Just beyond the effective focus, the scattering force on both the core and the shell equilibrates with the gradient force on the shell. Below the effective focus the scattering force has to compete with the negative gradient force on the water core. This causes the two local minima in the trapping efficiency. For particles with the larger inner radii that were found to be trapped deeper in Figure 5.36 c, the minimum just beyond the effective focus is not deep enough to trap the particle there. In fact the upward gradient force on the water droplet fills the minimum caused by the downward gradient force on the shell in some cases.

Also in the lateral directions there are traces of the competition between the gradient force on the shell and the oppositely oriented gradient forces on the core. Often the gradient forces on the shell cause the particles to be pushed back to the optical axis if the excursions are not too large. We conclude that trapping hollow shells of a higher index material immersed in and filled with a lower index medium are difficult to trap.

## 5.7 Acknowledgements

We thank Jacob Hoogenboom for synthesis of the 1.4  $\mu\text{m}$   $\text{SiO}_2$  particles. Dannis 't Hart is thanked for the 758 nm  $\text{SiO}_2$  particles. Johan Stiefelhagen is thanked for the synthesis of all the other particles used in this chapter. Michiel Hermes, Esther Vermolen, Mirjam Leunissen and Dirk Vossen are thanked for the experiments and simulations on the crystallization of hard spheres on trapped arrays of silica coated PS particle of PMMA particles in CHB-decalin. Marjolein Dijkstra, and Frank Smalenburg is thanked for useful discussions. It is a pleasure to thank Astrid van der Horst for many tips and interesting discussions. Peter Helfferich is thanked for many interesting discussions, technical support and the conductance of the experiments on the nonconservative forces and the influence of the position of lens L3 on the trapping depth. Timo Rozendal is thanked for careful proofreading.

## Bibliography

- [1] Neto, P. A. M. and Nussenzweig, H. M. Theory of optical tweezers. *Europhysics Letters* **50** 702 (2000).
- [2] Mazolli, A., Neto, P. A. M., and Nussenzweig, H. M. Theory of trapping forces in optical tweezers. *Proceedings of the Royal Society of London A* **459** 3021 (2003).
- [3] Viana, N. B., Rocha, M. S., Mesquita, O. N., Mazolli, A., Neto, P. A. M., and Nussenzweig, H. M. Towards absolute calibration of optical tweezers. *Phys. Rev. E* **75** 021914 (2007).

- [4] Lorenz, L. Lysbevægelsen i og uden for en af plane Lysbølger belyst Kugle. *Videnskaberne Selskabs Skrifter* **6** 1 (1890).
- [5] Lorenz, L. Sur la lumière réfléchie et réfractée par une sphère (surface) transparente. *Oeuvres scientifiques de L. Lorenz. revues et annotées par H. Valentiner. Tome Premier, Libraire Lehmann & Stage, Copenhague* 403 (1898).
- [6] Mie, G. Beiträge zur Optik trüber Medien, speziell kolloidaler Metallösungen. *Annalen der Physik* **25(3)** (1908).
- [7] Aden, A. L. and Kerker, M. Scattering of electromagnetic waves from two concentric spheres. *J. Appl. Phys.* **22** 1242 (1951).
- [8] Bohren, C. F. and Huffman, D. R. Absorption and Scattering of Light by Small Particles. Wiley Interscience, New York (1983).
- [9] Richards, B. and Wolf, E. Electromagnetic diffraction in optical systems. II. Structure of the image field in an aplanatic system. *Proc. R. Soc. Lond. A* **253** 358 (1959).
- [10] Nieminen, T. A., Heckenberg, N. R., and Rubinsztein-Dunlop, H. Forces in optical tweezers with radially and azimuthally polarized trapping beams. *Opt. Lett.* **33** 122 (2008).
- [11] Kawachi, H., Yonezawa, K., Kozawa, Y., and Sato, S. Calculation of optical trapping forces on a dielectric sphere in the ray optics regime produced by a radially polarized laser beam. *Opt. Lett.* **32** 1839 (2007).
- [12] Dutra, R. S., Viana, N. B., Neto, P. A. M., and Nussenzveig, H. M. Polarization effects in optical tweezers. *J. Opt. A Pure Appl. Opt.* **9** S221 (2007).
- [13] [http://diogenes.iwt.uni-bremen.de/vt/laser/wriedt/Mie\\_Type\\_Codes/body\\_mie\\_type\\_codes.html](http://diogenes.iwt.uni-bremen.de/vt/laser/wriedt/Mie_Type_Codes/body_mie_type_codes.html) .
- [14] Ashkin, A. Forces of a single-beam gradient laser trap on a dielectric sphere in the ray optics regime. *Biophys. J.* **61** 569 (1992).
- [15] Viana, N. B., Mazolli, A., Neto, P. A. M., and Nussenzveig, H. M. Characterization of objective transmittance for optical tweezers. *Appl. Phys. Lett.* **88** 4263 (2006).
- [16] van der Horst, A. High-refractive index particles in counter-propagating optical tweezers-manipulation and forces. PhD Thesis, Utrecht University (2006).
- [17] Ashkin, A., Dziedzic, J. M., Bjorkholm, J. E., and Chu, S. Observation of a single-beam gradient force optical trap for dielectric particles. *Opt. Lett.* **11** 288 (1986).
- [18] Svoboda, K., Schmidt, C. F., Schnapp, B. J., and Block, S. M. Direct observation of kinesin stepping by optical trapping interferometry. *Nature* **365** 721 (1993).
- [19] Neves, A. A. R., Fontes, A., de Y. Pozzo, L., de Thomaz, A. A., Rodriguez, E. C. E., Barbosa, L. C., and Cesar, C. L. Electromagnetic forces for an arbitrary optical trapping of a spherical dielectric. *Opt. Exp.* **14** 13101 (2006).
- [20] Richardson, A. C., Reihani, S. N. S., and Oddershede, L. B. Non-harmonic potential of a single beam optical trap. *Opt. Exp.* **16** 15709 (2008).
- [21] Lee, S.-H., Roichman, Y., Yi, G.-R., Kim, S.-H., Yang, S.-M., van Blaaderen, A., van Oostrum, P., and Grier, D. G. Characterizing and tracking single colloidal particles with video holographic microscopy. *Opt. Exp.* **15** 18275 (2007).
- [22] Florin, E.-L., Pralle, A., Stelzer, E. H. K., and Hörber, J. K. H. Photonic force microscope calibration by thermal noise analysis. *App. Phys. A* **66** S75 (1998).
- [23] Vermeulen, K. C., L.Wuite, G. J., Stienen, G. J. M., and Schmidt, C. F. Optical trap stiffness in the presence and absence of spherical aberrations. *Appl. Opt.* **45** 1812 (2006).

- [24] Rohrbach, A. Stiffness of Optical Traps: Quantitative Agreement between Experiment and Electromagnetic Theory. *Phys. Rev. Lett.* **95** 168102 (2005).
- [25] Zahkarian, A. R., Polynkin, P., Mansuripur, M., and Moloney, J. V. Single-beam trapping of micro-beads in polarized light: Numerical simulations. *Opt. Exp.* **14** 3660 (2006).
- [26] Roichman, Y., Sun, B., Stolarski, A., and Grier, D. G. Influence of Nonconservative Optical Forces on the Dynamics of Optically Trapped Colloidal Spheres: The Fountain of Probability. *Phys. Rev. Lett.* **101** 128301 (2008).
- [27] van Oostrum, P. D., van der Horst, A., and van Blaaderen, A. Mutual influence of time-shared optical traps studied by means of Video Holographic Microscopy. *Digital Holography and Three-Dimensional Imaging, OSA Technical Digest (CD) (Optical Society of America) DWD7* (2009).
- [28] Polin, M., Ladavac, K., Lee, S.-H., Roichman, Y., and Grier, D. Optimized holographic optical traps. *Opt. Exp.* **13** 5831 (2005).
- [29] Nemoto, S. Waist shift of a Gaussian beam by plane dielectric interfaces. *Appl. Opt.* **27** 1833 (1988).
- [30] Wiersma, S. H. and Visser, T. D. Defocusing of a converging electromagnetic wave by a plane dielectric interface. *J. Opt. Soc. Am. A* **13** 320 (1996).
- [31] Neuman, K. C., Abbondanzieri, E. A., and Block, S. M. Measurement of the effective focal shift in an optical trap. *Optics Letters* **30** (2005).
- [32] Im, K.-B., Kim, H.-I., Joo, I.-J., Oh, C.-H., Song, S.-H., Kim, P.-S., and Park, B.-C. Optical trapping forces by a focussed beam through two media with different refractive indices. *Optics communications* **226** 25 (2003).
- [33] Gong, Z., Wang, Z., Li, Y., Lou, L., and Xu, S. Axial derivation of an optically trapped particle in trapping force calibration using the drag force method. *Opt. Comm.* **273** 37 (2007).
- [34] Fontes, A., Ajito, K., Neves, A. A. R., Moreira, W. L., de Thomaz, A. A., Barbosa, L. C., de Paula, A. M., and Cesar, C. L. Raman, hyper-Raman, hyper-Rayleigh, two-photon luminescence and morphology-dependent resonance modes in a single optical tweezers system. *Phys. Rev. E.* **72** 012903 (2005).
- [35] Happel, J. and Brenner, H. *Low Reynolds Number Hydrodynamics*. Kluwer Academic, Dordrecht (1993).
- [36] Pure Component Properties (Queriable database), Chemical Engineering Research Information Center. <http://www.cheric.org/research/kdb/hcprop/showcoef.php?cmpid=818prop=VSL> (Retrieved 9 August 2010).
- [37] Roichman, Y., Sun, B., Roichman, Y., Amato-Grill, J., and Grier, D. G. Optical Forces arising from phase gradients. *Phys. Rev. Lett.* **100** 013602 (2008).
- [38] Wu, P., Huang, R., Tischer, C., Jonas, A., and Florin, E.-L. Direct Measurement of the Nonconservative Force Field Generated by Optical Tweezers. *Phys. Rev. Lett.* **103** 108101 (2009).
- [39] Asturian, R. D. and Hänggi, P. Brownian motors. *Physics Today* **55** (11) 33 (2002).
- [40] Sun, B., Lin, J., Darby, E., Grosberg, A. Y., and Grier, D. G. Brownian vortexes. *Phys. Rev. E.* **80** 10401 (2009).
- [41] Sun, B., Grier, D. G., and Grosberg, A. Y. *Phys. Rev. E* **82** (2010).
- [42] Visscher, K., Gross, S. P., and Block, S. M. Construction of multiple -beam optical

- traps with nanometer-resolution position sensing. *IEEE J. Sel. Top. Quant. Electron.* **2**(4) 1066 (1996).
- [43] Visscher, K., Brakenhoff, G. J., and Krol, J. J. Micromanipulation by multiple optical traps created by a single fast scanning trap integrated with the bilateral confocal scanning laser microscope. *Cytometry* **14** 105 (1993).
- [44] Fällman, E. and Axner, O. Design for fully steerable dual-trap optical tweezers. *Appl. Opt.* **36** 2107 (1997).
- [45] Vossen, D. L. J., van der Horst, A., Dogterom, M., and van Blaaderen, A. Optical tweezers and confocal microscopy for simultaneous three-dimensional manipulation and imaging in concentrated colloidal dispersions. *Rev. Sci. Instrum.* **75** 2960 (2004).
- [46] Deng, Y., Bechhoefer, J., and Forde, N. R. Brownian motion in a modulated optical trap. *J. Opt. A: Pure Appl. Opt.* **9** S256 (2007).
- [47] Shane, J. C., Mazilu, M., Lee, W. M., and Dholakia, K. Effect of pulse temporal shape on optical trapping and impulse transfer using ultrashort pulsed lasers. *Opt. Exp.* **8** 7554 (2010).
- [48] IntraAction Corporation Model DTD-274HA6 2 Axis Acousto-Optic Deflection System Instruction Manual .
- [49] Joykutty, J., Mathur, V., Venkataraman, V., and Natarajan, V. Direct Measurement of the Oscillation Frequency in an Optical-Tweezers Trap by Parametric Excitation. *Phys. Rev. Lett.* **95** 193902 (2005).
- [50] Pedersen, L. and Flyvbjerg, H. Comment on "Direct Measurement of the Oscillation Frequency in an Optical-Tweezers Trap by Parametric Excitation". *Phys. Rev. Lett.* **98** 189801 (2007).
- [51] Leunissen, M. Manipulating Colloids with Charges & Electric Fields. PhD Thesis, Utrecht University (2007).
- [52] Caruso, F. Nanoengineering of Particle Surfaces. *Adv. Mater* **13** 11 (2001).
- [53] van Blaaderen, A. and Vrij, A. Synthesis and characterization of colloidal dispersions of fluorescent, monodisperse silica spheres. *Langmuir* **8** 2921 (1992).
- [54] Graf, C., Vossen, D. L. J., Imhof, A., and van Blaaderen, A. A general method to coat colloidal particles with silica. *Langmuir* **19** 6693 (2003).
- [55] Guerrero-Martínez, A., Pérez-Juste, J., and Liz-Marzán, L. M. Recent Progress on Silica Coating of Nanoparticles and Related Nanomaterials. *Adv. Mater.* **22** 1182 (2010).
- [56] Demirörs, A. F., van Blaaderen, A., and Imhof, A. A general method to coat colloidal particles with titania. *Langmuir* **26** 9297 (2010).
- [57] Demirörs, A. F., Jannasch, A., van Oostrum, P. D. J., Schäffer, E., van Blaaderen, A., and Imhof, A. Seeded Growth of Titania Colloids with Refractive Index Tunability and Fluorophore-free Luminescence. *Langmuir*; DOI: 10.1021/la103717m (2010).
- [58] Luna-Xavier, J.-L., Bourgeat-Lami, E., and Guyot, A. The role of initiation in the synthesis of silica/poly(methyl methacrylate) nanocomposite latex particles through emulsion polymerization. *Colloid Polym. Sci.* **279** 947 (2001).
- [59] Luna-Xavier, J.-L., Guyot, A., and Bourgeat-Lami, E. Synthesis and Characterization of Silica/Poly (Methyl Methacrylate) Nanocomposite Latex Particles through Emulsion Polymerization Using a Cationic Azo Initiator. *J. Colloid Int. Sci.* **250** 82 (2002).
- [60] Zou, H., Wu, Z., and Shen, J. Polymer/Silica Nanocomposites: Preparation, Characterization, Properties, and Applications. *Chem. Rev.* **108** 3893 (2008).

- [61] Zoldesi, C. I., van Walree, C. A., and Imhof, A. Deformable Hollow Hybrid Silica/Siloxane Colloids by Emulsion Templating. *Langmuir* **22** 4343 (2006).
- [62] Lou, X. W., Archer, L., and Yang, Z. Hollow Mirco-/Nanostructures: Synthesis and Applications. *Adv. Mater.* **20** 3987 (2008).
- [63] Liu, J., Liu, F., Gao, K., Wu, J., and Xue, D. Recent developments in the chemical synthesis of inorganic porous capsules. *J. Mater. Chem.* **19** 6073 (2009).
- [64] Hu, Y., Nieminen, T. A., Heckenberg, N. R., and Rubinsztein-Dunlop, H. Antireflection coating for improved optical trapping. *J. Appl. Phys.* **103** 093119 (2008).
- [65] Bormuth, V., Jannasch, A., van Blaaderen, A., Howard, J., and Schäffer, E. Optical trapping particle and optical trapping method. *European Patent Application EP 08 15 2033.0* (filed 27 February 2008).
- [66] Bormuth, V., Jannasch, M., Ander, C. M. v. K., van Blaaderen, A., Howard, J., and Schäffer, E. Optical trapping of coated microspheres. *Opt. Exp.* **16** 13831 (2008).
- [67] Jannasch, A., Bormuth, V., van Kats, C. M., van Blaaderen, A., Howard, J., and Schäffer, E. Coated microspheres as enhanced probes for optical trapping. *Proc. of SPIE* **7038** (2008).
- [68] Bormuth, V., Varga, V., Howard, J., and Schäffer, E. Protein Friction Limits Diffusive and Directed Movements of Kinesin Motors on Microtubules. *Science* **325** 870 (2009).
- [69] Lin, K.-H., Crocker, J. C., Prasad, V., Schofield, A., Weitz, D. A., Lubensky, T. C., and Yodh, A. G. Entropically Driven Colloidal Crystallization on Patterned Surfaces. *Phys. Rev. Lett.* **85** 1770 (2000).
- [70] Gasser, U., Weeks, E. R., Schofield, A., Pusey, P. N., and Weitz, D. A. Real-space imaging of nucleation and growth in colloidal crystallization. *Science* **292** 258 (2001).
- [71] Yethiraj, A. and van Blaaderen, A. A colloidal model system with an interaction tunable from hard sphere to soft and dipolar. *Nature* **421** 513 (2003).
- [72] Frank, M., Anderson, D., Weeks, E. R., and Morris, J. F. Particle migration in pressure-driven flow of a Brownian suspension. *Journal of Fluid Mechanics* **493** 363 (2003).
- [73] Mohraz, A. and Solomon, M. J. Direct Visualization of Colloidal Rod Assembly by Confocal Microscopy. *Langmuir* **21** 5298 (2005).
- [74] Leunissen, M. E., Christova, C. G., Hynninen, A. P., Royall, C. P., Campbell, A. I., Imhof, A., Dijkstra, M., van Roij, R., and van Blaaderen, A. Ionic colloidal crystals of oppositely charged particles. *Nature* **437** 7056 (2005).
- [75] Cohen, I., Davidovitch, B., Schofield, A., Brenner, P., and Weitz, D. Slip, Yield, and Bands in Colloidal Crystals under Oscillatory Shear. *Physical Review Letters* **97** 215502 (2006).
- [76] Nugent, C. R., Edmond, K. V., Patel, H. N., and Weeks, E. R. Colloidal Glass Transition Observed in Confinement. *Physical Review Letters* **99** 025702 (2007).
- [77] Leunissen, M. E., van Blaaderen, A., Hollingsworth, A. D., Sullivan, M. T., and Chaikin, P. M. Electrostatics at the oil-water interface, stability, and order in emulsions and colloids. *Proceedings of the National Academy of Sciences of the United States of America* **104** 2585 (2007).
- [78] Leunissen, M. E., Sullivan, M. T., Chaikin, P. M., and van Blaaderen, A. Concentrating colloids with electric field gradients. I. Particle transport and growth mechanism of hard-sphere-like crystals in an electric bottle. *Journal of Chemical Physics* **128** 164508 (2008).
- [79] van Schooneveld, M. M., de Villeneuve, V. W. A., Dullens, R. P. A., Aarts, D. G. A. L.,

- Leunissen, M. E., and Kegel, W. K. Structure, Stability, and Formation Pathways of Colloidal Gels in Systems with Short-Range Attraction and Long-Range Repulsion. *The Journal of Physical Chemistry B* **113** 4560 (2009).
- [80] Hermes, M., Vermolen, E. C. M., Leunissen, M. E., Vossen, D. L. J., van Oostrum, P. D. J., Dijkstra, M., and van Blaaderen, A. Nucleation of colloidal crystals on configurable seed structures. *Soft Matter*, DOI: 10.1039/C0SM01219J (2011).
- [81] Sainis, S. K., Germain, V., and Dufresne, E. R. Statistics of Particle Trajectories at Short Time-Intervals Reveal Electrostatic Colloidal Interactions in Nonpolar Solvents. *Phys. Rev. Lett.* **95** 018303 (2007).



# 6

## Multiple traps together

---

The influence of a point trap is not limited to a point in space. In this Chapter we make use of the spatial extent of point traps. First, we show both with calculations and experimentally that counter-propagating traps can be used to trap particles that cannot otherwise be trapped. Particles with a high index of refraction sometimes scatter so much light that the scattering force exceeds the gradient force at all depths. By canceling the scattering force on the particles by means of a second focussed laser that propagates in the opposite direction, these particles can however be trapped. Another application of multiple traps lies in line-traps that limit the particles to a 1D line. We study an array of three traps to gain a better understanding of the physics. This is done both in calculations and in experiments. Under specific circumstances, it is found that particles larger than the laser focus can be trapped stiffer in an array of traps. This phenomenon is studied in more detail and a new type of optical tweezers is introduced that allows stiffer trapping with a more linear behavior.

## 6.1 Introduction

As can be seen in Chapter 5, the influence of a trap extends to an anisotropic region in 3D. This, one might use to combine the effects of multiple (time-shared) traps [1, 2], for instance to approximate a ‘line-trap’. Also when counter-propagating [2, 3] traps are used, multiple traps influence each other. In this Chapter we will first present counter-propagating tweezers, in section 6.2. These traps consist of two traps that are projected by two objectives and can be used to trap high index particles that cannot otherwise be trapped due to their large scattering. In this technique the sample is squeezed between two objectives and the particles are trapped in the overlapping focuses of two counter-propagating traps.

In section 6.3 we show that multiple traps can also be used to trap particles with a negative index contrast that cannot be trapped in a point trap because the gradient force in that case is directed down the intensity gradient.

Multiple traps together can also have the effect that the particles are localized much less strongly due to the smaller intensity gradients. In section 6.4 we look into the possibilities to form a line-trap that consists of multiple time-shared point traps. These line-traps might be used to measure interaction forces between the particles. Under certain circumstances, on the other hand, a pair of point traps next to each other can result in stiffer confinement. In section 6.5 we will present calculations and experiments that show stiff trapping in an array of point traps.

## 6.2 Counter-propagating tweezers to trap high index materials

To increase the scattering by a particle, and in order to increase the trapping forces, one might consider to use particles with a higher refractive index. This, however does not only make the gradient forces larger, but also the scattering forces. In the Rayleigh regime, the scattering forces increase faster with the index contrast than the gradient forces do, as can be understood from equations 4.11 and 4.13. This trend is also present in the Lorenz-Mie regime as can also be seen in Figure 5.22 and 6.1.

In Figure 6.1, we plot the trapping efficiency for 1.4  $\mu\text{m}$  particles with different refractive indices in ethanol. The first observation is that the trapping forces are larger for particles with a larger refractive index. But not only do the forces get larger. For the highest refractive indices, there is no height at which the gradient force counterbalances the scattering force completely. This results in an upward force everywhere and the particle is not trapped. The highest index common material that can still be trapped reasonably well is PolyStyrene, PS. Also melamine and amorphous titania particles with a diameter of 1.4  $\mu\text{m}$  are strictly speaking trappable but the restoring forces are small compared to thermal fluctuations.

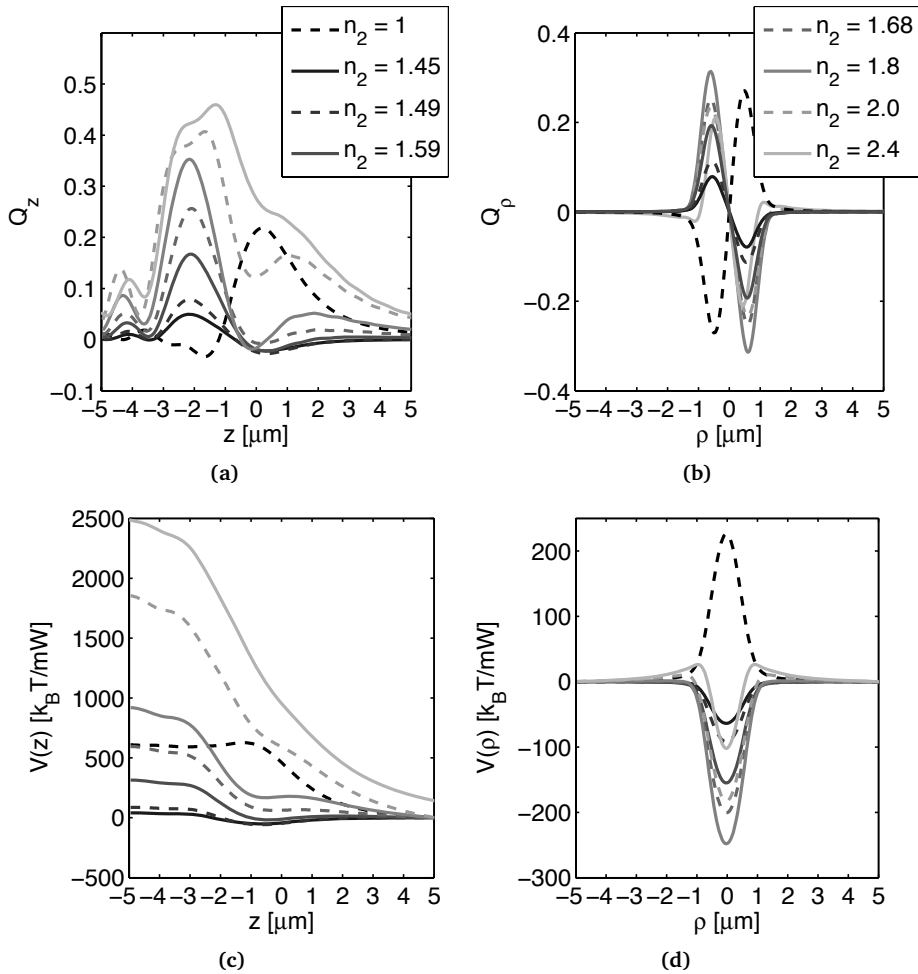


**Figure 6.1:** The influence of the refractive index on the trapping behavior. **a.** The axial trapping efficiency as a function of the distance in  $z$  from the geometrical focus,  $14 \mu\text{m}$  above the bottom glass plate for a  $1.4 \mu\text{m}$  particle at 8 different refractive indices in ethanol. The refractive indices are chosen to model particles of the following materials:  $n = 1$  for air,  $n = 1.45$  for silica,  $n = 1.49$  for PMMA,  $n = 1.59$  for PS (polystyrene),  $n = 1.68$  for melamine,  $n = 1.8$  and  $2.0$  for porous titania and  $n = 2.4$  for anatase titania. **b.** The lateral forces for the same particles calculated in the trapping plane for particles that are trappable in the axial direction and in the plane of the geometric focus for those that cannot be trapped. **c, d** The trapping efficiencies integrated in respectively the axial and the lateral direction.

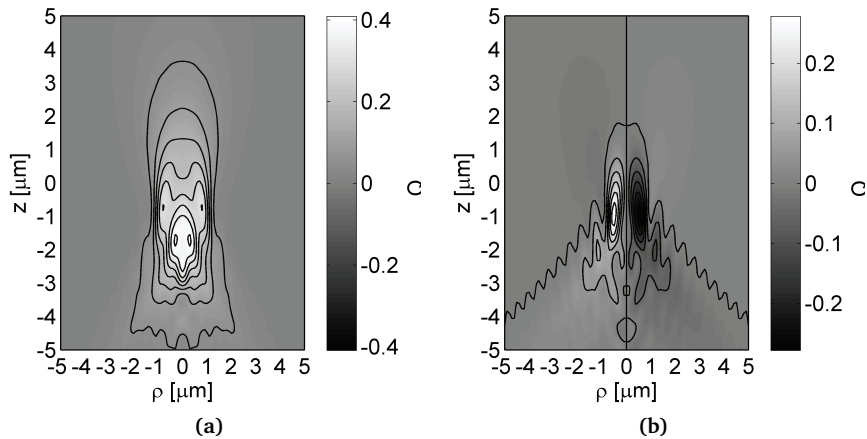


**Figure 6.2:** The force-field on a  $1.4 \mu\text{m}$  titania particle in ethanol. **a.** The axial trapping efficiency  $Q_z$  as a function of the position with the origin in the geometric focus for a  $1.4 \mu\text{m}$  titania ( $n = 2.4$ ) particle trapped in ethanol at a depth of  $14 \mu\text{m}$ . **b.** The lateral trapping efficiency  $Q_\rho$  as a function of the position with the origin in the geometric focus. The trapping efficiencies in both graphs are represented by grey values. For clarity some iso-force curves were added with the one for  $Q = 0$  slightly thicker.

The trapping forces have been integrated along the optical axis in Figure 6.1 **c**. The particle is effectively pushed upwards for all refractive indices. For this size, we observe a local minimum in the trapping ‘potential’ for particles with a refractive index up to 1.8. The higher the refractive index, the steeper the slope. Titania particles for instance, are practically shot upwards. Note that an air bubble, with an index of 1, lower than that of ethanol, does experience a local minimum in the trapping potential in the axial direction. Since the refractive index contrast for bubbles in ethanol is negative the gradient force points away from the highest intensity. This means that below the focus the gradient force points down, away from the focus. For air bubbles in ethanol the gradient force is larger than the scattering force at some point, suggesting trappability. As the gradient force points away from the focus also in the lateral directions however, the particle is pushed sideways, away from the focus.

Also in the lateral directions does a particle experience larger forces when its refractive index is larger. The differences in Figure 6.1 **b** are not as large as they are in the axial direction. This is due to the fact that in the lateral direction the only force that contributes is the gradient force. For the particles that cannot be trapped in the axial direction we calculated the lateral trapping efficiency at the depth of the geometrical focus. For the indices 2.0 and 2.4, the particle is laterally attracted to the trapping site when it is close enough. If it is positioned a bit further from the optical axis it is pushed even further away.

We plot the integrated lateral force in Figure 6.1 **d**. There is a clear minimum

but for the indices 2.0 and 2.4 there are two clear ‘shoulders’, barriers that need to be overcome. This is also visible for the  $n = 2.4$  case in Figure 6.2. For the lateral trapping efficiencies, there is a lighter rim to the right of the geometrical focus at depth  $z = 0$ , and a darker rim on the left. The fact that the particle gets pushed away in this direction is of minor importance because the particle is not even trapped stably in the axial direction.

Interaction of the light with the air bubble ( $n = 1$ ) in ethanol ( $n = 1.36$ ) in Figure 6.1 **b** and **d**, is inverted with respect to the other materials. The same behavior would be observed for air bubbles in water. Below the focus, the bubble is pushed further down rather than up. This is because the sign of the polarizability is different. Instead of pushed up the intensity gradient, the bubble is repelled by the focus as can also be seen from equation 4.13 for the gradient force in the Rayleigh regime. It is nevertheless possible to trap air bubbles in this size range by using for instance a *light cage* formed by a Laguerre-Gauss beam, counter balanced by the buoyant force as described in reference [4]. In this paper and references therein, the relevance of bubbles in medicine is elaborated. In section 6.3 the reader can find more information about the trapping of bubbles and other particles with an index of refraction smaller than that of the surrounding medium.

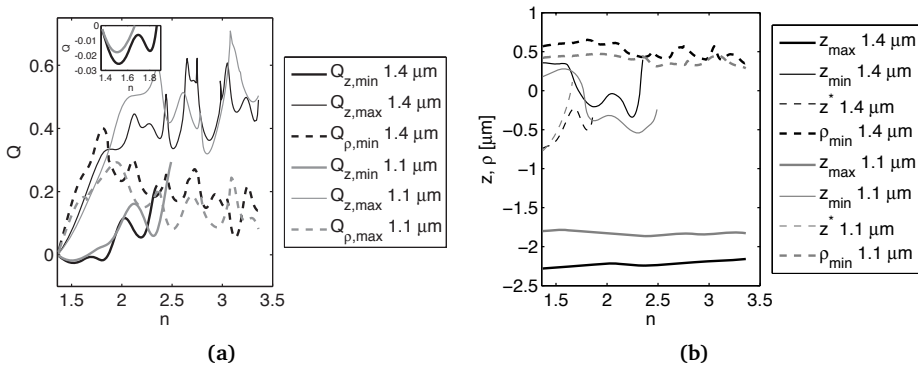


**Figure 6.3:** Restoring forces and trapping depths as a function of the particle refractive index. **a.** The maximum and minimum values of the trapping efficiency of a 1.4  $\mu m$  and a 1.1  $\mu m$  particle in ethanol, with the geometrical focus 14  $\mu m$  above the glass plate, as a function of the refractive index. Whenever there was a stable trapping location in the  $z$ -direction, the maximum lateral force is given at that height. Otherwise, the maximum lateral trapping efficiency is given at the plane of the geometrical focus. The minimal axial trapping efficiency is given for the primary trap, only when present. **b.** The axial and lateral position of the minimal and maximal trapping forces and the trapping location for these particles.

The maximum restoring forces beyond the trapping region ( $\min(Q_z)$ ) and the maximum pushing forces just below the trapping site as a function of the particle’s refractive index are plotted in Figure 6.3. We also included a curve for the maximum force in the axial direction, depending on the trap-ability either in

the trapping plane or in the plane of the geometrical focus. Clearly, the maximum forces pushing the particle up increase strongly with the particle's refractive index. This is due to the fact that the gradient force and the scattering force cooperate in this case. The maximal restoring force however (negative for stable trapping) rapidly diminishes as the scattering force gets larger faster than the gradient force does. That the gradient force also increases with the particle's refractive index can be seen from the trapping efficiency in the lateral directions. The maximal lateral trapping efficiency also increases with the refractive index of the particle, be it less strongly.

Depending on the particle size and above an index of refraction of 1.6 – 1.7, the maximal restoring force becomes positive. Higher index particles can thus not be trapped as can also be seen from Figure 6.1. These particles are pushed upwards. Due to Mie resonances, there are some exceptions to this. These resonances occur if an integer number of surface waves fits around the perimeter of the particle which makes the polarizability of the particle exceptionally high for one particular wavelength. The scattering cross-section of such particles is much larger than for comparable sized particles that do not show this resonance. For even higher indices, the minimum in the trapping efficiency even disappears as can be seen from the curve for particles with an index of refraction of 2.4, such as for instance anatase titania.

From Figure 6.3 **b** we learn that the position of the maximum forces in the axial and radial direction is mainly determined by the size of the particle and the shape of the focus rather than the refractive index. The depth at which the maximum force occurs for the 1.4  $\mu\text{m}$  particle shifts slightly upwards as the scattering force starts to dominate more and more. The depth at which the minimal force, or maximum restoring force occurs however, seems to start off constant and shifts quite suddenly with increasing trapping depth. This happens at indices for which there is no stable trapping to be expected. The plane of stable trapping moves up with the refractive index. This is the result of particles that are pushed further out of the focus by the increasing scattering force. It is also interesting to note that the maximal index at which stable trapping is possible depends on the size of the particle. For the 1.4  $\mu\text{m}$  it is predicted that stable trapping occurs for indices below 1.86 while for the 1.1  $\mu\text{m}$  particle this number is 1.66.

For actual trapping one does not only need a negative minimal trapping efficiency and a negative slope thereof. The restoring force should also be significantly large and extent over a significant area to be able to push the particle back to the trapping location against Brownian motion. Only a large stiffness is not enough. Indeed, the trapping forces increase with the refractive index of the particle. But, since the higher index particles cannot be trapped in the axial direction, we cannot directly make use of these larger forces.

A way to be able to trap high refractive index particles even stiffer and create larger forces is by using counter-propagating tweezers [3, 5–8]. The idea behind this counter-propagating trapping is simple. The radiation pressure of one laser

beam in its direction of propagation is canceled by a second laser beam propagating in the opposite direction while a great intensity gradient remains. The scattering forces associated with both beams point in opposite directions and cancel each other. To be able to do this, the sample containing the particle to be trapped has to be squeezed in between two objectives, focussing their respective laser beams to two overlapping, counter-propagating, focuses. See also Figure 6.4.

When the two counter-propagating traps are identical and overlap, the associated scattering forces will cancel in the focus. As a result the trap will be nearly conservative. Due to diffraction the light distribution just before a focus is not identical to the light distribution beyond the focus, so probably some non-conservativeness remains. See also sections 4.7.2 and 5.3.3.

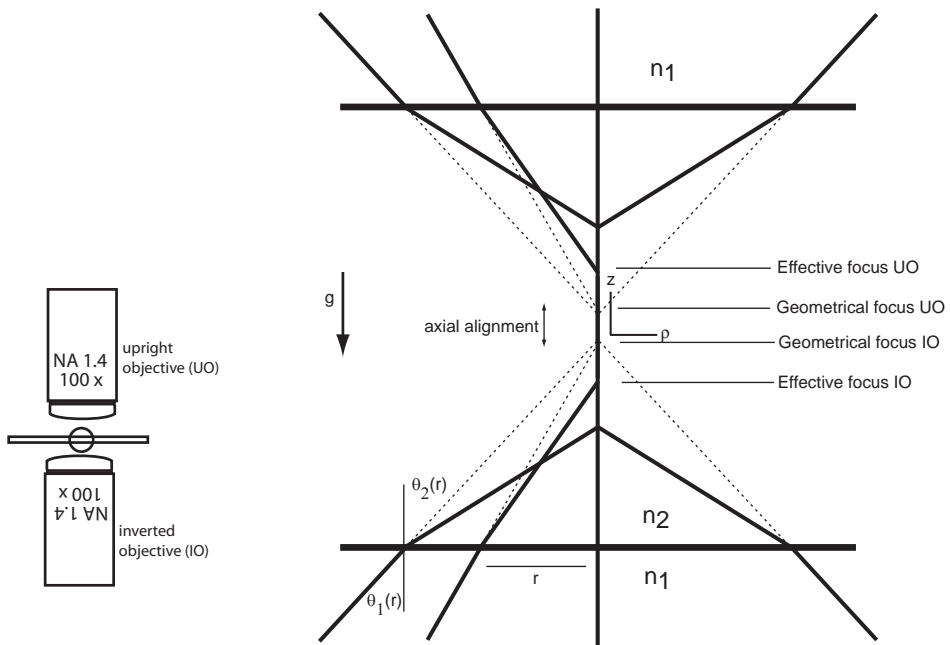


**Figure 6.4:** Schematic of counter-propagating traps. The dotted lines trace the path the light would follow if it were to be focussed in the geometrical focus, the full lines indicate how the light is refracted by the interface. Here the two focuses are not yet completely aligned.

Introducing an extra trap that propagates in the other direction unfortunately requires quite radical changes to a setup, see also the description of the setup in Chapter 1. It is quite simple to calculate the effect on the trapping behavior. In our setup we use time-shared traps, so the counter-propagating traps can be made such that they are never simultaneously present so that their time averaged force fields can simply be added. However, even when the two counter-propagating

traps are present simultaneously we do not expect any changes in the effective force field exerted by each individual trap because they are polarized in a mutually perpendicular manner, excluding interference. The result is that the total force in the  $z$ -direction of counter-propagating traps can be calculated by adding the negative of the mirrored force field. This is correct only in the absence of spherical aberration or, in case the distance between the ‘bottom’ of the sample and the trapped particle is equal to the distance between the ‘ceiling’ of the sample and the trapped particle. In all other cases, the counter-propagating trap will have a slightly different force curve due to different spherical aberration. This can be seen from the curves calculated for different trapping depths in section 5.3.2.

A way to align counter-propagating tweezers is to use a particle that can also be trapped with a single trap, such as a  $1.4\ \mu\text{m}$  silica particle. As extensively described in the previous section, this particle is trapped below (for the inverted trap) the geometrical focus due to spherical aberration. When the upper objective is aligned to create a counter-propagating trap, it is positioned such that both traps are at the same spot. The geometrical focus of the upper objective is then positioned below that of the lower objective. The  $z$ -component of the force field exerted by the focus of the upper objective is the negative of that associated with the lower objective, mirrored in the trapping plane of the particle that was used to do the alignment with. Of course, the symmetry between the upright and inverted focus that is broken by the spherical aberration when not trapping in the central plane of the sample remains intact when the immersion medium has the same refractive index as the glass.

Figure 6.5 gives a few force curves as exerted by counter-propagating optical traps that have been aligned using a  $1.4\ \mu\text{m}$  silica particle in a  $\sim 24\ \mu\text{m}$  thick sample of ethanol. The thickness of the sample is important to take into consideration because of spherical aberrations. For simplicity we assume the distance between the glass and the geometrical focus, and the laser power in the trap to be the same for both traps. The force curves are given for a  $1.4\ \mu\text{m}$  silica particle, a  $1.4\ \mu\text{m}$  titania ( $\text{TiO}_2$ ) particle ( $n_{\text{part}} = 2.4$ ) and two  $1.1\ \mu\text{m}$  particles, one made of titania and one made of silica.

As was to be expected from canceling the scattering force, the titania particles can be trapped, contrary to in the single traps, the exerted forces of which are plotted as dotted lines. The total power is distributed equally over the two traps. Not only can we now trap the titania particles, the force curves are also nicely symmetric around the trapping plane. From the slope of the trapping efficiency versus the depth can be concluded that the titania particles can be trapped much stiffer than the silica particles. For the  $1.4\ \mu\text{m}$  titania and silica particles we find axial stiffnesses of 863 and 192  $\text{pN}/\mu\text{m}/\text{W}$  respectively. For the  $1.1\ \mu\text{m}$  we find 877 and 217  $\text{pN}/\mu\text{m}/\text{W}$  for titania and silica respectively. The  $1.1\ \mu\text{m}$  titania particle therefore, is trapped about 4.6 times stiffer than the  $1.4\ \mu\text{m}$  silica particle.

In the lateral direction, the force curves and therefore the stiffnesses do not change when one traps the particles with counter-propagating tweezers. After all

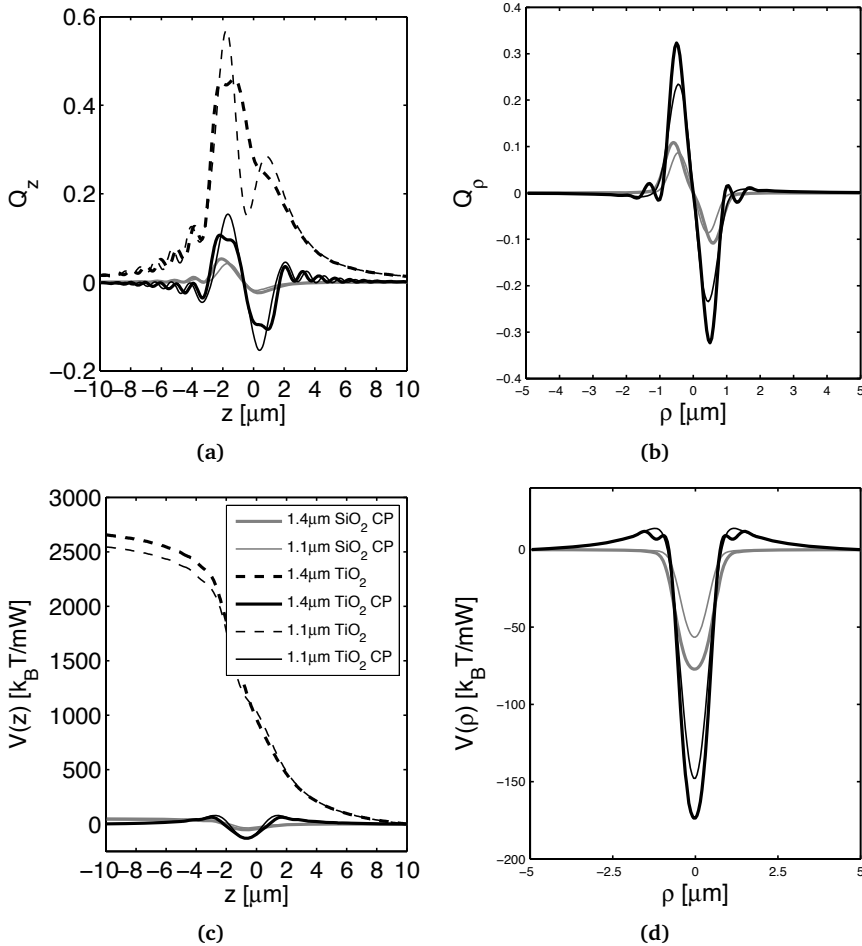


**Figure 6.5:** *Trapping high index particles in counter-propagating traps. a.* The axial trapping efficiency in counter-propagating traps, as a function of the distance in  $z$  from the geometrical focus, 12 μm above the bottom glass plate, for a 1.1 and 1.4 μm particles made of titania and silica. The thicker lines indicate the 1.4 μm particles. The grey lines indicate the silica particles. For the titania particles we also included the trapping efficiency for single traps. **b.** The lateral forces for the same particle. **c,d** The trapping efficiencies integrated in respectively the axial and the lateral direction.

the scattering force that is canceled by this technique, was not present in the lateral direction to begin with. In the lateral direction, for the 1.4 μm titania and silica particles we find axial stiffnesses of 2766 and 655 pN/μm/W respectively. For the 1.1 μm we find 3754 and 1284 pN/μm/W for titania and silica respectively.

Note that after canceling the scattering force, the only force that remains is the gradient force. Because of the limited numerical aperture of the objective used, the intensity gradients are much larger in the lateral direction than in the axial direction. This is reflected in the smaller maximum axial forces in the counter-propagating case. This is quite different in the single beam case as can be seen from Figure 6.3.

To test our theoretical predictions, we measured the lateral trapping stiffness by means of a Quadrant Photo Diode, see also section 4.4. The sample cell, consisting of two coverslips (Menzel No. 1) that were sealed together with candle wax, was filled with a dilute mixture of  $1.4\ \mu\text{m}$  diameter silica ( $n = 1.45$ ), particles and  $1.1\ \mu\text{m}$  titania particles ( $n = 2.4$ ) particles in ethanol ( $n = 1.36$ ). A pattern of time-shared traps, scanned by the AODs, is focussed in the sample by both objectives. The upright objective, the upper one, however, will give a mirror image of the pattern imaged by the inverted objective, see also the schematic of the setup in Chapter 1. To not be limited to symmetric patterns using a single pair of AODs, we scan both the desired pattern and its mirror image. Then, inside the sample, we overlap the pattern from the inverted beam with its mirror image from the upright beam, thus creating an array of counter-propagating traps. By scaling the added mirror image, we can also compensate for differences in magnification between the inverted and the upright beam paths introduced by the telescopes or by the use of objectives with different magnifications. Here, we used two identical  $100\times$  NA 1.4 PLAN APO objectives. We aligned the counter-propagating traps by visually checking on the camera image that a trapped silica particle did not change position when the inverted beam and the upright beam were alternately blocked. The imaging technique used to monitor the experiment is bright-field microscopy, where the upright objective acts as the condenser. As the numerical aperture of this objective is much larger than that of conventional condensers its depth of focus is particularly small,  $< \sim 5\ \mu\text{m}$ . To be able to properly illuminate the trapped array of particles, the position of the trapped array with respect to the illuminated plane needs to be controlled using the telescope of the upper beam path. Scanning a different set of traps for the upright microscope allows one to correct for a slightly different magnification of the array of traps by the upright objective.

Figure 6.6 shows stills from a movie where patterns of eight traps were combined to form four counter-propagating traps (plus eight single-beam traps that were not used). The array of counter-propagating traps, positioned at a depth  $D$  of  $12\ \mu\text{m}$  from either wall, was filled with one silica and three titania particles. The total power inside the sample was  $44\ \text{mW}$ , corresponding to  $5.5\ \text{mW}$  for each individual counter-propagating trap. The pattern was scanned at  $4.5\ \text{kHz}$  and changed in 34 steps over a total period of  $1.2\ \text{s}$ , yielding an average speed of the particles of  $\sim 20\ \mu\text{m/s}$ . In bright-field microscopy, the apparent size of the imaged particles is larger than the actual size [9]. For particles with a higher refractive index, this effect is more pronounced, causing the  $1.1\ \mu\text{m}$  diameter

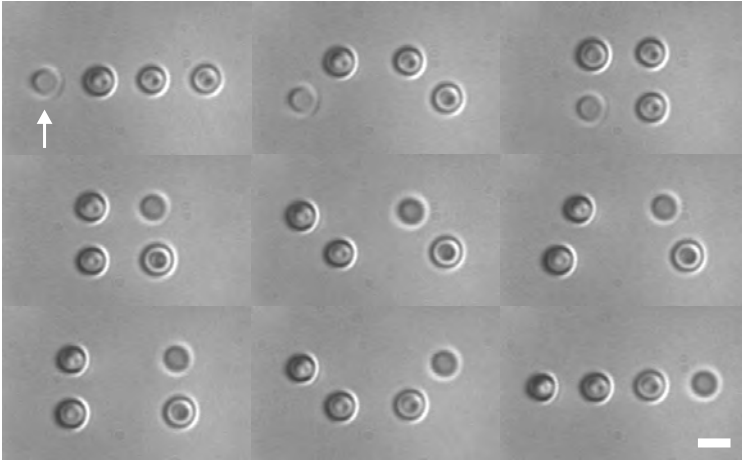


**Figure 6.6:** *Trapped array of titania and silica particles in ethanol.* Stills from a movie in bright-field microscopy of four counter-propagating traps filled with one  $1.4\ \mu\text{m}$  diameter silica particle (arrow) and three  $1.1\ \mu\text{m}$  diameter titania particles. The particles are positioned  $12\ \mu\text{m}$  away from either wall, and the pattern is changed in 34 steps in 1.2 s. The scale bar is  $2\ \mu\text{m}$ .

titania particles to appear larger than the  $1.4\ \mu\text{m}$  diameter silica particle.

Three-dimensional trapping of the titania particles in single-beam traps was not possible for any of the dozens of particles we tried to trap; they were pushed away along the beam axis by the excess scattering force. This is in accordance with the absence of a stable trapping position for these particles in the single-beam calculations.

For position detection of a particle in a non-shared trap, the fraction of the infrared beam that leaks through the dichroic mirror is imaged onto a quadrant photodiode (QPD) that is placed at the front camera port of the microscope.

We measured the radial trap stiffness  $\kappa_{\text{rho}}$  using QPD measurements. By fitting a Lorentzian to the normalized PSD curve of the QPD signal in Figure 6.7, we obtained the roll-off frequency  $f_0$  and used  $\kappa_{\text{rho}} = 12\pi^2\eta r f_0$ , with  $\eta$  the viscosity of the medium [10]. The high-frequency parts of the spectra for titania deviate from the -2 slope, typical for Brownian motion. This is possibly caused by not capturing all the light with the high-NA objective for these strongly scattering titania particles. However, we do not expect this to influence the fit value for  $f_0$  significantly. For these measurements, one stationary counter-propagating trap was used, with powers inside the sample of 22, 44, 88, and, only for the titania particle, 176 mW (measured using the two-objective method [11]). For a power of 44 mW in the sample we found  $f_0$  to be 499 Hz for the  $1.1\ \mu\text{m}$  diameter titania particle and, with  $\eta = 1.2 \times 10^{-3}\ \text{Ns/m}^2$  for ethanol, this yields a stiffness of  $\kappa_{\text{rho}} = 39\ \text{pN}/\mu\text{m}$ . The trap stiffness increased linearly with increasing laser power. Because of the mechanical noise in the curves for the  $1.4\ \mu\text{m}$  diameter

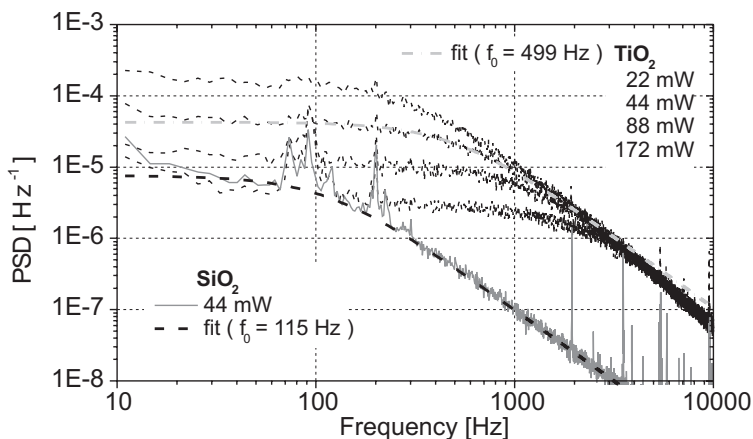


**Figure 6.7:** Power Spectrum Density curves for silica and titania particles in ethanol. PSD curves of the normalized signal for a  $1.4 \mu\text{m}$  diameter silica particle (grey solid curve) and a  $1.1 \mu\text{m}$  titania particle (black dotted curves) in ethanol for given laser powers inside the counter-propagating trap. For clarity only one curve is shown for silica. Lorentzian fits (dashed curves) are plotted for the 44 mW curves, with  $f_0$  at 115 Hz (silica) and 499 Hz (titania). Highest laser powers result in stiffest trapping and lowest plateau values.

silica particle which was more dominant due to the smaller scattering by these particles, we fitted these Lorentzians manually. Assuming an increase in stiffness linear with laser power, we found at 44 mW an  $f_0$  of  $115 \pm 10$  Hz, corresponding to  $\kappa_{\text{rho}} = 11.4 \text{pN}/\mu\text{m}$ , thus, a factor of 3.4 lower stiffness than for the smaller titania particle.

In our experiments, also described in reference [3] using Quadrant Photo diodes, we do indeed find a significantly larger lateral trapping stiffness for titania particles trapped by counter-propagating tweezers. However, the difference is not as large as predicted by our calculations (a factor of 3.4 rather than 5.7), which might be due to the difference between the spherical polarization in the calculations and the linear polarization used in the experiments.

However, the difference between the trapping by traps of these two polarizations is not very large [12]. By using counter-propagating tweezers the scattering force, which is more sensitive to the polarization of the light than the remaining gradient forces, is canceled. Another possible explanation for the smaller stiffness than expected for the titania particle may be found in the refractive index of the titania particles used. These particles may have had a lower refractive index than expected due to porosity, see also reference [13] and section 2.19. Last, but certainly not least, a slight misalignment could have caused a dramatic effect on the trapping stiffness. That the counter-propagating curve for the  $1.1 \mu\text{m}$  titania particle in Figure 6.5 is so similar to that of the  $1.1 \mu\text{m}$  titania particle is mere coincidence. The  $1.1 \mu\text{m}$  titania particle still has a rather pronounced minimum in

the trapping efficiency, as can be seen from the force curve for the same particles in single beam traps. A slight misalignment of the distance between the focuses in the  $z$ -direction could even cause the slope of the force curve for the counter-propagating trap to invert. The particle would be pushed away to be trapped at a different depth and with a different stiffness. The main point however holds; using counter-propagating tweezers we can trap high index particles that would otherwise be impossible to trap and it allows us to do so stiffer than with any other particle in a single beam trap.

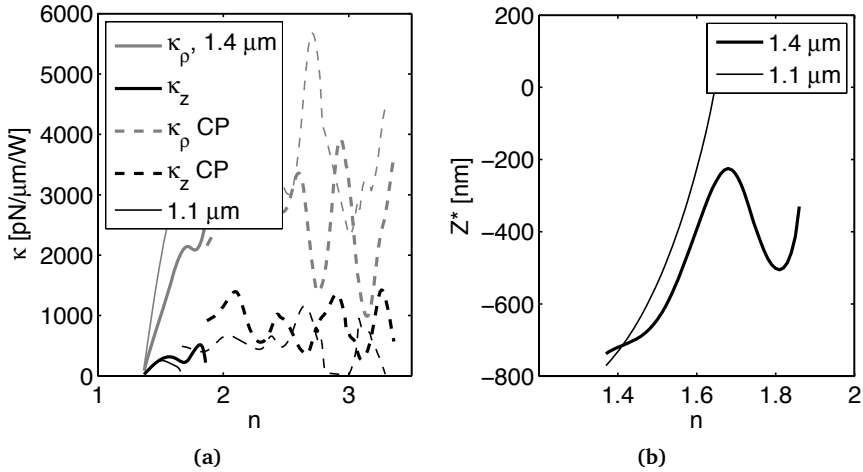


**Figure 6.8:** Trapping stiffness and trapping depth as a function of the particle refractive index using counter-propagating traps. **a.** The trapping stiffness in the axial and the lateral direction for a 1.1 and a 1.4 μm particle in ethanol, with the geometrical focus 14 μm above the glass plate, as a function of the refractive index. For indices that caused too large a scattering force we assumed counter-propagating traps, aligned in the  $z$ -direction using a 1.4 μm silica particle in a sample that was 24 μm thick. **b.** The trapping depths  $z_0$  with respect to the geometrical focus for these particles for those refractive indices that we were able to trap.

We plot the stiffness of trapping a 1.4 μm and a 1.1 μm particle in ethanol as a function of the refractive index of the particle in Figure 6.8. For the higher index particles, where this was necessary we assumed counter-propagating traps. It is clear an increasing index of the particles increases the stiffness with which they can be trapped. In Figure 6.1 the point of the steepest slope of the trapping efficiency is not always at the height where the two traps are made to overlap when using a 1.4 μm silica particle during the alignment. Obviously it is also possible to use samples with a different thickness or to not place the overlapping traps at the same distances from the respective glass/ethanol interfaces, so to not trap in the middle of the sample. For each particular experiment it is therefore worthwhile to do calculations to explore the proposed trapping conditions and

optimize the parameters.

A photonic crystal with wave-guides inside might be made out of silica particles with some strategically placed titania particles as doping to form the wave-guides. In 1887 Lord Rayleigh derived that in a one-dimensional array of periodic refractive index variations light of certain wavelengths cannot propagate [14]. One hundred years later, the idea arose of inhibition of spontaneous emission in 2D and 3D structures with periodic refractive index variations: photonic crystals [15, 16]. Under certain conditions photonic crystals have a band-gap for particular wavelengths that cannot propagate in any direction through the crystal. High refractive index particles can be used to dope photonic crystals to manipulate their interaction with light. An (artificial) defect in such a crystal, i.e. a missing particle or a particle with a different refractive index, can create a pass gap which can be used to create wave-guides [17, 18] or micro-cavities [19, 20], depending on their geometry. Optical tweezers can be used to trap individual particles and place them on lattice sites in a photonic crystal. With increasing thickness of the crystal this gets increasingly more difficult as the crystal will also interact progressively stronger with the light from the trapping laser. This effect can be strongly reduced by index matching the crystal matrix particles with a liquid medium.

### 6.3 Trapping particles with an index of refraction below that of the immersion medium

Air bubbles can normally not be trapped due to their negative contrast. In general, optical trapping is limited to particles with a higher index of refraction than that of the medium. Developing optical traps that can be used to localize also particles with a negative contrast would be interesting because it would allow for many experiments in which particles with a negative polarizability such as metals and gas bubbles are trapped. An interesting example of particles with a negative refractive index contrast without the high absorption of metals is found in gas bubbles in a liquid. These find application as contrast agent in medical ultrasound diagnostics and targeted drug delivery [21–23]. Optical tweezers can be used to localize these contrast bubbles to facilitate detailed studies of their dynamics [4, 24].

Figure 6.1 shows that bubbles with their low refractive index cannot be trapped due to the fact that the gradient force changes sign to point in the same direction as the scattering force. It is however possible to trap an air bubble in the axial direction with a point trap. Just below the focus, the light intensity increases with the height. So also for bubbles, with their negative index contrast, this results in a gradient force down. Unfortunately, the bubble will be rapidly pushed away from the optical axis by the gradient force. This trapping behavior is similar to the behavior we saw for some smaller particles in Figure 5.23. There is a fundamental difference though. The titania particle discussed in section 6.2 still experienced a gradient force towards the higher light intensity. The intensity distribution in

combination with its size made it such that the particle was pulled away from the optical axis. For bubbles the story is different. Even when the light intensity is highest on the optical axis, as it is usually, it is pushed away from the optical axis by the gradient force, towards the lower intensity.

In Figure 6.9 we plotted the trapping behavior for two bubbles (1 and 6  $\mu\text{m}$  in diameter) in ethanol, trapped in between two point traps. In Figure 6.9 **a** we plotted the axial forces that the bubbles experience on the optical axis. Just as for high index particles, the maximum trapping efficiency in the upward direction is much larger than the minimum trapping efficiency downward. This is where the gradient force cooperates with the scattering force. Below the effective focus, the bubbles experience a gradient force down that compensates the scattering force. Even further down the scattering force wins again. The bubble there is pushed upwards, with some wiggles caused by the spherical aberration. This results in an axial trap as there is a depth at which the bubble experiences a zero force in combination with a negative slope in the force.

In Figure 6.9 **b**, the particle is observed to be pushed away by the gradient force. With three or more carefully placed traps around the bubble it is, however, possible to confine the bubble also in the lateral directions. The bubble will then be pushed to the region with a lower intensity in between the traps and the bubble or particle with a lower refractive index, will be effectively trapped. In the axial direction it will be trapped just below the focus while in the lateral directions it will be confined in a cage of light. Such a trap is different from the traps formed by a Laguerre-Gauss beam used in reference [4]. Here, the multiple point traps confine the bubble in all directions so the buoyant force is not needed for the trapping of a bubble.

## 6.4 line-traps

Multiple traps can also be used to create a line of point traps that together act as a line-trap. Such a line-trap might be used to confine two particles to a 1D line to measure their mutual interaction [25], as has been demonstrated with line traps that have been generated using cylindrical lenses, scanning mirrors and spatial light modulators [26–28].

In practice it has proven to be hard to construct a line-trap that consists of time-shared point traps made with AODs. A possible explanation is that the respective point traps are not all of the same strength due to non-linear behavior in the AODs, creating effective potential barriers along the 1D trap. In the following we will look into the mutual influence of nearby traps in more detail. To do so, we study the simplest case of a line of point traps; a linear array of three traps. The observations may then be extended to line traps made of more point traps.

Once we have calculated the force fields like in Figure 5.11, we can also calculate the forces exerted by an array of time-shared traps. Because the traps are never simultaneously present, due to the time-sharing, we can exclude the oc-

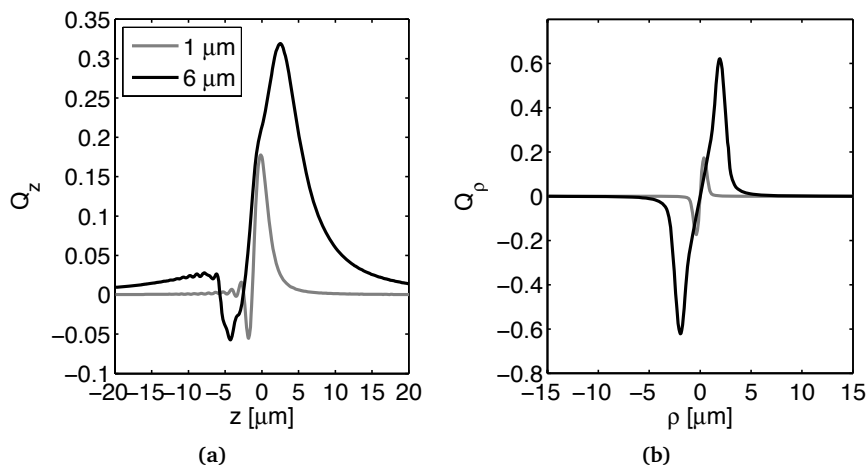


**Figure 6.9:** The trapping efficiency on an air bubble in water. **a.** The axial trapping efficiency  $Q_z$  as a function of the position with the origin in the geometric focus at a depth of  $14 \mu\text{m}$  for a  $1$  and  $6 \mu\text{m}$  air bubble in ethanol. **b.** The lateral trapping efficiency  $Q_\rho$  as a function of the distance from the optical axis at the depth at which the bubble finds a trapping location in the axial direction.

currence of interference of light of neighboring traps. We can therefore simply add the time averaged forces as they are exerted by the individual traps [3, 29–31]. Calculating the forces exerted by an array of traps is then simply a matter of bookkeeping. The fact that the two particles are never irradiated simultaneously greatly reduces the effects of optical binding which might be a disturbance to a force measurements [26], see also section 4.7.4.

In Figure 6.10, we show the force fields as exerted by three traps in a linear array with four different spacings in between the traps. Again, the particle under investigation is a  $1.4 \mu\text{m}$  silica particle in ethanol, with the geometrical focus  $12 \mu\text{m}$  deep in the sample. When the distance between the three traps is  $0 \text{ nm}$ , obviously the three traps add up to be one normal point trap. This can be seen in Figure 6.10 **a** and **d** for the axial and lateral trapping efficiencies respectively. When the spacing in between the traps is about as large as the traps themselves, as in Figure 6.10 **c** and **f**, the three traps exist independently and are only slightly influenced by the neighboring traps. Note that the forces are a third of those in the case that all three traps overlap.

For intermediate distances between the traps, something interesting happens. Just right of the middle trap, where the particle is normally pushed left, towards the trap, it is now simultaneously pushed to the right because is located to the left of the right trap. The result is that the net force on the particle is zero. In the axial direction however, see Figure 6.10 **b**, the particle is still confined. Also in the lateral direction ‘out of the paper’ the particle is still pushed back to the line.

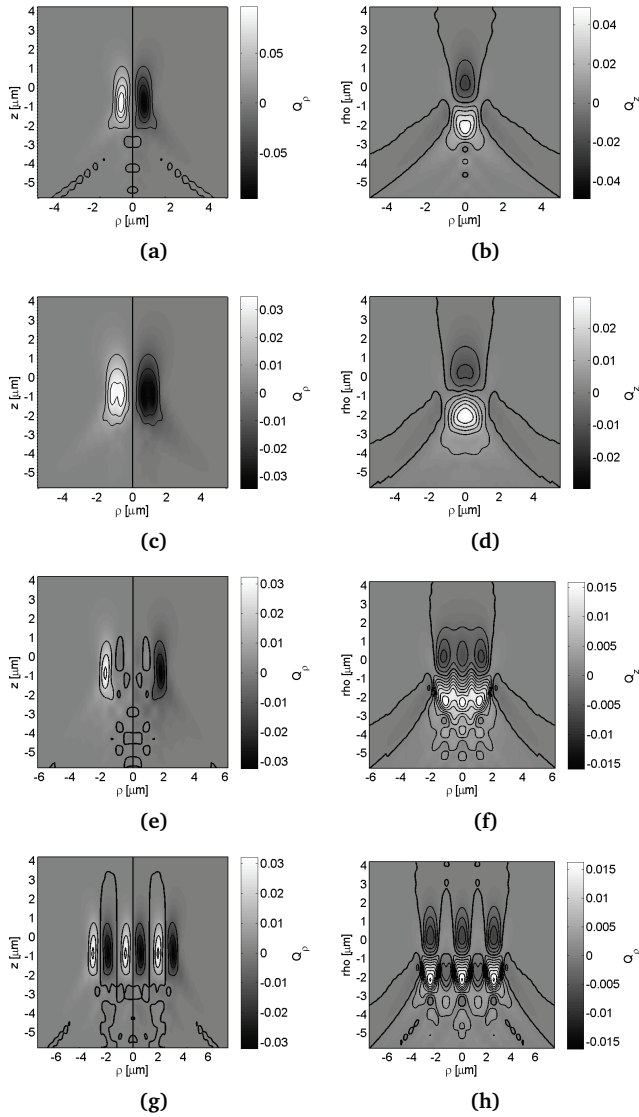


**Figure 6.10:** Force fields for three traps at different spacings. **a, b** and **c**. The axial trapping efficiency  $Q_z$  as a function of the position for a  $1.4 \mu\text{m}$  silica particle trapped in ethanol at a depth of  $12 \mu\text{m}$ . Between the three traps there is a spacing of respectively  $0$ ,  $1200$  and  $1560 \text{ nm}$ . **e, f** and **g**. The lateral trapping efficiency  $Q_l$  for the same cases. The trapping efficiencies in both graphs are represented by grey values.

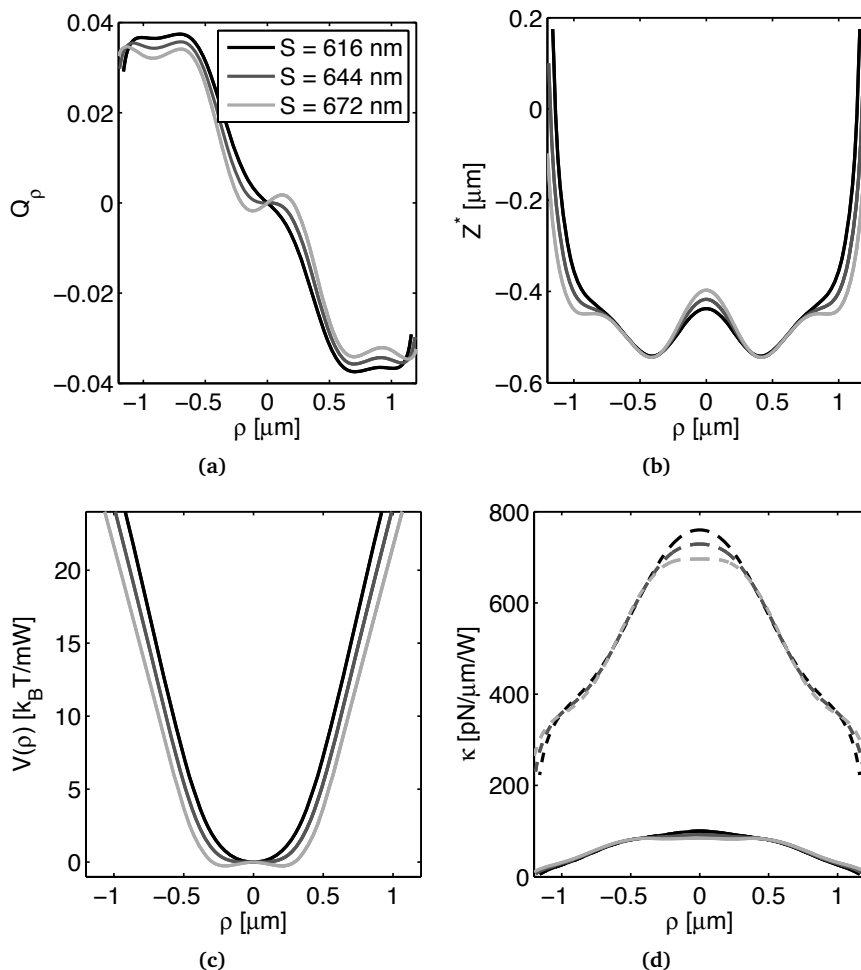


**Figure 6.11:** *Trapping forces on a line of three traps.* **a.** The trapping efficiency for a  $1.4 \mu\text{m}$  silica particle trapped in ethanol as a function of the distance along a line of three traps with a spacing of respectively 616, 644 and 672 nm. The geometrical focus is positioned at a distance of  $12 \mu\text{m}$  above the bottom glass plate. **b.** The depth, with respect to the geometric focus, at which the axial forces balance, as function of the distance along the line. **c.** The potential energy along the line traps. **d.** The trapping stiffness in the axial direction, full lines, and the trapping stiffness perpendicular to the line-trap, dashed lines, as a function of the distance along the line.

In Figure 6.11, we analyze the line-trap consisting of three traps in more detail. In Figure 6.11 **a** the trapping efficiency along the line is plotted for three different spacings, respectively 616, 644 and 672 nm. We note that a  $1.4 \mu\text{m}$  particle is still trapped along the direction of the line. When the particle is located

to the left of the three traps, it is pushed to the right. For the case in which the spacing between the traps is 644 nm, there is a small plateau in the trapping efficiency around the middle trap at  $\rho = 0$ . This means that along a small distance, the light exerts hardly any force on the particle in the direction of the line. When the spacing between the traps is slightly smaller (616 nm), the plateau is reduced to a mere inclination. When the spacing between the traps is increased by 28 nm the plateau is deformed significantly as well. The curve is no longer level in the middle of the line, instead the particle is pulled further away from the middle of the line. The middle of the line has become an unstable equilibrium.

The depth at which the axial scattering and gradient force balance varies as a function of the position along the line as can be seen in Figure 6.11 **b**. In this sense this Figure is similar to Figure 5.9. We note that the trapping depth is varying more than 200 nm with the position along the line. In other words: the line is not straight in space. Moreover, we note that the trapping depth in the middle of the line-trap is varying strongly as the spacing in between the three traps is changed.

We plotted the potential energy along the line in Figure 6.11 **c**. In this case we can indeed speak about potential energy as there is a clear path in space over which to integrate. This does not hold for all possible excursions the particle may make. We observe that the bottom of the minimum in the potential energy, in the case that the spacing in between the traps is 644 nm is indeed flat. A slight decrease of the spacing results in an effective point trap where the particle can minimize its free energy by going to the middle of the line-trap. If we make the spacing between the traps a little larger, two minima appear along the line, somewhere in between the constituent traps. When the spacing in between the traps is carefully chosen such that the bottom of the minimum in the potential energy is flat, the particle, itself 1.4  $\mu\text{m}$  in diameter, can travel about 1.3  $\mu\text{m}$  along the line with 1  $k_B T/W$  of thermal energy (to get that far at the same depth, perpendicular to the line takes 3.6  $k_B T/W$ , so indeed this minimum is elongated). In a single trap with the same total laser power it has a slightly smaller range of 0.6  $\mu\text{m}$ .

Finally, in Figure 6.11 **d** we plotted the trapping stiffness in the axial direction and in the lateral direction, perpendicular to the line. These are the stiffnesses associated with the forces that keep the particle on the line. Due to the presence of the neighboring traps, the particle experiences a smaller axial stiffness in the order of 100 pN/ $\mu\text{m}/W$ , which is significantly less than the stiffness the particle experiences in a single trap.

When the spacing between the traps was varied we saw that the potential energy along the line, for some spacings, shows a minimum which does not coincide with the middle trap. We note that the depth at which we trap the particle is a strong function of the spacing in between the three traps. In Figure 6.12 **a** we plotted in grey the position of the stable trapping location along the line as a function of the spacing in between the traps. This bifurcates at a certain point, the three traps form two minima, somewhere in between the traps. For larger

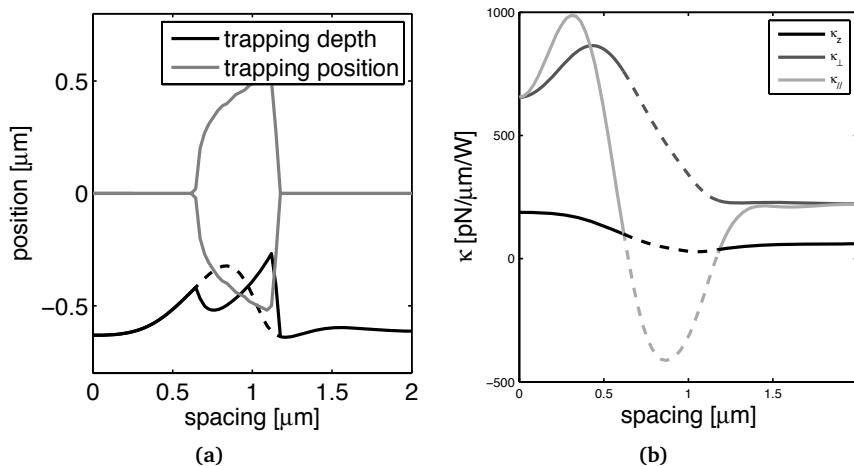


**Figure 6.12:** The trapping behavior as a function of the spacing between three traps. **a.** The trapping position of a  $1.4 \mu\text{m}$  silica particle trapped in ethanol as a function of the spacing between three point traps forming a line. The grey line represents the position along the line where the potential energy is minimal. The black line plots the axial position with respect to the geometrical focus. The dotted black line gives this distance for the middle of the line when that is not the stable trapping location. The geometrical focus is positioned at a distance of  $12 \mu\text{m}$  above the bottom glass plate. **b.** The trapping stiffness, i.e. the slope of the trapping efficiency, as a function of the spacing in between the traps. The dotted lines give the stiffnesses for the middle trap when this is not the most stable trapping location.

distances, the three traps separate into three separate traps, after which we give the position of the middle trap.

In black we depict the axial trapping position. Initially the particle is trapped deeper in the sample with increasing distance in between the traps. This is due to the fact that by increasing the distance between the traps we reduce the gradient in the intensity and thus the gradient force. As a result the scattering force becomes relatively more important and pushes the particle further up. There the gradient in the intensity is slightly larger and a new equilibrium is found. For completeness, we also give the trapping depth in the middle trap when this is not the stable trap (dashed line).

In Figure 6.12 **b** the trapping stiffness that the particle experiences are plotted as a function of the spacing in between the traps. Because in this case the cylindrical symmetry imposed by the assumption of circularly polarized light is broken, we give three different stiffnesses. The stiffness parallel to the line and the one perpendicular to the line are the same when the three traps are overlapping. When the traps are far apart, such that the traps no longer influence each other, the two stiffnesses are again equal to each other. In this case the trapping stiffnesses of all three traps have one third of the value they had when the three

traps were coinciding.

The stiffness parallel to the line goes to zero for a spacing of 644 nm. That is the distance between the traps that makes them form a line-trap. When the spacing in between the traps is made even larger, the ‘stiffness’ becomes negative. This means that the particle is effectively pushed away from the middle trap. Also the axial stiffness shows a minimum, be it for slightly larger spacing in between the traps. The axial stiffness the particle experiences in the secondary trap when this is the stable trapping location is even slightly higher than in the middle trap.

## Conclusion

For line-traps made by placing more than three point traps on a line we expect similar results. The potential along the line will depend very sensitively on the spacing between the constituent traps and the size of the particles. When the spacing between the traps is chosen slightly wrong, the particles trapped on the line will experience several energy barriers along the line. The limited axial stiffness will demand that a significant laser power be used to form the line-trap. This will only increase the energy barriers along the line. Another practical difficulty will be the fact that the trapping depth varies strongly with the position along the trap. This makes the particle tracking by means of conventional bright-field microscopy more challenging [9]. Of course this could be solved by applying Digital Holographic Microscopy, see Chapter 2. The analysis of the probability density distribution of multiple inter-particle-distances to study the inter-particle-interactions would also more complicated when the line is not straight. Finally, the great sensitivity of the trapping behavior on the line of the size of the particles demands that the particles between which the interaction potential should be measured are very similar in size (to about 3 nm). In conclusion, we think that using a linear array of time-shared point traps with a spacing comparable to the radius of the particles cannot be used to measure the pair-potential.

### 6.4.1 *line-traps: experiment*

We experimentally tested the above predictions. We trapped silica particles of respectively 758, 1080, 1400, 1640 and 1750 nm in diameter in an array of three time-shared traps. The spacing between the traps was varied using a LabVIEW (National Instruments) program. Digital Holographic Microscopy [32], was applied to track the particle movement. For each configuration of the traps we recorded between 400 and 500 frames at 200 frames per second. To signal the change in the trap configuration we placed the electronic shutter in the illuminating beam path rather than in the beam-path of the trapping laser. Whenever the conformation of the traps was altered, this resulted in a few dark frames that we used as a time stamp. We applied the algorithm as proposed by Marco Polin *et al.* [33] to solve the Langevin equation for an over-damped Brownian particle in a harmonic potential for the trap stiffness from the holographically measured

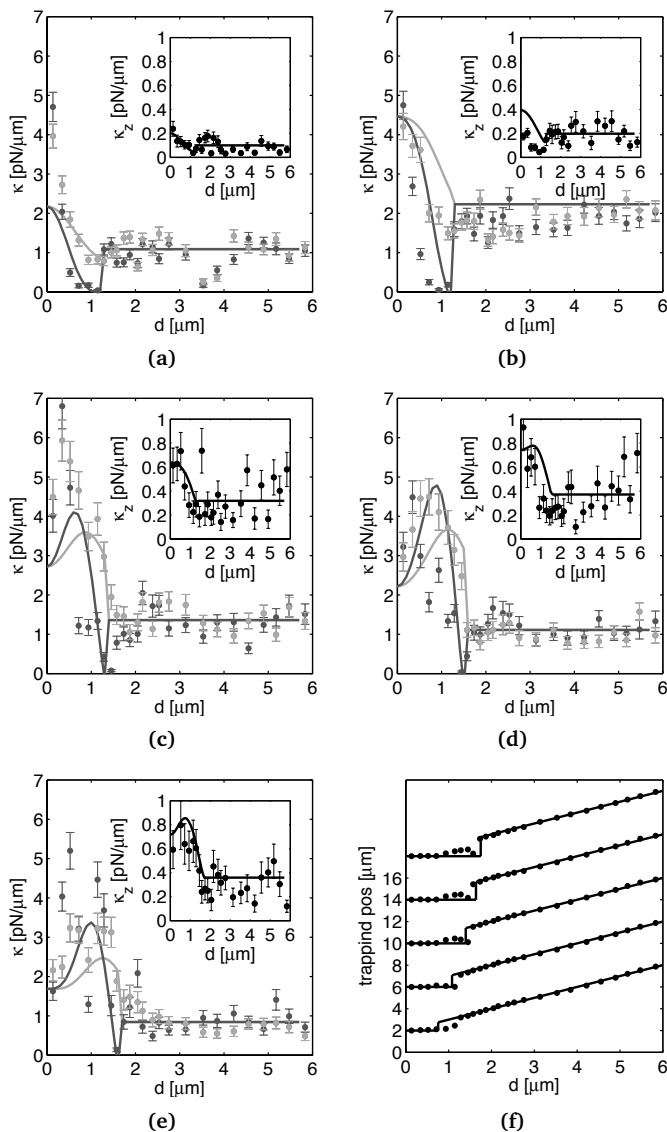


**Figure 6.13:** The experimental trapping stiffness on a line of three traps as function of the spacing between the traps. In a, b, c, d and e the trapping stiffnesses of a respectively 758, 1080, 1400, 1640 and 1750 nm diameter SiO<sub>2</sub> in ethanol in an array of three time-shared traps as a function of the distance between the traps. The geometric focus was placed 12  $\mu\text{m}$  above the bottom glass plate, the distance between the particle and the focal plane,  $d_h$  was 6  $\mu\text{m}$ . Dark grey and light grey was used respectively for the direction of the line and perpendicular to that. In the insets we present the results for the axial stiffness in black. The full lines represent the normalized results from calculations. The power of the laser was 500 mW, the stiffnesses are presented in pN/ $\mu\text{m}$  for 1 W of laser power. f. The trapping location as a function of the distance between the traps with respect to the middle trap. For clarity the lines were given different offsets. The full line represents the calculated most probable trapping location.

particle trajectories. The experiment was done at three different laser powers, 200 mW, 500 mW and 1000 mW.

At the beginning of each experiment care was taken to assure that the particle was approximately 12  $\mu\text{m}$  above the bottom glass plate. Then the spacing was set at its largest value and the particle was moved out of the frame using lens L3 to record the background for the holography, see also Chapter 2. Then the recording was started and after 1000 frames the traps were moved back into the frame. During the experiment the three traps were slowly brought together.

To see if any influence of interference can be observed we performed the experiments both with time-shared arrays of traps and with superimposed traps that were generated simultaneously by providing the AODs with a mixed signal containing the frequencies associated with the three trapping locations. The signal to the AODs was mixed with home built hardware.

The results of this experiment for a laser power of 500 mW are presented in Figure 6.13. In the same graphs we plot the calculated trapping stiffnesses. These stiffnesses were evolved at the predicted trapping location rather than in the central trap as was plotted in Figure 6.12 d. The experiment confirms the calculated behavior. When the spacing between the traps is of the order of the diameter of the particle we observe a clear minimum in the trapping stiffness in the direction of the line, while the particle remains confined to the line. However, slightly different spacings between the traps immediately result in larger stiffnesses, or energy barriers between along the lines. A similar effect is to be expected when trapping slightly smaller or larger particles. We also note that there is a clear increase in the trapping stiffness when the spacing between the traps is about half a diameter. The relative increase in the trapping stiffness seems to be larger for larger particles.

For continuous arrays of traps, generated by superimposing the traps rather than time-sharing the traps we found very similar results. The effect of possible interference between nearby traps may be studied gathering more statistics. However the strongest influence is to be expected when multiple particles are trapped and illuminated simultaneously. See also section 4.7.4.

The maximum increase in the trapping stiffness as a function of the spacing between the three traps with respect to the trapping in single traps, is for the 1400 and the 1750 nm particle was even larger than the calculated increase. We think this may be due to the relatively bad trapping in single traps due to imperfect alignment of the setup that caused the focus to not be diffraction limited.

## Conclusion

Summarizing, to make a line-trap of multiple time-shared point traps is hard because for the line to be 'flat' in the potential energy sense of the word, the spacing between the traps has to be exactly right. For a slightly larger or smaller particle this distance has to be different. As a result, line traps, made out of point traps in this way, will probably never allow one to measure the interaction between two

differently sized particles. When the particles are slightly different, the potential energy landscape of both particles needs to be measured in the absence of the other particle to correct for the influence of the line-trap while measuring the interaction between the two particles [25]. One would have to keep track of the two individual particles. Even worse is that at least one of the two particles is very likely not free to diffuse over the line. To make the line longer in order to allow more than one particle on the line one needs to add at more traps. In particular for the axial trapping, adding more traps may become problematic as this implies distributing the laser power over more traps. An interesting observation is the occurrence of effective traps in between the focuses at particular spacings that trap the particles even stiffer than in the constituent traps.

### 6.4.2 *line-traps: lines of many traps*

An alternative approach to form line-traps using point traps is to place many ( $O(100)$ ) traps close together on the scale of the particles. This allows the line-trap to be a line-trap independently of the size of the particles. When such a line-trap is to be made of time-shared traps, the laser has to be displaced even faster in order to be able to visit all the constituent point traps within less than a diffusion time. We can switch from one position to the other in about  $5 \mu\text{s}$ , so that a line of several hundreds of traps could be scanned in a millisecond, see also section 5.4.2. The effect of a deforming trap when the trap is switched on and off too fast, may be a little less strong when the trap is moved only to a nearby trap. Certainly the switching rate should be higher than the corner frequency [34] to have an effective trapping potential which justifies the application of the Boltzmann distribution in the analysis of the particle behavior.

To test this idea we trapped a  $1.4 \mu\text{m}$   $\text{SiO}_2$  particle in ethanol at  $14 \mu\text{m}$  above the bottom glass plate in an array of point traps. The traps formed a line with a length of  $5 \mu\text{m}$  and the number of traps on the line was varied from 2, 4, 8, 16, 32 through 64 equidistant traps. The laser was switched from one position to the next every  $4.8 \mu\text{s}$  for all conformations. As the traps all lay on the same line, any ‘ghost’ traps would be on the same position of the traps themselves, see also section 5.4.2. The particle was tracked by means of Digital Holographic Microscopy, see Chapter 2, with a frame rate of 100 Hz. For each conformation between 20,000 and 30,000 frames were recorded.

The trapping potentials as deduced from the observed probability density functions are presented in Figure 6.14 for the case that the line is formed by respectively 2, 16 and 64 traps. The trapping potential in the case the ‘line’ consisted of only two traps at a distance of  $5 \mu\text{m}$  is plotted Figure 6.14 a. The two traps are not influencing each other and we observe that the particle is confined in what looks like a harmonic well that is slightly less stiff in the axial direction. When the number of traps was increased to 16 this had two effects on the trapping potential.

First of all, the trapping stiffness in the direction of the line, represented by

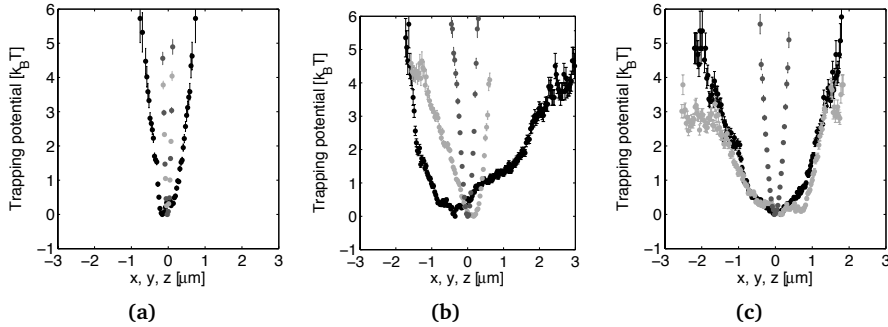


**Figure 6.14:** *line-trap made of many traps.* **a.** The trapping potential of a  $1.4 \mu\text{m}$   $\text{SiO}_2$  particle in a single trap. **b.** The trapping potential in 16 point traps that were placed equidistantly over a distance of  $5 \mu\text{m}$ . **c.** The trapping potential on the line with 64 traps over the same distance. The distance to the bottom glass plate was  $14 \mu\text{m}$ . Black was used for the trapping potential in the axial direction, grey and light grey were used for respectively the direction perpendicular to the line and parallel to the line.

the light grey symbols, is less stiff. The particle is free to diffuse over a larger range than in the direction perpendicular to the line. The array of traps starts to resemble a line-trap. The trapping potential along the line is less symmetric than before. This asymmetry we ascribe to nonlinearities in the AODs that do not diffract the light with the same efficiency in all directions.

Secondly, we notice that the particle is also less confined in the axial direction. This is due to the fact that the laser light is spread over more, nearby, positions such that the intensity gradients decrease. As a result the gradient forces in the axial direction are less strong and the particle is also more free to diffuse in the axial direction.

When the number of traps on the line is increased even further, to 64, the particle gained even more freedom in the direction of the line. The line is now effectively almost as long as in the axial direction. On the best section of the line the potential landscape is fairly flat with obstacles significantly smaller than  $1 k_B T$ .

Line traps created in this way may be used to measure inter-particle interactions using the analysis methods described in reference [25]. As can be understood from the above however, this technique cannot be applied to measure the interaction between the  $1.4 \mu\text{m}$  silica particles in ethanol using the present setup, as the particles are left with too much freedom in the axial direction. The particles would be free to hop over one another and the particles would tend to be trapped above each other. A better alignment and different choices of solvents minimizing spherical aberration will allow line traps to be made out of hundreds of point traps.

## 6.5 Line traps to increase the trapping stiffness; Double Traps

The most striking observation in Figure 6.12 and 6.13 is the observation of a maximum in the lateral stiffnesses at a spacing smaller than the spacing at which we observe a line-trap, at a spacing smaller than the particle itself. Although the intensity in the central trap is reduced to one third to form the two outer traps, the trapping stiffness is then observed to be larger than in a single trap with all the energy in one trap. This increase in the lateral stiffness can be explained by stating that the two side traps are placed such that their largest intensity gradient coincides with the edge of the particle. This way the polarization of the particle changes most with its position, which is equivalent to having a steeper intensity gradient. We make the focus effectively larger, more similar in size to the particle. This results in a larger stiffness. This is a significant increase in the lateral stiffness, as can be seen from Figure 6.12 and 6.13. Unfortunately, this does not increase the stiffness in the axial direction. The axial stiffness is slightly less when the spacing in between the traps is chosen such that the stiffness in the direction of the line is maximum.

The observation that the axial trapping stiffness can be increased by making the effective focus larger, motivated us to also calculate the trapping stiffness of a combination of only two traps. We choose to call this new type of optical traps *double traps*. Effectively, the focus can then be made similar in size to the particle, such that the intensity slope is maximized at the edge of the particle to increase the stiffness. Doing so we use the stiffening of the traps of larger particles at larger distances that was reported in [35, 36] to trap the particles stiffer. This stiffening clearly occurs for the largest particle in Figure 5.19 **b**.

We plot the experienced stiffness in three directions, the axial direction, parallel to the line spanned by the two traps and perpendicular to the line, all as a function of the spacing in between the two traps in Figure 6.15 **a**. We only consider spacings small enough so that the particle is trapped in the middle between the two traps.

Similar to the left side of Figure 6.12, there is an increase of the trapping stiffness in the direction of the double trap for the smallest spacings. Then, while the parallel stiffness is already going down with increasing spacing between the two traps, the stiffness in the direction perpendicular to the spacing shows a maximum. The main difference between Figure 6.15 and Figure 6.12 is that the maximum stiffness is even higher in Figure 6.15, for the case with two traps. Apparently the middle trap in the case with three traps contributes relatively little to the stiffness. It is more efficient to concentrate the laser light only in the outer two traps forming a double trap.

In Figure 6.15 **b**, **c** and **d** we plot the trapping efficiency or dimensionless force, as a function of the position of the particle in the three directions, the  $z$  axis, parallel to the spacing between the particles and the direction perpendicular

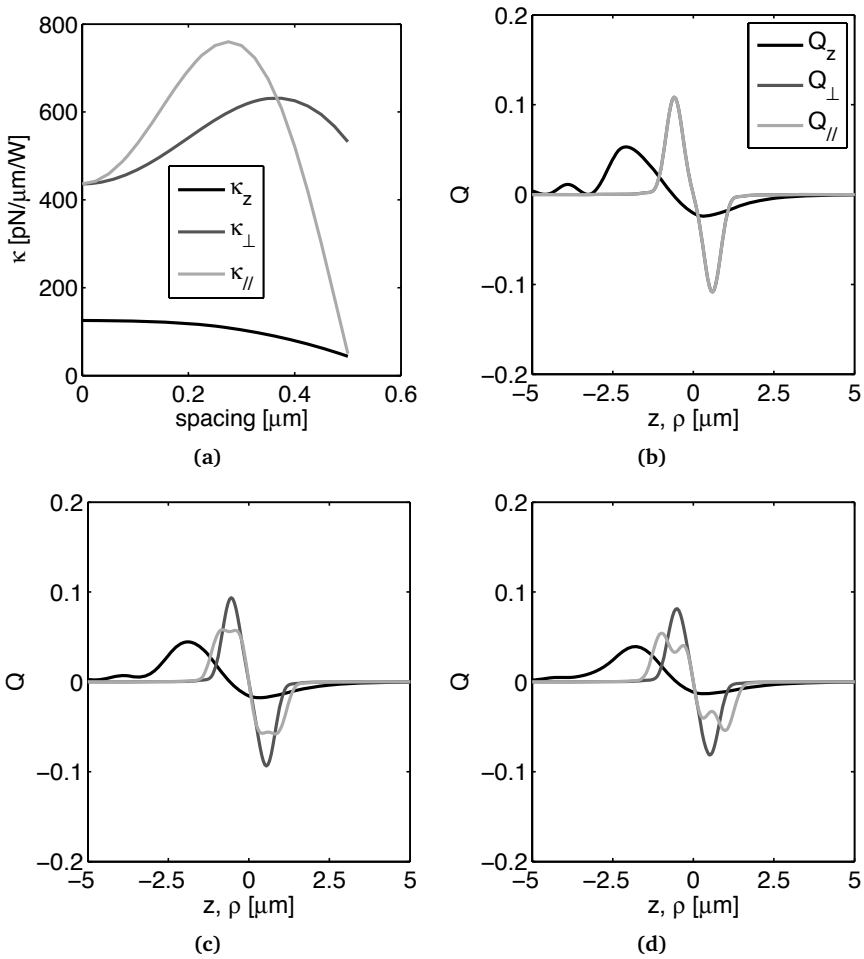


**Figure 6.15:** The trapping behavior in a double trap, an array of two traps as a function of the distance between them. **a.** The trapping stiffness of a 1.4  $\mu\text{m}$  silica particle trapped in ethanol, with the geometrical focus 12  $\mu\text{m}$  above the glass, as a function of the spacing between two point traps. **b.** The trapping efficiencies in the three directions, along the propagation direction of the light, in the direction of the spacing in between the two traps and perpendicular thereto, as a function of the position, when the spacing between the two traps is zero. **c.** The same as in **b**, but with a spacing of 600 nm between the traps, when the parallel stiffness is maximum. **d.** The same as in **b**, but with a spacing of 800 nm between the traps, when the perpendicular stiffness is maximum.

to that for a  $1.4\ \mu\text{m}$  silica particle in ethanol. These curves have been calculated for zero spacing between the traps and for spacings of 600 and 800 nm for which the trapping stiffness in the parallel and perpendicular direction respectively, is maximum. The effective trap in Figure 6.15 **b** where both traps overlap is symmetric such that the trapping efficiency in the parallel and the perpendicular direction overlap. We note that the trapping efficiency has a very small bend in it, the curve is steeper further away from the optical axis in accordance with references [35] and [36].

The spacing between the traps in Figures 6.15 **c** and **d** causes the particle in the middle to experience the steeper part of the curve in Figure 6.15 **a**. The result is a more linear force-extension curve and a higher stiffness. Obviously, spreading the laser power over two trap decreases the power in each trap and thus the maximum trapping efficiency. The lateral trapping efficiency is still considerable. In the axial direction the maximum restoring force is respectively  $-0.0240$ ,  $-0.0133$  and  $-0.0179$  Figure 6.15 **b**, **c** and **d**. We note that the loss in restoring force is smaller than a factor two. The gain in parallel and perpendicular trapping efficiency is at maximum respectively a factor 1.7 and 1.5 (corresponding to stiffnesses of 1135 and 947 pN/ $\mu\text{m}/W$ ), while the maximum restoring force is weakened by a factor 1.8 and 1.3 respectively. It may be interesting to sacrifice some axial restoring force to gain lateral stiffness.

Larger particles are generally trapped less stiff, as we have seen in section 5.5. This does not mean that the maximum trapping force is less for larger particles. To the contrary, the maximum lateral trapping efficiency increases with the particle size (Figure 5.24). The dependence of the optical force on the position of the particles is more non-linear for larger particles. The decreasing stiffness in the trapping location is the result of the fact that the polarization of the particle does not decrease significantly at small deviations from the trapping position. Double traps use the larger polarizability of larger particles to traps these particle stiffer.

Figure 6.16, is analogous to Figure 6.15, for an even large particle,  $4\ \mu\text{m}$  in diameter. Again, in Figure 6.16 **a** the stiffnesses that the particle in between the two traps experiences in all three directions is plotted as a function of the distance between the two traps. The trapping efficiencies are plotted in Figure 6.16 **b** as a function of the position when the two traps are overlapping. This particle is a few times larger than the focus, the interaction between the edge of the particle and the intensity gradient of the trap is rather small when the particle is in the middle and thus totally engulfs the focus. The non-linearity in the trapping efficiency with the displacement is evident. The slope in the trapping efficiency varies significantly with the particle position. This variation in the slope of the trapping efficiency leads to the appearance of multiple maxima in the trapping stiffnesses in Figure 6.16 **a** where the spacing between the two traps is varied.

With increasing spacing between the two traps there is a general increase in all three stiffnesses. Particularly for the trapping stiffness in the axial direction this is surprising. With increasing spacing between the traps the particle is trapped

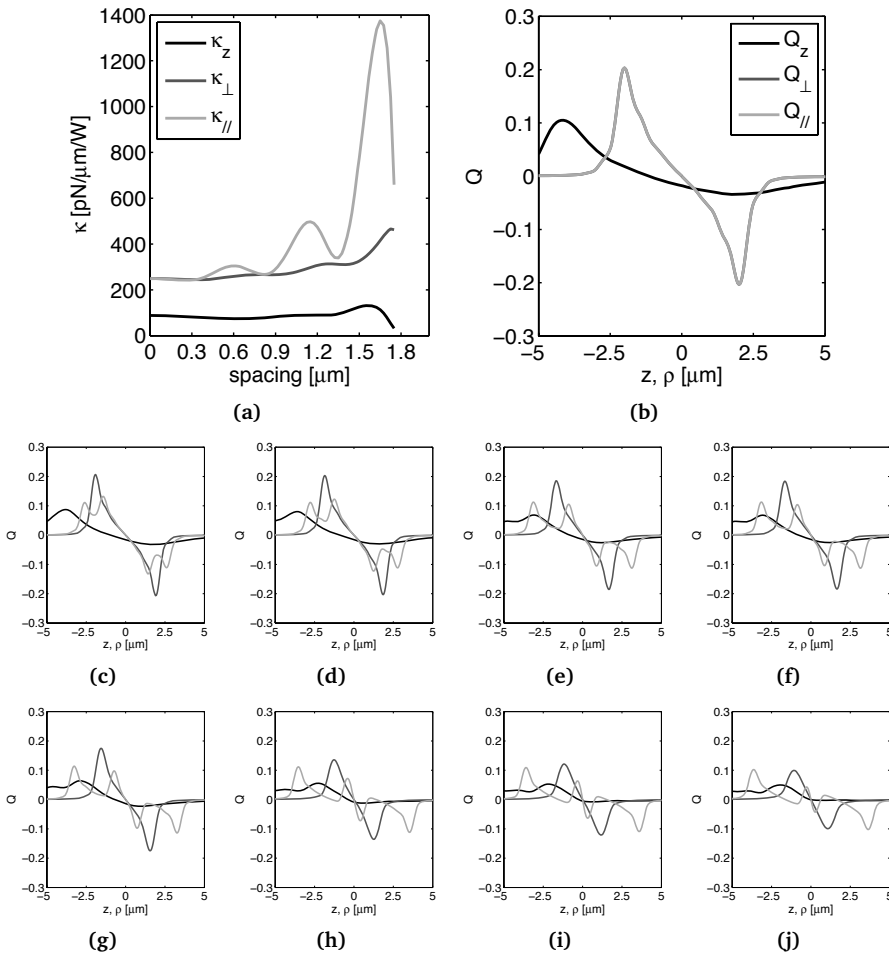


**Figure 6.16:** The trapping behavior in a double trap a function of the distance between them for a 4  $\mu\text{m}$  particle. **a.** The trapping stiffness of a 4.0  $\mu\text{m}$  silica particle trapped in ethanol, with the geometrical focus 12  $\mu\text{m}$  above the glass, as a function of the spacing between two point traps. **b.** The trapping efficiencies in the three directions, along the propagation direction of the light, in the direction of the spacing in between the two traps and perpendicular thereto, as a function of the position, when the spacing between the two traps is zero. **c-j.** The same as in **b**, but with a spacing of respectively 1200, 1550, 2250, 2300, 2550, 3150, 3300 and 3450 nm between the traps corresponding to the various local maxima in the trapping stiffnesses.

further upwards. This indicates that the particle effectively experiences a larger scattering force. However, also the gradient force is influenced by the varying spacing between the traps. In table 6.5 we quote the trapping stiffnesses and the maximum restoring forces in all three directions for the spacings at which either stiffness experiences a (local) maximum. From the restoring forces in the  $z$ -direction we gather that there is no particular trend in the evolution of the maximum restoring force.

The trapping efficiency is plotted as a function of the distance to the middle between the two geometrical focuses in Figure 6.16 **c** through **j**, each with the two traps at which a maximum in the trapping stiffness was observed. With each next maximum in either one of the stiffnesses we effectively remove one more wobble in the curve for the trapping efficiency in Figure 6.16 **b**. These wobbles are the result of the interference effect that was discussed in section 5.5. The result is that the force on the particle becomes more and more linear with the displacement. A linear relation between force and displacement is very useful for force measurements [35–37]. We effectively iron the interaction between the light and the particle.

Because the edge of the particle experiences a steeper intensity gradient with increasing spacing between the traps, the stiffness generally increases with increasing spacing between the traps. This increase takes place at the cost of the maximum restoring force. For the spacings larger than 3200 nm in Figure 6.16 **i** and **j**, the trapping efficiency in the parallel direction locally, at a distance of about 50 nm, points away from the middle between the two point traps. At even larger distances, the force points back to the middle between the traps. The particle can also be trapped close to either one of the constituent point traps.

A trap like the one in Figure 6.16 **i** would be ideal for force measurements where large forces in one direction need to be measured. The force could be measured in the perpendicular direction providing a linear behavior over more than two micron up to a trapping efficiency of more than 0.1. The even higher stiffness in the parallel direction would guarantee that the particle remains on the line along which the interaction of interest acts. All this at the cost of a relatively small reduction of the axial restoring force while we even increase its axial stiffness. The size of the particle would facilitate easy position detection, which, due to the extent over which the trap is linear is not even too critical any more.

### 6.5.1 Double traps: experiment

We experimentally tested the increase in the trapping stiffness for larger particles in double traps. We trapped silica particles of respectively 758, 1080, 1400, 1640 and 1750 nm in diameter in a double trap. As in section 6.4.1, the spacing between the traps was varied using a LabVIEW (National Instruments) program and Digital Holographic Microscopy [32], was applied to track the particle movement. For each configuration of the traps we recorded between 400 and 500 frames at 200 frames per second. We applied the algorithm as proposed by Marco Polin *et*

Panel of Figure 6.16	Spacing nm	$\kappa_z$ $\frac{\text{pN}}{\mu\text{mW}}$	$\kappa_{//}$ $\frac{\text{pN}}{\mu\text{mW}}$	$\kappa_{\perp}$ $\frac{\text{pN}}{\mu\text{mW}}$	$Q_z$	$Q_{//}$	$Q_{\perp}$
<b>b</b>	0	88	248	248	-0.034	-0.203	-0.203
<b>c</b>	1200	74	305	259	-0.026	-0.113	-0.186
<b>d</b>	1550	76	271	266	-0.016	-0.115	-0.136
<b>e</b>	2250	90	494	292	-0.031	-0.123	-0.204
<b>f</b>	2300	90	498	298	-0.023	-0.114	-0.175
<b>g</b>	2550	89	385	313	-0.003	-0.102	-0.100
<b>i</b>	3150	130	1155	361	-0.032	-0.132	-0.203
<b>j</b>	3450	53	1041	466	-0.008	-0.109	-0.121

**Table 6.1:** The spacings between the two traps, the trapping stiffnesses and the restoring forces for the maximal trapping stiffness in two traps for a 4.0  $\mu\text{m}$  silica particle trapped in ethanol, with the geometrical focus 12  $\mu\text{m}$  above the glass, corresponding to the curves in b – j of Figure 6.16.

al. [33] to solve the Langevin equation for an over-damped Brownian particle in a harmonic potential for the trap stiffness from the holographically measured particle trajectories. The experiment was done at three different laser powers, 200 mW, 500 mW and 1000 mW.

At the beginning of each experiment, care was taken to assure that the particle was approximately 12  $\mu\text{m}$  above the bottom glass plate. Then the spacing was set at its largest value and the particle was moved out of the frame using lens L3 to record the background for the holography, see also Chapter 2. Then the recording was started and after 1000 frames the traps were moved back into the frame. During the experiment the two traps were slowly brought together. At a certain moment in time a double trap formed and the particle is trapped in the middle between the two traps.

To check for the influence of interference, we performed the experiments both with time-shared arrays of traps and with superimposed traps that were generated simultaneously by providing the AODs with a mixed signal, consisting of a superposition of the frequencies associated with the two trapping locations. The signal to the AODs was mixed with home built hardware. As in section 6.4.1 we did not observe any appreciable difference between the trapping behavior in time-shared and continuous arrays.

Similar to Figure 6.13 we give the trapping stiffness as a function of the distance between the two traps for the particle sizes under investigation. The full lines represent calculated trapping stiffnesses while the symbols are the measured trapping stiffnesses. The calculated stiffnesses in the lateral and axial directions were normalized separately, to correct for the afore mentioned lesser stiffness in the axial direction.

For the particles with a diameter of 1400, 1640 and 1750 nm we observe that the calculations predict an increase in the trapping stiffness in the lateral directions for certain spacings between the two traps. The experimental stiffnesses confirm these results. The maximum stiffness in the direction of the double trap is slightly larger than in the direction perpendicular to that. For the largest two particles, with diameters of 1640 and 1750 there is even a slight increase in the axial trapping stiffness.

### 6.5.2 More calculations on double traps

In Figure 6.18 we give an overview of the trapping depth and the stiffnesses of silica particles in a trap with the geometrical focus 12  $\mu\text{m}$  above the glass ethanol interface. Grey values represent the trapping depth with respect to the geometrical focus and the stiffnesses in the three directions of interest, as a function of both the radius of the particle and the spacing between the two traps. When the particle does not experience a trap in the middle between the two point traps the corresponding pixel is left white.

We depict the trapping depth in double trap in Figure 6.18 **a** as a function of the spacing between the traps and the particle size. The smallest particles, up to a radius of about half a micron, can be trapped at spacings that are slightly larger than the particle itself. The focus is larger than these particles and the spacing in between them is small compared to their extent. For larger particles, the largest spacing in between the two point traps for which we can still trap the particle in the middle increases more or less linearly with the particle radius. The maximum spacing is always smaller than the diameter of the particle itself.

The trapping stiffness in the axial direction is plotted in Figure 6.18 **b**. The particle size which is trapped stiffest over all, is about half a micron in radius as was also seen in section 5.5. For particles that are significantly larger than the focus, roughly a micron and larger in radius, for each particle the highest axial stiffness is achieved just before the two traps separate. Possibly, the destabilizing effect of the scattering force on the particle is minimized at these spacings. A larger fraction of the total light misses the particle which means it does not transfer momentum to the particle and as a result the scattering force is reduced. The particle/spacing combinations that yield the largest axial stiffness coincide with those for which the particle is trapped deepest, as can be seen from Figure 6.18 **a**.

In the larger particles trapped in double traps at relatively small spacings, so in the south eastern quadrants of the Figure 6.18 **a** and **b**, the interference

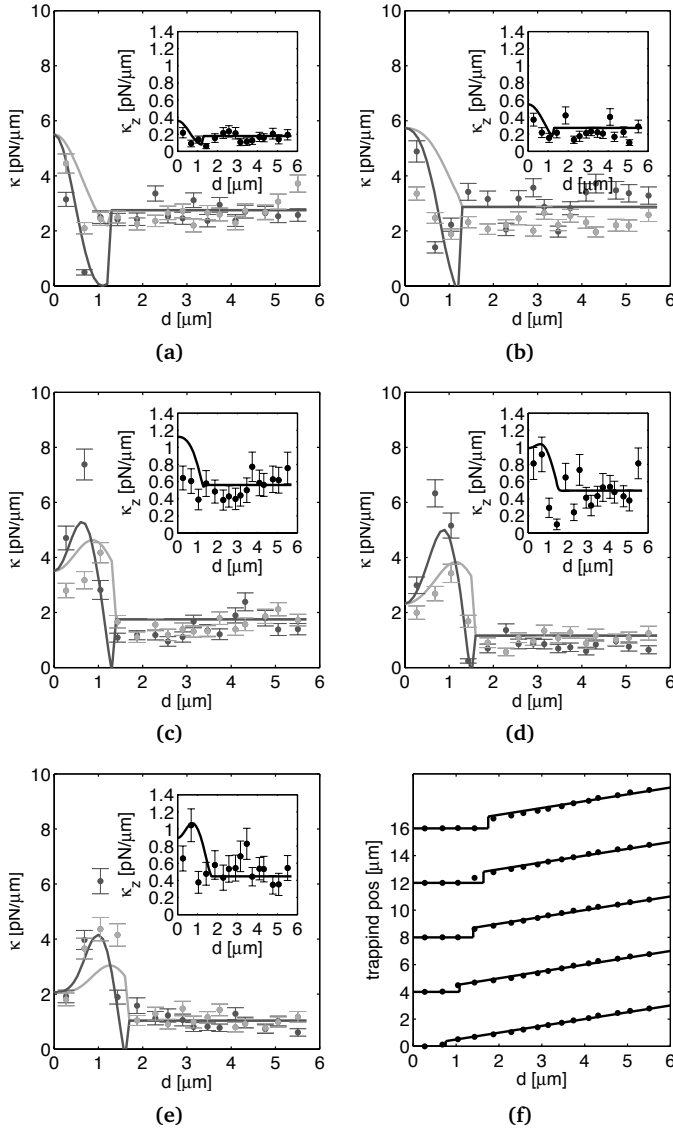


**Figure 6.17:** The experimental trapping stiffness in a double trap as function of the spacing between the traps. In a, b, c, d and e the trapping stiffnesses of a respectively 758, 1080, 1400, 1640 and 1750 nm diameter SiO<sub>2</sub> in Ethanol in a double trap consisting of two continuous traps are plotted as a function of the distance between the traps. The geometric focus was placed 12  $\mu\text{m}$  above the bottom glass plate, the particle was trapped  $z_z = 6 \mu\text{m}$  above the focal plane. Dark grey and light grey was used respectively for the direction of the line and perpendicular to that. In the insets the results for the axial direction are plotted in black. The full lines represent the normalized results from calculations. The power of the laser was 500 mW, the stiffnesses have been normalized to 1 W of laser power. f. The trapping location as a function of the distance between the traps with respect to the center of the double trap. For clarity the lines have been given offsets. The black line represents the middle of the array when that is the most probable trapping location and the position of one of the two traps when the calculations suggest that the particle would be trapped there.

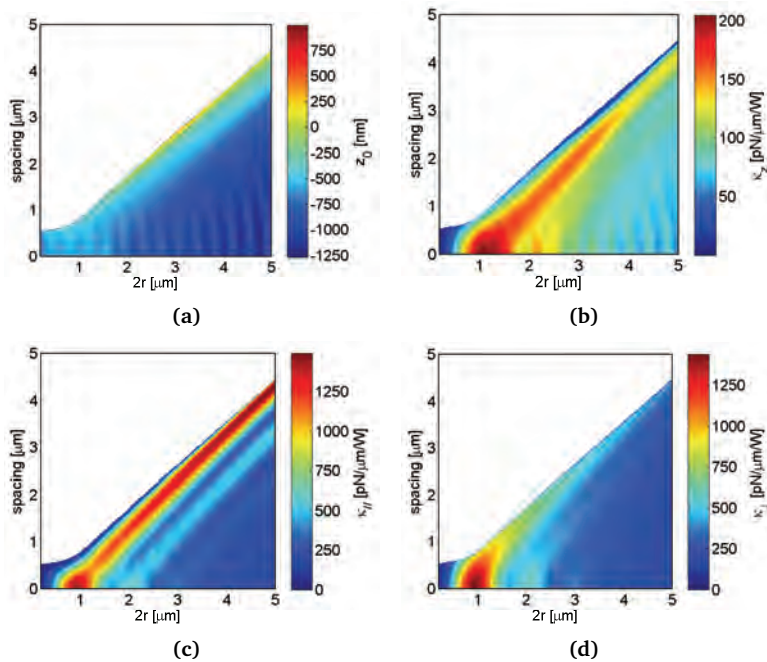


**Figure 6.18:** The trapping stiffnesses and trapping depths of silica particles in two traps in ethanol as a function of the distance between the traps and the particle size. **a.** The trapping depth with respect to the geometrical focus at  $12\ \mu\text{m}$  above the glass of a silica particle in ethanol, as a function of the spacing between two point traps and the radius of the particle, both in microns, represented false colors. For those combinations of particle radius and trap spacing that did not result in stable trapping in the middle between the traps, we left the corresponding pixel white. **b.** The axial trapping stiffness of the same configurations. **c.** The stiffness in the direction of the spacing between the two constituent traps. **d.** The trapping stiffness perpendicular to the spacing between the two traps.

effect discussed in section 5.5 is still present. This effect diminishes for the larger spacings at which the stiffness is optimized.

Also in the direction perpendicular to the spacing between the two traps, in Figure 6.18 **d**, the larger particles experience a maximum stiffness just before the two traps separate. The maximal trap stiffness in the direction perpendicular to the two traps never exceeds the maximal lateral trapping stiffness achieved for an optimal size,  $430\ \text{nm}$  in radius, in a single trap,  $1437\ \text{pN}/\mu\text{m}/W$ .

In 6.18 **c** we give the trapping stiffness along the direction of the two traps. Again the maximum stiffness for the larger particles occurs at a spacing between the two traps that is slightly smaller than the distance at which the traps separate. That is what we expect because in that case the interaction between the intensity gradient of the trap and the refractive index jump at the edge of the particle coincide. The maximum stiffness in the direction of the separation between the two

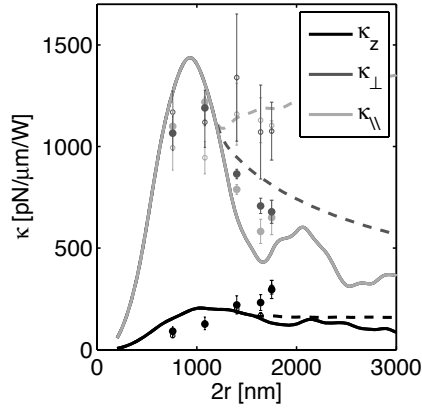


**Figure 6.19:** The trapping stiffnesses as a function of the particle size, optimized by using double traps compared to the trapping stiffnesses in a single trap. Full lines, the axial (black) and lateral (light grey) trapping stiffness for a silica particle with geometrical focus at 12  $\mu\text{m}$  above the glass, in ethanol, as a function of the radius of the particle. The dashed lines correspond the maximal trapping stiffness in either the axial direction (black), the direction parallel (light grey) and the direction perpendicular (dark grey) to the spacing in between the two traps. The closed symbols are the trapping stiffnesses as measured in single traps, the open symbols represent the maximum stiffness as experimentally observed in the experiments in section 6.5.1. The experiments performed at 200, 500 and 1,000 mW of laser power were normalized to 1 W of laser power and averaged.

traps is even larger than the optimal stiffness in a single trap for the optimal size for some of the largest particles. We find a trapping stiffness of 1491  $\text{pN}/\mu\text{m}/\text{W}$  for a particle with a radius of 2730 nm in two traps at a mutual distance of 2560 nm.

The dependence of the trapping stiffnesses on the radius of a silica particle in ethanol, similar to Figure 5.18, is plotted in Figure 6.19. Here, the geometrical focus was at a depth of 12  $\mu\text{m}$  above the glass plate. Once again, there is a clear maximum in the trapping stiffness for a particle that is about as large as the focus itself. The dotted lines represent the maximum trapping stiffnesses we calculated for double traps when varying the spacing between two traps. The maximum stiffness are plotted for the axial direction, the direction of the spacing between the two traps and the direction perpendicular thereto. Note that the spacing for which the trapping stiffness in a particular direction is maximal is not necessary the same for the stiffnesses in all three directions.

For particles that are larger than about 600 nm in radius, the lateral trapping stiffnesses can be increased by trapping the particle in two traps with a suitable spacing between them. In the axial direction the trapping stiffness for particles that are larger than about 800 nm in radius can be increased.

In the direction parallel to the spacing between the two traps the maximum trapping stiffness continues to increase with increasing particle radius. Particles

that are larger than roughly  $2\ \mu\text{m}$  in radius, so about 4 times larger than the focus, the stiffness can even be larger than the maximum stiffness in a single trap of an optimally sized particle.

In the direction perpendicular to the spacing between the two point traps, the maximum stiffness still decreases with increasing particle size. The two traps together however, are significantly stiffer than the stiffness of a single trap with the same total laser power. The oscillations in the lateral trapping stiffness that are the result of the interference between light that was reflected by the first interface of the particle with light that has transferred the particle twice, see section 5.5, have been ironed out by the optimal splitting of the two traps. Effectively, the scattering force is minimized in a double trap with the correct spacing.

In the axial direction a similar behavior is observed. The maximal stiffness in a double trap goes down with the particle size, but is significantly higher than in a single trap with the same total laser power.

Another interesting observation is that the spacing between the two traps that optimizes the trapping stiffness effectively renders the interference effect on the axial and lateral stiffness, as discussed in section 5.5, negligible. The periodic variation of the trapping stiffness with increasing particle radius is not visible in the value of the maximal stiffnesses at optimized spacing between the two traps. In Figure 6.18, the spacings at which the optimal stiffnesses are found do not show any periodic variation with the particle size. Apparently, the scattering force is reduced so significantly by splitting the laser light over two traps that the actual reflection coefficient of the particle is of scarce relevance.

The symbols represent the trapping stiffnesses from the experiments in section 6.5.1. The closed symbols represent the experimental stiffness in single traps. The open symbols represent the experimental maximum trapping stiffness as observed in the double traps in Figure 6.17. The experiments show a clear increase in the trapping stiffness as predicted by the calculations for double traps.

## Conclusion

Double traps can be used to increase the trapping stiffness with which the larger particles are trapped. The technique also allows one to make the dependence of the trapping efficiency and thus the force-displacement curve more linear. The asymmetry in the lateral trapping stiffnesses can actually be useful. It is also possible to use three point traps in a triangle to make the trap more symmetric. Spreading the laser light to increase the trapping stiffness is better than increasing the laser power as the latter would increase the risk of heating and photo damage in biological experiments. The spreading of the laser light over more traps decreases the maximum intensity in the sample and could be used to increase the total power of laser light in the array of traps without inducing damage.

## 6.6 Acknowledgements

We thank Jacob Hoogenboom for synthesis of the 1.4  $\mu\text{m}$   $\text{SiO}_2$  particles. We also thank A. I. Campbell, J. S. Schütz-Widoniak and Ahmet Demirörs for the  $\text{TiO}_2$  particles used in section 6.2. A. Moroz and M. Dogterom re thanked for calculations and discussions on counter-propagating trapping. Dannis 't Hart is thanked for the 758  $\text{nm}$   $\text{SiO}_2$  particles. Johan Stiefelhagen is thanked for the synthesis of all the other particles used in this Chapter. Peter Helfferich is thanked for the mixing hardware and assistance with the experiments on arrays of traps. Astrid van der Horst is thanked for guidance and useful discussions.

## Bibliography

- [1] Visscher, K., Brakenhoff, G. J., and Krol, J. J. Micromanipulation by multiple optical traps created by a single fast scanning trap integrated with the bilateral confocal scanning laser microscope. *Cytometry* **14** 105 (1993).
- [2] Vossen, D. L. J., van der Horst, A., Dogterom, M., and van Blaaderen, A. Optical tweezers and confocal microscopy for simultaneous three-dimensional manipulation and imaging in concentrated colloidal dispersions. *Rev. Sci. Instrum.* **75** 2960 (2004).
- [3] van der Horst, A., van Oostrum, P., Moroz, A., van Blaaderen, A., and Dogterom, M. High trapping forces for high-refractive index particles trapped in dynamic arrays fo counterpropagating optical tweezers. *Appl. Opt.* **47** 3196 (2008).
- [4] Garbin, V., Cojoc, D., Fabrizio, E. D., J.Overvelde, M. L., van der Meer, S. M., de Jong, N., Lohse, D., and Versluis, M. Changes in microbubble dynamics near a boundary revealed by combined optical micromanipulation and high speed imaging. *Applied Physics Letters* **90** 114103 (2007).
- [5] Ashkin, A. Acceleration and trapping of particles by radiation pressure. *Phys. Rev. Lett.* **24** 156 (1970).
- [6] Smith, S. B., Cui, Y., and Bustamante, C. Overstretching B-DNA: the elastic response of individual double-stranded and single-stranded DNA molecules. *Science* **271** 795 (1996).
- [7] Wang, W., Chiou, A. E., Sonek, G. J., and Berns, M. W. Selfaligned dual-beam optical laser trap using photorefractive phase conjugation. *J. Opt. Soc. Am. B* **14** 40 (1997).
- [8] Rodrigo, P. J., Daria, V. R., and Glückstad, J. Real-time threedimensional optical micromanipulation of multiple particles and living cells. *Opt. Lett.* **29** (2004).
- [9] Baumgartl, J. and Bechinger, C. On the limits of digital video microscopy. *Europhys. Lett.* **71** 487 (2005).
- [10] Allersma, M. W., Gittes, F., de Castro, M. J., Stewart, R. J., and Schmidt, C. F. Two-dimensional tracking of ncd motility by back focal plane interferometry. *Biophys. J.* **74** 1074 (1998).
- [11] Misawa, H., Koshiokaa, M., Sasaki, K., Kitamura, N., and Masuhara, H. Three-dimensional optical trapping and laser ablation of a single polymer latex particle in water. *J. Appl. Phys.* **70** 3829 (1991).

- [12] Dutra, R. S., Viana, N. B., Neto, P. A. M., and Nussenzeive, H. M. Polarization effects in optical tweezers. *J. Opt. A Pure Appl. Opt.* **9** S221 (2007).
- [13] Demirörs, A. F., Jannasch, A., van Oostrum, P. D. J., Schäffer, E., van Blaaderen, A., and Imhof, A. Seeded Growth of Titania Colloids with Refractive Index Tunability and Fluorophore-free Luminescence. *Langmuir*; DOI: 10.1021/la103717m (2010).
- [14] Rayleigh, L. The propagation of waves through a medium endowed with a periodic structure. *Philosophical Magazine* **24** 145 (1887).
- [15] Yablonovich, E. Inhibited spontaneous emission on solid-state physics and electronics. *Phys. Rev. Lett.* **58** 2059 (1987).
- [16] John, S. Strong localization of photons in certain disordered dielectric superlattices. *Phys. Rev. Lett.* **58** 2486 (1987).
- [17] Noda, S., Tomoda, K., Yamamoto, N., and Chutinan, A. Full three-dimensional photonic bandgap crystals at near-infrared wavelengths. *Science* **289** 604 (2000).
- [18] Rinne, S., Garcia-Santamaria, F., and Braun, P. Embedded cavities and waveguides in three-dimensional silicon photonic crystals. *Nature Photonics* **2** 52 (2008).
- [19] Wostyn, K., Zhao, Y., de Schaezen, G., Hellemans, L., Matsuda, N., Clays, K., and Persoons, A. Insertion of a two-dimensional cavity into a self-assembled colloidal crystal. *Langmuir* **19** 4465 (2003).
- [20] Qi, M., Lidorikis, E., Rakich, P. T., Johnson, S. G., Joannopoulos, J. D., Ippen, E. P., and Smith, H. I. A three-dimensional optical photonic crystal with designed point defects. *Nature* **429** 538 (2004).
- [21] Gramiak, G. and Shah, P. Echocardiography of the aortic root. *Invest. Radiol.* **366** 356 (1968).
- [22] Bouakaz, A., Frigstad, S., ten Cate, F. J., and de Jong, N. Super harmonic imaging: a new imaging technique for improved contrast detection. *Ultrasound Med. Biol.* **28** 59 (2002).
- [23] Klibanov, A. L. Microbubble Contrast Agents: Targeted ultrasound imaging and ultrasound-assisted drug-delivery applications. *Invest. Radiol.* **43** 354 (2006).
- [24] Garbin, V., Dollet, B., Overvelde, M., Cojoc, D., Fabrizio, E. D., van Wijngaarden, L., Prosperetti, A., Jong, N., Lohse, D., and Verluis, M. History force on coated microbubbles propelled by ultrasound. *Phys. Fluids* **21** 092003 (2009).
- [25] Polin, M., Roichman, Y., and Grier, D. G. Autocalibrated colloidal interaction measurements with extended optical traps. *Phys. Rev. E.* **77** 051401 (2008).
- [26] Burns, M. M., Fournier, J.-M., and Golovchenko, J. A. Optical Binding. *Phys. Rev. Lett.* **63** 1233 (1989).
- [27] Crocker, J. C., Matteo, J. A., Dinsmore, A. D., and Yodh, A. Entropic Attraction and Repulsion in Binary Colloids Probed with a Line Optical Tweezer. *Phys. Rev. Lett.* **82** 4352 (1999).
- [28] Roichman, Y., Sun, B., Roichman, Y., Amato-Grill, J., and Grier, D. G. Optical Forces arising from phase gradients. *Phys. Rev. Lett.* **100** 013602 (2008).
- [29] Visscher, K., Gross, S. P., and Block, S. M. Construction of multiple -beam optical traps with nanometer-resolution position sensing. *IEEE J. Sel. Top. Quant. Electron.* **2(4)** 1066 (1996).
- [30] van der Horst, A., Campbell, A. I., van Vugt, L. K., Vanmaekelbergh, D. A. M., Dogterom, M., and van Blaaderen, A. Manipulating metal-oxide nanowires using counter-propagating optical line tweezers. *Opt. Exp.* **15** 11629 (2007).

- [31] van Oostrum, P. D., van der Horst, A., and van Blaaderen, A. Mutual influence of time-shared optical traps studied by means of Video Holographic Microscopy. *Digital Holography and Three-Dimensional Imaging, OSA Technical Digest (CD) (Optical Society of America) DWD7* (2009).
- [32] Lee, S.-H., Roichman, Y., Yi, G.-R., Kim, S.-H., Yang, S.-M., van Blaaderen, A., van Oostrum, P., and Grier, D. G. Characterizing and tracking single colloidal particles with video holographic microscopy. *Opt. Exp.* **15** 18275 (2007).
- [33] Polin, M., Ladavac, K., Lee, S.-H., Roichman, Y., and Grier, D. Optimized holographic optical traps. *Opt. Exp.* **13** 5831 (2005).
- [34] Deng, Y., Bechhoefer, J., and Forde, N. R. Brownian motion in a modulated optical trap. *J. Opt. A: Pure Appl. Opt.* **9** S256 (2007).
- [35] Neves, A. A. R., Fontes, A., de Y. Pozzo, L., de Thomaz, A. A., Rodriguez, E. C. E., Barbosa, L. C., and Cesar, C. L. Electromagnetic forces for an arbitrary optical trapping of a spherical dielectric. *Opt. Exp.* **14** 13101 (2006).
- [36] Richardson, A. C., Reihani, S. N. S., and Oddershede, L. B. Non-harmonic potential of a single beam optical trap. *Opt. Exp.* **16** 15709 (2008).
- [37] Masri, D. E., van Oostrum, P., Smallenburg, F., Vissers, T., Imhof, A., Dijkstra, M., and van Blaaderen, A. Measuring Colloidal Forces from Particle Position Deviations inside an Optical Trap. *Soft Matter*, DOI:10.1039/COSM01295E (2011).







## Summary

Colloids are microscopic particles that are finely distributed in some other material. Colloids are ubiquitous in many aspects of daily life in the form of many types of dispersions in various liquids; for example as blood cells they provide our bodies with oxygen and crucial nutrients, as pigment particles in paint they are responsible for the right flowing behavior and they stick (ideally) when they should to color and protect. As fat droplets in milk, they feed us. Colloids are comparable in size to the wavelength of visible light. As a result, the interaction of light with colloids is a rather rich phenomenon. Colloids scatter light in many directions. In dense suspensions, light might even be scattered multiple times by different particles. Light scattering is what makes milk look white.

Apart from the fascinating ways in which light interacts with colloids, colloids themselves show interesting collective behavior. Colloids interact with each other over distances that can sometimes be many times longer than their diameter. Typical forces between colloids are the van der Waals attraction, screened charge repulsion, dipolar interactions and depletion attractions. Because most forces scale with the volume of objects, most external forces such as gravity and the influence of inertia on colloid dynamics are relatively small with respect the erratic forces on the colloids that are caused by collisions with the solvent molecules excited by thermal motion. Colloids perform Brownian motion and are therefore a thermal system. The balance between the interaction forces between colloids and the entropy of a colloidal system makes some configurations more favorable than others, depending on the conditions. By changing parameters such as the volume fraction, the temperature or the strength of the interactions, colloidal dispersions can be put in conditions in which they undergo a phase transition. Colloids can form crystals, liquids, gasses but also gels and glasses. A famous example of a colloidal phase transition in daily life is the clustering of colloids in milk that is induced by the addition of chemicals that change their interactions. This is what happens when milk is used to make cheese. The phase behavior of colloidal dispersions is very interesting for many applications. Also for fundamental research are colloids of major interest as they can, contrary to molecules and atoms that also show phase transitions, be directly observed using light microscopy techniques.

In this thesis we studied and applied the scattering of light by colloids. In Chapter 2 we focussed on the way in which monochromatic light that is scattered by individual colloids interferes with the remaining, un-affected light. Such an interference pattern is called a hologram. We used an inverted microscope in transmission mode to magnify such holograms so that the individual fringes in the interference patterns could be recorded by different pixels off a CCD camera. The technique of recording holograms of small objects by taking snapshots of the interference pattern underneath such particles is called in-line Digital Holographic Microscopy, DHM. It is called in-line because the angle between the illuminating light and the reference beam with which the scattered light interferes is zero.

After recording, the holographic snapshots can be analyzed in basically two ways.

One such a technique called 'back scattering'. Here the recorded 2D interference pattern is used as input to calculate the light distribution in a volume in the sample using the well known interference behavior of light. From the 3D light distribution it is then possible to track individual scatterers. This we demonstrated by tracking the 3D positions in a very dilute suspension of titania particles in cyclohexyl chloride. From the coordinates, we were able to determine the radial distribution function, which is often used in the study of the phase behavior of colloidal dispersions. We demonstrated that DHM can be a powerful tool in soft matter research because it allows one to measure the distribution of colloids in very dilute dispersions. The positions are determined from a single snapshot, which on the timescales of colloids is instantaneous. The conventional technique, confocal microscopy, cannot be used to study the distribution in such dilute dispersions because of its limited speed. The last particles recorded in a 3D stack would have moved significantly with respect to where they were at the instant of time when the first particles were recorded. We also showed that backscattering can be used to track anisotropic colloids. We described how it is possible to determine the position and the orientation of silica rods in 3D from single holographic snapshots.

One of the main assumptions made to be able to perform backscattering is that the refractive index in the sample is homogeneous. The fact that the particles can be detected is due to the light scattering which occurs when their refractive index is different from that of the surrounding liquid. The error that is made by the simplification of a homogeneous refractive index results in a relatively large error in the position detection of a scattering particle and it certainly makes the characterization of such particles from a back-scattered 3D stack extremely challenging. To address this problem we present a second method to analyze digital holographic micrographs in Chapter 2. The scattering of light by spherical particles that are comparable in size to the wavelength of the light can be quantitatively calculated as a series expansion in spherical harmonics. The interference between the calculated scattered light field with non-scattered light waves can then be calculated to come to a simulated hologram. We presented an overview of possible holograms for a wide variety of particles. The characteristics of a particle, its radius and refractive index, and its three dimensional position can be determined by numerically solving the inverse problem posed by the interference and scattering that resulted in an experimentally obtained hologram. Using an implementation of the Levenberg-Marquardt algorithm we minimized the summed squared differences between corresponding pixels in experimental and simulated holograms. The fit-values for the particle characteristics and its position were then regarded as measured parameters.

This method of analyzing the properties of individual colloidal particles in situ was used to follow the evolution of the radius and refractive index of titania particles when they were dried or sintered before being redispersed. We also

demonstrated that it is possible to determine that melamine particles are porous by observing that the fit-values of the refractive index of these particles are lower than what can be expected for solid particles.

From the analysis of the holographic snapshots we also obtained the coordinates of colloidal particles in space. By analyzing the frames of holographic movies we were able to measure the trajectories that individual colloidal particles followed in space. Analysis of these trajectories allowed us to measure the hydrodynamic radius of the particles and to confirm the error estimates of the minimization algorithm. Using DHM, it is possible to track colloidal particles in space with an accuracy of a single nm in the lateral directions and to within 10 nm in the axial direction. We studied the sedimentation of a silica colloid in ethanol and concluded that the sedimentation speed was in accordance with what was to be expected based on the literature value of the densities of both materials. From the distribution of distances at which colloids were observed in the axial direction as they bounced around on the bottom of a sample, by using the Boltzmann distribution, we were able to measure the interaction potential between the particles and the glass bottom as well as the buoyant mass of the particles. Using this method, we were able to measure the increased mass of polystyrene particles when they were coated with a layer of silica.

By adding the scattered light fields of multiple particles to the non-scattered light wave, it is possible to calculate holograms of ensembles of particles. Here, multiple scattering and the scattering of near-fields around the particles are neglected. We showed in Chapter 2 that when the particles are far enough apart, or when they are at a similar distance from the focal plane, it is possible to holographically measure the individual particle positions and characteristics. Analysis of the trajectories of 2 silica particles in ethanol and of seven particles in tetrahydrofuran simultaneously demonstrated that the accuracy with which the positions could be measured in this way was to a large extent independent of the distance between the particles.

By exposing colloids to an alternating electric field in the MHz range it is possible to induce dipoles in them. These dipoles then attract each other and form strings by so-called dipolar focussing. Dipolar focussing was used to make polystyrene particles in dimethylsulfoxide form strings. These strings were then made permanent by a thermal annealing step. In Chapter 2 of this thesis we studied the rotational and translational diffusion of two such strings by means of digital holographic microscopy. In the case of a longer string we could also study the bending behavior of a semi-flexible string. The translational and rotational diffusion of the strings agreed qualitatively with theory for the diffusion of cylinders. The quantitative disagreement between theory and the measured diffusivity of the semi-flexible string might stem from its flexibility. From the trajectories of the constituent particles we could calculate different estimates for the dispersion length of the string according to different definitions. Using optical tweezers we were able to construct strings of silica particles in tetrahydrofuran that became

permanent by the van der Waals attraction. These, and the polystyrene strings in dimethylsulfoxide were bent using three optical tweezers while tracking the bending using DHM.

The same physics of light scattering that allows one to holographically track and characterize colloidal particles can also be used to manipulate them. Light carries an amount of energy and momentum. When the light is scattered by interaction with a particle, its direction of propagation changes. As a result, the momentum of that light is also changed. The rate of change of momentum of the light at the particle results in a force that is exerted on the particle. When a powerful laser is focussed using a high numerical aperture objective, the optical forces on a colloidal particle close to the focus can be considerable when compared to the Brownian forces. Depending on the particle size, and in particular the refractive index contrast with the solvent, the particle can experience forces towards the focus and become trapped there. This technique is referred to as optical tweezers and is widely applied in soft condensed matter research but also in bio-medical research, as cells and bacteria are also colloids. In Chapter 4 we gave an overview of the available literature on optical tweezers.

To a first approximation, the potential by which an optically trapped particle is confined to its trapping site is harmonic. For small forces and small displacements in the trap, the so called force-extension curve is linear. In Chapter 3 we use this property of optical traps to measure the interaction force between two trapped PMMA colloids in cyclohexyl chloride while varying the distance between the particles. The effective distance between the particles was determined from confocal micrographs and from the positions with respect to the equilibrium positions of the particles in the traps we determined the forces between the particles. The forces that were measured in this way were the result of screened charge repulsion and were several hundreds of pico-Newtons large. The screening lengths observed were several microns long. As a result, the charge repulsion could be modeled using the Derjaguin approximation. We successfully fitted the resulting force equation to the measured interaction forces. We varied the ion concentration in the solvent by adding a salt to the dispersion and observed that both the charge of the particles and the screening length decreased. We demonstrated, that by shining UV light on the sample, the ion concentration increased, reducing the screening length. This strongly suggests that UV light degraded the solvent. The irradiation with UV light did not measurably affect the charge of the particles.

More sensitive measurements on the order of femto-Newtons were conducted by letting trapped particles loose for short amounts of time. During these amounts of time the particles freely diffused and drifted apart under the influence of their mutual interactions. During these intervals, we recorded holographic snapshots from which we measured the diffusion and thus the hydrodynamic friction factors as well as the drift velocities. From these, it was possible to calculate the interaction force. In this way we measured the charge repulsion between two silica particles in ethanol from which we could determine the screening length in

the ethanol. We showed that for these measurements on the interaction between silica particles in tetrahydrofuran the possibility to measure the out-of-plane position is indispensable, as can be done by means of the holographic microscopy technique that we introduced in Chapter 2. Using this method to measure interaction forces, we demonstrated that in the interaction between silica coated polystyrene particles in purified cyclohexyl bromide, the screening length can be as long as 10 micron, roughly 10 particle diameters. In this case the simplification of modeling the particles as a point charge in their center was justified and the Yukawa equation for the screened charge repulsion could be fitted to the measured interaction forces. Moreover, we demonstrated that by using this method to measure forces on colloidal particles it is possible to directly measure the forces of external fields such as gravity and an applied electric field.

The precise shape and magnitude of the forces exerted by optical tweezers depend on many parameters. It is possible to calculate these forces. We used a Debye-type integral of the radiation pressure on spherical particles in a diffraction limited focus, the description of which takes the effect of spherical aberrations into account, to calculate the forces that we can exert with the optical tweezers in our group. In Chapter 5 we give an overview of the possibilities. We start by varying the position of a silica particle in ethanol to show the effects on the trapping behavior. Then, we proceeded by varying the radius and refractive index of the particle. With increasing particle size the trap stiffness initially increased until the particles were comparable in size to the diffraction limited focus. After that, the trapping stiffness was observed to decrease with a further increase in the particle radius. We performed experiments where we trap a particle while we track it in 3D using the DHM as introduced in Chapter 2. We show that the trapping stiffness does indeed increase linearly with the laser power. Contrary to previous reports, we do experimentally observe a clear maximum in the trapping stiffness for particles of about the size of the wavelength. We also investigate experimentally the effect of the blinking rate in time-shared tweezers on the trapping stiffness. It was already known in literature that the blinking rate should be chosen faster than the characteristic timescale of the motion of a particle in a trap. We found that the switching rate can also be chosen too fast which severely degrades the laser focus and thus the trap stiffness.

We extended the calculations by introducing a shell around the particles and explored the consequences for the trapping behavior for various combinations of solvents, core- and shell-materials. Particles with a core-shell structure may be trapped stiffer than solid particles when the coating reduces the reflection and thus the backscattering. Silica coated polystyrene particles were trapped in arrays in concentrated dispersions of refractive index matched PMMA particles in a mixture of cyclohexyl bromide and cis-decalin to study the effect on the formation of a crystal nucleus.

In Chapter 6 we looked into the possibilities that arise when multiple optical tweezers are used simultaneously. When two counter-propagating focuses are

overlapped, it is possible to trap particles that cannot otherwise be trapped. Some particles have an index of refraction that is so high that the scattering force dominates and causes the particle to be pushed away in a single trap. When trapped in counter-propagating traps, these particles can be held stiffer. This allows the exertion of larger forces than particles that are trapped in single traps. This was demonstrated both in calculations and in experiments.

Additionally, arrays of traps next to each-other offer interesting possibilities. In general, it is not possible to trap particles with a refractive index that is lower than that of the dispersing medium because they are pushed away from the focus. We showed that it should be possible to trap these particles in 3D using three traps around the particle that act as bars forming a cage.

An alternative method to measure the interaction potential between colloidal particles is to trap two of them on a so-called line-trap. In this technique, the particles are confined to an essentially 1 dimensional line. The interaction potential can then be determined from the probability density function of observed inter-particle distances. The potential that the particles on the line experience should be flat enough for the particles to freely diffuse over the line. Moreover, the potential of interaction with the trap should be known to be able to correct for its influence on the apparent interaction between the particles. In Chapter 6 we explored both by calculations and by experiments the possibilities of forming line-traps for interaction measurements by placing multiple point traps on a line. As a test-case we studied the trapping behavior in an array of three traps. We concluded that this is extremely challenging when the number of point traps is limited to several tens of traps. In that case the spacing between the point traps along the line needs to be chosen with extreme precision to fit the individual particles. Any amount of polydispersity in particle size would cause the line-trap to not be flat for one of the two particles between which the interaction is to be measured. The line would not be straight in space and it would also show energy barriers along the line. Experimentally we demonstrated that when hundreds of traps very close to each other are used, it is possible to form an effective line-trap. The length of the trap is limited by the switching rate of the tweezer. Careful optimization may make it possible to form line-traps in this manner, but this is by far not the easiest way to measure inter-particle interactions.

We observed in the results of the calculations and the experiments conducted to explore the possibility to form a line-trap out of point traps, that sometimes the particles were trapped even stiffer by the array of point traps than they were trapped by single traps. When a particle is larger than the diffraction limited focus of the laser, it is trapped less stiffly by an optical tweezer. By placing multiple traps at carefully chosen distances, an effectively larger focus that is comparable in size to a larger particle, can be created. In Chapter 6, we studied, both in calculations and in experiments, how this can be used to trap larger particles more stiff in an array of two traps. We found that the trap stiffness can be significantly increased in this way. For the largest particles considered we even predict that in

the direction of the array they can be trapped stiffer by two traps than optimally sized particles can in a single trap with the same laser power. Surprisingly, we also observed an increase in the axial trapping stiffness for these particles. Moreover, the force-extension curves for these stiffer trapped particles were found to be more linear than those in single traps, making these so-called double traps an interesting technique to measure the generally rather large forces in biological systems.

## Samenvatting in het Nederlands

‘Colloïden’ is een verzamelnaam voor kleine microscopisch kleine deeltjes van een materiaal dat fijn verdeeld is in een ander materiaal. Colloïden in allerhande dispersies spelen een belangrijke rol in vele aspecten van het dagelijkse leven. Als rode bloedcellen voorzien zij onze lichaamscellen van zuurstof en voedingsmiddelen. Als pigmentdeeltjes in verf zorgen ze voor de juiste stromingseigenschappen en plakken ze aan een voorwerp vast om het meer kleur te geven en het te beschermen. Colloïden zijn vergelijkbaar in grootte met de golflengte van zichtbaar licht. Daardoor is de lichtverstrooiing door colloïden een rijk fenomeen. Ze verstrooien het licht in vele richtingen. In geconcentreerde suspensies kan het zelfs zo zijn dat licht meerdere keren door verschillende deeltjes wordt verstrooid. Lichtverstrooiing is het fenomeen waardoor melk wit kleurt.

Los van de fascinerende wijze waarop colloïden licht verstrooien, vertonen ze zelf ook zeer interessant collectief gedrag. Colloïden zijn interactief over afstanden van soms een aantal keer hun eigen diameter. Typische krachten tussen colloïden zijn de van de Waals attractie, afgeschermded ladingsafstoting en uitputtings attracties. Door de beperkte grootte van colloïden zijn de meeste krachten zoals de zwaartekracht en de invloed van inertie, die met het volume schalen, relatief klein. Een gevolg daarvan is dat de grillige krachten die worden uitgeoefend door botsingen met de moleculen van het oplosmiddel niet te verwaarlozen zijn. Colloïden vertonen Brownse beweging en vormen daardoor een thermisch systeem. De balans tussen de interactie-krachten tussen de colloïden en de entropie zorgt ervoor dat sommige configuraties beter zijn dan andere. Door de omstandigheden zoals de volumefractie, de temperatuur of de kracht van de interacties te variëren kunnen colloïdale dispersies ertoe bewogen worden een faseovergang te ondergaan. Colloïden kunnen kristallen, vloeistoffen, gassen maar ook gelen en glazen vormen. Een bekend voorbeeld van een colloïdale faseovergang uit het dagelijkse leven is het klonteren van colloïden in melk dat wordt geïnduceerd door toevoeging van chemicaliën die hun interacties veranderen. Dit gebeurt wanneer uit melk kaas gemaakt wordt. Het fasegedrag van colloïden is zeer interessant met het oog op mogelijke toepassingen. Ook voor fundamenteel onderzoek zijn colloïden van groot belang doordat ze in tegenstelling tot moleculen en atomen, direct in beeld kunnen worden gebracht met behulp van lichtmicroscopie en bovendien bewegen colloïden een stuk trager dan atomen.

In dit proefschrift beschrijf ik hoe we het verstrooien van licht door colloïden hebben bestudeerd en toegepast. In hoofdstuk 2 richtte ik mij op de interferentie tussen door colloïden verstrooid monochromatisch licht en het overgebleven niet-verstrooide licht. Dergelijke interferentiepatronen heten hologrammen. We hebben een geïnverteerde microscoop in transmissie modus gebruikt om de interferentiepatronen te vergroten zodat de buiken en knopen op verschillende pixels van een CCD vallen. Deze methode om hologrammen op te nemen door foto's te nemen van het interferentiepatroon onder kleine objecten wordt in-lijn Digitale

Holografische Microscopie, DHM genoemd. Het heet zo omdat de hoek tussen de beschijnende bundel en de referentiebundel waarmee het verstrooide licht interfereert nul is. Na de opname kunnen de hologrammen op twee fundamenteel verschillende manieren worden geanalyseerd.

Ten eerste is er een techniek die golfreconstructie heet. Hierbij wordt een tweedimensionaal plaatje gebruikt als invoer voor de berekening van de lichtverdeling in een volume van een monster door gebruik te maken van het bekende interferentiegedrag van licht. Uit deze driedimensionale lichtverdeling kunnen dan vervolgens de posities van de deeltjes worden bepaald. Dit hebben we laten zien door de driedimensionale posities van een verdunde dispersie van titania deeltjes in cyclohexyl chloride te bepalen. Uit deze driedimensionale verdeling van deeltjes hebben we vervolgens de radiële dichtheidsverdeling gedestilleerd, een techniek die veel wordt toegepast bij het bestuderen van het fasegedrag van colloïden. We hebben laten zien dat DHM een krachtig gereedschap kan zijn bij het onderzoek van zachte materie omdat het ons in staat stelt om de verdeling van deeltjes in zeer verdunde dispersies te meten. Alle deeltjesposities worden bepaald uit één enkele momentopname. Voor de colloïden is dat instantaan. De conventionele methode, confocale microscopie, kan niet gebruikt worden voor dergelijk verdunde dispersies in verband met de beperkte opname snelheid. Het laatst opgemerkte deeltje in een driedimensionale verzameling van informatie zou significant verplaatst zijn sinds het moment waarop het eerste deeltje werd opgemerkt. We hebben tevens laten zien dat het mogelijk is om golfreconstructie te gebruiken om de positie en oriëntatie van an-isotrope colloïden te bepalen. We hebben dit laten zien aan de hand van holografische momentopnamen van een silica staafje.

Eén van de vereenvoudigingen die wordt toegepast bij het analyseren door middel van golfreconstructie is de aanname dat de brekingsindex in het monster homogeen is. Het feit dat de deeltjes opgemerkt kunnen worden is het gevolg van de lichtverstrooiing die plaatsvindt wanneer de brekingsindex verschilt van die van de omringende vloeistof. De fout die door deze vereenvoudiging wordt gemaakt, resulteert in een relatief grote onnauwkeurigheid bij de bepaling van de positie van de deeltjes en het maakt het bepalen van de eigenschappen van de deeltjes een grote uitdaging. In hoofdstuk 2 introduceren we daarom een tweede techniek om digitale microscopisch-holografische afbeeldingen te analyseren. De lichtverstrooiing door sferische deeltjes die vergelijkbaar zijn in grootte met de golflengte van licht kan kwantitatief worden berekend aan de hand van een expansie serie van sferische harmonischen. De interferentie tussen het berekende verstrooide licht en niet-verstrooid licht kan dan berekend worden om te komen tot een gesimuleerd hologram. We gaven een overzicht van de mogelijke hologrammen van een ruime selectie aan deeltjes. De eigenschappen van een colloïde, zijn straal en brekingsindex en zijn driedimensionale positie, kunnen worden bepaald door het inverse probleem dat wordt opgeworpen door een interferentiepatroon tussen verstrooid licht en onveranderd licht numeriek op te lossen.

Met behulp van een zogenaamd Levenberg-Marquardt algoritme minimaliseerden we de opgeteld kwadratische verschillen tussen corresponderende pixels in experimentele en gesimuleerde hologrammen. De fitwaarden voor de deeltjeseigenschappen en posities werden vervolgens als meetwaarde beschouwd.

Deze methode om de eigenschappen van individuele colloïdale deeltjes *in situ* te meten is gebruikt om de ontwikkeling van de straal en brekingsindex van titania deeltjes te meten nadat de deeltjes gedroogd en gesinterd waren alvorens weer te zijn gedispergeerd. We hebben tevens laten zien dat het mogelijk is op te merken dat melamine deeltjes poreus zijn doordat de fitwaarden voor de brekingsindex lager zijn dan wat verwacht zou mogen worden.

Uit de analyse van holografische momentopnamen bepaalden we ook de coördinaten van colloïden. Door opeenvolgende momentopnamen van holografische filmpjes te analyseren konden wij de trajecten in de ruimte van individuele deeltjes bepalen. Analyse van dergelijke trajecten stelde ons in staat de hydrodynamische straal van een deeltje te meten en ook om de nauwkeurighedsinschatting van het minimalisatiealgoritme te bevestigen. Met gebruikmaking van DHM is het mogelijk om colloïden in de ruimte te volgen met een nauwkeurigheid van één nm in de laterale richtingen en tot binnen 10 nm in de axiale richting. We bestudeerden de sedimentatie van een silica colloïde in ethanol en concludeerden dat de sedimentatiesnelheid in overeenstemming was met wat kon worden verwacht op basis van literatuurwaarden voor de dichtheden van deze materialen. Uit de verdeling van afstanden tot de wand van deeltjes die vrij diffundeerden konden we met behulp van de Boltzmann-distributie de interactiepotentiaal met het glas en tevens de effectieve dichtheid van die deeltjes bepalen. Op deze manier zijn we erin geslaagd de gewichtstoename te meten van polystyreendeeltjes waar een silica laagje op aangegroeid werd.

Het is mogelijk door optelling van de verstrooide velden van meerdere deeltjes bij een niet verstrooid veld hologrammen van ensembles van deeltjes te berekenen. Hierbij worden meervoudige verstrooiing en het verstrooien van nabijgelegen velden verwaarloosd. We laten in hoofdstuk 2 zien dat als twee colloïden ver genoeg van elkaar zijn verwijderd, of als ze zich nagenoeg op dezelfde afstand van het focale vlak bevinden, dat het dan mogelijk is de posities en eigenschappen van de individuele deeltjes te bepalen. Analyses van de trajecten van twee silica deeltjes in ethanol en van zeven silica deeltjes in tetrahydrofuraan lieten zien dat de nauwkeurigheid waarmee de posities van de deeltjes kon worden bepaald nagenoeg onafhankelijk is van de afstand tussen de deeltjes.

Door colloïden bloot te stellen aan een alternerend elektrisch veld met een frequentie van enkele MHz is het mogelijk dipolen in de deeltjes aan te slaan. Deze dipolen trekken elkaar aan en vormen ketens door middel van zogenaamde dipool focussing. Dit werd gebruikt om ketens van polystyreen deeltjes in dimethylsulfoxide te maken. Deze ketens werden permanent gemaakt door een eenvoudige thermische stap. In hoofdstuk 2 van dit proefschrift bestudeerden wij de rotationele en translationele diffusie van twee van zulke ketens door ze te volgen

met behulp van DHM. De translationele en rotationele diffusie kwamen kwalitatief overeen met een theorie voor de diffusie van een cylinder. De kwantitatieve verschillen tussen de gemeten en de theoretische diffusie van een semi-flexibele keten zouden kunnen worden herleid tot de flexibiliteit. Uit de trajecten van de individuele deeltjes in de keten konden we de dispersielengte van de keten schatten aan de hand van verschillende definities. Met gebruikmaking van optische pincetten zijn we in staat gebleken ketens te vormen van silica deeltjes in tetrahydrofuraan die permanent werden door de van der Waals attractie. Deze ketens en die van polystyreen in dimethylsulfoxide konden worden gebogen in een reeks van drie vallen terwijl zij gevolgd werden met behulp van DHM.

Dezelfde fysica van lichtverstrooiing die ons in staat stelt om colloïden holografisch te volgen en te karakteriseren, stelt ons tevens in staat hen te manipuleren. Met licht is een hoeveelheid energie en impuls geassocieerd. Verstrooiing verandert de voortplantingsrichting van het licht. Daarbij wordt ook de impuls van het licht veranderd. De veranderingssnelheid van de impuls van het licht resulteert in een kracht op het deeltje. Als een krachtige laser wordt gefocuseerd met behulp van een hoge numerieke apertuur objectief dan kunnen deze optische krachten groot worden in vergelijking met de Brownse krachten. Afhankelijk van de grootte en in het bijzonder de brekingsindex van een deeltje kan het een kracht in de richting van de focus ondervinden om daar vervolgens als het ware in een val gevangen te blijven. Deze techniek staat bekend als optische pincetten en wordt veel toegepast in onderzoek naar zachte materie maar ook in biologisch en biomedisch onderzoek, aangezien cellen ook colloïden zijn. In hoofdstuk 4 gaven wij een overzicht van de beschikbare literatuur over optische pincetten.

In eerste benadering is de potentiaal waarmee optisch vastgepakte deeltjes worden beperkt in hun vrijheid harmonisch. Bij kleine krachten en kleine uitwijkingen is de kracht-uitwijkingcurve lineair. In hoofdstuk 3 gebruikten we deze eigenschap van optische pincetten om de interactiekracht tussen twee vastgepakte PMMA deeltjes in cyclohexyl chloride te meten terwijl we de afstand tussen de deeltjes varieerden. De effectieve afstand tussen de deeltjes werd daarbij bepaald uit confocale microscopische afbeeldingen. Uit de posities ten opzichte van de evenwichtspositie in de optische val bepaalden wij tevens de kracht tussen de deeltjes. De krachten die op deze wijze werden bepaald waren het resultaat van afgeschermdeladingsafstoting en ze waren enkele honderden pico-Newtons groot. De afscherminglengten die werden gemeten waren enkele micrometers lang zodat de ladingsafstoting moest worden beschreven met behulp van de Derjaguin benadering. De resulterende kracht vergelijking kon met succes worden gefit aan de gemeten interacties. We varieerden de ionen concentratie in het oplosmiddel door zout toe te voegen aan de dispersie en we observeerden dat zowel de lading op de deeltjes als de afscherminglengte afnam. Door de dispersie met UV licht te beschijnen konden we laten zien dat dan de concentratie van ionen in het oplosmiddel toeneemt, waardoor de afscherminglengte afneemt. Het beschijnen van de dispersie met UV licht resulteerde niet in een meetbaar ver-

schillende lading op de deeltjes.

Gevoeliger krachtmetingen van femto-Newtons werden uitgevoerd door de vastgepakte deeltjes los te laten gedurende korte periodes. Gedurende deze periodes konden de deeltjes zich vrijelijk bewegen onder invloed van de Brownse beweging en onderlinge interacties. Tijdens deze periodes van relatieve vrijheid werden de deeltjes gevolgd door middel van DHM, en uit de trajecten werden de diffusie snelheid, en dus de wrijvingsfactor, alsmede de gemiddelde snelheid afgeleid. Hieruit konden vervolgens de interactiekrachten worden berekend. Op deze manier hebben we de ladingsafstoting gemeten tussen twee silica deeltjes in ethanol. Hieruit konden we de afschermafstand in de ethanol bepalen. We hebben laten zien dat het voor het meten van de krachten tussen silica deeltjes in tetrahydrofuraan op deze wijze noodzakelijk is om ook de bewegingen uit het vlak te kunnen volgen, zoals kan worden gedaan met behulp van de holografische methode die we in hoofdstuk 2 hebben geïntroduceerd. Met behulp van deze nieuwe methode om de interactiekrachten tussen colloïden te meten hebben we tevens laten zien dat de interactiekracht tussen twee met silica bedekte polystyreen deeltjes in gezuiverde cyclohexyl bromide wel 10 micron in afscherminglengtes, dus ook ongeveer 10 deeltjes diameters lang kunnen zijn. In deze gevallen waren de vereenvoudigingen van de lading als een puntlading in het centrum van de deeltjes verantwoord en kon de Yukawa vergelijking voor de afgeschermdeladingsafstoting worden gefit aan de gemeten interactiekrachten. We hebben bovendien aangetoond dat het mogelijk is om deze methode om krachten op colloïdale deeltjes te meten ook kan worden toegepast om direct de krachten te meten die externe velden zoals de zwaartekracht en toegepaste elektrische velden op de deeltjes uitoefenen.

De precieze vorm en grootte van de krachten zoals die worden uitgeoefend door optische pincetten hangen af van veel parameters. Het is mogelijk om deze krachten uit te rekenen. We gebruikten een Debye-type integraal van de stralingsdruk op sferische deeltjes in een diffractie-gelimiteerde focus waarbij we rekening hielden met het effect van sferische aberratie om de krachten die we kunnen uitoefenen met de optische pincetten in onze groep te berekenen. In hoofdstuk 5 gaven we een overzicht van de mogelijkheden. We begonnen door de positie van de val die een silica deeltje in ethanol vasthoudt te variëren om het effect op het gedrag van het deeltje in een optische val te bestuderen. Daarna varieerden wij de straal en de brekingsindex van het deeltje. Met toenemende grootte van het deeltje neemt de stijfheid van de val eerst toe, totdat het deeltje ongeveer even groot is als de diffractie gelimiteerde focus. Hierna neemt de stijfheid weer af met een verder toenemende straal van de deeltjes. We voerden experimenten uit waarbij we de deeltjes vingen terwijl we ze volgden in 3D met behulp van de DHM uit hoofdstuk 2. We lieten zien dat de stijfheid van de val lineair is met de laservermogen. In tegenstelling tot eerdere meldingen, hebben wij experimenteel kunnen aantonen dat er een duidelijk maximum is in de valstijfheid van deeltjes die ongeveer even groot zijn als de golflengte van het licht. Ook bestudeerden

wij experimenteel het effect van de schakelsnelheid van een in de tijd gedeeld optisch pincet op de stijfheid van de val. Het was al bekend in de literatuur dat de snelheid waarmee een optisch pincet knippert sneller gekozen moet worden dan de tijdschaal waarop deeltjes in een val zich typisch bewegen. Wij vonden dat de knippersnelheid ook te snel gekozen kan worden waardoor de focus minder goed wordt, wat resulteert in een tegenvallende valstijfheid.

We breidden de berekeningen uit voor deeltjes met een schil van een ander materiaal en verkenden de consequenties voor het gedrag van optische pincetten voor een breed scala aan combinaties van oplosmiddelen en materiaal keuzes voor de kernen en de schillen. Deeltjes met een gelaagde structuur kunnen in sommige gevallen stijver worden vastgepakt dan massieve deeltjes doordat de schil als een antireflectiecoating werkt. Meerdere van een silica schil voorziene deeltjes zijn vastgehouden in bepaalde geometrische vormen in een mengsel van Cyclohexyl Bromide en decaline waarin zeer veel, in brekingsindex aan dit mengsel gelijke, PMMA deeltjes waren gedispergeerd, met als doel het effect hiervan op het fasegedrag van de PMMA deeltjes te bestuderen.

In hoofdstuk 6 bestudeerden we de mogelijkheden die het vastpakken van deeltjes in meerdere optische pincetten tegelijkertijd bieden. Als de in tegengestelde richting propagerende foci over elkaar heen worden gelegd, is het mogelijk deeltjes te pakken die niet op andere wijze kunnen worden gepakt. Sommige deeltjes hebben een brekingsindex die zo hoog is dat de verstrooiingskracht domineert en ervoor zorgt dat de deeltjes weggedrukt worden uit één enkele val. Als zij echter worden vastgepakt in tegengesteld-propagerende vallen, kunnen ze stijver worden vastgepakt en dit stelt ons dan tevens in staat om grotere krachten uit te oefenen dan met deeltjes die in enkelvoudige vallen kunnen worden vastgehouden. Dit hebben we aangetoond met zowel berekeningen als metingen.

Ook reeksen van nabije vallen bieden interessante mogelijkheden. We toonden aan dat het mogelijk moet zijn om deeltjes met een brekingsindex die lager is dan die van de immersievloeistof, waardoor zij worden weg geduwd van de focus, in 3D te vangen door drie vallen rondom hen heen te plaatsen, die als het ware dienen als de tralies van een kooi.

Een alternatieve methode om de krachten tussen colloïden te meten is om ze met zijn tweeën te vangen in een zogenaamde lijnval. In dat geval worden de deeltjes in feite in hun vrijheid beperkt tot een één dimensionale lijn. De interactiepotentiaal tussen de deeltjes kan dan worden bepaald aan de hand van de geobserveerde verdeling van afstanden tussen de deeltjes. De potentiaal die de deeltjes op de lijn ervaren moet vlak genoeg zijn opdat de deeltjes vrijelijk langs de lijn kunnen diffunderen. Daarnaast moet deze potentiaal bekend zijn om te kunnen corrigeren voor de versturende invloed die zij heeft op de schijnbare interactiepotentiaal tussen de deeltjes. In hoofdstuk 6 verkennen wij de mogelijkheden om lijnvallen te maken door meerdere puntvallen in een rij op te stellen. Dit hebben wij zowel in berekeningen als in metingen gedaan. Bij wijze van proef hebben we het gezamenlijke gedrag van drie vallen bestudeerd. Hierbij kwamen

wij tot de conclusie dat het een uitzonderlijke uitdaging vormt om een lijnval te construeren uit slechts enkele tientallen puntvallen. De afstanden tussen de puntvallen langs de lijn moeten zeer nauwkeurig worden gekozen om bij de deeltjes te passen. De kleinste grootteverdeling zou ertoe leiden dat de lijnval niet vlak zou zijn voor één van de twee deeltjes waartussen de interactie gemeten zou moeten worden. De lijn zou de ruimte niet recht doorkruisen en tevens zouden zich energetische barrières langs de lijn opwerpen. Experimenteel hebben we aangetoond dat het wel mogelijk is om een lijnval te maken door honderden vallen op zeer korte afstanden van elkaar te plaatsen. De lengte van een dergelijke lijnval is dan beperkt door de schakelsnelheid van het optische pincet. Zorgvuldige optimalisatie zou het mogelijk moeten kunnen maken om lijnvallen te maken, maar dit is zeker niet de eenvoudigste wijze waarop interactiekrachten tussen colloïden gemeten kunnen worden.

Het viel ons op in de berekeningen en tijdens de experimenten die ten doel hadden de mogelijkheden tot het vormen van de een lijnval te verkennen, dat de deeltjes in sommige gevallen zelfs stijver gevangen werden door de reeks van puntvallen dan het geval was in één enkele val met dezelfde totale lichtintensiteit. Als een deeltje groter is dan de diffractiegelimiteerde focus van de laser, dan wordt hij minder stijf gevangen door een optische val. Door meerdere vallen op strategisch gekozen afstanden te plaatsen kan een effectief grotere val worden gevormd die vergelijkbaar in grootte is met een groter deeltje.

Zowel in berekeningen als in experimenten hebben we de mogelijkheden bestudeerd om dit effect te gebruiken om grotere deeltjes stijver vast te houden in twee vallen, samen een dubbelval genoemd. We vonden dat de stijfheid van de val op deze manier significant kan toenemen. Voor de grootste deeltjes die we in beschouwing namen voorspellen we zelfs dat zij stijver vastgehouden kunnen worden dan deeltjes met een voor stijf vasthouden optimale grootte in één enkele val met hetzelfde totale laservermogen. Verbazingwekkend genoeg namen wij zelfs een toename van de axiale stijfheid waar voor deeltjes die groter waren dan de optimale grootte. Daar komt bij, dat de kracht-uitwijkingscurves voor stijver vastgehouden deeltjes in dubbelvallen, meer lineair waren dan die in het geval van een enkele val. Hierdoor vormen zogenaamde dubbelvallen een interessante techniek om de, in het algemeen grotere krachten in biologische systemen te meten.

## Samenvatting voor Leken

Colloïden zijn kleine deeltjes, ongeveer één honderdste van de dikte van een haar groot. Ze komen voor in allerhande oplossingen. Denk aan rode bloedcellen, rookdeeltjes, pigment in verf en vetdruppeltjes in melk. Colloïden zijn ongeveer even groot als de golflengte van licht. Daardoor verstrooien colloïden licht op zeer karakteristieke wijze. Hierdoor is melk bijvoorbeeld 'wit'. Door botsingen met vloeistofdeeltjes in hun omgeving vertonen colloïden 'Brownse' beweging. Colloïden oefenen kleine krachten op elkaar uit die er samen met de Brownse beweging voor zorgen dat ze zich soms ordenen. Ze vormen dan bijvoorbeeld spontaan een kristal, een geordende structuur waarbij de deeltjes als het ware op een rooster liggen. Ook atomen en moleculen kunnen kristallen vormen. Door toevoeging van chemische stoffen kunnen de krachten tussen colloïden worden aangepast. Dit doe je als je van melk kaas maakt door stremsel of een zuur toe te voegen om ervoor te zorgen dat de deeltjes in de melk aan elkaar plakken. Hoewel colloïden erg klein zijn, kun je ze met een microscoop bekijken. Dit kan met atomen niet, doordat ze té klein zijn en té snel bewegen. Dit maakt colloïden tot een ideaal studieobject om naar dergelijke ordeningsprocessen te kijken. In dit proefschrift wordt een nieuwe microscopietechniek, 'holografische microscopie', geïntroduceerd. Hierbij gebruik je de karakteristieke wijze waarop colloïden licht verstrooien om hun grootte te meten en ze in 3D te volgen. Met een zogenaamde 'optische pincet' is het bovendien mogelijk colloïden met licht vast te pakken en ze te verplaatsen. Met behulp van optische pincetten en holografische microscopie kun je de zeer kleine krachten tussen colloïden meten.

## Acknowledgements

The past years have been long, tiring and very enervating. The group here in Utrecht forms a very exciting surrounding full of interesting people and lots of fancy, new, old, dusty and unknown, and sometimes creatively adapted equipment. The perfect playground for a curious boy like me! It's time to say goodbye and thank some people. Let me start by excusing for forgetting everyone I will forget!

Alfons, ik ben je dankbaar voor het bij elkaar brengen van al deze leuke mensen en het mooie speelgoed. Ik heb een heleboel kunnen leren in deze stimulerende omgeving. Dank ook voor de vrijheid om mijn eigen pad uit te stippelen, en voor de begeleiding. The friday morning workdiscussions I found very educative. My curiosity was often stimulated at these meetings and I will miss the sunny Friday mornings behind these terrible grey curtains trying to see the little red dots projected on the wall. Often the tension was a little like at Sinterklaasavond: what cool stuff would we find in the folder this time? I should thank everyone ever present at these meetings, for presenting, asking questions or for laughing at the right moments.

Carlos, hartelijk dank voor je introductie in het lab. Bedankt voor de leuke uren achter de confocal op zoek naar rooie puntjes die verdaaid groen werden, als we ze weer terug vonden... Dank ook voor de vele interessante discussies over silica jassen, goud staven en petroleum jelly! Je was de sociale ruggegraad van de groep met je bijdrages aan groepsuitjes en sinterklaasvieringen. Los van alles heb je je belangrijkste bijdrage aan mijn proefschrift waarschijnlijk geleverd tijdens de vele koffiepauzes! Esther, fijn je kamergenoot te zijn. Geweldige afleiding, heerlijk geleuter :) Maar ik wil niet badinerend doen over je bijdrage aan mijn werk hier. Je hebt me een hoop geleerd over photonische kristallen en over de mensen in Utrecht en daarbuiten. Ik bewonder je nauwgezette werkwijze, en nu mijn boekje ook bijna af is temeer ook voor de planning!

Teun! Spring-in-het-veld-Teun! Esther zei al dat je vol energie zou zitten! Dank daarvoor. Dank voor de leuke experimentjes die we samen hebben bedacht. Bedankt voor het Kritisch lezen van mijn proefschrift. Bedankt dat je me hebt overtuigd van het feit dat het 'iets' is en niet 'iets', het voorbeeld van de Telegraaf is spot-on! Laura, thank you very much for the beers, the chatting, the discussions on phase-diagrams, hard spheres and Canadian politics! Johan bedankt voor de deeltjes en de gezelligheid!

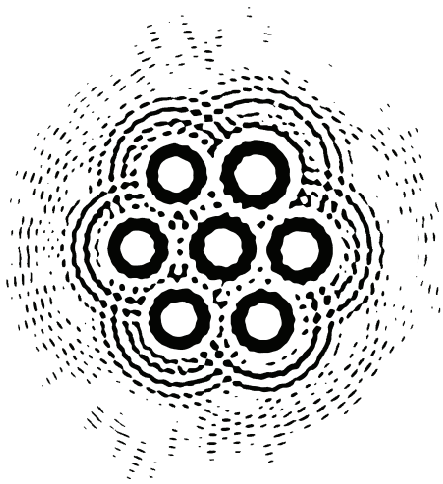
María Delgado Flores, nogmaals complimenten voor je mooie naam, dank voor de coca en je gezelligheid! Arnout bedankt dat je je inzicht in lichtvertrooiing met me hebt willen delen. Voor de geduldige antwoorden op mijn naïeve vragen. Bedankt voor het jarenlang lenen van Bohren & Huffman! Marjolein, bedankt voor je mooie Britse accent en het zo goed begeleiden van Laura, Michiel, Matthieu en Frank. Ik heb veel aan ze gehad! Michiel, Frank, Matthieu, bedankt voor de geduldige uitleg van hoe simulaties,  $\LaTeX$  en computers werken!

Peter, waarde naamgenoot, bedankt voor het meedenken met de nieuwste experimenten. Bedankt voor het doen van sommige experimenten. Bedankt voor de computers en bedankt voor het gezelschap achter het gordijn met de mooie groene brillen als het duo *Peter & Peter*. Bedankt voor het optuigen van Tweezer, de nieuwe kerstboom. Heel veel succes en plezier ermee! Hans, ook bedankt voor je inspanningen en de geleden frustratie om tricky ondanks zijn naam werkend te krijgen. Astrid bedankt voor de introductie in het trappen van deeltjes! Ik wil je samen met Dirk bedanken voor de mooie opstelling. Bedankt voor de goede ideeën voor experimentjes en bedankt voor de gezelligheid!

Timo, bedankt voor het lezen, bedankt voor de muziek, bedankt voor de kaft. Dank dat je er voor me was. Ik wil ook Eisse bedanken, heerlijk met je geleuterd! Op de fiets en te voet in de bergen hou je me maar met moeite bij, maar dat maak je meer dan goed met je kookkunsten! Matthijs, Lisette, Jorien en Roos, bedankt voor alles! Gijs, geweldig hoe je me aan het einde van mijn promotie van mijn werk kon houden op regenachtige dinsdagen met je prachtige lach! Pa, Ma, bedankt dat jullie me hebben ondersteund bij mijn promotie, zonder jullie diverse bijdragen had ik het niet af kunnen maken. Bedankt voor jullie geduld bij het mij grootbrengen. Voor de derde keer, na de middelbare school, na de universiteit en nu na mijn promotie is het klaar en hoef ik nooit meer naar school! Een geweldig gevoel! Manu, grazie mille per tutto, per la tua compagnia, la tua cucina e per la tua bellissima lingua. Grazie per il supporto ed il fatto che mi hai potuto sopportare durante gli ultimi mesi pesantissimi della scrittura della mia tesi. Grazie per le tue poche ma appuntissime critiche sullo *consecutio temporum* e il percorso logico di quel che tentavo di mettere su carta. Grazie per le distrazioni indispensabili. Grazie per essere chi sei. Grazie.

René, Jos, Eelco, Niels en Simone bedankt voor jullie interessante kijk als theoretici op de dingen en voor jullie bijdragen aan de werkbijeenkomsten en dienstreizen! Maurice, Lia, Rob, Jan en Daniela, dank voor jullie aanwezigheid op conferenties en andere gelegenheden. Kamergenoten! Roommates! Esther, Joan, Andy, Matthew, Daisuke, Zuocheng, Linh, Bo (thanks for the PS particles and Asian perspective), Bas, thank you all for sharing the office with me! Mensen: Alfons, Arnout, Marjolein, René, Matthew, Bing, Jamal (merci bien pour les experiments beaux), Linh, Teun, Thijs, Nina, Laura, Arjen, Joost (bedankt voor de methyloxiperfluorobutaan en het lezen), Jissy, Marlous, Anke, Bas, Marjolein, Kristina, Ran, Bart, Bo, Frank, Hanumantha Rao (thanks for the strings), Peter, Judith, Bas, Carlos, Gulşen, Marjoke (je staat nog steeds niet op de website!), Krassimir, Ernest, Stéphane, Faik a.k.a. Ahmet, Anita, Andrew, Michiel, Jacob (bedankt voor de 1.4  $\mu\text{m}$  silica deeltjes in ethanol), Ingeborg, Alessandro (grazie per le spiegazioni del caso Italiano), Jader, Zuocheng, Alejandro, Eduardo, Chantal, Emanuela, Denise, Daisuke, Hans, Didi, Andrea, Dannis, Michiel, Astrid, Andrei, Dave, Hans, Gerhard (thanks for the reading), María, Thea, Antti-Pekka, Mirjam, Matthieu, Joan, Svytoslav, Job, Krassimir, Esther, Yu Ling, Carmen, Menno, Thijs, Thomas (bedankt dat ik je mocht begeleiden), Georgi (thank you

for letting me teach you stuff), Tristan, Rianne, Ronen, Anne, Floor, Wessel, Rob, Lucas, Timo, Eisse, Esther, Quirine, Matthijs, Jorien, Gijs, Lisette, Roos, Harry, Marijke, Maurice, Lia, Jan, Daniela, Myrthe, Ana, Sanja, Piero, Steffi, Piero and all those I may have forgotten: Bedankt!



## List of Publications

This thesis is partially based the work that has been published in the following papers:

- S.-H. Lee, Y. Roichman, G.-R. Yi, S.-H. Kim, S.-M. Yang, A. van Blaaderen, P. van Oostrum, and D. G. Grier, Characterizing and tracking single colloidal particles with video holographic microscopy, *Optics Express* **15**, 18275 (2007). (Chapter 2)
- A. van der Horst, P. D. J. van Oostrum, A. Moroz, A. van Blaaderen, and M. Dogterom, High trapping forces for high-refractive index particles trapped in dynamic arrays of counterpropagating optical tweezers, *Applied Optics* **47**, 3196 (2008). (Chapter 6)
- P. D. van Oostrum, A. van der Horst, and A. van Blaaderen, Mutual influence of time-shared optical traps studied by means of Video Holographic Microscopy, *Digital Holography and Three-Dimensional Imaging, OSA Technical Digest (CD)* (Optical Society of America, 2009)). (Chapter 6)
- M. Hermes, E. C. M. Vermolen, M. E. Leunissen, D.L.J. Vossen, P.D.J. van Oostrum, M. Dijkstra and A. van Blaaderen Nucleation of colloidal crystals on configurable seed structures, *Soft Matter*, DOI: 10.1039/C0SM01219J, (2011). (Chapter 5)
- A. F. Demirörs, A. Jannasch, P.D.J. van Oostrum, Erik Schäffer, A. van Blaaderen and Arnout Imhof Seeded Growth of Titania Colloids with Refractive Index Tunability and Fluorophore-free Luminescence, *Langmuir*, DOI: 10.1021/la103717m, (2011). (Chapter 2)
- D. El Masri, P. D. J. van Oostrum, F. Smalenburg, T. Vissers, M. Dijkstra, A. Imhof, A. van Blaaderen Measuring Colloidal Forces from Particle Position Deviations inside an Optical Trap, *Soft Matter*, DOI: 10.1039/C0SM01295E, (2011). (Chapter 3)

### In preparation:

- P. D. J. van Oostrum, D. El Masri, F. Smalenburg, T. Vissers, M. Dijkstra, A. Imhof, A. van Blaaderen Measuring Colloidal Forces in Dense Long-Range Dispersions, *in preparation*. (Chapter 3)